Title
Rotating detonation rocket engine analysis with high-speed optical diagnostics

Author
Nair, Anil Pradeep

Publication Date
2022

Peer reviewed|Thesis/dissertation

UNIVERSITY OF CALIFORNIA

Los Angeles

Rotating detonation rocket engine analysis with high-speed optical diagnostics

A dissertation submitted in partial satisfaction

of the requirements for the degree

Doctor of Philosophy in Mechanical Engineering

by

Anil Pradeep Nair

2022

ABSTRACT OF THE DISSERTATION

Rotating detonation rocket engine analysis with high-speed optical diagnostics

by

Anil Pradeep Nair
Doctor of Philosophy in Mechanical Engineering
University of California, Los Angeles, 2022
Professor R. Mitchell Spearrin, Chair

This dissertation details design and experimental analysis of the rotating detonation rocket engine (RDRE) propulsion concept, which offers potential gains in specific impulse and thrust-to-weight relative to conventional deflagration-based rockets. A liquid bi-propellent RDRE test article has been designed for use with hypergolic space-storable propellants leveraging additive manufacturing to improve hydraulic performance. High-speed imaging is performed to characterize detonation formation times, measure detonation wave-speeds, and assess the detonation wave modes in the combustor during hot-fire testing. These detonation characteristics are correlated with combustor performance metrics, such as thrust and specific impulse. These data are also used to make the first estimates of the detonation cell size for these propellants, which cannot be measured using conventional techniques. Additionally, MHz optical diagnostics have been developed using laser-absorption spectroscopy (LAS) with distributed-feedback (DFB) lasers for sensing time-resolved pressure, temperature, and CO/CO_2 concentrations in the exhaust of a methane-oxygen fueled RDRE. These diagnostics are used to assess the variation in these exhaust thermodynamic properties over a variety of test conditions to assess the effect of varying mass flux, equivalence ratio and propellant mixedness. The wavelength tunability and average output power of DFB lasers are enhanced and optimized for use at MHz rate, extending the utility of the absorption diagnostics to more extreme detonation environments. The optical pressure sensing technique

is then demonstrated in laboratory environments and uncertainties are rigorously quantified. Lastly, the CO temperature-sensing technique is extended to extreme temperatures near 10,000 K using a fit of the Boltzmann population fractions across CO energy states. In addition to the presented sensing strategies, a DFB-laser tuning model and comprehensive measurement uncertainty analyses are included in the Appendix to aid in the future design of LAS systems. Additionally, the design and drawings for two facilities used in this work, the UCLA Propulsion Test Platform and Detonation-Impulse Tube, are provided in the Appendix.

The dissertation of Anil Pradeep Nair is approved.

Ann Karagozian

Richard Wirz

Artur Davoyan

R. Mitchell Spearrin, Committee Chair

University of California, Los Angeles

2022

TABLE OF CONTENTS

LIST OF FIGURES

LIST OF TABLES

ACKNOWLEDGMENTS

Firstly, I would like to thank my advisor, Professor Mitchell Spearrin for his mentorship over the last five years. I have been greatly inspired by your passion, confidence, and ambition when it comes to research. I am indebted to you for the time you have dedicated to helping me grow as an engineer and scientist, and I will always remember the lessons you have taught me. I would also like to thank Professor Richard Wirz for being my undergraduate faculty advisor, helping nurture my interests in rocket propulsion, and encouraging me to pursue a Ph.D. Over the course of my Ph.D., he has given me valuable feedback on my research. I thank Professor Wirz, Professor Ann Karagozian, and Professor Artur Davoyan for their guidance as members of my thesis committee.

I would also like to thank the members of UCLA Rocket Project who helped foster my interest in rocket engineering. I see my time in UCLA Rocket Project as a direct precursor to my decision to pursue graduate school. Specifically, I would like to thank my seniors: Kai Matsuka, Anny Lin, Rafael Gutierrez, Hayden Johnson, Aaron Tiscereno, Alex Omar, Justin Nguyen, Sam Dupas, Kari Kawashima, Anthony Vong, and Eric Hidalgo. You all pushed me into leadership/technical roles and provided me with so many opportunities. I would also like to thank the other individuals who I was lucky to be able to work with during my time in Rocket Project: John Flores, Daniel Kerr, Rudy Crespo, Angelo Pacumio, Ben Walsh, Victor Huyan, David Lu, Katherine Lee, Josh Lee, Stacey Lewis, Nick Kuenning, Daniel Pineda, Jacob Dipietro, John Harnsberger, Alex Blaya, Ryan Weber, Caleb Lessard, Edward Shen, Alex Cusianovic, Eric Sangret, Calvin Huynh, Alex Lima, Anneliese Peterson, China Hagström, Dante Bruno, and Christopher Vincent. I learned so much from you all as engineers, and I am proud of what were able to accomplish for Rocket Project.

I would like to give a special thanks to Foster Stanback of the Foundation for the Carolinas. Mr. Stanback provided funding for the liquid bi-propellant rocket project I had the privilege of leading during my final year as an undergraduate. The experience allowed me to be immersed in all aspects of rocket propulsion, including theory, manufacturing, rocket

testing, and analysis. This immersion helped me realize that I wanted to learn more about propulsion and ultimately inspired me to pursue graduate school and eventually a Ph.D.

During my time as an undergraduate, I also had the pleasure of meeting Dave Crisalli of Polaris Propulsion. Dave taught me the lessons of rocket engineering that you couldn't find in a textbook and was instrumental in the success of the liquid rocket project. I was lucky to continue to work with Dave throughout my Ph.D. over three hot-fire test campaigns. He has been a great role model, and I hope to be able to help the next generation of rocket scientists in the way he has helped me. I would also like to acknowledge Tai Yu of Polaris Propulsion for his support and attention to detail during the hot-fire test campaigns.

My graduate work would not have been possible without the support of the various organizations and people I have had the chance to collaborate with. From the Air Force Research Laboratory, I would like to thank John Bennewitz, Bill Hargus, Blaine Bigler, Jason Burr, Steve Dancyzk, and Alex Schumaker. From NASA, I would like to thank Thomas Teasley for his support of our work with additive manufacturing and space-storable RDREs. I would also like to thank Jason Kriesel and Ilya Dunayevskiy for their support in the laser diagnostic project.

Beyond faculty, there are many staff members at UCLA who have been instrumental to the success of my research over the course of the past few years. In particular, I would like to thank Jose Sanchez of the UCLA machine shop for his patience and guidance during my year-long endeavor to build the detonation tube during my first year. Jose taught me almost everything I know about machining and was always willing to help me with the most outrageous manufacturing procedures. I would also like to thank Travis Widick, Anthony Redon, and Dirk Williams of the UCLA machine shop for their support. Additionally, I would like to thank Miguel Lozano and Ben Tan of the MAE department for their assistance during my TAship and machining. I would also like to thank the administrative staff for the MAE department—in particular, Amanda Gordillo, who has always gone above and beyond to support our lab when it comes to navigating purchasing or reimbursements.

The long nights of experiments, paper-writing, and preparing meeting slides would not

have been bearable without a positive and supportive team in the lab.While it has been great to work with everyone in the SpearrinLab group over the years, I would like to give a special thanks to individuals I have had to the chance to work with closely. Dr. Daniel Pineda, thank you for helping spark my initial interest in graduate studies and for being a great role model with regards to work ethic and being willing to sacrifice to help others. Dr. Fabio Bendana, your attention to detail and persistence has inspired me to produce high quality work, and I greatly appreciated all of the times we tried to get to the bottom of a question that stumped us both. Dr. Daniel Lee, thank you for your guidance during my first couple of years. I learned a lot of the basics of LAS from you during our test campaigns at AFRL, and I always found it very easy to talk to you about issues I was facing in the lab. Kevin Schwarm, you are one of the hardest workers in the lab. I always admired your dedication and passion to your research. David Morrow, thank you for being a great friend and research partner during my first two years—it was great to work with you on the detonation tube, and I also appreciated you introducing me to weight-lifting as a form of stress relief. Alex Cusianovic, thank you for your help with the detonation tube—I was lucky to have the chance to see your growth over the years, and I am excited to see what all of the things you'll launch into space. Anneliese Peterson, I'd also like to thank you for your help in building the detonation tube. It was also awesome to get to talk to astronauts with you, even though the experience was quite stressful. Nick Kuenning, despite you being three years younger than me, I often find myself going to you with questions, especially when something is broken. You are a talented engineer and problem solver, and I am excited to see what you accomplish next. Alex Keller, your excitement for our work is contagious. Thank you for your enthusiasm and hard work over the past couple of years. I know the hypergol project is in good hands with you taking the lead. Alex Lima, I am glad we had the chance to work closely during the 2021 RDRE testing. I always found myself inspired by your great engineering sensibilities and work ethic. Barathan Jeevaretanam, thank you for helping build the test-stand control system and for being a great friend over the last couple of years. I could always count on you for a great Trader Joe's recommendation. Miles Richmond, thank you for the energy you brought to the lab. I am glad we got to work together, and thank you for being my

"guru" when I needed it. Isabelle Sanders, Nick Kuenning, Chuyu Wei, David Morrow, Travis Fujimoto, and Daniel Lee: it was great TAing with you all for MAE 157A. Teaching that class was challenging, but I am grateful for the time we got to spend together while preparing labs, helping students with their projects, and traveling to the desert. Christopher Jelloian, you always inspired me with your passion for your project and your work ethic. I am glad we got to work together on the bias-tee development. China Hagström, it was great getting to work with you in Rocket Project and in the lab. I am excited to see what you accomplish during your Ph.D. Joel Otomize, I am glad we were able to collaborate during the summer you were in the lab, and I am grateful that you continued to stay in touch. I would especially like to thank Dr. Nicolas Minesi. I have always been able to count on you for support, and I have been inspired by your positive attitude and outlook on life (as well as your "spontaneous" approach to challenges). Thank you for always making the time to review my meeting slides and writing. You have also truly made the lab a better place by advocating for myself and the other graduate students. I know you will be a great professor.

I would like to express my gratitude for the co-authors who were instrumental in several of the papers included in this dissertation: Fabio Bendana, David Morrow, Daniel Pineda, Christopher Jelloian, Daniel Lee, Alex Keller, Alex Lima, Nick Kuenning, Nicolas Minesi, Miles Richmond, Jason Kriesel, John Bennewitz, Blaine Bigler, Bill Hargus, Steve Danczyk, and Professor Spearrin.

I would also like to thank my parents, Pradeep and Geetha, for instilling in me an appreciation for education and pushing me to work hard from a young age. I would also like to thank my siblings, Sunil and Uma, for always being there for me over the years.

Last but not least, I would like to thank my girlfriend and life partner, Lanzel Patawaran. You have been with me through all of the ups and downs of my graduate school experience and have always been extremely patient and understanding during all those nights when I was sure "I'll be done in an hour." You have always pushed me to be the best version of myself, and I could not have done this without your support. I am so excited for the next chapter in our life. I love you.

CURRICULUM VITAE

2014-2018	B.S., Aerospace Engineering, UCLA
2018-2020	M.S., Mechanical Engineering, UCLA
2018-2022	Ph.D. Candidate, Mechanical Engineering, UCLA

PEER-REVIEWED PUBLICATIONS

[1] **A.P. Nair**, N.Q. Minesi, N.M. Kuenning, A.R. Keller, R.M. Spearrin. Optical pressure sensing at MHz rates via collisional line broadening of carbon monoxide: uncertainty quantification in reacting flows. In *Applied Physics B* (Under Review).

[2] N.Q. Minesi, **A.P. Nair**, M.O. Richmond, N.M. Kuenning, C.C. Jelloian, R.M. Spearrin. Excited-oxygen kinetics at electronvolt temperatures via 5-MHz RF-diplexed laser absorption spectroscopy. In *Applied Optics* (Accepted).

[3] N.Q. Minesi, M.O. Richmond, C.C. Jelloian, N.M. Kuenning, **A.P. Nair**, R.M. Spearrin. Multi-line Boltzmann regression for near-electronvolt temperature and CO sensing via MHz-rate infrared laser absorption spectroscopy. In *Applied Physics B* (2022).

[4] **A.P. Nair**, A.R. Keller, N.Q. Minesi, D.I. Pineda, R.M. Spearrin. Detonation cell size of liquid hypergolic propellants: estimation from a non-premixed combustor. In *Proceedings of the Combustion Institute* (2022).

[5] **A.P. Nair**, N.Q. Minesi, C.C. Jelloian, N.M. Kuenning, R.M. Spearrin, Extended tuning

of distributed-feedback lasers in a bias-tee circuit via waveform optimization for MHz-rate absorption spectroscopy. In *Measurement Science and Technology* (2022).

[6] **A.P. Nair**, A.R. Keller, D.S. Morrow, A.B. Lima, D.I. Pineda, R.M. Spearrin. Hypergolic continuous detonation with space-storable propellants and additively-manufactured injector design. In *Journal of Spacecraft and Rockets* (2022).

[7] **A.P. Nair**, D.D. Lee, D.I. Pineda, J. Kriesel, W.A. Hargus, J.W. Bennewitz, B. Bigler, S.A. Dancyzk, R.M. Spearrin. Methane-oxygen rotating detonation exhaust thermodynamics with variable mixing, equivalence ratio, and mass flux. In *Aerospace Science and Technology* (2021).

[8] D.D. Lee, F.A. Bendana, **A.P. Nair**, S.A. Dancyzk, W.A. Hargus, R.M. Spearrin. Exploiting line-mixing effects for laser absorption spectroscopy at extreme combustion pressures. In *Proceedings of the Combustion Institute* (2021).

[9] J. Li, **A.P. Nair**, K.K. Schwarm, D.I. Pineda, R.M. Spearrin. Temperature-dependent line mixing in the R-branch of the ν_3 band of methane. In *Journal of Quantitative Spectroscopy and Radiative Transfer* (2020).

[10] D.D. Lee, F.A. Bendana, **A.P. Nair**, D.I. Pineda, R.M. Spearrin. Line mixing and broadening of carbon dioxide by argon in the ν_3 bandhead near 4.2 µm at high temperatures and high pressures. In *Journal of Quantitative Spectroscopy and Radiative Transfer* (2020).

[11] **A.P. Nair**, D.D. Lee, D.I. Pineda, J. Kriesel, W.A. Hargus, J.W. Bennewitz, S.A. Dancyzk, R.M. Spearrin. MHz laser absorption spectroscopy via diplexed RF modulation for pressure, temperature, and species in rotating detonation rocket flows. In *Applied Physics B* (2020).

CHAPTER 1

Introduction

1.1 Rocket-propulsion fundamentals

The power-to-weight ratio of combustion devices is an inescapable necessity for escaping Earth's gravity to propel people and scientific instruments into space. This power is harnessed and directed using chemical rocket propulsion. A typical chemical rocket system can be visualized in Fig. 1.1. A full treatise on rocket propulsion can be found in many texts on the subject [1, 2, 3]. For the purposes of this thesis, only key relations and concepts will be presented to help provide context for the research conducted herein. In rocket systems, a payload is accelerated to high speeds via the jet propulsion principle, which involves ejecting high-velocity gases (termed the propellant) from the aft end of the vehicle. The thrust force F produced by such a process is related to the exhaust velocity u_{ex} by the thrust equation[1], which is based on the conservation of fluid momentum:

$$F = \dot{m} u_{\text{ex}}, \tag{1.1}$$

where $\dot{m}$ is the mass flow rate of the propellant. Using the thrust equation, and basic kinematics, the Tsiolkovsky rocket equation may be derived, which relates the exhaust velocity, vehicle mass, and total vehicle speed change (termed the delta-V, ΔV):

$$\Delta V = u_{\text{ex}} \ln\left(1 + \frac{m_{\text{propellant}}}{m_{\text{payload}} + m_{\text{propulsion}}}\right). \tag{1.2}$$

[1]For simplicity, the exhaust is assumed to be "perfectly expanded", such that the exit pressure is equal to the ambient pressure.

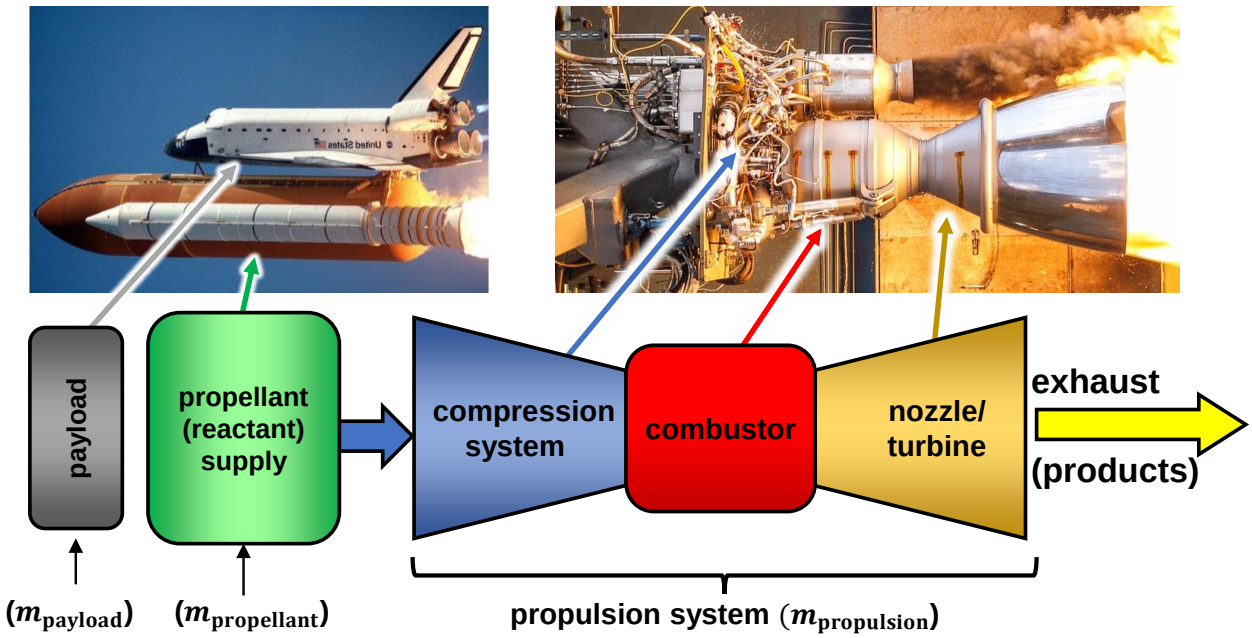

Figure 1.1: *Top Left*: Image of Space Shuttle (NASA). *Top Right*: Image of SpaceX Merlin Engine during hot fire test (SpaceX). *Bottom*: Simplified diagram of conventional chemical rocket vehicle.

Here, $m_{\text{propellant}}$ is the total mass of propellant stored on the vehicle before it is expended, m_{payload} is the mass of the non-propulsion related components of the rocket vehicle, including the structural mass of the vehicle, and $m_{\text{propulsion}}$ is the mass of the propulsion system. These masses are indicated at the bottom of Fig. 1.1. Here, the structural mass of the vehicle is neglected, and is considered part of the payload.

In these systems, for a given ΔV set by the mission objective, it is desirable to increase the total amount of payload that can be carried by the rocket. To reflect this, Eqn. 1.2 can be rearranged, solving for m_{payload}:

$$m_{\text{payload}} = \frac{m_{\text{propellant}}}{\exp\left(\frac{\Delta V}{u_{\text{ex}}}\right) - 1} - m_{\text{propulsion}} \tag{1.3}$$

. It can be clearly seen that the allowable amount of payload may be increased in a few ways. Increasing the amount of propellant can increase payload capability, and this is the reason why large payloads typically require very large launch vehicles with high propellant

mass fractions. The propellant mass fraction f_p is the ratio of the total mass of propellant at takeoff to the total mass of the vehicle (including propellant) at takeoff:

$$f_\mathrm{p} = \frac{m_\mathrm{propellant}}{m_\mathrm{propellant} + m_\mathrm{payload} + m_\mathrm{propulsion}}. \tag{1.4}$$

Likewise, the inert mass fraction f_i represents the fraction of non-propellant mass for the vehicle at takeoff:

$$f_\mathrm{i} = \frac{m_\mathrm{payload} + m_\mathrm{propulsion}}{m_\mathrm{propellant} + m_\mathrm{payload} + m_\mathrm{propulsion}} = 1 - f_\mathrm{p}. \tag{1.5}$$

The high propellant mass fraction of launch vehicles can be easily observed for the Space Shuttle in Fig. 1.1, for which the propellant comprises over 95% of the total vehicle mass [4]. However, larger launch vehicles require higher thrust levels to help them overcome their substantial weight when launching from Earth. This requires a heavier vehicle frame, which cuts into the mass that can be spent on payload. This fundamentally limits the total amount of payload that can be launched from a single-stage rocket vehicle. Typically, for large payloads, staging is used, although this greatly increases system complexity and risk of failure.

Alternatively, the allowable payload mass can be increased by increasing the propellant exhaust velocity to make propellant consumption more efficient. Higher exhaust velocities allow for more thrust per unit mass expended per second or, in other words, more impulse per unit mass of propellant. For this reason, the exhaust velocity is often expressed as the "specific impulse" or I_sp:

$$I_\mathrm{sp} = \frac{u_\mathrm{ex}}{g} = \frac{F}{\dot{m}g} = \frac{J}{m_\mathrm{propellant}}. \tag{1.6}$$

Here, g is the gravitational acceleration on the surface of the earth, and J is the total impulse (integral of thrust over time) imparted to the rocket vehicle. Increasing I_sp has a nearly exponential effect on the allowable payload mass, so incremental improvements in propellant exhaust velocity can have large ramifications on the payload capacity of launch vehicles. Lastly, the allowable payload mass can be increased directly by reducing the mass allocated to the propulsion system, kg for kg. There is often a trade-off between these

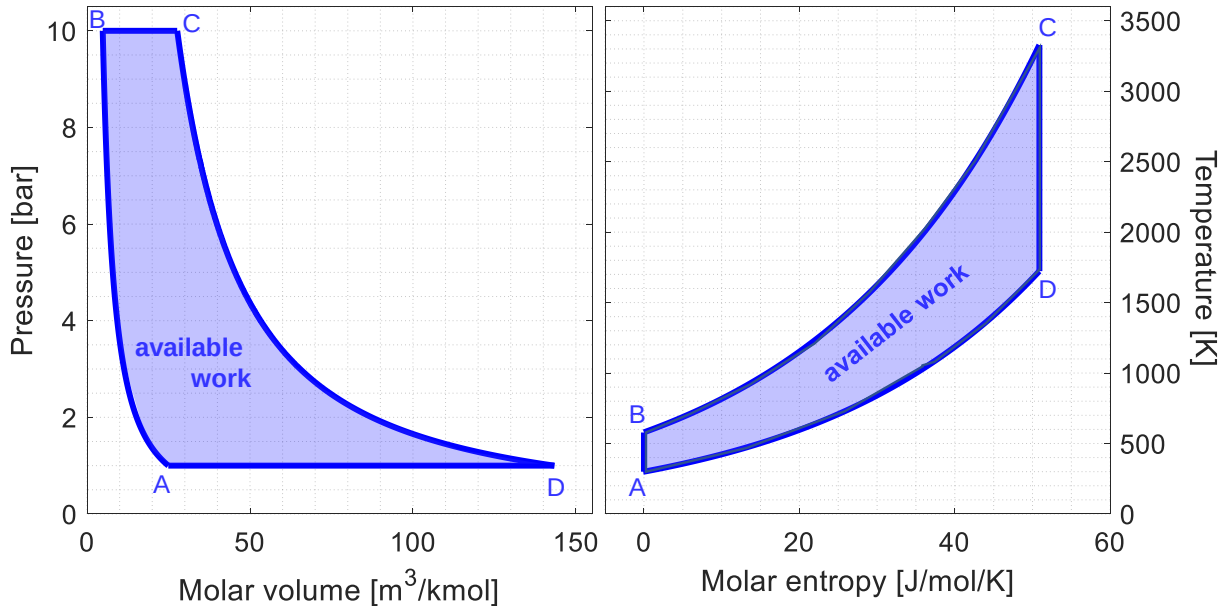

Figure 1.2: Example pressure-volume (*left*) and temperature-entropy (*right*) diagrams for the Brayton cycle. The initial conditions are 1 bar and 300 K. γ is assumed to be 1.4 and the heat input is 80 kJ/mol.

last two factors. Before assessing how the propulsion system mass and performance can be optimized, the basic operation of the propulsion system must be discussed.

The propulsion system can usually be divided into three major components: the compression system, the combustor, and the nozzle, which are pictured schematically and for SpaceX's Merlin Engine in Fig. 1.1. Across these components, various thermodynamic processes occur. These processes are typically represented by the Brayton cycle for a conventional rocket engine. A sample pressure-volume (P-v) diagram and temperature-entropy (T-s) diagram for this process are shown in Fig. 1.2.

The compression system pressurizes the propellants to a high pressure via high-pressure inert gas (blowdown system), a compressor (for gaseous propellants), or a pump (for liquid propellants). This is typically represented with an isentropic compression process in the Brayton cycle, represented by process A→B in Fig. 1.2. At this stage, the propellants, which are typically combustion reactants (fuel and oxidizer) have a high level of chemical potential

energy. In the combustor, these propellants/reactants are mixed and a combustion reaction between them is induced. During the burning of the propellants, their chemical potential energy is converted into thermal energy, which manifests in extremely high temperatures, typically in excess of 3000 K in rocket combustors. For the Brayton cycle, this combustion process is conducted at a constant pressure, represented by process B→C in Fig. 1.2.

The nominal combustion performance of a rocket engine is typically given by the "characteristic velocity" or c^*, which for an ideal rocket with a calorically perfect gas is given by:

$$c^*_{\text{ideal}} = \sqrt{\frac{\gamma}{\gamma - 1}\frac{\bar{R}T_{\text{C}}}{M}} \times f(\gamma) = \sqrt{h_{\text{C}}} \times f(\gamma). \tag{1.7}$$

Here, h_{C} is the specific enthalpy of the post-combustion gas, $\bar{R}$ is the universal gas constant, M is the average molecular weight of the combusted gas, and $f(\gamma)$ is a function of the the ratio of specific heats, γ, of the combustion gas. For γ between 1.2–1.3 $f(\gamma)$ ranges from 0.63–0.72. Various propellant combinations have different values for c^*, depending on their specific energy content. Additionally, c^* is a function of the oxidizer-to-fuel mixture ratio of the propellants. For oxygen-combustion, c^* tends to be optimized at mixture ratios that are fuel-rich, due to the reduced post-combustion molecular weight and consequently higher specific gas enthalpy of fuel-rich products (H_2, H, CH_4) relative to oxygen-rich products (O_2, O). For this reason, rocket engines are typically run at a fuel-rich mixture ratio. The post-combustion gas properties such as temperature and composition are typically evaluated with knowledge of the thermodynamics properties of the reactants and products using chemical equilibrium solvers such as NASA CEA [5]. The actual achieved c^* in a real engine may be lower than the ideal value calculated via chemical equilibrium due to incomplete mixing of the reactants, heat transfer out of the engine, or chemical non-equilibrium effects. To assess this in a real system, the c^* is usually measured with the following equation, which defines c^*

$$c^* \equiv \frac{P_{\text{C}} A_{\text{th}}}{\dot{m}}. \tag{1.8}$$

Here, P_{C} is the combustion pressure, A_{th} is the flow area of a nozzle throat that would accelerate the flow to sonic velocity (as discussed below). The measured c^* is compared to

the ideal c^* from Eqn. 1.7 to obtain a "c^* efficiency" η_{c^*}:

$$\eta_{c^*} = \frac{c^*_{\text{meas}}}{c^*_{\text{ideal}}}. \tag{1.9}$$

For modern liquid rocket engines, η_{c^*} regularly exceed 95%, so little improvement can be made to performance in this regard.

After combustion, the propellant is accelerated to high velocities (supersonic) via a thermal-to-kinetic energy conversion process, which typically occurs in a converging-diverging (de Laval) nozzle. This process is typically approximated as isentropic, and is represented by process C→D in Fig. 1.2. When assessing the energy that can be extracted from the propellants in this cycle, it is useful to consider the work done on the gases, which in the case of a rocket system is equivalent to the kinetic energy imparted to the combustion gases. This can be visualized by the area bound by the P-v or T-s diagrams in Fig. 1.2. This area is dominated by the area under the P-v curve in the expansion phase (C→D). It is desirable to have the highest level of work output for a given heat input (dictated by the chemical energy content of the propellants). This can be expressed by the thermal efficiency η_{therm}, which is defined for a generic heat engine as the ratio of the net work output of the heat engine, W_{net}, and the total heat input into the engine, Q_{in}:

$$\eta_{\text{therm}} = \frac{W_{\text{net}}}{Q_{\text{in}}}. \tag{1.10}$$

Assuming a calorically perfect gas, negligible work done to compress the reactants, and that $T_{\text{C}} >> T_{\text{A}}$, the efficiency may be expressed in terms of the gas temperatures as:

$$\eta_{\text{therm}} = 1 - \frac{h_{\text{ex}}}{h_{\text{C}}} \approx 1 - \frac{T_{\text{ex}}}{T_{\text{C}}}. \tag{1.11}$$

Here, the exhaust gas temperature is represented by T_{ex}. This relation indicates that the total work that can be extracted in the nozzle is increased if the gas is allowed to expand and cool by a greater degree. In other words, it is desirable for the exhaust gas to be as cool as possible relative to the post-combustion gas.

The level of gas cooling and expansion is dictated by the drop in gas density and pressure across the nozzle. Typically, the gases are expanded from the combustor pressure P_{C} down

to atmospheric pressure P_∞. This is quantified with the pressure ratio, PR:

$$\mathrm{PR} = \frac{P_\mathrm{C}}{P_\infty}. \tag{1.12}$$

The ratio of the combustor temperature and nozzle exhaust temperature is defined as the temperature ratio TR:

$$\mathrm{TR} = \frac{T_\mathrm{C}}{T_\mathrm{ex}}. \tag{1.13}$$

The temperature ratio is related to the pressure ratio via the following, assuming calorically-perfect, isentropic expansion:

$$\mathrm{TR} = (\mathrm{PR})^{1-\frac{1}{\gamma}}. \tag{1.14}$$

Since γ ranges from 1 to 5/3, the exponent of PR is between 0 and 0.4, indicating that for a target change in temperature, the change in pressure must be significantly larger and that there are diminishing returns in performance as combustion pressure is increased. By combining Eqn. 1.14 with Eqn. 1.11, the thermal efficiency may be cast in terms of the

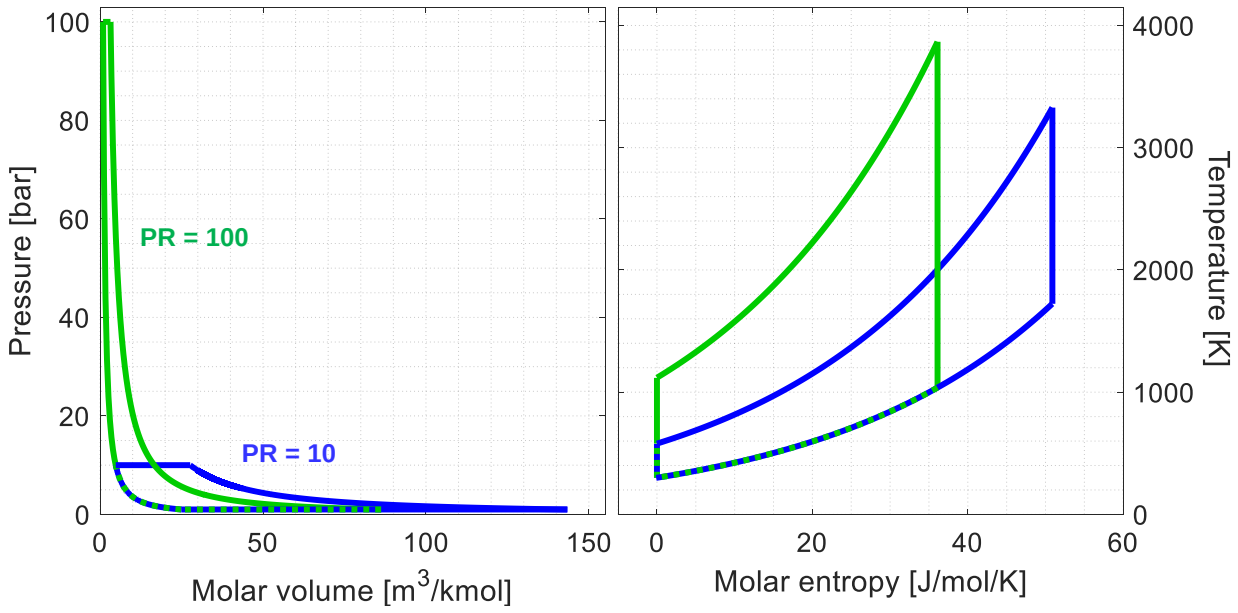

Figure 1.3: pressure-volume (*left*) and temperature-entry (*right*) diagrams for the Brayton cycle at two different pressure ratios. The initial conditions, heat input, and γ are the same for the two cases, and are equivalent to those of Fig. 1.2.

pressure ratio:

$$\eta_{\text{therm}} \approx 1 - \frac{1}{(\text{PR})^{1-\frac{1}{\gamma}}}. \tag{1.15}$$

This relation clearly indicates that increasing combustion pressure relative to the ambient pressure causes the exhaust gas to be cooler, resulting in improved thermal-to-kinetic energy conversion[2]. The increase in work output and thermal efficiency with higher pressure combustion can be visualized in Fig. 1.3, where the P-v and T-s diagrams for the Brayton cycle are shown for two different pressure ratios (10 and 100) but the same heat input. The area bound by the thermodynamic cycles is clearly higher for the pressure ratio of 100. The T-s diagram also reveals that higher pressure combustion occurs at a lower entropy value, which means that more of the energy released via combustion can be used for useful work. The trend of increasing thermal efficiency with pressure ratio can also be seen in Fig. 1.4, where the PR = 10 case (point i) and the PR = 100 case (point ii) are highlighted. The increase of thermal efficiency in this sample case, where $\gamma = 1.4$, $P_{\text{A}} = 1$ bar, $T_{\text{A}} = 300$ K, and $Q_{\text{in}} = 80$ MJ/mol, the efficiency increases from 48% to 73%.

In conclusion, despite the relatively minor gains to be made in improving the chemical-to-thermal energy conversion process in rockets, substantial improvement in the thermal-to-kinetic energy conversion process can be made by combusting at higher pressures. This has been the focus of recent research and development for launch vehicle rocket engines [6, 7]. The increased efficiency at higher pressures lead to a higher propellant exhaust velocity and would lead to a resulting increase in payload capability, but this efficiency comes at a cost. Combustion at higher pressures requires the compression system and combustor to be designed with thicker wall to withstand the increased pressure load. Turbomachinery and valves designed for extreme pressures are also larger and more complex than at low

[2]For rockets, typically the thrust coefficient C_{F}, which is effectively the ratio of the thrust force to the characteristic force generated by the chamber pressure ($P_{\text{C}}A_{\text{th}}$) represents the effect of thermal efficiency. For a calorically perfect gas, the relation is:

$$C_{\text{F}} \equiv \frac{F}{P_{\text{c}}A_{\text{th}}} = g(\gamma)\sqrt{1 - \frac{h_{\text{C}}}{h_{\text{ex}}}} = g(\gamma)\sqrt{\eta_{\text{therm}}}. \tag{1.16}$$

pressures. Additionally, heat transfer rates in the combustor and nozzle are much higher at higher pressures, requiring additional cooling system capacity. All of these factors increase the mass of the propulsion system to a degree that can offset the performance gains made from increasing propellant exhaust velocity.

To summarize, Eqn. 1.3 describes the fundamental limit on payload mass for a rocket vehicle based on basic mass/momentum conservation and kinematics. Payload capability can be improved by increasing propellant mass, decreasing propulsion system mass, or improving propulsion system efficiency, typically by combusting at higher pressures. These factors are often competing, making advancements in rocket technology challenging. Recent interest in democratizing access to space has sparked new demand in improving the current state-of-the-art towards lower cost, higher performance engines.

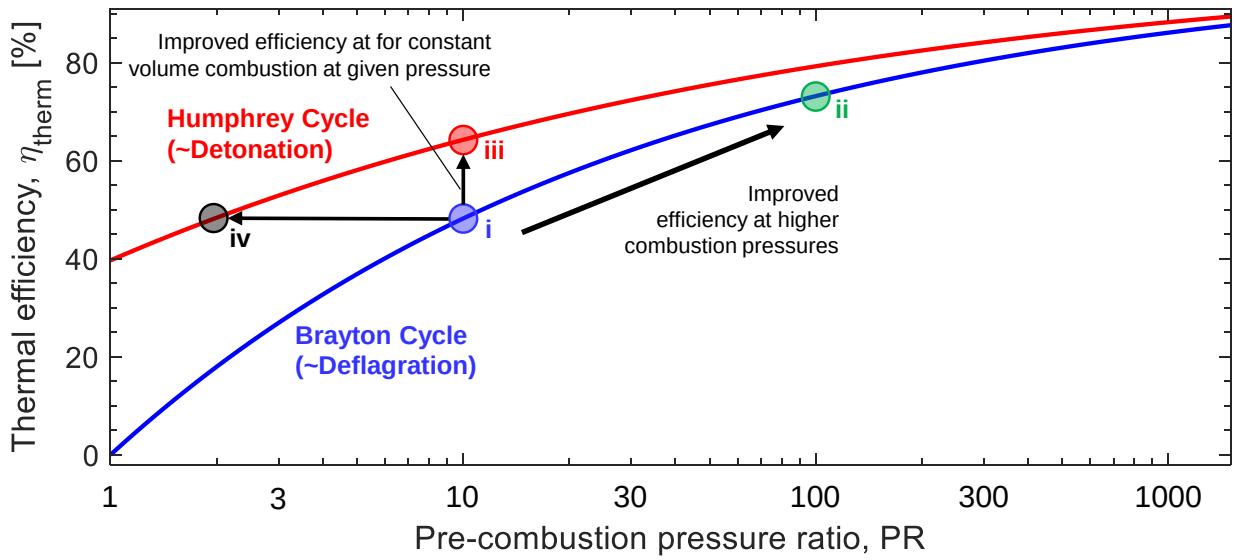

Figure 1.4: Thermal efficiency *versus* nozzle pressure ratio for the Brayton cycle (blue) and the Humphrey cycle (red).

1.2 Detonation thermodynamics

The constant-pressure combustion process used in conventional rocket engines is also known as a "deflagration". Detonation-based combustion, also known as pressure-gain combustion, offers an alternative method for energy conversion, one in which higher post-reaction pressures and temperatures can be achieved at similar pre-combustion pressures than in deflagration-based combustion [8]. A detonation is often approximated by constant-volume combustion. The Brayton cycle may be modified to substitute the constant-pressure heating/combustion step with a constant-volume heating step. This modified cycle is called the Humphrey cycle [9]. The P-v and T-s diagrams for the Humphrey cycle is compared to that for the Brayton cycle in Fig. 1.5. For both cycles, the initial pressure/temperature are set to ambient conditions (1 bar, 300 K), $\gamma = 1.4$, $Q_{\text{in}} = 80$ MJ/kg. The pre-combustion compression ratio ($P_{\text{B}}/P_{\text{A}}$) is also 10 for both cycles. When combusting at a constant volume,

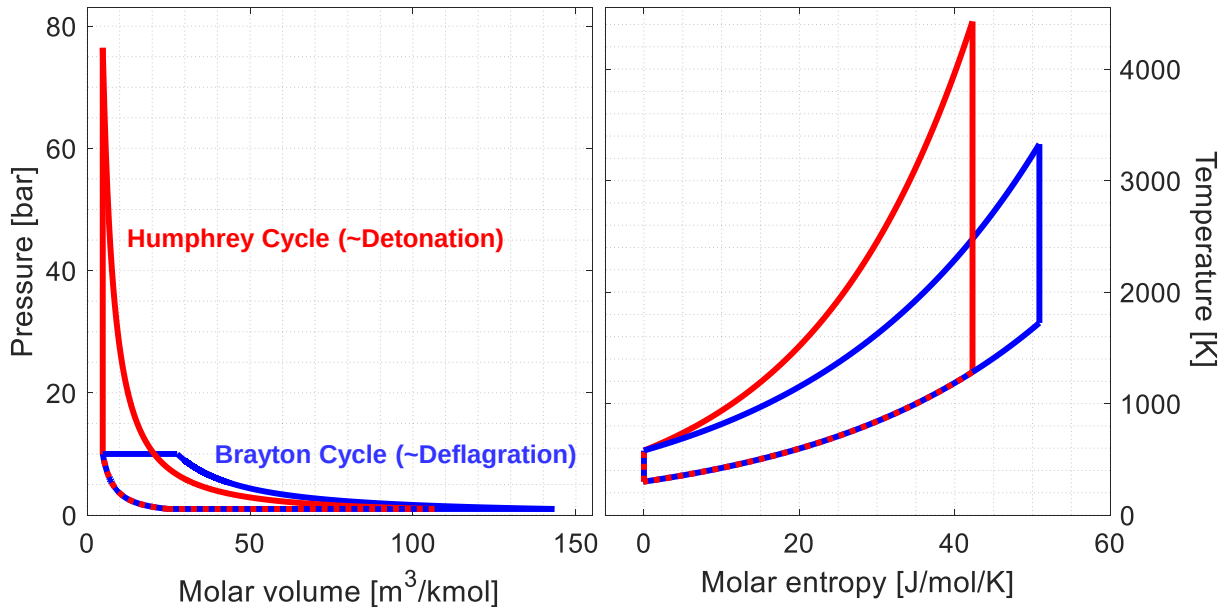

Figure 1.5: pressure-volume (*left*) and temperature-entropy (*right*) diagrams for the Brayton cycle (blue) and Humphrey cycle (red). The initial conditions, compression ratio (PR), heat input, and γ are the same for the two cases, and are equivalent to that of Fig. 1.2.

the pressure greatly increases (hence the term *pressure-gain combustion*), by a factor of ∼76 in this case. There is also a corresponding increase in post-combustion temperature, by a factor of ∼1.3 in this case. It can clearly be seen that the area bound by the cycle diagram for the Humphrey cycle is greater than that of the Brayton cycle for the same heat input, implying greater thermal efficiency. This is due to the higher pre-expansion pressure for the Humphrey cycle, which allows for a greater drop in temperature as the gas is expanded to ambient pressure. It can be seen on the T-s diagram that the post-expansion temperature is nearly 35% lower for the Humphrey cycle compared to the Brayton cycle, despite the higher combustion temperature. Additionally, the post-combustion entropy is reduced for the Humphrey cycle compared to the Brayton cycle. The improved thermal efficiency of the detonation cycle can also be seen in Fig. 1.4, which plots the thermal efficiencies of the two cycles versus pre-combustion pressure ratio. For a given pressure ratio, the Humphrey cycle outperforms the Brayton cycle. For the case considered here, at a pre-combustion compression ratio of 10, the thermal efficiency of the Humphrey cycle is 64%, compared to the 48% of the Brayton cycle. This can be visualized by comparing points (i) and (iii) in Fig. 1.4.

The improved thermal efficiency of the Humphrey cycle, implies that for a rocket engine utilizing constant-volume combustion, the propellants may be accelerated to a higher exhaust velocity without the penalty of increased pressurization system mass. Alternatively, for a fixed propellant exhaust velocity, the upstream pressure requirement may be reduced when using constant-volume combustion. For the case considered here, the Humphrey cycle at a pre-compression ratio of nearly 2 has the same thermal efficiency of the Brayton cycle at a pressure ratio of 10. This can be visualized by comparing points (i) and (iv) in Fig. 1.4. Since the mass of pressure vessels scales nearly linearly with pressure, this can yield a near factor 5 reduction in propulsion system mass. These theoretical advantages have spurred interest in detonation-based combustion for rocket-propulsion applications [10, 11, 12].

The significance of the efficiency gains of detonation combustion can be quantitatively examined by referring back to the rocket equation (Eqn. 1.2). For a launch vehicle with a target ΔV of 11.2 km/s (Earth escape velocity) and 300 s specific impulse, the required

propellant mass fraction is $f_{\mathrm{p}} = 0.9778$. If the specific impulse is improved by just 10%, the required propellant mass fraction for the same ΔV drops to $f_{\mathrm{p}} = 0.9686$. While this represents only a sub-percent change in propellant mass fraction, the inert mass fraction increases from $f_{\mathrm{i}} = 0.0222$ to 0.0314, representing a 41% increase. If 50% of the inert mass was originally budgeted as payload mass, and if the propulsion system mass remained constant with the I_{sp} increase, this means that the allowable payload mass increases by about 83%, representing an increase of nearly double. For cases of low inert mass fraction, a linearized sensitivity analysis indicates that a given percent change x in I_{sp} translates to a percent change in f_{i} approximately equal to $\frac{\Delta V}{u_{\mathrm{ex}}} x$, which in this case is $\sim 4x$. With the aforementioned assumption regarding the payload mass starting as 50% of the inert mass, the percent change in payload mass is $\sim 8x$.

1.3 The physical mechanism of a detonation

Detonations and deflagrations are two types of flames, or interfaces between unburnt reactants and burnt products. The two flame types are classified by their speed of propagation relative to the unburnt reactants. A deflagration propagates at subsonic speeds, and a detonation propagates at supersonic speeds. The sonic velocity is taken as the speed of sound in the unburnt gas. The speed of these two types of flames is related to the fundamental mechanism by which the flames propagate. In a deflagration, the flame propagates via mass and heat transfer from the hot combustion products to the reactants, which are diffusion-dominated processes that rely on molecular collisions. Once the reactants are heated above their auto-ignition temperature, they begin to react and release heat, which sustains the flame. Diffusion is relatively slow, which leads to deflagration flame speeds being on the order of cm/s [13]. Additionally, across a gaseous deflagration, the density drops (gas expands) by the same order of magnitude as the temperature increases. A schematic of a deflagration reaction zone is shown at the top of Fig. 1.6.

In a detonation, combustion is driven by supersonically propagating shock waves which travel on the order of km/s. These shock waves compress the reactants to temperatures above

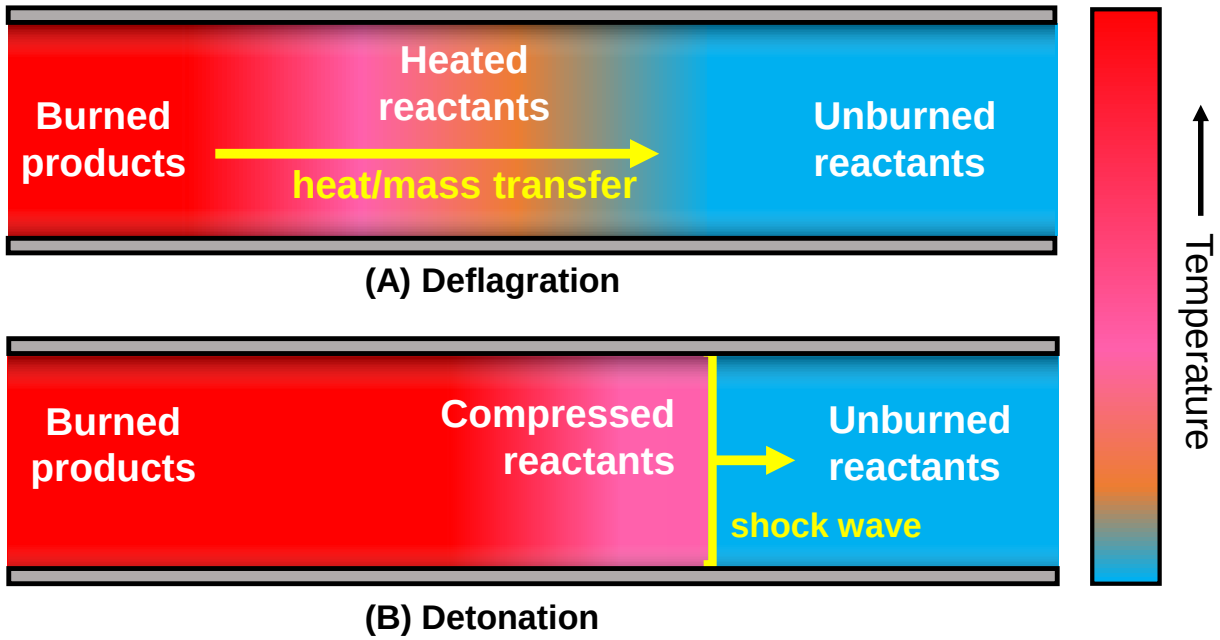

Figure 1.6: Comparison of a deflagration flame structure (A) to a detonation flame structure (B).

their auto-ignition temperature, causing post-shock combustion. As such, a detonation is a coupled shock and reaction front. The shock wave is driven forward by the expansion of the product gases in the reaction zone. The temperatures behind the leading shock wave lead to rapid combustion kinetics, which consequently lead to a short reaction zone compared to deflagration. Thus, detonation combustion features exceptionally high power densities, orders of magnitude higher than for deflagration combustion [14]. Due to the shock mechanism of a detonation wave, detonation combustion is not truly a constant-volume process. In fact, the specific volume across an ideal gaseous detonation can decrease, resulting in higher pressure-gain compared to the Humphrey cycle discussed in the previous section. A more realistic thermodynamic cycle reflecting the shock compression of real detonations is provided by Zel'dovich von Neumann Döring (ZND) cycle [9]. A schematic of a detonation wave can been seen compared to a deflagration wave in Fig 1.6.

For a deflagration-based rocket engine, the flame front is usually stationary relative to the combustor. This is because the subsonic flame speed matches the subsonic flow speed

of reactants and products through the combustor in a process known as flameholding [15]. For a detonation however, the flame speed generally exceeds the speed of the flow, except in the case of supersonic combustion, as in a scramjet. As such, a detonation wave cannot be held steady at a fixed location in the combustor. Detonation waves must propagate within the combustor, leading to an unsteady and spatially non-uniform flow field. This greatly increases the complexity of analysis, design, and modeling for a detonation-based engine compared to a conventional deflagration-based engine.

1.4 Detonation-engine architectures

Initial work on detonation engines used an engine architecture known as the pulse detonation engine (PDE) [16]. In a PDE, a tube is filled with reactants, which are then ignited on one end of the tube. As the combustion wave propagates through the mixture, the wave accelerates and transitions from a subsonic deflagration to a supersonic detonation due to volumentric confinement in a process known as deflagration-to-detonation transition (DDT) [17]. The hot pressurized combustion products are then expelled from the downstream end of the tube, generating thrust. The tube is then re-filled with fresh reactants and the process is then repeated. This process can be visualized in Fig. 1.7 with a diagram from Ref. [18]. The figure also shows a five-tube PDE being hot-fire tested at the China Lake Naval Surface Warfare Center along with sample pressure traces for a PDE—both also from Ref. [18]. The PDE has been shown to harness the theoretical thermodynamic benefits of detonation engines but have practical shortcomings that limit their use in real propulsion systems: (1) the repetition rate of the combustion event is limited by the feasibility of opening and closing valves at high speeds and on reliably igniting the reactant mixture repeatedly, (2) the length of tube required for DDT increases propulsion system dry mass, (3) not all combustion occurs in a detonation mode, and (4) the drop in pressure as the combustion products are exhausted makes it impractical to design a nozzle to optimally expand all of the combustion gas [19].

In recent years, the rotating detonation engines (RDE) concept has been studied as an alternative engine architecture that resolves the aforementioned challenges associated with

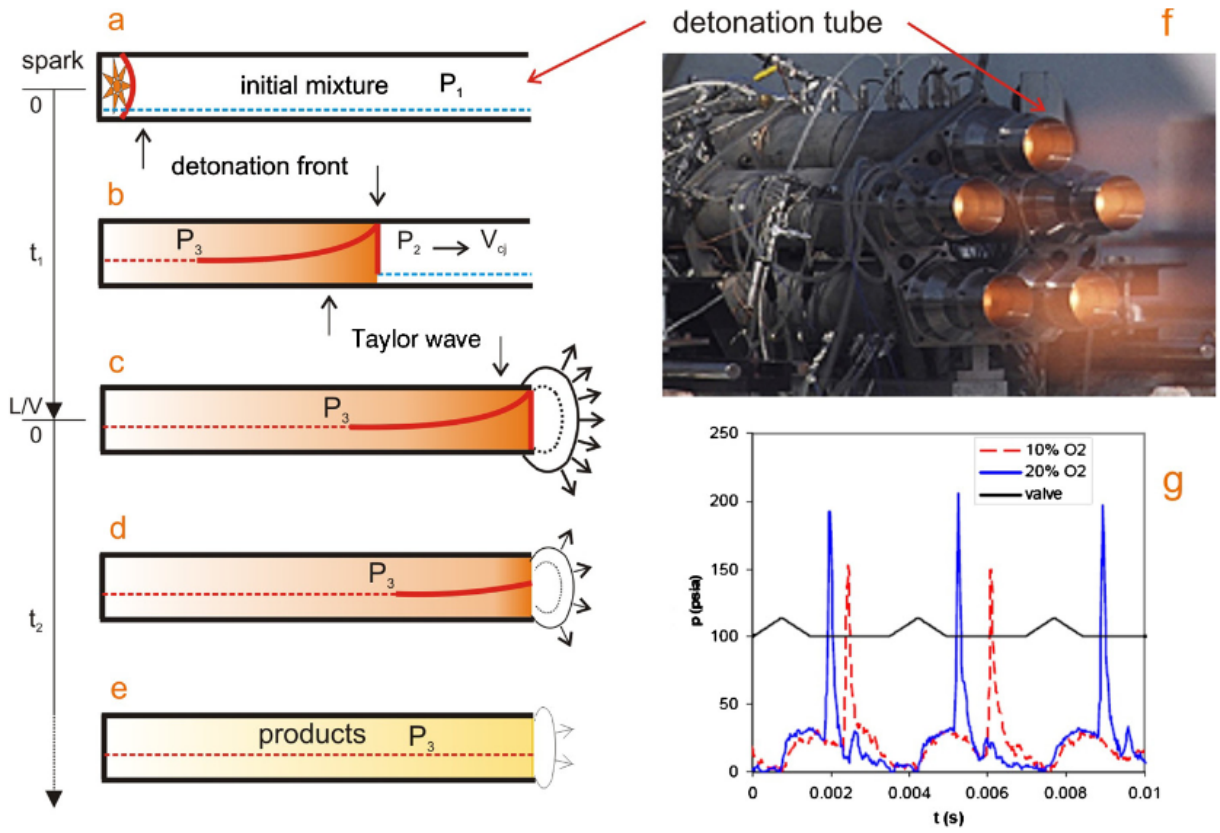

Figure 1.7: *Left*: Schematic of pulse detonation engine operation. *Top right*: Five-tube pulse detonation engine during hot-fire testing at China Lake Naval Surface Warface Center. *Bottom right*: Sample pressure traces from a pulse detonation engine firing. All images from Ref. [18].

PDEs [19]. In RDEs, propellant is fed steadily into an annular combustion chamber and consumed by one or more transverse detonation waves which continuously propagates (or rotates) around the annulus as shown in Fig. 1.8, creating a steady level of thrust from an otherwise unsteady detonation process. This architecture eliminates the need for precision-timed valves, as the transverse detonation wave meters the flow of reactants into the combustor. As the detonation wave passes a propellant injector, the propellant feed is temporarily cut off and after the wave passes, propellant flow is re-established. Additionally, DDT only has to occur once during engine startup, as the same transverse detonation wave(s) will continuously propagate around the annulus consuming new propellant. Thus the length needed

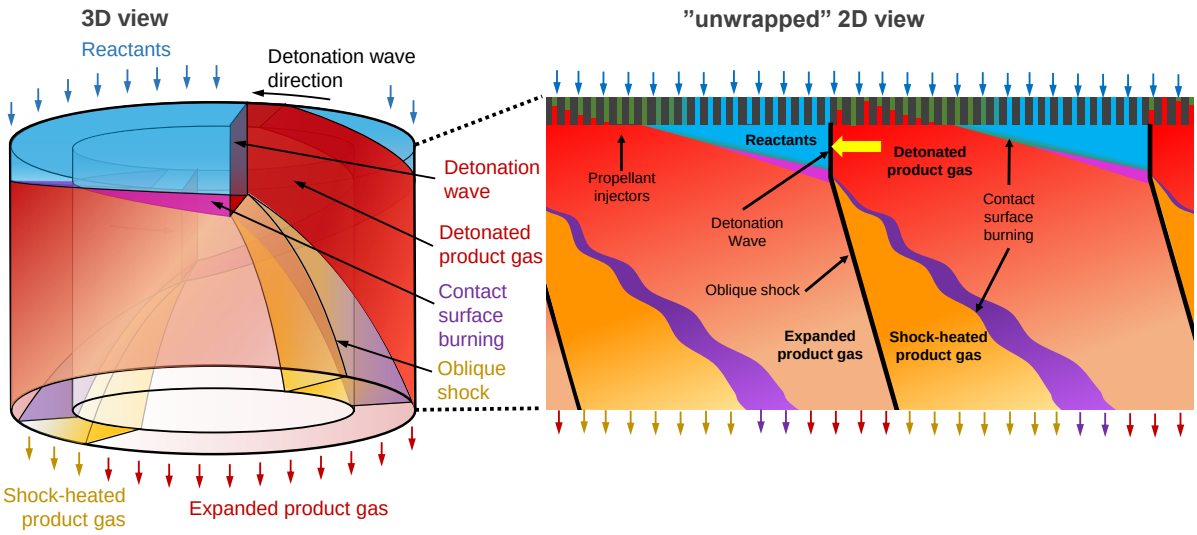

Figure 1.8: *Left*: Diagram of rotating detonation rocket engine combustor with two simultaneous co-rotating detonation waves consuming propellants injected from the top of the annular chamber. *Right*: "Unwrapped" view of RDRE.

for DDT is wrapped around the annulus, which leads to a smaller engine size compared to a PDE. RDEs also allow combustion to happen on very short spatial scales, due to rapid consumption of reactants by the supersonically propagating detonation waves near the propellant injector face. In the rotating reference frame of the detonation wave(s), geometric area expansion can occur without the need for a nozzle [20]. The last two factors suggest that RDEs may have significantly reduced combustor/nozzle size compared to PDEs and conventional deflagration based engines, which further complements the potential mass reduction promised by the thermodynamic advantages of detonation based combustion.

Due to the advantages of RDEs over PDEs, the rotating detonation rocket engine (RDRE) has become the subject of considerable research and development efforts [21, 22, 23, 24, 25, 26, 27, 12, 28]. Many researchers have conducted experimental, numerical, and analytical investigations of RDREs, overcoming initial experimental hurdles to sustain continuous detonation, establishing operational regimes relevant to rocket propulsion, examining the effects of different system geometries, and producing a framework with which to compare and analyze results. Regardless, RDREs are still at a relatively low technology readiness

level (TRL), and significant higher-level challenges remain for measuring and understanding RDRE efficiency, experimental realization of stagnation pressure-gain, as well as characterization of relationships among propellant combustion and expansion [23, 25, 26, 12, 27, 29]. To date, most experimental RDREs have not produced higher specific impulse than traditional deflagration-based rocket engines.

Much experimental [25, 30, 31, 32, 33, 34, 35, 36, 37, 38] and computational work [39, 40, 41, 42, 43] has been conducted to accelerate technical readiness and investigate the causes of sub-optimal RDRE performance. These studies typically utilize simple gaseous fuels—such as H_2, C_2H_4, and CH_4—with simplified modular engine designs allowing for various parametric studies. Such has been the approach at the Air Force Research Laboratory (Edwards, CA) over the last several years [12], wherein several concerted experimental and numerical investigations have been conducted using a single RDRE architecture [24] fueled almost exclusively by gaseous methane and oxygen. These investigations, among others, have yielded valuable insights into the relationships among operating conditions, rotating detonation behavior, and overall engine performance, which are summarized in the following paragraphs.

The effects of injection, mixing, and mass flow rate on thrust, specific impulse, and detonation propagation have been systematically examined, revealing many observed trends for the conditions tested:

- rotating-detonation stability is strongly dependent on propellant mixing [44]
- the number of concurrent detonation waves in the annulus is linked to the total propellant flow rate [28, 37, 45]
- tighter annular gaps generally yield higher performance [46]

RDRE propulsive performance has traditionally been linked with higher detonation wave-speeds, as detonation wave-speed is proportional to the speed of sound of the detonated gases, which generally increase with post-detonation temperature [13]. A benchmark for detonation wave-speed to which experimental results are often compared to [34, 47, 36, 37, 48]

is the maximum possible wave-speed as predicted by Chapman-Jouguet theory, often denoted as the CJ wave-speed, which represents the speed of an ideal, fully-formed, 1-dimensional detonation wave propagating into a pre-mixed reactants. This optimal wave-speed varies with the selection of fuel and oxidizer, equivalence ratio, and pre-detonation pressure and temperature. Caveats to the correlation between performance and wave-speed have been recently noted [49], wherein increased specific impulse for an RDRE is observed even in circumstances where detonation wave-speed is reduced. It is thus apparent that detonation wave-speed and overall propulsive performance (i.e. measured engine thrust and specific impulse) hold a complex relationship convoluted by local transport effects, fluid mechanics, and thermochemistry.

Various mechanisms have been proposed to explain the suboptimal performance seen in real RDREs. One such mechanism is parasitic deflagration [50, 51], which is defined as the undesirable burning of propellants in a deflagration mode. This parasitic deflagation can occur prior to the passage of a detonation wave, due to pre-heating by products of the previous detonation wave. This effect is known as "contact-surface burning" and is indicated in Fig. 1.8. Parasitic deflagration can also occur after the passage of a detonation wave in the case that the reactants were not well mixed before the passage of the detonation wave. The heat released via parasitic deflagrative reaction both pre- and post-detonation is energy unavailable to the detonation, reducing post-detonation pressure gain and specific impulse [49].

Additionally, the short timescales between detonation waves (on the order of microseconds) allows for a short window of time for non-premixed reactants to fully mix before the passage of a detonation. Reactants are being injected into detonation products from the previous detonation wave, which also begin to mix with the reactants [52]. Both of these effects have the combined result of providing an inbound detonation wave with an under-mixed and partially combusted reactant mixture, which limits the energy released across the wave. This has the effect of weakening the detonation wave, which reduces both detonation wave-speed and performance [53, 44, 54].

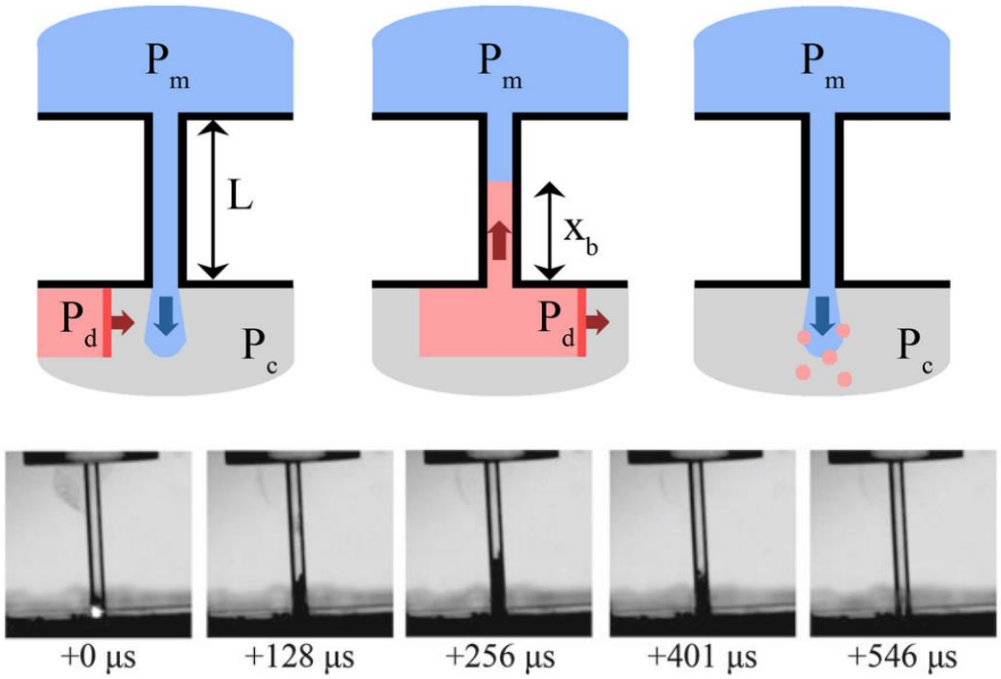

Figure 1.9: *Top*: Depiction of injector back flow and recovery behind a detonation wave. *Bottom*: Experimental observation of back flow using water as the injected fluid and a gaseous premixed detonation wave. Both images from Ref. [55] .

Another potential cause of reduced RDRE performance relates to the propellant injection system. The high pressures behind strong detonation waves cause a temporary reversal of the pressure gradient across a propellant injection element [56]. This can cause a dramatic reduction of reactant inflow to the combustion chamber or in certain cases, a full cutoff of propellant inflow, or in the worst case, a back flow of combustion products into the injection orifices [43]. If the upstream injection pressures are not sufficiently high, then the propellants streams may take a long time to re-establish forward flow, which is not desirable due to the aformentioned microsecond timescales between detonation waves [55]. Longer injector recovery timescales compared to the period of detonation passage leads to a weakening and slowing of the detonation wave to allow time for the propellants to fully refresh, and ultimately limits the energy release across the detonation wave. In extreme cases, this process can prevent the stable formation of detonation waves at all, allowing for

a deflagration mode of combustion to prevail [38]. In addition to this, if one propellant stream (say the fuel stream) reestablishes flow quicker than than the oxidizer stream, then a mixture with an off-nominal mixture ratio may be temporarily produced. This effect can further reduce the energy released by the reactants when they are consumed by a detonation wave. The solution to this problem has typically been to increase the feed pressure of the propellants, allowing for a faster injector response time [39]. However, this solution negates some of the system-level benefits of pressure-gain combustion in which lower feed system pressures and ultimately lower propulsion system mass is promised.

Besides the issues related to the combustion heat release, there is also the question of gas expansion downstream of the combustion zone. In a typical deflagration-based rocket engine, all gas particles undergo a similar thermodynamic process during expansion in the nozzle [1]. This permits the nozzle designer to size the nozzle expansion ratio (exit area to throat area) for a single pressure ratio. In a RDRE however, all of the gas particles undergo a slightly different thermodynamic process [20]. As shown in Fig. 1.8, some of the combusted gas encounters an oblique shock wave, which changes its entropy, temperature, pressure, and velocity compared to the gas unaffected by the oblique shock. This causes the exhaust gas flow being to be stratified in thermodynamic state, making it hard to design a nozzle to perfectly expand the flow to atmospheric pressure. Both computational studies [57] and experimental efforts [25, 33, 58] have been conducted using aerospike nozzles on RDREs, which theoretically permit for the automatic adjustment of area ratio to changing pressure ratio. These studies have generally indicated a positive benefit from the addition of a nozzle, although further research is needed to determine if this benefit is related to perfect gas expansion, reduced base drag, or higher average chamber pressures associated with a nozzle throat [59, 60].

In addition to the aforementioned issues regarding sub-optimal RDRE performance, there are additional thermal challenges associated with the dynamic flow-fields in RDREs. In deflagration-based rocket engines, the flow is typically steady in nature, which promotes the development of a thermal boundary layer in which the temperature of the gas is dropped

by a couple thousands of kelvin. This permits rockets to operate at temperatures upward of 3000 K using combustion chambers made of metals that fail structurally above 700–1000 K [3]. In an RDRE, the flow-field is highly transient, so no such thermal boundary layer can be established, leading to convective heat transfer coefficients that are much higher than in conventional rocket engines [61]. Additionally, the combustion zone in RDREs are much denser and hotter than in normal rocket engines, which only exacerbates the problem. The center-body in the RDRE annulus is also difficult to access and cool using conventional methods such as regenerative cooling. These high thermal loads currently limit the run time of most RDREs to a couple of seconds, after which thermal damage may begin to occur [62, 63]. Some research groups have attempted to characterize and address these thermal issues, such as the RDRE research group at the Japan Aerospace Exploration Agency (JAXA). This group has assessed the heat flux from a C_2H_4–O_2-fueled RDRE and extended the run time of the RDRE to 6 s using C/C composites [64, 65]. The group has also used film-cooling by injecting propellant directly onto the walls and mitigated the difficulties of cooling the center-body by removing it entirely [35]. This method has allowed for the RDRE wall to nearly reach a thermal steady state [66]. While these recent developments are encouraging, to date, no RDRE has been run for longer than 10 s at a time.

The numerous technical challenges associated with RDREs highlight a need for further experimental efforts to characterize the loss mechanisms described above. The evaluation of the relative contribution of each loss mechanism depending on the combustor design and operating condition is difficult due to their convolution into the usual global parameters such as thrust and specific impulse. Optical diagnostics present the prospect of making direct measurements of combustion properties. However, the propagation speed of detonation waves, coupled with their high pressure and temperature, renders these diagnostics challenging. In the next section, we discuss the development of optical diagnostics sufficiently resolved in time and space and adapted for these harsh environments.

1.5 Optical diagnostics for RDREs

A critical issue in evaluating RDRE technology has been a lack of diagnostic capability that is sufficiently quantitative and granular to provide useful feedback. In this dissertation, we utilize both existing optical methods for RDRE diagnostics and we address the need for additional diagnostic advancement by furthering the state-of-the-art in high-speed laser diagnostics for harsh combustion environments.

The steep gradients in temperature, pressure, and species concentrations of detonation waves over small spatial (<1 mm) and temporal (<100 µs) scales have posed unique diagnostic challenges in the quantitative evaluation of RDREs. Although measurements of thrust, chamber pressure, and mass flow rate have long been used to calculate specific impulse and characteristic velocity in rocket applications [1], these global metrics represent the end-result of several energy conversion processes.

Various techniques have been developed in an attempt to measure local gas properties such as pressure and temperature in RDREs. An accurate and reliable assessment of the peak pressure is valuable for determining the "pressure-gain" achieved via detonation, which is correlated with propulsive efficiency [67]. The extreme thermal environment in detona-

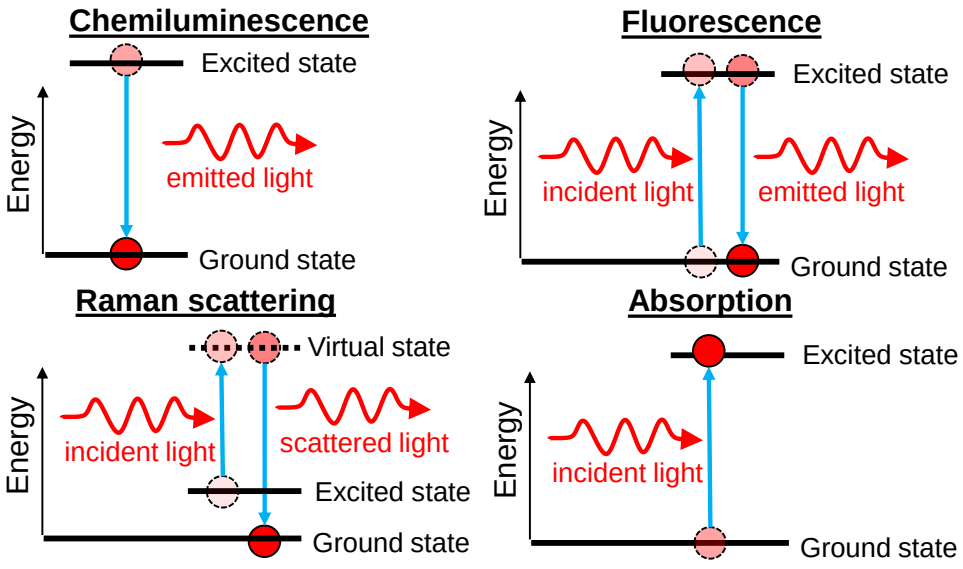

Figure 1.10: Molecular energy diagrams representing various optical diagnostic techniques.

tion combustors tend to damage conventional electro-mechanical pressure transducers when operation times last longer than a few seconds [68, 69]. To compensate for this, pressure transducers are often stood off from the combustion chamber with a recess or standoff. The presence of the cavity created by this offset can attenuate high-frequencies while resonances in the cavity can amplify certain frequencies which have the effect of attenuating and distorting measured pressure profiles, causing errors in peak pressure readings up to 50% [70, 71]. As a result, most approaches to measuring pressure in detonation engines do not involve measurement of peak pressure but instead opt to either measure frequency content to infer detonation wavespeed or attenuate high-frequency content altogether to measure time-averaged pressure, also known as capillary-tube attenuated pressure (CTAP) [70]. Temperature measurements for RDREs have been conducted using thermocouples [72], but the temperatures measured are those of the combustion chamber wall, not of the combustion gas itself, as thermocouples are unable to survive at combustion gas temperatures.

Various optical techniques have been developed and utilized in detonation engines. A brief review on these techniques is given below:

- *High-speed videography*: High-speed cameras have been the fundamental diagnostic tool used to obtain useful information about RDRE flow-fields [73, 36]. The basic theory of operation behind this technique is to capture the luminosity associated with the spectral emission of the high-temperature combustion gas. As molecules in excited energy states naturally relax down to a lower energy level, they emit light. This can be visualized in the top left of Fig. 1.10. Regions of high luminosity correspond to the locations of detonation waves in an RDRE flowfield, allowing for the tracking of the position of detonation waves over time. Cameras are usually positioned a few meters downstream of the RDRE exhaust plane as to image the entire annulus, although some groups have imaged the exhaust at an angled view [66]. High-speed imaging permits a direct calculation of detonation wave-speeds and the observation of detonation wave dynamics such as the formation and destruction of multiple detonation waves. A sample set of high-speed video stills from Bennewitz et al [37] demonstrating a tran-

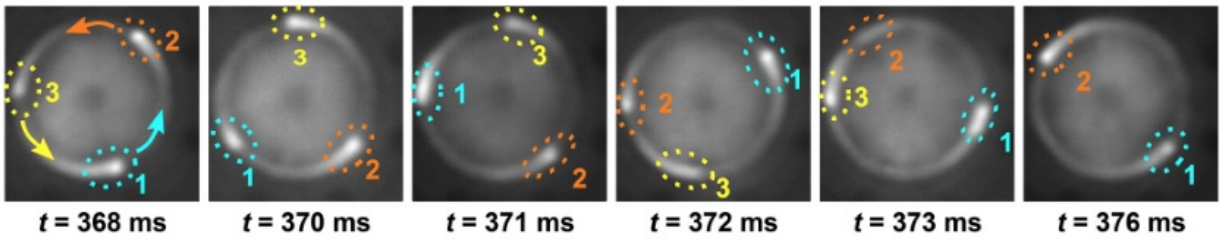

Figure 1.11: Sample high-speed video stills from Bennewitz et al [37] showing a transition between a three-wave detonation mode to a two-wave detonation mode in an RDRE annulus

sition from a three-wave detonation mode to a two-wave detonation mode is shown in Fig. 1.11. While this technique allows for excellent spatial resolution, the luminosity measurement represents a path-integration of the emission from all gas particles at a particular azimuthal location in the RDRE, preventing the determination of localized gas properties. Some engine designs feature an optically-accessible RDRE [48, 74] with transparent walls to allow for a direct view of the combustion gases, as shown in Fig. 1.12. Despite this, the light intensity is only loosely correlated with actual gas temperature, as visible light is produced as a result of many separate physical mechanisms, such as soot radiation, chemical reactions, and chemiluminescence of radical species. Nevertheless, the technique provides good time resolution, on the order of 10s of microseconds, with the main limitation being the camera frame rate. This technique is utilized in Chapters 2 and 3 to detonation wave formation, speeds, and modes in an RDRE.

Figure 1.12: Example of an optically-accessible RDRE using a quartz outerbody for high--speed videography, from Wang et al [48].

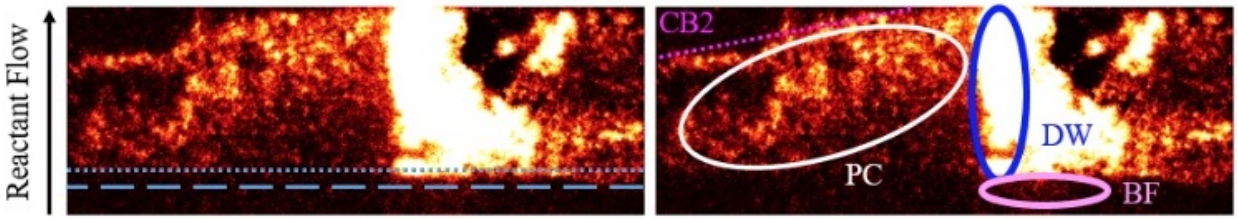

Figure 1.13: A sample OH* chemiluminescence measurement from Chacon et al [50]. The x-axis represents the azimuthal position along the circumference of the annulus and the y-axis represents the axial position from the injector face. On the right, regions of high chemiluminescence are correlated to specific flow features, with DW representing the detonation wave and PC representing zones of parasitic combustion.

- *OH* Chemiluminescence*: This technique is a specific version of the aforementioned high-speed videography in which the luminosity outside of the light associated with the OH* radical at 308 nm is filtered using a spectral bandpass filter. The chemiluminescence measurement has an advantage over the conventional videography technique because it directly identifies flame fronts where OH* is produced [75, 50, 76]. An example of an OH* chemiluminescence measurement is shown in Fig. 1.13. While useful, this technique has difficulty in providing quantitative information about local gas properties and is again limited in measurement rate by the camera frame rate.

- *Laser-induced fluorescence (LIF)*: LIF is a technique which involves the excitation of a species (e.g. OH, NO, CH, acetone) to an electronic state by intense laser radiation, followed by the measurement of the radiative electronic relaxation of that species. This process can be visualized in the top right of Fig. 1.10. This technique allows the measurement of species concentrations. If performed on two electronic transitions (two-color LIF), this diagnostic can also resolve temperature. However, LIF is subject to several perturbations, the most important being the quenching of the electronic excited states by other molecules, and therefore requires calibration for quantitative results. This technique can be extended into two-dimensions by using a laser sheet, which is known as Planar laser-induced fluorescence (PLIF). PLIF has been utilized for

imaging of many combustion systems, but quantitative measurements become difficult in highly dynamic flowfieds at extreme combustion conditions [77]. As a result, the application of PLIF to RDREs has largely been confined to qualitative assessment of RDRE injector mixing and refresh dynamics in cold flows where the temperatures are low using seeded acetone as a target molecule [78, 79, 80] but more recent work demonstrates the potential for use of OH PLIF in making measurements in the reacting flow-field of an RDRE [81].

- *Particle image velocimetry (PIV)*: PIV involves the measurement of instantaneous fluid velocity by the use of tracer particles which are seeded into the flowfield. A light source (typically a pulsed laser) is used to illuminate the particles, which can be tracked with a high-speed camera. The change in particle position over time can be used to infer the local fluid velocity, assuming the tracer particles move with the local gas. PIV has been used to make measurements of gas velocity in RDREs [82, 83, 84, 85] but critical limitations include measurement rate (limited to 10s of kHz) and the effect of the injection of tracer particles on the RDRE gas dynamics.

- *Raman Spectroscopy*: Raman spectroscopy utilizes the scattering of photons by molecules. Anti-Stokes Raman scattering involves a molecule transferring energy to an incoming photon, which results in a decrease of the photon's wavelength. This process can be visualized in the bottom left of Fig. 1.10. Coherent anti-Stokes Raman spectroscopy (CARS) is a specific type of anti-Stokes Raman spectroscopy in which multiple light sources are combined to produce a new coherent beam at the anti-Stokes frequency. CARS allows for accurate sensing of gas properties with a high spatial resolution, but it is not an absolute measurement and its application to RDREs is limited due to its low measurement rate, which has not exceeded 1 kHz [86].

- *Laser absorption spectroscopy (LAS)*: LAS exploits the absorption of light at wavelengths resonant with differences in molecular energy levels to infer thermophysical flow properties such as: temperature, species concentration, pressure, and number density. The absorption of light by a molecule can be visualized at the bottom right of Fig. 1.10.

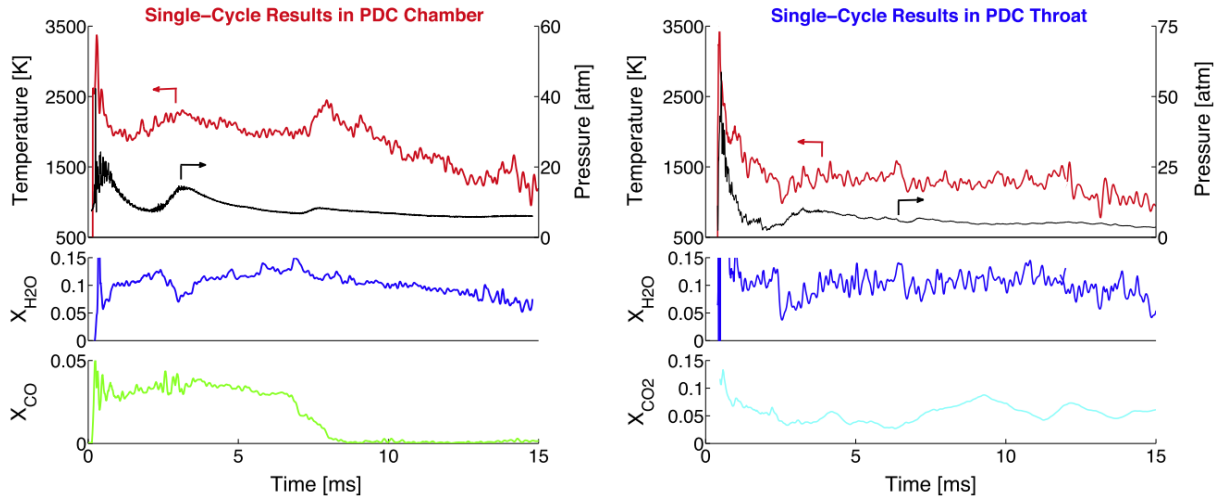

Figure 1.14: Time-resolved temperature and species concentrations at two locations in a pulse detonation combustor [88].

Molecules have unique absorbance spectra; therefore, this technique can be used to target numerous species relevant to combustion, including: reactants (CH_4), intermediates (CO, OH, CH), and products (CO_2, H_2O). Unlike the aforementioned techniques, LAS is calibration-free and strong absorption interactions enable the use of low-power, relatively inexpensive light sources for sensitive measurements. LAS has been used for measurements in detonation environments [87, 88, 89, 90, 91, 92]. Specifically, wavelength-scanning (or -modulating) LAS techniques have been used for robust PDE/RDE measurements of absorption by water vapor in the near-infrared [92, 93, 88, 94] and by the carbon oxides in the mid-wave infrared [89, 95, 30, 87]. Sample LAS measurements of species and temperature from a PDE are shown in Fig. 1.14, from Ref. [88]. Compared to the other techniques mentioned above, LAS has been shown to both provide quantitative measurements of localized thermophysical gas properties, while also allowing for high-speed measurement rates (>100 kHz) which are potentially high enough to resolve intra-cycle gas properties.

Due to the advantages of LAS, in this work, we leverage this technique to make measurements of gas properties in an RDRE. A persistent challenge to deploying LAS to the

harsh transient environment of a detonation engine has been balancing the need for fast measurement rates and robustness to environmental noise. Early LAS efforts on PDEs deployed fixed-wavelength laser absorption methods to probe hydrocarbon fuels [96, 97] and water vapor [91]. While fixed-wavelength absorption techniques are typically only limited in measurement rate by detector bandwidth, the methods are generally not robust against beam steering, particle scattering, window fouling, and thermal emission which are highly dynamic in detonation engines. To address these issues, more recent LAS work in the context of detonation engines has focused on wavelength-scanning or wavelength-modulation techniques that allow for reliable correction of thermal emission and active recovery of a non-absorbing baseline signal (or insensitivity to baseline signal) that mitigates issues of steering, scattering, and window fouling. Wavelength-scanning (or -modulating) spectroscopy techniques have been utilized for more robust PDE/RDE measurements of water vapor absorption in the near-infrared [92, 93, 88, 94] and the carbon oxides in the mid-wave infrared [89, 90, 30, 87]. However, the effective measurement rates for these wavelength scanning methods (10–100 kHz) are insufficient to fully resolve thermophysical gradients in many detonation-based engines. Specifically, rotating detonation rocket engines often possess cycle frequencies (which may involve multiple waves) in the range of 5–30 kHz, for which MHz measurement rates are desired for temporal resolution of intra-cycle transients. Part of this work is dedicated to the extension of LAS temporal resolution in order to sufficiently resolve intra-cycle RDRE flow properties.

1.6 Scope and organization

This dissertation focuses on the implementation of existing high-speed optical diagnostics and the development of new optical diagnostic techniques for RDRE analysis. The central goal of these efforts is to gain deeper understanding of the many physical mechanisms in detonations and the relative influence of the various loss mechanisms introduced in Section 1.4.

Chapters 2 and 3 focus on the testing of an RDRE developed by UCLA for use with liquid space-storable hypergolic propellants. Liquid-fueled RDREs have thus far been rela-

tively unexplored by the research community, with experimental efforts focusing primarily on gaseous-fueled RDREs. We examine the effects of varied injector design, propellant flow rate, and combustion chamber geometry on the detonation characteristics and performance of the RDRE by using current state-of-the-art diagnostic techniques, such as high-speed videography and capillary-tube attenuated pressure (CTAP) measurements. Additionally, the feasibility of using additive manufacturing for enhanced propellant injector design is studied. Chapter 3 presents a novel technique for assessing the fundamental spatial scales for detonation of hypergolic propellants by utilizing the high-speed video data.

In Chapter 4, we demonstrate a new LAS sensor designed to measure multiple combustion parameters (pressure, temperature, species number densities) at MHz rates in the exhaust of a gaseous CH_4–O_2-fueled RDRE. The opto-electronic advancements in mid-infrared distributed-feedback (DFB) lasers and spectroscopic theory that provides the basis for the sensor are discussed along with some demonstration results. Chapter 5 investigates the exhaust thermodynamics of the same gaseous CH_4–O_2-fueled RDRE utilizing the sensor developed in Chapter 4. The intra-cycle variation of pressure, temperature, and CO number density are observed across a variety of test conditions (flow rate, equivalence ratio, injector geometry) and various trends are observed. These data are then used to infer energy content/conversion and loss mechanisms in the RDRE, highlighting the potential of this new granular diagnostic for assessing RDRE physics.

Chapter 6 entails a more detailed exploration of how to optimize MHz-rate DFB laser tuning to provide improved spectral wavelength tuning and signal-to-noise ratio. This chapter serves as a broadly applicable guide for high-speed DFB laser tuning for a wide variety of high-speed sensing applications. This paves the way for high-speed sensing at more extreme pressure and temperature conditions that can be found near the RDRE injector face.

Chapters 7 and 8 utilize the tuning benefits provided by the tuning optimization of Chapter 6 to develop sensors for more extreme/varied combustion environments. Chapter 7 specifically details a more broadly applicable pressure sensing strategy for a wider range of fuels, combustion modes, and pressure conditions. Chapters 8 details a sensor for ex-

treme temperatures, up to nearly 10,000 K, with reduced uncertainties, utilizing a fit of the Boltzmann distribution of the gas.

Lastly, Chapter 9 summarizes the findings of the thesis and discusses current/future research directions to further increase the understanding of the operation of RDREs. Various appendices are included which provide additional details on the work presented in the main body of this thesis. Appendix A provides details on the MMH–NTO RDRE testing of Chapters 2 and 3, such as the design/operation of the mobile Propulsion Test Platform and Mojave Test Area. Appendix B provides details on the Detonation-Impulse Tube facility used in Chapters 6 and 7 to create 1-D detonation conditions in the laboratory for optical sensor validation/demonstration. Appendix C presents a first-order analytical model for high-speed DFB laser tuning dynamics that provide insight on some of the experimental trends noted in Chapter 6. Appendices D, E, and F each provide detailed uncertainty analyses for the laser-absorption sensing techniques presented in Chapters 4, 7, and F respectively. Appendix G provides details on the combustion-kinetics analysis presented in in Chapter 7 and Appendix H provides uncertainty analysis for the post-reflected-shock conditions generated in the UCLA High-Enthalpy Shock Tube facility used in Chapters 4, 6, 7, and 8. Lastly, Appendices I and J provide full drawing packages respectively for the hypergol RDRE combustor used in Chapters 2/3 and the Detonation-Impulse Tube described in Appendix B.

CHAPTER 2

Rotating detonation of hypergolic space-storable propellants using an additively-manufactured injector design

The contents of this chapter have been published in the ***AIAA Journal of Spacecraft and Rockets*** *under the full title "Hypergolic Continuous Detonation with Space-Storable Propellants and Additively Manufactured Injector Design'' [98] and portions have been published in the journal* ***Proceedings of the Combustion Institute*** *[99] under the full title "Detonation cell size of liquid hypergolic propellants: Estimation from a non-premixed combustor''. Portions of the chapter's content have been presented / included in the conference proceedings for the* ***AIAA Propulsion and Energy Forum, 2021*** *[100] the* ***AIAA SciTech Forum, 2022*** *[101] and the 39th International Symposium on Combustion.*

2.1 Introduction

Several experimental and computational efforts in recent years have yielded considerable progress in understanding and maturing rotating detonation engines operating on gaseous propellants such as hydrogen, methane, and ethylene in air or in gaseous oxygen, but experimental work dedicated to the detonation of liquid bi-propellant combinations for rocket propulsion has been limited [21, 102], particularly for in-space applications [103, 104]. The development of reliable liquid bi-propellant systems is key to practical implementation of RDREs, owing to the higher energy density of liquid propellants and—consequentially—reduced volumetric requirements and decreased structural mass fraction in spacecraft and

launch vehicles [1, 3].

The dynamic unsteady nature of detonations and extreme range of thermodynamic conditions covered across short time scales (<ms) and convoluted spatial domain pose significant challenges for RDRE control, modeling, and design [23], and consequently have kept RDREs at a relatively low technological readiness level (TRL). Critical technology limitations to date include (1) under-mixed propellant injection yielding relatively low wavespeeds [53, 105, 44, 54], (2) extreme heat transfer and associated lack of chamber durability [72, 106, 102], and (3) undesirably high pressure-loss feed systems required to avoid injection back flow and to shorten propellant refresh timescales for continuous operation; these losses offset the pressure gain associated with detonation combustion [39, 43, 38]. All three of these issues can be related to or influenced by injector design, which has magnified influence on the detonation characteristics, operability, and practicality of RDREs [107, 3].

For liquid-fueled detonation combustors, injector design is additionally complicated compared to their more common gas-phase counterparts. Liquid-injection systems must support the conversion of the reactants into a gas phase, to enable combustion, by colliding propellant streams to encourage stream breakup and subsequent atomization into droplets small enough to vaporize on timescales short enough to support stable operation. Because of this, the performance of liquid injectors is highly sensitive to injector element size, placement, and orientation. Because of the aforementioned phase-change, liquid injection flows are fundamentally two-phase. This, combined with the additional physics associated with effects such as surface tension, complicates analysis compared to gas-phase propellants. Lastly, due to the significantly higher energy density of liquid propellants, it is unsafe to premix liquid propellants to any degree before injection, meaning that liquid injectors are also entirely responsible for complete propellant mixing.

Despite limited prior development of liquid bi-propellant detonation combustion devices, in-space propulsion systems using space-storable propellants may expedite the overall timeline to technical and flight-readiness for RDREs. First, most in-space propulsion systems/thrusters are much smaller in scale and thrust than launch/boost propulsion systems,

thereby more rapidly enabling full-scale engine testing at a more moderate design-build-test cycle cost [108]. Second, the typical pulsed-mode operation of in-space thrusters with short-duration burns may help avoid the worst of heat transfer challenges inherent to RDRE geometries, which otherwise complicate the design and development for boost or orbit-transfer engines with longer burn durations. Third, the ignition reliability and stability of hypergolic space-storable propellants partly reduces system and testing complexity. Lastly, in-space propulsion systems typically require lower chamber pressures, lessening the pressure-gain requirement of an RDRE. All of these reasons suggest that research and development of RDREs operating on space-storable propellants may offer an expedient path to technical readiness of RDREs in general.

Typically, rotating detonation engines are started in a deflagration mode, with a detonation wave being introduced via an external source, usually a small tube with a large l/d filled with a detonable gas mixture, ignited using a separate ignition system, such as a sparkplug [24, 109]. These pre-detonator systems are not desirable for in-space applications, as the requirement for an external ignition system increases the likelihood of propulsion system failure in an environment where troubleshooting and maintenance are not easily conducted. The mitigation of ignition-associated failure is the principal reason that hypergolic propellants are typically used for in-space applications.

The hypergolicity of conventional space-storable propellants provides for a unique mode of detonation initiation. Detonatability has been shown to scale inversely with reaction activation energy [110]. Hypergolic propellants inherently have low activation energy and therefore have a theoretically higher propensity to detonate. Xue et al recently demonstrated the feasibility of initiating rotating detonations with monomethylhydrazine (MMH) and dinitrogen tetroxide (NTO) without the use of a pre-detonator [103, 104], indicating that hypergolically-initiated rotating detonation rocket engines (RDREs) may be feasible. Additionally, Anderson et al [102] recently demonstrated usage of a small hypergolic slug to initiate detonation behavior with a non-hypergolic propellant combination in a rotating detonation engine.

Deflagration-to-detonation transition timescales are particularly important for in-space propulsion. Small bipropellant thrusters (5–500 N or 1–100 lbf thrust) are often used in a *pulse firing mode* [111], in which the thruster is operated in short bursts, which can be as short as 10s of milliseconds [112]. This firing mode is typically for precise in-space attitude control and station-keeping. In addition to the precise control enabled by pulse firing, this operation mode limits the total heating to the walls of the thruster in time, reducing the requirements of the engine cooling system relative to thrusters operated in a continous mode. If RDREs are to be used for pulsed-mode operation, it is important that any thruster be able to reach its design operating state as quickly as possible for accurate delivery of an incremental impulse. To this end, a good understanding of the hypergolic deflagration-to-detonation transition (DDT) in an annular combustor is required.

Most RDEs (rocket and airbreathing) described in the public literature have employed subtractively-manufactured simple impingement or jet-in-crossflow style injectors [21, 103, 104, 12, 113], contrasting with more advanced rocket injector geometries that minimize mixing scales at the cost of complexity [114, 107], including those more recently enabled by additive manufacturing [115, 116]. However, key challenges associated with additive manufacturing include the production of small features on the order of 0.5 mm (0.020"), below which the resolution of 3D printers is typically insufficient to produce high-precision injection orifices [117]. Moreover, additively-manufactured components typically possess increased surface roughness, leading to potentially increased frictional losses [115]. To date, the benefits and drawbacks of additive manufacturing have not been rigorously explored in the context of rotating detonation engine injection.

In this study, we describe the development and testing of a modular liquid bi-propellant combustor with additively-manufactured (AM) injectors used to assess the detonability of the space-storable hypergolic propellants monomethylhydrazine (MMH) and dinitrogen tetroxide (NTO) in an annular combustor. We first describe the computational fluid dynamics-driven design methodology and manufacturing process, including pre- and post-manufacturing cold-flow assessments of injector hydraulic performance. We then describe an experimental hot-

fire testing campaign, detailing the infrastructure, instrumentation, procedures, and operating parameter test matrix used to assess MMH–NTO detonability. Following the setup, we present results from testing, including a novel dataset on the detonation behavior of hypergolic propellants and the conditions under which they form, highlighting key trends associated with mass flow rate, DDT timescales, and detonation modal characteristics.

2.2 Design and analysis

A novel injector plate was developed for use in the test article using iterative computational analysis to generate a design specifically manufacturable by laser-powder bed fusion (L-PBF). The baseline reference injector design is a conventionally-machined impinging style injector, based on a design employed by Xue et al [103, 104], which uses 24 unlike-doublet injector elements distributed circumferentially around the annulus, with both the fuel and oxidizer streams oriented 30° from the injector-face normal. The reference injector orifices were approximately 0.31 mm (0.0122") and 0.37 mm (0.0145") in diameter for the fuel and oxidizer streams respectively. A modified additively-manufacturable injector design was developed with the goal of establishing consistent rotating detonation operability over a range of mass flow rates with lower injection pressure loss. One change to the new injector relative to the baseline design was increasing the density of injection elements ($> 40\%$) to promote increased secondary mixing between injector elements. Additionally, the orifice sizes were increased slightly ($\sim$10%) relative to the baseline, though this varied based on surface treatment, as discussed in later sections. Notably, to improve the hydraulic performance of the injector, the propellant passageways from the plenum to the injection orifices were tapered, allowing for a gradual transition in flow area which was predicted to reduce viscous losses and increase the relative back-flow resistance of the injector [55]. Conventional subtractive manufacturing techniques are not particularly well-suited to achieve this type of variable tapering. Conversely, additive manufacturing allows for the fabrication of continuously-tapered geometries. A diagram indicating the difference in injection orifice tapering between the two manufacturing approaches is shown in Fig. 2.1.

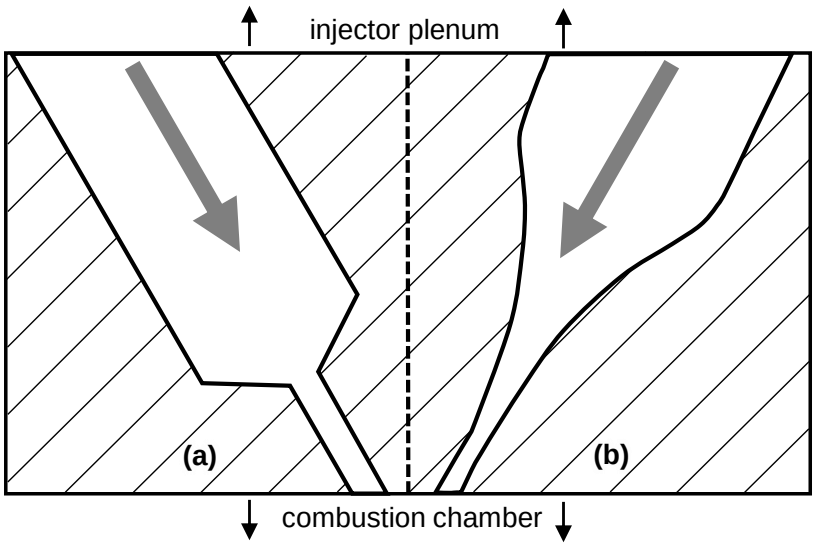

Figure 2.1: (a) Cross-section of impinging injection element fabricated using subtractive manufacturing techniques such as drilling. (b) Cross-section of tapered impinging injector element enabled by additive manufacturing.

The primary metric used to assess hydraulic performance is the injector discharge coefficient C_{D}, unique to each propellant stream i, defined by the following equation [1, 3]:

$$C_{\mathrm{D},i} = \frac{\dot{m}_i}{A_i\sqrt{2\rho_i \Delta P_i}}. \tag{2.1}$$

Here, $\dot{m}_i$ is the mass flow rate of propellant i with density ρ_i through a set of orifices with total reference flow area A_i, driven by a pressure drop ΔP_i.

Computational fluid dynamics (CFD) analysis was conducted to assess the change in discharge coefficient between the injector designs. A steady, three-dimensional, single-phase, non-reacting, pressure-based CFD model using the SST-k-ω turbulence model was implemented in ANSYS Fluent using water as the working fluid. Water was selected as the working fluid due to its similar density and viscosity to the propellants and to facilitate direct comparison to cold-flow testing with water for model validation. In the model, a wedge of the injector geometry was evaluated to isolate a single fuel and oxidizer pair, leveraging axial symmetry to reduce computational costs. Pressure boundary conditions were placed on the manifold inlet and injection orifices to generate a pressure drop representative of that expected during typical engine operation. Figs. 2.2a and 2.2b show the fluid domain for the

fuel and oxidizer with the associated boundary conditions, as well as the mesh of the fluid domains. Fig. 2.2c shows the velocity contours for the CFD solution. Once a solution was converged upon, the mass flow rate through each injector element was obtained from the CFD model. Equation 2.1 was then used to evaluate the discharge coefficient for the fuel and oxidizer streams independently, using the injector orifice areas as reference areas. The gradual tapering of the AM design was shown to increase the discharge coefficient from 0.80 to 0.91 for the fuel stream and from 0.77 to 0.92 for the oxidizer stream, representing an increase in effective flow area of 14% and 19%, respectively.

In addition to an increase in the effective flow area, the CFD modeling quantified a difference in back-flow resistance between the two injector designs. As mentioned in Chapter 1, propellant back flow behind a passing detonation wave is suspected to be a primary culprit in suboptimal RDRE performance [55]. Back-flow resistance was assessed by reversing the boundary conditions of the CFD simulation, simulating a condition where the combustion chamber was at an elevated pressure relative to the propellant plenums, representative of conditions after a detonation wave passes an injector orifice. Velocity contours for reverse flow in the AM injector are shown on the bottom of Fig. 2.2c. The primary metric used to evaluate back-flow resistance was diodicity, Di, defined as the ratio of pressure drop for reverse flow to the required pressure drop in forward flow for the same mass flow rate. This

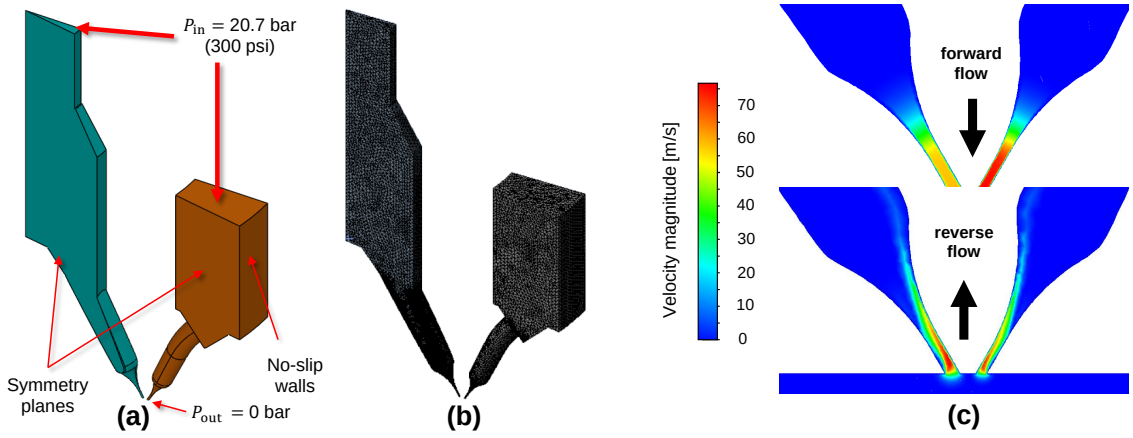

Figure 2.2: (a) Slice of fluid domain with boundary conditions indicated. (b) Mesh of fluid domain. (c) Velocity contours for the additively-manufactured injector.

can be expressed in terms of forward and reverse discharge coefficients for each propellant stream i as follows:

$$\mathrm{Di}_i = \left(\frac{\Delta P_{\mathrm{rev},i}}{\Delta P_{\mathrm{fwd},i}}\right)_{\dot{m}} = \left(\frac{C_{\mathrm{D,fwd},i}}{C_{\mathrm{D,rev},i}}\right)^2. \tag{2.2}$$

The tapered design enabled by additive manufacturing increased the predicted diodicity by 10% and 29% for the fuel and oxidizer streams, respectively, compared to the baseline injector design. Table 2.1 compares the hydraulic characteristics of the two injector designs predicted by CFD.

Two AM injectors were printed from stainless steel 630 using laser-powder bed fusion. The injectors were printed upside-down to ensure the injection orifices were left exposed after printing and not attached to the baseplate of the printer. The injectors were printed with three hollow internal cavities to reduce the weight and build time of the part. Drainage holes were printed between these cavities and various exterior surfaces of the injector to allow for the flushing of unused powder from these cavities after the printing process. After printing, the injectors underwent a hot isostatic pressing (HIP) process to improve mechanical properties. The injectors were then sandblasted to reduce external surface roughness and machined to further improve the surface finish on the sealing surfaces and injector face, as well as to add O-ring grooves. In order to produce the small diameter injector orifices for the AM injectors—which were below the typical 0.5 mm (0.020") resolution achievable by L-PBF printers—additional post-processing steps were taken. L-PBF was used to create the tapered passageways and create undersized injection orifices. These holes were printed misshapen

Table 2.1: Summary of predicted discharge coefficients and diodicities for the baseline and additively-manufactured (new) injectors, with percent changes indicated.

Metric	**Baseline**	**New (% change)**
$C_{\mathrm{D,fwd,fuel}}$	0.80	+14%
$C_{\mathrm{D,fwd,ox}}$	0.77	+19%
$\mathrm{Di}_{\mathrm{fu}}$	1.27	+10%
$\mathrm{Di}_{\mathrm{ox}}$	1.14	+29%

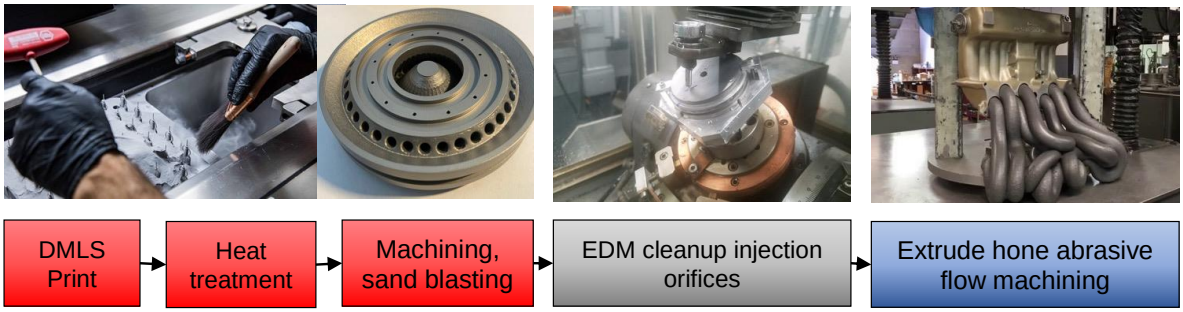

Figure 2.3: Manufacturing workflow for AM injectors. *Left*: Example of L-PBF printing process (Image source: Protolabs) yielding AM injector. *Middle*: EDM drilling of injector holes. *Right*: Example of abrasive flow machining (Image source: Extrude Hone).

and partially closed, and were opened up using electron-discharge machining (EDM) drilling. EDM drilling ensured the holes were rounded and uniform in size from element to element. In order to ensure the surface roughness of the propellant passageways was minimized, an extrude-hone abrasive flow machining (AFM) process was used on one of the two injectors, during which the holes were opened up in size by about 0.05–0.08 mm (0.002–0.003"). The manufacturing workflow can be visualized in Fig. 2.3.

The injectors were cold-flow tested using water as a propellant simulant, as seen in Fig. 2.4. Cold-flow testing on the conventionally-manufactured injector was used to obtain discharge coefficients of 0.79 and 0.64 for the fuel and oxidizer streams. Cold-flow testing for the unhoned AM injector yielded discharge coefficients of 0.87 and 0.69 for the fuel and oxidizer streams respectively. This represented an increase of 10% and 8% for the fuel and

Table 2.2: Cold-flow results for the baseline injector and the two additively-manufactured injectors along with the percent change for the additively-manufactured injectors relative to the baseline injector.

	Baseline	**AM injector**		**Percent change**	
Metric	**injector**	unhoned	honed	unhoned	honed
$C_{\mathrm{D,fwd,fuel}}$	0.79	0.87	0.96	+10%	+22%
$C_{\mathrm{D,fwd,ox}}$	0.64	0.69	0.79	+8%	+23%

Figure 2.4: Image of simultaneous cold-flow testing of the fuel and oxidizer flow paths for the unhoned additively-manufactured injector using water.

oxidizer streams respectively. These percent increases are lower than predicted by CFD, likely due to the omission of surface roughness from the CFD model. Cold-flow testing for the honed AM injector yielded discharge coefficients of 0.96 and 0.79 for the fuel and oxidizer streams respectively. These values represent a 22% and 23% increase for the fuel and oxidizer streams respectively compared to the machined injector. These percent increases are greater than the increases predicted by CFD, indicating that AFM helps to further reduce the relative fluid resistance of the AM design relative to the conventionally-machined design. All experimental discharge coefficients are tabulated in Table 2.2.

While the AFM honing process resulted in higher discharge coefficients and geometric flow areas and consequentially lower pressure drops across the honed injector, it should be noted that the AFM process resulted in non-uniform sizes among the holes around the annulus. The spread in orifice sizes was about ±10% for both the fuel and oxidizer streams and the resulting spread in the orifice area ratios was approximately ±25% around the annulus. This may have led to mixture-ratio variations throughout the annulus which may have impacted detonation performance, as is discussed later in Section 2.4.

2.3 Experimental setup

A modular test article with an annular combustion chamber was developed to assess the rotating detonation characteristics of monomethylhydrazine (MMH) and dinitrogen tetrox-

ide (NTO). The test article is shown in Fig. 2.5. A drawing package for the test article components/assembly is provided in Appendix I.

The test article consists of a stainless-steel propellant manifold, in which various injector plates can be installed. The injectors assessed here were all unlike impinging doublets. The manifold features a central oxidizer plenum surrounded by an annular fuel plenum. The two plenums are sealed from each other by two O-ring seals, between which a nitrogen purge prevents incidental mixing of the propellants across the plenums in case of a leak. The annular combustion chamber is a modular design, assembled axially using stackable beryllium-copper spools. The modularity enables multiple configurations for testing (varying chamber length, width, and injector design), and grants the ability to quickly replace or modify the test article in the event of hardware loss. The aftmost inner spool can be replaced with an aerospike plug nozzle, which can be used to assess effects of downstream flow-area constrictions on the detonation behavior of the propellants. The test-article hardware

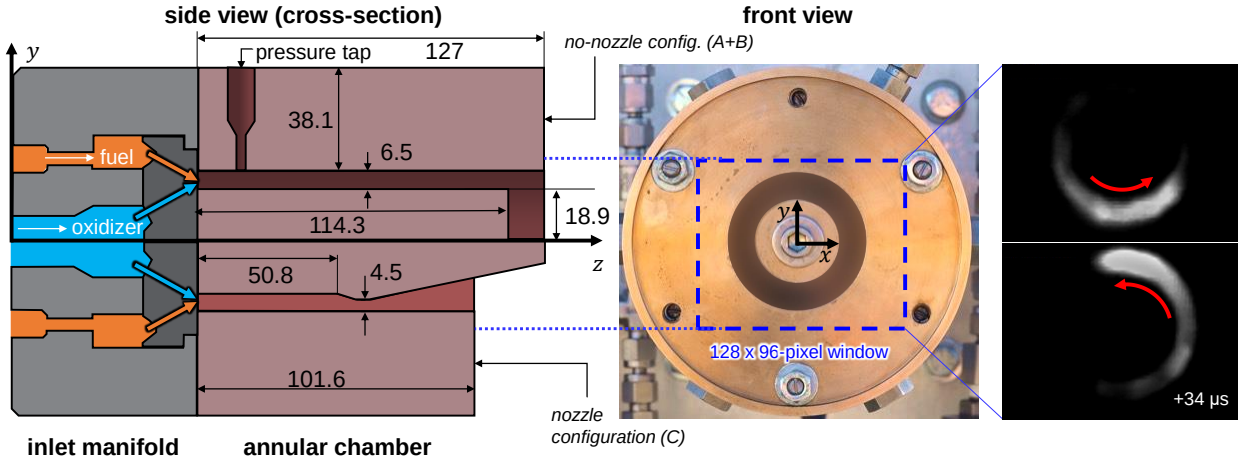

Figure 2.5: *Left*: Cross-section view of the MMH–NTO combustor with all dimensions in mm. The top half of the cross-section represents the chamber configuration with no nozzle. The bottom half of the cross section represents the chamber configuration with the nozzle. *Middle*: Downstream view of combustor, with the 128×96-pixel window captured by the high-speed camera indicated in blue. *Right*: Sample high-speed video stills indicating the presence of a detonation wave in the combustor.

Table 2.3: Relevant parameters for the combustor configurations used in the experiments. $C_{\mathrm{D}}A$ values refer to the product of the discharge coefficient and total geometric flow area. L_{outer} is the outer-body length. g_{min} and g_{max} are the minimum and maximum annular gaps respectively.

Configuration	A	B	C
Injector	unhoned	honed	honed
Nozzle	N	N	Y
$(C_{\mathrm{D}}A)_{\mathrm{fu}}$ (relative)	1.00	1.66	1.66
$(C_{\mathrm{D}}A)_{\mathrm{ox}}$ (relative)	1.31	2.17	2.17
L_{outer}, mm (in)	127 (5.0)	127 (5.0)	102 (4.0)
g_{min}, mm (in)	6.5 (0.255)	6.5 (0.255)	5.2 (0.204)
g_{max}, mm (in)	6.5 (0.255)	6.5 (0.255)	6.5 (0.255)

includes instrumentation spools, allowing for the connection of multiple sensors and pressure transducers, detailed in Section 2.3. The outer diameter of the annular chamber was 50.8 mm (2.00"), and the inner diameter was 37.8 mm (1.49"), yielding a nominal annular gap of 6.5 mm (0.255"). The length of the outer-body was 127 mm (5.0") for tests without the nozzle and 102 mm (4.0") for tests with the nozzle. The nozzle-less center-body was 89 mm (3.5") long. The nozzle had a throat diameter of 40.4 mm (1.59"), yielding a minimum annular gap of 5.2 mm (0.204") and a contraction ratio of 1.25.

Over the course of the test campaign, three test-article configurations (A, B, and C) were used. Configuration A used the unhoned AM injector without a nozzle. Configuration B used the honed AM injector without a nozzle. Configuration C used the honed AM injector with the aerospike nozzle. The pertinent information regarding the three configurations are summarized in Table 2.3.

Hot-fire testing was conducted at the Mojave Test Area (MTA) located near Cantil, CA. A portable test stand, termed the UCLA MMH–NTO Propulsion Test Platform, with a propellant-tank blow-down configuration was used to hot-fire the test article during the

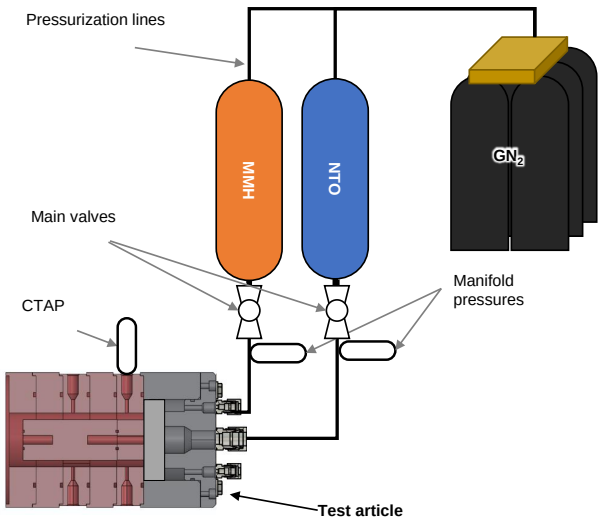

Figure 2.6: A simplified schematic of the propellant feed system including pressure transducers are shown on the right.

campaign. A simplified schematic of the test stand is shown on the right side of Fig. 2.6. Further detail of the design and operation of the Propulsion Test Platform are given in Appendix A. Images of the test stand along with relevant instrumentation are shown in Fig. 2.7. For this hot-fire testing campaign, MMH was used as the fuel, while a MON-3 (3% nitric oxide by weight) variant of NTO was used as the oxidizer. Prior to each hot-fire of the test article, knowledge of the fluid resistance of the injectors (obtained via cold-flow testing) was used to set the propellant-tank pressures to target specific propellant flow-rate combinations. This process set the mixture ratio and total flow rate for each test. Propellant tank pressures were set and maintained using a network of manually-operated regulators on the mobile test stand. Test duration was typically about 700 ms—long enough to allow the test article to reach a quasi-steady operating state, but short enough to mitigate thermal damage to the hardware. Each hot fire was followed by an automatic N_2 purge through both propellant lines to remove residual propellant from the lines, reducing personnel risk and corrosion of the test article. Sample images of various hot-fire tests can be seen in Fig. 2.8.

Various instrumentation was used to monitor combustion dynamics in the annular chamber, including (1) a high-speed visible-wavelength camera (Photron FASTCAM SA4) oper-

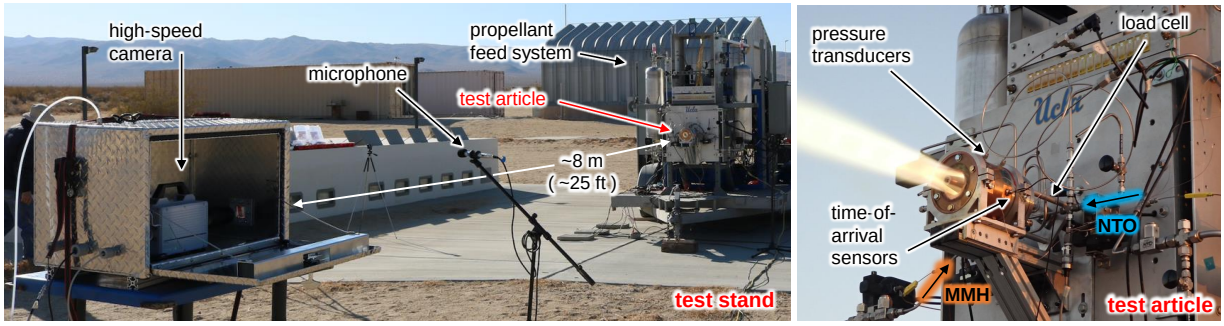

Figure 2.7: *Left*: Liquid bi-propellant test stand with instrumentation and test article labeled. *Right*: Test article during hot-fire test with propellant feed lines and instrumentation labeled.

Figure 2.8: Photographs of hot-fire tests conducted in March 2021 at the Mojave Test Area.

ating at a frame rate of 150 kfps with a resolution of 128×96 pixels (The effective spatial resolution of ∼0.5 mm), (2) two condenser microphones (Samson C02) with verified frequency measurement up to 24 kHz, and (3) time-of-arrival piezoelectric pins (Dynasen CA-1135) mounted in the outer chamber. An S-type load cell was used to measure the thrust produced by the test article Additionally, two capillary-tube attenuated pressure (CTAP) [70] measurements monitored the average combustion chamber pressure at two axial locations (13 mm / 0.5" and 64 mm / 2.5" from the injector face) using pressure transducers (Trafag 8252). This pressure was used along with propellant manifold pressure measurements to obtain a measurement of injector pressure drop Δp_i across each propellant manifold i which was used to determine the mass flow rate of each propellant $\dot{m}_i$ using the following equation, obtained by re-arranging Eqn. 2.1:

$$\dot{m}_i = (C_\mathrm{D} A)_i \sqrt{2 \rho_i \Delta p_i}. \tag{2.3}$$

Here ρ_i is the propellant density and $(C_\mathrm{D} A)_i$ refers to the effective flow area of each side of the injector, which can be predicted via compuational analysis or measured experimentally in cold-flow testing. The mass flow rate measurements of each propellant stream were summed to assess the total mass flow rate into the combustor. The oxidizer-to-fuel mixture ratio R was also calculated using the flow rate measurements:

$$R = \frac{\dot{m}_\mathrm{ox}}{\dot{m}_\mathrm{fu}}. \tag{2.4}$$

2.4 Results and discussion

Over the course of the measurement campaign, the mixture ratio, total flow rate, and chamber geometry were varied over approximately 50 hot-fire tests in which rotating-detonation behavior was observed. The conditions where detonation behavior was observed are plotted in Fig. 2.9. Notably, all observed detonation behavior arose spontaneously, without the use of a pre-detonation tube or an explosive charge to initiate the detonation behavior. The mixture ratio was varied from approximately 1.3 to 1.9. Beyond these mixture ratios,

combustion was not supported in the combustor. The total flow rate for which detonation behavior was observed ranged from approximately 0.27–0.53 kg/s (0.60–1.17 lbm/s) for configuration A and from 0.33–0.68 kg/s (0.73–1.50 lbm/s) for configurations B and C. At flow rates lower than the ranges indicated, detonation behavior was not observed. Configuration A supported detonation behavior at lower flow rates than configurations B and C, likely due to the higher resistance of the unhoned injector, which induced higher injector pressure drops for a given flow rate. This higher resistance can be expressed in terms of the stiffness of the injector (pressure drop over chamber pressure), which was generally 3–7 compared to the stiffness values of the honed injector which were 1–2. This higher pressure differential may have increased the injector's resistance to propellant back flow or flow-rate modulation due to the passage of detonation waves and may have additionally improved propellant mixing due to the increased momentum of the propellant streams. Both of these effects are likely to help support the formation and stability of detonation behavior [38, 53]. For configurations A and B, this lower flow-rate limit appeared to increase with increasing mixture ratio. The upper limit in flow rate was limited by the supply of ullage gas (N_2) and the maximum operating pressure of the system, ∼100 bar (1500 psi). The higher flow rates

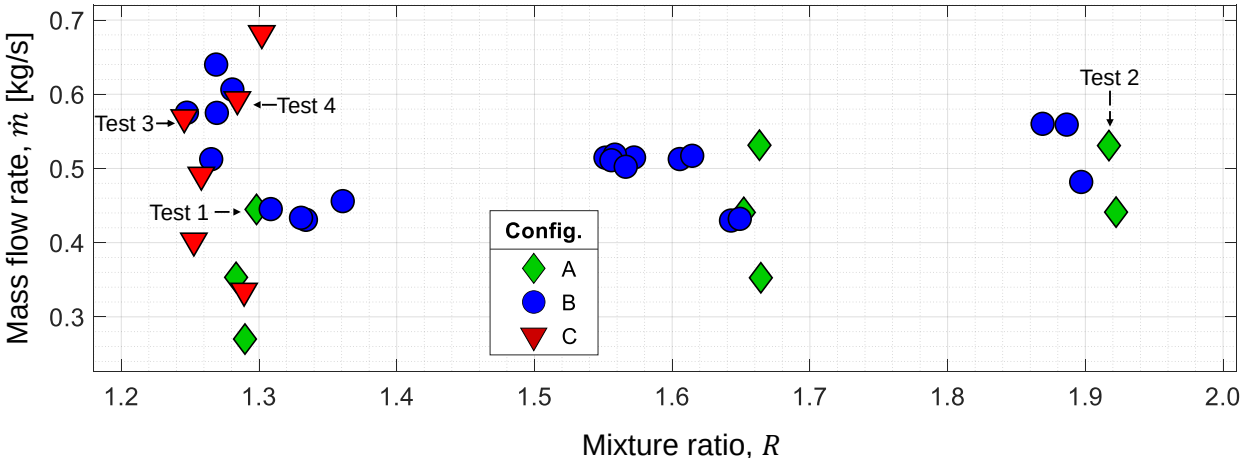

Figure 2.9: Plot of mixture ratio / mass flow rate conditions for which detonation behavior was observed. The color of the markers represents combustor configuration used for each test. Tests 1 through 4 are specifically labeled.

achievable for configurations B and C are due to the increased flow area ($C_{\mathrm{D}}A$) of the honed injector, which reduced the required upstream pressure for a given flow rate. Configuration A was able to produce consistent detonation behavior across the range of mixture ratios whereas configuration B had inconsistent behaviors at mixture ratios greater than 1.5. At these higher mixture ratios, similar operating conditions could sometimes provide divergent results, with detonations forming some of the time, but not all of the time. Configuration C with the nozzle supported detonation behavior only in a limited band of mixture ratios around 1.2–1.3. The inability of configurations B and C to consistently support detonation formation at high mixture ratios may be linked to the non-uniformity in the injector hole sizes caused by the honing process, which may have led to large discrepancies in the mixture ratio from injector element to element. This would have caused one or more element pairs to perform anomalously during the higher mixture ratio tests, which may have lead to locally non-detonable mixtures being produced.

Test hardware was inspected visually between tests and more closely examined at the close of the test series after hardware disassembly. Green emission in the exhaust plume suggested some atomic copper erosion, which would come from the inner or outer chamber spools, but for most of the test series this was not noticeable or measurable with regards to the hardware. Visual inspection during the test series revealed only minor discoloration near the injector face presumably associated with regions of high thermal loading. When changing injectors near the midpoint of the test series, the chamber pieces could be inspected more closely and were measured to be within original manufacturing tolerances. In the latter half of the test series, higher flow rates and chamber pressure conditions were examined. While test hardware appeared to sustain no noticeable damage upon visual inspection through the annulus, post-test disassembly revealed some erosion and pitting in the chamber center body near the injector face. Recessions on the order of 0.3 mm (0.01") deep, 4 mm (0.16") long, and 3 mm (0.12") wide were located immediately downstream of the injector face, in line azimuthally with the injector elements. While specific test conditions could not be assigned to this erosion, it is likely associated with test conditions at highest propellant flow rates.

Four tests in particular, labeled Tests 1–4, are examined in more detail below to illustrate the data-processing technique used to obtain meaningful information about the detonation behavior of the examined propellants. The flow conditions for these tests are indicated in Fig. 2.9. Test 1 was conducted with configuration A (unhoned injector, no nozzle) at a mixture ratio of 1.30 and a total flow rate of 0.45 kg/s (0.99 lbm/s). Test 2 was also conducted with configuration A, but at a mixture ratio of 1.91 and total flow rate of 0.53 kg/s (1.17 lbm/s). Test 3 was conducted with configuration C (honed injector, with nozzle) at a mixture ratio of 1.25 and a total flow rate of 0.57 kg/s (1.26 lbm/s). Test 4 was also conducted with configuration C, but at a mixture ratio of 1.28 and total flow rate of 0.59 kg/s (1.30 lbm/s).

2.4.1 Detonation detection via high-speed imaging

As mentioned above, the presence of rotating detonations was verified with multiple methods. The data from the microphones, time-of-arrival sensors, and high-speed videography could be analyzed for temporal frequency content using a Fast Fourier Transform (FFT). The top and middle rows of Fig. 2.10 indicate the frequency content obtained from a microphone and time-of-arrival sensor for a sample test (Test 1), indicating a peak in frequency content near 9.5 kHz, with apparent overtones near 19 kHz.

The data from the high-speed camera provided temporally and spatially resolved information about the detonation behavior present in the annulus. An image post-processing technique was used to measure the number and speed of the waves in the annulus [36]. The method entailed examining a 1000-frame ($\sim$6.67-ms) subsection of the video, drawn from the halfway point in the duration of the steady-state operation in the test. 1000 frames were chosen to 1) provide sufficient temporal frequency resolution on subsequent FFT analysis (temporal frequency is inversely proportional to data duration), and 2) provide a short enough interval such that any subtle motions of the camera during the test did not compromise the analysis (the annulus will move around the field of view on long enough timescales). First, the 1000 frames are averaged into a single image, and this average image is subtracted

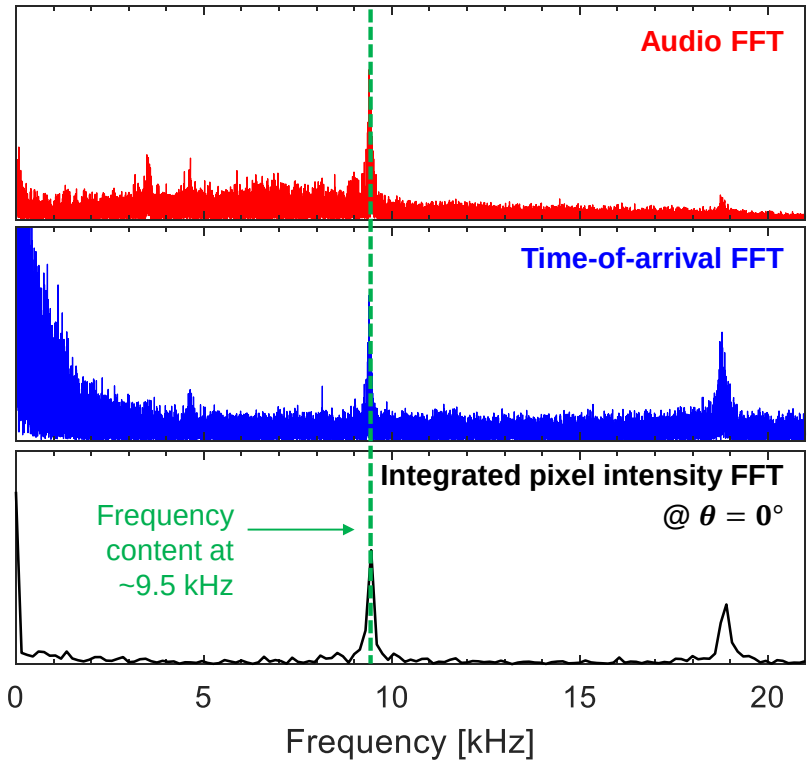

Figure 2.10: Fast Fourier Transform (FFT) of the audio, time-of-arrival, and luminosity signals for Test 1. All three signals share a common dominant frequency near 9.5 kHz.

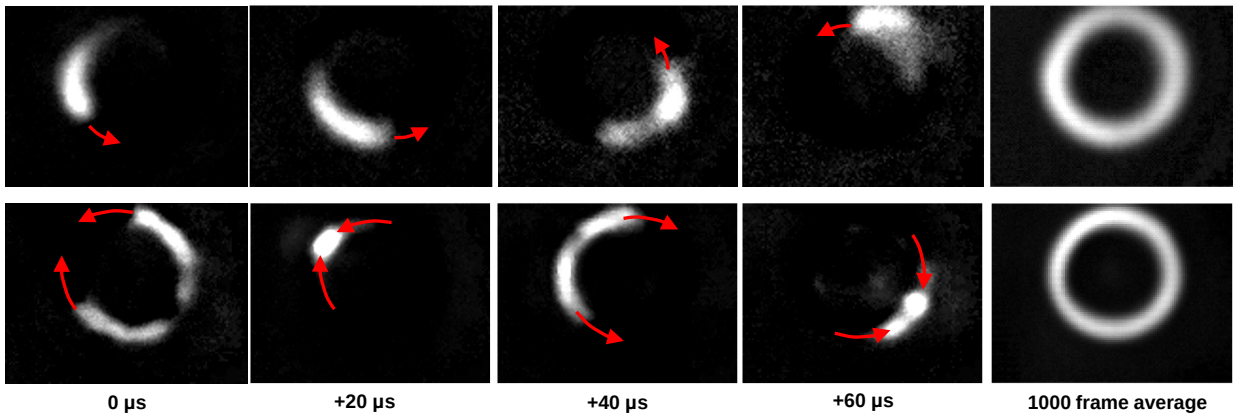

Figure 2.11: Video stills for Tests 1 (top) and 2 (bottom) The fifth image is the averaged image over 1000 frames.

from each of the 1000 individual frames, highlighting the differential light intensity associated with periodic disturbances in the annulus. Representative single video frames from Tests 1 and 2 are shown in Fig. 2.11, along with the corresponding 1000-frame averaged image. The location of the annulus in the image is found by noting the pixels associated with maximum light intensity in the average image and performing a Taubin fit [118] on these points to find the center and radius of the circle that defines the annulus.

The coordinates of the circle are used to generate a polar mesh dividing the image into angular sectors, each with an angular size of 3.6°. The pixel intensity located in each sector was integrated to obtain a map of integrated intensity versus angular position θ. This was performed for each frame and the results were compiled into a matrix which contained integrated pixel intensity values corresponding to each angular location and each frame. These results could be plotted as a contour plot called a "detonation surface" [36]. Sample detonation surfaces are shown in Fig. 2.12.

2.4.2 Detonation modal characteristics

Four detonation surfaces are shown here as observed across the four different tests with varying flow condition and chamber geometry. In these detonation surfaces, wave behavior can be readily observed for tests where rotating detonations were produced as indicated by lines of high light intensity propagating with a finite slope in the angular direction. The slope of these lines is inversely proportional to the propagation speed of these periodic disturbances. In the four different tests, four different wave behaviors can be observed. In Test 1, a single wave is observed to propagate around the annulus in the counter-clockwise (CCW) direction, which is denoted as the positive angular direction in the detonation-surface plot (bottom left to top right). This single-wave behavior is the dominant behavior for configuration A. Configuration B also displays the single-wave mode for low mass flow rates. In Test 2, one wave is observed propagating CCW with another propagating clockwise (CW). This mode is known as a "counter-propagating" or "slapping" mode [37]. The slapping mode is the dominant mode for configuration B, with configuration A displaying this mode only for the

highest total flow-rate value and configuration C displaying this mode only for the lowest total flow-rate value. In Test 3, a single dominant detonation wave propagates CCW around the annulus, with two slower waves travelling in the opposite CW direction. In Test 4, two sets of counter-propagating waves are shown in the annulus, with two waves travelling CW and two waves travelling CCW. The wave modes involving more than two waves are only seen with configuration C, implying some link between the downstream flow restriction of the nozzle and the development of more than two detonation waves.

In order to extract quantitative information about the wave behavior from the detonation-surface plots, a 2-D Fast Fourier Transform was performed on the data, which entailed performing a time-based FFT on the integrated intensity for each angular sector, followed by performing a spatial FFT on the azimuthally-resolved results. This allowed for the extraction of spatial (or angular) and temporal frequencies in the data, as performed by Bennewitz et al. [36]. The bottom row of Fig. 2.10 shows the time-based FFT for the angular sector at position $\theta = 0°$, which corresponds to the location of the time-of-arrival sensor and the right-most point on the annulus when viewed by the high-speed camera. The frequency content of the optical signal matches those of the time-of-arrival and microphone data. The 2-D FFT is visualized for three tests in Fig. 2.10, where the FFT for a single-wave, counter-propagating

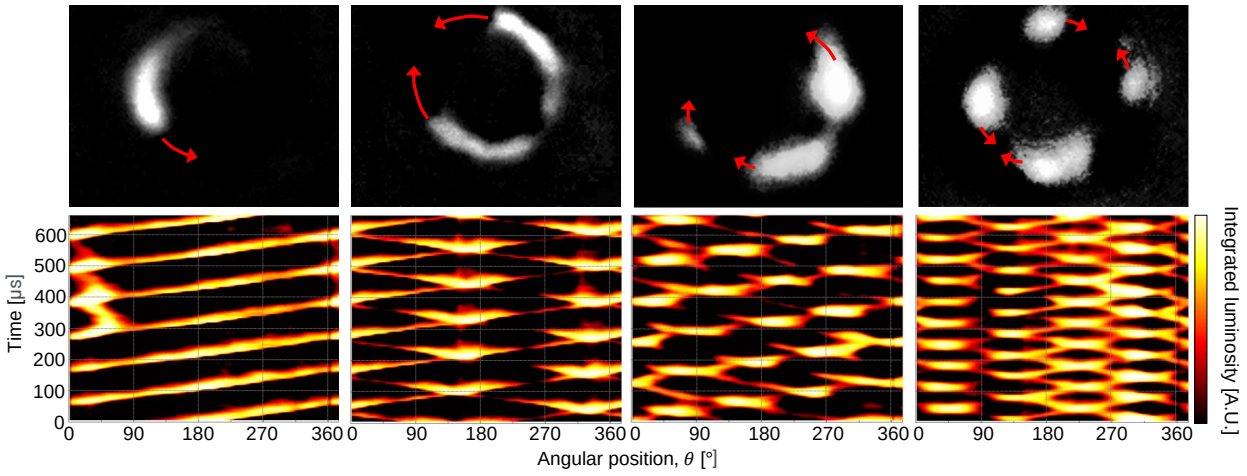

Figure 2.12: *Top*: Images from Tests 1–4 (left to right) indicating single-, two-, three-, and four-wave behavior. *Bottom*: Corresponding detonation surfaces for a ∼600 μs time interval.

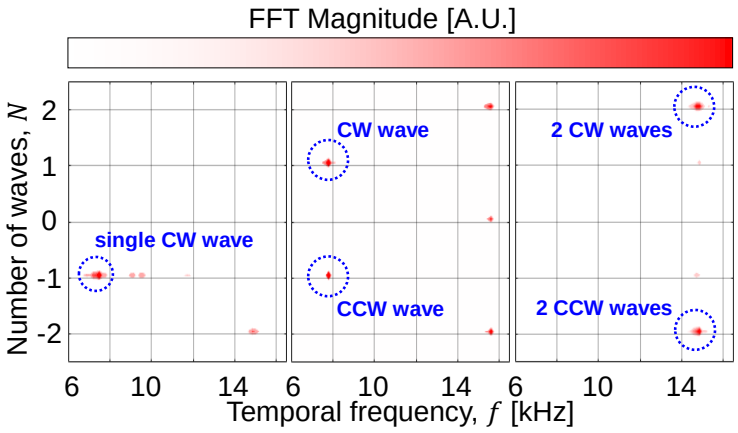

Figure 2.13: 2-D Fast-Fourier Transform of detonation-surface plot for a single clockwise wave (*left*), two counter-propagating waves (*middle*), and four counter-propagating waves (*right*).

two-wave, and counter-propagating four-wave mode can be seen. Each maximum on the 2-D FFT surface plot corresponds to a unique set of co-rotating waves in the annulus. If the spatial frequency (in units of $^{\circ -1}$) is multiplied by the total angle associated with the annulus (360°), then the number of waves n associated with the detonation mode can be extracted.

Once the number of waves is known, and the temporal frequency f of the mode is known, the wave-speed U associated with the mode can be obtained with the following equation:

$$U = \frac{\pi D f}{n} \tag{2.5}$$

where D is the average annulus diameter. For Test 1, a single CCW wave traveling at ∼1.29 km/s was identified using the FFT. For Test 2, two counter-propagating waves are identified as travelling at ∼1.22 km/s. For Test 3, the CCW wave was found to travel at ∼1.13 km/s and the two CW waves were found to travel at ∼1.00 km/s. For Test 4, all four of the waves the annulus were found to travel at ∼1.01 km/s. These wave-speeds are on the order of 50–60% of the ideal one-dimensional wave-speeds predicted by Chapman-Jouguet detonation theory for gas-phase MMH–NTO detonation [100] and are 3–4 times the gas-phase speed of sound of the MMH-NTO mixture.

Figure 2.14 shows the wave-speeds obtained from the high-speed video plotted against

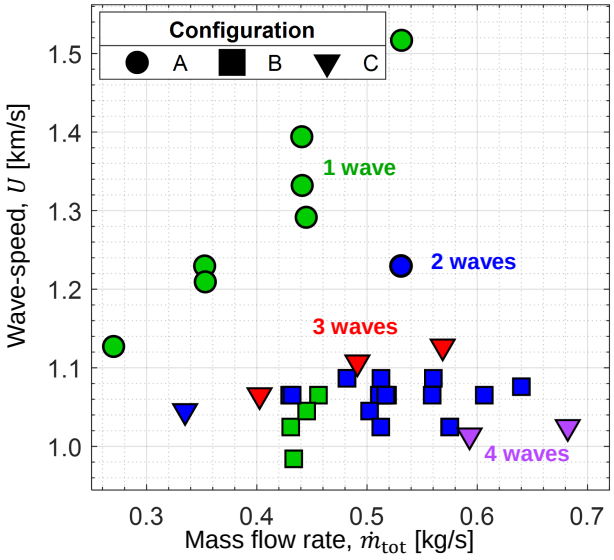

Figure 2.14: Wave-speed *versus* mass flow rate. Combustor configurations are indicated by marker shape and various wave modes are indicated by the marker color.

mass flow rate, with the number of waves for each test condition indicated by the color of the marker and the combustor configuration indicated by the shape of the marker. In some of the multi-wave mode cases, not all waves shared the same speed (this is always true for the three-wave mode). For these cases, the speed of the dominant/fastest wave [119] was plotted. For a given combustor configuration, a general trend is observed that for higher mass flow rates, there is an increased number of detonation waves. This trend is consistent with previous RDRE studies [37] wherein it was postulated that relatively fixed wave-speeds (perhaps limited by evaporation rate, mixing rate, reaction rate, thermodynamics, or some other intrinsic rate-limiting factor) result in the need for an increasing number of waves to consume more propellant per unit time at higher mass flow rates. Configuration A primarily supported the presence of single detonation waves, with a single test resulting in the formation of two detonation waves at the highest tested flow rate, ∼0.53 kg/s (1.17 lbm/s) with this configuration. With a few exceptions, configuration B featured single-wave behavior at flow rates below 0.50 kg/s (1.1 lbm/s), and only exhibited two-wave behavior above 0.50 kg/s. Notably, all of the single-wave cases featured a counter-clockwise propagating wave. Configuration C did not demonstrate any single-wave behavior and uniquely produced multi-wave

modes. This may have been caused by reflections of the detonation waves and associated shock waves off the converging portion of the nozzle [120, 59].

The wave-speeds associated with the unhoned injector (configuration A) were generally higher than the wave-speeds associated with the honed injector (configurations B and C). It is also noteworthy that the range of wave-speeds for the honed injector were much lower than the range of wave-speeds associated with the unhoned injector. For certain wave-modes and combustor configurations, a positive correlation is noted between wave-speed and mass flow rates. This is true for the single-wave cases for configurations A and B, as well as for the three-wave cases for configuration C. In general, there is also an inverse correlation between the wave-speed and the number of waves in the annulus for a given combustor configuration, although this trend is more prominent for configurations A and C than for configuration B.

2.4.3 Performance evaluation

In addition to the high-speed video data, axial thrust performance during detonation-mode operation was also assessed using an S-type load cell with a 1000-lbf (4.45-kN) operating range. A representative thrust curve is shown in Fig. 2.15 with corresponding average chamber pressures. In general, each test comprised an initial transient startup period lasting approximately 0.2 s, after which quasi-steady-state detonation behavior was observed, corresponding to a near-constant thrust measurement. At the conclusion of each test, a stepped-down thrust associated with the N_2 purge is observed. The steady thrust values were on the order of 1 kN (100s of lbf) across various test conditions. Thrust measurements F were combined with the total mass-flow-rate measurement $\dot{m}_{\text{tot}}$ to measure the specific thrust F_{sp} delivered by the test article using the following equation, analogous to a specific impulse [1, 3]:

$$F_{\text{sp}} = \frac{F}{\dot{m}_{\text{tot}}}. \tag{2.6}$$

Specific thrust values higher than 2 km/s were achieved, albeit limited by a lack of optimal expansion (as discussed later).

Specific thrust normalized against the maximum value obtained during the test series

is plotted versus total mass flow rate in Fig. 2.16, with the various wave modes identified. From this plot, a few key trends are noted. First, a general correlation between the total flow rate and thrust generation per unit mass flow rate is noted, indicating more efficient energy and/or momentum conversion with increasing propellant flow rate. Second, the total number of waves also generally corresponds with higher performance. This observation aligns with the results of other RDRE studies [36, 49], which have noted that a higher number of waves results in higher-frequency operation, leaving fresh propellants in contact with hot combustion products from previous detonation cycles for less time, potentially mitigating parasitic deflagration losses. It is noted that all of the multi-wave modes observed in these experiments are counter-propagating in nature and that the increased performance with additional waves may not apply to cases where co-rotating waves are generated. In terms of combustor configurations, configuration C is the best performer, which may be attributable to either the higher number of detonation waves generated when the nozzle is present or the increased thrust production as a result of additional flow expansion due to the presence of

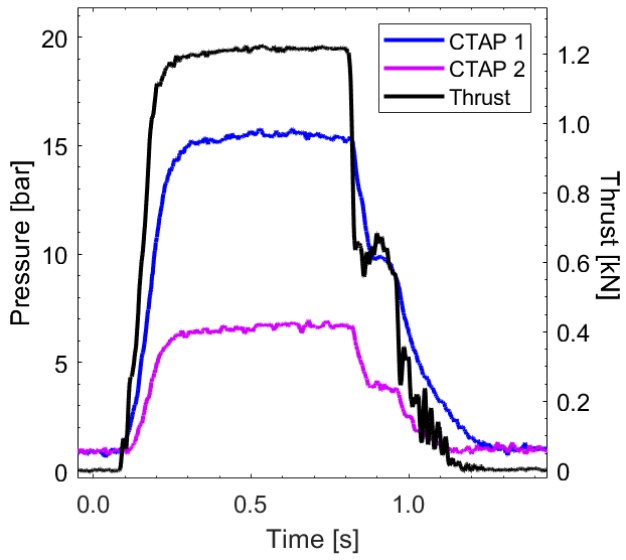

Figure 2.15: Representative thrust and capillary-tube attenuated pressure (CTAP) measurements at locations 13 mm (#1) and 64 mm (#2) from injector. Time zero indicates when propellant valves are opened.

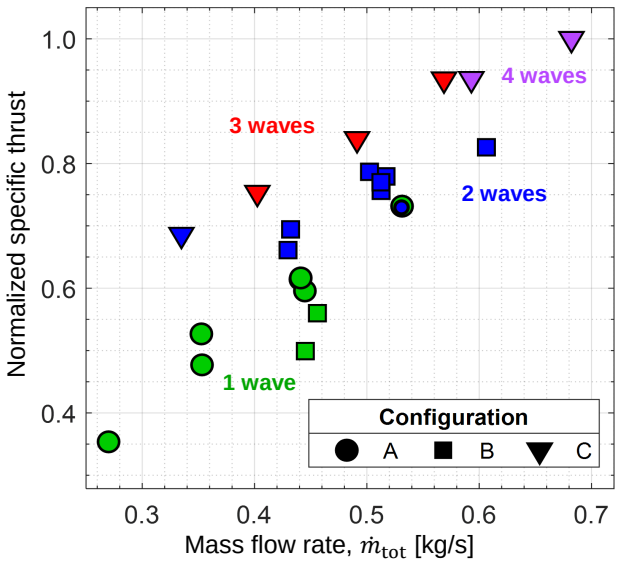

Figure 2.16: Normalized specific thrust *versus* total propellant flow rate. Combustor configurations are indicated by marker shape, and various wave modes are indicated by the marker color.

the diverging section of the nozzle. Configuration A appears to be the worst performer in this regard despite the high wave-speeds it produced. This may be due to the inability of the unhoned injector to operate at higher flow rates where the higher-performing multi-wave modes may be achievable. However, for the single-wave mode operation and a propellant flow rate of ∼0.45 kg/s (1 lbm/s), configuration A out-performs configuration B. This may suggest that the unhoned injector is allowing the propellants to mix more uniformly than the honed injector due to the consistent hole sizes of the injector elements around the annulus. It is also worth noting that performance did not vary significantly across the range of mixture ratios where detonation behavior was observed.

In order to isolate the performance associated with the combustion process from the performance enhancement associated with downstream flow expansion, the average chamber pressure P_C can be estimated based on the capillary-tube attenuated pressure (CTAP) measurement located 13 mm (0.5”) from the injector face. Figure 2.15 shows represetative time-resolved CTAP measurements at both axial locations. The steady-state CTAP measurements generally ranged from 3 to 18 bar (40–260 psi) near the injector face across the

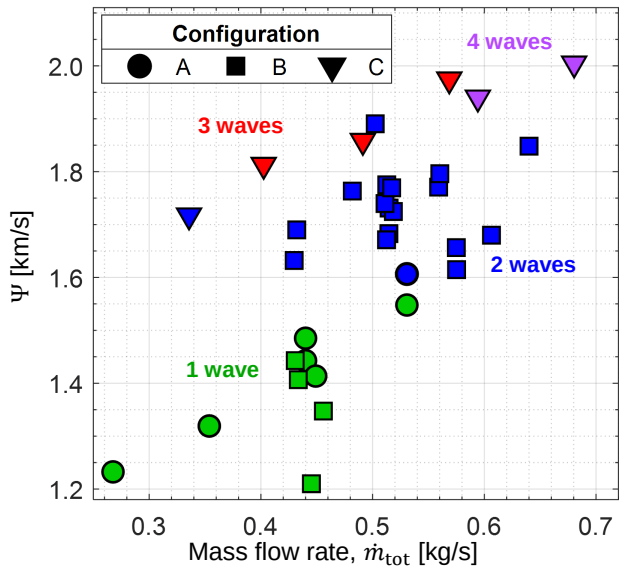

Figure 2.17: Ψ *versus* total propellant flow rate. Combustor configurations are indicated by marker shape, and various wave modes are indicated by the marker color.

various test condition. The CTAP measurements typically featured noise on the order of ± 0.15 bar (± 2 psi), which amounted to an uncertainty on the order of 1–5 %. The upstream CTAP measurement can be used to calculate a metric analogous to a characteristic velocity, c^*, which has traditionally been used as a metric of combustion performance [1, 3]. Although not able to capture the pressure extremes associated with individual detonation waves in the annulus, this CTAP measurement can be used to assess the relative performance of the combustor for various test conditions, which we define by the following figure of merit Ψ:

$$\Psi = \frac{P_C A_{min}}{\dot{m}_{tot}}. \tag{2.7}$$

Here, A_{min} is the cross-sectional area of the combustor at location of minimum area (for configurations A and B, this is the cross-sectional area of the chamber and for configuration C, this is the cross-sectional area at the nozzle throat), and $\dot{m}_{tot}$ is the total mass flow rate into the combustor. Though analogous to c^*, Ψ is not directly comparable since the measurement of P_C does not capture the stagnation pressure of the combustion gases, which has a spatial and temporal distribution. Ψ is plotted versus total mass flow rate in Fig. 2.17, with the various wave modes and combustor configurations identified. It can be seen that

configuration C is generally the best performer, indicating that the increased number of detonation waves and the associated detonation efficiency is a strong contributor to the overall performance of the combustor.

In order to assess the ability of the engine to convert the average pressure near the injector face into useful thrust, we define another performance metric, τ, as the ratio of thrust produced F to the product of the upstream CTAP pressure P_{C} and minimum combustor cross-sectional area A_{min}:

$$\tau = \frac{F}{P_{\mathrm{C}} A_{\mathrm{min}}}. \tag{2.8}$$

τ is analogous to a thrust coefficient [1, 3]; however—as with the calculation for Ψ—it is not directly comparable since P_{C} is only an averaged value of the chamber pressure at a particular axial position. Values of τ normalized against the maximum value obtained in the campaign are plotted against total flow rate in Fig. 2.18. It can be seen that τ varies most strongly with total propellant flow rate, which can be explained by the increased chamber pressures at higher flow rates which allow for increased levels of gas expansion. Values of τ were lower than the thrust coefficients predicted for equivalent pressure ratios for a perfectly-

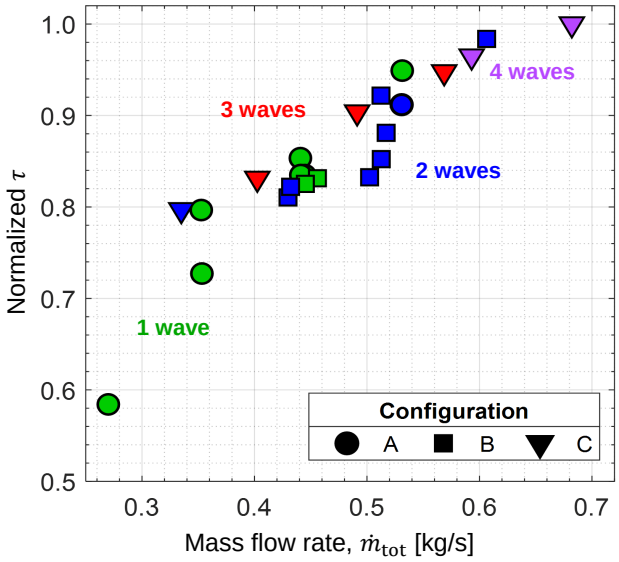

Figure 2.18: Normalized τ *versus* total propellant flow rate. Combustor configurations are indicated by marker shape, and various wave modes are indicated by the marker color.

expanded deflagration-based rocket [5]. This was to be expected as the nozzle configuration was not designed to optimize expansion, but rather to examine upstream influences of flow constriction on combustion. Notably, configuration C with the nozzle did not exhibit a higher value for τ than the other configurations at a given flow rate, clearly indicating that the nozzle needs to be further optimized to augment thrust production compared to the nozzle-less configurations.

Specific thrust F_s is the product of Ψ and τ. The individual assessments of Ψ and τ suggest two reasons for the increase in F_s with flow rate—the combustion/detonation efficiency increases with an increased number of detonation waves at higher flow rates (likely due to decreased parasitic deflagration) and enhanced gas expansion due to the higher chamber pressures achieved at higher flow rates.

2.4.4 Deflagration-to-detonation transition timescales

In this section, assessment of deflagration-to-detonation transition timescales is made across the various test conditions. A sample CTAP measurement (made 13 mm (0.5") downstream of the injector face) from a hot-fire test is shown in the top of Fig. 2.19. Ignition is seen to occur approximately 70 ms after the main propellant valves are opened, as evidenced by the rapid increase in chamber pressure and in light captured by the high-speed camera at that time. Approximately 174.5 ms after the main propellant valves were opened, a change in the combustion behavior is noted. High-speed camera data capturing this transition are shown in the bottom of Fig. 2.19. Initially, at 174.32 ms, no periodic behavior is observed, and the light intensity is relatively uniformly distributed around the annulus. At around 174.47 ms, the uneven distribution of light intensity around the annulus can be observed, with light intensity being concentrated in the bottom-right sector of the annulus. This bright region begins to propagate in a counter-clockwise direction around the annulus. By 174.60 ms, the bright region increases significantly in intensity and by 174.64 ms the disturbance becomes steep-fronted and continues to propagate around the annulus until propellants are cut-off from the combustor around 600 ms later. This wave is observed to propagate at supersonic

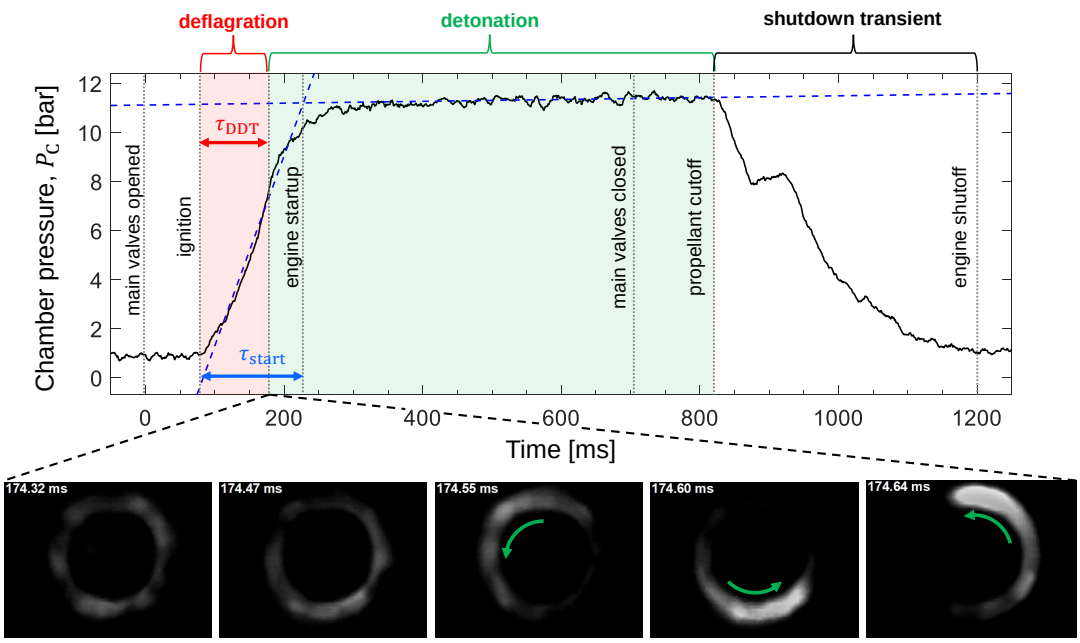

Figure 2.19: Chamber pressure data for a sample MMH–NTO hot-fire test (*top*), with key events labeled. The deflagration-to-detonation transition ∼174 ms after the main valves are commanded open is shown in more detail with stills from the high-speed camera footage (*bottom*).

speeds, approximately 2000 m/s, implying that it is a detonation wave.

Additionally, at around 175 ms, the frequency spectrum associated with the microphone and time-of-arrival sensor data develops a peak near 10 kHz, which corresponds to the frequency at which the wave seen propagating by the high-speed camera travels around the annulus, providing further evidence of the presence of a detonation wave. The data therefore indicate that the formation of a spontaneous detonation wave can occur in approximately 105 ms. This delay between ignition and the formation of a detonation wave is defined as the "detonation formation time" τ_{DDT}. The above video analysis accompanied by analysis of the microphone and time-of-arrival data was repeated for each of the test conditions to identify the detonation formation time.

In order to decouple the transition from deflagration to detonation from the startup transient of the combustor, the time required for the combustor to reach steady state was assesed.

This assessment was made using the CTAP trace for each test, as indicated in Fig.2.19. For each CTAP trace, the ramp-up period of the engine was identified by observing when the chamber pressure first rose above atmospheric pressure (noted as the time corresponding to ignition) and observing when the rate of pressure increase began to level off. A linear fit was made to this region. The beginning of the steady phase of the pressure trace was identified by noting when the rate of change of pressure increase arrived at zero. The end of the steady phase was marked by when the rate of change of pressure began to significantly decrease. A linear fit was also made through the steady phase, and the time corresponding to the intersection of the best fit lines for the ramp-up phase and steady phase was used as a metric for how long engine startup took, which we denote as τ_{start}. The aforementioned linear fits and τ_{start} are indicated in Fig. 2.19. The combustor startup times are generally between 130 ms and 320 ms.

To illustrate how the detonation formation time compared to the combustor startup time, τ_{DDT} was normalized by τ_{start}. These normalized values are plotted against propellant flow

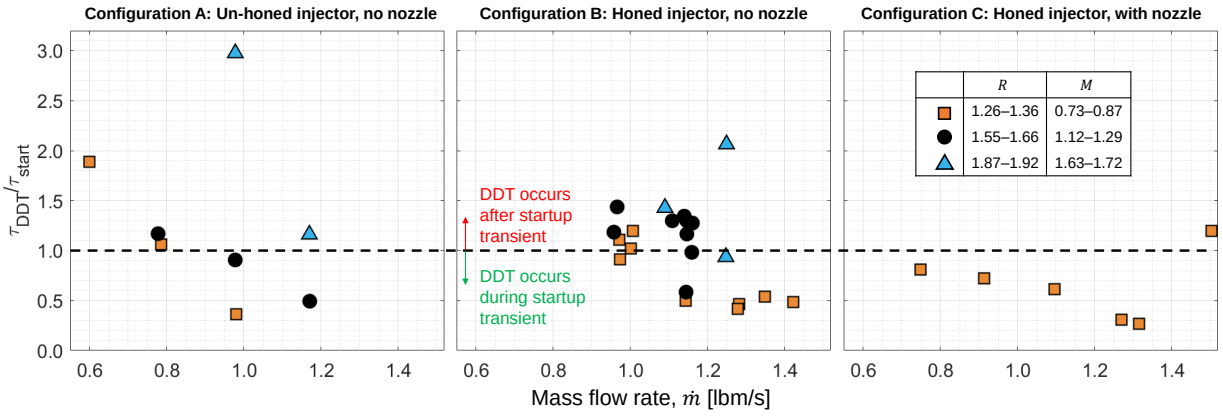

Figure 2.20: Plot of detonation formation times normalized by engine startup time *versus* mass flow rate for the three combustor configurations. The marker colors represent the mixture ratio groupings of the tests, with black points representing the nominal mixuture ratio near 1.6 (momentum ratio near 1.2), orange representing a more fuel-rich mixture ratio near 1.3 (momentum ratio near 0.8), and blue representing a more fuel-lean mixture ratio near 1.9 (momentum ratio near 1.7).

rate in Fig. 2.20. Values $\tau_{\mathrm{DDT}}/\tau_{\mathrm{start}}$ less than unity indicate that deflagration-to-detonation transition occurs during the startup transient of the combustor, whereas value greater than 1 indicate that DDT occurs after the engine has reach steady state. The marker color distinguishes the tests by the approximate mixture ratio. Black markers represent tests with mixture ratios R between 1.55 and 1.66, which is a nominal mixture ratio for MMH–NTO rocket systems [121]. Orange markers represent tests with R = 1.25–1.36, which is more fuel-rich than the nominal mixture ratio. Blue markers represent tests with R = 1.87–1.92 which is more fuel-lean than the nominal mixture ratio.

By examining the leftmost window of Fig. 2.20, which corresponds to combustor configuration A, with the unhoned injector, a few trends can be observed. For a given mixture ratio range, the relative detonation formation time is seen to decrease with increasing propellant flow rate. This could be attributed to the higher chamber pressures achieved at higher propellant flow rates, which has been observed to promote transitions from deflagration to detonation [122]. Additionally, the nominal mixture ratio generally results in the lowest detonation formation times, although at higher flow rates, the richer mixture ratios begin to yield similar relative formation times. The leaner mixture ratios perform considerably worse, with the longest relative detonation formation time approximately three times greater than the combustor startup time being produced at these mixture ratios (corresponding to a detonation formation time of approximately 600 ms). This is a bit counter-intuitive, as this mixture ratio is closer to the stoichiometric value of 2.5, which implies higher propellant reactivity which increases reactant detonability [123]. It is postulated that the mixing performance is the limiting factor at these higher mixture ratios, not chemical kinetics. This is evidenced by the fact that at slightly higher mixture ratios (above 2), ignition did not occur, and unburned propellant was ejected from the combustor, implying extremely poor mixing.

The mixing performance of the injector can be predicted by examining the *momentum ratio* M, which is the ratio of the momentum flux of the oxidizer stream to the fuel stream. For an injector where the fuel and oxidizer streams are angled to the injector plane by the same amount, M can be expressed in terms of the oxidizer and fuel flow rates $\dot{m}_{\mathrm{ox}}$ and $\dot{m}_{\mathrm{fu}}$,

as well as the oxidizer and fuel injection velocities v_{ox} and v_{fu} as:

$$M = \frac{\dot{m}_{\mathrm{ox}} v_{\mathrm{ox}}}{\dot{m}_{\mathrm{fu}} v_{\mathrm{fu}}}. \tag{2.9}$$

For each propellant stream i, the injection velocity v_i can be estimated using the following relationship:

$$v_i = \sqrt{\frac{2\Delta p_i}{\rho_i}}. \tag{2.10}$$

Combining Equations 2.1, 2.9, and 2.10 yields a simplified expressure for M:

$$M = \frac{\rho_{\mathrm{fu}} (C_{\mathrm{D}} A)_{\mathrm{fu}}}{\rho_{\mathrm{ox}} (C_{\mathrm{D}} A)_{\mathrm{ox}}} R^2. \tag{2.11}$$

From cold-flow measurements and knowledge of the propellant densities, the coefficient in front of R^2 is approximately 0.466 for both injectors. This enables direct calculation of the momentum ratio from the mixture ratio.

For ideal mixing, the momentum ratio of an injector should be near unity. For both of the injectors, an average momentum ratio of 1 is obtained at a mixture ratio near 1.45. At the nominal mixture ratio (R = 1.55–1.66), the achieved momentum ratio was between 1.12 and 1.29. For the richer mixture ratios (R = 1.26–1.36), the achieved momentum ratio was between 1.12 and 1.29. For the leaner mixture ratios (R = 1.87–1.92), the achieved momentum ratio was between 1.63 and 1.72. The exceptionally high momentum ratio for the most lean (near stoichiometric) conditions helps explain the long DDT times, as mixing performance was likely poor for these tests. This poor mixing performance also explains the lack of ignition at mixture ratios greater than 2, as the momentum ratio would have exceeded 1.85.

In the middle window of Fig. 2.20, the relative detonation formation time for combustor configuration B, with the honed injector, is plotted against propellant flow rate. Here the richer mixture ratios perform the best, with the lowest relative detonation formation times at any given propellant flow rate. Tests at the leaner mixture ratios again yield the longest relative detonation formation time at a given flow rate. The nominal mixture ratios have DDT times between those of the richer and leaner mixture ratios. Again, a general trend

of decreasing τ_{DDT} is observed with increasing flow rate, particularly for the richer mixture ratios.

The tests conducted with configuration C (honed injector with nozzle) only supported detonations at the richer equivalence ratios. In general, configuration C features the relative lowest detonation formation time of the three combustor configurations, with some tests featuring detonations forming within the first 32% of the startup transient, corresponding to formation times as low as 65 ms. This might be attributable to the increased chamber pressure associated with the presence of the downstream flow constriction provided by the nozzle, which increases reactant detonability. For all tests except one (which happened to feature the lowest value for τ_{start}), the detonation formation time was shorter than the combustor startup time when the nozzle was used, which corresponds to detonation formation times below 215 ms.

Overall, these results indicate that detonation behavior can occur during the process of engine startup if the engine is operated at appropriate flow conditions for proper mixing, and at high enough propellant flow rates or chamber pressure. Lastly, we should note that the observed timescales themselves are likely dependent on mixing, valve opening times, annulus width, injector stiffness, and feed system geometry that are somewhat specific to our facility and test-article design. The reader is thus cautioned in using these values as absolute reference.

2.5 Summary

An impinging injector produced by additive manufacturing was designed using computational analysis to assess the rotating detonation characteristics of the space-storable hypergolic propellants MMH and NTO in an annular combustor. Non-reacting, three-dimensional computational fluid dynamics analysis was performed to show the design increased forward discharge coefficient and diodicity compared to an analogous baseline injection design developed for conventional machining. Two new injectors were additively manufactured based on

this design, one of which went through an extrude-hone process to reduce internal surface roughness and one that did not. Cold-flow testing results showed that a smoothly tapered injector element enabled by additive manufacturing could reduce pressure loss, and that the extrude-honing process further increased the discharge coefficient to realize the hydraulic gains estimated by simulations. Both injectors were hot-fire tested using a mobile test stand supplying monomethylhydrazine and a MON-3 variant of dinitrogen tetroxide as the fuel and oxidizer respectively. High-speed videography was used to identify the number of waves present in the combustor annulus and the speeds of these waves. Additionally, mass flow rate and thrust measurements were obtained and used to calculate specific thrust and relative performance values. These measurements indicated a positive correlation between the number of waves in the annulus and the mass flow rate of propellants and specific thrust, which is consistent with previous results presented in the available literature.

Additionally, the range of operating conditions and wave-speed was shown to depend on the type of injector used. In particular, the non-uniformity in hole sizes related to the honing process was seen to reduce the detonation wave-speed and operability over a wide range of mixture ratios. Additionally, it was seen that at lower flow rates, detonation behavior was not observed, with the unhoned injector achieving lower flow rates than the honed injector, suggesting that higher flow resistance mitigates post-detonation injector flow-rate reduction.

It was also observed that the presence of a downstream flow constriction in the form of a plug nozzle restricted the range of mixture ratios where detonation was supported. However, the nozzle also led to the formation of three-wave and four-wave modes, which correlated to higher combustor performance. It is noted that while the performance of the various combustor configurations are compared in this work, more exhaustive testing over a wider range of operating conditions is required to make a definitive conclusion regarding which configuration is the best performer. In particular, it is not completely clear if the performance increases exhibited by the nozzle configuration are due to the increased number of waves or due to the effect of adding a flow constriction on the fluid mechanics of the exhaust flow.

Timescales associated with the spontaneous transition between a deflagration and detonation combustion mode were also examined experimentally. Results suggest that detonation waves can form spontaneously on the orders of tens to hundreds of milliseconds after ignition, which in many cases were well below the time required for the engine to ramp up to its nominal operating condition, which bodes well for application of hypergol-fueled RDREs to in-space propulsion systems. Additionally, trends with propellant mixing, flow rate, and combustion chamber geometry were noted, which imply that deflagration-to-detonation transition occurs more quickly at higher flow rates, when a downstream flow constriction is present (most likely associated with higher chamber pressure), and near injector momentum ratios of 1. The latter observation is presumed dependent on injector design.

This work represents an early step in the development of practical RDREs using space-storable liquid propellants for in-space propulsion applications, demonstrating the ability to initiate and sustain continuous detonation with these hypergolic propellants over a range of conditions. The effort also highlights potential of additive manufacturing for RDRE applications, as well as some new considerations for manufacturing process control. Future work will involve improving the consistency of the surface-treatment process and further increasing the diodicity of the propellant injectors to enable detonation behavior of liquid propellants at lower injection pressures, increasing the technical readiness level of RDREs towards practical use in various propulsion systems.

In the remaining chapters, the focus will be turned towards the development of high-speed quantitative laser diagnostics for RDRE/combustion environments.

CHAPTER 3

Estimation of detonation cell size for liquid hypergolic propellants

The contents of this chapter have been published by the journal ***Proceedings of the Combustion Institute*** *[99] under the full title "Detonation cell size of liquid hypergolic propellants: estimation from a non-premixed combustor".*

3.1 Introduction

Detonation cell size (λ) is a characteristic length scale that is fundamental to reactant or propellant combinations and is important to designing detonation combustors for such propulsion or energy systems [124]. For example, in a ducted or tubular flow, as may be used in a pulse detonation engine, the minimum diameter that supports detonation formation is λ/π [125]. In an annular geometry—as typically used for a rotating detonation engine—the cell size also helps determine critical combustor dimensions. The minimum chamber diameter is $\sim 40\lambda$, the minimum annular gap size is $\sim 2.4\lambda$, and the minimum chamber length is $\sim 24\lambda$ [21]. Detonation cell size has been characterized for a range of reactant combinations, including fuels such as hydrogen and hydrocarbons detonated in air or pure oxygen [126, 127]. However, detonation cell sizes for liquid hypergolic propellants lack experimental study, in part due to inherent complexities.

For most fuels and oxidizers, detonation cell size can be measured directly. Premixed reactants may transition to a detonation combustion mode and cell size can be observed using "soot foil" traces, which involve placing soot-covered sheets of foil in a detonation tube [128].

When a detonation wave passes over the soot foil, its cellular structure leaves an imprint which can be used to measure the average cell size for a particular reactant combination. Alternative methods to measure cell size have involved optical diagnostics including Schlieren imaging, planar laser-induced fluorescence, and Rayleigh scattering [129, 130].

As mentioned in Chapter 2, for in-space chemical propulsion, hypergolic propellants are desired for fast and reliable ignition. Complications for direct observation of detonation cell size for these propellants are: (1) the propellants cannot be premixed, (2) their toxicity have precluded much research with these reactants, and (3) the detonation cell sizes are expected to be very small (<0.1 mm). The latter arises from the relationship of detonation cell size and required ignition energy for combustion. Reactant combinations with relatively large required ignition energy will have a long ignition delay and induction length, leading to a large cell size [131]—the converse is also observed. For example, hydrocarbon detonation in air at 1 atm produces cell sizes of 10–1000 mm, whereas hydrocarbon detonation in pure oxygen produces cell sizes of 1–10 mm [126]. Hypergolic propellants inherently have low required ignition energy—their auto-ignition temperatures are below room temperature. Thus, their cell size is expected to be sub-mm, precluding accurate resolution with the aforementioned techniques [132]. Catoire et al. measured cell sizes for various forms of hydrazine in oxygen using soot foils at low pre-detonation pressures. The measurable cell sizes ($\geq$20 mm) are much larger than that expected for hypergols at realistic pressures (>1 atm) [133].

Due to the aforementioned practical limitations, there is—to our knowledge—no experimental cell size data for hypergolic propellants at realistic detonation conditions. In this chapter, we present an approach to experimentally assess the detonation cell size for hypergolic propellants at practical conditions by leveraging the relationship between the cell size and critical combustor length scales the non-premixed annular combustor presented in Chapter 2. We use the method to produce the first estimates of cell size for the common space-storable rocket propellant combination: monomethylhydrazine (MMH) and the MON-3 (3 % NO by weight) variant of nitrogen tetroxide (NTO).

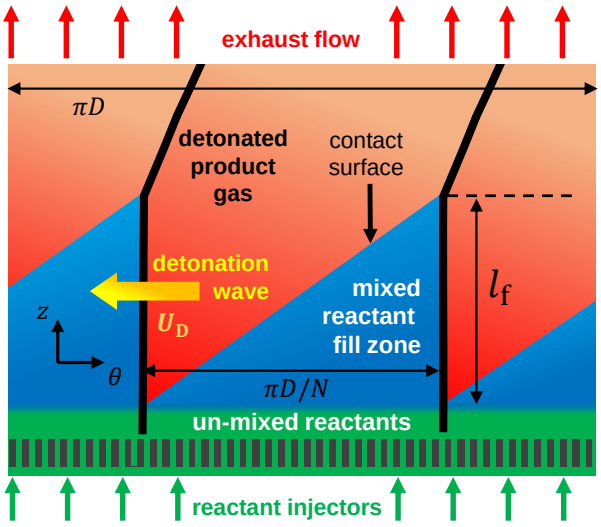

Figure 3.1: Unwrapped view of RDRE with two detonation waves (not to scale). Reactants are fed from below through propellant injectors and combustion product gas is exhausted at the top.

3.2 Methodology

In this section we present the analytical framework used to estimate detonation cell size from a non-premixed annular combustor. A generic "unwrapped" annular RDRE flow field is pictured in Fig. 3.1. Here the reactant is injected into the combustor from below, after which it is consumed by a detonation wave and converted into hot product gases which are then exhausted at the top of the chamber. From the point where the propellants mix sufficiently to combust, the distance the mixture penetrates into the combustor before the detonation wave consumes it is known as the *fill height*, l_f. If the detonation wave-speed is constant, as the reactant flow rate decreases, the fill height decreases until it reaches a critical value, $l_{f,cr}$. After reaching this critical value, decreasing reactant flow rate does not lead to an additional decrease in l_f—rather, the number of detonation waves in the annulus will decrease in order to increase the fill height per detonation wave in what is termed as a descending mode transition [37, 134].

The critical fill height relates to the detonation cell size, λ, through the following rela-

tionship [21]:

$$l_{\mathrm{f,cr}} = (12 \pm 5)\lambda. \tag{3.1}$$

Thus, λ can be estimated though the measurement of $l_{\mathrm{f,cr}}$ in an RDRE. To assess l_{f}, the analysis presented by Wolanski [135] is used and briefly summarized here. The volume of the reactant fill zone, V_{f}, consumed by a single detonation wave is assumed to be in the shape of a triangular prism—as indicated in Fig. 3.1—and can be written as:

$$V_{\mathrm{f}} = \frac{1}{2}\frac{\pi D}{N}\bar{l}_{\mathrm{f}} w. \tag{3.2}$$

Here, D is the mean annulus diameter, N is the number of detonation waves in the annulus, w is the annular gap size and $\bar{l}_{\mathrm{f}}$ is the average fill height at the detonation surface. For co-rotating waves, the fill height is constant, so the average fill height is equal to the instantaneous value. For counter-propagating waves, the fill height is unsteady, so an average must be used. The time t_{f} required for one detonation wave to consume volume V_{f} of propellant can be written as:

$$t_{\mathrm{f}} = \frac{\pi D/N}{U_{\mathrm{D}}}. \tag{3.3}$$

Here, U_{D} is the detonation wave-speed. The ratio of the fill-zone volume and the consumption time can be taken to find the reactant consumption rate for a single detonation wave, $\dot{V}_{\mathrm{single}}$:

$$\dot{V}_{\mathrm{single}} = \frac{V_{\mathrm{f}}}{t_{\mathrm{f}}} = \frac{1}{2}\bar{l}_{\mathrm{f}} w U_{\mathrm{D}}. \tag{3.4}$$

The consumption rate of all N detonation waves can summed and this sum must equal the incoming reactant flow rate $\dot{V}_{\mathrm{tot}}$:

$$\dot{V}_{\mathrm{tot}} = N\dot{V}_{\mathrm{single}} = \frac{1}{2}N\bar{l}_{\mathrm{f}} w U_{\mathrm{D}}. \tag{3.5}$$

Here, we assume that the density of the reactants does not change significantly between the time of injection and the passage of the detonation wave, i.e. the reactants remain in the liquid phase until they are consumed by the detonation wave. Measurements of propellant temperatures and manifold pressures indicate that the propellants were in the liquid phase prior to entering the combustor. The timescales for MMH–NTO propellant

droplet vaporization in rocket combustors have been assessed to be on the order of 10–100 ms [136], whereas the time between passage of successive detonation waves is typically on the order of 10–100 µs, as assessed in Section 3.3 with high-speed videography. This implies that propellants do not have enough time to vaporize in the reactant fill zone. Numerical studies have shown that the leading shock wave of a detonation for liquid fuel can vaporize the reactants [137],providing for a mechanism for the abrupt phase transition in the detonation structure itself and supporting the notion of liquid reactants prior to detonation-wave passage and subsequent gas-phase chemistry. The phase change is endothermic and has the effect of reducing the detonation wave velocity [138, 139].

Equation 3.5 may be solved for the averaged, uniform, liquid-equivalent reactant fill height:

$$\bar{l}_{\mathrm{f}} = \frac{2\dot{V}_{\mathrm{tot}}}{NwU_{\mathrm{D}}}. \tag{3.6}$$

The calculation of the uniform liquid-equivalent fill height provides a lower bound on the actual reactant fill height due to non-uniform injetion. For brevity, the bar is dropped from $\bar{l}_{\mathrm{f}}$ hereafter. With Eqn. 3.6, measurements of $\dot{V}_{\mathrm{tot}}$, U_{D}, N, and w can be used to find the effective reactant fill height for a given flow condition. As discussed previously, if a descending modal transition is observed as the incoming volumetric flow rate is decreased, the critical minimum value of the fill height $l_{\mathrm{f,cr}}$ can be ascertained. This value of $l_{\mathrm{f,cr}}$ can then be used to estimate the detonation cell size using Eqn. 3.1.

3.3 Experimental results

The modular annular combustor from Chapter 2 was used to assess the rotating-detonation characteristics of MMH and MON-3. A cross-sectional view of the test article is shown on the left side of Fig. 2.5. A detailed description of the test article is presented in Chapter 2. The hot-fire tests from Chapter 2 for configurations B and C were utilized for this study. Both configurations utilized the honed AM injector. As a reminder, configuration B used a center body of uniform diameter and is termed here as the *no-nozzle configuration*. The center body

was 114.3-mm long and its outer body length was 127 mm. In configuration C, referenced here as the *nozzle configuration*, a center body in the shape of an aerospike plug nozzle was used to assess effects of downstream flow constrictions (and chamber pressurization) on the detonation fill height.

For this study, only the experiments conducted at an oxidizer-to-fuel mixture ratio of 1.25–1.30 with mass flow rates between 0.3 to 0.7 kg/s were considered, as to assess the detonation cell size for a particular mixture ratio. Chapter 2 details the experimental procedure for executing the hot-fire tests, as well as the instrumentation used for assessing detonation dynamics.

3.3.1 Cell-size calculations

The volumetric propellant flow rate into the chamber was determined by dividing the mass flow rate measurement of each propellant stream by the density of the propellant, which was determined by measuring the temperature of the propellant immediately before entering the combustor. To obtain the number of detonation waves present in the annulus, N, and the detonation wave-speed, U_{D}, footage from the high-speed camera was used in combination with image post-processing detailed in Chapter 2.4.1. The high-speed video was used to generate contour plots of integrated light intensity versus time and angular position in the annulus, termed a "detonation surface" [36]. Sample detonation surfaces are shown for tests with various wave modes in Fig. 3.2. In these detonation surfaces, wave behavior can be readily observed for tests where rotating detonations were produced as indicated by lines of high luminosity propagating with a finite slope in the angular direction. The slope of these lines is inversely proportional to the propagation speed of these periodic disturbances. As mentioned in Chapter 2, four different wave behaviors were observed across the experiments. In some tests, a single wave is observed to propagate around the annulus in the counter-clockwise (CCW) direction, which is denoted as the positive angular direction in the detonation-surface plot. This mode can be seen in the leftmost detonation-surface plot in Fig. 3.2. In other tests, one wave is observed propagating CCW with another propagating

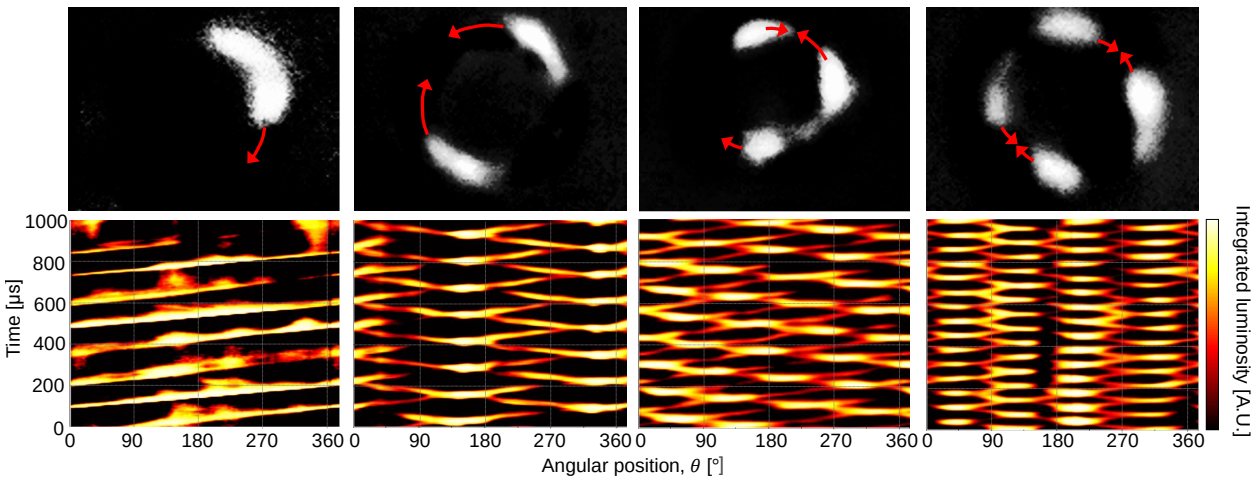

Figure 3.2: *Top*: High-speed video frames from four different detonation experiments from the cell-size study, showing the different wave modes present in the combustor. *Bottom*: Detonation-surface plots of integrated pixel intensities *versus* time and angular position in the annulus.

clockwise (CW), as seen in the second detonation-surface plot from the left in Fig. 3.2. This mode is known as a "counter-propagating" or "slapping" mode [37]. In some other tests, a single dominant detonation wave propagates CCW around the annulus, with two slower waves travelling in the opposite CW direction, as seen in the third detonation-surface plot from the left in Fig. 3.2. Lastly, another mode features a total of four waves, with two waves travelling CW and two waves travelling CCW, as seen in the rightmost detonation-surface plot in Fig. 3.2.

Equation 3.6 can be used to obtain the reactant fill height, l_{f}, from the volumetric flow rate and the number/speed of the detonation waves in the annulus obtained from image processing. In Fig. 3.3, the fill height is plotted against the inlet volumetric flow rate for the two configurations with and without a nozzle. From this plot, a few trends can be observed. For both configurations, as reactant flow rate decreases, the fill height decreases for a given number of waves. When the fill height reaches a critical minimum value, the number of detonation waves in the annulus decreases by one. As the number of waves is decremented, the fill height is increased above the critical value. Blue-to-green and purple-

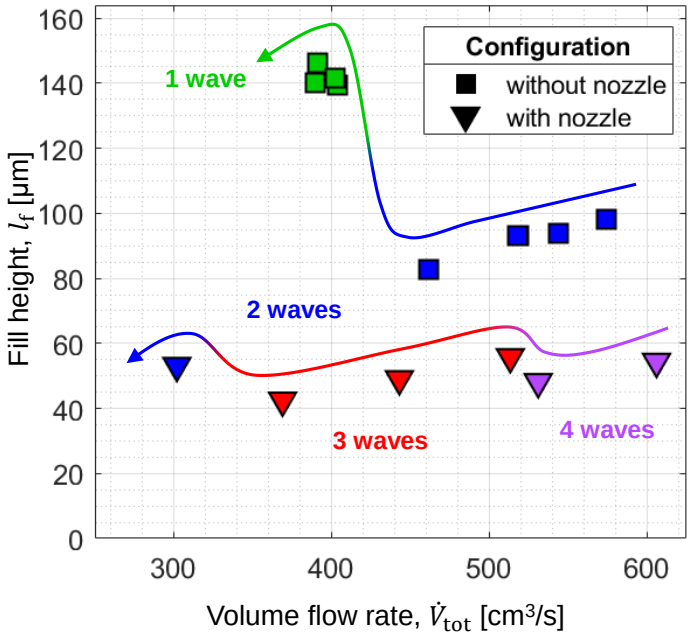

Figure 3.3: Liquid-equivalent reactant fill-zone height *versus* propellant volumetric flow rate for both combustor configurations. The mode transitions with decreasing flow rate can be observed by following the arrows.

to-red-to-blue arrows illustrate the jumps in fill height across descending mode transitions as the volumetric flow rate is decreased across experiments. It is also interesting to note that as flow rate increases, there appears to be a maximum fill height that is nearly double the minimum fill height, which is consistent with previous observations in rotating detonation combustors [21].

It can be seen that using the nozzle configuration, the fill heights are generally lower—the modal transition occurs for smaller critical values of the effective fill height. This also has the effect of causing an increased number of detonation waves at similar or lower flow rates. This reduced critical fill height implies that the detonation cell size is smaller for the nozzle configuration.

The critical minimum liquid-equivalent fill height is 70–80 µm for the nozzle-less configuration and 30–50 µm for the nozzle configuration. By using Eqn. 3.1, we can obtain an

estimate of the cell size: 4.1–11 µm for the nozzle-less configuration and 1.8–7.1 µm for the nozzle configuration. The decreased cell sizes for the nozzle configuration is postulated to be linked to increased pre-detonation pressure induced by the downstream flow constriction induced by the nozzle.

Equations 3.1 and 3.6 were applied to the operating conditions from the CH_4–O_2 rotating detonation engine at the Air Force Research Laboratory at Edwards Air Force Base, CA [38, 113]. We found that the minimum fill height inferred across a 2-to-3 wave modal transition near stoichiometric conditions is ∼7.4 mm for an average chamber pressure of 4 atm, corresponding to a cell size of 0.44–1.1 mm. A similar cell size of ∼1 mm was measured using a soot-foil technique and matches our value [140].

3.3.2 Evidence of critical fill height in transient case

The knowledge of the critical fill height and cell size can be used to predict descending modal transitions. This technique is demonstrated for a test conducted at a mass flow rate of 0.61 kg/s and mixture ratio of 1.29 without the nozzle. In Fig. 3.4, the time-resolved mass flow rate can be seen on the top left during the shutdown transient once the main propellant valves are commanded closed (700 ms after they are commanded opened). For ∼100 ms, the mass flow rate is constant, as there is some delay in the closing of the main propellant valves due to the response time of the pneumatic control system and the inertia of the valve.. After $t = 800$ ms, the main propellant valves begin to close. The isolation of the propellant lines from the pressurized propellant supply upstream causes the pressure in these lines to drop as the residual propellant is fed into the combustor. As the pressure in these lines drop, the mass flow rate begins to ramp down. This is accompanied by a drop in the effective reactant fill height, which is also plotted in Fig. 3.4. Once the fill height drops below the critical value between 70 and 80 µm, the two-wave detonation mode is no longer stable, and a descending mode transition occurs from a two-wave mode to a single-wave mode. The decreased number of waves allows for the fill height to again be above the critical value.

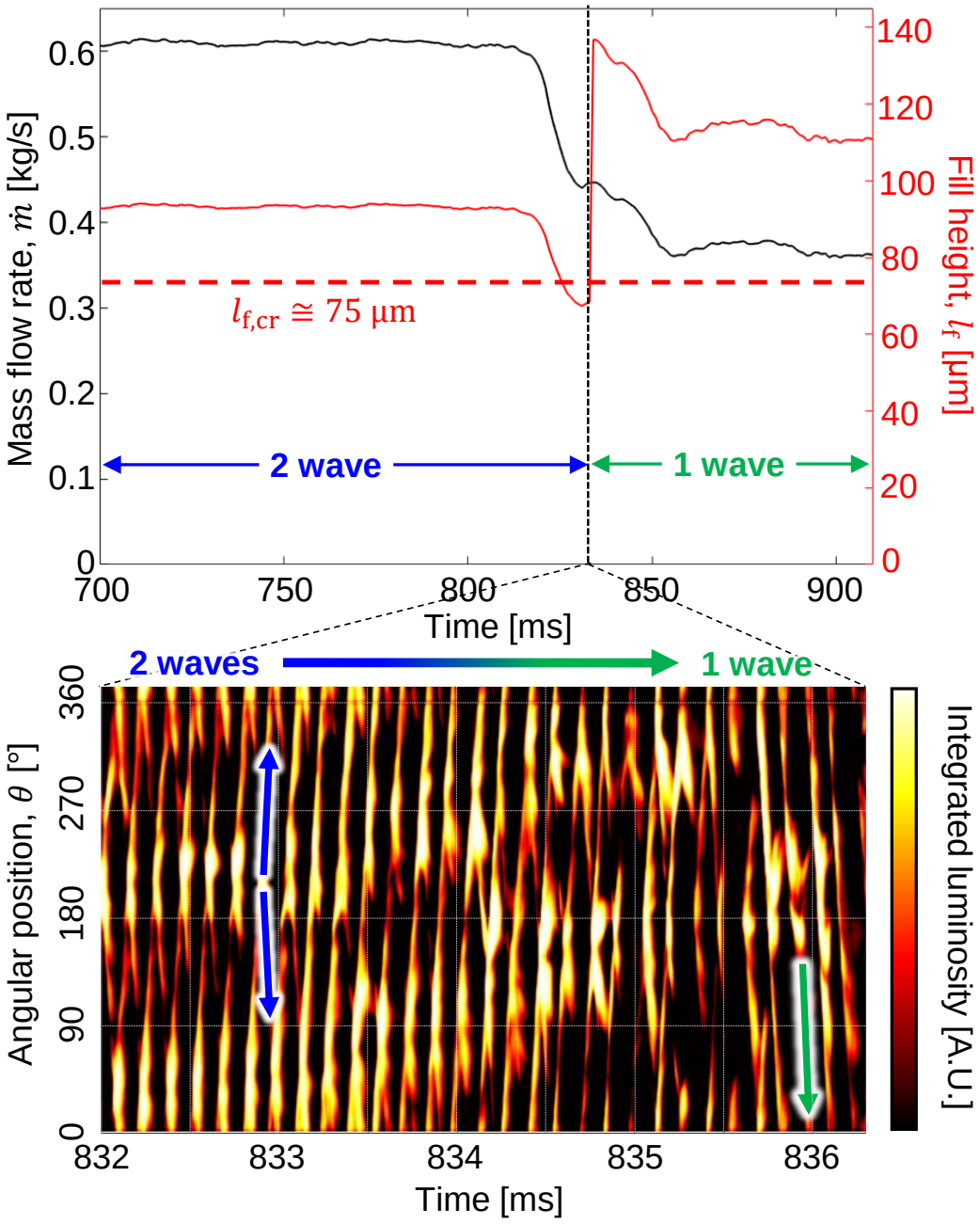

Figure 3.4: *Top*: Plot of total propellant mass flow rate *versus* time (black) and liquid-equivalent reactant fill height *versus* time (red) during a shutdown transient.When the fill height drops below the critical value, the two-wave detonation mode becomes unstable and transitions to a single-wave mode. *Bottom*: Detonation-surface plot indicating the descending mode transition from a two-wave mode to a single-wave mode.

3.3.3 Correlation with theoretical induction length

As indicated in Section 3.1, the detonation cell size is linked to the induction distance Δ_i behind the leading shock wave in a detonation. Here, we compare these parameters for various reactant mixtures, including hydrocarbons detonated in air and oxygen, as well as MMH–MON3.

The detonation cell size for various hydrocarbon fuels detonated in air or oxygen are obtained from Caltech's Detonation Database [126], which were measured using a soot-foil technique. These data were obtained for stoichiometric mixtures at a room-temperature initial condition. The initial pressure condition for these hydrocarbon detonations are nominally ∼1 atm, except for C_2H_6–O_2, C_2H_4–O_2, C_3H_8–O_2, and C_2H_2–O_2, where the initial pressures are 15 kPa, 13 kPa, 50 kPa and 66 kPa, respectively. For MMH–MON3, the cell-size estimates come from the methods presented in this work.

The detonation induction length is assessed in the gas-phase using the Caltech Shock and Detonation Toolbox [141] in Cantera [142]. The ZND reaction zone [143] behind the leading shock wave is computed using the GRI-Mech 3.0 mechanism [144], for the hydrocarbons, and ARL's MMH-RFNA reaction mechanism [145], for MMH–MON3. For the hydrocarbon simulations, the pre-detonation equivalence ratio, temperature, and pressure were set to the same values as in the cell-size experiments. For the MMH–MON3 simulations, the pre-detonation oxidizer-to-fuel mixture ratio was set to 1.27 ($\phi = 1.97$) and the initial temperature was set to 300 K. Two NO_2 were used as surrogate for N_2O_4 to maintain numerical stability. Since the pre-detonation pressure was unknown for the RDRE experiments, multiple simulations were conducted at various initial pressures. For each combustor configuration, the pre-detonation pressure in the ZND simulation was set to the midrange of CTAP pressures. Additional simulations were performed at the minimum and maximum CTAP values accounting for the spread across the various tests in the Caltech database and our experiments. An additional uncertainty of 40% was added to these bounds to account for the fact that the CTAP value is not exactly equal to the pre-detonation pressure.

A sample simulated reaction zone for MMH–MON3 can be seen in Fig. 3.5 for a pre-

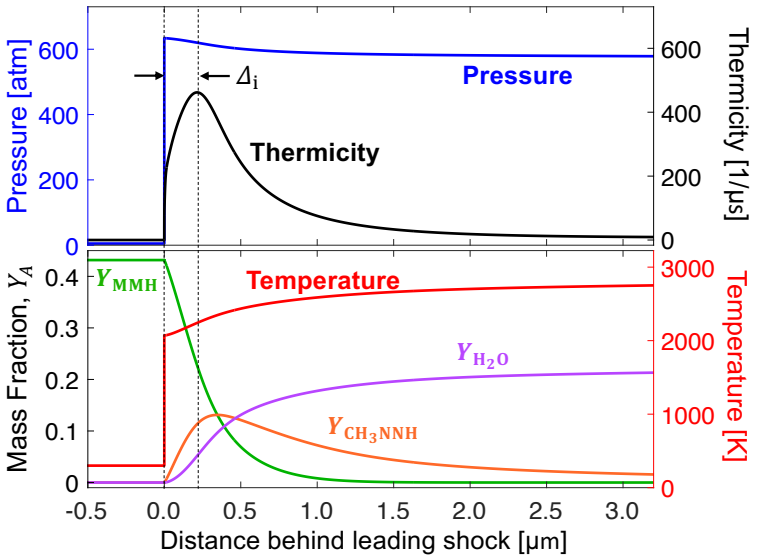

Figure 3.5: ZND simulated pressure, thermicity, temperature, and select species mass fractions *versus* distance behind leading shock wave for a MMH–MON3 detonation wave with an initial temperature and pressure of 300 K and 5 atm with induction length labeled. For the species evolution, a reactant (MMH), intermediate (CH_3NNH), and product (H_2O) are shown.

detonation pressure of 5 atm. The induction length is found by finding the distance between the leading shock wave and the point of maximum thermicity (non-dimensional rate of heat release). Select measured/inferred cell sizes and simulated induction lengths are tabulated in Table 3.1.

In Fig. 3.6, the experimentally-assessed cell sizes are plotted against the simulated values for the induction length for all of the considered mixtures. The induction length and cell size for the hydrocarbon-oxygen mixtures are both lower than for the hydrocarbon-air mixtures due to the more favorable ignition characteristics of oxygen-enriched combustion. The induction length for the hypergolic reactants at the high-pressure and fuel-rich conditions used in this work are predicted to be sub-μm which is a couple of orders of magnitude smaller than for the hydrocarbon fuels due to rapid hypergol ignition behavior. A clear correlation between cell size and induction length can be seen for the various reactant combinations. Using the data from the hydrocarbon reactants, a power law was fitted to relate cell size λ_{fit}

Table 3.1: Simulated induction length and experimental cell size for select reactant combinations.

Reactants	P_1 [atm]	Δ_i [µm]	λ [µm]
CH_4–Air	1.0	17,000	350,000
C_2H_6– Air	1.0	2,000	54,000
C_3H_8– Air	1.0	2,000	46,000
C_2H_4– Air	1.0	600	20,000
C_2H_2– Air	1.0	780	9,200
H_2 – Air	1.0	250	8,000
C_2H_6–O_2	0.15	180	7,700
C_2H_4–O_2	0.13	160	4,000
CH_4–O_2	1.0	200	3,000
C_3H_8–O_2	0.49	69	2,500
C_2H_2–O_2	0.65	33	1,500
H_2–O_2	0.97	51	1,400
MMH–MON3 (no nozzle)	3.0	0.10–0.21	4.1–11
MMH–MON3 (nozzle)	12.5	0.08–0.17	1.8–7.1

[mm] and induction length Δ_i [mm], using $\lambda_0 = \Delta_{i,0} = 1$ mm.

$$\lambda_{fit} = 23.7\lambda_0 \left(\frac{\Delta_i}{\Delta_{i,0}} \right)^{0.90}. \tag{3.7}$$

The exponent of 0.90 indicates an approximate linear relationship between induction length and detonation cell size. The coefficient in front of λ_0 indicates that detonation cells tend to be an order of magnitude larger in width compared to the length of their reaction zones. This scaling coefficient has been shown to vary for different reactant types, and seems to have a dependence on the ratio of reactant activation energy and the thermal energy behind the leading shock of the detonation [146, 147]. This ratio relates to the stability of the detonation wave [143].

The power law of Eqn. 3.7 is plotted as a red curve in Fig. 3.6. It can be seen that the inferred values of the MMH–MON3 cell sizes result in good agreement with the trend

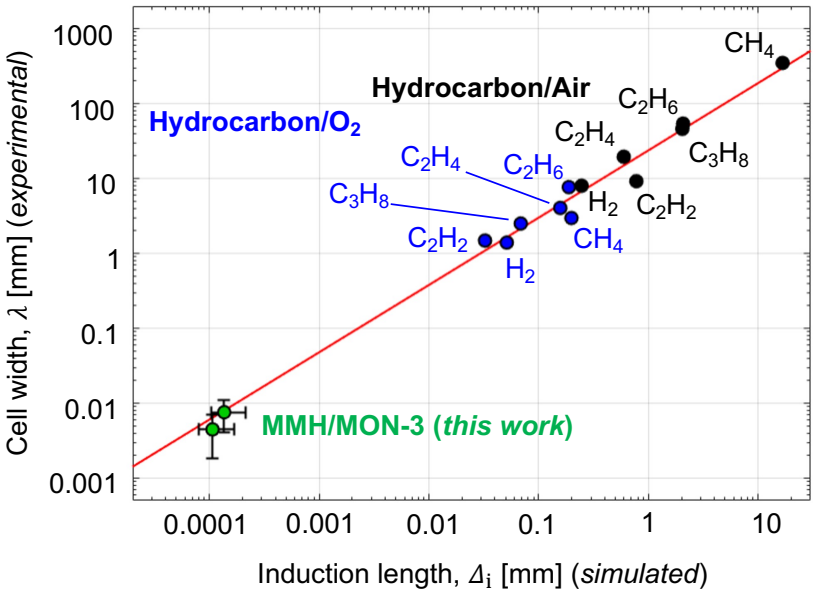

Figure 3.6: Experimental detonation cell width *versus* simulated detonation induction length for hydrocarbon-air mixtures (black), hydrocarbon-oxygen mixtures (blue), and MMH—MON3 (green). For MMH–MON3, pressures from 5–13 atm were simulated for the no-nozzle configuration, and 7–18 atm for the nozzle configuration.

predicted by the hydrocarbon detonation data and significantly extend the range of cell size assessment by two orders of magnitude below the lowest values in the literature.

3.4 Summary

An experimental technique for estimating detonation cell size of hypergolic propellants is presented and used for the first measurements of the cell size for the common space-storable rocket propellants MMH and MON-3. Cell size is estimated using a known correlation between critical liquid-equivalent reactant fill height and cell size. Reactant fill height is inferred using a control-volume analysis to relate the geometry of the reactant fill zone to the propellant flow rate, detonation wave-speed/quantity (measured using high-speed videography), and annular gap size. The critical fill height is identified by monitoring the decrease of number of waves across experiments (1) at steady state and (2) in transient

conditions. Given the limits of conventional methods, the current approach represents a practical alternative for estimating the detonation cell size of hypergolic propellants and other propellants at high initial pressures where cell sizes are expected to be much less than 1 mm.

CHAPTER 4

MHz laser absorption spectroscopy via diplexed RF modulation for pressure, temperature, and species in rotating detonation rocket flows

The contents of this chapter have been published in the journal ***Applied Physics B*** *under the full title "MHz laser absorption spectroscopy via diplexed RF modulation for pressure, temperature, and species in rotating detonation rocket flows" [148]. Portions of the chapter's content have been presented / included in the conference proceedings for the* ***AIAA SciTech Forum, 2020*** *[149] and the* ***AIAA Propulsion and Energy Forum, 2020*** *[150].*

4.1 Introduction

A critical issue in evaluating RDE technology has been a lack of diagnostic capability that is sufficiently quantitative and granular to provide useful feedback. In this chapter, we address this need by advancing the state-of-the-art in high-speed laser diagnostics for harsh combustion environments. As mentioned in Chapter 1, laser absorption spectroscopy (LAS) has several advantages compared to other optical diagnostic techniques for assessing gas properties in harsh environments such as that of an RDRE. A persistent challenge to deploying LAS to detonation engines has been balancing the need for very fast measurement rates (to resolve steep property gradients) and the desire for robust methods for reliable quantitative data interpretation in such a harsh environment. Rotating detonation rocket engines often possess cycle frequencies (which may involve multiple waves) in the range of 5–30 kHz (as in Chapter 2), for which $\geq$ MHz measurement rate is desired for temporal

resolution of intra-cycle transients. Early LAS efforts on PDEs deployed fixed-wavelength laser absorption methods [96, 97, 91] which are typically only limited in measurement rate by detector bandwidth. However, these methods are generally not robust against beam steering, particle scattering, window fouling, and thermal emission, which are common and highly dynamic in detonation engines and pronounced in rocket combustors [151]. Fixed-wavelength LAS methods also require assumptions about spectral line shapes to be quantitative. To address these issues, more recent LAS work in the context of detonation engines has focused on wavelength-scanning or wavelength-modulation techniques that allow for reliable correction of thermal emission and active recovery of a non-absorbing baseline signal (or insensitivity to baseline signal) that mitigates issues of steering, scattering, and window fouling. Wavelength-scanning (or -modulating) spectroscopy techniques have been utilized for more robust PDE/RDE measurements [92, 93, 88, 94, 89, 90, 30, 87]. However, the effective measurement rates for these wavelength scanning methods (10–100 kHz) are insufficient to fully resolve thermophysical gradients in many detonation-based engines. For detonations and other highly transient physical processes, microsecond time resolution of thermodynamic and thermochemical properties required. LAS at MHz rates has been demonstrated by various methods [152, 153, 154, 155], and has proven useful in measuring gas properties in detonation environments [156, 148], planetary-entry shock layers [153, 157], and characterization of energetic materials [158]. Continuous-wave distributed feedback lasers (CW-DFBs) are highly stable, narrow-linewidth semiconductor light sources with convenient injection-current tunability. CW-DFB lasers have been used extensively in wavelength-scanning or wavelength-modulation techniques for gas-phase absorption spectroscopy [159], with low scan-to-scan output variation/noise relative to pulsed operation. Over the past two decades, CW-DFB lasers have been developed throughout the mid-wave infrared, via quantum cascade or interband cascade architectures, providing access to the strongest vibrational absorption bands of most molecules, and thus enabling gas detection of many species at relatively short optical pathlengths, which has attracted new applications.

In this chapter, we present a mid-infrared laser absorption sensing method enabling MHz

measurements of temperature, pressure, and two major combustion species (CO and CO_2) in the annular exhaust flow of a rotating detonation rocket engine (RDRE). We first discuss the opto-electronic sensor design that enables radio-frequency (RF) wavelength modulation at MHz rates with mid-infrared CW sources. This is followed by details of the spectroscopic methods used to infer temperature, pressure, and species density from absorption spectra. We then describe the experimental setup involving a rotating detonation rocket test rig at the U.S. Air Force Research Laboratory (in Edwards, CA USA), including a retro-reflection optical configuration. Demonstration results are shown and discussed, with a corresponding analysis of uncertainties.

4.2 Opto-electronic design

A key enabling element of this work is the integration of bias-tee circuitry with distributed feedback (DFB) quantum cascade and interband cascade lasers to facilitate RF wavelength modulation (or scanning). Bias-tees are diplexers which combine a constant electromagnetic signal, such as a direct laser injection current (DC), with a modulated signal or alternating current (AC). The ideal bias-tee consists of an inductor which admits DC signal (the bias) but blocks AC signals, teed with a capacitor which admits AC signals while blocking DC signals. The maximum modulation frequency is limited by the parasitic elements inherent to circuit components (e.g. the parasitic inductance in the capacitor).

For typical DFB laser control and modulation, a laser driver is used which stabilizes injection current and temperature with a closed-loop circuit. In these drivers, modulation is typically achieved by varying the laser set-point current. Modulation bandwidth is usually limited by the phase error or lag introduced by the various elements in the circuit, some of which are used for current stabilization, as well as preventing reverse bias or exceeding prescribed current limits. Bandwidth can be increased by using faster or fewer circuit elements, such as to minimize the phase error. However, given that commercial laser drivers are designed and built to minimize the risk of instability over a wide range of loads, the phase error resulting from the components used to achieve this stability results in a lower band-

width than might be achieved by the laser. For quantum cascade lasers, injection current controllers with current range on the order of 1 Amp have typical modulation bandwidths on the order of 10^5 Hz [160], lower than can be achieved with diode laser controllers [155].

Approaching bandwidth limits renders an attenuation in the current modulation intensity and diminishing wavelength modulation. To circumvent this limitation, we integrate a bias-tee into the laser control circuit, using the conventional laser driver to set the bias or mean direct current (prescribing the center wavelength), while diplexing a radio frequency (RF) alternating current between the driver and laser. This effectively bypasses many circuit elements in the driver that constrain modulation bandwidth, but adds some risk of laser damage. Bias-tee circuits have been implemented (with commercial packaging) for near-infrared diode lasers [161], and have more recently been demonstrated with DFB quantum cascade lasers [162]. We note that this approach to rapid wavelength tuning is an alternative to laser pulsing, which can achieve similar rates, but has been observed to increase intensity noise and lower periodic stability [163, 164].

In this work, a continuous-wave distributed-feedback (DFB) quantum cascade laser (QCL) (ALPES Lasers), tunable from 2001 to 2012 cm^{-1}, and an interband cascade laser (ICL) (Nanoplus), tunable from 2382 to 2389 cm^{-1}, were used as the narrow-band light sources to probe rovibrational transitions of CO and CO_2 respectively. Both light sources were modulated using bias-tee circuitry as shown in Fig. 4.1. To avoid the 200 kHz bandwidth limitation of the laser controllers (Arroyo 6310-QCL and Arroyo 6305), the controllers are used solely to set the mean injection current, or DC bias, going into the laser and to control the temperature of the laser chip using thermoelectric cooling (TEC). Sinusoidal radio frequency current modulation is supplied by function generators (SRS DS345).

The direct current (DC) and alternating current (RF) signals are combined using commercial bias-tee diplexers (SigaTek SB12D2D) with a frequency range of 100 kHz to 12.4 GHz. A representative setup with the DFB QCL is shown on the top of Fig. 4.1. Since the lasers each accept a current modulation, and the function generator outputs a voltage modulation, a voltage-to-current transfer function H for each laser (which depends on effective impedance)

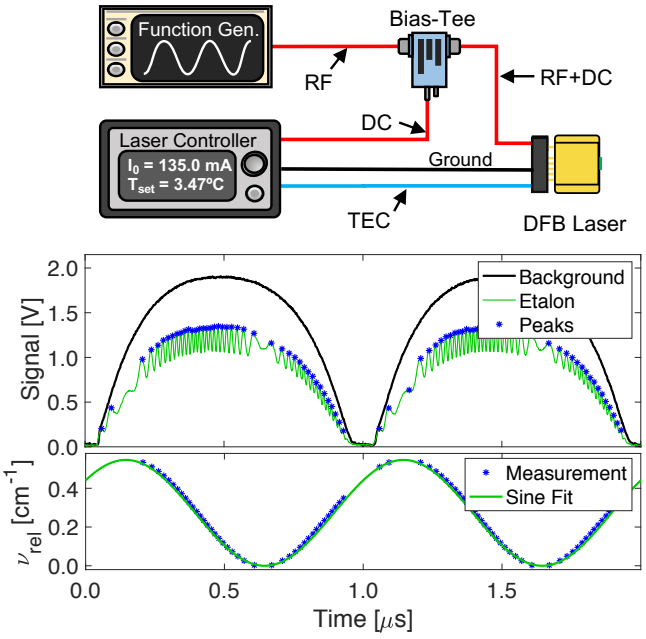

Figure 4.1: Bias-tee laser control schematic (*top*). Sample MHz laser scans showing background and etalon scans (*middle*). Plot of resulting relative wavenumber vs. time calculated from the etalon peaks with sinusoidal fit (*bottom*).

required experimental determination to prevent unintentional current overloading of the light sources. The transfer function was determined by biasing the DC injection current on the laser controller to just below the mean (i_{mean}) of the lasing threshold current i_{th} and maximum allowable current specified by the manufacturer, i_{max}, and subsequently increasing the AC (or RF) voltage amplitude by small increments until the lasing threshold was observed (no signal on the photovoltaic detector). This voltage amplitude is termed V_{A}. The transfer function is then calculated:

$$H = \frac{i_{\text{mean}} - i_{\text{th}}}{2V_{\text{A}}}. \tag{4.1}$$

For a scan rate of 1 MHz, the transfer function was determined to be ∼11.9 mA/V for the QCL and ∼2.15 mA/V for the ICL. Furthermore, we observed that the transfer function varied with modulation frequency, and this effect was pronounced with the interband cascade laser, for which H decreased by nearly a factor of five between 100 kHz and 2 MHz (shown

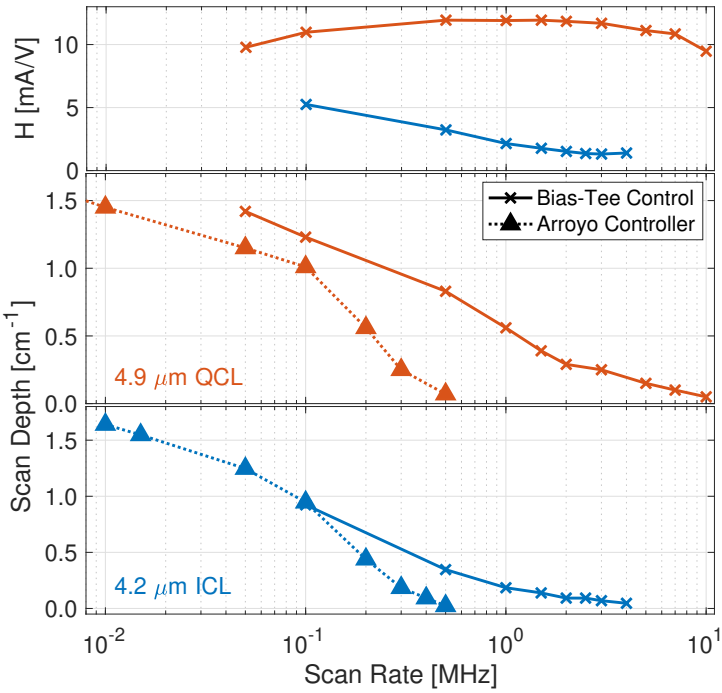

Figure 4.2: Plot of voltage-to-current transfer function versus scan frequency for the bias-tee circuits (*top*). Plot of scan depth vs. scan frequency with and without bias-tee control for both the QCL and ICL (*bottom*).

at top of Fig. 4.2).

The maximum achievable peak-to-peak scan depths (in wavenumber) for the bias-tee configurations were determined for a given modulation frequency and compared to those enabled by the commercial laser drivers. The optical setup involved pitching the modulated laser radiation through a 2-inch germanium etalon and scaling the spacing of time-resolved intensity peaks by the etalon free spectral range (FSR). The peaks are then fitted to a sine function, which quantifies the modulation amplitude in the wavenumber domain [cm^{-1}]. Representative intensity signals with and without the etalon present as well corresponding wavelength modulation for the QCL are shown in the bottom of Fig. 4.1.

For the QCL, a modulation rate of 1 MHz produces approximately 25 peaks in the etalon signal over a time interval of approximately 300 ns over the upscan. This 300 ns represents an effective integration time for the measured spectra and inferred gas properties

(at 1 MHz). In order to temporally resolve these etalon peaks, an optical detector with bandwidth $\geq$ 85 MHz must be utilized. In this work, detectors with bandwidth greater than 190 MHz were utilized.

The respective scan depths and transfer function of each laser were determined as a function of modulation frequency and plotted in Fig. 4.2. As depicted, the bias-tee configuration extends the scan frequency up to several MHz with substantial corresponding RF wavenumber modulation amplitude. Divergence in maximum achievable scan depth is observed between the two modulation schemes at frequencies above 100 kHz. For the bias-tee circuit, reference scan depths of 0.55 cm^{-1} and 0.18 cm^{-1} were achieved at 1 MHz for the QCL and ICL, respectively. During measurements in the detonation environment, the laser is scanned below its lasing threshold to account for thermal emission on the detector. We note that the phase lag between laser output intensity and wavelength (or wavenumber) renders the downscan less usable, occurring at a time of minimum laser power and yielding poor signal-to-noise ratio (SNR).

4.3 Spectroscopic methods

In this section, we describe the spectroscopic methods used to quantitatively infer temperature, pressure, and species density for CO and CO_2 from absorption data. Estimations of measurement uncertainty along with uncertainty dependencies for each of these variables (including the effects of simplifying assumptions) are presented in a detailed analysis in Appendix D.

4.3.1 Temperature and CO-density measurement

A cluster of three P-branch transitions in the fundamental vibrational bands of CO was probed for evaluation of temperature, pressure, and CO column number density of the detonated gases. The specific rovibrational transitions are indicated in the top of Fig. 4.3, which shows the P(2,20), P(0,31), and P(3,14) lines where the nomenclature P(v'',J'') indi-

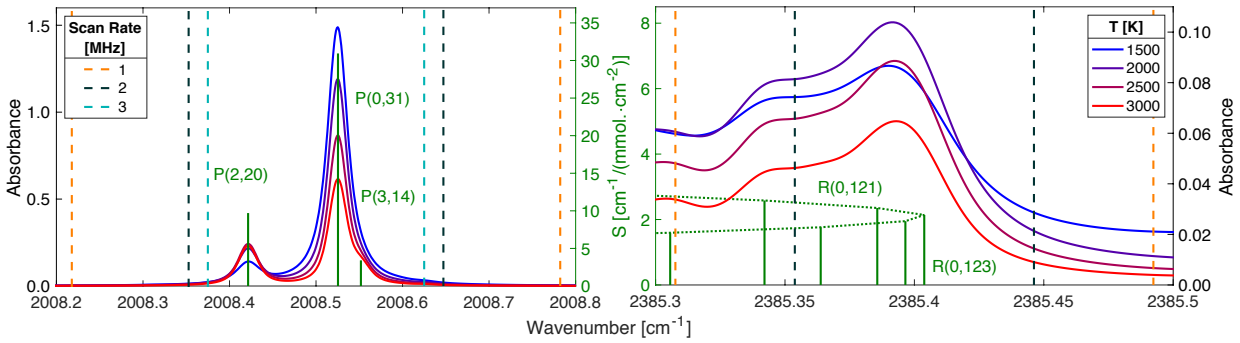

Figure 4.3: Target CO (*left*) and CO_2 (*right*) absorption spectra across a range of temperatures for $X_{CO} = 0.20$, $X_{CO_2} = 0.15$, atmospheric pressure, and a 1 cm optical path-length. Linestrengths for the target transitions are plotted overlaid at 2500 K. Vertical dashed lines indicate the scan depth achievable by the laser targeting the spectra at various scan rates.

cates the respective lower vibrational (v'') and rotational (J'') quanta. These CO transitions were primarily selected for their strength, relative spectral isolation from other combustion species, and divergent temperature-dependence due to their differences in lower state energy [151, 165]. Line intensities and positions are shown in Fig. 4.3 with representative absorbance spectra at various conditions of interest.

The Beer-Lambert law, shown in Eqn. 4.2, relates spectral absorbance α of transition k of absorbing species j to gas properties, including the number density of species j, n_j [molec·cm^{-3}], and temperature T [K] in a gas medium at a particular wavenumber ν [cm^{-1}] [166]:

$$\alpha_{kj,\nu} = -\ln\left(\frac{I_t}{I_0}\right)_\nu = \int_0^L n_j S_{kj}(T)\varphi_{kj}(\nu, T, P_Y)dl, \tag{4.2}$$

where l [cm] is the coordinate describing the position along the optical path (line-of-sight), L [cm] is the total optical path-length through the gas medium, $S_{kj}(T)$ [cm^{-1}/molec·cm^{-2}] is the temperature-dependent linestrength or intensity of transition k of species j, $\varphi_{kj}(\nu)$ [cm] is the lineshape function, and P_Y is the set of partial pressures of all species Y in the gas mixture. I_0 is the incident intensity provided by the light source, while I_t is the transmitted light intensity that exits the absorbing medium.

If the path length is known and the absorbing species is uniformly distributed along the

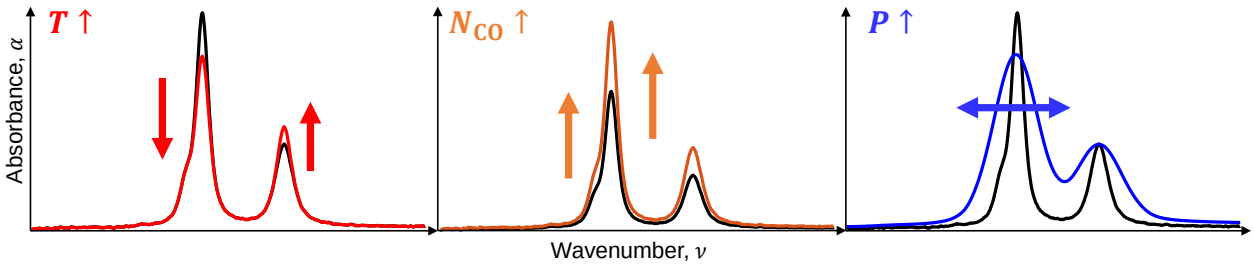

Figure 4.4: Dependence of target CO spectrum on the key measured gas properties: temperature, CO density, and pressure.

line of sight, the terms inside the path integral in Eqn. 4.2 may be factored out and the the absorbance can be directly related to the absorbing species number density. However, in this experiment, both the path length and the distribution of absorbing species along the line-of-sight are unknown. The gas composition can still be quantified using a quantity known as the column density, N_j [molec./cm^2] [167], which is an integral of the number density of species j along the optical line-of-sight:

$$N_j = \int_0^L n_j dl. \tag{4.3}$$

We may also define $\bar{T}$ as the path-averaged temperature weighted by the number density of the absorbing species [167]:

$$\bar{T} = \frac{\int_0^L n_j T dl}{\int_0^L n_j dl}. \tag{4.4}$$

Although path-integrated, quantitative measurements of $\bar{T}$ and N_j can be directly compared to the results of computational fluid dynamics (CFD) simulations to aid in the development and refinement of multi-physical models.

Since the lineshape function, $\varphi_{kj}(\nu)$, is dependent on wavenumber, collisional partners, pressure, and temperature, it is convenient to integrate absorbance over the entire transition to yield an absorbance area A_{kj} [cm^{-1}] independent of lineshape, utilizing the fact that the spectrally integrated lineshape function is equal to 1:

$$A_{kj} = \int_{-\infty}^{+\infty} \alpha_{kj,\nu} d\nu = N_j S_{kj}(\bar{T}). \tag{4.5}$$

This is usually achieved in practice by fitting an assumed lineshape function to the spectra. Eqn. 4.5 is valid when the linestrength of transition k is approximately linear with temperature, such that the path-averaged number density-weighted linestrength $\overline{S_{kj}(T)}$ is approximately equal to $S_{kj}(\bar{T})$, regardless of the temperature distribution across t he pathlength [167]. For the lines selected and conditions studied in this work, the linear linestrength approximation is valid to within 1% error, as discussed in Appendix D.0.3. For simplicity, we drop the overbar notation in all subsequent equations in this paper such that T refers to the number density weighted pathlength-averaged temperature.

If two spectral transitions (A and B) of a single species are probed, the ratio of their absorbance areas R_{AB} reduces to a function dependent only on temperature T:

$$R_{\mathrm{AB}}(T) = \frac{A_{\mathrm{A}j}}{A_{\mathrm{B}j}} = \frac{S_{\mathrm{A}j}(T)}{S_{\mathrm{B}j}(T)}. \tag{4.6}$$

Temperature-dependent linestrengths $S_{Aj}(T)$ and $S_{Bj}(T)$ can be calculated from reference

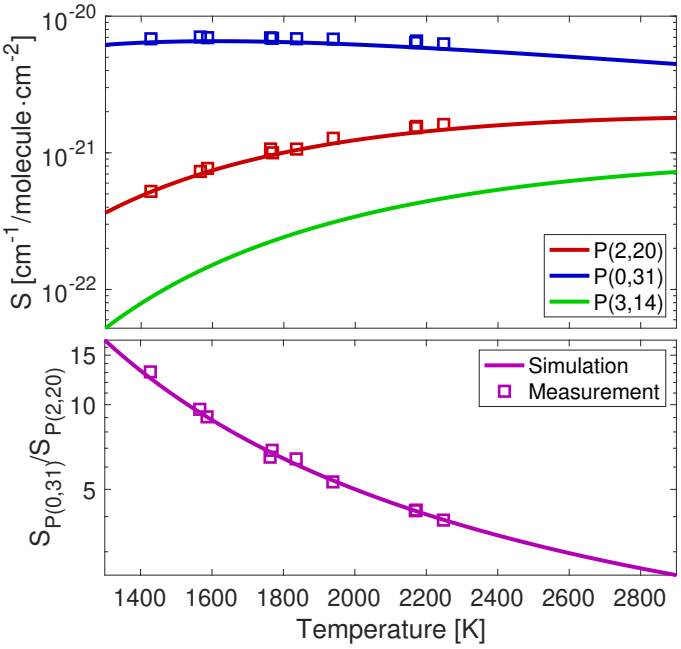

Figure 4.5: Linestrengths *versus* temperature for the three target transitions. The ratio of linestrengths between the P(0,31) and P(2,20) line are also shown vs. temperature. Both simulated values of the linestrength ratio using the HITEMP database [168] and measurements from the UCLA High-Enthalpy Shock Tube facility are shown.

temperature linestrengths $S_{Aj}(T_0)$ and $S_{Bj}(T_0)$, which for all transitions used in this work are sourced from the HITEMP database [168]. Thus, by simultaneously resolving at least two transitions for species j and determining their absorbance areas, the temperature of the gas can be inferred without requiring detailed information about the broadening parameters of the lineshape, providing a measurement independent of gas composition and total pressure. The temperature dependence of the CO spectrum can be seen on the let side of Figs. 4.3 and 4.4. With temperature inferred, a re-arranged form of Eqn. 4.5 can be used to find species column density:

$$N_j = \frac{A_{kj}}{S_{kj}(T)}. \tag{4.7}$$

This linear scaling of absorbance area and CO density can be visualized in the middle of Fig. 4.4.

The accuracy and robustness of the measurements of T and N_j therefore depend on the confidence in the temperature-dependence of the transition linestrengths, $S_{kj}(T)$. The linestrengths of the P(2,20) and P(0,31) transitions and their temperature-dependent ratio R_{AB} were validated experimentally in a High-Enthalpy Shock Tube facility at UCLA over a range of temperatures up to 2300 K, as shown in Fig. 4.5. Details of the shock tube apparatus and operation are described in previous work [165, 169]. In both the validation experiments, as well as measurements in the target detonation environment, a scanned-wavelength direct absorption technique [159] was utilized to scan across the wavelength domain of the three transitions. Some slight nominal disagreement is noted for the values of $S_{kj}(T)$, though this was determined to be within experimental uncertainty considering the linestrength uncertainties reported in the HITEMP database [168]. Nevertheless, the measured linestrength ratio $R_{AB}(T)$ is in excellent agreement with theoretical calculations, and this line pair has been used successfully for thermometry in previous work [165].

While the measurements rely primarily on the two strongest lines, the weak P(3,14) transition becomes more significant at very high temperatures (>1800 K), contributing to the absorbance measurement $\alpha_{\nu,\text{meas}}$ and blending with the P(0,31) line. We account for this influence with an iterative simulation procedure depicted in Fig. 4.6. In this procedure, the

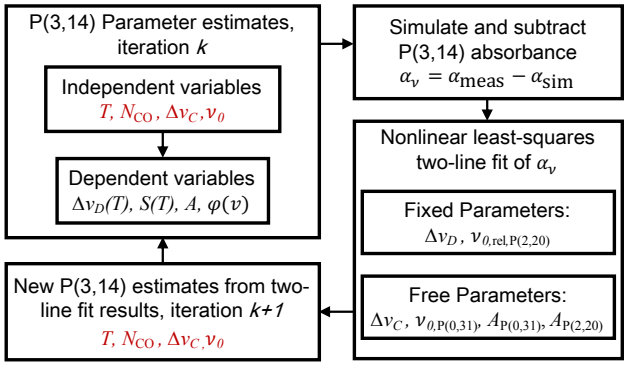

Figure 4.6: Flow chart describing iterative spectral fitting procedure to account for the influence of the CO P(3,14) line in measured absorbance.

absorbance specifically associated with the CO P(3,14) transition is modeled utilizing the Voigt lineshape [170] and subtracted from the measured absorbance prior to a two-line spectral fit of the P(0,31) and P(2,20) lines. In the first step (iteration k), temperature and CO column number density, N_{CO} are estimated from Chapman-Jouguet simulations (discussed further in Section 4.3.2) and used in combination with a guess for collisional width $\Delta\nu_C$ and P(3,14) line position $\nu_{0,\mathrm{P(3,14)}}$ to simulate the absorbance from the P(3,14) line, $\alpha_{\nu,\mathrm{sim}}$. In the next steps, this $\alpha_{\nu,\mathrm{sim}}$ is then subtracted from $\alpha_{\nu,\mathrm{meas}}$, and a two-line Voigt fit is applied to the remaining P(2,20) and P(0,31) spectra to determine their respective absorbance areas A_i, which are treated as free parameters along with the P(0,31) line position $\nu_{0,\mathrm{P(0,31)}}$ ($\nu_{0,\mathrm{P(2,20)}}$ is fixed relative to $\nu_{0,\mathrm{P(0,31)}}$) and a single collisional width $\Delta\nu_C$. In this study, the collision widths of all three CO lines are assumed equal; the associated consequences are discussed more in section 4.3.2 and Appendix D.0.2. In the final steps, T is inferred from the ratio of fitted absorbance areas (as described by Eqn. 4.6) and is used to obtain N_{CO} using Eqn. 4.7, while a new estimate for $\nu_{0,\mathrm{P(3,14)}}$ is determined from the fitted $\nu_{0,\mathrm{P(0,31)}}$. These values of T, N_{CO}, and $\nu_{0,\mathrm{P(3,14)}}$, along with the fitted $\Delta\nu_C$, are new parameter estimates for the next iteration (iteration $k+1$) in the loop described by Fig. 4.6. The iterations continue until T, N_{CO}, $\nu_{0,\mathrm{P(3,14)}}$, and $\Delta\nu_C$ converge. The temperature- and CO-sensing strategy was tested on the UCLA Detonation-Impulse facility, as discussed in Appendix B.

4.3.2 Pressure measurement

The measured collisional line-width, $\Delta\nu_C$, obtained from the aforementioned fitting procedure, contains information about the pressure of the gas medium, and is independent of the absorbance area. The collisional width is related linearly to total pressure P_{tot} as follows [166]:

$$\Delta\nu_C = P_{\text{tot}} \sum_Y X_Y (2\gamma_{\text{CO}-Y}(T)) = 2P_{\text{tot}}\gamma_{\text{CO}-\text{mix}}(T), \tag{4.8}$$

where $\gamma_{\text{CO}-Y}(T)$ is the temperature-dependent collisional-broadening coefficient for an absorber (CO) and collision partner Y, X_Y is the mole fraction of collision partner Y, and $\gamma_{\text{CO},-textmix}(T)$ is the mixture-weighted collisional-broadening coefficient. The dependence of the spectral broadening with pressure can be visualized on the right side of Fig. 4.4. Rearranging Eqn. 4.8, pressure can be determined given a measurement of $\Delta\nu_C$ and knowledge of the broadening coefficient for the gas mixture:

$$P_{\text{tot}} = \frac{\Delta\nu_C}{2\gamma_{\text{CO}-\text{mix}}(T)}. \tag{4.9}$$

The temperature dependence of $\gamma_{j-Y}(T)$ in Eqn. 4.8 for any absorbing species j is often modeled with a power-law expression [166]:

$$\gamma_{j-Y}(T) = \gamma_{j-Y,0} \left(\frac{T_0}{T}\right)^{N_Y}, \tag{4.10}$$

where $\gamma_{j-Y,0}$ is the collisional-broadening coefficient at the reference temperature T_0 (typically 296 K) and N_Y is the temperature-dependent power-law exponent (not to be confused with species column density). Both $\gamma_{j-Y,0}$ and N_Y are specific to collisional partner, as well as the quanta of the associated rovibrational transition. For CO, these parameters have been theoretically calculated by Hartmann et. al [171] as a function of rotational quantum number for high-temperatures with the collision partners CO_2, H_2O, N_2, and O_2. These tablulated values can be used with independent estimates of temperature and gas composition to determine $\gamma_{\text{CO}-\text{mix}}(T)$ in Eqn. 4.9, and thereby determine gas pressure P_{tot}. Owing to the number of assumptions made in order to determine P_{tot} from laser absorption measurements, we provide a rigorous derivation of uncertainty estimates for all of these calculations in Appendix D.0.4.

Informed by the operating conditions of the methane-oxygen RDRE experiment described in Section 4.4, we estimate mixture composition of the post-detonation gases with CalTech's Shock & Detonation Toolbox [141] in CANTERA [142] using the GRI-MECH 3.0 mechanism [144]. We perform the thermodynamic calculations using a Chapman-Jouguet (CJ) detonation model assuming ambient pre-detonation conditions (300 K, 1 atm), and an initial reactant mixture composition (parameterized by the fuel-oxidizer equivalence ratio, ϕ) determined from the methane and oxygen flow rates measured in the experiment. For each operating condition, the calculation yields a post-detonation composition, temperature, and pressure. From here, we make two different assumptions to produce a range of possible mixture compositions: First, the mixture composition is frozen, while the gas is expanded isentropically to 1 atm. The frozen composition and resulting temperature comprise the "frozen" assumption conditions. Second, the gas is allowed to equilibrate while holding entropy and pressure constant. The resulting composition and temperature comprise the "equilibrium" assumption conditions.

For determination of $\gamma_{\mathrm{CO-mix}}(T)$ in Eqn. 4.9, only species with mole fractions above 0.01% in the simulation results are considered, while experimentally-measured temperature T determined from Eqn. 4.6 is used. Considered species include CO, CO_2, H_2O, OH, H_2, O_2, O, and H. The mole fractions over ϕ from 0.6–1.6 for these species are shown as ranges in Fig. 4.7, reflecting variation between a frozen composition (post-detonation) assumption and an equilibrium composition assumption at one atmosphere. For broadening coefficient estimation in Eqn. 4.9, the equilibrium mole fractions are utilized.

In reality, the detonations in the RDRE are non-ideal, as some combustion may be occurring in a deflagration mode. To assess the effect of this on the exhaust plane composition, Cantera simulations were executed for constant-pressure combustion over a range of pressures near the estimated injection pressure (3-6 atm). Again, the exhaust was isentropically expanded to one atmosphere under both a frozen and equilibrium composition assumption. In general, the ranges of mole fractions of each of the combustion species in the deflagration simulation lay within the bounds shown in Fig. 4.7, supporting the use of the detonation

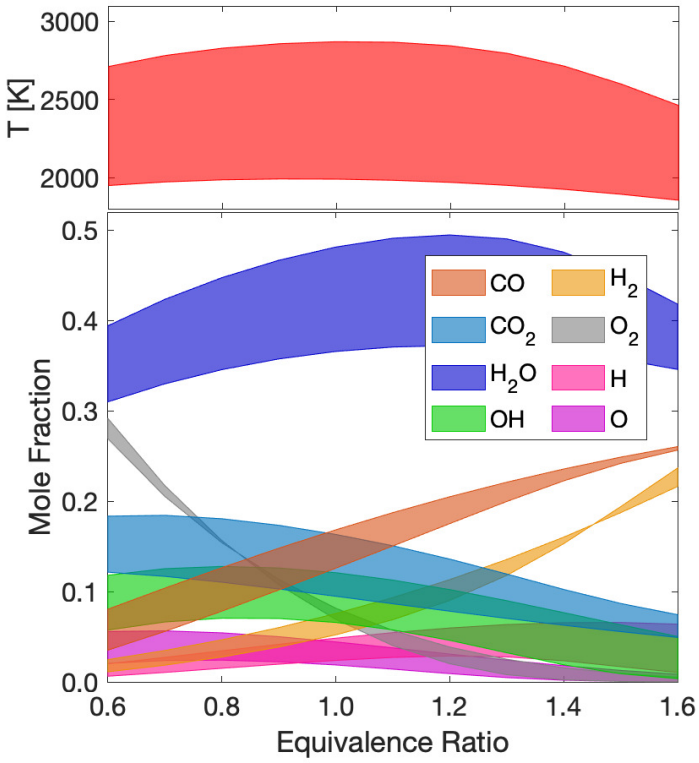

Figure 4.7: Plot of the temperature (*top*) and gas composition (*bottom*) for a CH_4–O_2 detonation gas expanded isentropically to one atmosphere. Each quantity is plotted as a range to indicate the variation in gas properties between equilibrium and frozen flow.

model to capture the possible range of gas composition. Additionally, it is noted that the expansion process may not be exactly isentropic, due to effects such as heat loss and friction. However, these entropy sources (while affecting gas temperature) are not expected to significantly change gas composition.

As mentioned, calculated broadening parameters for CO with collision partners CO_2, H_2O, and O_2 are tabulated in the literature [171]. Broadening parameters for CO with the collision partner H_2 are obtained from Sur et. al [172] and are scaled to account for the higher rotational quanta in this work by multiplying by the ratio of CO–N_2 broadening for different rotational quanta from Hartmann et. al [171]. To obtain the remaining broadening parameters for CO, OH, O, and H, we scale the broadening coefficient for N_2 by the optical collision diameter, σ_{CO-Y}, between CO and species Y, and reduced mass, μ_{CO-Y} of CO and

species Y through the following relationship [159]:

$$\gamma_{\mathrm{CO-}Y}(T) = \gamma_{\mathrm{CO-N_2}}(T) \left(\frac{\sigma_{\mathrm{CO-}Y}}{\sigma_{\mathrm{CO-N_2}}} \right)^2 \sqrt{\frac{\mu_{\mathrm{CO-N_2}}}{\mu_{\mathrm{CO-}Y}}}. \tag{4.11}$$

The optical collision diameter $\sigma_{\mathrm{CO-}Y}$ is calculated according to intermolecular potential parameter combination rules developed for the Lennard-Jones 6-12 potential [173]:

$$\sigma_{\mathrm{CO-}Y} = \frac{1}{2}(\sigma_{\mathrm{CO}} + \sigma_Y). \tag{4.12}$$

Although the optical collision diameter is not necessarily equal to the kinetic collision diameter, they are assumed to scale proportionally for the collision partners of interest [174]. The reduced mass is defined as:

$$\mu_{\mathrm{CO-}Y} = \frac{m_{\mathrm{CO}} m_Y}{m_{\mathrm{CO}} + m_Y}. \tag{4.13}$$

Values of σ_Y for CO, N_2, OH, O, and H are estimated from the collision diameters used in combustion species transport modeling [175], while values of m_Y are determined from species atomic and molecular weights. The uncertainties associated with this estimation procedure are included in our uncertainty analysis, discussed in more detail in Appendix D.0.5.

To simplify and increase the robustness of the iterative spectral fitting procedure described by Fig. 4.6, we assume that the collisional widths $\Delta\nu_C$ of the three target CO transitions P(0,31), P(2,20), and P(3,14) are equal to one another. This implies that the mixture-weighted collisional-broadening coefficients, $\gamma_{\mathrm{CO-mix}}(T)$, are also equal for the three rovibrational transitions. We show the validity of this assumption in Fig. 4.8, in which $\gamma_{\mathrm{CO-mix}}(T)$ for each of the three CO lines is plotted as a function of temperature for an equilibrium-assumed detonation exhaust composition at a nominal operation equivalence ratio of $\phi = 1.1$. It can be seen that the predicted values for all three lines converge within 5% at temperatures between 2000 and 3000 K, confirming the appropriateness of the assumption for the RDRE exhaust measurements performed in this work. Fig. 4.8 also shows the variation of $\gamma_{\mathrm{CO-mix}}$ for different equivalence ratios covering the range of frozen and equilibrium flows. It is observed that the broadening coefficient does not change significantly with species mole fraction variation associated with equivalence ratio and with frozen

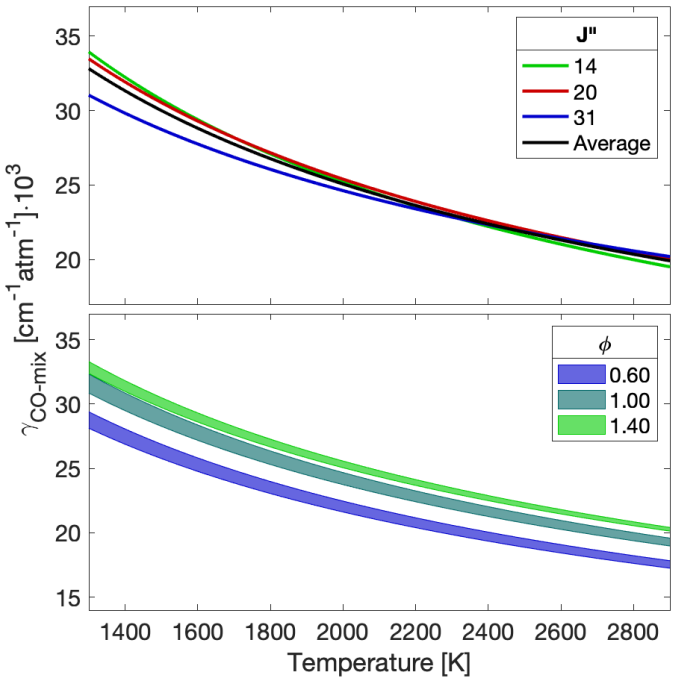

Figure 4.8: $\gamma_{\mathrm{CO-mix}}(T)$ plotted as a function of temperature for different rovibrational transitions J'' (*top*) as well as for different gas compositions corresponding to varying RDRE operation conditions and frozen vs. equilibrium assumptions (*bottom*).

or equilibrium conditions, particularly at higher temperatures and equivalence ratios, reducing the error introduced with the assumption of equilibrium composition, as detailed in Appendix D.0.5.

It is important to note that the total pressure P_{tot} determined in Eqn. 4.9 assumes insignificant pressure shifting [166] of the targeted CO transitions, that $\gamma_{\mathrm{CO-mix}}(\overline{T}) = \overline{\gamma_{\mathrm{CO-mix}}(T)}$, and that $\gamma_{\mathrm{CO-mix}}(T) \approx \sum_{\mathrm{Y}} X_{\mathrm{Y}} \gamma_{\mathrm{CO-Y}}(T)$. For the temperature range for this sensor (1500–3000 K), the anticipated pressure shifts of the transitions are lower than the measurement resolution (< 0.005 cm^{-1}), and $\gamma_{\mathrm{CO-mix}}(T)$ is approximately linear with T. Furthermore, in this temperature range, collisional-broadening behavior is largely insensitive to variations in gas composition—within the bounds of frozen and equilibrium mixture composition—along the integrated line of sight, resulting in only small potential deviations in parameters derived from a Voigt lineshape fit, estimated to be on the order of 2%.

4.3.3 CO_2-density measurement

A group of R-branch transitions comprising the bandhead of the $v_1 v_2{}^{l_2} v_3(01^10 \rightarrow 01^11)$ fundamental vibrational band of carbon dioxide was targeted for sensing of CO_2 column number density in the detonated gases. The specific rovibrational transitions are indicated in the bottom of Fig. 4.3, which shows the R(119)-R(129) lines in the bandhead. Unlike the targeted lines for CO, the lines of CO_2 in this bandhead are too spectrally blended to infer temperature and mole fraction utilizing the methods outlined in Section 4.3.1. Moreover, rovibrational bandheads at high temperatures and even moderate pressures are susceptible to collision-induced rotational energy transfers that distort molecular spectra at high collision frequencies, via a phenomenon known as line-mixing [176]. By accounting for line-mixing with additional spectral modeling, rovibrational bandheads have been successfully used to quantitatively interpret thermochemistry in rocket propulsion flows [177]. To interpret the absorption measurements of CO_2 in rotating detonation rocket flows, we implement a line-mixing model for the $v_1 v_2{}^{l_2} v_3(00^00 \rightarrow 00^01)$ bandhead developed in prior work [178]. The model, which uses the HITEMP database [168], is a function of J''-dependent broadening parameters $\gamma_{CO_2-Y}(T)$, temperature T, total pressure P_{tot}, and column number density N_{CO_2}. The absorbance is modeled as:

$$\alpha_{CO_2,\nu} = N_{CO_2} \frac{\text{Im}(\mathbf{d} \cdot \mathbf{G}^{-1} \cdot \boldsymbol{\rho} \cdot \mathbf{d})}{\pi}, \tag{4.14}$$

where the matrix $\boldsymbol{\rho}$ and vector $\mathbf{d}$ $[\text{cm}^{-1}/(\text{molec} \cdot \text{cm}^{-2})]^{\frac{1}{2}}$ are temperature dependent sets of spectral parameters that describe lower state Boltzmann population fraction and transition amplitudes. $\mathbf{G}$ $[\text{cm}^{-1}]$ is a complex matrix defined as:

$$\mathbf{G} = \nu \mathbf{I} - \boldsymbol{\nu}_0 - i P_{\text{tot}} \mathbf{W}_{CO_2-\text{mix}}(T), \tag{4.15}$$

where $\mathbf{I}$ is the identity matrix, $\boldsymbol{\nu}_0$ $[\text{cm}^{-1}]$ is a diagonal matrix of transition linecenters, and $\mathbf{W}_{CO_2-\text{mix}}(T)$ $[\text{cm}^{-1}/\text{atm}]$ is the temperature dependent relaxation matrix, which contains mixing rates for all relevant rovibrational transitions that scale with the collisional-broadening coefficients of the transitions. Thus, with independent knowledge of the temperature, pressure, and mixture-weighted broadening parameters, the absorbance at the

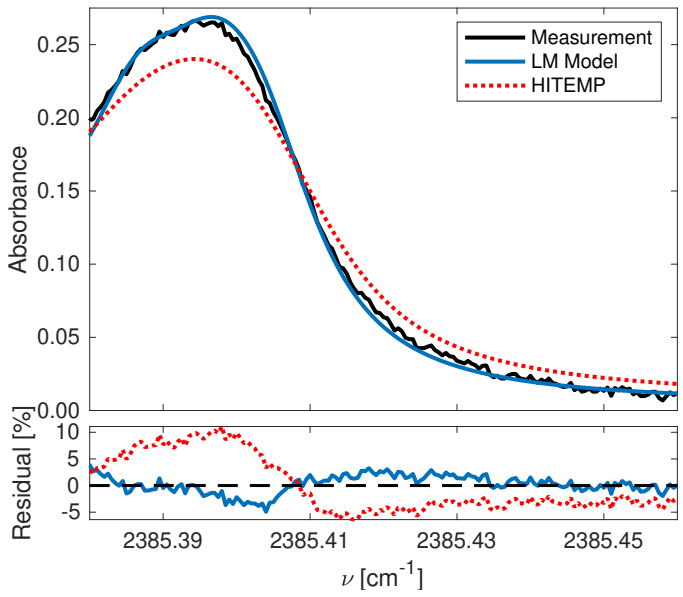

Figure 4.9: Absorbance for the targeted ($01^10 \rightarrow 01^11$) bandhead of CO_2 in an Ar bath gas measured in the UCLA High-Enthalpy Shock Tube facility, alongside predictions with and without the line-mixing model implemented. $X_{CO_2} = 0.03$, $P_{tot} = 0.95$ atm, $T = 2221$ K, $L = 10.32$ cm.

bandhead can be modeled as a function of a single variable (N_{CO_2}). More detail on the molecular physics governing line mixing is available in previous work [169].

Using values of $\gamma_{CO_2-Ar}(T)$ previously measured for the rovibrational transitions of interest [178] in an argon bath gas, we construct a modified relaxation matrix for the ($01^10 \rightarrow 01^11$) bandhead based on the experimentally determined $\mathbf{W}_{CO_2-Ar}(T)$ for the neighboring ($00^00 \rightarrow 00^01$) bandhead. The model includes measured broadening parameters from the CO_2 lines with rotational quanta J''=99–145, wholly encompassing the lines targeted in this work (J''=117–131). The predictive capability of this modified line-mixing model for the targeted wavelength region is examined using the high-enthalpy shock tube (described previously), and a representative case is shown in Fig. 4.9. The spectral simulation incorporating the line-mixing model exhibits much better agreement with the measured CO_2 bandhead spectra than the spectral simulation that neglects line-mixing, capturing the peak-to-valley differential absorption with lower residuals ($\sim$3%).

The relaxation matrix for Ar is scaled to determine the relaxation matrix in the RDRE exhaust mixture by:

$$\mathbf{W}_{\mathrm{CO_2-mix}}(T) = \mathbf{W}_{\mathrm{CO_2-Ar}}(T)\left(\frac{\gamma_{\mathrm{CO_2-mix}}(T)}{\gamma_{\mathrm{CO_2-Ar}}(T)}\right). \tag{4.16}$$

Here, $\gamma_{\mathrm{CO_2-Ar}}(T)$ is the collisional-broadening coefficient for CO_2 in Ar and $\gamma_{\mathrm{CO_2-mix}}(T)$ is the mixture-weighted collisional-broadening coefficient for CO_2, defined as:

$$\gamma_{\mathrm{CO_2-mix}}(T) = \sum_{Y} X_Y(\gamma_{\mathrm{CO_2-}Y}(T)). \tag{4.17}$$

$\gamma_{\mathrm{CO_2-Y}}(T)$ for the collision partners CO_2, H_2O, N_2, and O_2 are obtained using tabulated values for J''=101 provided by Rosenmann et. al [179] and $\gamma_{\mathrm{CO_2-Ar}}(T)$ is obtained using measured values for collisions with argon at J''=101 [178]. Broadening parameters for CO_2 with collision partner H_2 are determined using the same method as those for CO—the $\gamma_{\mathrm{CO_2-H_2}}(T)$ value reported by Sur et. al [172] is scaled to account for the higher rotational quanta in this work. As with CO, the remaining CO_2 broadening parameters for collision partners CO, OH, O, and H are estimated by scaling $\gamma_{\mathrm{CO_2-N_2}}(T)$ according to Eqns. 4.11 through 4.13. The mole fractions X_Y are estimated from the CJ detonation model described in Section 4.3.2.

For every wavelength modulation period, the measured temperature and pressure from the previously discussed CO spectroscopy, as well as estimated mixture composition (determined through the methods described in Sections 4.3.1 and 4.3.2) are used as inputs for the line-mixing model for CO_2. The line-mixing model is fitted to the measured spectra using a nonlinear least-squares solver with $N_{\mathrm{CO_2}}$ as a free parameter, while holding T and P_{tot} constant. To simplify the fitting procedure, a peak-to-valley differential absorption is specifically targeted, wherein only the absorbance at the bandhead peak ($\approx$2385.39 $\mathrm{cm^{-1}}$) and at a low-absorbance valley region ($\approx$2385.50 $\mathrm{cm^{-1}}$) are used for the fit. Due to the larger number of assumptions and estimates for the inputs to the CO_2 spectral model, the inferred column density has inherently higher uncertainty, as discussed in Appendix D.0.6.

4.4 Experimental setup

Fig. 4.11 illustrates the optical configuration for the absorption sensing technique and hardware interface for conducting measurements at the exit plane of an RDRE combustor. The design of the modular RDRE test article is described thoroughly in previous work [24, 28], and so only the information most relevant to the optical interface, operating conditions, and data analysis are detailed here for brevity. The outer diameter of the copper test article annulus is 7.62 cm, and the width of the annulus is 0.5 cm. The RDRE operates on gaseous methane (CH_4) and gaseous oxygen (O_2) as the main propellants, which are ignited with a pre-detonation system near the exit of the chamber. The propellants are injected through impingement-style elements around the annulus, and their flowrates are measured using sonic orifices. These measured flow rates are used to determine overall operating equivalence ratio, ϕ. During a test, pressures in the injection manifolds are high enough to provide choked

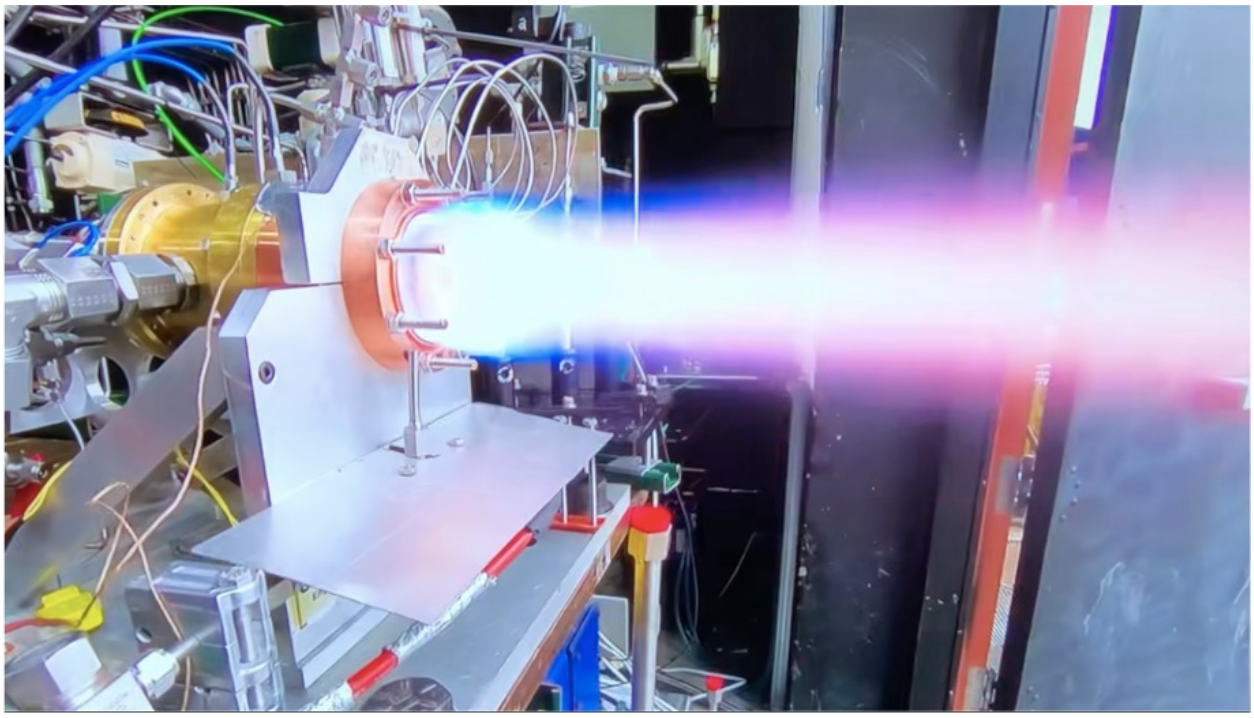

Figure 4.10: Hot-fire test of CH_4–O_2 RDRE at AFRL with optical diagnostics installed (obscured by plume)

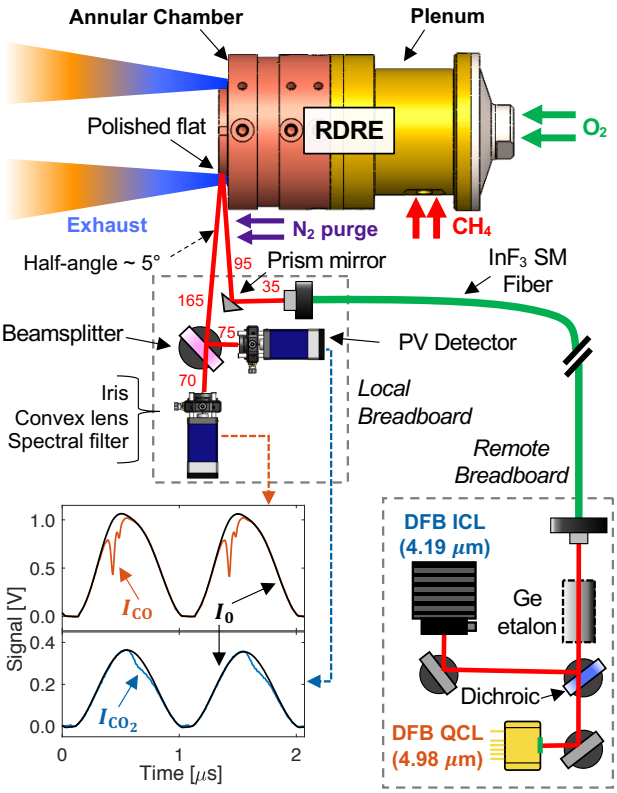

Figure 4.11: Optical interface for RDRE data collection. Beam path lengths are provided in millimeters.

flow, though this may not be the case during the presence of a passing detonation wave. Capillary tube attenuated pressure (CTAP) static probes are used to monitor pressure at various locations in the annular combustion chamber. Additionally, measurements of the test article thrust are made using a 500-lbf (2.2-kN) load cell. The test article can be observed during a hot-fire test in Fig. 4.10.

A notable feature of the RDRE hardware is the polished copper center body protruding out of the exit plane. Four 0.635 cm × 0.635 cm square flats are machined onto the center-body, providing retro-reflective surfaces for the laser beams. As the annular gap is 0.5 cm, the optical path length is approximately 1 cm.

To probe the targeted lines of CO near 4.98 µm and the CO_2 bandhead near 4.19 µm, the DFB QCL with ∼50 mW output power and the DFB ICL with ∼5 mW output power described in Section 4.2 are utilized as the single-mode light sources, respectively. A dichroic

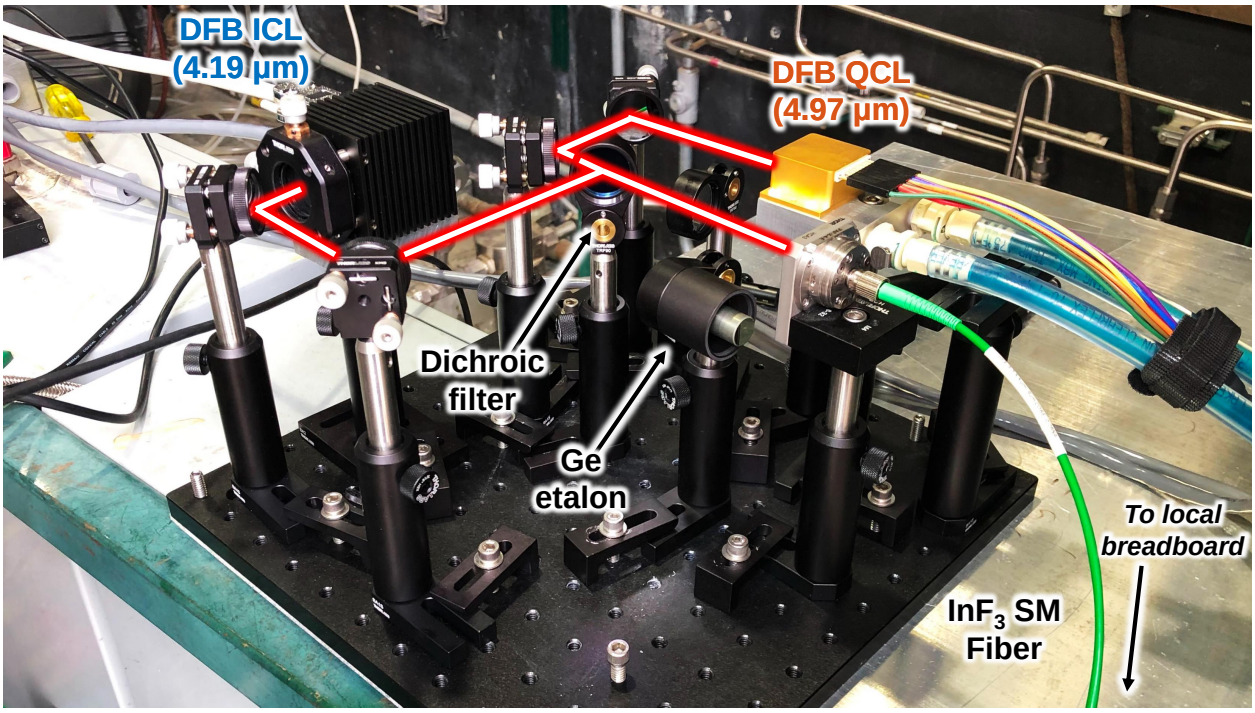

Figure 4.12: Image of remote breadboard which multiplexed lasers using a dichroic filter and coupled the beams into a fiber optic cable.

filter is used to multiplex the laser beams, acting as a beamsplitter with minimal power loss. Both incident beams are aligned colinearly and free-space coupled into one single-mode InF_3 fiber with a 9 µm core diameter. The fiber delivers the light from a remote breadboard, on which the lasers are mounted, to a local breadboard mounted to the RDRE thrust structure. The remote breadboard is pictured in Fig. 4.12 and the local breadboard is pictured in Fig. 4.13. The fiber output is then re-collimated using a CaF_2 lens and reflected off a small right-angle prism mirror. The beam is then pitched across the exit of the RDRE annulus through the exhaust gases and onto the polished center body flat surface, which reflects the light back towards the detector assembly, as shown in the top of Fig. 4.11. A beam splitter separates the transmitted light so that each beam can be spectrally filtered for its respective wavelength (Electro Optical Components, 4210±42 nm and Spectrogon, 4960±148 nm) before being collected on distinct thermo-electrically cooled photodetectors. The spectral filters also mitigate interference caused by thermal emission

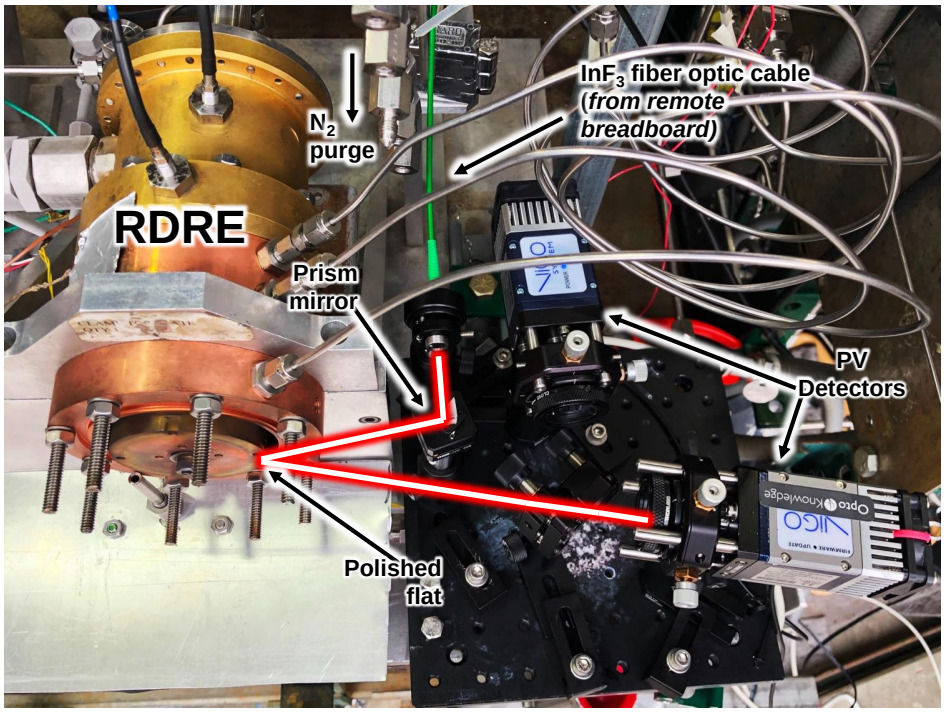

Figure 4.13: Image of local breadboard which reflected light of RDRE center body back into PV detectors for LAS measurements.

from the hot exhaust gases. The two MCT photovoltaic detectors (Vigo PVMI-4TE-8-1x1)[1] have ∼200-MHz bandwidth each to resolve the RF modulation. The pitch and catch optics (detectors, beamsplitter, prism mirror, lenses) were all mounted on the aforementioned local breadboard using standard optical posts adjusted in height to be in a horizontal plane passing through the centroid of the RDRE. The optical setup includes kinematic mounts for beam pointing and translation, which were used to optimize alignment and maximize the transmitted light intensity during the experiment.

Raw detector voltages were collected at sample rates of 250 MS/s and 500 MS/s, for 1.0 s intervals (0.5 s intervals for 500 MS/s tests) of hot-fires spanning approximately 1.0 s in duration. A nitrogen purge system directed along the side of the test article displaces

[1]It was found that these high-bandwidth detectors had alignment-dependent non-linearity above voltage levels of 0.5–1 V. This limited the maximum signal and signal-to-noise ratio (SNR) of these measurements. In Chapters 6–8, AC-coupled detectors (Vigo PVI-4TE-6-1x1) were instead used, with linearity up to 3 V, greatly improving measurement SNR.

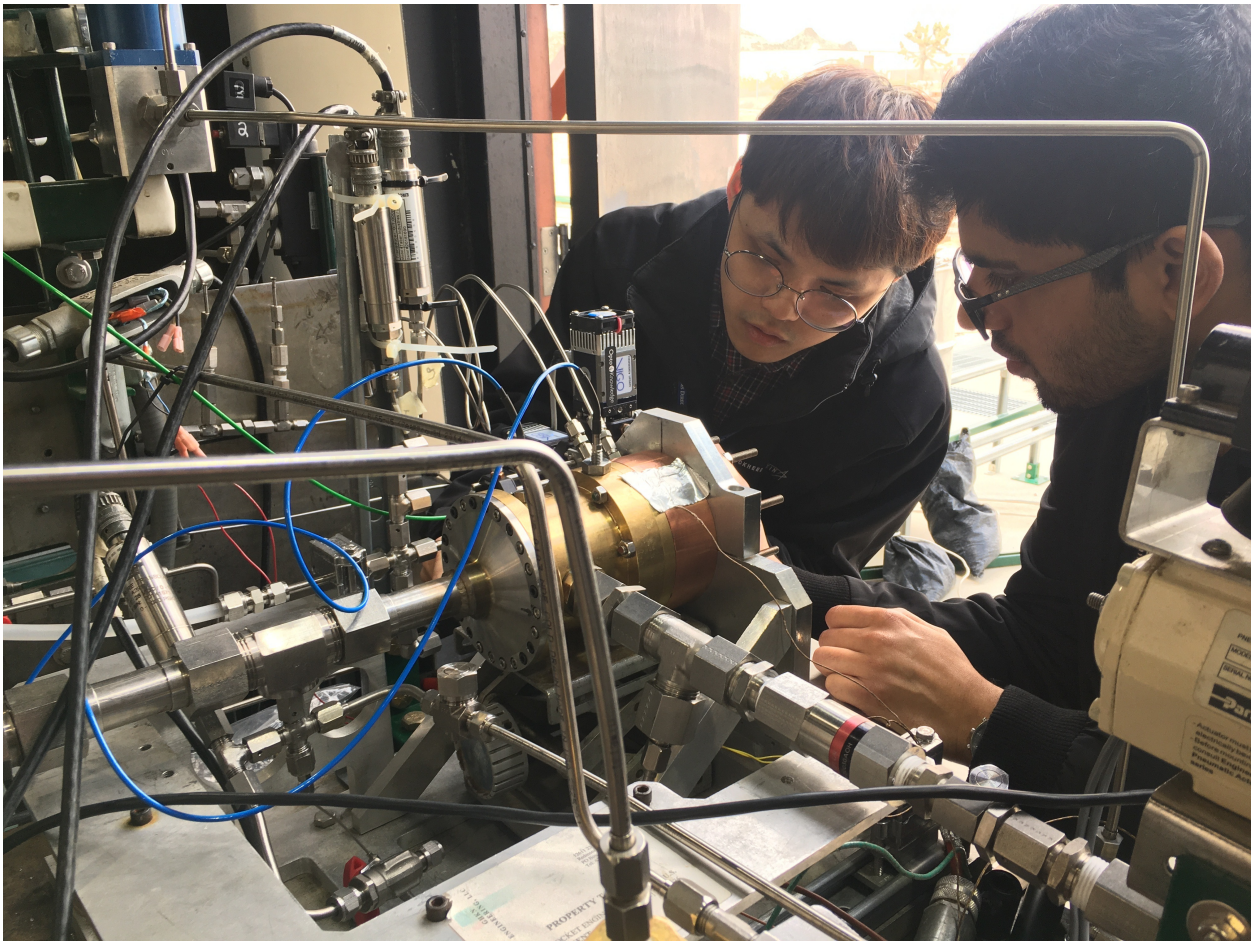

Figure 4.14: UCLA graduate students Daniel Lee (*left*) and Anil Nair (*right*) aligning retro-reflection optics for RDRE LAS measurements.

ambient H_2O vapor and CO_2 and mitigates exhaust gas recirculation in the optical line-of-sight, which can otherwise spectrally interfere with the absorbance spectra of CO and CO_2, respectively. The QCL targeting CO is modulated at rates varying from 1 MHz to 3 MHz, while the ICL targeting CO_2 is modulated at 1 MHz. Prior to each test, the incident light intensity I_0 is recorded for each light source, along with a measurement of the light intensity with the germanium etalon in the line-of-sight to determine the relative frequency of the laser scan.

4.5 Sensor demonstration

Time-resolved laser absorption measurements were performed on the RDRE combustor over a range of propellant flow rates ($\dot{m}$ = 0.2–1.0 lbm/s) and mixture ratios (ϕ = 0.6–1.6) with CH_4–GOx as propellants. All tests were completed at the Air Force Research Laboratory on Edwards Air Force Base in Edwards, CA USA. Raw detector voltage data, such as those shown in the inset of Fig. 4.11, are processed using Eqn. 4.2 to obtain spectral absorbance α_ν for both species of interest. We note that the transmitted light intensity I_t required subtraction of thermal emission and the background light intensity I_0 required temporal shifting and multiplication by a scalar to match the non-absorbing portion of the transmitted intensity. Due to the large frequency separation between laser modulation and environmental noise, common baseline convoluting factors such beam steering appear frozen during a single modulation period and do not distort the scan shape (enabling correction by a simple scalar multiplier). The aforementione frequency separation can visualized in Fig. 4.15 where a Fast-Fourier transform of the raw 1-s long LAS data trace is taken in three conditions: (1) when the laser light is not incident upon the detector, but the RDRE is hot-firing (black), (2) when the laser is modulating at 1 MHz, but the RDRE is not operating (blue), and (3) when the laser is modulating and the RDRE is hot-firing (red). It can bee seen that the frequency content above 1 MHz, associated with the laser modulation is well above the frequency content associated with RDRE cycle dynamics (15–100 kHz). Additionally, while the noise is constant in the MHz regime, the noise begins to increase as $1/f$ in the sub-MHz regime, representing the effect of mechanical vibrations, thermal emission, and other convoluting factors. This $1/f$ noise is also well-separated from the laser-modulation frequency and associated overtones.

In the remainder of this section, we first present time-histories of temperature, CO, and pressure calculated from the absorption measurements provided by the QCL at MHz rates, stepping through the intermediate analyses required to determine those values. We then follow with a demonstration of simultaneous multi-species CO and CO_2 sensing enabled by the additional absorption measurements provided by the ICL and revealing ability to

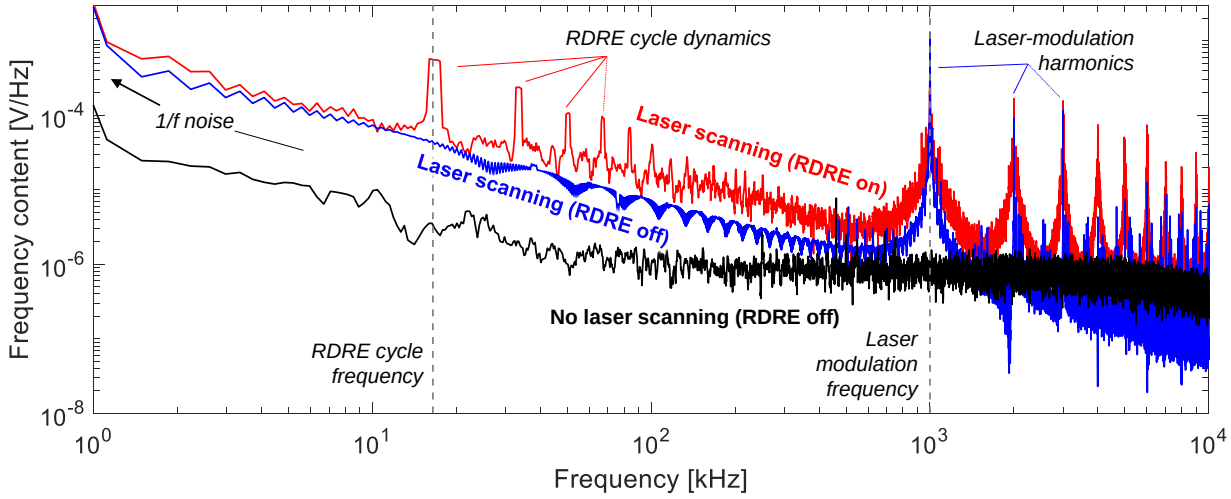

Figure 4.15: Fast-Fourier Transform of raw detector data with laser on (red and blue curves) or laser off (black curve). Also, the variation with the RDRE operating (black and red curves) and not operating (blue curve) is shown.

account for total carbon oxidation. Finally, we demonstrate enhanced time resolution of the technique, pushing the thermochemistry measurements to rates up to 3 MHz. As mentioned previously, a rigorous uncertainty analysis for the reported values of temperature, column number density, and pressure is presented in Appendix D.

4.5.1 Time-resolved CO spectroscopy

The spectra targeting CO are fitted according to the iterative procedure described in Section 4.3.1 and by Fig. 4.6. Figure 4.16 shows the measured absorbance spectra from a representative single sub-microsecond scan (no averaging) along with the corresponding spectral fits of the three targeted CO transitions. The residual between measurement and overall spectral fit with the Voigt lineshape model is typically under 2%, demonstrating the appropriateness of the iterative fitting procedure for this sensing application and the relatively high SNR. The behavior of the CO spectra as the detonation waves pass through the line-of-sight can be visualized more readily by plotting the spectra in three dimensions as a function of time, as shown in Fig. 4.17. A distinct periodicity in the time-resolved behavior

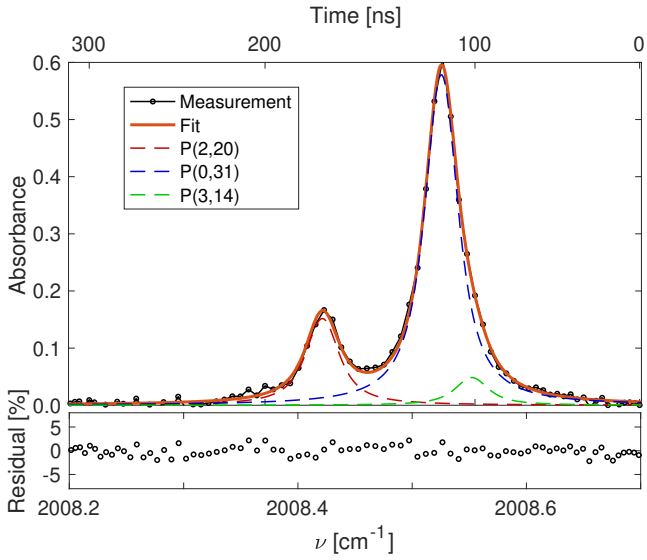

Figure 4.16: Example scanned-wavelength Voigt fitting of data from the RDRE experiments, showing an effective measurement integration time of 300 ns.

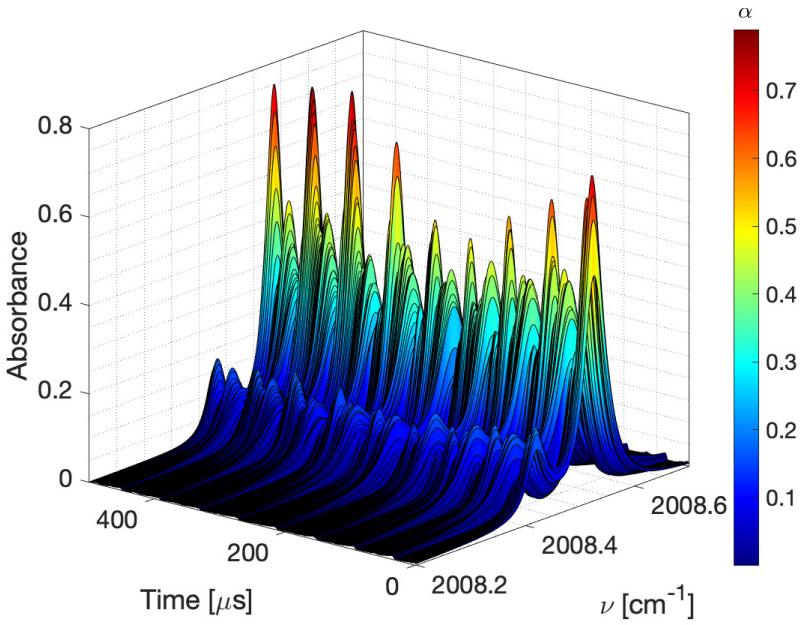

Figure 4.17: Visualization depicting changing spectra of the P(0,31), P(2,20) and P(3,14) lines of CO in time during a representative measurement of RDRE exhaust.

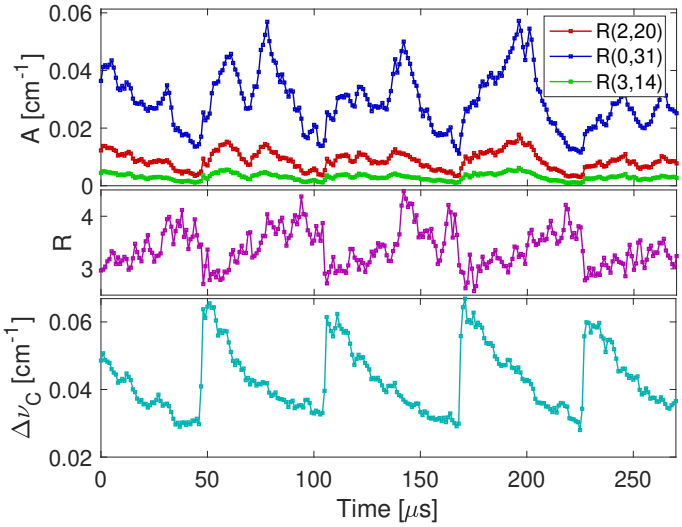

Figure 4.18: Time-resolved absorbance areas of the P(0,31), P(2,20) and P(3,14) lines of CO (*top*). The time-resolved ratio of absorbance areas of the P(0,31) and P(2,20) lines (*middle*). Time-resolved collisional-width (*bottom*).

of the spectra is observed, evidenced by sharp increases in both the peak absorbance α and the collisional broadening in the lines. The rapidly changing thermodynamic conditions in the flowfield associated with each detonation cycle affect the spectral parameters for each transition differently, which can be discerned by plotting absorbance area A_{kj} and collisional width $\Delta\nu_C$ as a function of time for the P(0,31), P(2,20) and P(3,14) lines as shown in Fig. 4.18. As with the spectral absorbance shown in Fig. 4.17, periodic behavior is observed in time for all absorbance areas A_{kj}, with the the P(0,31) and P(2,20) lines consistently demonstrating the largest values in every detonation cycle. The fitted collisional width $\Delta\nu_C$ for all lines shows a very clear sharp rise and decay behavior, indicative of a large pressure rise associated with a shock or detonation wave. The ratio of the absorbance areas for the P(0,31) and P(2,20) lines, R, is also plotted as a function of time in Fig. 4.18. At the start of every cycle, there is a distinct drop in R associated with an increase in temperature, as indicated by temperature-dependence shown in Fig. 4.5.

Once temperature is determined from R, column number density N_{CO} and total pressure P_{tot} can be determined via the methods described in Sections 4.3.1 and 4.3.2, respectively.

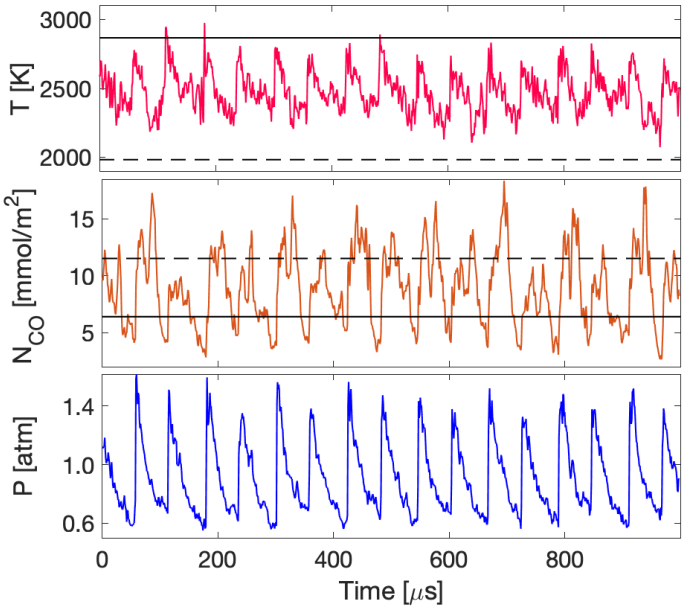

Figure 4.19: Time-resolved temperature (*top*), CO column density (*middle*) and pressure (*bottom*) over 1000 µs. The temperature and column density values predicted from CANTERA at P_{tot} =1 atm are shown for equilibrium flow as solid black curves and for frozen flow as dashed black curves. A path length of 1 cm is assumed for the column density.

Representative results are shown in Fig. 4.19 for 1000 µs of a hot-fire test conducted with a propellant mass flow rate of $\dot{m}$=0.6 lbm/s and a nominal operating equivalence ratio of ϕ=1.1. For this test, periodicity in temperature, column density, and pressure characteristic of the cyclic nature of RDREs are readily observed. Precision error for all variables is calculated by dividing measurement noise (1-σ of a 5-point moving average) by the mean variable value for the entire test. Measured temperature is observed to oscillate between 2250 K and 2800 K with a precision error of approximately 2.1%, and nominally within the bounds set by the frozen and equilibrium conditions predicted by the CJ detonation model. Likewise, the CO column number density oscillates about the range of predicted values with a precision error of about 3.1%. Additionally, there is a noticeable second peak in N_{CO} in many of the cycles. The time-history of the total pressure determined from fitted collisional width $\Delta\nu_C$ shows very sharp peaks to values as high as 1.5 atm and decay to valleys as low as 0.6 atm, with

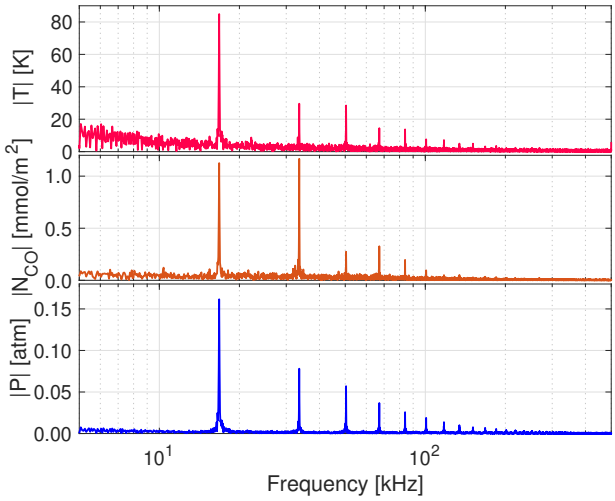

Figure 4.20: Fast-Fourier transform of 10 ms of time-resolved temperature, CO column density and pressure data. A strong peak near 16.78 kHz is observed.

a precision error of approximately 3.7%. Uncertainty associated with these measurements is detailed in Appendix D.

A harmonic analysis of the thermodynamic conditions can allow us to examine these distinct behaviors among the thermodynamic state variables in more detail. A discrete-Fourier transform is performed on a 10 ms interval of the temperature, column number density, and pressure time-histories, and the resulting dominant temporal frequencies [kHz] are shown in Fig. 4.20. For this RDRE test, the single-sided amplitude spectra of these thermodynamic state variables reveals common peaks at 16.78 kHz as well as associated overtone frequencies (33.56 kHz, 50.34 kHz, 67.12 kHz, etc). Interestingly, although 16.78 kHz represents the strongest frequency for both temperature and pressure and corresponds to the detonation frequency determined through high-speed video [28], the strongest frequency observed for CO column number density is 33.56 kHz, likely a consequence of the second peak observed in N_{CO} during many of the detonation cycles, as shown in Fig. 4.19.

4.5.2 Simultaneous CO and CO_2 measurement

To achieve simultaneous measurement of CO_2, the spectra targeting CO_2 are fitted with a line-mixing model using the time-resolved thermodynamic parameters measured from the CO spectra as inputs, as described in Section 4.3.3. Fig. 4.21 shows the measured absorbance spectra from a representative single scan along with the least-squares fit of the line-mixing model. A corresponding simulation of the spectra without implementing the line-mixing model is also shown, highlighting the line mixing model's ability to better capture differential absorption between the maximum and minimum absorbance regions in the CO_2 bandhead spectra. The signal-to-noise ratio (SNR) of the measurement is much lower than that of CO, resulting in spectral fit residuals of approximately 10%. There are a few causes, including the low detector signal of the laser light intensity from the ICL as shown in Fig. 4.11 and the generally lower CO_2 absorbance relative to that of CO for these thermodynamic conditions. Nevertheless, the absorbance measurement can be quantitatively interpreted to provide a

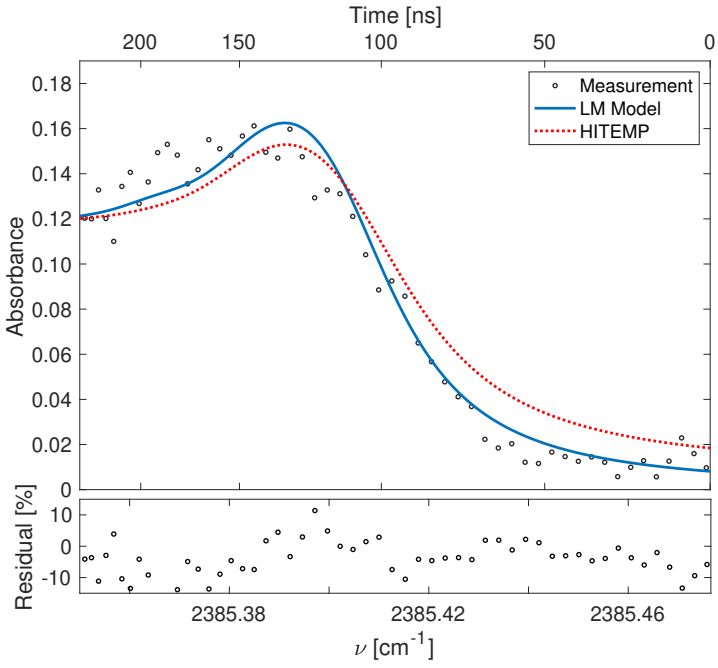

Figure 4.21: Example scanned-wavelength CO_2 bandhead data from the RDRE experiments, showing an effective measurement integration time of 250 ns.

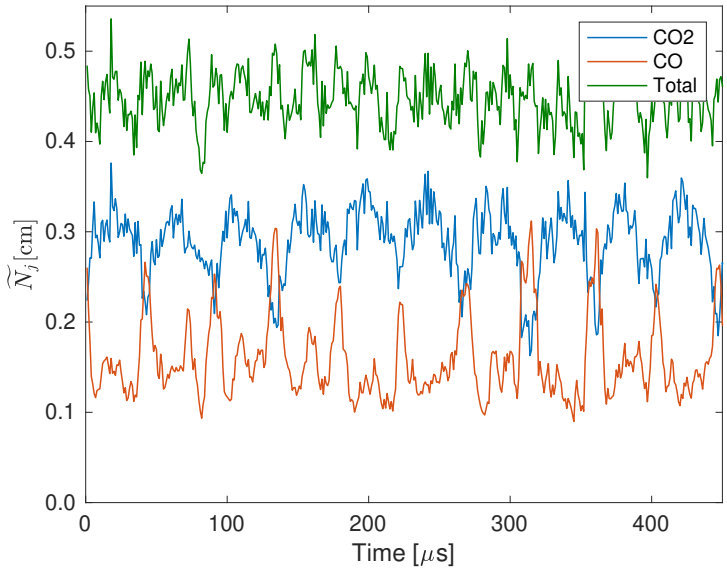

Figure 4.22: Time-resolved profiles of temperature and pressure normalized column number densities $\widetilde{N}_j$ for CO, CO_2, and their sum.

time-resolved measurement of CO_2 density in the detonation exhaust with a measurement precision of approximately 6.2%. To better quantitatively interpret the relative concentrations of CO and CO_2 and separate the time-resolved species concentration behavior from the time-resolved temperature and pressure, we normalize the CO and CO_2 column densities by the ratio of pressure and temperature to yield $\widetilde{N}_j$:

$$\widetilde{N}_j = N_j \frac{k_B T}{P_{\text{tot}}}, \tag{4.18}$$

which we expect to trend with the relative concentration or mole fraction of species across the line-of-sight.

Representative $\widetilde{N}_{\text{CO}}$ and $\widetilde{N}_{\text{CO}_2}$ values from a hot-fire test conducted with a propellant mass flow rate of $\dot{m}$=1.0 lbm/s and an equivalence ratio of ϕ=1.1 are shown in Fig. 4.22 along with their sum. Important trends among the simultaneous species measurements are immediately noted; periodic spikes in CO correspond to dips in CO_2, while their sum (total) oscillates with a lower amplitude about a constant value, indicating a conservation of total carbon oxides in the RDRE exhaust with some potential variation in oxidizer-to-fuel ratio

over time. The power of the simultaneous CO–CO_2 sensing strategy coupled with the MHz-measurement rates is highlighted by examining intra-cycle species evolution. In each cycle, a sudden large increase in CO is immediately followed by an increase in CO_2 which occurs on a longer timescale as CO decreases. As was seen in Figs. 4.19 and 4.20, some cycles exhibit a second—albeit less pronounced—increase and decrease in CO accompanying the larger increase and decrease, implying some potential chemical kinetic evolution within each cycle (convolved with post-detonation fluid dynamics). It should further be noted that chemistry (carbon oxidation) in the exhaust plume (related to entrained air) may influence the ratio of CO and CO_2 and their quantitative comparison. Such a biasing effect is minimized by the nitrogen purge and close axial proximity of the beam to the RDRE chamber.

4.5.3 Multi-MHz sensing

To demonstrate the high-speed RF wavelength modulation capability of the opto-electronic configuration used in this work, we conducted scanned-wavelength direct absorption spectroscopy measurements of the target CO lines at 1, 2, and 3 MHz using the DFB QCL. Fig. 4.23 shows the measured temperature, CO column number density, and pressure time-history of three independent RDRE tests operating at the same mass flow rate of $\dot{m}$=0.6 lbm/s and reactant equivalence ratio of ϕ=1.1. The time-histories in Fig. 4.23 have been phase-adjusted for simpler comparison amongst the measurements. Additionally, the values of P_{tot} have been plotted as deviation about their common mean. As noted in Fig. 4.2, the scan depth of the QCL decreases as the scan rate increases—for the 3 MHz measurements, the P(0,31) and P(3,14) lines were only partially resolved. This reduced the robustness of the spectral fit and introduced more noise into the time-histories of absorbance area A_{kj} and thereby more noise into the area ratio R, precluding clean measurements of T and N_{CO}. Fortunately, the spectral fits of collisional width $\Delta\nu_C$ were found to be more robust against this phenomenon, since the P(2,20) line was completely resolved, enabling 3 MHz measurement rates of total pressure P_{tot} using the single line (with a modest increase in uncertainty). Some test-to-test and cycle-to-cycle variation is observed between the three experiments; however,

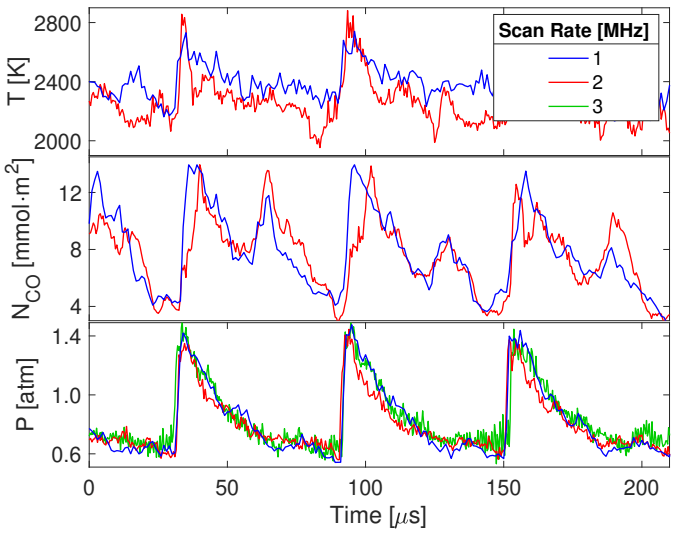

Figure 4.23: Time-resolved temperature, CO column density, and pressure at the RDRE exhaust for 1, 2, and 3 MHz measurement rates. Pressure is shown as a deviation from mean pressure.

distinct common thermochemical behavior is observed, most notably the secondary peak in the N_{CO} time-histories. The higher speed measurements clearly show a resolution of sharp changes in temperature and species density, as well as the peaks and valleys of the pressure rise and fall associated with each of the detonation waves (capturing temporal behavior more difficult to resolve at the lower measurement rates).

4.6 Summary

A laser absorption sensing strategy for CO, CO_2, temperature, and pressure has been developed for MHz measurements in annular detonation exhaust flows using diplexed RF modulation (bias-tee circuitry) with mid-infrared distributed feedback lasers. Temperature, pressure, and CO column number density were inferred from an iterative multi-line Voigt fitting procedure applied to a spectrally-resolved cluster of P-branch transitions in the fundamental infrared band near 4.98 µm. CO_2 column number density measurements were obtained by fitting a line-mixing model of absorption to the peak and valley of the rovibrational band-

head near 4.19 µm, using the temperature and pressure inferred from CO as inputs. The multi-parameter sensing method was demonstrated on a rotating detonation rocket combustor at measurement rates up to 3 MHz with integration times as short as 100 ns, elucidating transient gas properties not previously observable. Beyond the unique application, the RF modulation technique using bias-tee circuitry with mid-infrared DFB sources was proven both exceptionally fast and robust, with broader utility to other highly transient harsh environments.

In the next chapter, this sensor is used to analyze the thermodynamics and fluid mechanics of the CH_4–O_2 rotating detonation engine across various operating conditions. Chapter 6 focuses on extending the scan depth capability of bias-tee-modified DFB lasers to extend the technique to more extreme applications. Chapter 7 focuses specifically on the pressure sensing method of this chapter, extending the sensor to general combustion environments and providing a more comprehensive uncertainty analysis for these various applications. Chapter 8 extends the thermometry / CO species sensing to extremely high temperatures (near 10,000 K) by using a multi-line Boltzmann population fit.

CHAPTER 5

Methane-oxygen rotating detonation exhaust thermodynamics with variable mixing, equivalence ratio, and mass flux

The contents of this chapter have been published in the journal ***Aerospace Science and Technology*** *under the full title "Methane-oxygen rotating detonation exhaust thermodynamics with variable mixing, equivalence ratio, and mass flux" [113]. Portions of the chapter's content have been presented / included in the conference proceedings for the* ***AIAA Propulsion and Energy Forum, 2020*** *[150].*

5.1 Introduction

In this chapter, the MHz diagnostic developed in Chapter 4 is used to examine the thermodynamics of the gaseous methane-oxygen RDRE developed by the Air Force Research Laboratory (Edwards, CA) over the last several years [12]. This engine [24] has been the subject of several concerted experimental and numerical investigations, collectively known as the model validation for propulsion (MVP) effort [180]. These investigations, among others, have yielded valuable insights into the relationships among operating conditions, rotating detonation behavior, and overall engine performance. Specifically, the effects of injection, mixing, and mass flow rate on thrust, specific impulse, and detonation propagation have been systematically examined, revealing that—among many observed trends for the conditions tested—performance is generally independent of injector orifice size [38], rotating detonation stability is strongly dependent on propellant mixing [44], and that the num-

ber of concurrent detonation waves in the annulus is linked to the detonation wave-speed and propellant flow rate [28, 37, 45]. Though RDRE propulsive performance has traditionally been linked with higher detonation wavespeeds, caveats to this observation have been recently noted [49], wherein increased specific impulse for an RDRE is observed even in circumstances where detonation wavespeed is reduced. It is thus apparent that detonation wavespeed (often measured by high-speed cameras) and overall propulsive performance (i.e. measured engine thrust and specific impulse) hold a complex relationship convoluted by local transport effects and thermochemistry. These factors influence the degree of parasitic deflagration in the flow, which is suspected as the primary culprit in suboptimal RDRE performance [50, 51] as indicated in Chapter 1. The heat released via parasitic deflagrative reaction both pre- and post-detonation—shown as contact surface burning in Fig. 1.8—is energy unavailable to the detonation, reducing post-detonation pressure gain and specific impulse [49].

These critical nuances highlight limitations of current diagnostic capability in providing sufficiently resolved data to determine underlying localized thermochemical behavior responsible for non-ideal global RDRE performance. In particular, the steep gradients in temperature, pressure, and species concentrations of detonation waves over small spatial ($<$1 mm) and temporal ($<$100 µs) scales have posed unique diagnostic challenges in the quantitative evaluation of RDREs. Although measurements of thrust, chamber pressure, and mass flow rate have long been used to calculate specific impulse and characteristic velocity in rocket applications [1], these global metrics represent the end-result of several energy conversion processes and lack granularity to quantify local combustion progress. Capillary tube attenuated pressure (CTAP) measurements are only able to capture averaged pressure measurements [24] and cannot distinguish individual detonation waves in these engines. Detonation wavespeed—often considered a metric of detonation ideality—is usually measured in RDREs using high-speed videography and compared to the corresponding theoretical Chapman-Jouguet detonation condition [34, 47, 36, 37, 48]. These measurements have provided a basis for evaluation of local thermochemistry, but cannot readily distin-

guish the individual contributions of deflagrative vs. detonative combustion to overall heat release. Moreover, as computational power has increased, these experimental measurement techniques are unable to characterize RDREs with sufficient detail to compare with the increasingly sophisticated models used in RDRE development.

The laser-absorption diagnostic methods developed in Chapter 4 can provide non-intrusive means to interrogate quantitative flow-field thermochemical properties, elucidating the underlying local combustion behavior as well as propulsion system performance. The high measurement rate for this diagnostic (MHz) allows for time-resolved intra-cycle analysis. As employed in the current chapter, this method provides quantitative thermodynamics measurements of temperature, pressure, and CO density with sufficient granularity to assess temporal and spatial characteristics associated with RDRE operation.

In this chapter, we present a novel and comprehensive dataset of rotating detonation combustor exhaust thermodynamics for gaseous methane and oxygen propellants with a doublet impingement-style injector. MHz laser-absorption measurements of pressure, temperature, and CO are analyzed over a sequence of tests with varying nominal equivalence ratio, mass flux, and mixing characteristics. We first review the methods used to obtain and analyze time-resolved gas properties as well as the RDRE test article and operational characteristics. We then describe the results from the tests performed and conclude with a discussion of RDRE performance, including transient behavior, cycle-average property evolution, and other reacting flow dynamics revealed by the time-resolved quantitative data.

5.2 Methods

In this section, we define the methods used to analyze the rotating detonation rocket combustor. We first describe the experimental setup involving a rotating detonation rocket test rig at the U.S. Air Force Research Laboratory (in Edwards, CA USA) and the optical interface of the mid-infrared laser absorption sensing system, illustrated in Fig. 5.1. We then describe the spectroscopic methods used to quantitatively infer temperature, pressure, and

CO species density from time-resolved absorption data.

5.2.1 RDRE test rig

The design of the modular RDRE test article is described thoroughly in previous works [24, 28], so here we briefly review information most relevant to the optical measurement location, selected test article configuration, and operating conditions. The outer diameter of the copper test article annulus was 7.62 cm, and the width of the annulus was 0.5 cm. The overall chamber length was 7.62 cm. A notable distinction of the RDRE hardware relative to prior work is the polished copper center body protruding out of the exit plane—Four 0.635 cm × 0.635 cm square flats were machined onto the centerbody, providing retro-reflective surfaces off which laser beam can reflect.

The RDRE operated on gaseous methane (CH_4) and oxygen (O_2) as the main propellants, which were ignited with a pre-detonation system near the exit of the chamber. The propellants entered the annular chamber through 72 unlike doublet impingement-style elements distributed circumferentially about the injector face. The fuel and oxidizer hole diameters were 0.787 mm and 1.24 mm respectively. Each propellant stream was angled 30 degrees from the vertical. The fuel and oxidizer holes were drilled into separate concentric face-

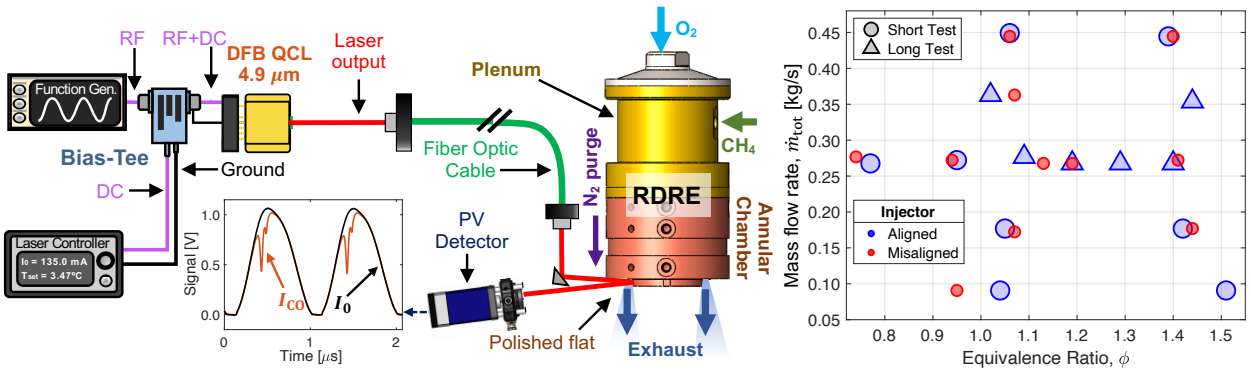

Figure 5.1: Bias-tee laser control schematic and optical interface for RDRE data collection with sample raw detector data (*left and center*). Mass flow rate and equivalence ratio test matrix (*right*).

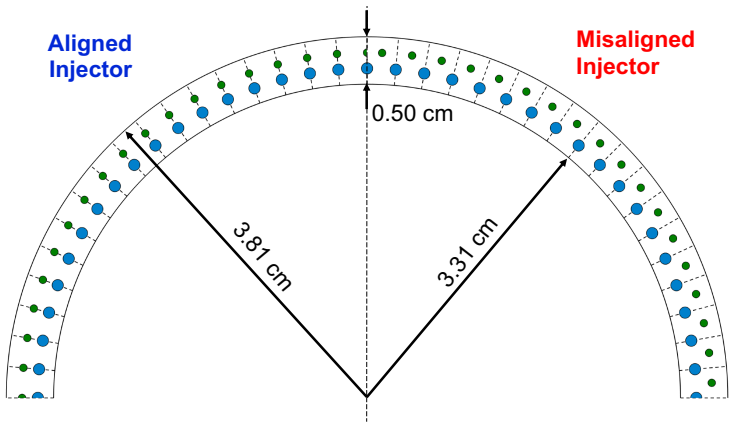

Figure 5.2: Schematic of injector face with key annulus dimensions. The aligned injector configuration is shown on the left and the misaligned injector configuration is shown on the right.

plates that were aligned such that the fuel and oxidizer streams directly impinge upon each other. The concentric faceplates could also be configured into a staggered or "misaligned configuration" such that the fuel and oxidizer streams would be alternating and azimuthally equidistant, separated by 2.5 degrees [44, 54]. This configuration represented poor reactant mixing. The two configurations are depicted graphically in Fig. 5.2. Notably, for all tests performed here, there was no nozzle attached to the annular combustor.

Propellant flowrates were measured using critical flow nozzles; these measured flow rates were then used to determine the flow condition, comprised of the equivalence ratio, ϕ, and total mass flow rate, $\dot{m}_{\text{tot}}$. During the various tests, pressures in the injection manifolds were high enough to provide choked flow, though not necessarily during passage of a detonation wave. Capillary tube attenuated pressure (CTAP) static probes were used to monitor pressure at various locations in the annular combustion chamber. The furthest upstream CTAP probe was located 8.9 mm from the injector face. Additionally, measurements of the test article thrust were made using a 2200-N load cell. A high-speed visible camera (Phantom v2511) was positioned 6 m downstream of the test article to image and track the detonation waves present in the annulus. Video data from the camera was used to ascertain the number of waves, wave-speed, and the cycle frequency associated with the operating mode of the

Table 5.1: Summary of the LAS, high-speed camera, and CTAP measurements. Camera data was not successfully collected for test 25. Note: in all misaligned injector runs, wave modes were not sustained for the entire test duration with the sporadic creation and destruction of waves. Where multiple waves are indicated for the misaligned injector runs, smaller counter-propagating waves were present in addition to a dominant wave.

Test no.	ϕ	$\dot{m}_{\text{tot}}$ [kg/s]	CTAP [atm]	Cycle frequency [kHz]	wave-speed [km/s]	No. of Waves	LAS Record Length [s]	Thrust [N]	Specific Impulse [s]
Aligned injector									
1	1.09	0.277	4.1	16.8	1.88	2	1.0	387	143
2	1.18	0.268	4.0	16.7	1.87	2	1.0	378	143
3	1.29	0.268	4.0	16.4	1.83	2	1.0	374	144
4	1.40	0.268	4.0	16.3	1.82	2	1.0	378	143
5	0.77	0.268	3.6	15.4	1.72	2	0.5	334	126
6	0.95	0.272	3.9	16.8	1.88	2	0.5	360	136
7	1.04	0.091	1.4	14.0	1.56	2	0.5	62	70
8	1.05	0.177	2.6	16.2	1.81	2	0.5	200	114
9	1.02	0.363	5.3	16.4	1.83	2	1.0	543	151
10	1.06	0.449	6.1	22.1	1.65	3	0.5	690	167
11	1.51	0.091	1.5	13.5	1.51	2	0.5	71	77
12	1.42	0.177	2.7	15.5	1.73	2	0.5	209	120
13	1.44	0.354	5.1	16.5	1.84	2	1.0	543	157
14	1.39	0.445	6.3	21.0	1.56	3	0.5	734	168
Misaligned injector									
15	0.74	0.268	3.7	4.8	1.08	1	0.5	334	124
16	0.94	0.272	3.8	4.4	1.07	1	0.5	338	126
17	1.13	0.268	3.9	9.0	1.00	2	0.5	316	128
18	1.19	0.268	3.9	5.0	1.11	1	0.5	343	130
19	1.41	0.272	4.1	9.0	1.01	2	0.5	351	132
20	0.95	0.091	1.4	4.8	1.07	1	0.5	53	58
21	1.07	0.172	2.5	8.8	0.98	2	0.5	178	104
22	1.07	0.363	5.1	5.0	1.07	1	0.5	485	137
23	1.06	0.445	6.3	4.4	0.99	2	0.5	618	143
24	1.44	0.177	2.6	12.3	0.92	3	0.5	292	110
25	1.40	0.445	6.6	–	–	–	0.5	636	145

combustor via analysis techniques described in previous work [36].

During the test campaign, laser absorption data was successfully collected for 25 different test conditions, depicted graphically in the right of Fig. 5.1 and summarized in Table 5.1. One subset of these tests (6 total) featured a variation in equivalence ratio from $\phi = 0.77$ to 1.40 at an approximately constant mass flow rate of $\dot{m}_{\text{tot}} = 0.268 - 0.277$ kg/s. Another subset of these tests (5 tests) involved varying the mass flow rate from $\dot{m}_{\text{tot}} = 0.091$ to 0.449 kg/s at a near-stoichiometric equivalence ratios ($\phi = 1.02 - 1.09$). The final subset of interest (5 tests) involved varying mass flow rate from $\dot{m}_{\text{tot}} = 0.091$ to 0.445 kg/s at more fuel-rich equivalence ratios ($\phi = 1.39$ to 1.51). In addition to the variations in equivalence ratio and mass flow rate, the misaligned injector configuration was utilized for some of the tests, providing a binary input parameter with which to examine the effects of reactant mixedness. These tests are shown as red markers in Fig. 5.1. The same set of conditions in equivalence ratio and mass flow rate were targeted as for the aligned injector, although LAS data was not collected for certain test conditions.

All hot-fire tests were approximately one second in duration, but a full second of LAS data was only collected for 6 of the 25 tests; these are indicated in Fig. 5.1 with a circle marker (0.5 s test) or a triangle marker (1.0 s test). For the 19 remaining tests, only the latter 0.5 s of laser absorption data were saved.

5.2.2 Laser-absorption diagnostic

The mid-infrared, retro-reflection optical setup described in Section 4.4 was utilized to measure gas properties in situ via laser absorption at the exit plane of the rotating detonation rocket combustor. In this chapter, only the gas properties obtained using the absorbance spectrum of CO (temperature, pressure, and CO column density) are investigated, so the portion of the optical setup involving the this portion of the diagnostic are detailed here. For this optical configuration, a continuous-wave distributed feedback (DFB) quantum cascade laser (QCL, ALPES Lasers) with ∼50 mW output power, tunable from 2001 to 2012 cm^{-1} was used as the narrow-band light source to probe rovibrational transitions of CO. The

details of the opto-electronic hardware used to enable 1-MHz modulation of this laser are provided in Section 4.2.

The incident beam was free-space coupled into one single-mode InF_3 fiber with a 9 µm core diameter. The fiber delivers the light from a remote breadboard—on which the laser is mounted—to a local breadboard mounted to the RDRE thrust structure. The fiber output is then re-collimated using a CaF_2 lens and reflected off a small right-angle prism mirror. The beam is then pitched across the exit of the RDRE annulus through the exhaust gases and onto the polished center body flat surface, which reflects the light back towards the detector assembly, as shown on the right of Fig. 5.1. The annular gap is 0.5 cm, resulting in a retro-reflected optical path length of approximately 1 cm. The beam is then passed through an optical bandpass filter (Spectrogon, 4960±148 nm) and subsquently focused onto a thermo-electrically cooled photodetector (Vigo PVMI-4TE-8-1x1). Raw detector voltage signals were collected at sample rates of 250 MS/s and 500 MS/s, for measurement intervals of 1.0 s and 0.5 s respectively. A nitrogen purge system directed along the side of the test article displaces ambient H_2O vapor in the quiescent air which can otherwise spectrally interfere with the absorbance spectra of CO.

Representative time-resolved spectra, pressure, temperature and CO column density are shown on the left side of Fig. 5.3 for 1 ms of a hot-fire test conducted at the nominal operating condition. For this test, periodicities in temperature, column density, and pressure characteristic of the cyclic nature of RDREs are readily observed. The right side of Fig. 5.3 shows the measured absorbance spectra from a representative single sub-microsecond scan (no averaging) along with the corresponding spectral fits of the three targeted CO transitions. The LAS theory used to obtain temeperature, pressure, and CO column density from the absorbance spectra of CO are detailed in Section 4.3.

To obtain more insight into the relative concentration of CO in the exhaust gases, the CO column density can be normalized by n, the number density of the exhaust gas (which is found using the ratio of measured pressure and temperature), and $\overline{L}$, the retro-reflected optical path length assuming no radial expansion of exhaust gases as they leave the combustor.

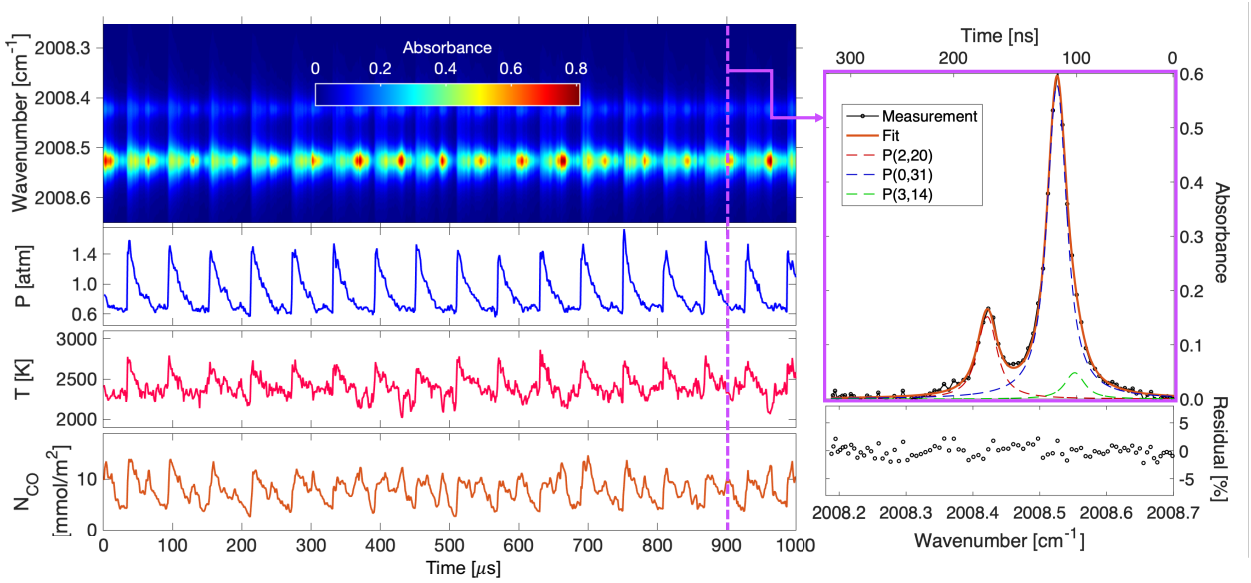

Figure 5.3: Contour plot depicting changing absorbance spectra of the P(0,31), P(2,20), and P(3,14) lines of CO in time during a sample measurement (test 1) of RDRE exhaust (*top left*). A single scan in time corresponding to the vertical dashed line is shown (*right*), showing the raw data with Voigt fits overlaid. The pressure, temperature and CO column density inferred from the spectra is shown on the bottom left.

This quantity—which we label $\overline{N}_{\mathrm{CO}}$—scales with the average mole fraction of CO ($\overline{X}_{\mathrm{CO}}$) in the exhaust gases:

$$\overline{N}_{\mathrm{CO}} = \frac{N_{\mathrm{CO}}}{n\overline{L}} = \frac{N_{\mathrm{CO}} k_B T}{P_{\mathrm{tot}} \overline{L}} = \overline{X}_{\mathrm{CO}} \frac{L}{\overline{L}}. \tag{5.1}$$

Notably, an increase in $\overline{N}_{\mathrm{CO}}$ can be caused both by an increase in the average mole fraction of CO in the exhaust gases as well as an increase in effective optical path length due to the radial expansion of the exhaust flow as it leaves the annulus.

5.3 Results

This section summarizes the experimental results from the test campaign. Table 5.1 details the test operating conditions (equivalence ratio and mass flow rate) for each reported test along with measurements of capillary tube averaged pressure (CTAP, 8.9 mm from the

injector face), wave-speed u_{wv}, number of waves, and cycle frequency obtained from high-speed video f_{det}, the duration of the LAS measurements, thrust F and specific impulse I_{sp}.

5.3.1 Transient properties

In this subsection, the time histories of the gas property measurements (pressure, temperature, and CO) are examined over the course of an entire 1.0 s hot-fire test (test number 1), which is representative of a typical test. Fig. 5.4 shows the static gas pressure P, temperature T, and normalized CO column density $\overline{N}_{\text{CO}}$ for a full-length test at the nominal flow condition ($\phi \approx 1.1$, $\dot{m}_{\text{tot}} \approx 0.6$ m/s), plotted on a logarithmic time scale to highlight the details and disparate timescales involved in the transient behavior. Time "0" corresponds to the time at which CO was initially detected—approximately 112 ms after the main propel-

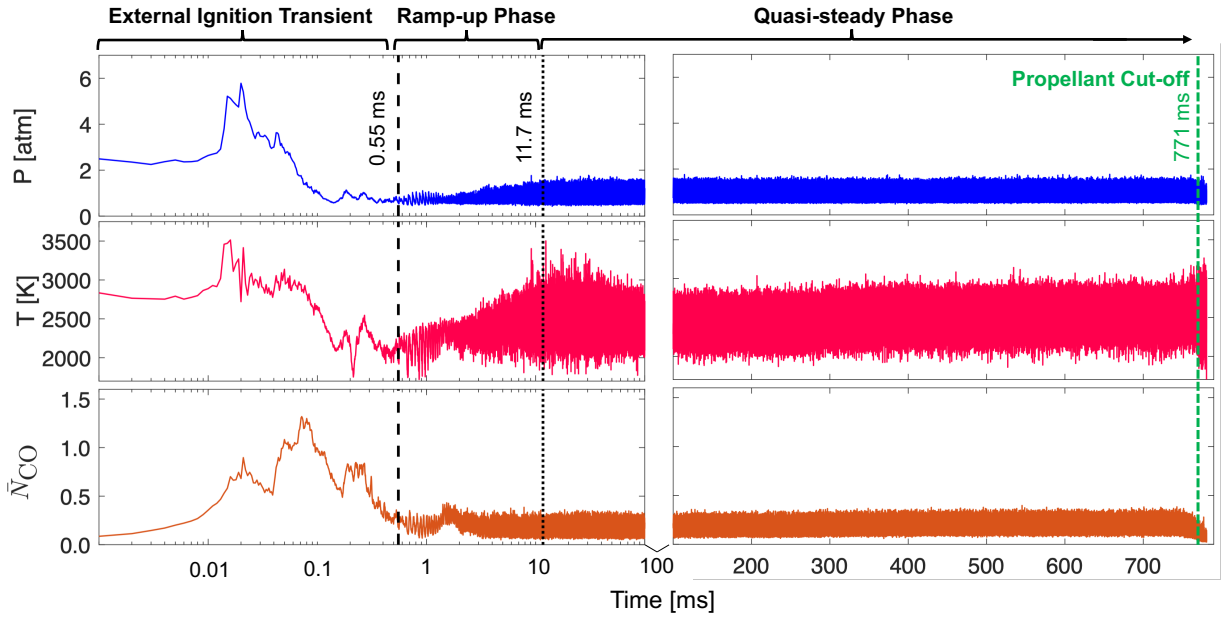

Figure 5.4: Left: Gas properties over the first 100 ms of a nominal flow condition test (test 1) using a logarithmic time scale. The dashed vertical line indicates the onset of stable oscillatory behavior, the dotted line indicates a quasi-steady state in the cyclic thermochemical properties. Right: The remainder of the test is shown in a linear time scale.

lant valves were commanded open. The data in Fig. 5.4 show a localization of the startup transient behavior to the initial 100 ms of the test, which—for this test—contain the peak values for the pressure, temperature, and normalized CO column density. This transient behavior is likely associated with the external ignition system at the exit plane. Notably, the normalized CO column density $\overline{N}_{\mathrm{CO}}$ calculated using Eqn. 5.1 reaches a value greater than one during this time—the high pressures associated with this transient event blend the targeted spectral transitions and distort the measurement. Accordingly, these early-time data are used only for comparison of physical time scales associated with the establishment of a steady operating mode.

The measurement rates achieved in this study produced a large volume of LAS data (>8 gigabytes per test), necessitating the development of an efficient data analysis routine to interpret and characterize the time-varying thermodynamic behavior for each test, which we describe here. We first performed a short-time Fourier transform (SFST) to reveal time-varying harmonic content in the data by dividing the full time-resolved signal into smaller sections/windows of a specified duration and applying a Fourier transform to those windows [45, 181]. As the temporal window size gets smaller, the time resolution of the SFST increases; however, the frequency resolution drops due to a reduction in available sample points. For this study, a window size of 0.5 ms was used, with neighboring windows overlapping by 0.25 ms, yielding a time resolution of 0.25 ms with an approximate frequency resolution of 2 kHz. Resulting spectrograms of P, T, and $\overline{N}_{\mathrm{CO}}$ generated using SFSTs on test number 1 are shown in Fig. 5.5. The dominant frequency is consistently $\approx$16 kHz for all three quantities, and the power spectral density of pressure at this frequency increases over the duration of the test, implying an increase in strength of the oscillatory mode over time. While changes over time in the temperature spectra are less pronounced, the overtone of the CO column density spectra is observed to increase during the test.

With knowledge of the dominant frequencies in the data provided by the harmonic analysis, the data were partitioned into wave cycles, enabling investigation of changes in intra-cycle behavior throughout the duration of the test. Moreover, partitioning the data into cycles

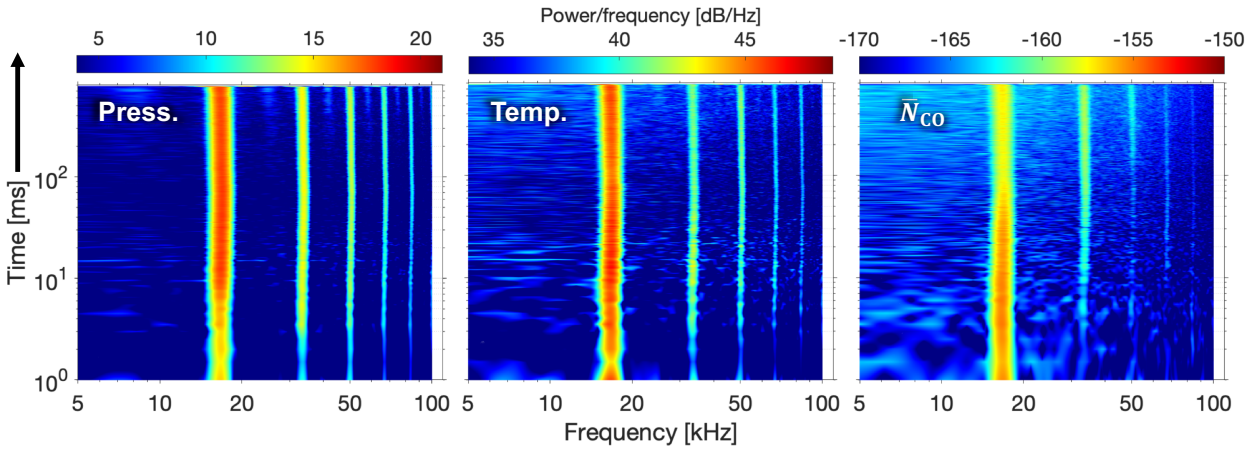

Figure 5.5: Short-time Fourier transform of pressure (*left*), temperature (*center*) and CO column density (*right)* data, using a window size of 0.5 ms for test 1. A dominant frequency of ≈16 kHz can be observed with additional harmonics being present at higher frequencies.

readily allows calculation of cycle-averaged thermodynamic behavior, which is of significant utility to performance analyses and comparisons with high-fidelity modeling. However, the exact length of a wave cycle was not constant during any given hot-fire test, and so a simple division of the data into equal length cycles was not possible [182]. To address this data nonideality, the pressure profile was used to partition the data, owing to its large gradients in the wave-fronts and the antecedence of its increase within a cycle relative to subsequent increases in temperature or CO density. A successful strategy for wave-front detection was developed by finding the region of maximum cumulative pressure change inside a time window informed by the inverse of the wave frequency provided by the harmonic analysis. This method also allowed for the identification of the base and peak of the wave-front.

After partitioning the data into cycles, the cycle lengths throughout the test were examined; during the initial transient startup, the cycle lengths were often short and erratic from cycle to cycle, likely due to competing wave propagation modes. In the data examination, stable oscillatory behavior is assumed when the cycle length first reaches 80% of the overall median cycle length. For the test presented in Fig. 5.4, this occurred about 0.55 ms after CO formation, and this time is shown as a dashed vertical line. The pressure, temperature,

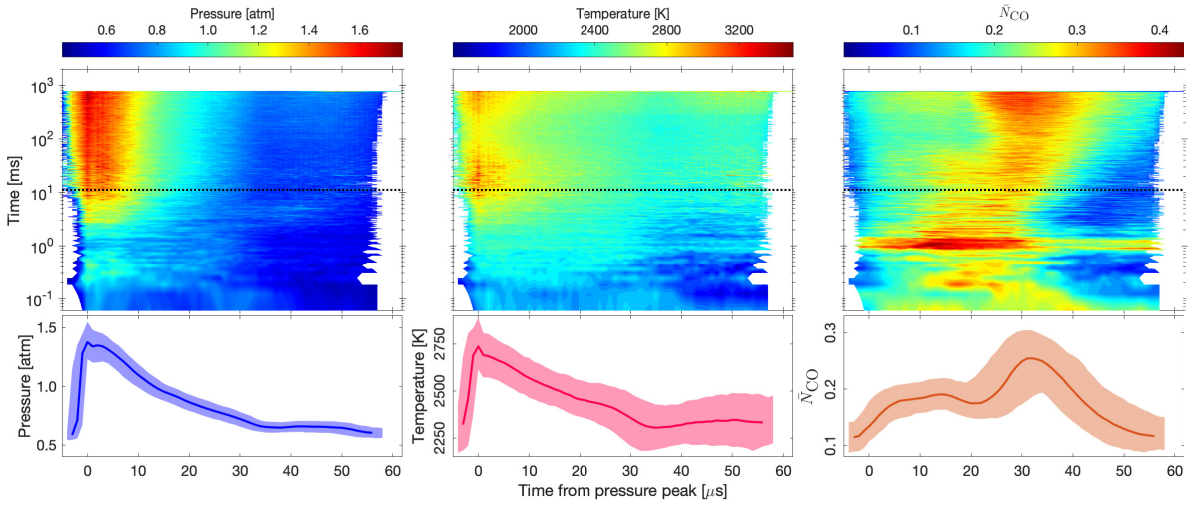

Figure 5.6: *Top:* Temporal evolution of cyclic pressure P, temperature T, and normalized CO column density $\overline{N}_{\mathrm{CO}}$ from initiation of stable oscillatory behavior for test 1. Time "0" for the y-axis indicates the onset of cyclic behavior. Black dashed lines note the onset of steady cyclic behavior. *Bottom:* Intra-cycle ensemble profiles for P, T, and $\overline{N}_{\mathrm{CO}}$ during steady state operation. The shaded regions represent the "regions of variability" related to each intra-cycle ensemble profile.

and CO column density evolution across the stable cycles are shown in the top of Fig. 5.6 as a function of time. A ramp up in the peak cycle pressure over time is readily observed, as also indicated by the harmonic analysis. Additionally, the peak in the CO profile recedes over time relative to the wave front, corresponding to an increase in strength of the $\overline{N}_{\mathrm{CO}}$ overtone observed in the harmonic analysis.

Even after commencement of initial oscillations—which imply the onset of rotating detonation behavior—an additional transient associated with the establishment of quasi-steady state wave behavior was observed, as seen in Figs. 5.4, 5.5, and 5.6.

The peak pressure for each cycle is plotted versus time in Fig. 5.7. The quasi-steady state is established within the first ∼10 ms of the test —indicated by the dashed blue line in Fig. 5.7 and the black line in Fig. 5.6—and was characterized by the peak cycle pressure reaching a steady value. This steady peak pressure was obtained by averaging the peak cycle

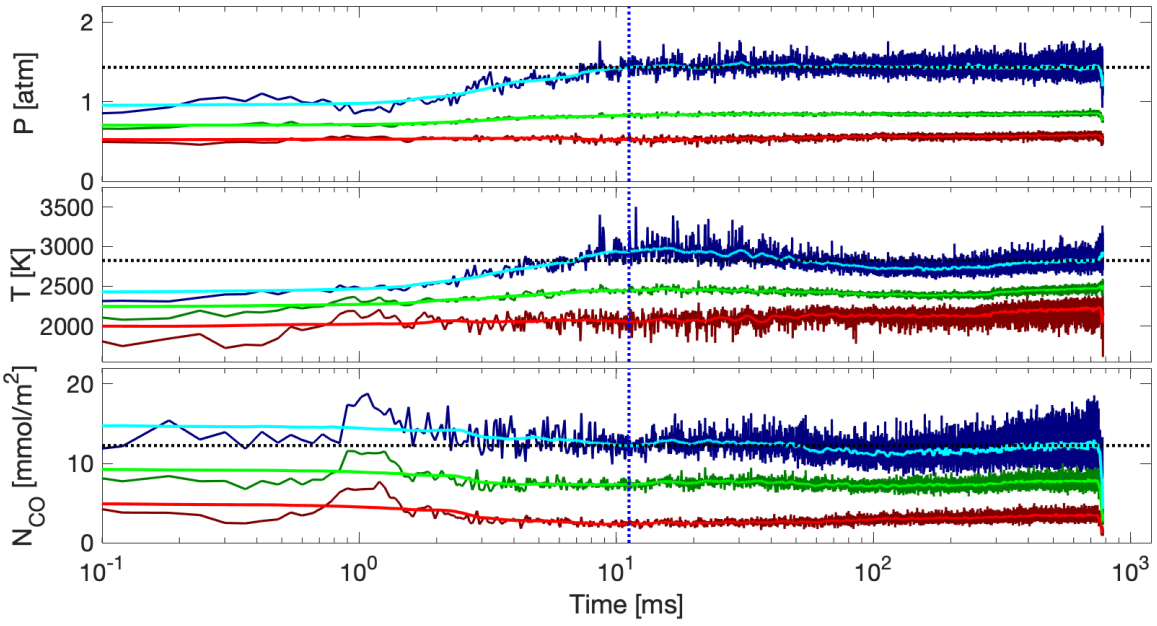

Figure 5.7: Temporal evolution of cycle properties. The blue, green, and red curves represent cycle maximums, mean values, and minimums, respectively. Brighter curves are 50 cycle moving averages of the blue, green, and red curves, respectively. Black dashed lines indicate the steady-state cycle maximum, and the blue dashed line denotes the onset of steady state behavior. Time "0" indicates the onset of cyclic behavior.

pressure in a region of approximately 200 ms in the latter half of the test. We define the "rise time" to reach steady state behavior as the time between the start of the test and the time when the peak pressure first reaches this value [183]. For test 1, the "rise time" was approximately 11.7 ms after initial CO formation.

Across the 6 tests for which startup transient data was collected, the time from propellant valve opening to the first observation of CO at the measurement location was on the order of 100 ms.

For 5 of these tests, the CO-formation time was 110–124 ms. The remaining test (4) was an outlier, with a CO-formation time of 142 ms. The elapsed time between CO formation and oscillatory behavior—the "lock-in" time—was typically on the order of 0.5 ms, with 5 of the 6 tests having a lock-in time between 0.42 and 0.67 ms. Test 9 was an outlier, however,

Table 5.2: Summary of the transient time scales for the applicable tests.

Test no.	ϕ	$\dot{m}_{\text{tot}}$ [kg/s]	CO-formation time [ms]	Lock-in time [ms]	Rise time [ms]
1	1.09	0.277	112	0.55	11.7
2	1.18	0.268	114	0.53	16.6
3	1.29	0.268	110	0.67	15.0
4	1.40	0.268	142	0.42	33.1
9	1.02	0.363	113	1.49	13.9
13	1.44	0.354	114	0.54	6.2

with a lock-in time of 1.49 ms. After oscillations were established at the measurement location, the time (relative to the CO- formation time) it took for the oscillations to reach a quasi-steady state was on the order of 10 ms, with most tests having a rise time between 6 and 17 ms. Test 4 was again an outlier, with a rise time of 33.1 ms. All of the measured transient timescales are summarized in Table 5.2.

5.3.2 Intra-cycle properties

With the data partitioned into cycles, and the steady-state region identified, the pressure P, temperature T, and CO column density $\overline{N}_{\text{CO}}$ were averaged (using median values to increase robustness against outliers) across the various cycles to obtain characteristic intra-cycle profiles from the ensemble means of the repetitive cycles for P, T, and $\overline{N}_{\text{CO}}$. The time "0" for these cycles is defined as the time of peak-pressure, right after the wave-front. As mentioned previously, the exact length of each cycle (and the rise and decay periods) varied from cycle to cycle, likely due to small variability in the detonation wavespeeds. In order to simplify the averaging procedure, only cycles as long as the median cycle length were ensemble-averaged to generate the intra-cycle mean gas property profiles (solid lines) shown in the bottom of Fig. 5.6. To represent the variability in the thermodynamic profiles at various cycle lengths, and from cycle-to-cycle, a "region of variability" is also plotted

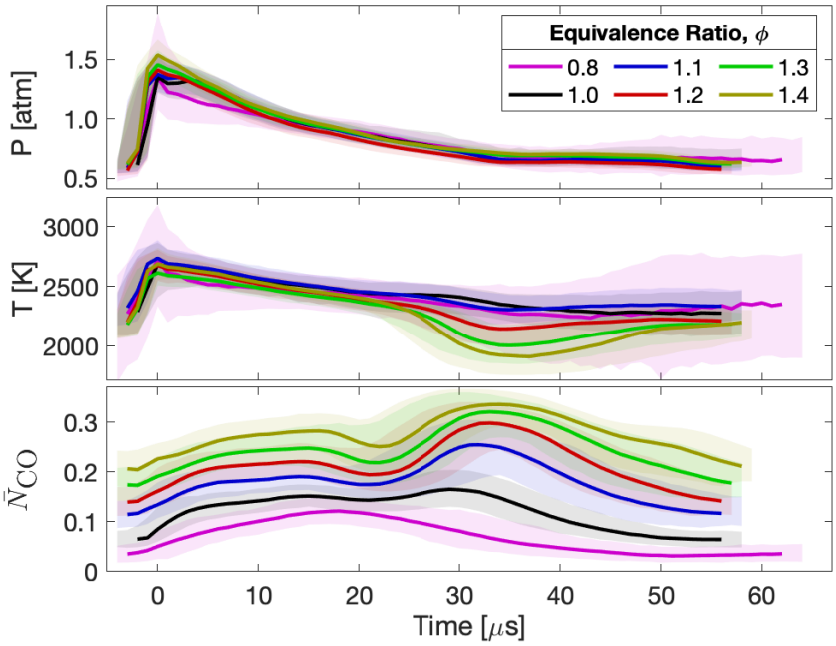

Figure 5.8: Intra-cycle ensemble thermochemical profiles for various equivalence ratios at a constant mass flow rate of 0.27 kg/s.

around each profile. This region was obtained by first considering the distribution of cycle lengths and identifying the interdecile range (10th to 90th percentile) of cycle lengths. For each cycle length within this range, an ensemble mean profile was generated, with error bars representing the interdecile ranges of P, T, and $\overline{N}_{\mathrm{CO}}$ at each point in time along the cycle. The maximum and minimum value of each gas property among these ensemble profiles of various lengths were used to bound the region of variability. The region of variability is represented as a shaded region bounding the intra-cycle mean profiles in Fig. 5.6. The intra-cycle thermodynamic evolution of the cycles can be clearly observed in these ensemble mean profiles: pressure abruptly increases at the beginning of the cycle, followed by an abrupt increase in temperature and subsequently a more gradual increase in normalized CO column density. As pressure and temperature decay in time, the normalized CO column density increases slowly until a second flow feature is encountered, wherein the normalized CO column density rises abruptly and is accompanied by a dip in the temperature profile.

Once the intra-cycle mean profiles have been calculated, the thermodynamic flow struc-

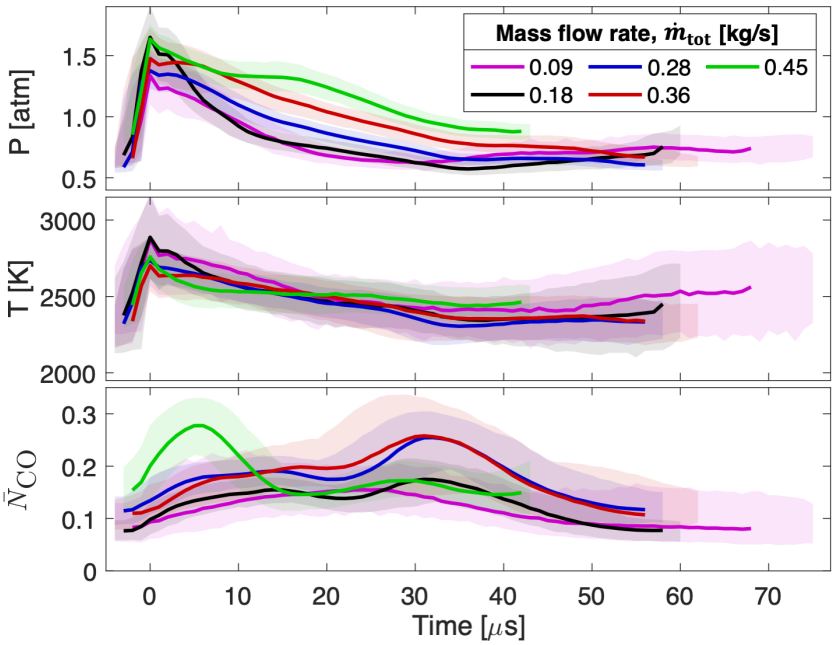

Figure 5.9: Intra-cycle ensemble thermochemical profiles for various mass flow rates at near stoichiometric ($\phi = 1.0$–1.1) conditions.

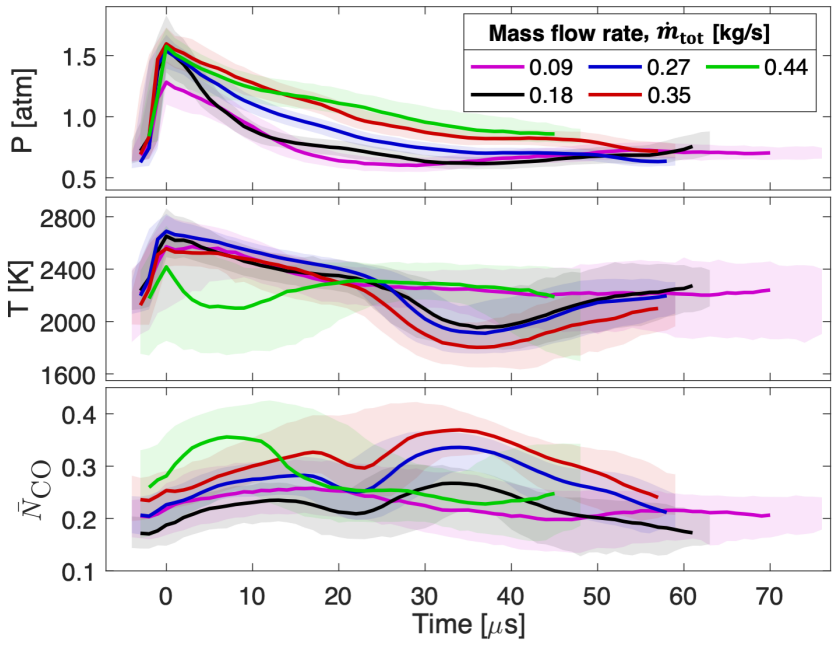

Figure 5.10: Intra-cycle ensemble thermochemical profiles at fuel-rich ($\phi = 1.4$–1.5) conditions for various mass flow rates.

tures associated with different test conditions can readily be compared. Fig. 5.8 shows the intra-cycle mean pressure, temperature and CO density profiles of tests at different equivalence ratios (at a constant total flow rate of ≈0.27 kg/s).

The pressure profiles and post-shock temperature profiles are fairly consistent among equivalence ratios. The temperature drop in the latter half of the cycle is strongly affected by equivalence ratio, however, with a larger drops observed with increasingly fuel-rich conditions. Additionally, the overall normalized CO column density is higher for fuel-rich conditions; the CO increase in the latter half of the cycle is more pronounced at fuel-rich equivalence ratios, and virtually nonexistent at the fuel-lean equivalence ratio.

Fig. 5.9 shows the thermodynamic intra-cycle profiles of tests at different mass flow rates (at a near constant equivalence ratio $\phi = 1.0$–1.1). Here, the pressure and normalized CO column density are generally higher for higher mass flow rates. At the lowest flow rate (0.091 kg/s), the abrupt shift in CO level in the latter half of the cycle is undetectable. The temperature evolution in the cycle, however, demonstrates approximately constant behavior among test conditions. Between 0.363 kg/s and 0.454 kg/s, there is a modal transition [37], wherein rotating detonation behavior in the combustor assumes a 3-wave mode instead of a 2-wave mode, as evidenced by the decrease in the cycle length and by corresopnding high-speed camera footage. This increase in the number of waves is consistent with prior investigations indicating an increase in number of waves with mass flux [38]. The structure of the intra-cycle thermodynamic profile shifts substantially with the mode transition—the peak in CO and associated drop in temperature are shifted to the first half of the cycle.

In Fig. 5.10, the thermodynamic intra-cycle profiles of tests at various mass flow rates at more fuel-rich equivalence ratios ($\phi = 1.4$–1.5) are plotted. Similar trends are observed as when varying mass flow rate at near-stoichiometric equivalence ratios: The pressure profile and peak CO level generally increase as the mass flow rate increases. Since these tests are conducted at a more fuel-rich equivalence ratios, the temperature drop and associated CO rise in the latter half of the cycle are more pronounced than they are in Fig. 5.8. Again, at the lowest mass flow rate, this feature is not observed and at the highest mass flow rate,

there is a mode transition from 2 to 3 waves accompanied by a shift in the thermodynamic structure, with the CO rise/temperature drop moving to the first half of the test.

5.3.3 Modal transitions

For some tests, the number of waves present in the annulus abruptly changed. This is evidence by high-speed video and from a change in the characteristic frequency in the gas property data measured by LAS. One such test was test number 5. Both the spectrogram and high-speed video stills for this test can be seen in Fig. 5.11. High-speed video indicated that this was an "ascending" mode transition [37] from 2 waves to 3 waves. This was accompanied by an increase in the characteristic frequency from about 17 kHz to 22 kHz . The cycle averaged gas property profiles for the two modes can be observed in Fig. 5.8. While the pressure and temperature profiles are observed to be fairly similar between the two modes (albeit shorter for the 3 wave mode versus the 2 wave mode), the normalized CO column density profile is drastically different between the two modes. For the 2 wave mode,

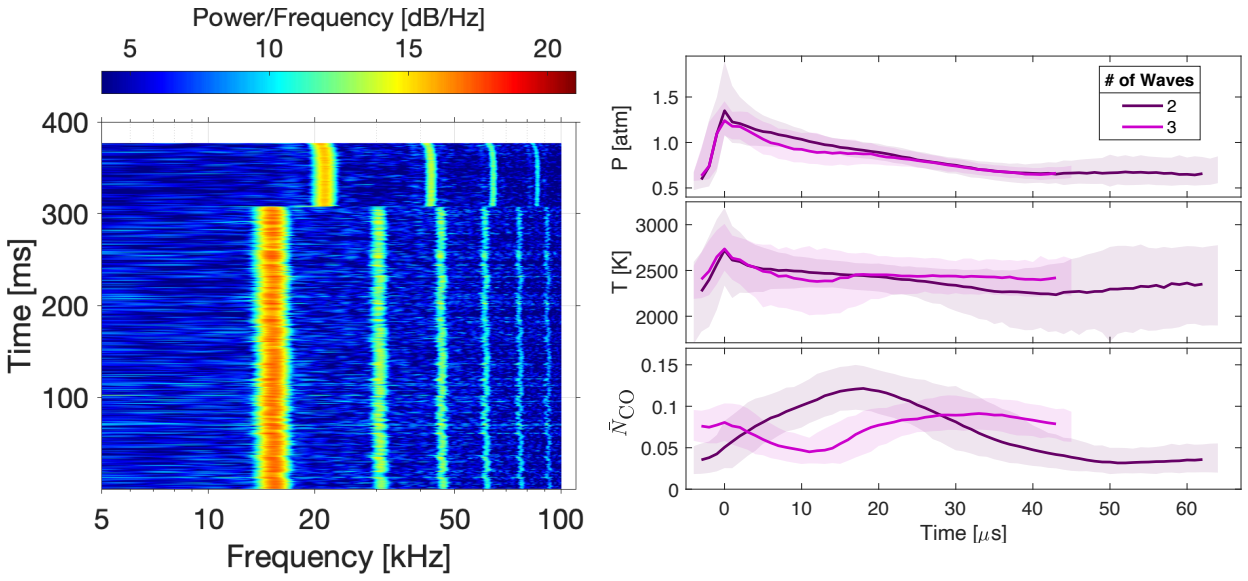

Figure 5.11: Evidence of a mode transition during test 6 via harmonic analysis (*left*), with the pressure spectrogram displaying and abrupt shift to a higher frequency around 300 ms after CO formation. Intra-cycle gas property evolution across mode transition (*right*).

the CO profile starts and ends at a low value, peaking in the first half of the cycle. In the 3 wave mode, the CO level starts and ends at a relatively high value, reaching a minimum in the first half of the cycle.

5.3.4 Low-flowrate modal oscillation

For the tests conducted at the lowest mass flow rate (0.09 kg/s), a low frequency oscillation in the temperature and CO column density was observed at around 50 Hz, with the detonation frequency of approximately 14 kHz superimposed upon this low frequency oscillation. This behavior can be observed in Fig. 5.12 for test 7. The periods of increased CO column density corresponded to decreased temperature. The pressure profile seemed to be less affected by this low frequency phenomenon.

CTAP measurements indicated that pressure near the injector face was very close to the pressure measured at the exit plane by LAS measurements. This is likely due to the reduced propellant feed pressure for these low flow rate tests. This lack of pressure drop through the

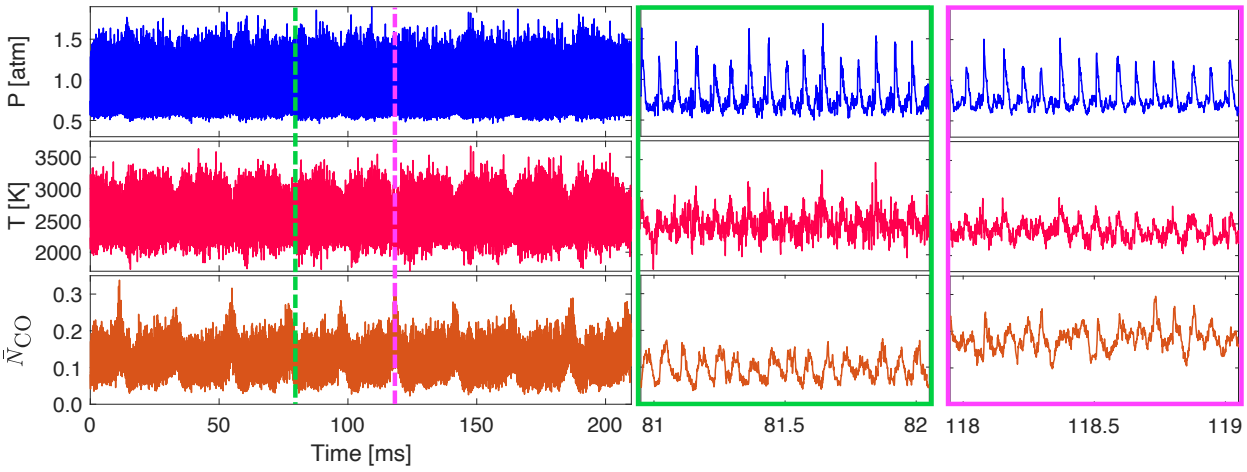

Figure 5.12: A 200-ms chunk of test 8 (*left*), showing a low-frequency oscillation in the gas properties superimposed on the higher-frequency structure associated with the detonation phenomena. Two excerpts of this data around 2 ms long (*center and right*) are shown at the valley and peak of this low-frequency oscillation, demonstrating a shift in the mean CO concentration and in the intensity of the high-frequency temperature fluctuations.

annulus may have allowed for combustion instabilities to more easily propagate through the system, leading to the observed behavior.

5.3.5 Non-cyclic gas properties

The misaligned injector produced weak rotating detonation wave behavior according to both the high-speed video and LAS data, which showed that 1 or 2 waves would become prominent occasionally, moving at relatively slow speeds (∼1 km/s), occasionally changing propagation direction. Furthermore, when the video data revealed the presence of multiple waves, they were often counter-propagating instead of co-rotating. Fig. 5.13 compares the results of two tests (tests 1 and 17) conducted at the same equivalence ratio and mass-flow rate ($\phi = 1.1$

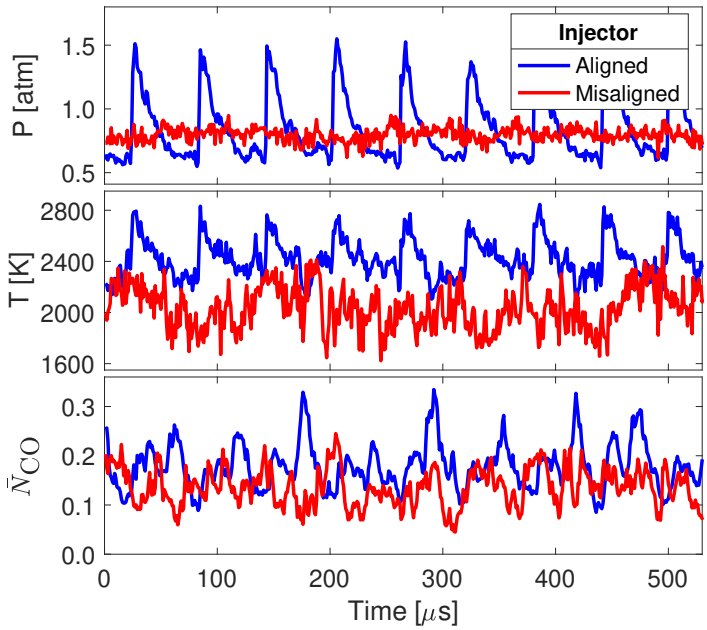

Figure 5.13: A comparison of the thermodynamic measurements made at the same flow condition (tests 1 and 17) using two different injectors. The gas properties for the aligned injector exhaust are shown in blue and the properties for the misaligned injector are shown in red.

and $\dot{m}_{\text{tot}} = 0.27$ kg/s respectively), but with the two different injectors. The pressure time-history profile produced by the misaligned injector is relatively flat and unchanging compared to the pressure profile produced by the aligned injector, which clearly displays sharp gradients in pressure. Subtle wave-fronts are noticeable, however, appearing with significantly lower frequency than with the aligned injector; this reduced frequency is reflective of the low wave-speed and number of waves present within the annulus. Unlike the pressure profile, the temperature and normalized CO column density properties measured in the misaligned injector exhaust oscillate significantly. The oscillations in these profiles are not as structured as those measured in the aligned injector exhaust, consistent with a lower mixture thermicity and weaker detonation behavior.

Due to the lack of cyclic time-resolved thermodynamic structure in the misaligned in-

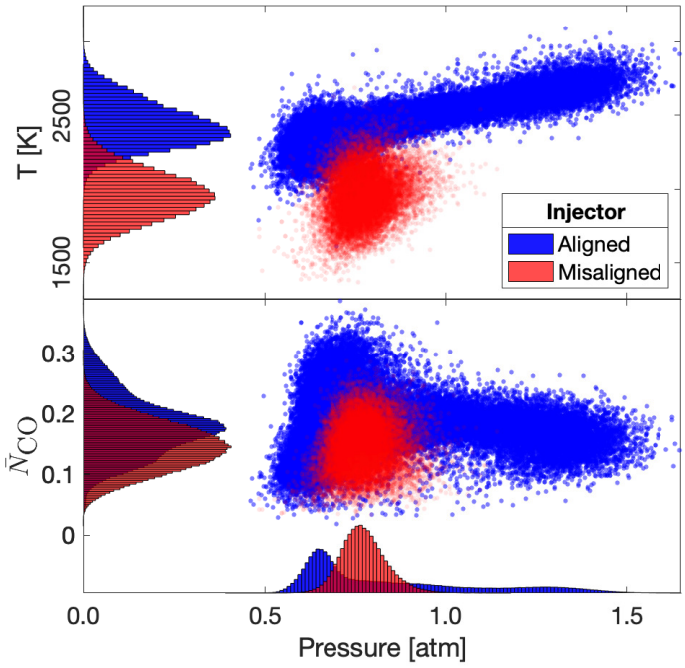

Figure 5.14: Normalized histograms of pressure, temperature, and normalized CO column density plotted from tests 1 and 17 which were conducted at an equivalence ratio of ∼1.1 and mass flow rate of ∼0.27 kg/s with the aligned and misaligned injectors respectively. Scatter data of a random sample of 10% of the data points is also plotted to show how the variables trend with one another.

jector exhaust, a different data analysis framework was developed to fairly compare aligned and misaligned injector results. We employed a statistical analysis in which histograms were constructed based on the distribution of time-resolved thermodynamic properties over an entire test. These histograms were normalized by number of time-resolved measurements per test (on the order of 400–800 thousand, depending on test record length) and by the bin-width of the histograms: 0.01 atm, 25 K, and 0.003 for the pressure P, temperature T, and normalized CO column density $\overline{N}_{\mathrm{CO}}$ measurements, respectively. Histograms for tests 1 and 17 are shown in Fig. 5.14 comparing the distributions for the thermodynamic exhaust measurements between the aligned and misaligned injectors. Scatter plots are also overlaid to highlight any correlation among the thermodynamic variables. The thermodynamic variables are nearly normally distributed (Gaussian) for the misaligned injector exhaust, whereas the aligned injector exhaust properties demonstrate distinctly skewed (non-Gaussian) structure in their distributions. Notably, the aligned injector exhaust spent more time at lower pressures than the misaligned injector exhaust, but was skewed towards higher pressures by short-lived—but significantly larger—peak pressure values. Additionally, the temperature and CO distributions of the aligned exhaust displayed higher mean values than the

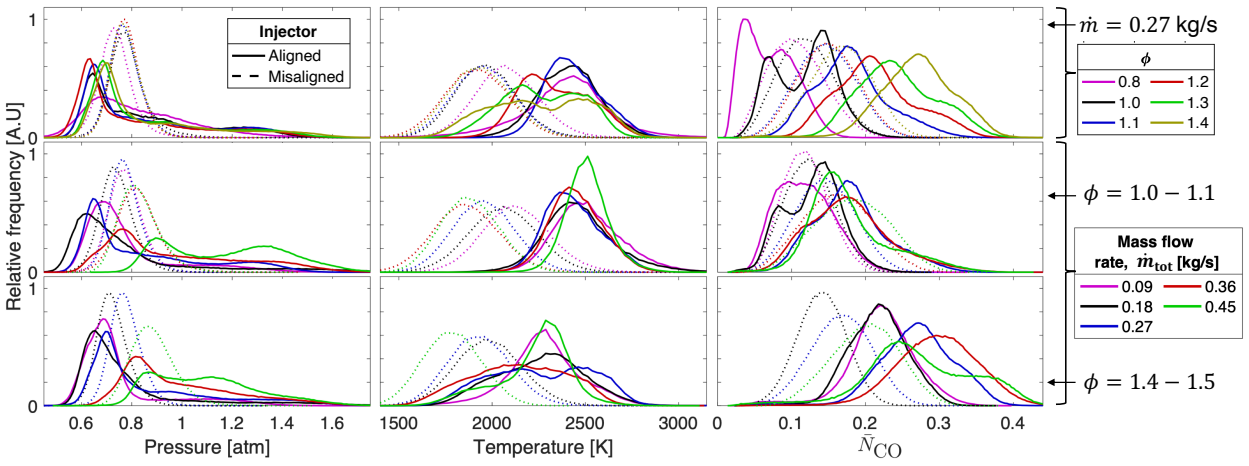

Figure 5.15: Histograms of the thermodynamic data across the various test conditions. Solid curves represent aligned injector tests, dashed curves represent misaligned injector tests. All curves are normalized such that the areas under each curve are the same.

misaligned exhaust distributions. In Fig. 5.15, the histograms for all 25 test conditions are shown, including aligned and misaligned injector cases.

5.3.6 Comparison to 1-D Chapman-Jouguet model

To provide context to the measured gas properties and associated trends, a 1-dimensional thermodynamic model [184] was developed using CANTERA [142] and Caltech's Shock and Detonation Toolbox [141]. It is well-established that in an RDRE flowfield, not all fluid particles undergo the same thermodynamic cycle [20]. Accordingly, for this modeling comparison, a fluid was assumed to follow one of two thermodynamic paths: (1) deflagration or (2) detonation, each followed by isentropic expansion. Both possible paths involved reactants being injected at an initial pressure P_0 (based on the CTAP measurement for a corresponding test) and ambient temperature (300 K) at a particular equivalence ratio ϕ (determined from the measured mass flow rates of the corresponding test). In our model of the first path, the reactant mixture is allowed to reach thermodynamic equilibrium at constant pressure and enthalpy, modeling a deflagration-based combustion process. Our model of the second path allowed the reactants to undergo a Chapman-Jouguet (CJ) detonation process. After combustion, the reacted gases in the models of each path are isentropically expanded to an exit pressure of one atmosphere (representing perfectly expanded flow). Gas expansion in the exhaust considering both a frozen composition and equilibrium composition were evaluated. Fig. 5.16 shows the predicted exhaust CO mole fraction and temperature across varying equivalence ratio for both deflagration and detonation, with both frozen and equilibrium composition expansion assumptions. The initial pre-combustion pressure assumed in these calculations was 4 atm, since most of the tests at the nominal flow rate of 0.27 kg/s had a CTAP value near this pressure. Interestingly, the exit temperature predicted for a given deflagration-based path is higher than the temperature predicted for the corresponding detonation-based path; the detonation path expands the reacted gas from a higher pressure (approximately 30 times higher, $\approx$120 atm) than the deflagration path, which is modeled as a constant pressure process. This results in a greater conversion of thermal to kinetic energy

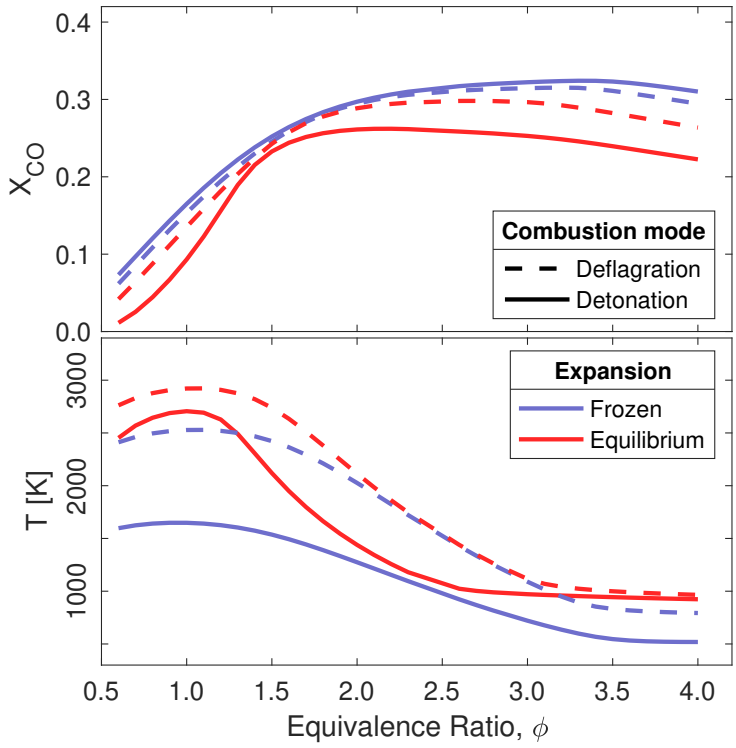

Figure 5.16: Predictions of exhaust CO mole fraction (*top*) and temperature (*bottom*) at various equivalence ratios based on the 1-D CANTERA model. Solid curves represent values from CJ detonation exhaust, dashed curves represent values from deflagration exhaust, blue curves represent frozen composition exhaust and red curves represent equilibrium composition exhaust.

for the detonation-based path, yielding a theoretically higher cycle efficiency.

Fig. 5.17 presents measurements of wave-speed u_{wv}, pressure P, temperature T, and normalized CO column density $\overline{N}_{\mathrm{CO}}$ for the various flow condition variations. For u_{wv}, T, and $\overline{N}_{\mathrm{CO}}$ (assuming a path length of 1 cm), predictions from the 1-D CANTERA model are plotted alongside the measurements. Temperature is—on average—lower than the values predicted for an equilibrium deflagration or detonation exhaust, except in the fuel-rich condition. The $\overline{N}_{\mathrm{CO}}$ measurements are in close agreement with model predictions at the leaner equivalence ratios, but begin to diverge at the more fuel-rich equivalence ratios. As mass flow rates increase from low flow rates to higher flow rates, average $\overline{N}_{\mathrm{CO}}$ values accordingly transition

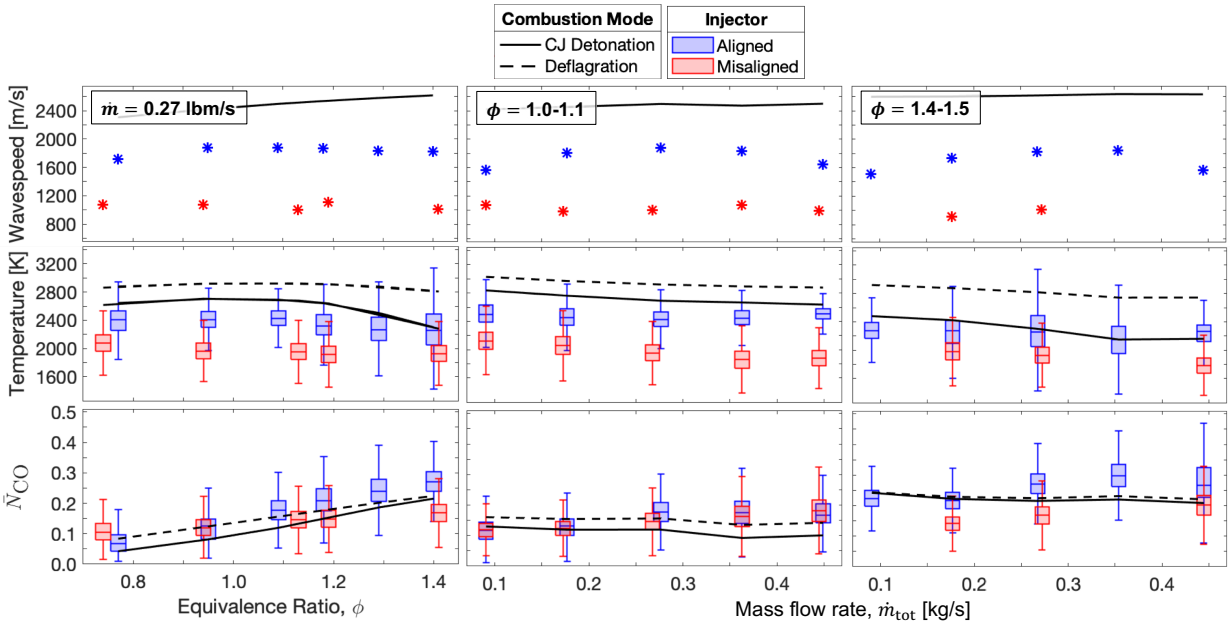

Figure 5.17: Measurements of wave-speed (from high-speed camera) and statistical summary temperature and CO column density measurements, represented using box plots that indicate the median value, interquartile range, and total range (excluding outliers). CANTERA predictions of wave-speed, exit-plane temperature, and exit-plane CO mole fraction are plotted against measurements, with solid curves representing values from CJ detonation exhaust, dashed curves representing values from deflagration exhaust. Trends vs. equivalence ratio at a constant mass flow rate of 0.27 kg/s are shown in the left column. Trends vs. mass flow rate are shown in the middle and right columns for near stoichiometric and fuel-rich equivalence ratios respectively.

from lower-than-predicted levels to higher-than-predicted levels. For a given mixture ratio, higher $\overline{N}_{CO}$ levels are traditionally associated with CO_2 dissociation in higher-temperature and lower-pressure deflagration-based rocket exhaust [1]. In these tests, however, the pressures were all distributed around one atmosphere and the temperatures were lower than predicted, so the higher-than-predicted $\overline{N}_{CO}$ levels are likely due to some other effect. Due to the path-integrated nature of the column density measurement, it is possible that radial flow expansion would cause a larger perceived CO column density—however, the intra-cycle profiles in Figs. 5.8–5.10 show that the peak in $\overline{N}_{CO}$ did not typically occur at times of

maximum P, when maximum radial expansion would be considered most likely. Rather, the intra-cycle $\overline{N}_{CO}$ peak typically occurred after the chronological mid-point of the cycle, associated with a temperature drop. Studies of methane-oxidation kinetics in nozzle flows [185] and cursory chemical kinetic simulations considering expanding flow [186] performed in CANTERA indicate that kinetically frozen flow is highly unlikely for the flow rates and geometry considered in these tests. In order to better understand the flow-phenomena that could lead to these mismatches in temperature and CO column density, the flow dynamics and structure at the exhaust of the RDRE combustor should be considered, as discussed in the following section.

5.4 Data analysis and discussion

5.4.1 Correlation with RDRE flow dynamics

The cycle-averaged gas property profiles can be compared to a commonly understood model of the two-dimensional "unwrapped" flow structure in an RDRE [187, 23] which is visualized in Fig. 5.18. In an RDRE, one or more detonation waves propagate tangentially in the annulus, consuming fresh propellant introduced into the annular chamber by the injector. Most of the RDRE exhaust gas is nearly-isentropically expanded from behind these detonation waves. One of the primary flow structures that can be observed are oblique shocks, which are attached to the detonation waves. These oblique shocks compress some the expanded gas from the previous detonation cycle, abruptly increasing pressure and temperature. The oblique shocks are postulated to be the primary pressure wave-front observed in our experimental data. This pressure/temperature increase is also accompanied by a delayed increase in measured normalized CO column density, which is potentially linked to incremental CO formation / CO_2 dissociation in the high-temperature region behind the shock or time-varying equivalence ratio.

Additionally, contact surfaces separate the shock-heated exhaust gas from unshocked exhaust, shown in purple in Fig. 5.18. These contact surfaces begin between the detonated gas

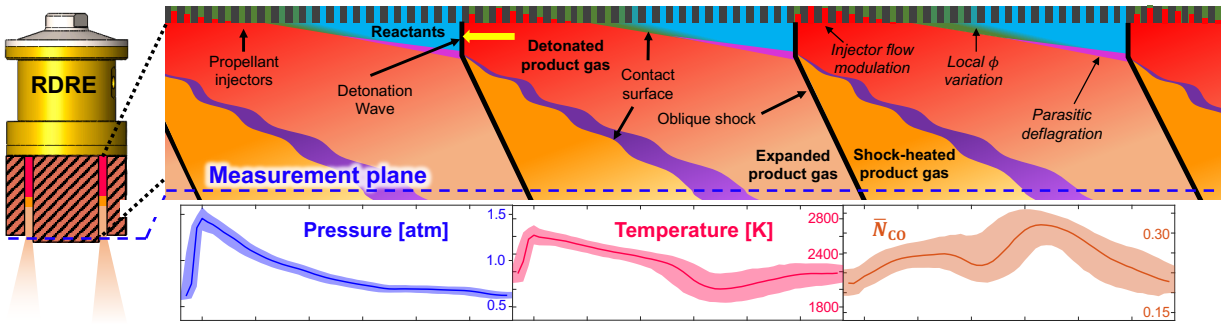

Figure 5.18: Flow structure visualization in an "unwrapped" RDRE (*top*). Cycle-averaged pressure, temperature, and normalized CO column density (*bottom*) during the steady state operating mode for test 3. The thermochemical profiles are aligned with the flow features they span.

and the freshly injected propellants from the following cycle, shown in pink. The contact surfaces are postulated to correlate in time with the large rise in measured normalized CO column density and associated temperature drop, as the chemical composition may be variable across the contact surface. The pressure across a contact surface is constant, thus no pressure change is observed in the pressure profile. There can be a slip velocity between the gases on either side of the contact surface—this can induce fluid instabilities at the contact surface, causing mixing between the shocked and unshocked gases. This has the effect of reducing the sharpness of the contact surface boundaries at the exit plane.

By examining the thermochemical measurements through this lens of the two-dimensional flow dynamics, we provide further experimental evidence supporting hypothesized loss mechanisms in the RDRE: (1) parasitic deflagration and (2) injector flow rate modulation. First, it has been established via computational modeling and experimental works [50] that the freshly injected reactants can be sufficiently heated by the detonation products from the previous cycle such that the reactants burn in a deflagration mode at the contact surface, termed *parasitic deflagration*. These deflagrated products cannot be reacted within the detonation wave, and therefore represent a loss mechanism for the RDRE. The deflagrated products are instead processed by the oblique shock and are transported to the exit plane along the

contact surface. This is a potential cause for the temperature drop seen at the postulated contact surface.

The second non-ideal effect in the RDRE is the modulation of the propellant injectors flow rates upon detonation wave passage [188, 80]. The high pressure behind the detonation wave can cause a periodic unchoking event in the propellant injectors, which momentarily drops the mass flow rate through a given injection orifice. If one propellant stream recovers faster than the other, a local variation in the equivalence ratio of the reactants may occur. This effect has been predicted analytically [58] and has been observed in CFD simulations of this RDRE geometry [38]—in the case where the fuel injector recovers more quickly than the oxidizer injector, a locally fuel-rich mixture may be generated. When this locally rich mixture is combusted, a lower temperature and higher concentration of CO can be expected. This may be linked to the measured rise in CO and drop in temperature behind the contact surface, since the gases immediately behind the contact surface are produced by reactants injected during the injector recovery period. This hypothesis is consistent with the trends observed in Fig. 5.8—as the equivalence ratio was increased, the rise in CO associated with the contact surface passage increases. To physically increase the equivalence ratio for a test, the pressure at which the fuel was being fed to the injector increased, which could cause the fuel injector to recovery more quickly than the oxidizer injector. This is also consistent with the increasing characteristic temperature drop with increasing equivalence ratio, with the injector dynamics rendering more extreme fuel-rich conditions for short periods within the cycle despite the global equivalence ratio expected to yield a similar combustion temperature according to chemical equilibrium.

5.4.2 Energy-flux analysis

To further examine the experimental measurements in the context of detonation ideality and propulsive efficiency, we develop an analytical framework in this section to assess RDRE performance by evaluating the various forms energy in the RDRE exhaust and assessing the completeness of the energy conversion mechanisms in the combustor. This framework can

be used to assess what types of losses contribute to the performance reduction in an RDRE based on time-resolved thermodynamic data.

In the RDRE (and any rocket engine) there are two main energy conversion processes: (1) chemical-to-thermal and (2) thermal-to-kinetic. The first process, chemical-to-thermal energy conversion, primarily occurs across the combustion wave (deflagration or detonation). Poor injector mixing can cause locally-rich and locally-lean reaction zones in the combustor, burning off-nominal mixture ratios and limiting the release of all the chemical energy stored in the reactants [53]. Even with perfect mixing however, high-temperature dissociation of carbon dioxide and water inhibits the full release of chemical energy [1].

The second energy conversion process involves the conversion of thermal energy to kinetic energy. This typically occurs via gas expansion from high pressures to low pressures. Higher expansion ratios (ratio of initial pressure to final pressure) yield higher temperature drops in the flow, converting more thermal energy into kinetic energy; therefore, expansion is most efficient when the expansion starts at a higher pressure, as the final pressure for expansion is typically set to the local atmospheric pressure for maximum performance. Due to the rotational flow dynamics in an RDRE, some fluid leaves the combustor with some azimuthal velocity $u_{\perp}$, instead of pure axial velocity $u_{\parallel}$. This represents a loss mechanism, as the azimuthal kinetic energy is not useful in imparting momentum to the combustor. Chemical reactions may continue during the expansion process as the temperature drops, allowing for product recombination and promoting the continued release of chemical potential energy into thermal and kinetic energy.

The exhaust gas measurements can be used to measure some of the forms of energy present in the gas as it exits the combustor. The exhaust gas thermal energy, in the form of sensible enthalpy h_{sensible}, can be measured using temperature. For an ideal gas without composition change, the isobaric heat capacity c_P is solely a function of temperature for a given gas composition. The sensible enthalpy of a gas mixture here is defined as the enthalpy of the gas at temperature T relative to its enthalpy at the reference temperature

($T_{\text{ref}} = 300$ K):

$$h_{\text{sensible}} = \int_{T_{\text{ref}}}^{T} c_P(T) dT. \tag{5.2}$$

The heat capacity of the gas for a given test is approximated with the aformentioned 1-D thermodynamic model using the reactant equivalence ratio and pre-detonation pressure as inputs and assuming the gas has been detonated and expanded to 1 atm at chemical equilibrium. The specific kinetic energy of the flow k is the sum of the axial (parallel to direction of thrust) and azimuthal (perpendicular to direction of thrust) components $k_{\parallel}$ and $k_{\perp}$, respectively:

$$k = k_{\parallel} + k_{\perp} = \frac{1}{2}u^2 = \frac{1}{2}u_{\parallel}^2 + \frac{1}{2}u_{\perp}^2. \tag{5.3}$$

u is the total velocity magnitude and $u_{\parallel}$ and $u_{\perp}$ are the axial and azimuthal components respectively.

In this work, we estimate axial velocity via the time-averaged continuity equation:

$$\dot{m}_{\text{tot}} = \overline{\rho u}_{\parallel} A_{\text{annulus}}. \tag{5.4}$$

This can be rearranged to obtain the average axial velocity:

$$\overline{u}_{\parallel} = \frac{\dot{m}_{\text{tot}}}{\overline{\rho} A_{\text{annulus}}}. \tag{5.5}$$

The mass flow rate is known for each test, and the annulus cross-sectional area may be calculated with the annulus dimensions listed in Section 5.2.1. The time-resolved density ρ may be obtained from the pressure and temperature measurements using the ideal gas law:

$$\rho = \frac{PM}{\overline{R}T}. \tag{5.6}$$

The gas molecular weight M is estimated using the average of the equilibrium exhaust detonation and deflagration composition from the aforementioned 1-D thermodynamic model and is not expected to vary more than 13% between these two conditions. When considering concurrent uncertainties in temperature and pressure [148], the uncertainty of ρ is not larger than 15%. The time-resolved density can be averaged to obtain the average density, which can then be used to find $\overline{u}_{\parallel}$. The key assumption above is that the average mass flux $\overline{\rho u_{\parallel}}$ is

equal to the product of the average density $\overline{\rho}$ and average axial velocity $\overline{u_{\parallel}}$. We acknowledge that this assumption is not strictly true, and that the velocity measurement is approximate in nature as a result. A measurement of time-resolved velocity can be used with this analytical framework in future studies to provide for a more accurate assessment of the kinetic energy in the flow.

The sum of the sensible enthalpy and kinetic enthalpy can be summed up to obtain the stagnation enthalpy h_{stag}, which is the quantity representative of the total amount of flow energy:

$$h_{\text{stag}} = h_{\text{sensible}} + k. \tag{5.7}$$

Since only the axial velocity is inferred in this work, a quantity called the axial stagnation enthalpy is defined, which represents the total thermal and axial kinetic energy in the flow:

$$h_{\text{stag},\parallel} = h_{\text{sensible}} + k_{\parallel}. \tag{5.8}$$

Following the analysis presented by [184], the azimuthal kinetic energy is an order of magnitude smaller than the axial kinetic energy, so the axial stagnation enthalpy is a close approximation of the actual stagnation enthalpy.

Fig. 5.19 plots the spread of sensible enthalpy, axial velocity, and axial stagnation enthalpy in the flow over all 25 tests. While the latter two properties are only approximations due to the velocity estimate, some relevant trends can be observed. We also note the spread in axial velocity is determined by using individual time-resolved density values to obtain individual measurements of velocity. The misaligned injector clearly resulted in less conversion of chemical energy to useful thermal and kinetic energy, as the sensible enthalpy, axial kinetic energy, and axial stagnation enthalpy are all lower for the misaligned injector. There is a greater spread in energy for the aligned injector exhaust, which is representative of the unique thermodynamic states of different pathlines in an RDRE. The variation in the exhaust energy is clearly seen to be more strongly linked to the mass flow rate than the equivalence ratio of a given test condition, at least over the range of conditions explored in this study. This is likely linked to the increased combustion pressures associated with

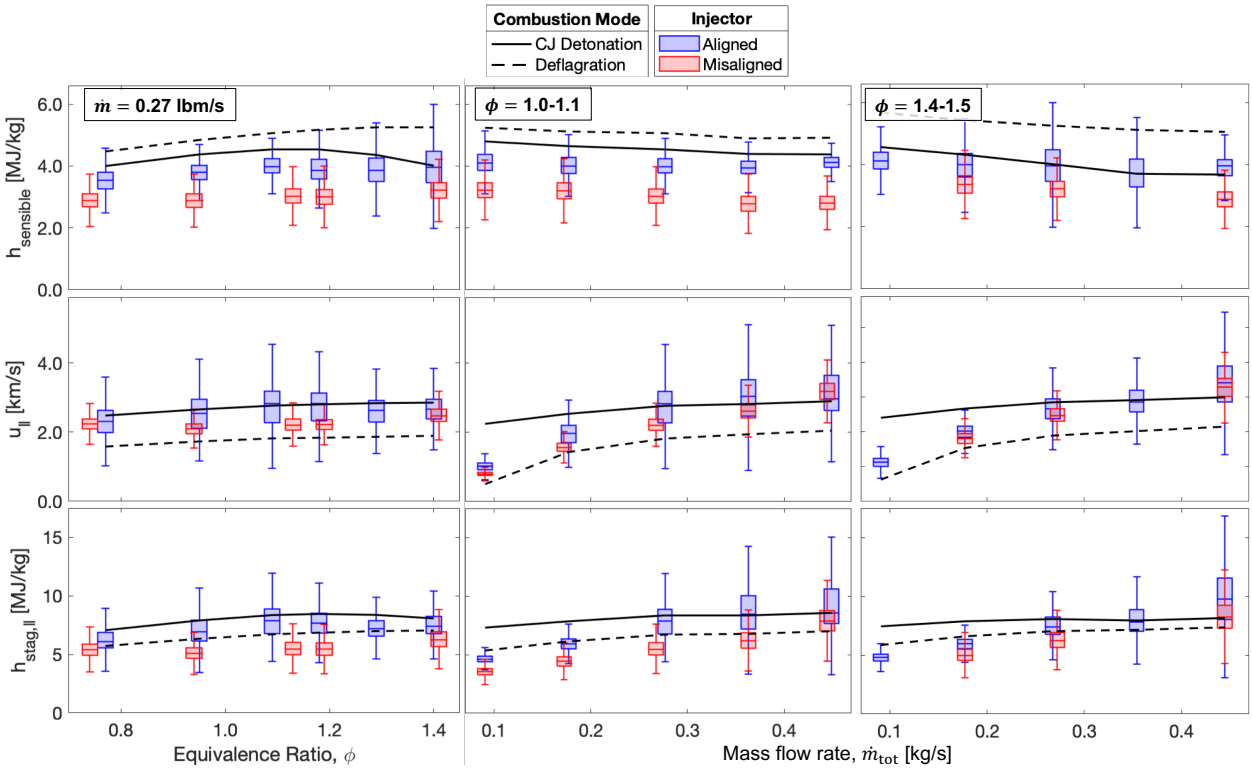

Figure 5.19: Measurements of exit plane sensible enthalpy (t*op*), axial velocity (*middle*) and axial stagnation enthalpy (*bottom*) represented as box plots to indicate variation in the properties over time. Both aligned and misaligned injector results are shown in blue and red respectively. Theoretical predictions based on the 1-D thermodynamic model are shown as black curves, with the solid curves representing detonation exhaust and the dashed curves representing deflagration exhaust.

higher flow rates, as indicated in Table 5.1, which allow for greater flow expansion as the products travel towards the combustor exit. The results exhibit generally consistent trends with simulations and reasonable quantitative agreement, though at some of the high mass flow rates the kinetic energy appears higher than the simulation. This can be attributed to a slight over-estimate of the axial velocity, likely attributable to increasing flow area at the exit plane.

In Fig. 5.20, $h_{\mathrm{stag},\parallel}$ is plotted against the specific impulse (I_{sp}) measurements derived from the load cell and tabulated in Table 5.1. For specific impulse values greater than 100 s,

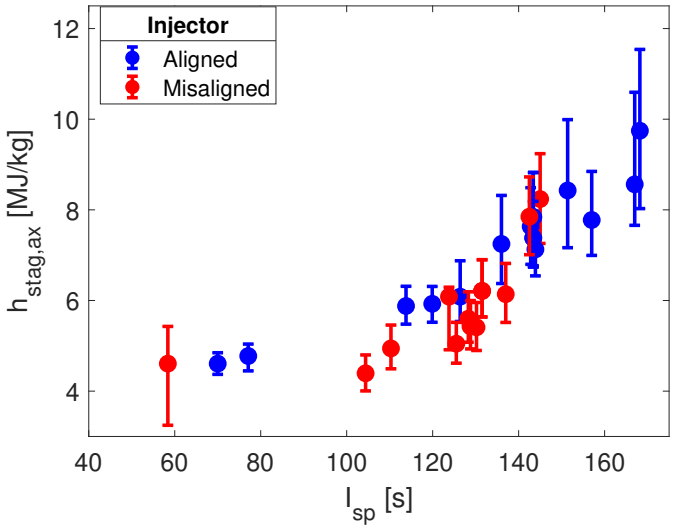

Figure 5.20: Measured axial stagnation enthalpy obtained via LAS measurements *versus* specific impulse from thrust and mass flow rate measurements for both injectors.

there is a clear correlation between I_{sp} and the measured stagnation enthalpy, indicating that $h_{\text{stag},\parallel}$ is a good predictor of engine performance.

To gauge the completeness of the energy conversion mechanisms, various efficiencies can be defined. A combustion efficiency η_{comb} can be defined as the fraction of energy actually released via chemical reaction (which at the combustor exhaust can manifest as thermal energy h_{sensible} or kinetic energy k) to the total chemical energy in the propellants:

$$\begin{aligned}\eta_{\text{comb}} &= \frac{\text{total energy extracted via chemical rxn}}{\text{total chemical energy available}} \\ &= \frac{h_{\text{sensible}} + k}{h_{\text{f,react}} - h_{\text{f,prod,min}}} \approx \frac{h_{\text{stag},\parallel}}{h_{\text{f,react}} - h_{\text{f,prod,min}}}.\end{aligned} \tag{5.9}$$

Here $h_{\text{f,react}}$ is the enthalpy of formation of the unburned propellants and $h_{\text{f,prod,min}}$ is the minimum energy level of the product gas attained in a frozen equilibrium condition (only the major product species CO_2, H_2O, CO, and H_2 are present for fuel-rich mixtures) [13]. Both of these terms can be calculated a priori using tabulated thermodynamic properties. The combustion efficiency can be reduced by poor propellant mixing and by high-temperature dissociation of CO_2 and H_2O. The denominator in this efficiency is related to the metric of c^* (which is proportional to the square-root of the combustion heat release) used to characterize

the maximum combustion performance obtained for a constant-pressure rocket engine. The combustion efficiency is therefore akin to the c^*-efficiency of conventional rocket engines.

Thermal efficiency η_{therm} is based on its classical definition for a heat engine, here defined as the ratio of kinetic energy produced (work done on working fluid) to the total thermal energy released via chemical reaction:

$$\eta_{\text{therm}} = \frac{\text{exhaust kinetic energy}}{\text{total energy extracted via chemical reaction}} = \frac{k}{h_{\text{sensible}} + k}. \tag{5.10}$$

This efficiency can be likened to the "thrust-coefficient" metric defined for conventional rocket propulsion, which characterizes the level of post-combustion gas expansion offered by a rocket nozzle. In a similar way to how the c^* and thrust coefficient can be multiplied to yield the specific impulse for a conventional rocket vehicle, η_{therm} and η_{comb} can be combined to yield an overall engine efficiency η_{tot}:

$$\eta_{\text{tot}} = \frac{\text{exhaust kinetic energy}}{\text{total chemical energy available}} = \eta_{\text{comb}}\eta_{\text{therm}} = \frac{k}{h_{\text{f,react}} - h_{\text{f,prod,min}}}. \tag{5.11}$$

For an ideal stoichiometric methane-oxygen deflagration at 5 bar, the combustion efficiency is around 74% and the thermal efficiency is around 24%, yielding an overall efficiency of around

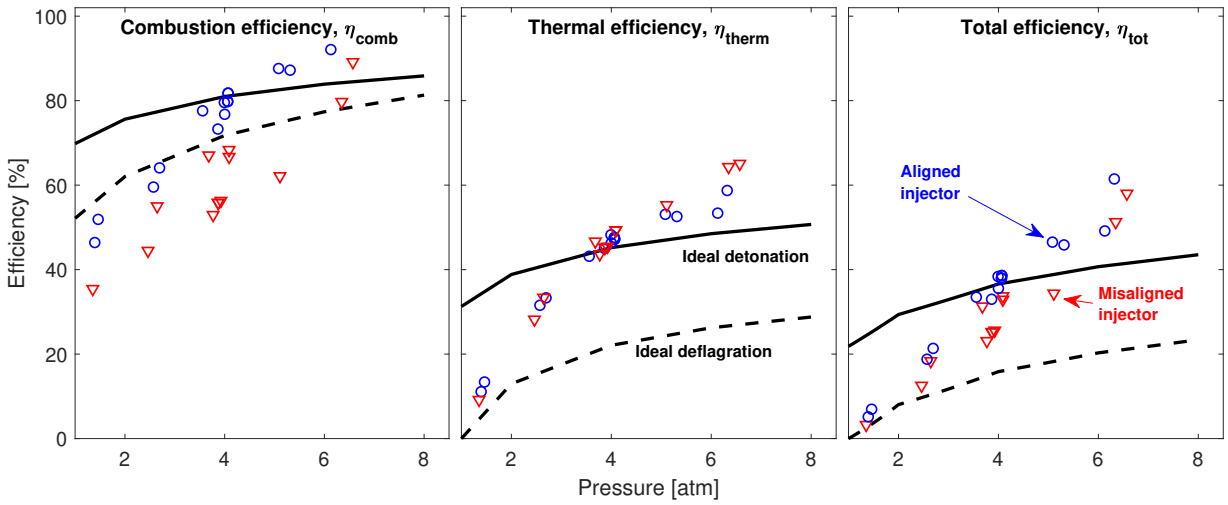

Figure 5.21: Plot of theoretical (black) and measured efficiencies for the aligned injector (blue points) and misaligned injector (red points). Theoretical detonation results are represented by the solid curves and theoretical deflagration results are represented by the dashed curves.

18%. For an ideal stoichiometric methane-oxygen detonation with a pre-detonation pressure of 5 bar, the combustion efficiency is approximately 82% and the expansion efficiency is around 47%, yielding an overall efficiency of around 37%. It is important to note that for ideal methane-air combustion the combustion efficiency is nearly 100%, as the combustion and exhaust temperatures are typically 1000 K cooler than for methane-oxygen combustion, suppressing product gas dissociation. In these airbreathing engine architectures, the overall efficiency is essentially equal to the expansion efficiency which is representative of the thermal/cycle efficiency.

Fig. 5.21 plots the theoretical combustion, thermal, and total efficiencies versus pre-combustion pressure. Both the combustion efficiency and thermal efficiency increase at higher combustion pressures, based on the 1-D thermodynamic model from above. For combustion efficiency, this is due to the suppression of the dissociation of CO_2 and H_2O at higher pressures. For thermal efficiency, this is due to the higher potential for expansion work when expanding from higher pressures. The detonation combustion and thermal efficiencies are likewise higher than the deflagration values at the same pre-combustion pressure, as the detonation induces a higher post-combustion pressure, suppressing product gas dissociation and allowing for greater levels of gas expansion.

The measurements of the efficiency values for the RDRE experiments are also plotted against the CTAP pressure for each experiment in Fig. 5.21. The plot experimentally indicates the increase in both efficiencies with combustion pressure. The combustion efficiency is generally higher for the aligned injector compared to the misaligned injector, likely due to better mixing leading to more complete combustion. Interestingly, for a given flow rate, the misaligned injector seems to exhibit a higher expansion efficiency than the aligned injector. This may be linked the typically lower exit pressure of the misaligned injector exhaust and weak nature of the oblique shocks in the misaligned exhaust, which would yield a greater conversion of thermal to kinetic energy. As indicated earlier, direct time-resolved velocity measurements would help with more accurate accounting of the energy in the exhaust gas. Nevertheless, the results presented in Fig. 5.21 are still indicative of the correlations between

the energy release mechanisms and operating conditions.

5.5 Summary

MHz laser-absorption measurements of pressure, temperature, and CO density have been made on a methane-oxygen rotating detonation rocket engine at variable operating conditions. Time-histories of the thermodynamic properties over the full test durations were analyzed to identify key transient features. A cycle partitioning strategy was employed using Fourier analysis and the time-resolved pressure profile for indicating the wave front. This enabled calculation of ensemble average intra-cycle thermodynamic profiles during the quasi-steady test time. A quantitative comparison of RDRE cycle properties across different engine operating conditions ($\dot{m}_{\text{tot}}, \phi$, injector alignment) was also conducted. Comparisons of measurement data with a 1-D thermodynamic model and a 2-D gas dynamic model reveal disagreements and intra-cycle trends that elucidate non-ideal mechanisms present in the RDRE operation, such as parasitic deflagration and post-detonation injector recovery. An energy flux analysis was also conducted to assess the completion of the conversion of chemical energy to thermal energy and the subsequent conversion of thermal energy to kinetic energy, with clear performance improvement with better mixing and higher mass flux.

CHAPTER 6

Extended tuning of distributed-feedback lasers in a bias-tee circuit via waveform optimization for MHz-rate absorption spectroscopy

The contents of this chapter have been published in the journal ***Measurement Science and Technology*** *[189] under the full title "Extended tuning of distributed-feedback lasers in a bias-tee circuit via waveform optimization for MHz-rate absorption spectroscopy". Portions of the chapter's content have been presented / included in the conference proceedings for the* ***AIAA SciTech Forum, 2022*** *[190].*

6.1 Introduction

As indicated in Chapter 4, spectral tuning across multiple spectral lines enables the measurement of multiple gas properties such as temperature, pressure, and species concentration. Extended spectral tuning can additionally support potential application at higher pressures where spectral transitions are broadened. Unfortunately, for CW-DFB lasers, there is an intrinsic trade-off in scan rate and scan spectral range (termed spectral scan depth $\Delta\nu$ [cm^{-1}]). Traditionally, the rate-limiting component in CW-DFB modulation schemes is the laser-controller bandwidth, which attenuates the external modulation signal before it reaches the laser. This has typically limited CW-DFB laser absorption measurements to rates of 10s to 100s of kHz, which is insufficient to resolve physical phenomena occurring at microsecond timescales. The rapid drop in scan depth with scan rate is indicated by the red curve in Fig. 6.1 for the CW-DFB QCL used in Chapters 4 and 5 for which the current modulation

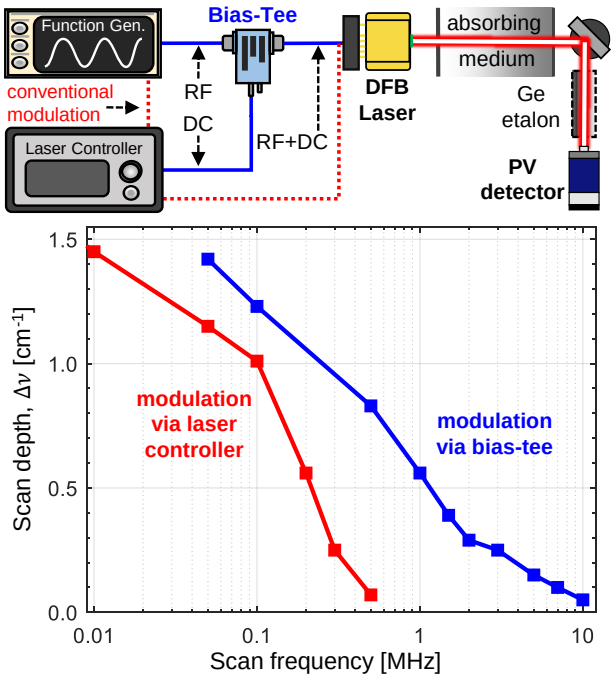

Figure 6.1: *Top left*: Schematic of DFB laser-control setup with conventional modulation in red and RF-modulation hardware with bias-tee in blue. *Top right*: Optical setup for typical laser absorption measurement. *Bottom*: Scan depth *versus* scan frequency with and without bias-tee circuit for quantum cascade laser used in Chapter 4.

was mediated by an Arroyo 6310-QCL controller [160].

The bandwidth limitation of the laser controller can be bypassed by directly diplexing the current modulation with the DC output from the controller using a bias-tee (see Fig. 6.1). In Chapter 4, bias-tee circuits coupled with CW-DFB lasers enabled a significant improvement in the achievable spectral scan depth at a given scan frequency, particularly near and above 1 MHz. This is highlighted by the blue curve in Fig. 6.1, which also shows an order of magnitude increase in the effective scan frequency for a given scan depth. The scan depth achievable in Chapter 4 was on the order of 0.5 cm^{-1} at 1 MHz (equivalent to $\Delta\lambda = 1.25$ nm at 5 µm). While useful, it remains desirable to increase the tuning range or scan depth to collect additional spectral information at such high measurement rates.

In addition to spectral scan depth, the quality of LAS measurement data during a scan

period depends heavily on the optical signal-to-noise ratio (SNR)[1] of the detected light intensity, and this depends, in part, on the modulation waveform. Given the coupling of injection-current modulation waveform with CW-DFB laser output intensity, typical modulation waveforms (e.g. sinusoidal, sawtooth) involve periods of high and low output intensity and correspondingly high and low optical SNR. In many cases, large regions of the scan period are not usable due to low optical SNR, and this can be pronounced when maximizing the scan depth and thus scanning near the lasing threshold. As such, in addition to the scan depth extension, there is a further need to improve and maximize the optical SNR of scanned-wavelength CW-DFB laser absorption measurements to increase the quantity and quality of spectral information collected at MHz rates.

In this chapter, we explore variations of modulation waveform to maximize spectral scan depth and optical SNR for a continuous-wave distributed feedback quantum cascade laser (QCL) in a bias-tee circuit with application to MHz-rate laser absorption spectroscopy. We first describe the optical configuration and methods for characterizing DFB laser tuning dynamics in the context of laser absorption spectroscopy. Subsequent waveform exploration shows significant gains to be made using square-waveform modulation and modulating below the lasing threshold. The high laser chirp rates produced by these waveforms also reveal limitations associated with the detection system bandwidth for measurement of narrow spectra. To compromise these issues, we outline a waveform-optimization strategy to generate a waveform that maximizes laser spectral scan depth and optical SNR without exceeding typical detector bandwidth constraints. This study shows that the combination of the bias-tee circuit and injection-current waveform optimization yields more than an order of magnitude gain in temporal frequency (and effective measurement rate) for a target spectral tuning depth relative to conventional laser modulation. The aforementioned methods are demonstrated for laser absorption sensing in dynamic high-temperature environments

[1]The optical SNR of a laser signal is defined here as the ratio of the mean value of a laser signal divided by the standard deviation of the signal due to noise. This "optical" SNR is proportional to the SNR of the end LAS measurement of quantities such as temperature, pressure, or species concentrations (termed "measurement SNR"), but is not not necessarily equal to it, with the relationship between the two influenced by other factors such as absorption strength, temperature sensitivity, and fitting method.

(detonation and shock tubes) for MHz-rate measurements of gas pressure and temperature. In Appendix C, a first-order model is developed for high-speed distributed feedback laser wavelength tuning dynamics and provides physical explanations for the experimental trends noted in this chapter.

6.2 Methods

This chapter presents a deeper exploration of the characteristic tunability of continuous-wave distributed feedback lasers in the infrared with single-mode monochromatic light output. Distributed-feedback lasers consist of a periodic grating structure embedded in the laser gain medium, which acts a distributed Bragg reflector (DBR) [191] that selectively provides optical feedback to a narrow band of wavelengths (10^{-4}–10^{-3} cm^{-1} linewidth [192]) related to the spatial periodicity of the grating, enabling stable, single-mode operation. DFB lasers are wavelength-tuned by changing the temperature of the DBR grating, which has the effect of changing its spatial periodicity, which shifts the laser output wavelength [193]. The temperature of the laser can be set using Peltier thermoelectric cooling (TEC) supplied by the laser controller. The temperature of the laser chip can be further increased via resistive heating from the laser injection current, which shifts the laser output wavelength higher than the TEC alone. The laser temperature can be rapidly modulated by injection-current modulation, enabling fast wavelength tuning around the center wavelength set by the TEC and average resistive heating. The relationship between laser temperature and output wavelength and the resulting tuning dynamics are discussed in more detail in Appendix C.

In this work, a continuous-wave DFB-QCL (ALPES Lasers), tunable from 2002 to 2012 cm^{-1} was used as the representative light source for scan-depth maximization in a bias-tee circuit. This wavelength was selected due in part to demonstrated utility for LAS measurements of spectral transitions in the fundamental band of carbon monoxide for numerous sensing applications [194, 151, 165, 157] as well as in Chapters 4 and 5. Note that this *continuous-wave* laser must be differentiated from *pulsed* DFB lasers used in other high-speed sensing techniques [195, 196, 197, 198, 199, 200, 163, 201], and typically offers better

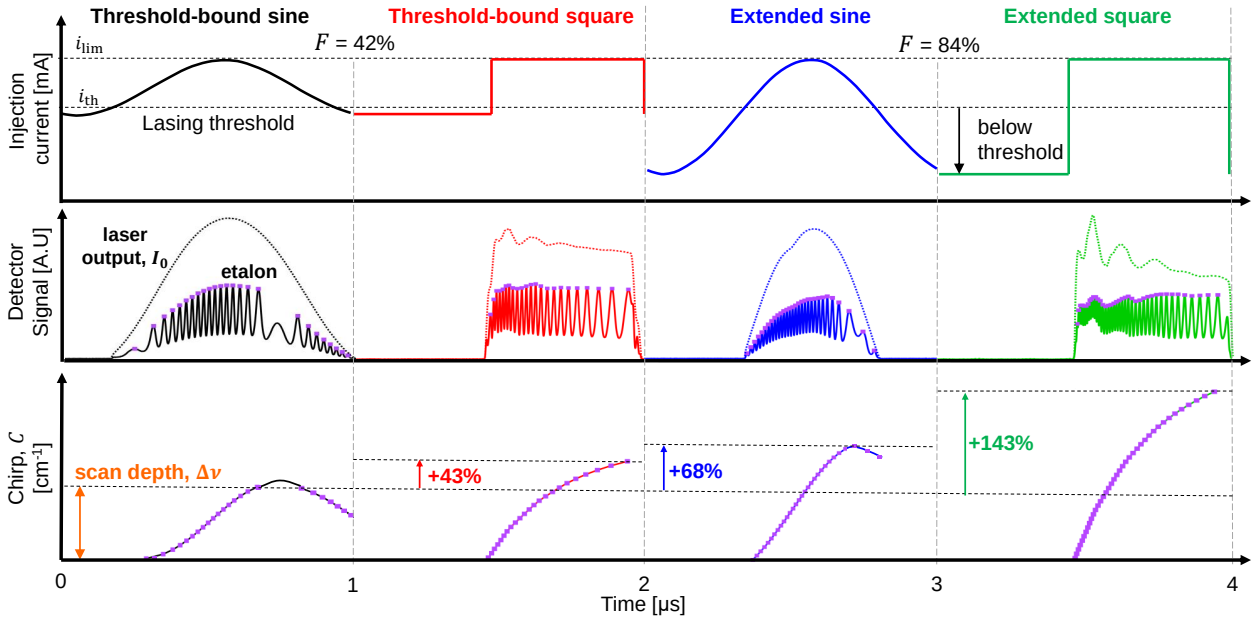

Figure 6.2: *Top*: Injection current *versus* time for various MHz waveforms. *Middle*: Detector signals produced by laser output (dotted curves) and signal when germanium etalon in beam path (solid curves). *Bottom*: Inferred laser chirp *versus* time (solid curves) obtained from the etalon signal peaks (purple dots).

scan-to-scan repeatability in output intensity. The laser temperature and mean injection current are set using an Arroyo 6310-QCL controller. A radio frequency (RF) signal is supplied by a digital function generator (Rigol DG1032Z) which can supply a maximum output frequency of 30 MHz. The function generator can output various waveforms: sine waves, square waves, as well as user-defined arbitrary waveforms. The DC current from the laser driver and the RF current from the function generator are diplexed using a bias-tee circuit to create a modulating injection-current waveform going into the laser. The bias-tee circuitry used to operate the laser is shown at the top left of Fig. 6.1 and a representative sinusoidal waveform is pictured at the top left of Fig. 6.2.

A coupled optical detection system was configured to assess the laser tuning dynamics, including output intensity and wavelength variation in time for a given input waveform. The laser beam is focused onto an AC-coupled MCT photovoltaic detector (Vigo PVI-4TE-6-1x1)

with a bandwidth that spans between 10 Hz and 200 MHz. The detector output was sampled at 1.25 GS/s using a Textronix MSO44 oscilloscope with a 200-MHz bandwidth. A typical laser output trace is shown for a sinusoidal injection-current waveform on the left of the middle row of Fig. 6.2. To additionally assess the wavelength scanning or tuning range of the laser, a 50.8-mm germanium etalon was placed into the beam path. The detector and etalon location in the beam path is shown at the top right of Fig. 6.1. The effective wavelength-dependent transmissivity due to the internal resonance of the etalon induces an oscillatory signal on the detector as the laser wavelength changes in time. This signal is pictured in the middle row of Fig. 6.2. The etalon peaks are evenly spaced in the spectral domain by the etalon's free spectral range (FSR) of $\sim$0.025 cm^{-1}. By identifying the peak locations, the change in laser wavelength/frequency over time can be assessed. The instantaneous change in wavenumber magnitude over the scan is termed the *chirp*, C [cm^{-1}] [202]. The chirp profile for a representative sine wave is plotted in the bottom left of Fig. 6.2. Two regions of the scan period can be identified by increasing or decreasing intensity, also termed upscan and downscan. In the upscan, the laser wavelength is increasing as the laser chip is being heated by the injection current. In the downscan, the laser chip is being cooled and the wavelength is decreasing. Typically, the output intensity of the laser responds within nanoseconds to the injection current, and the laser temperature lags behind, yielding a corresponding lag in wavelength or wavenumber. This lag is pronounced at MHz scan frequencies, which often leads to the wavelength downscan occurring during the portion of the scan with the lowest or zero output intensity, as seen for the sinusoidal waveform in Fig. 6.2 (see also Eqn. C.24). This results in poor optical SNR for the downscan, preventing the collection of meaningful spectral information during this part of the scan.

Given that current modulation via the bias-tee circuit involves bypassing the laser driver, which protects the laser from reverse bias, careful procedural steps must be taken when characterizing the laser tuning. Notably, the function generator outputs a voltage signal whereas the laser output depends on the injected current signal. Thus, a transfer function H [$\text{A}\cdot\text{V}^{-1}$] between the voltage amplitude from the function generator and the injection-current am-

plitude to the laser must be established, as in Chapter 4. This was determined by first setting the DC current of the laser to some value i_{DC} [A] above the lasing threshold using the laser driver and then slowly increasing the amplitude of an RF sinusoidal waveform from the function generator. By measuring the laser output intensity and noting when the bottom of the sine wave flattens (zero intensity signal), the minimum injection current is assumed to be reaching the lasing threshold current i_{th}. By using the known peak-to-peak voltage amplitude of the function generator output, V_{pp} [V], the transfer function, H, can be determined:

$$H = \frac{2(i_{\mathrm{DC}} - i_{\mathrm{th}})}{V_{\mathrm{pp}}}. \tag{6.1}$$

For the bias-tee and laser system used in this work, the transfer function was approximately 14 mA/V. Knowledge of the transfer function enables the user to identify the actual minimum and maximum current values being applied to the laser for any given function generator output.

With the transfer function known, bounds on the mean injection current and RF voltage amplitude from the function generator can be prescribed. For arbitrary waveforms, the average value of the RF voltage is not necessarily equal to the "midrange" RF voltage V_{mid} [V], or the average of the maximum and minimum voltage (V_{max} and V_{min}). As such, the offset of such waveforms should be adjusted on the function generator such that the cycle-averaged mean value of the output waveform is zero, to prevent unpredictable leakage of a DC (or low frequency) signal across the bias-tee. Failure to do so can cause laser overvoltage or reverse-biasing. Also, the DC current supplied by the laser driver should be set such that the maximum RF+DC current i_{max} does not exceed the current limit of the laser, i_{lim}. This condition can be met by ensuring the following:

$$i_{\mathrm{DC}} \leq i_{\mathrm{lim}} - HV_{\mathrm{max}}. \tag{6.2}$$

Likewise, to prevent reverse-biasing the laser, the minimum RF+DC injection current must be positive. This is enforced by ensuring the DC current satisfies the following condition:

$$i_{\mathrm{DC}} \geq HV_{\mathrm{min}}. \tag{6.3}$$

The spectral tuning and signal-to-noise ratio objectives of this work are aimed towards laser absorption spectroscopy (LAS). The basics of LAS methods are well-described in prior literature [159, 166] and in Section 4.3 of Chapter 4, and thus largely omitted here. While the waveform optimization methods are mostly independent of the target absorption features, the effective temporal frequency content of the target absorptivity must be considered. To acquire LAS measurements, a laser beam is directed through an absorbing medium as pictured in Fig. 6.1. Before the absorbing medium is present, a measurement of the laser raw intensity I_0 is taken, known as the "background" signal. Once the absorbing gas is present in the line-of-sight, a second measurement of the transmitted intensity I_{tr} is taken. The ratio of these signals is used to obtain the spectral absorbance α_ν using the following relation:

$$\alpha_\nu = -\ln\left(\frac{I_{\mathrm{tr}}}{I_0}\right)_\nu . \tag{6.4}$$

The time-resolved absorbance spectrum can be mapped to the wavenumber domain by using the chirp profile obtained with the etalon signal. This absorbance spectrum can then be analyzed to extract information about the properties of the medium in question, such as gas temperature, pressure, and composition. In Section 3, the relevance of the characteristic temporal frequency associated with changes in α_ν from wavelength scanning is described in the context of laser tuning dynamics. Demonstrations of LAS measurements at MHz rates are also presented.

6.3 Results and analysis

6.3.1 Laser tuning dynamics

The periodic injection-current waveform used to modulate the laser impacts its wavelength-tunability and power-output characteristics. At very high scan rates, a sinusoidal waveform is commonly used for injection-current modulation, which gradually changes the heating applied to the laser between a maximum and minimum value. The harmonics of sinusoidal modulation may also be conveniently analyzed [158]. Here we rigorously examine the benefits and potential drawbacks of square-waveform modulation, which has previously shown

some benefit to improving optical SNR for under-sampled spectra [203]. In square-wave modulation, the laser heating no longer changes gradually. Instead, during the upscan, a step change to maximum current and heating occurs, and during the downscan, the maximum level of cooling occurs when the current changes step-wise to the minimum value. These dramatic variations of heating and cooling allow the laser grating to reach greater extremes of temperature, resulting in greater spectral scan depth. For the present setup, applying a sine wave which is scanned between the lasing threshold (approximately 110 mA) and the maximum allowable current (190 mA), a scan depth of 0.40 cm^{-1} is achievable. With a square wave operating with the same current amplitude, a scan depth of 0.57 cm^{-1} is achievable, representing a significant increase of $\sim$43%, which corresponds closely to the predictions from Eqs. C.23 and C.49. The aforementioned sinusoidal and square waveforms are indicated in the first two columns of Fig. 6.2.

Beyond the increase in scan depth due to the waveform change, it is clear that the optical signal-to-noise ratio (SNR) associated with the laser output increases with the square wave, as the laser ramps up to its maximum output power much more quickly and for longer in time than for a sine wave. Additionally, compared to the sine wave modulation, the optical SNR remains roughly constant across the scan, mitigating bias of the spectral measurement between regions of high and low optical SNR. It should be noted that square-wave modulation necessarily results in the downscan having near-zero optical SNR. However, as mentioned in Section 2, for MHz-rate modulation, even for sinusoidal waveforms, the downscan already typically has poor optical SNR due to the lag between wavelength and intensity modulation and is consequently not usually utilized for spectral information.

In addition to square-wave modulation, and by a similar principle, scan depth was shown to increase by modulating below the lasing threshold current. In this case, the amplitude of the modulated current signal was extended to span between near-zero current and the maximum current limit of the laser. This technique increases heat dissipation and causes the amplitude of the temperature modulation to increase, which explains why the scan depth increases, despite the fact that the observed intensity is lower as the laser is not outputting

light when it is scanned below the lasing threshold. We normalize the peak-to-peak current amplitude i_{pp} by the maximum current amplitude $i_{\mathrm{pp,max}}$ (modulating from zero current to the current limit) to define a variable termed the *fractional current*, F:

$$F = \frac{i_{\mathrm{pp}}}{i_{\mathrm{pp,max}}} = \frac{i_{\mathrm{pp}}}{i_{\mathrm{lim}}}. \tag{6.5}$$

For the laser used in this work, scanning between the lasing threshold and maximum current limit corresponds to a *threshold-bound* fractional current of $F_{\mathrm{th}} = 42\%$. In other words, the fraction of injection-current range (from zero to max current) for which lasing occurs is 42%, and the current range below the threshold represents the other 58%. To mitigate the risk of reverse-biasing the laser, a minimum current limit value was set at approximately 1/3 of the lasing threshold current (30 mA for this work) corresponding to a maximum fractional current of $F = 84\%$. The injection-current profiles for these two values of fractional current are shown in Fig. 6.2, with the first two columns featuring waveforms at $F_{\mathrm{th}} = 42\%$ and the second two columns featuring waveforms at $F = 84\%$. For the remainder of the paper, to emphasize the improved scan depth of this technique, we will call waveforms with $F > F_{\mathrm{th}}$ "extended", i.e., *extended sine* or *extended square*. Waveforms that are modulated between the lasing threshold and current limit ($F = F_{\mathrm{th}}$) are termed "threshold-bound". The effect

Table 6.1: Variation of the scan depth as a function of fractional current from 42% (threshold-bound) to 84% (extended).

	Scan depth, $\Delta\nu$ [cm^{-1}]	
Fractional current, F [%]	Sine wave	Square wave
42 (threshold-bound)	0.40 cm^{-1}	0.57 cm^{-1}
84 (extended)	0.64 cm^{-1}	0.99 cm^{-1}

of the fractional current variation can be directly seen in Table 6.1. When the waveforms are modulated at the maximum fractional current, the scan depths increase to 0.64 cm^{-1} for the sine wave, and 0.99 cm^{-1} for the square wave. This represents a 60% and 148% increase respectively in scan depth compared to the threshold-bound sine wave modulated at the threshold-limited fractional current modulation.

An interesting and notable side effect of the MHz-rate current modulation below the lasing threshold is an effective extension of the temperature tuning range of the laser. DFB lasers are typically designed to operate in a range of wavelengths limited by the temperature range achievable by the Peltier TEC. We observed that extended current modulation at high speeds allows for the DFB-QCL to lase at wavenumbers that would otherwise be inaccessible. Typically, when the current applied to the laser decreases, the wavenumber output of the laser increases (wavelength decreases) as the laser drops in temperature. When the current drops below the threshold current, the laser continues to cool, tuning the laser DFB grating to higher wavenumbers. However, these frequencies of light are not outputted by the laser, as the laser power drops to zero below the lasing threshold. In the case of high-speed modulation, however, the lag between the laser intensity output and the laser temperature allows for the laser cavity to be tuned to a wavenumber associated with a "below-threshold" temperature while the power is quickly ramped up above the threshold. By shifting the fractional current from $F = 42\%$ to $F = 84\%$ the spectral domain accessible by the laser was effectively extended by $\sim$1.5 cm^{-1}, which is equivalent in this case to shifting the laser TEC setpoint $\sim$10°C colder.

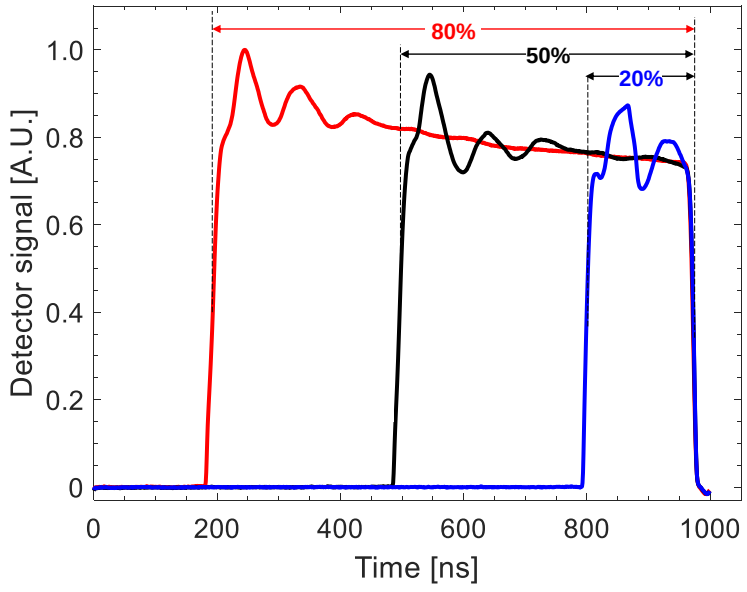

Figure 6.3: Detector signals for extended square waves ($F = 84\%$) with varying duty cycle.

In addition to the influence of waveform shape and fractional injection-current amplitude, the effects of injection-current duty cycle were also examined, specifically for the square waveform. As the duty cycle is varied, there is a tradeoff between the amount of time spent heating and cooling the laser. For instance, a duty cycle above 50% involves longer periods of heating than cooling, and the opposite for a duty cycle below 50%. In Fig. 6.3, representative laser output intensity traces are shown for three square waves of varying duty cycle (20%, 50%, and 80%) which all share a fractional current of 42%. As might be expected, the spectral scan depth is maximized for a duty cycle of 50%, which agrees with observations made by Chrystie et al. for pulsed QCLs [200] and is supported by the mathematical arguments presented in Appendix C. The variation of the scan depth with duty cycle can be seen with the black curve in Fig. 6.4 for extended waveforms with $F = 84\%$.

It should be noted that the aforementioned effects are pronounced at very high scan rates because chip heating and cooling are too slow to change to a fixed wavelength (top of square wave) within the scan period. At slower scan rates, the spectral scan depth would presumably be less sensitive to duty cycle, as the laser would likely be able to reach the

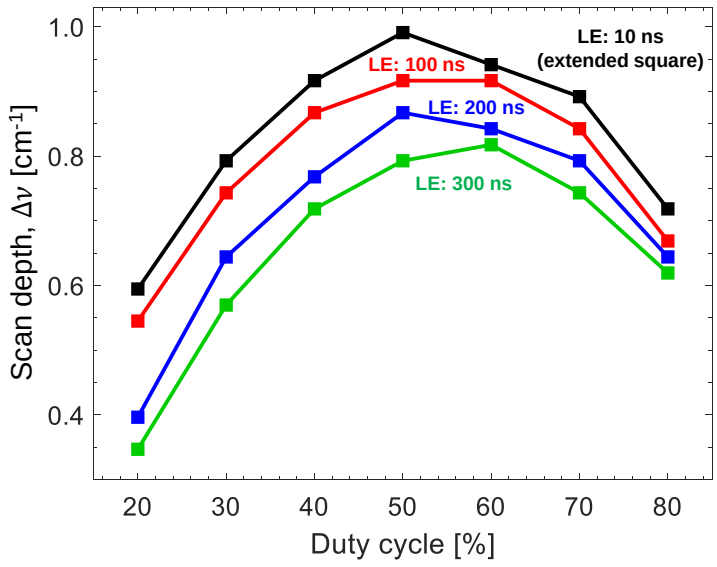

Figure 6.4: Scan depth *versus* duty cycle for extended square waveforms ($F = 84\%$) varying leading-edge (LE) ramp times.

output wavelength associated with maximum current level, regardless of the time spent in the upscan relative to the downscan. Accordingly, as laser scan rate is reduced, the relative gain in spectral scan depth would be reduced. Additionally, it should be expected that the thermal responsivity and heat dissipation rates vary from one laser chip to another, but in the examination of several CW-DFB lasers in our laboratory, similar effects (with regards to the gain in spectral scan depth) on the same order of magnitude were observed under MHz modulation. We further note that the relative gain from sub-threshold extended current modulation depends on the baseline fractional threshold current. Specifically, DFB interband cascade lasers (ICLs) typically have lower threshold current values relative to their maximum current limit compared to quantum cascade lasers. This means that the threshold-limited fractional current for these lasers are typically high ($> 60\%$) relative to QCLs. As such, the opportunity for spectral scan depth improvement via extended scanning is limited for these types of lasers. As an example, for a Nanoplus ICL with an output wavelength near 4.19 µm tested in our laboratory, the threshold-limited fractional current was 75%. The spectral scan depth increased 32% for a square waveform when increasing the fractional current from 75% to 95%. However, square-wave modulation was still greatly beneficial relative to sine-wave modulation for this same ICL, with the threshold-bound square wave having 72% higher spectral scan depth relative to a threshold-bound sine wave.

6.3.2 Detection bandwidth limitations

The aforementioned methods for extending the spectral scan-depth capability of DFB lasers can generate optical signals with very high temporal frequency content, and thus spectral resolution may become limited by the detection system. If the frequency content of the optical signal is near or above the detection-system bandwidth (related to the bandwidth of the detector and oscilloscope), then the recorded signal can become distorted as the high-frequency components of the signal become attenuated and phase-shifted due to effective low-pass frequency filtering. Distortion of the background or transmitted light intensity causes the measured absorbance (obtained using Eqn. 6.4) to be similarly distorted. An

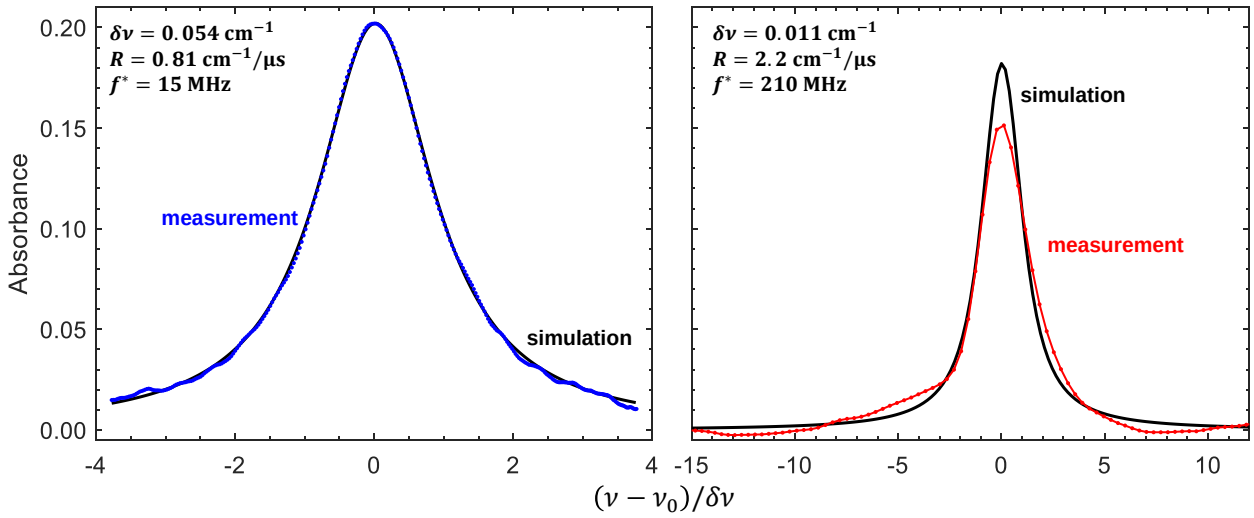

Figure 6.5: Absorbance measurement of the $^{12}C^{16}O$ P(0,22) line *versus* wavenumber normalized by the linewidth (relative to linecenter). *Left*: Close agreement between low characteristic frequency measurement (15 MHz, blue) and a Voigt profile simulation (black). *Right*: Lineshape distortion of high characteristic-frequency measurement (210 MHz, red) compared to a Voigt profile simulation (black).

example of such a distorted absorbance measurement is shown on the right side of Fig. 6.5.

High frequency content in the optical signals may come about due to (1) fast scanning across a narrow spectral feature when making an absorption measurement (I_{tr} distortion) or (2) high-frequency oscillation of the raw laser output intensity (I_0 distortion). Narrow spectral features can cause rapid changes in transmitted light intensity as the laser wavelength rapidly scans across the feature. This type of distortion will occur when either the spectral features have a narrow linewidth $\delta\nu$ [cm^{-1}] or when the rate of change of the laser output wavenumber is high. The magnitude of the rate of change of wavenumber output (or chirp, C) of the laser is termed the "chirp rate", R [cm^{-1}·s^{-1}] [191]:

$$R = \left|\frac{\mathrm{d}\nu}{\mathrm{d}t}\right| = \frac{\mathrm{d}C}{\mathrm{d}t}. \tag{6.6}$$

For infrared absorption spectra of small gaseous species (i.e. CO, CO_2, H_2O) at near-atmospheric pressures, the dominant contributor to the linewidth is collisional broadening ($\delta\nu \approx \delta\nu_{\text{C}}$) [204] which scales linearly with gas pressure. As such, the bandwidth related

distortion will be pronounced at lower pressures. It is postulated that for a given detector bandwidth, there will be a maximum "characteristic frequency" f^* [Hz] associated with the light intensity change due to the narrow spectral absorption feature:

$$f^* = \frac{R}{\delta\nu}. \tag{6.7}$$

Here, $\delta\nu$ is the full-width half maximum (FWHM) of the target spectral feature. Equivalently, a "characteristic time" τ^* [s] may be defined which intuitively represents the time required to scan the FWHM of the spectral feature:

$$\tau^* = \frac{1}{f^*} = \frac{\delta\nu}{R}. \tag{6.8}$$

In order to identify the maximum allowable characteristic frequency for the target line used in this work with a 200-MHz bandwidth detection system, a series of measurements of carbon monoxide (CO) absorption at room temperature were conducted by placing a 33.94-cm static gas cell into the optical path. This gas cell was filled with pure CO to various fill pressures. Before the cell was filled, we measured the background intensity with and

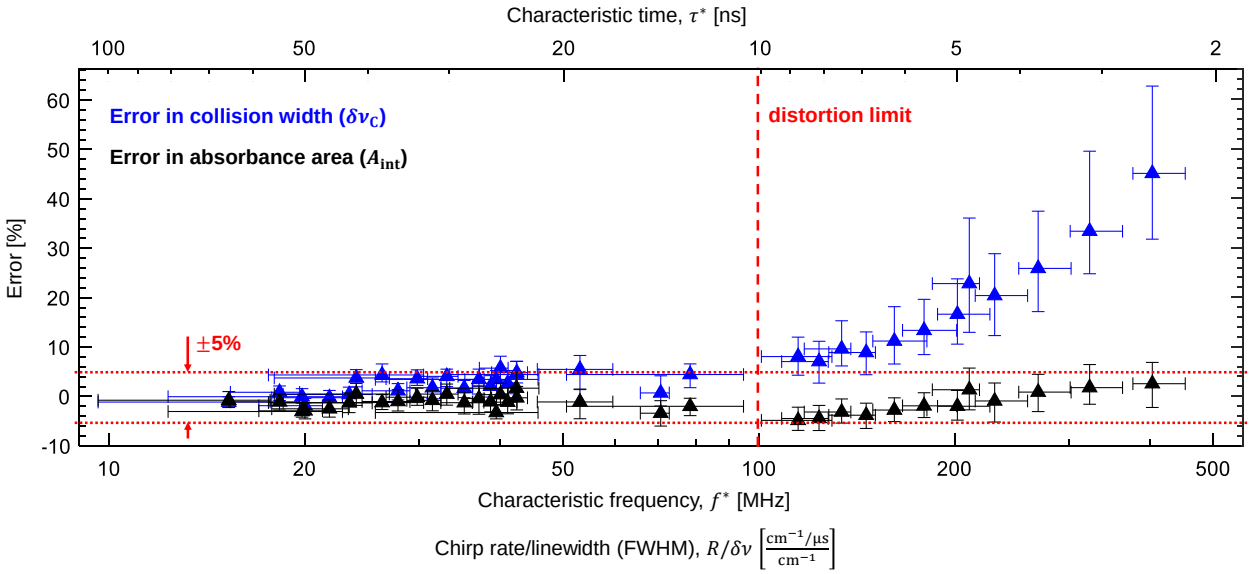

Figure 6.6: Error in fitted collision linewidth and absorbance area of the $^{12}C^{18}O$ P(0,22) line at various characteristic frequencies (chirp rate over FWHM). The error in the fit of $\delta\nu_C$ is seen to increase significantly past $f^* = 100$ MHz

without the etalon in the beam path, to transform the results from the time domain to the spectral wavenumber domain. After the cell was filled, the transmitted light intensity was recorded, and an absorbance measurement was calculated using Eqn. 6.4. The laser's center wavelength was tuned to the P(0,22) line of $^{12}C^{18}O$ at 2004.28 cm^{-1}, which was selected due to its isolation from other CO lines and from the spectra of ambient water. Measurements were performed using sine waves in order to isolate the effects of the potential high-frequency content in other waveforms. The chirp rate of these sine waves was adjusted by varying the fractional current and the laser modulation frequency. In addition, the characteristic frequency of the measurement is adjusted by filling the gas cell to different pressures, resulting in variation in the FWHM of the spectral feature.

Sample room-temperature absorbance measurements are shown in Fig. 6.5. A range of characteristic frequency measurements were collected spanning from 10 MHz to 400 MHz. At low characteristic frequencies, the measured absorbance spectra agrees closely with a Voigt simulation of the target line using linestrength and self-broadening parameters from HITRAN 2020 [205], as indicated on the left side of Fig. 6.5. At high characterstic frequencies the measured lineshape becomes distorted, as indicated on the right side of Fig. 6.5. There is a reduction in the measured peak absorbance, along with signal artifacts in the wings of the line. This distortion precludes accurate fitting of the absorption lineshape.

In order to assess the magnitude of the detector induced distortion on the measured lineshape parameters, a Voigt profile [170] was fitted to the measured spectra over a range of characteristic frequencies. In this lineshape fitting routine, the Doppler linewidth of the Voigt profile was fixed whereas the collision linewidth ($\delta\nu_C$), absorbance area (A_{int} [cm^{-1}]), and absolute line position of the line were allowed to float. The three parameters were varied until a solution minimizing the sum of squared errors between the measurement and fit was found. The error in fitted collision linewidth and absorbance area is plotted in Fig. 6.6 against the characteristic frequency of the absorption measurement. It can be seen that for lower characteristic frequencies, the error in the measured spectral parameters is low and on the order of the scan-to-scan variation in the error, as indicated by the vertical error bars.

At higher frequencies however, the fitted collision width ends up being higher than the true collision width, revealing in an instrument-induced broadening of the line. It is interesting to note that the fitted absorbance area is more robust to the detector induced distortion, with the error in the fitted areas staying within ±5% even at the highest tested characteristic frequencies. The critical characteristic frequency beyond which the collisional linewidth measurement error exceeds 5% is approximately 100 MHz (corresponding to $\tau^* = 10$ ns), which is 1/2 the detection system bandwidth $f_{\mathrm{BW}} = 200$ MHz, implying that the following criteria should be met to mitigate detector induced distortion of absorption signals:

$$f^* < \frac{1}{2} f_{\mathrm{BW}}. \tag{6.9}$$

The above criteria may be used to establish a maximum allowable laser chirp rate for a given detection system bandwidth and target spectral feature. For example, if the $^{12}C^{16}O$ P(0,22) line was to be measured down to pressures of 0.25 atm ($\delta\nu = 0.027$ cm^{-1}) using a 200-MHz bandwidth detection system, a maximum allowable measurement error of 5% imposes a

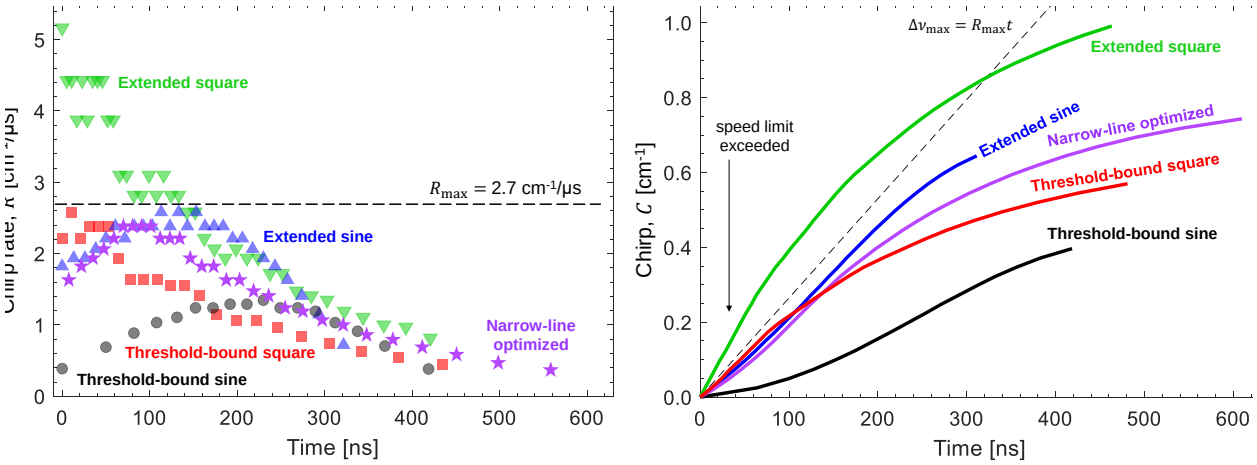

Figure 6.7: *Left*: Chirp rate *versus* time for the threshold-bound sine, threshold-bound square, extended sine, extended square, and optimized waveform. The extended square is observed to exceed the chirp-rate limit defined for scanning CO at 0.25 atm (2.7 cm^{-1}·μs^{-1}). *Right*: Chirp *versus* time for the same waveforms. The extended square yields the highest scan depth but exceeds the bandwidth-limited chirp rate. The optimized waveform achieves high scan depth while remaining below the speed limit.

maximum chirp rate of $R_{\max} = 2.7\ \mathrm{cm}^{-1}\cdot\mu\mathrm{s}^{-1}$. In light of this limit, the waveforms discussed in Section 6.3.1 can be re-evaluated. The left side of Fig. 6.7 indicates the chirp rate versus time during a single modulation period for the various waveforms. Some of these waveforms resulted in chirp rates that exceeded this limit during some portion of the scan. We can define a usable scan depth, $\Delta\nu_{\mathrm{use}}$, which corresponds to the scan depth, $\Delta\nu$, restricted to the portion of the scan where the chirp rate is below $R_{\max}$:

$$\Delta\nu_{\mathrm{use}} = \Delta\nu\big|_{R<R_{\max}}. \tag{6.10}$$

For the threshold-bound sine wave ($F = 42\%$), the extended sine wave ($F = 84\%$), and the threshold-bound square wave ($F = 42\%$), the chirp rate never exceeds the maximum allowable value. Thus, their usable scan depths are equal to the actual scan depths. However, for the extended square wave, the chirp rate does exceed the limiting value at the beginning of the upscan, meaning that spectral features positioned at the beginning of the scan could be potentially distorted. The usable scan depth for the extended square is therefore reduced from 0.99 cm^{-1} to 0.50 cm^{-1}, rendering it less useful than the threshold-bound square wave and extended sine, for this particular narrow-linewidth absorption. In fact, when considering usable scan depth, maximizing F does not maximize $\Delta\nu_{\mathrm{use}}$. For a square wave, the usable scan depth is similar for fractional current values between 40 and 65%, yielding an approximate usable scan depth of 0.5 cm^{-1}. The chirp versus time for the aforementioned waveforms during a single modulation period are indicated on the right side Fig. 6.7. A dashed line is plotted with the slope equal to the maximum chirp rate. This corresponds to the maximal chirp achievable while respecting the bandwidth-limited chirp-rate limit. The extended square clearly overtakes this maximal chirp profile at early times. It must be noted that for FWHMs above $\sim$0.05 cm^{-1} (corresponding to pressures above $\sim$0.5 atm for CO), the full extended square waveform (with 0.99-cm^{-1} scan depth) can be used without an expected distortion of the spectra—limitations on the broad tuning offered by this technique are only relevant for measurements of narrow spectral features.

The other potential source of high-frequency content relates to the oscillations in raw laser intensity. This appears as a *ringing* at the beginning of a scan due to the overshoot in

laser output power when the injection current undergoes a large step-change, on the order of nanoseconds [206, 207], induced by the square waveform (which can be related to the Gibbs phenomenon). Ringing can be observed at the beginning of the various square-wave pulses shown in Figs. 6.2 and 6.3. The amplitude of ringing increases as the fractional current is increased because the laser current is changing more drastically. For the laser studied in this work, it was found that the ringing frequency was on the order of 10 MHz, which is well below the detection bandwidth of 200 MHz used in this work. Additionally, to validate that the ringing associated with the extended square waveform did not lead to distortion of the measured spectra, room-temperature measurements of CO at 0.5 atm were conducted across the waveform. In each test, the laser temperature was tuned to position the spectral feature at various positions along the scan waveform. Whether or not the feature was positioned in a region of high ringing, the error in the measured absorbance area and collision width was below 5%, validating the lack of ringing-induced distortion. When ringing is present in the background signal, proper temporal alignment of the background and transmitted intensity profiles must be enforced. Otherwise, the absorbance signal will include non-trivial baseline artifacts that are difficult to remove in post-processing techniques. On the other hand, the absence of these residual artifacts is a good indicator of proper alignment or phasing between the incident and transmitted light intensities when calculating absorbance—this utility is not typical of conventional waveforms. Ringing also results in a loss of potential optical SNR due to the short-lived nature of the peak laser intensity. In the next section, we will show that an optimal compromise between the extended sine and the extended square can be found using arbitrary waveform generation to mitigate ringing and detection-system induced distortion while maximizing optical SNR and scan depth.

6.3.3 Waveform optimization

It is clear that the extended square waveform maximizes spectral scan depth, but high initial chirp rates and ringing can reduce the usefulness of the full waveform. To mitigate the limitations of detector bandwidth for narrow spectral-feature detection and reduce ringing,

one can presumably slow the initial rate of change of the laser output power and output frequency. One method to accomplish this involves modifying the duty cycle of the waveform. As discussed in Section 6.3.1, spectral scan depth is optimized at a duty cycle of 50%. However, increasing the duty cycle has the effect of reducing the amount the laser cools during the downscan. This makes the temperature change at the beginning of the upscan less drastic, reducing the chirp rate, leading to more of the scan being usable. This effect can be seen in the left and middle columns of Fig. 6.8, where square pulses with duty cycles of 50% and 70% are compared. The increase in the duty cycle increases the usable scan depth from 0.42 cm^{-1} to 0.52 cm^{-1}. On the other hand, reducing the duty cycle causing the laser temperature to drop more significantly during the downscan, causing more rapid heating during the beginning of the upscan leading to high initial chirp rates, reducing the usable scan depth. This is exacerbated by the short duration of the upscan, meaning that there is minimal time for the laser chirp rate to return to slow enough speeds. In fact, at 20% duty cycle, the usable scan depth is zero.

Increasing the waveform duty cycle improves usable scan depth to a point, and additional gains can be made by adding a linear ramp to the beginning of the pulse, turning the square into a trapezoid. The length of the ramp (LE) has a maximum value for a given duty cycle, as detailed in Appendix C. When using a ramp, the definition of duty cycle is the fraction of the scan period for which the current is above the midrange value, i_{mid}, which is the arithmetic mean of the maximum and minimum current. This ramp has the effect of providing more gradual heating to the laser, resulting in slower initial wavelength tuning while also mitigating ringing in the optical output signal. This effect can be seen in the right column of Fig. 6.8 where a 300-ns leading-edge ramp is added to the waveform with 70% duty cycle. As the length of the leading-edge ramp is increased, the overall scan depth achieved by the laser is necessarily reduced, along with a reduction in optical SNR during the initial part of the scan. At 50% duty cycle, changing the leading edge ramp does not improve the usable scan depth, as the reduction in initial chirp rates is almost exactly compensated by the reduction in overall spectral scan depth. On the other hand, at higher duty cycles, the

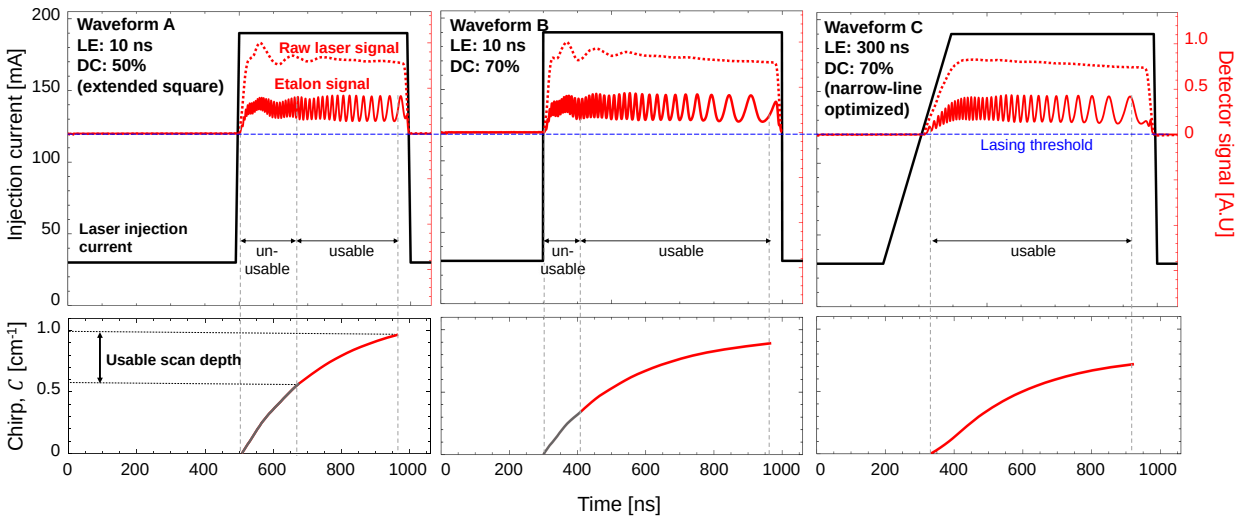

Figure 6.8: Laser injection current, detector signals (*top*) and chirp profiles (*bottom*) for a 10 ns leading-edge square waveforms with 50% duty cycle (waveform A, *left column*) and 70% duty cycle (waveform B, *middle column*). The narrow-line optimized trapezoidal waveform with a 300-ns ramp and 70% duty cycle (waveform C) is shown in the right column. The combined effect of the leading-edge ramp and increased duty cycle keep the chirp rate below the detector limit, making the entire scan usable.

addition of a leading-edge ramp improves the usable scan depth for narrow-line measurement. For the 70% duty-cycle waveform, shifting from a 10-ns ramp to a 300-ns ramp boosts the usable scan depth from 0.52 cm^{-1} to 0.74 cm^{-1}. The entire scan also becomes completely usable, as the chirp rate limit is not exceeded at any point. It is also interesting to note that as the length of the leading-edge ramp is increased the optimal duty cycle for maximizing overall spectral scan depth also shifts to higher values than 50%. This effect can be seen in Fig. 6.4 and a physical explanation for this phenomenon is presented in Section C.5 of Appendix C.

In order to find a trapezoidal waveform that maximizes usable scan depth while $R_{max} < 2.7$ $cm^{-1} \cdot \mu s^{-1}$ (for narrow-spectra measurement), a multi-parameter optimization was conducted. Laser output intensity and etalon signal were recorded for the various trapezoidal waveforms and the scan depth and peak chirp rate were identified for each waveform. The

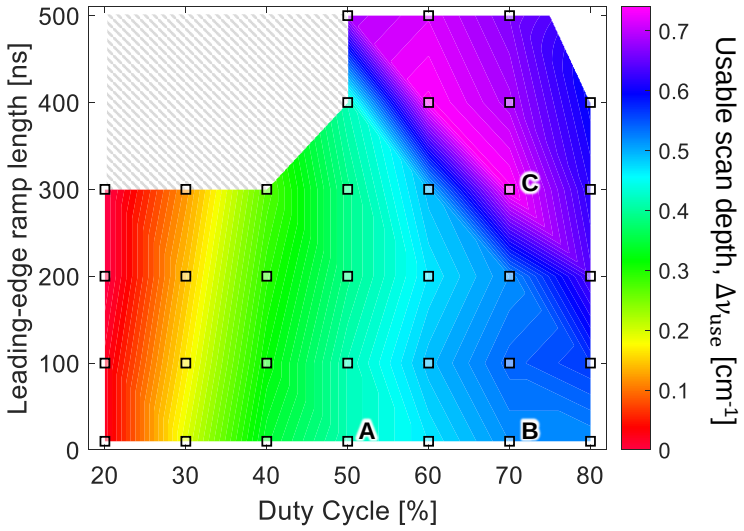

Figure 6.9: Contour plot of usable scan depth as a function of duty cycle and leading-edge ramp length at a fixed fractional current $F = 84\%$. The points A, B, and C correspond to waveforms A, B, and C from Fig. 6.8, with point C (narrow-line optimized waveform) clearly corresponding to a waveform of high usable scan depth. The gray region in the top left corner of the plot represents waveforms that were not investigated due to sub-optimal usable scan depth.

usable scan depth was mapped as a function of the leading-edge ramp time (varied in increments of ∼100 ns), duty cycle (varied in increments of 10%), and fractional current. A contour plot of the variation in usable scan depth with duty cycle and leading-edge ramp time at a fixed value of fractional current ($F = 84\%$) is shown in Fig. 6.9. The aforementioned trends of improved usable scan depth at increased duty cycle and leading-edge ramp times can clearly be observed. The usable scan depth maximized at a value near $\Delta\nu_{\text{use}} = 0.74$ cm^{-1} in a region where duty cycle is 60–70% and the leading edge ramp time is 300–400 ns and the maximal fractional current $F = 84\%$. Given this range of options, the waveform with the longer duty cycle and shorter leading edge ramp is chosen (DC = 70% and LE = 300 ns) as this choice maximizes optical SNR and increases the length of the scan, enabling higher temporal resolution of the target spectra at a fixed measurement sampling rate. This optimized waveform is termed the "narrow-line" optimized waveform.

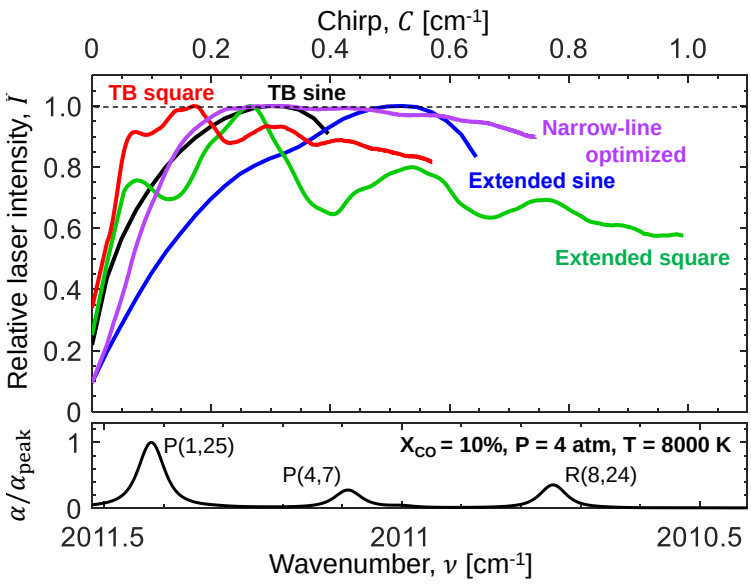

Figure 6.10: *Top*: Normalized laser power *versus* chirp for the various waveforms ("TB" refers to threshold-bound waveforms). *Bottom*: Sample absorbance spectrum of 10% CO in air near 5 µm at 4 atm, 8000 K.

The chirp rate and chirp profiles for this waveform are compared to the other waveforms in Fig. 6.7. The injection-current profile, laser output intensity, etalon signal, and chirp versus time are shown on the right side of Fig. 6.8. Figure 6.10 compares the chirp and laser output intensity profiles (normalized by peak intensity to obtained the *relative intensity* $\hat{I} = I/I_{\text{peak}}$) of the various waveforms. The effect of the scan depth variation in the waveforms can also be observed in relation to a sample spectrum of high-temperature CO, where the higher scan-depth waveforms are able to scan across more transitions. It can be clearly seen that the optimized waveform does not induce ringing in the laser power output. This allows for an increase in the optical SNR of measurements with this profile, as the laser spends more of its time at peak power compared to the cases with ringing, where the laser is only momentarily at the maximum power output. This compensates for the initial reduction in optical SNR over the first 0.2 cm^{-1} of the scan. This can be assessed quantitatively by finding the spectrally-averaged relative laser power $\overline{I}$ across the scan:

$$\overline{I} \equiv \frac{1}{\Delta\nu} \int_0^{\Delta\nu} \hat{I} dC. \tag{6.11}$$

Table 6.2: Comparison of the average laser intensity metrics for the various waveforms in this study. NL refers to"narrow-line".

Waveform	$\overline{I}$	$\overline{\Delta\nu}$ [cm^{-1}]	$\overline{\Delta\nu}_{\text{use}}$ [cm^{-1}]
TB sine	0.83	0.33	0.33
Extended sine	0.76	0.49	0.49
TB square	0.87	0.50	0.50
Extended square	0.71	0.71	0.42
NL optimized	0.88	0.65	0.65

The values of $\overline{I}$ for the main waveforms studied in this work are included in Table 6.2. The narrow-line optimized waveform has the highest value of $\overline{I}$, which is indicative of how long the waveform spends at maximum power.

To incorporate the effect of scan depth on this power analysis, another figure of merit, the "weighted scan depth" $\overline{\Delta\nu}$ may be defined, which integrates the relative laser intensity $\hat{I}$ over the the chirp of the laser, which is the product of $\overline{I}$ and $\Delta\nu$:

$$\overline{\Delta\nu} \equiv \int_0^{\Delta\nu} \hat{I} dC = \overline{I}\Delta\nu. \tag{6.12}$$

This is essentially the scan depth of the laser, weighted by the relative laser output intensity across the scan and can be visualized as the area under the curves in Fig. 6.10. $\overline{\Delta\nu}$ is also tabulated in Table 6.2 for the various waveforms analyzed in this work. The narrow-line optimized waveform, has a value of $\overline{\Delta\nu}$ only 6% lower than the value for the extended square, despite the fact that the optimized waveform scan depth is 20% lower. The spectral information collected with the optimized waveform is therefore of higher average optical SNR than the extended square. If only integrating over the usable part of the scan in a sensing application involving narrow spectra features, a "weighted usable scan depth" $\overline{\Delta\nu}_{\text{use}}$ can also be defined. This is also tabulated in Table 6.2, which indicates a 55% improvement with the narrow-line optimized waveform over the extended square. While neither $\overline{I}$, ν, nor ν_{use} are used in the waveform optimization procedure presented above, they may be incorporated in future optimization for sensing strategies where optical SNR is of high importance, such as

for the measurement of optically thick/thin spectra or in power-limited applications.

The previous analysis reveals that the key constraint in waveform optimization is the maximum allowable chirp rate. This maximum chirp rate is obtained using Eqs. 6.7 and 6.9 based on the detection system bandwidth and the linewidth of the target spectral features. Notably, the maximum allowable chirp rate can be increased by using a higher bandwidth detection system or by targeting broader spectral features. By considering these two parameters, waveforms with maximum useful scan depths can be employed without spectral distortion. It should be noted that the analysis here used a specific but representative quantum cascade laser. For other CW-DFB lasers, a different optimum point may exist with varying scan depth and chirp profiles, but the same general trends and principles are expected to apply. Waveform variations beyond adding a linear ramp were not explored for the sake of simplicity, but it is possible that a more complex waveform could yield further improvements . These waveforms would likely follow the dashed chirp profile from the right side of Fig. 6.7.

6.3.4 Sensing demonstrations

6.3.4.1 Dynamic pressure measurements

To demonstrate the utility of the high scan depth offered by the extended square waveform (F = 84%, DC = 50%, and LE = 10 ns), MHz-rate LAS measurements of gas pressure were performed in a dynamic combustion environment. The experiment was conducted on UCLA's Detonation-Impulse Tube (DIT) facility [149]. In these experiments, a mixture of stoichiometric ethylene (C_2H_4) and oxygen (O_2) at an initial pressure of 207 Torr was spark ignited at one end of a 196-cm long, 3.81-cm ID tube with a Shchelkin Spiral to aid in deflagration-to-detonation transition (DDT). DDT was confirmed via wave-speed measurements made by piezoelectric sensors located near the end of the tube (1.5–1.8 m from the sparkplug)[2]. The wave-speeds were seen to match (within measurement uncer-

[2]More details on the DIT are provided in Appendix B.

tainty) values predicted for an ideal 1-dimensional Chapman-Jouguet (CJ) detonation wave, as predicted using CalTech's Shock & Detonation Toolbox [141] in CANTERA [142] using the GRI-MECH 3.0 mechanism [144].

The laser discussed in the previous sections was tuned to target the P(0,31), P(2,20), and P(3,14) rovibrational transitions of $^{12}C^{16}O$ near 2008.5 cm^{-1} with the goal of measuring gas pressure by fitting the measured spectra as in a similar method as in Chapter 4. During these experiments, the laser light was pitched through the detonation tube via two wedged sapphire windows providing optical access. These windows are located 1.5 m from the sparkplug. Raw laser background and transmitted intensity scans are shown 0–4 µs after the passage of the detonation wave at the top of Fig. 6.11. A fit of the measured spectra for the first scan after detonation-wave passage is pictured below, which leads to a pressure measurement of 9.5 atm. The residuals between the fit and measurement are generally within ±3%. It should be noted that the raw data are not smoothed in any way prior to fitting. The ringing in the background intensity signal is also present in the transmitted signal, although the magnitude of the signal oscillations is lower due to the high levels of absorption by the combustion gas. The absorbance does not go to zero at the ends of the scan due to the high pressure of the gas which induces significant collisional broadening. Additionally, at high temperatures (>3000 K), there is some broadband interference from CO_2 in this spectral region, which causes additional absorption across the scan. This broadband interference is fitted as a constant in fitting procedure and rejected, with the remaining fitted CO Voigt lineshapes being used to solve for the pressure and temperature of the gas.

The time history of the measured gas pressure is shown at the bottom of Fig. 6.11 at a measurement rate of 1 MHz, without any averaging. The low scatter (measurement SNR∼100)[3] in the measured pressure is a result of the high optical SNR, spectral scan depth, and scan-to-scan stability of the CW laser and the selected injection-current waveforms. The measured peak pressure of 9.5 atm can be compared to the value predicted

[3]Measurement SNR is found by taking the ratio of a measured parameter (smoothed using a 5-point moving average) and the signal noise. The signal noise is found by subtracting the signal by the aforementioned moving average and taking the standard deviation of the resulting difference over the same 5 points.

by the CJ theory obtained using the aforementioned Shock and Detonation Toolbox. This value is indicated as a horizontal dashed line in Fig. 6.11; close agreement is observed with the measured peak pressure. The measurement also captures decay in pressure from the CJ values after the initial passage of the detonation wave, associated with the Taylor expansion wave [208]. Additionally, the measurement captures the effect of reflected pressure waves resulting from the impact of the detonation wave on the plastic burst diaphragm located at

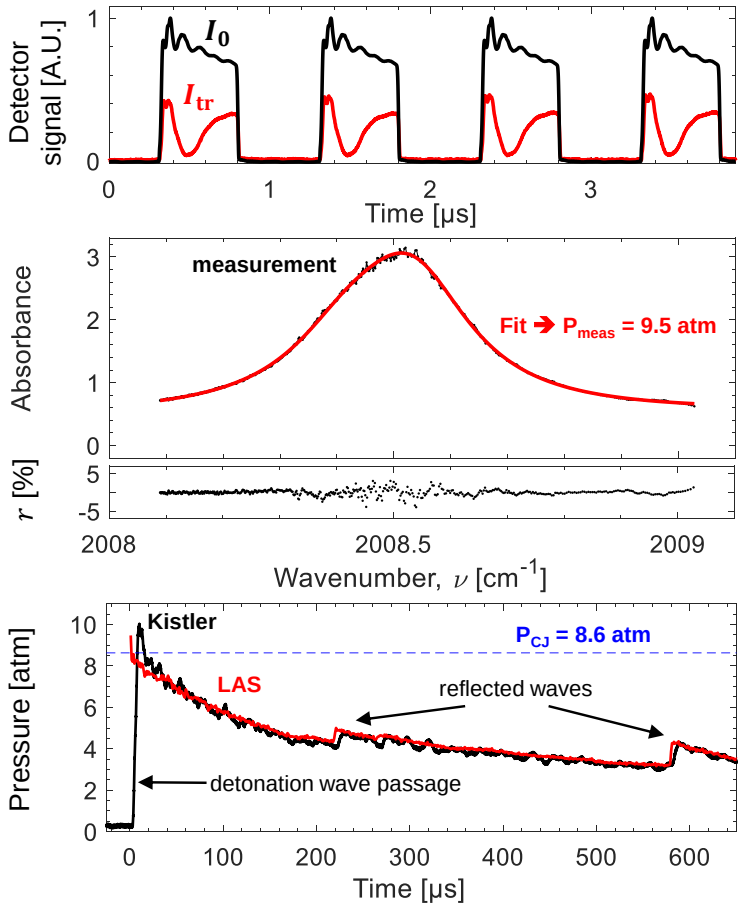

Figure 6.11: *Top*: Measured background (black) and transmitted signals (red) for in detonation tube for the first 4 μs after detonation wave passage. *Middle*: First post-detonation absorbance spectrum (black) along with spectral fit (red). Residuals on the order of $|r| < \pm 3\%$ pictured below (black dots). *Bottom*: Pressure trace obtained using LAS (red) and a Kistler pressure transducer (black) compared to the value computed using CJ detonation theory (dashed line).

the end of the tube. These reflected waves result in an increase in pressure at the measurement location. The optically-measured pressure dynamics and magnitudes agree very well with the piezoelectric pressure transducer (Kistler 603CAA) located at the same axial plane in the detonation tube. Notably, the large spectral scan depth facilitates measurements at elevated pressure (up to ∼10 atm) at MHz rates. The presssure sensing technique and detonation-tube experiments are further detailed in Chapter 7.

6.3.4.2 Multi-line thermometry

To demonstrate the ability of the extended spectral tuning method to resolve multiple discrete spectral transitions in a 1-µs scan period, a transient multi-line temperature measurement was conducted in the UCLA High-Enthalpy Shock Tube (HEST) facility [169, 165, 209]. In this experiment, 10% CO in argon was shock-heated by a helium driver gas bursting aluminium diaphragms. The driven section of the tube over which the shock forms is 4.9 m long. Optical access is provided by two wedged sapphire windows located 2 cm from the endwall of the driven section. The optical path length through the inner diameter of the tube is 10.32 cm.

Temperature is determined by fitting a simulated spectrum to the measured spectrum of three transitions of $^{12}C^{16}O$ — P(1,25), P(4,7), and R(8,24) — near 2011 cm^{-1} indicated in Figs. 6.10 and 6.12. These three lines have a large spread in lower state energies (∼14,000 cm^{-1}) and have appreciable absorption strength at temperatures above 5,000 K, enabling sensitive thermometry [166]. In the fitting procedure, temperature, CO number density, line broadening, and absolute line position are varied until the squared sum of the residuals between the measurement and simulation is minimized. The simultaneous fitting of these three lines (rather than two) provides more precise and accurate temperature measurements.

Although having a similar center wavelength and tuning range, the DFB-QCL used in this particular experiment is not the same as discussed in Sections 6.2–6.3.4.1. Notably, the achievable scan depth for this second laser is slightly higher, with scan depths up to 1.15 cm^{-1}

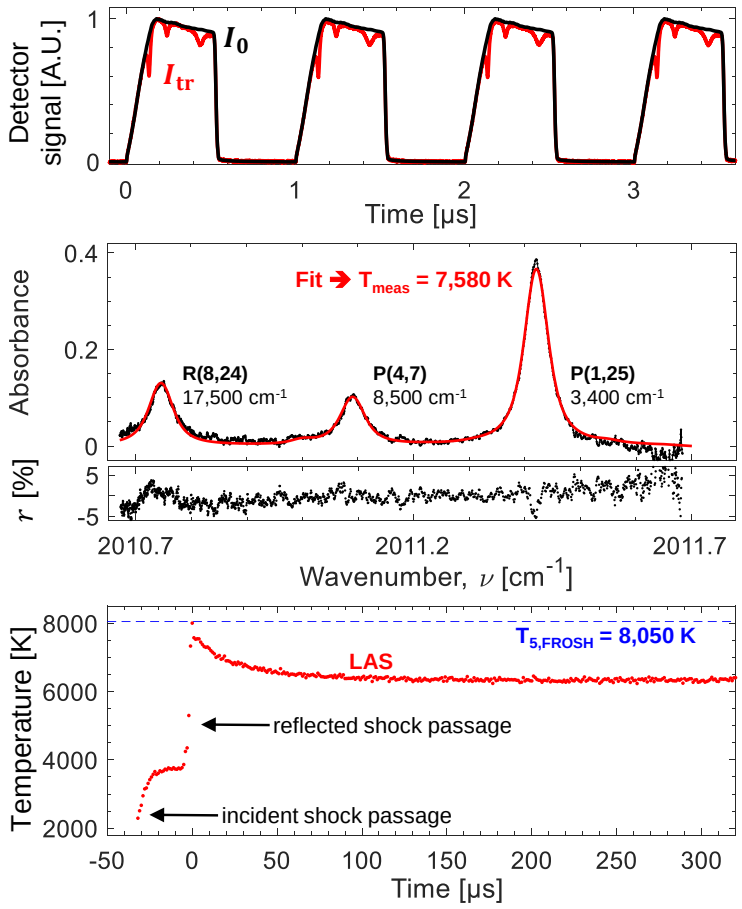

Figure 6.12: *Top*: Measured background (black) and transmitted signals (red) in shock tube for the first 4 μs after the reflected shock wave. *Middle*: 1-cm^{-1} measured absorbance spectrum (black) along with spectral fit (red) for the first post-reflected-shock measurement. Residuals on the order of $|r| < \pm 5\%$ plotted below (black dots). The names and corresponding lower state energies in cm^{-1} are written next to each major transition. *Bottom*: Temperature time history obtained using LAS (red) compared to post-reflected-shock temperature predicted using ideal-shock relations (dashed line).

attainable using the extended square waveform at 1 MHz. Due to the low expected pressures behind the incident shock wave (< 1 atm) and to mitigate ringing, a short leading-edge ramp of 200 ns was added to the waveform. For the present application, the maximum chirp rate was set to 3.5 cm^{-1}·μs^{-1}. Even with this leading-edge ramp added, the scan depth achieved was slightly greater than 1 cm^{-1} at 1 MHz.

Sample raw LAS measurements are shown at the top of Fig. 6.12 for 0–4 µs after the passage of the reflected shock wave at the measurement location. The absorbance spectrum for the first post-reflected-shock measurement is indicated in the middle of Fig. 6.12. Here the full 1-cm^{-1} scan depth enabling three-line detection is readily apparent. Residuals are on the order of ±5%. At the bottom of Fig. 6.12, the temperature versus time is plotted, with time 0 indicating the time of reflected-shock passage at the measurement location. Some vibrational relaxation is observed to occur immediately after the incident shock passage, on the order of 10s of microseconds, with the temperature eventually reaching an equilibrium value near 3760 K. The temperature is rapidly increased to a value near 8010 K across the reflected shock wave. This temperature is in close agreement with the value predicted by ideal shock-tube relations [210, 211] of 8050 K. After the reflected-shock passage, the temperature rapidly drops over 10s of microseconds, as CO dissociates. The post-reflected-shock temperature eventually reaches an equilibrium value of 6350 K. Using this temperature sensing strategy, a measurement SNR of ∼200 is achieved, again as a result of the high optical SNR, spectral resolution, and scan-to-scan stability of the CW laser and the selected injection-current waveforms. The measurement SNR for temperature is found in the same way as for the pressure measurements in Section 6.3.4.1, using the standard deviation in the difference between the measured temperature and a moving average to find the noise of the temperature signal.

The multi-line temperature sensing strategy is further developed in Chapter 8, where a more accurate fitting method leveraging the large spread in rovibrational energy levels among the transitions. The sensor is also used to investigate CO dissociation kinetics at high temperature.

6.4 Summary

Injection-current waveform variations were analyzed for extending and optimizing spectral tuning of CW-DFB lasers via MHz modulation in a bias-tee circuit. Laser chirp rates and signal-to-noise ratio were found to significantly increase by modulating the laser using square

waves instead of sine waves and by scanning the laser below the lasing threshold. These techniques ultimately yielded scan depths on the order of 1 cm^{-1} at 1 MHz, representing an increase of more than a factor of 2 relative to threshold-bound sinusoidal modulation. The effect of waveform duty cycle and leading-edge ramp were examined, with a longer leading-edge ramp mitigating output ringing and excessive chirp rate, while requiring a longer duty cycle to maximize useful scan depth. The attenuation of the high-frequency laser signals due to detector bandwidth was also examined, and limiting criteria are defined based on the characteristic frequency of target absorption features. Based on common detector limitations, an optimized trapezoid waveform was established for a 200-MHz bandwidth detection system for use in sub-atmospheric sensing where narrow spectral features are expected. This study revealed that the combination of the bias-tee circuit and injection-current waveform optimization yields more than an order of magnitude gain in temporal frequency (and effective measurement rate) for a target spectral tuning depth (1 cm^{-1}) relative to conventional laser modulation via bandwidth-limiting controllers. The various MHz waveform strategies were finally demonstrated for high-speed gas sensing in two impulse facilities. In a detonation tube, we measured transient gas pressure based on collisional linewidth up to $\sim$10 atm; in a shock tube, we performed dynamic temperature measurements based on three discrete transitions resolvable in a single microsecond modulation period. The pressure sensor and high-temperature sensing strategy are further developed in Chapters 7 and 8. The analysis presented here may serve as a broadly applicable guide to optimizing injection-current waveform for CW-DFB lasers modulated at MHz rates for absorption spectroscopy. In the next chapter, a first-order model is developed for high-speed distributed feedback laser wavelength tuning dynamics and provides physical explanations for some of the experimental trends noted in this chapter.

CHAPTER 7

Optical pressure sensing at MHz rates via collisional line broadening of carbon monoxide: uncertainty quantification in reacting flows

The contents of this chapter have been submitted to the journal ***Applied Physics B*** *[212] under the full title "Optical pressure sensing at MHz rates via collisional line broadening of carbon monoxide: uncertainty quantification in reacting flows".*

7.1 Introduction

Pressure measurements are critical to understanding the behavior of thermo-fluid systems. Pressure is indicative of the fluid-mechanical force on solid surfaces in both aerodynamic and propulsive contexts, which is important for understanding thrust/lift/drag generation and structural loading. In many systems, the pressure field is unsteady, with pressure fluctuations traveling at or above the speed of sound. These pressure oscillations may arise from shock/detonation waves, rapid gas compression, turbomachinery [213], or acoustic phenomena, which may be coupled to chemical reactions in the case of combustion instabilities. The timescales associated with these unsteady pressure fluctuations are often in the 100 Hz–100 kHz range. As such, there is a need for high-speed pressure measurements in reacting flows. Conventionally, pressure is measured (electro)mechanically by detecting the force applied by a fluid on a small surface. This force causes the transducer material to strain, which is often linked to a change in an electrical characteristic of the transducer (resistance, capacitance) which then leads to a change in voltage across the sensor. Piezoelectric (PE)

or piezoresistive (PR) transducers can perform measurements at up to 100s of kHz through the sensing of charge generation (PE) or mechanical stress (PR) and represent the current state-of-the-art in high-speed pressure measurements for harsh environments.

Despite their broad utility, PE and PR sensors have a few shortcomings in highly dynamic reacting flows. Because of charge migration from the crystal to its surroundings in PE sensors, the pressure measurement changes over long timescales, leading to signal drift [214]. This makes PE sensors unsuitable for measuring static pressure values. Both PE and PR sensors also are susceptible to spurious output signal generation from mechanical vibrations and high temperatures, which are ubiquitous in harsh environments. At combustion-relevant temperatures (>1000 K) the sensor materials begin to degrade, which can lead to total sensor failure after prolonged exposure, on the order of seconds [68, 69]. To combat this, in environments with sustained high heat flux, such as detonation combustors, pressure transducers are often stood off or recessed from the flowfield. This leads to attenuation and distortion of pressure profiles, which can cause errors in peak pressure readings up to 50% [70, 71]. As a result, most approaches to measuring pressure in detonation engines opt to either measure frequency content to infer detonation wave-speed or attenuate high-frequency content altogether to measure time-averaged pressure, also known as capillary-tube attenuated pressure (CTAP) [70].

In addition to the aforementioned practical issues, conventional pressure transducers are constrained to measurements at the boundary of a flowfield. It is often desirable to assess pressure away from solid surfaces, such as for supersonic flows. Boundary-layer effects such as shock bifurcation in dynamic flow fields can induce an offset between pressure in the bulk flow and pressure in the boundary layer [215, 216]. This effect is especially problematic in shock tubes [216], where boundary layer effects can convolute side-wall pressure measurements made with conventional pressure transducers, increasing the uncertainty in the thermodynamic conditions produced by reflected shocks, particularly for polyatomic driven gases (e.g. CO_2, fuels) [215]. This presents difficulties for shock tube experiments involving chemical kinetics, as reaction rates are sensitive to combustion pressure. As such, it is

desirable to have a measurement of the pressure in the bulk gas.

Laser-based optical methods can overcome many of the presented challenges, achieving high-speed, non-intrusive, in-situ measurements for which the sensor hardware is not directly exposed to the harsh test gas [159]. Pressure measurements can be made by assessing the collisional line broadening of gaseous spectra, which scales linearly with pressure. Kranendonk et al. [217] measured pressure based on this principle using broadband measurements of the $v_1 + v_3$ band of H_2O. Caswell et al. [92] applied this concept to time-resolved measurements of gas pressures in a pulse-detonation combustor, whereas Goldenstein et al. [218] also applied this method to measure pressure in a propane-air flame. Mathews et al. [219] used collisional broadening obtained with wavelength-modulated planar laser-induced fluorescence of CO_2 to make spatially-resolved pressure measurements in a room-temperature CO_2–Ar jet. A caveat to collisional-broadening based pressure measurements is that the scaling factor between pressure and line broadening (known as the collisional-broadening coefficient γ) is both temperature and composition dependent. In the above works, either simple gas mixtures were studied or simplifying assumptions about the gas composition were made. In Chapter 4, a sensor was developed to measure gas pressure at the exhaust of CH_4/O_2 rotating-detonation rocket engine using laser absorption spectroscopy of CO. In that chapter and the associated Appendix D, pressure uncertainty was estimated specifically for the RDRE application.

In this chapter, the MHz-rate optical pressure-sensing strategy based upon collisional line broadening of CO is presented as a broadly applicable method for interrogating a wide range of dynamic combustion environments, with analysis of a comprehensive range of uncertainty factors. First, in Section 7.2, the high-speed pressure-measurement methodology based on infrared laser absoprtion spectroscopy is detailed. Then, in Section 7.3, an updated uncertainty-analysis methodology from that of Chapter 4/Appendix D is introduced to account for the influence of various sources of the uncertainty in the pressure measurement. Uncertainty sources include measurement signal noise, spectroscopic uncertainties, and uncertainty in gas composition. These uncertainties are quantified over a range of conditions,

reflecting different fuels, equivalence ratios, reaction progress, and combustion modes (deflagration and detonation), which influence gas composition and temperature. Correlations between uncertainty sources are also assessed. This uniquely comprehensive uncertainty analysis indicates broad utility of the method and enables uncertainty estimation in a variety of applications. Finally, in Section 7.4, the utility and precision/accuracy of the sensor is demonstrated and compared to conventional techniques in laboratory environments in (1) a high-enthalpy shock tube and (2) a detonation-impulse facility, at temperatures from 1500–3000 K and pressures from 0.5–10 bar. Appendix E provides an extended uncertainty analysis, and Appendix G provides details on the combustion kinetics analysis employed in this work.

7.2 Methodology

Pressure is inferred in this method from spectrally-resolved lineshapes obtained using laser absorption spectroscopy (LAS) [166], as in Chapter 4. The details of LAS that are relevant to this sensor will be repeated here for clarity, and to introduce to slightly different symbols used throughout this chapter and the associated Appendix E. The absorbance α is determined from the attenuation of laser light intensity through an absorbing medium, as pictured in the top left of Fig. 7.1. A distributed feeback (DFB) quantum cascade laser (QCL) is used as a narrowband mid-infrared light source. The transmitted laser intensity is recorded on a photovoltaic (PV) detector. If I_0 is the light intensity before attenuation and I_{tr} is the light intensity after attenuation, absorbance is defined as:

$$\alpha = -\ln\left(\frac{I_{\mathrm{tr}}}{I_0}\right). \tag{7.1}$$

An absorbance spectrum may be probed during a single measurement by modulating/tuning the laser output wavelength. For DFB lasers, this wavelength tuning is accomplished by changing the temperature of the laser, which changes the resonance of the laser cavity. High-speed tuning is typically achieved using current modulation, which has been traditionally limited in bandwidth to 100s of kHz by the laser controller. A bias-tee tuning configuration

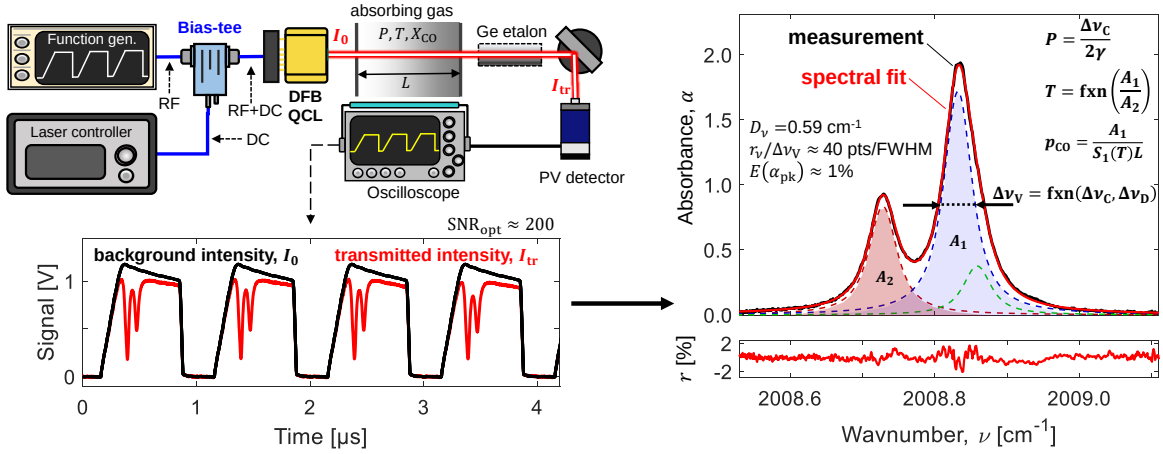

Figure 7.1: *Left*: Bias-tee laser control schematic used to inject trapezoidal MHz waveform into DFB QCL. Laser light is attenuated by absorbing gas, which is measured by a PV detector and oscilloscope. A germanium etalon may be inserted into the beam path to assess the chirp profile of the laser over a modulation period. Sample raw MHz laser absorption data is shown below. *Right*: Measured sub-microsecond absorbance spectrum of target CO line cluster along with spectral fit. The spectral parameters (areas, linewidth) used to obtain pressure, temperature, and CO partial pressure are indicated on the spectrum. The peak-normalized residual r between the measurement and fit is plotted below.

(pictured in Fig. 7.1) can be used to directly inject a current-modulation waveform into the laser, bypassing the controller, enabling wavelength tuning at MHz rates as introduced in Chapter 4. This has enabled MHz measurements of line clusters with a total output wavenumber amplitude (scan depth) up to 1 cm^{-1} using the methods of Chapter 6. Assuming a uniform gas medium across the line-of-sight[1], the absorbance α_i from single spectral transition i is described by the Beer-Lambert law:

$$\alpha_i(\nu) = S_i(T) p_j L \phi_i(\nu, P, T, X_1, ..., X_N), \tag{7.2}$$

where ν is the wavenumber [cm^{-1}] of the incident light, $S_i(T)$ [cm^{-2}/atm] is the absorption linestrength of transition i at temperature T, p_j [atm] is the partial pressure of gas species

[1]The case of non-uniform gas medium is discussed in Appendix E.0.5.

Y which is absorbing light, X_1–X_N are the set of mole fractions of all N species in the gas, and L [cm] is the optical path length.

The lineshape function ϕ is modeled as a Voigt profile [170], which is a convolution of a Lorenztian and a Gaussian profile, resulting from two dominant broadening mechanisms. The Gaussian lineshape is due to the Doppler broadening of the line, whose FWHM termed "Doppler width", $\Delta\nu_{\mathrm{D}}$ [cm^{-1}], is given by:

$$\Delta\nu_{\mathrm{D}} = \nu_0\sqrt{\frac{8k_{\mathrm{B}}T\ln 2}{mc^2}}. \tag{7.3}$$

ν_0 [cm^{-1}] is the center wavenumber of the transition, k_{B} [$\mathrm{erg{\cdot}K}^{-1}$] is the Boltzmann constant, m [g] is the mass of the gas species, and c [$\mathrm{cm{\cdot}s}^{-1}$] is the speed of light. The Lorentzian lineshape results from collisional broadening (also termed pressure broadening). The Lorentzian FWHM arising from collisional broadening (termed the "collision width"), $\Delta\nu_{\mathrm{C}}$ [cm^{-1}], is related to the total collision rate $Z_{j-\mathrm{mix}}$ [s^{-1}] of absorbing species j with the "mix" of gas species in the mixture:

$$\Delta\nu_{\mathrm{C}} = \frac{Z_{j-\mathrm{mix}}}{\pi c}. \tag{7.4}$$

For an ideal gas, the total collision rate of Eqn. 7.5, is proportional to the gas pressure P and inversely related to the temperature T.

$$Z^{\mathrm{id}}_{j-\mathrm{mix}} = P\ [\mathrm{Ba}]\cdot\sum_Y X_Y\pi\sigma^2_{j-Y}\left(\frac{8}{\pi\mu_{j-Y}k_{\mathrm{B}}T}\right)^{1/2}. \tag{7.5}$$

Here, the subscript Y refers to each species present in the gas mixture that can act as a "collision partner" to the absorbing species. σ_{j-Y} [cm] is the "optical collision diameter" of the absorbing species and a collision partner Y, given by:

$$\sigma_{j-Y} = \frac{1}{2}(\sigma_j + \sigma_Y). \tag{7.6}$$

σ_j and σ_Y refer to the individual effective diameters of the molecules. μ_{j-Y} [g] is the "reduced mass" of j and Y and is given by:

$$\mu_{j-Y} = \frac{m_j m_Y}{m_j + m_Y}. \tag{7.7}$$

The temperature and gas mixture dependence of the collisional broadening can be lumped into a single coefficient, termed the "collisional broadening coefficient" γ [$\mathrm{cm^{-1}}\cdot\mathrm{atm^{-1}}$], such that Eqns. 7.4 and 7.5 can be combined as:

$$\Delta\nu_{\mathrm{C}} = 2\gamma P, \tag{7.8}$$

with P in units of atm. γ is the half-width at half maximum (HWHM) per unit pressure for a collisionally broadened lineshape. It is this simple linear dependence of the collision width on pressure in Eqn. 7.8 that is exploited to infer pressure from absorption lineshapes. The pressure dependence of the target CO absorption spectrum for this work, due to the increase in $\Delta\nu_{\mathrm{C}}$, can be seen in Fig. 7.2.

γ can be expressed as the weighted sum over each collision partner with broadening coefficient γ_{j-Y}:

$$\gamma = \sum_{Y} X_Y \gamma_{j-Y}. \tag{7.9}$$

Ideally, each γ_{j-Y} takes the approximate form:

$$\gamma_{j-Y} \approx (9.87\cdot 10^{-7})\frac{\sigma_{j-Y}^2}{c}\left(\frac{2}{\pi\mu_{j-Y}k_{\mathrm{B}}T}\right)^{1/2}. \tag{7.10}$$

In reality, this temperature scaling of γ_{j-Y} is not exact, with the exponent on T deviating from 1/2. To capture this non-ideal effect, γ_{j-Y} is often modeled with a power law:

$$\gamma_{j-Y}(T) = \gamma_{j-Y,0}\left(\frac{T_0}{T}\right)^{N_{j-Y}}. \tag{7.11}$$

Here, $\gamma_{j-Y,0}$ is a reference value of the collisional broadening coefficient at reference temperature T_0, and N_{j-Y} is the "temperature exponent" of the power law. These parameters not only depend on collision partner, but also vary across different spectral transitions for a given molecule. Typically both γ_0 and N decrease with rotational quantum number and are a weak function of vibrational quantum number [220]. These parameters have been characterized and catalogued for many absorbing species and collision partners in the literature [205]. From Eqns. 7.9 and 7.11, knowledge of the collisional broadening parameters (γ_0 and N) as well as gas composition and temperature T can enable knowledge of the collisional

broadening coefficient γ for a given gas mixture and condition. This knowledge can be used along with measurement of collision line width to measure pressure using Eqn. 7.21.

As a convolution of two simple lineshapes, the Voigt lineshape may be expressed as a function of $\Delta\nu_{\mathrm{D}}$ and $\Delta\nu_{\mathrm{C}}$. In order to isolate changes in linewidth to collisional processes, it is advantageous to fix the value of $\Delta\nu_{\mathrm{D}}$ in spectral fitting routines. As such, knowledge of the gas temperature is required to calculate $\Delta\nu_{\mathrm{D}}$ (and γ).

Temperature can be obtained using two-line thermometry [166]. In this technique, the spectrally-integrated area under an absorption feature, A_i, is utilized. This "absorbance area" is related to the gas properties by spectrally integrating the Beer-Lambert law using $\int_{-\infty}^{+\infty}\phi_i(\nu)d\nu = 1$.

$$A_i = \int_{-\infty}^{+\infty}\alpha_i(\nu)d\nu = S_i(T)p_jL. \tag{7.12}$$

If the ratio R_{12} of the absorbance areas of two transitions 1 and 2 (as in Fig. 7.1) are taken, the resulting ratio is purely a function of temperature:

$$R_{12} = \frac{A_2}{A_1} = \frac{S_2(T)}{S_1(T)} = \frac{S_2^0}{S_1^0}F_{12}(T). \tag{7.13}$$

Here, S_i^0 refers to the room-temperature linestrength of transition i and $F_{12}(T)$ is a temperature-dependent function that depends exponentially on the difference in lower state energies of the two transitions, $\Delta E''_{12} = E''_1 - E''_2$. Knowledge of the ratio of two absorbance areas of transitions with a large difference in lower-state energy enables sensitive temperature measurements, providing knowledge of the Doppler width and collisional-broadening coefficient.

Temperature is also used to evaluate the linestrengths of the spectrally-resolved transitions, which enables a quantitative determination of species. Specifically, the linestrength is used with the integrated Beer-Lambert law of Eqn. 7.12 to find the partial pressure of the absorbing gas:

$$p_j = \frac{A_2}{S_2(T)L} = \frac{A_1}{S_1(T)L}. \tag{7.14}$$

Using the total pressure P determined from collision linewidth, the mole fraction of the absorbing gas X_j can also be determined:

$$X_j = \frac{p_j}{P}. \tag{7.15}$$

For this work, rovibrational transitions of CO in the mid-infrared are used to simultaneously probe gas pressure, temperature, and CO concentration. Carbon monoxide was selected for several reasons: (i) CO is ubiquitous in hydrocarbon combustion systems as stable intermediate that is a precursor to carbon dioxide CO_2 for fuel-lean systems, or a major product for fuel-rich hydrocarbon combustion systems, (ii) CO can remain in the product gas due to incomplete carbon oxidation or due to the dissociation of CO_2, (iii) CO can be present in reactant gases due to exhaust gas recirculation, and (iv) and CO can be employed as a fuel for some applications [221]. Therefore, the significant concentrations of CO in many modes of combustion make it an attractive target for gas property measurement in combustion systems.

In addition to these combustion-related arguments, CO is one of the strongest absorbers in the infrared, enabling highly sensitive measurements. Due to its simple diatomic structure and singlet electronic ground state, the CO lines are typically well separated which permits accurate fitting and high confidence to spectral parameters. Recent advances in mid-infrared photonics [222] have enabled access to the CO fundamental band, which has orders of mag-

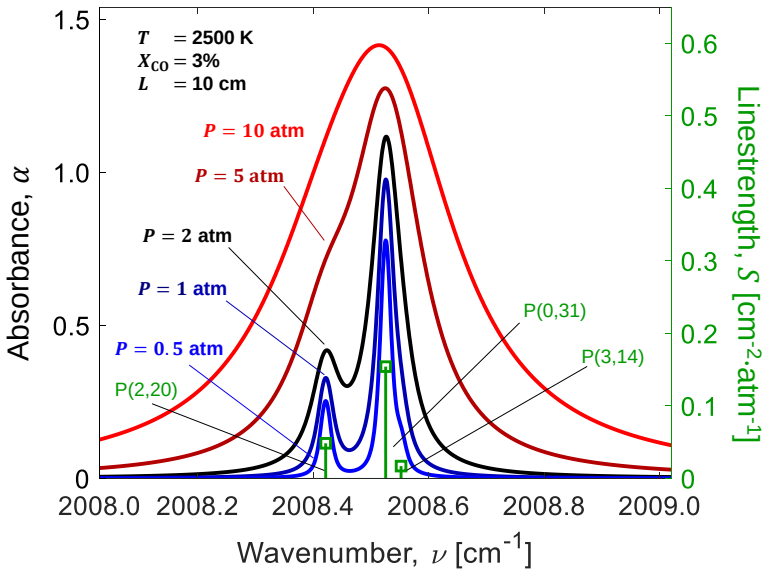

Figure 7.2: Simulation of target CO line cluster at fixed temperature, CO mole fraction, and pathlength, with pressure varied. Linestrengths at 2500 K are shown in green.

nitude stronger absorption strength compared to the overtone bands in the near-infrared. In this work, two transitions near 5 µm ($\nu_0 \sim 2008.5$ cm^{-1}) in the fundamental rovibrational band of CO are targeted: P(2,20) and P(0,31). This line selection has been used in previous works [151, 165, 157] and in Chapter 4, due to its high absorption strength, relative spectral isolation from other significant combustion species, the close spacing of the two transitions to enable two-line thermometry with a single narrowband laser, and the large difference in lower-state energy $\Delta E''$ of these transitions. A measurement of the absorbance spectrum of this line cluster is shown on the right side of Fig. 7.1, and is simulated at various pressures in Fig. 7.2, highlighting the sensitivity of the spectrum to pressure. The next section of this chapter details the precision and accuracy of pressure measurement with these specific spectral transitions of CO. Nevertheless, the methods of this work can be applied to any significantly collisionally-broadened line selection for any number of gas species of interest.

7.3 Uncertainty analysis

In this section, we rigorously analyze the uncertainties in the optical pressure measurement arising from several sources. First, Section 3.7.3.1 details the framework used to integrate the influences of various error sources into the overall uncertainty in a measured variable (i.e. pressure). The overall uncertainty in pressure is related to the uncertainty in the measured collision width, $\Delta\nu_C$, and the inferred collisional broadening coefficient, γ. As such, Section 3.7.3.2 details the uncertainties influencing $\Delta\nu_C$ and Section 3.7.3.3 examines the uncertainties influencing γ. Section 3.7.3.4 combines the potential errors from these two parameters to derive the total uncertainty in pressure. Some extra details of the uncertainty analysis are included in Appendix E.

7.3.1 Uncertainty-analysis framework

We use the Taylor Series Method (TSM) [223] to propagate uncertainties between related quantities, as in Chapter 4/Appendix D, with some modifications to account for the direc-

tionality and correlation of uncertainties. Uncertainty represents an aggregation of potential errors or deviations between a measurement result and its true value. Because errors are often not known *a priori* and cannot always be obtained for certain types of measurements, uncertainty is used to reflect the confidence with which a stated measurement result represents the true value of a measured quantity given such unknowns. For a given variable g, the uncertainty in g is written as $\delta g^{\{\theta\}}$. $\delta g^{\{\theta\}}$ is always a positive number, where the superscript $\{\theta\}$ refers to the directionality of the potential error. If $\theta = +1$ (or "+" for short), the potential error is considered positive and if $\theta = -1$ (or "-" for short), the error is considered negative, such that $g^{\text{meas}} - \delta g^{-} \leq g^{\text{true}} \leq g^{\text{meas}} + \delta g^{+}$. If g depends on N independent variables x_1–x_N, the uncertainty in g is assumed to take the following form:

$$\delta g^{\{\theta\}} = \sum_{k=1}^{N} \left| \frac{\partial g}{\partial x_k} \right| \delta {x_k}^{\{d_k\}} = \sum_{k=1}^{N} (\delta g)_{x_k}^{\{\theta\}}. \tag{7.16}$$

${\delta x_k}^{\{d_k\}}$ is the uncertainty in the k^{th} input variable x_k and $(\delta g)_{x_k}^{\{\theta\}}$ is the contribution to the uncertainty in g from the uncertainty in x_k, which is the potential error in g from x_k. It is assumed that each uncertainty in x_k is small, albeit potentially different in magnitude depending on direction, and that g is locally linear from $x_k - {\delta x_k}^{-}$ to $x_k + {\delta x_k}^{+}$. It should be noted that this summation of potential errors is performed linearly rather than in quadrature in order to more easily account for directionality. A correction factor of $\sqrt{2}$ is later introduced to make overall uncertainty estimates consistent with the more common sum of squared error (SSE) approach. The directionality of the potential error contribution of x_k, $\{d_k\}$, depends on the sign of $\partial g / \partial x_k$:

$$d_k = \theta \cdot \text{sgn} \left(\frac{\partial g}{\partial x_k} \right). \tag{7.17}$$

If $\partial g / \partial x_k$ is positive, then the positive potential error in x_k contributes to the positive uncertainty in g. If $\partial g / \partial x_k$ is negative, then the negative potential error contribution of x_k contributes to the positive uncertainty in g. This is especially important for errors that are potentially higher in one direction. In this chapter, if the directionality superscript is dropped from an equation, it is implicit that positive potential error contributions sum to the positive uncertainty in g and negative potential error contributions sum to the negative

uncertainty in g.

Often, the relative uncertainty ($\delta g/g$) of a parameter is of greater importance than the absolute uncertainty (δg). The individual contributions to $\delta g/g$ (potential errors) from each x_k are notated as $E(g, x_k)$, where:

$$E(g, x_k) = \left(\frac{\delta g}{g}\right)_{x_k} = \frac{(\delta g)_{x_k}}{g}. \tag{7.18}$$

The *total relative uncertainty* in g is notated as $E(g)$. $E^+(g)$ and $E^-(g)$ refer to the positive and negative relative uncertainties in g. Sometimes, x_k will not refer to a numerical variable, but a general uncertainty source, such as noise in the measured absorbance spectra ($x_k = \alpha$), uncertainty in fundamental spectroscopic parameters ($x_k = \text{spec.}$), or compositional uncertainty ($x_k = \text{mix}$).

The sensitivity of g to one of its inputs x_k, $s(g, x_k)$, is of importance to quantifying aggregate uncertainty and is defined as:

$$s(g, x_k) = \frac{x_k}{g}\frac{\partial g}{\partial x_k}. \tag{7.19}$$

For small changes in x_k, such that g is linear with x_k, $s(g, x_k)$ is the percent change in g per percent change of input x_k. A sensitivity s can represent an approximate local relationship between g and x_k of the form $g = {x_k}^s$. Using s, Eqn. 7.16 may be rewritten in terms of relative uncertainty as Eqn. 7.20 for uncorrelated potential errors:

$$E^{\{\theta\}}(g) = \sum_{k=1}^{N} |s(g, x_k)|\, E^{\{d_k\}}(x_k) = \sum_{k=1}^{N} E^{\{\theta\}}(g, x_k). \tag{7.20}$$

In the remainder of this chapter, we also included correlation terms in Eqns. 7.16 and 7.20, as per Eqns. E.1 and E.2 in Appendix E.0.1.

Pressure is the primary measured variable in this chapter, inferred from the re-arranged form of Eqn. 7.8:

$$P = \frac{\Delta\nu_{\mathrm{C}}}{2\gamma}. \tag{7.21}$$

The uncertainty in pressure is linked to the uncertainties in the collision width, $\Delta\nu_{\mathrm{C}}$, and the collisional-broadening coefficient, γ. The collision width is measured directly from a

fitted Voigt lineshape to experimental data. As such, the uncertainty in collision width is the potential error due to signal noise in the measurements, $E(\Delta\nu_C, \alpha)$. The uncertainty in the collisional broadening coefficient is dominated by the potential errors in the species-specific spectroscopic broadening parameters and the composition of the gas being examined, which largely affect the accuracy of the measurement (rather than precision). Additionally, the collisional-broadening coefficient is temperature-dependent, so there is additional uncertainty associated with the temperature measurement. The temperature measurement has potential error contributions from the signal noise and bias from the measurements, $E(T, \alpha)$ and $E(T, \text{bias})$, and therefore is not independent from the collision-width potential error contributions. In the following subsections, we investigate the various sources of potential error in the pressure measurement technique and ultimately discuss the relative impact of each uncertainty source on the overall pressure measurement uncertainty.

7.3.2 Collision-width uncertainty

To provide a general description of the factors influencing the measurement of collision-width from a measured absorption spectrum, a single Voigt lineshape with measurement noise was simulated and fitted across many pressure/temperature and noise conditions. Several details of this single-line analysis are given in Appendix E.0.2. Only the most important takeaways are described here.

The potential error in collision-width is related to the noise in the absorption measurement, which either presents as high-frequency random "white noise" in the absorbance signal or as low-frequency noise which manifests as a distortion of the non-absorbing baseline of the spectrum. The effect of white noise on precision error is evaluated numerically by fitting Voigt profiles with added white noise. The spread in the fitted collision width is taken as the precision error. It is determined that the precision error in the collision-width measurement, notated $E(\Delta\nu_C, \alpha)$, scales linearly with the relative noise in the absorbance measurement $E(\alpha_{pk}) = (\delta\alpha/\alpha)_{pk}$. Additionally, the precision error is minimized when collision width is approximately equal to the full Voigt FWHM (termed the Voigtian width $\Delta\nu_V$), as is

the case at moderate pressures (here the Voigt lineshape can be closely approximated by a Lorentzian). Spectral sampling parameters, such as scan depth D_ν [cm^{-1}], and spectral wavenumber resolution, r_ν [cm^{-1}], also affect precision error. Figure 7.3 plots the collision width precision error (normalized by absorbance white noise amplitude $E(\alpha)$) versus the ratio of scan depth to linewidth. When examining the black and blue curves, it can been seen that increasing the scan depth reduces precision error up to approximately five times the transition linewidth, i.e. $D_\nu = 5\Delta\nu_\mathrm{V}$. Additionally, in comparing the black and blue curves, it can be seen that the precision error scales with the number of data points per linewidth, i.e. $E(\Delta\nu_\mathrm{C}, \alpha) \propto 1/\sqrt{n}$, where $n = r_\nu/\Delta\nu_\mathrm{V}$ is the number of data points per FWHM. A convenient summary of the aforementioned trends is encapsulated in the

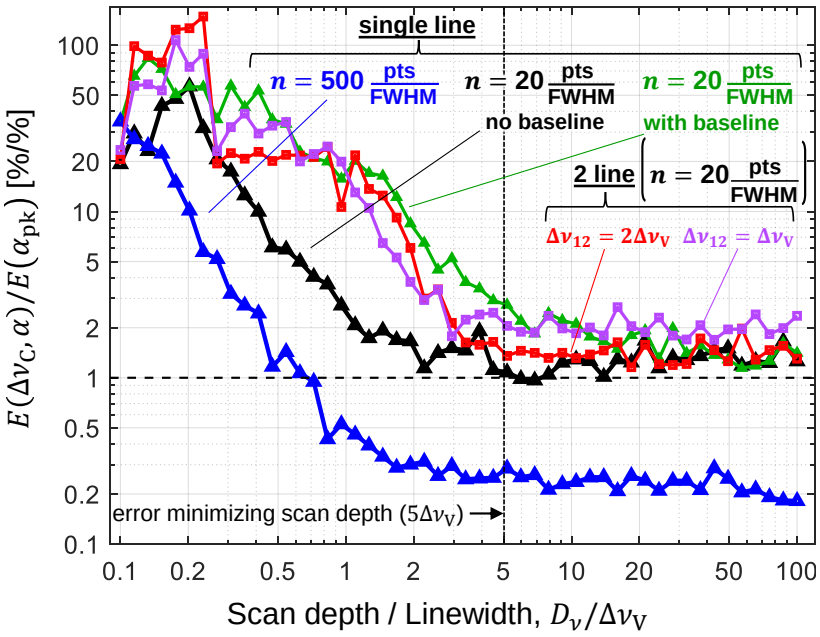

Figure 7.3: Collision linewidth precision error, normalized by absorbance noise, *versus* the ratio of scan depth to linewidth for fitted Lorentzian lineshapes. The blue, black, and green curves represent fits of a single line with varied spectral resolution and baseline uncertainty (fitted with a 2nd-order polynomial). The red and purple curves represent fits of blended lineshapes at various line spacings.

following approximation:

$$E(\Delta\nu_C, \alpha) \approx \sqrt{\frac{20}{n}} \frac{\Delta\nu_V}{\Delta\nu_C} E(\alpha_{pk}). \tag{7.22}$$

When time-averaging over $\eta = f_{scan}/f_{req}$ measurement samples, precision error is reduced by a factor $\sqrt{\eta}$.

The variation of precision error with changing baseline distortion was also examined. The baseline distortion was modeled as a low-frequency sine wave with random amplitude, frequency, and phase. This distortion increases precision error, as observed by comparing the green and black curves of Fig. 7.3. A convenient rule of thumb is established: in order to fit the noise with a 1st- or 2nd-order polynomial with minimal precision error, the scanning frequency should be at least ten times or twice the temporal frequency of baseline noise, respectively (see Appendix E.0.2.4).

Lastly, two overlapping transitions are simulated at variable line spacing $\Delta\nu_{12}$ to investigate the effect of line blending on precision. Blended lines increase the aforementioned scan depth threshold to $D_\nu = 5\Delta\nu_V + \Delta\nu_{12}$. Even when the lines are well resolved, there is significant increase in precision error (factor $\approx 1 + 2\Delta\nu_V/\Delta\nu_{12}$) when the line spacing is below the linewidth due to the difficulty in separating the contributions of each transition to the spectrum. The red and purple curves of Fig. 7.3 show the precision versus scan depth for select values of line spacing. While the above analyses of generic Voigt/Lorentzian lineshapes provide valuable insights, a more accurate evaluation accounting for the specific absorption characteristics (temperature dependence, line blending, broadening parameters, etc.) of the multi-line CO spectrum near 2008.5 cm^{-1}, used for the particular sensing strategy of this chapter, was conducted.

For the multi-line analysis, the two primary CO features discussed previously, P(2,20) (line 1) and P(0,31) (line 2), are simulated along with the smaller P(3,14) (line 3) line which contributes significantly to the spectrum at temperatures above 2000 K. Line 3 is not used for thermometry and blends significantly with P(0,31), which adds complications to the spectral fitting procedure. The error analysis was performed over a range of representative conditions: $T = 1000$ – 4000 K, $P = 0.1$ – 10 atm, with $r_\nu = 0.002$ cm^{-1}, $D_\nu = 0.7$ cm^{-1}, $X_{CO} = 3\%$, and

$L = 10.32$ cm. The lines are simulated using the HITEMP database [205] and the CO–N_2 collisional-broadening model discussed below in subsection 7.3.3.1. Low-frequency sinusoidal baseline (BL) noise is added to the simulated spectra ($\overline{f}_{\mathrm{BL}} > 0.25$ cycles/cm^{-1}, $\Delta\alpha_{\mathrm{BL}} < 0.5$). White noise is added to each simulation using Eqn. E.3, using the absorbance value at each point in the spectrum to generate a spectrally-varying noise profile. The resulting absorbance noise is $< 2\%$, with variation across gas conditions (discussed further in Appendix E.0.2). This absorbance noise scales inversely with $X_{\mathrm{CO}}L$. 50 randomly generated baseline and white noise combinations are added to the spectral simulations, resulting in 50 fitted results.

The noisy profiles are fitted using a non-linear least squares fitting routine to the sum of 3 Voigt profiles along with a quadratic polynomial (to fit the baseline noise). This fitting routine is based of that of Chapter 4, with some modifications. In this fitting routine, the relative line positions between the three transitions ($\nu_{0,1} - \nu_{0,2}$ and $\nu_{0,3} - \nu_{0,2}$) are fixed, with the absolute line position $\nu_{0,2}$ floated. The absorbance areas of the two major lines, A_1 and A_2, are floated, and temperature is obtained using Eqn. 7.13 from the ratio $R_{12} = A_1/A_2$. The absorbance area of the P(3,14) line, A_3 is fixed at the value corresponding to the

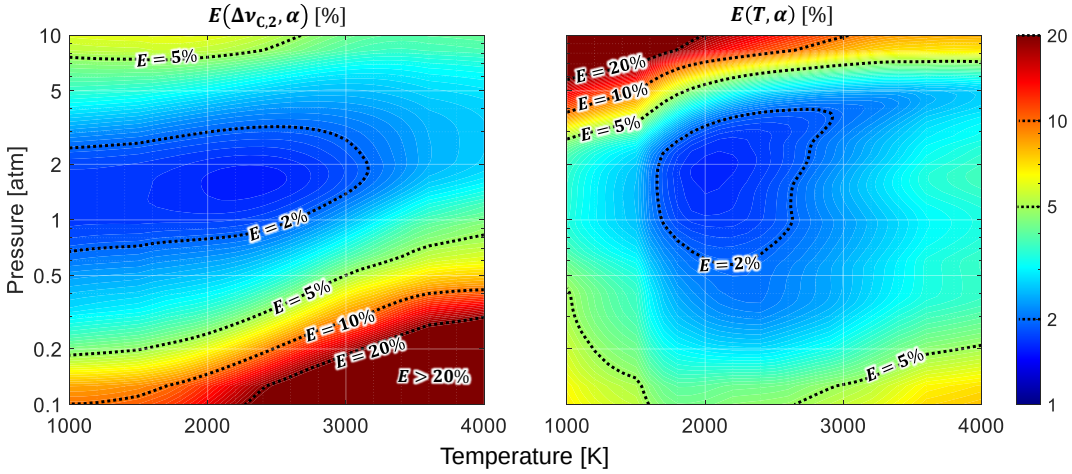

Figure 7.4: Precision error in the collision-width of the P(0,31) line (*left*) and in temperature (*right*) versus pressure and temperature for the multi-line fitting procedure. $X_{\mathrm{CO}}L = 0.3$ cm, $\mathrm{SNR}_{\mathrm{opt}} = 250$, $D_\nu = 0.7$ cm^{-1}, $r_\nu = 0.002$ cm^{-1}, $\overline{f}_{\mathrm{BL}}^{\mathrm{max}} = 0.25$ cycles/cm^{-1}, and $\Delta\alpha_{\mathrm{BL}}^{\mathrm{max}} = 0.5$. Black dashed lines represent level curves of fixed error values.

temperature derived from the ratio of the other two line areas. The Doppler widths for the three lines are also fixed at the value derived from this temperature. The collision width of the dominant P(0,31) line, $\Delta\nu_{C,2}$, is floated, with the collision-widths of the other two lines fixed at the temperature-dependent ratio predicted by the CO–N_2 broadening model developed in subsection 7.3.3.1. The initial guesses for the floated Voigt parameters ($\nu_{0,2}$, A_1, A_2, $\Delta\nu_{C,2}$) are randomized by ±2% of their known values (or of r_ν for the line position) and the guesses for the baseline polynomial coefficients are set to 0. Each of the 50 noisy profiles for each condition are fitted and the range in the resulting fitted collision width and temperature are assessed. These range values are normalized by the known value of the parameters to obtain $E(\Delta\nu_{C,2}, \alpha)$ and $E(T, \alpha)$ for each pressure and temperature condition. These measurement errors are plotted in Fig. 7.4 to show the dependence on temperature and pressure.

For many combustion-relevant conditions, the precision error in $\Delta\nu_C$ and T is 1–5% ($SNR_{meas} > 20$–100). As shown in Fig. 7.4, precision error is minimized between 1 and 2 atm for temperatures between 2000 and 2500 K, with a minimum error of around 1.5%. At higher temperatures and lower pressures, the reduced spectral resolution and weaker absorption reduces precision. The reduced collision width relative to overall linewidth further increases $E(\Delta\nu_C, \alpha)$ at low P / high T conditions, whereas reduced sensitivity of the absorbance area ratio R_{12} with temperature and the increased convoluting effect of the P(3,14) line increase $E(T, \alpha)$ for $T > 2500$ K. At $T \leq 1000$ K, the strength of the P(2,20) line decreases, decreasing the precision on its area measurement thus increasing the temperature precision error. At $P \geq 5$ atm, the increased effect of baseline distortion and the blending of the two primary transitions begins to preclude accurate separation of the absorbance features from each other and from low-frequency noise, increasing precision error. The baseline/blending affects temperature much more significantly due to the increased propensity for absorbance area to become convoluted by these factors than linewidth, as discussed in Appendix E.0.2.4 and E.0.2.5. In addition to the collision width and temperature, the partial pressure of CO may be obtained from the fitting results using Eqn. 7.14. The precision error on p_{CO} is

discussed in Appendix E.0.4 and is in the 1–5% range ($\mathrm{SNR}_{\mathrm{meas}}(p_{\mathrm{CO}}) \sim$ 20–100) between 1 and 10 atm. It should be noted that above 10 atm, the three-line model is insufficient to characterize real CO spectra, as the wings of neighboring CO transitions begin to overlap with the three lines simulated here.

In addition to the precision error, the potential bias errors associated with assumptions in the fitting procedure were also examined: (1) the linestrength of the perturbing P(3,14) line, whose value from HITEMP 2019 has an uncertainty between 5 and 10%, (2) uncertainty in the collisional-broadening assumptions, namely the relative value of γ_1 and γ_3 with respect to the collisional-broadening coefficient of the main line, γ_2, and (3) potential error associated with the fixed Doppler width. Each of these parameters were evaluated independently, by assuming they were actually 10% higher when generating the simulated spectrum. The spectra were then fitted as normal and the fitting results were compared to the originally generated spectra. This was repeated for all of the temperature/pressure conditions of interest. The effect of an underestimation of S_3^0 has the effect of causing an overestimate of $\Delta\nu_{\mathrm{C},2}$. This potential error is more pronounced at higher temperatures and lower pressures, and is about 1.2% at $P = 1$ atm and $T = 2500$ K. If a 10% uncertainty in γ_1/γ_2 is assumed, the potential error associated with an incorrect assumption for γ_1 relative to γ_2 contributes about 1% uncertainty at $P = 1$ atm and $T = 2500$ K, with a more pronounced effect at higher temperatures and lower pressures. The potential error associated with an incorrect assumption for γ_3 relative to γ_1 contributes about 0.8% uncertainty at $P = 1$ atm and $T = 2500$ K when a 10% uncertainty on γ_3/γ_2 is assumed. This error is minimized at lower temperatures, and at moderate pressures near 3 atm. In general, error in the Doppler width is less consequential because the broadening is typically collision dominated in conditions of interest to combustion systems, see Appendix E.0.2.1. Nevertheless, the sensitivity of the collision width measurement to the assumed Doppler width is useful to cases where there is collisional narrowing [166, 224]. At 1 atm and 2500 K, if an uncertainty in the Doppler width of 1% is assumed, the contribution to the uncertainty on $\Delta\nu_{\mathrm{C},2}$ is 0.3%.

The aforementioned potential errors in the collision width from measurement noise and

biases introduced by the fitting procedure are assumed to be independent, and can be combined using Eqn. 7.20 to obtain the overall uncertainty $E(\Delta\nu_{\mathrm{C}})$ in the collision-width at a given temperature and pressure condition:

$$E(\Delta\nu_{\mathrm{C}}) = E(\Delta\nu_{\mathrm{C}}, \alpha) + E(\Delta\nu_{\mathrm{C}}, \mathrm{bias}) \tag{7.23}$$

$$E(\Delta\nu_{\mathrm{C}}, \mathrm{bias}) = E(\Delta\nu_{\mathrm{C}}, S_3^0) + E(\Delta\nu_{\mathrm{C}}, \gamma_1) + E(\Delta\nu_{\mathrm{C}}, \gamma_3) + E(\Delta\nu_{\mathrm{C}}, \Delta\nu_{\mathrm{D}}). \tag{7.24}$$

This uncertainty may be combined with the potential errors in the collisional broadening coefficient γ using Eqn. E.2 to obtain the overall uncertainty in the pressure measurement. The following subsection will detail the uncertainty in γ.

7.3.3 Broadening coefficient-uncertainty

In this section, we detail the model used to estimate the collisional-broadening coefficients of CO. Section 3.7.3.3.1 details the assumptions made for the species-specific collisional-broadening parameters and their associated uncertainty. Section 3.7.3.3.2 then shows how these parameters are combined including composition uncertainty.

7.3.3.1 Species-specific broadening-coefficient uncertainty

This subsection details the uncertainties in species-specific broadening coefficients which are used to estimate γ. The effect of errors in $\gamma_{\mathrm{CO}-Y,0}$ and $N_{\mathrm{CO}-Y}$ on $\gamma_{\mathrm{CO}-Y}(T)$ (labelled as γ_{Y0}, N_Y, and γ_Y for brevity) is obtained by applying Eqn. 7.20 to Eqn. 7.11:

$$E(\gamma_Y) = E(\gamma_Y, T) + E(\gamma_Y, \gamma_{Y0}) + E(\gamma_Y, N_Y). \tag{7.25}$$

The relative potential error due to temperature uncertainty scales with NY:

$$E^+(\gamma_Y, T) = |-N_Y|\frac{\delta T^-}{T} = N_Y E^-(T). \tag{7.26}$$

The potential error contribution to γ_Y from γ_0 is exactly the uncertainty error in γ_{Y0}:

$$E(\gamma_Y, \gamma_{Y0}) = \frac{\delta\gamma_{Y0}}{\gamma_{Y0}} = E(\gamma_{Y0}). \tag{7.27}$$

The relative potential error in γ_Y scales with the relative uncertainty in N times N and a temperature dependent scale factor:

$$E^{+}(\gamma_Y, N_Y) = \left|\ln\left(\frac{T}{T_0}\right)\right| N_Y \times \begin{cases} E^{+}(N_Y), & \text{if } T \leq T_0 \\ E^{-}(N_Y), & \text{if } T > T_0 \end{cases} . \tag{7.28}$$

The scale factor increases from 0 to $2.3N_Y$, as T is increased from T_0 to $10T_0$. For example, at $T = 10T_0$, if $N_Y = 0.7$ and the assumed value of N_Y was 10% high, γ_Y would be underestimated by ∼16%. The above analysis indicates that accurate knowledge of γ_0 and N are required for accurate determination of γ and pressure.

The collisional broadening parameters γ_{Y0} and N_Y for CO have been tabulated for a variety of collision partners Y (Y = CO, CO_2, H_2, and He) and rotational quantum numbers [205]. The N_Y tabulated in HITRAN are typically valid up to 1000 K and high-temperature coefficients must be used above this limit [89, 225]. At combustion-relevant temperatures, the variation of γ_Y with rotational quantum number is significantly reduced (see Chapter 4) and the analysis of 7.3.2 indicates that the exact knowledge of J''-dependence is not crucial to the fitting of the target spectra. As such, the determination of the broadening parameters of the main P(0,31) line, whose collision width is directly used for the pressure measurement, is of the utmost importance. For combustion in air, a majority of the exhaust gas is N_2, with the bulk of the remaining gas composed of CO, CO_2, H_2O, O_2, and H_2. As such CO-N_2 broadening is critical for an accurate assessment of the overall broadening coefficient in air combustion. Hartmann et al. [171] provided CO broadening parameters γ_0 and N for the collision partners N_2, O_2, CO_2, and H_2O up to $J'' = 77$. These parameters were calculated *ab initio*, and the resulting mixture-weighted broadening in flames using these parameters were shown to be accurate within 10% via scattering experiments. Since then, various studies have measured select broadening parameters at $T \geq 1000$ K and are employed in this chapter to refine the values of Hartmann et al.

Medvecz and Nichols [229] noted that the CO–N_2 coefficients from Hartmann may be overestimated. Chao et al. [227] measured CO broadening by CO, N_2, CO_2, and H_2O for the R(0,11) line in the first overtone band of CO near 2.3 µm up to 1100 K. Cai et al. [230]

Table 7.1: Summary of species-specific collisional broadening coefficients with CO. γ_0 is at a reference temperature of $T_0 = 1000$ K. For each collision partner: 1st/2nd/3rd line corresponds to P(2,20)/P(0,31)/P(3,14).

Collision partner, Y	$\gamma_{CO-Y,0}$ [10^{-3} cm^{-1}·atm^{-1}]	N_Y	Ref.
CO	22.7	0.592	[226]
	20.1	0.470	
	24.0	0.661	
N_2	22.5	0.550	[171, 89]
	21.5	0.453	
	25.6	0.626	
CO_2	24.9	0.500	[171, 227]
	20.0	0.471	
	29.2	0.526	
H_2O	40.2	0.716	[171, 227]
	36.4	0.609	
	39.9	0.769	
O_2	22.0	0.561	[171, 228]
	20.2	0.562	
	22.3	0.594	
H_2	35.3	0.471	[172, 171]
	31.3	0.388	
	37.2	0.536	

measured CO–N_2 broadening up to 1000 K for the R(0,1) and R(0,2) lines in the same overtone band of CO. Spearrin et al. [89] measured CO–N_2 broadening from 1150–2600 K for the P(0,20) transition near 4.8 µm in the CO fundamental band. When the measurements of Chao, Cai, and Spearrin are used to generate $\gamma(T = 1000\text{K})$, the measurements indicate

that Hartmann's CO–N_2 broadening predictions are about 20% high. Similarly, comparing Spearrin's measurement of N to Hartmann's values, we find that Hartmann's model over-predicts N by about 4%. For this chapter, Spearrin's broadening parameters are used to model the P(2,20) line of CO. The broadening parameters of the P(0,31) and P(3,14) line are found by scaling Spearrin's P(20) values by the ratio of the parameters in Hartmann's model and averaging these with Hartmann's values.

Chao's CO–CO_2 and CO–H_2O broadening measurements indicate that Hartmann's predictions of $\gamma(T = 1000\text{K})$ were overestimated by ∼14% and ∼24%, respectively [227]. As such, for this chapter, Hartmann's predicted values at 1000 K are adjusted to the experimental values of [227]. Hartmann's N values are retained for these collision pairs. Chao's CO–CO measurements agree closely with that of Rosasco et al. [226], so Rosasco's values at $T = 1000$ K are used for $\gamma_{\text{CO}-\text{CO},0}$ and Rosasco's measurements from 700–1500 K are used to retrieve $N_{\text{CO}-\text{CO}}$. Finally, Hartmann's $\gamma_{\text{CO}-\text{O}_2,0}$ at 1000 K is rescaled using Mulvihill et al. [228] measurements at 1100–2100 K, whereas Hartmann's $N_{\text{CO}-\text{O}_2}$ value is used un-altered.

There is a lack of data in the literature for high-temperature values of CO–H_2 broadening across the rotational states used in this work. Sur et al. [172] performed measurements of CO–H_2 broadening up to 700 K for the R(0,11) overtone line. In this chapter, the values of $\gamma_{\text{CO}-\text{H}_2,0}$ at the J'' of interest are estimated by multiplying the $J'' = 10$ value from Sur et al. by the J''-dependent ratio of $\gamma_{\text{CO}-\text{N}_2}$ from Hartmann. N values for the CO–H_2 broadening are assumed to be equal to that of Hartmann's CO–N_2.

The aggregated broadening coefficients of CO as aforementioned are summarized in Table 7.1. For all other species, the broadening is estimated using the scaling argument of Chapter 4, based on Eqn. 7.10. For collision partner Y, the broadening value for CO–N_2 is multiplied by a factor indicating the relative collision rate with CO between Y and N_2. Therefore, lighter molecules, with smaller reduced mass, present higher broadening coefficients:

$$\gamma_{\text{CO}-Y} = \gamma_{\text{CO-N}_2} \left(\frac{\sigma_{\text{CO}-Y}}{\sigma_{\text{CO-N}_2}} \right)^2 \sqrt{\frac{\mu_{\text{CO-N}_2}}{\mu_{\text{CO}-Y}}}. \tag{7.29}$$

Implicit in this is the assumption $N_{\mathrm{CO}-Y} = N_{\mathrm{CO\text{-}N_2}}$. The scale factors between CO-N_2 broadening and the collision diameters of select broadening partners are summarized in Table 7.2.

In this chapter, the contribution of each species to the overall collisional broadening (Eqn. 7.9) is defined by Γ, the "partial collisional-broadening coefficient":

$$\Gamma_{\mathrm{CO}-Y} = X_Y \gamma_{\mathrm{CO}-Y}. \tag{7.30}$$

This term is analogous to partial pressure, and is proportional to CO–Y collision rate. The sum of the partial broadening coefficients is the total mixture-weighted broadening coefficient, combining Eqns. 7.9 and 7.30: $\gamma = \sum_Y \Gamma_{\mathrm{CO}-Y}$.

The uncertainties in the broadening model presented here will lead to potential errors in the mixture-weighted broadening coefficient. For each collision partner Y, uncertainty in $\gamma_{\mathrm{CO}-Y,0}$ and $N_{\mathrm{CO}-Y}$ will lead to spectroscopic potential error in $\gamma_{\mathrm{CO}-Y}$ by Eqns. 7.25–

Table 7.2: Tabulation of assumed broadening scale factors, collision diameters, and references for select species with no tabulated broadening in the literature. The diameters for CO and N_2 are provided, as they are used in Eqns. 7.6 and 7.29 to find the scaled broadening values for the other species in the table.

Collision partner, Y	$\frac{\gamma_{\mathrm{CO}-Y}}{\gamma_{\mathrm{CO}-\mathrm{N_2}}}$	σ_Y [nm]	Ref.
N_2	1.00	362	[144]
CO	—	365	[144]
OH	0.88	275	[144]
H	2.32	205	[144]
O	0.90	275	[144]
NO	0.90	333	[231]
CH_4	1.20	374	[144]
C_2H_4	1.09	397	[144]
$nC_{10}H_{22}$	1.55	668	[232]

7.28. The relative spectroscopic potential errors in each collision pair's broadening coefficient $E(\gamma_{\mathrm{CO}-Y}, \mathrm{spec})$ are obtained from Eqns. 7.27 and 7.28:

$$E(\gamma_{\mathrm{CO}-Y}, \mathrm{spec.}) = E(\gamma_{\mathrm{CO}-Y,0}) + E(\gamma_{\mathrm{CO}-Y}, N_{\mathrm{CO}-Y}). \tag{7.31}$$

The total spectroscopic potential error in the mixture-weighted collisional broadening coefficient, $E(\gamma, \mathrm{spec.})$, can be expressed as by:

$$E(\gamma, \mathrm{spec.}) = \sum_{Y} \frac{\Gamma_{\mathrm{CO}-Y}}{\gamma} E(\gamma_{\mathrm{CO}-Y}, \mathrm{spec.}). \tag{7.32}$$

In short, the above equation indicates that the error in broadening parameters for collision partners that are present in high quantities and have high broadening coefficients are the most significant.

7.3.3.2 Compositional uncertainty

As the gas composition changes, the relative contribution of each collision partner's broadening coefficient with CO changes. In Chapter 4, the error in γ associated with this was found by summing $\gamma_{\mathrm{CO}-Y}\delta X_Y$ over the various collision partners Y. The error δX_Y was found by assessing the change in each X_Y with fuel-to-oxidizer equivalence ratio ϕ and with a change between chemically frozen and equilibrium composition. This previous approach overestimates the potential error in γ due to composition change, as each X_Y are not independent of one another during a composition change, see Appendix E.0.1. Since all X_Y must sum to one, as one mole fraction increases and the collision rate from that collision partner increases, other mole fractions must necessarily decrease, reducing the collision rates associated with those collision partners. As such, the change in γ with compositional change must be assessed by observing how the entire gas composition varies.

To assess the variation of the collisional-broadening coefficient with gas composition, simulations of combustion chemistry were performed in Cantera version 2.7. The primary fuels studied were the hydrocarbons methane (CH_4), ethane (C_2H_6), ethylene (C_2H_4), acetylene (C_2H_2), propane (C_3H_8), and Jet-A (using n-decane, $nC_{10}H_{22}$, as a surrogate). Additionally,

non-carbon fuels such as hydrogen (H_2) and ammonia (NH_3) were investigated as extreme cases. Both combustion using air and pure oxygen were studied to extend the range of applications from air-breathing to rocket applications. Various chemical mechanisms were used to simulate the different fuel chemistries[2].

The variation in composition is considered for (1) chemical equilibrium versus fuel-to-oxidizer equivalence ratio ϕ, (2) kinetically in terms of reaction progress as reactants are turned into products, and (3) as the combustion products expand and cool post-combustion. For the equilibrium simulations, each fuel/oxidizer combination was initially set to 1 atm and 1500 K with reactant composition set by the equivalence ratio. Afterwards, the mixture was equilibrated at constant pressure and enthalpy (HP). After equilibration, the "major products" are identified. The major products are defined as those with a mole fraction greater than 1% anywhere across the equivalence ratio range and are shown for C_2H_4–air and C_2H_4–O_2 at the top of Fig. 7.5. Using broadening coefficients selected in subsection 3.7.3.3.1, the partial broadening coefficients (evaluated at a constant $T = 2500$ K) are plotted versus equivalence ratio of C_2H_4–air and C_2H_4–O_2 in the middle row of Fig. 7.5. The spectroscopic potential error contribution to γ from each partial broadening coefficient (represented by each term in the summation in Eqn. 7.32 times γ) is represented by the shaded regions. Since only the major products are considered, in order to better estimate the broadening contribution from the minor products, γ is multiplied by a correction factor of $(\sum_Y X_Y)^{-1}$. This factor typically increases γ by less than 1%. γ is plotted along with the partial broadening coefficients in the middle row of Fig. 7.5 in black. For hydrocarbon-air combustion, the total spectroscopic potential error is dominated by the uncertainty in CO–N_2 broadening, as N_2 makes up a majority of the product gas composition. For hydrocarbon–O_2 combustion, the spectroscopic potential error has more diverse contributions, with CO–H broadening uncertainty being most substantial, due to the high broadening of this collision pair (H has the lowest mass of the collision partners) and due to the high uncertainty in the

[2]The GRI-3.0 High-Temperature mechanism [144] was used to simulate CH_4 and H_2. The USC Mechanism Version II [233] was used to simulate the C_2 hydrocarbons (C_2H_6, C_2H_4, C_2H_2), as well as C_3H_8. The mechanism developed by Glarborg et al. [231] was used to simulate NH_3 combustion. The JetSurF 2.0 mechanism [232] was used to simulate Jet-A combustion.

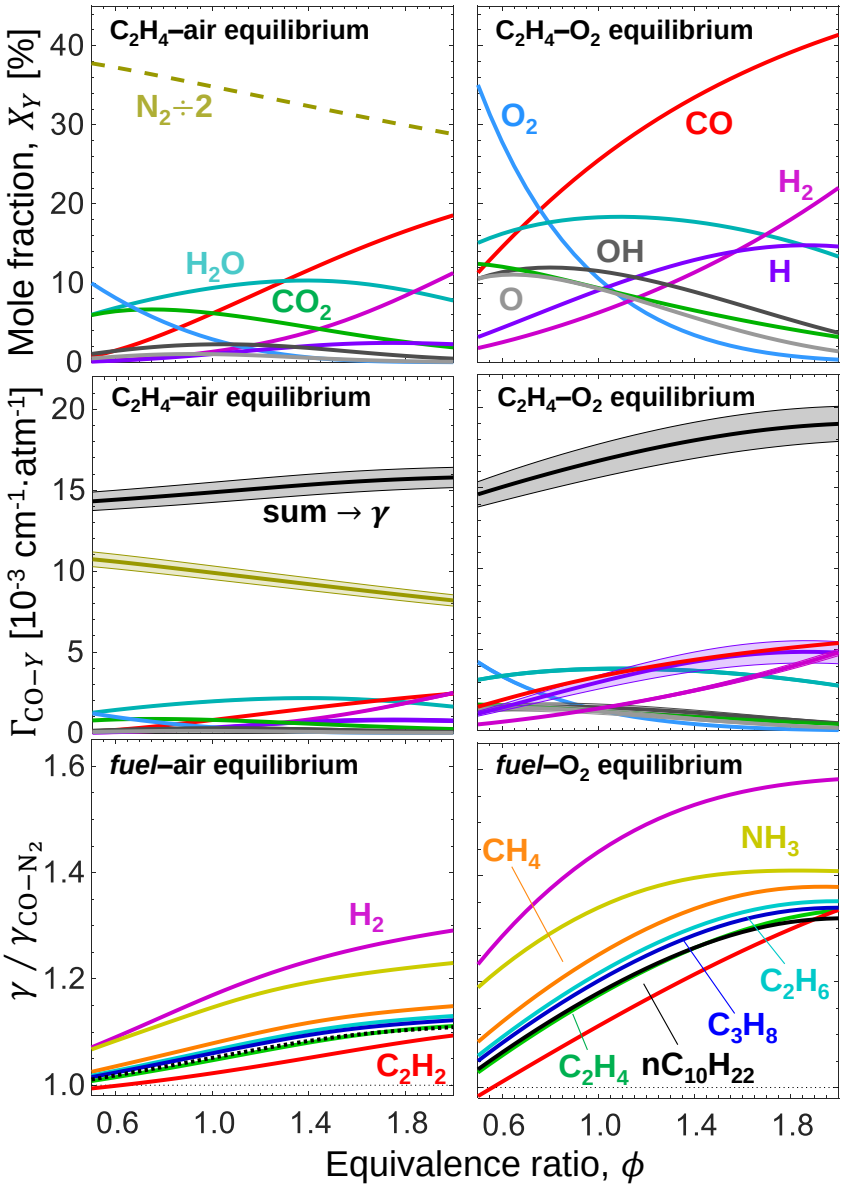

Figure 7.5: *Top*: Equilibrium composition versus ϕ for C_2H_4–air (*left*) and for C_2H_4–O_2 (*right*) at 1 atm. Only the species whose concentrations exceed 1% across the equivalence ratio range are plotted. *Middle*: Partial broadening coefficients for the P(0,31) line at $T = 2500$ K with total mixture-weighted broadening coefficient shown in black. Spectroscopic potential error is indicated by the shaded region around each curve. *Bottom*: Mixture-weighted collisional broadening coefficient, normalized by the CO–N_2 broadening coefficient.

CO–H broadening parameters, which are obtained from scaling relations.

γ/γ_{CO-N_2} is plotted versus equivalence ratio for each studied fuel at the bottom of Fig. 7.5. For all studied conditions with the hydrocarbons, γ was within 40% above γ_{CO-N_2}. γ is higher for O_2 combustion compared to air combustion, as there is a larger concentration of lighter molecules. In general, for each studied fuel-oxidizer combination, γ increases with increasing equivalence ratio. This is due to the increasing concentration of H_2 and H, which are light molecules that are frequent colliders with CO. At leaner equivalence ratios on the other hand, an excess of O_2 and N_2 is present, which are a relatively heavy molecules with a lower collision rates with CO, leading to reduced broadening. As the equivalence ratio is reduced significantly below 1, the γ approaches a weigted sum of γ_{CO-N_2} and γ_{CO-O_2}, which reduces the potential error associated with composition.

The broadening coefficients for the hydrocarbons in air change by about 11% from $\phi = 0.5$ to $\phi = 2$. For O_2 combustion, the differences between the broadening of the various fuel products is higher. For hydrocarbon–O_2 combustion, γ changes by about 25% from $\phi = 0.5$ to $\phi = 2$. It was found that the sensitivity of γ to ϕ, $s(\gamma, \phi)$, is typically below 0.1 %/% for the hydrocarbons in air and below 0.2 %/% for the hydrocarbons in O_2, with a peak in sensitivity typically near stoichiometric conditions. Thus, a 5% accuracy in the broadening coefficient is achieved if ϕ is known within 20–50%. It is also interesting to note a reduced sensitivity of γ to ϕ at higher values of ϕ, particularly for the O_2-combustion cases. This is largely due to the plateauing production of H in the exhaust at very high ϕ.

When comparing the various fuels, the broadening generally increases as the H/C ratio in the fuel increases, with the C_2H_2 (H/C=1) products having the lowest broadening, and C_2H_6 (H/C=3) products having the highest broadening. This is due to the higher concentration of H_2O, H_2, and H in the exhaust versus CO and CO_2 for the fuels carrying more hydrogen atoms. In general for equilibrium, the exact knowledge of the fuel-oxidizer mixture is not required to obtain gas composition. The equilibrium composition at a given temperature and pressure is dictated by the proportions of the elements C, H, O, and N in the reactant mixture. For many common hydrocarbons (CH_4, C_2H_6, C_2H_4, and Jet-A) the broadening of

the product gas in air combustion have almost the same ϕ dependence, with the broadening coefficients being within a few percent of each other, due to the fact that their H/C ratios are very similar (2–4). The H_2 product gas has the highest broadening as a majority of the non-N_2 product gas composition is H_2O, H_2 and H. NH_3 represents an intermediate case, with the presence of additional N_2 in the product gas reducing the broadening from that of the case of pure H_2 but higher than that of the hydrocarbons.

Often for in-situ measurements, combustion may be in-progress or incomplete. This means the combustion gas is not well-represented by the equilibrium products discussed in the previous paragraph. To investigate how the collisional-broadening coefficients vary across a combustion reaction, 0-D kinetic simulations were performed using CANTERA in a constant-pressure and constant-enthalpy (HP) reactor ($\phi = 1$ and $T_{\text{init}} = 1500$ K). Simulations were run until the mole fractions of H_2O, CO_2, and NO were within 0.1% of the equilibrium value predicted by the equilibrium simulations. Reaction progress Z was defined in terms of the mass fraction of the products and reactants, as defined in Appendix G.0.1.

For C_2H_4–air and C_2H_4–O_2, the mole fractions of the major species (present in $\geq$1% during the reaction) versus the reaction coordinate Z are shown at the top of Fig. 7.6. In the middle row of Fig. 7.6, the partial collisional-broadening coefficient, $\Gamma_{\text{CO}-Y}$, evaluated at $T = 2500$ K is plotted for each collision partner, with the spectroscopic potential error in each partial broadening coefficient represented by the shaded region around each curve. The sum of the partial broadening coefficients is plotted in black along with its spectroscopic potential error as the black shaded region. As for the equilibrium case, in hydrocarbon–air combustion, this potential error is dominated by the uncertainty in CO–N_2 broadening. For hydrocarbon–O_2 combustion, the potential error is largely dominated by the uncertainty in the CO–fuel broadening coefficient at early points in the reaction and by CO–H broadening towards the end of the reaction.

$\gamma/\gamma_{\text{CO-N}_2}$ at $T = 2500$ K is plotted versus reaction progress Z for each studied fuel at the bottom of Fig. 7.6. In general, for each studied fuel-oxidizer combination, γ increases with increasing reaction progress, as the composition shifts from fewer/heavier molecules to

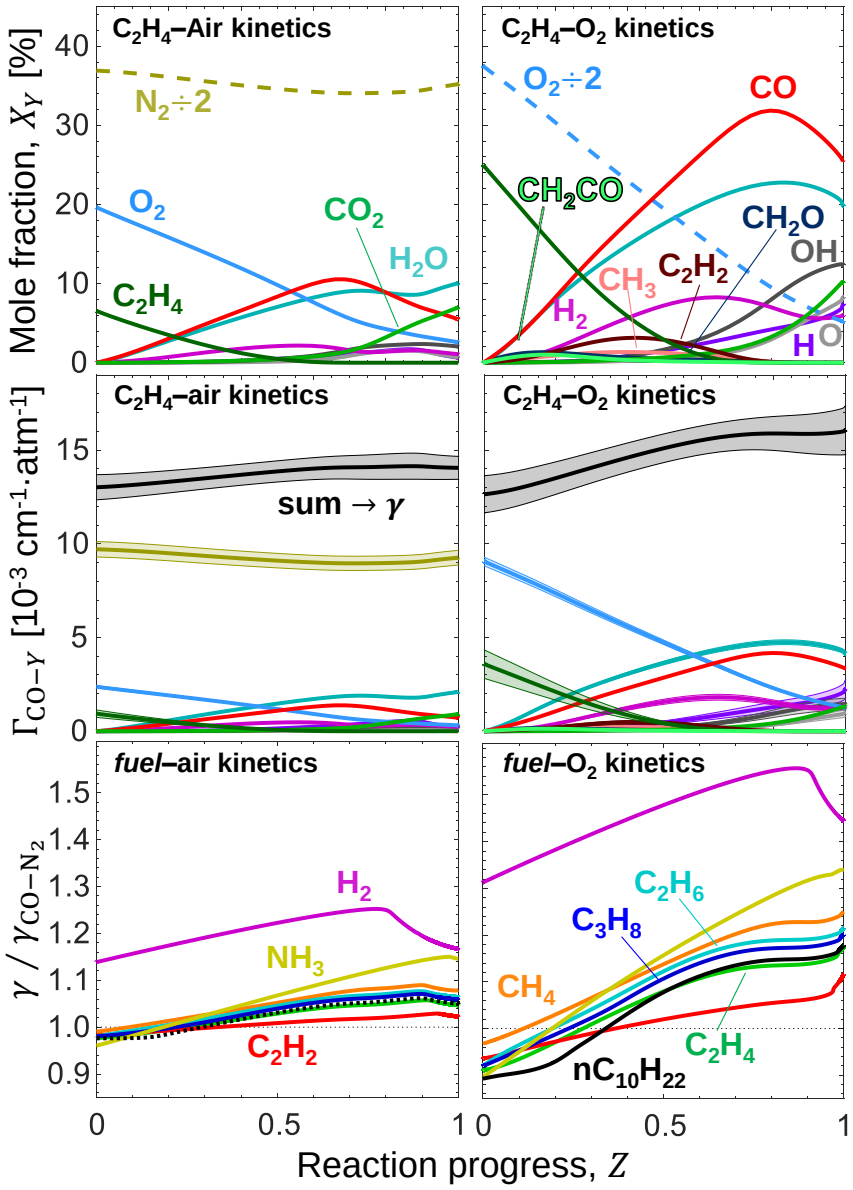

Figure 7.6: *Top*: Gas composition versus reaction progress, Z, for C_2H_4–air (*left*) and for C_2H_4–O_2 (*right*). *Middle*: Partial broadening coefficients for the P(0,31) line for the major collision partners versus Z, evaluated at $T = 2500$ K, with $\gamma = \sum \Gamma_{\mathrm{CO}-Y}$ shown in black. Spectroscopic potential error is indicated by the shaded region around each curve. *Bottom*: Mixture-weighted collisional broadening coefficient, normalized by the CO–N_2 broadening coefficient, versus Z for various fuels.

more/lighter molecules across the reaction, resulting in an increased collision rate per unit pressure. An exception to this trend is H_2, which features a dip in γ towards the tail-end of the reaction, due to water dissociation. Air mixtures present some stability to γ versus Z, due to the large quantity of N_2 in air. Interestingly, at early times, γ is very close to the value for CO–N_2 broadening for the hydrocarbon fuels and NH_3, both for air and O_2 combustion. This is due to the very similar collision diameter and molecular weight of many of these fuels to nitrogen, leading to a very similar collision rate with CO. While the presence of fuel tends to increase the broadening coefficient of the reactant mixture, the presence of oxygen has the opposite effect due to its higher molecular weight. These two effects tend to compensate each other, leading to an overall mixture-weighted broadening coefficient similar to that of pure N_2. H_2 is an exception because H_2 is very light and has a high broadening coefficient compared to N_2 as a result. These results imply that for hydrocarbon mixtures at early phases in the combustion process, CO–N_2 broadening provides a very good estimate of the broadening coefficient, with the uncertainty in the fundamental spectroscopic parameters (γ_0, N) dominating the potential error.

For most of the hydrocarbons studied (CH_4, C_2H_6, C_2H_4, and Jet-A) the broadening of the mixture have nearly the same Z dependence, with the broadening coefficients being within a few percent of each other. These fuel-air combinations see an 8–10% increase in γ across the reaction coordinate. For O_2 combustion, the differences between the broadening values for the different fuel mixtures across the reaction space are higher but still on the order of a few percent. These fuel–O_2 combinations see an approximately 30% increase in γ across the reaction coordinate. NH_3 has a similar dependence with Z as these hydrocarbons at early points in the reaction, but then diverge to a higher value of γ towards the end of the reaction, closer to that of H_2. C_2H_2 diverges from the other hydrocarbons early on in the reaction space due to the high production of CO compared to other exhaust products. It was found that the sensitivity of γ to Z is typically $s(\gamma, Z) = \pm 0.1$ %/% range for the hydrocarbons in air and in the $s(\gamma, Z) = -0.05$–0.2 %/% range for the hydrocarbons in O_2. Most of the hydrocarbons present a reduced sensitivity of γ to Z towards the last 20% of

the reaction. This implies that a single value of γ could be used for most mixtures that are in the final oxidation phase of the reaction. It should be noted that at higher equivalence ratios, the change in γ across the reaction is magnified, whereas at lower equivalence ratios, the change in γ is reduced—the lean mixtures are mainly composed of N_2 (or pure O_2 for oxy-combustion).

In addition to the variation of γ with equivalence ratio and reaction progress, the change in γ during gas cooling was investigated. This is particularly of interest for O_2 combustion, since the higher temperatures achieved in O_2 combustion lead to higher levels of dissociation of H_2O and CO_2 into light molecules/atoms such as H, O, OH, H_2, O_2, and CO. As the gas temperature drops, recombination reactions occur which convert these dissociation products back into H_2O and CO_2. To investigate this, the gas objects from the end of the kinetic simulations had their temperature reduced isobarically and were allowed to equilibrate at constant pressure and temperature. For each gas, the temperature was reduced from the equilibrium temperature to half the equilibrium temperature. This cooling effect resulted in at most a 2% increase in γ in air, and a 6% increase in γ for O_2 combustion. To achieve this effect, the gas temperature needs to drop by about 25% ($\sim$750 K), which for isentropic expansion would correlate with a 70–80% drop in pressure. Lower pressures tend to encourage dissociation, so a pressure drop may reduce the composition change[3].

The uncertainty assigned to γ from compositional uncertainty is context-dependent. In certain scenarios, the equivalence mixture ratio, reaction progress, and degree of departure from chemical equilibrium may be more or less certain. In a pure reactant mixture for example, the reaction progress is known to be 0 and for a pre-mixed combustor, ϕ can be known precisely. Discretion must be used when choosing the composition at which to evaluate γ and when assigning potential error. In general, the compositional potential error

[3]These effects may be more pronounced for combustion at extreme pressures or for detonation combustion, where temperatures exceeding 4000 K are possible, leading to large levels of product-gas dissociation. This compositional change from cooling may not be fully realized—as combustion gas cools, the kinetics of recombination will slow down, resulting a "kinetically frozen" state.

may be written as:

$$E(\gamma, \text{mix}) = E(\gamma, \phi) + E(\gamma, Z) + E(\gamma, \text{eq.}), \tag{7.33}$$

where "eq." refers to the potential error associated with the thermodyanmic state and non-equilibrium of the gas mixture, which may include effects of certainty in combustion mode, such as deflagration versus detonation. The total uncertainty in γ may be written as:

$$E(\gamma) = E(\gamma, \text{mix}) + E(\gamma, \text{spec.}) + E(\gamma, T). \tag{7.34}$$

In the following subsection, the uncertainty in γ is combined with the uncertainty in $\Delta\nu_{\text{C}}$ to obtain the overall uncertainty in P.

7.3.4 Total uncertainty in pressure

The three main sources of potential error in the pressure measurement have been identified in the preceding subsections: (1) precision/bias error resulting from the data collection and processing, (2) uncertainties in the spectroscopic constants which characterize CO collisional broadening, and (3) uncertainty in the combustion gas composition. In this subsection, we detail how these potential errors can be combined to assess the overall uncertainty in the pressure measurement.

The uncertainty in the collision-width comes entirely from measurement noise and biases from the fitting model. The uncertainty in γ also has contributions from these sources via the potential error contribution from the temperature measurement, as indicated in Eqn. 7.34. These potential errors cannot be simply added due to correlations, so Eqn. E.2 must be used. The other potential error sources stem from the uncertainties in the broadening parameters and composition of the bath gas. The potential error in γ from temperature uncertainty can be written as:

$$E^{+}(\gamma, T) = \sum_{Y} \frac{\Gamma_{\text{CO}-Y}}{\gamma} N_{\text{CO}-Y} E^{-}(T). \tag{7.35}$$

This may be further broken down into a potential error in γ from precision error, $E(\gamma, \alpha)$, bias error, $E(\gamma, \text{bias})$, and error from uncertainty in S_1^0 and S_2^0, $E(\gamma, S^0)$, stemming from these potential errors in the temperature measurement. The precision and bias errors may

be quantified using the methods of Section 3.7.3.2 through the fitting of noisy absorbance profiles. Of particular note is the potential bias error associated with the uncertainty of the P(3,14) linestrength. This potential error is near-zero at pressures near 2.5 atm, and is generally sub-1% for higher pressures. At $P \leq 1$ atm, this potential error increases beyond 1% when $T \geq 2500$ K. $E(\gamma, S^0)$ can be found using the dependence between temperature and the reference linestrengths in Appendix E.0.3:

$$E^+(\gamma, S^0) = \frac{kT}{hc\Delta E''_{12}} \frac{\sum_Y N_Y \Gamma_{\mathrm{CO}-Y}}{\gamma} \times (E^+(S_1^0) + E^-(S_2^0)). \tag{7.36}$$

Using Eqn. 7.20 and 7.21, the uncertainty in P can be expressed as:

$$E^+(P) = E^+(P, \alpha) + E^+(P, \mathrm{bias}) + E^-(\gamma, \mathrm{spec.}) + E^-(\gamma, \mathrm{mix}) + E^-(\gamma, S^0). \tag{7.37}$$

Note that $E(P, \alpha)$ and $E(P, \mathrm{bias})$ are related to the precision error and bias error for $\Delta\nu_{\mathrm{C}}$ and γ (via the temperature measurement), accounting for correlation from measurement noise. These errors may be assessed using the methods of Section 7.3.2 but are closely approximated by the errors in the collision-width measurement due to the weak dependence of γ on T. In addition, potential bias error due to line-of-sight non-uniformity is typically below 1% for the conditions of the sensor demonstrations of Section 7.4 and are neglected in this section, see Appendix E.0.5.

Sample pressure uncertainty values for the combustion products of C_2H_4–air and C_2H_4–O_2 are shown in Fig. 7.7 for $P = 1$ atm, $X_{\mathrm{CO}}L = 3\%\cdot$cm, $\mathrm{SNR}_{\mathrm{opt}} = 250$ at three different temperatures. The figure indicates the potential error contributions from various sources as bars below the top set. Values greater than 0 indicate the upper uncertainty/error bound and values less than zero indicate the lower uncertainty/error bound. Here, the following arbitrary assumptions are made as an example: $E^{\pm}(\phi) = 10\%$, $E^+(Z) = 0$, $E^-(Z) = 10\%$, $E(\gamma_1/\gamma_2) = E(\gamma_3/\gamma_2) = 3\%$. The uncertainties in the reference linestrengths are taken from the HITEMP Database. Here, the final uncertainties/errors are multiplied by a "coverage factor" [223] of $1/\sqrt{2}$ to account the linear addition of errors, as opposed to adding in quadrature. In general, the dominating error contribution comes from uncertainty in the broadening parameters for CO, which increases modestly at higher temperatures. Other spectroscopic

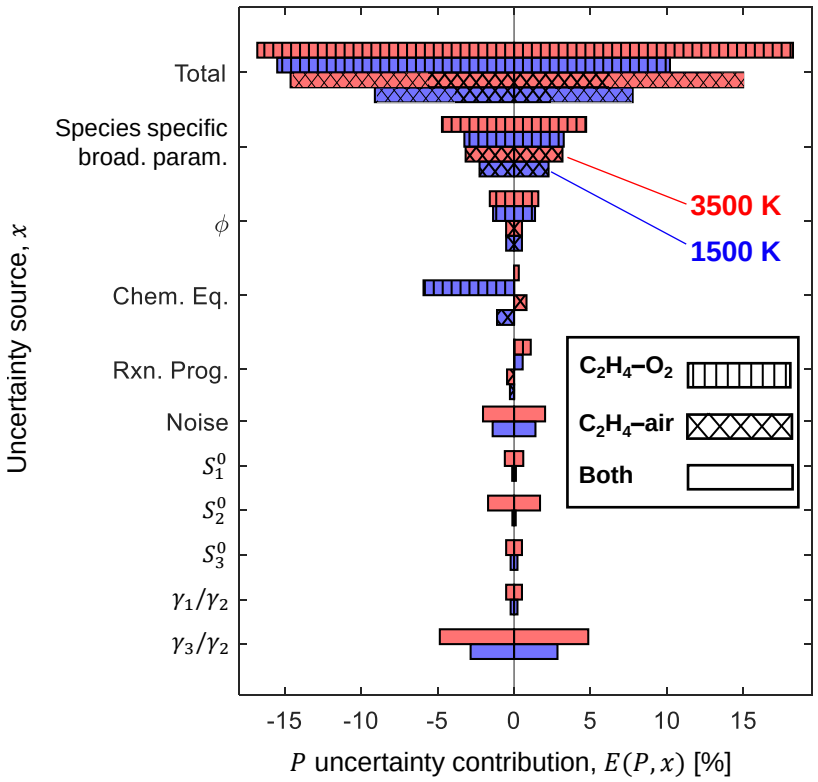

Figure 7.7: Contributions of potential error sources to total pressure uncertainty (top 4 bars) for C_2H_4-fueled combustion product gas. Bar color corresponds to temperature condition. Bar hatching pattern indicates if composition-related errors/uncertainties are for air or oxygenated combustion.

errors (linestrenghs) add a few percent uncertainty to the pressure measurement. The potential error from compositional uncertainty is dominated by the uncertainty in the chemical equilibrium state of the gas for oxygenated combustion at lower temperatures, furthest from the adiabatic flame temperature of the gas, where the composition may have changed the most. This can add up to a 5% bias in the pressure measurement. Overall, the uncertainty in pressure is around $\pm 10\%$.

7.4 Sensor demonstrations

The pressure sensing strategy was demonstrated in two laboratory facilities at UCLA: a high-enthalpy shock tube and a pulse-detonation tube. For all experiments, a common optical setup was used. A distributed-feedback quantum cascade laser (DFB QCL) was maintained a constant temperature using thermoelectric cooling supplied by an Arroyo 6310-QCL laser controller, which also set the DC current input to the laser. The laser output wavelength was modulated at MHz rates using a Rigol DG1032Z function generator multiplexed with the DC current via a bias-tee [148]. The laser modulation waveform is trapezoidal, with the leading-edge ramp rate selected depending on the expected broadening of the target spectral features. Based on the guidelines established in Chapter 6, narrow spectral features at low pressures are scanned using a lower ramp rate to reduce the rate of output wavelength change (chirp rate). This procedure avoided the distortion of narrow spectral features due to detector bandwidth limitations. The waveform duty cycle is typically between 50–70%, adjusted to maximize the scan depth for a given ramp rate. This yields an integration time for the measurement on the order of 500–700 ns for each modulation period or laser "scan",

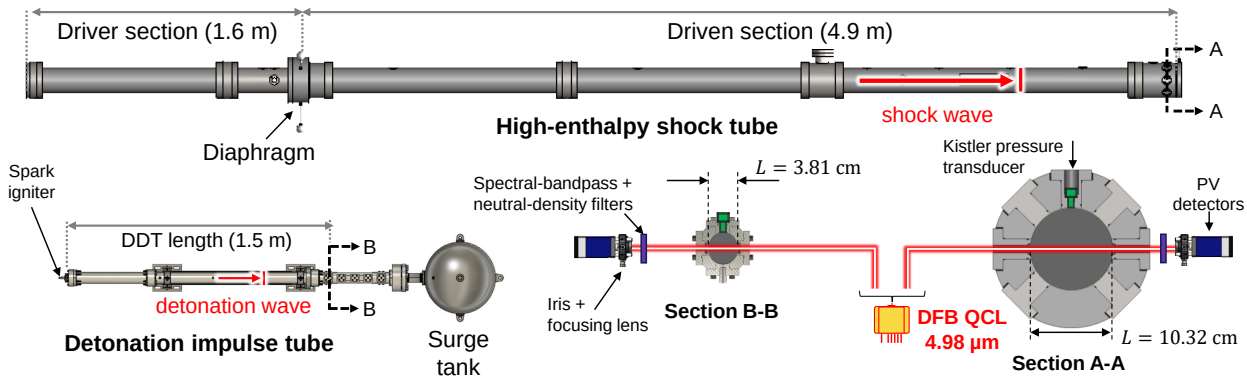

Figure 7.8: Experimental setup used for sensor demonstrations. High-enthalpy shock tube facility (*top*) with key dimensions and features labeled. Detonation-impulse tube (*bottom left*) with deflagration-to-detonation transition length and key components labeled. The optical setup (*bottom right*) is shown at the cross sections of the measurement planes (Section A–A and Section B–B).

see Fig. 7.9.

Laser light is directed through the flow of interest onto a thermoelectrically-cooled, AC-coupled, photovoltaic detector (Vigo PVI-4TE-6-1x1) with a 200-MHz bandwidth coupled with narrow bandpass / neutral density filters, an iris, and a CaF_2 convex lens. The voltage output of the detector is recorded on a Tektronix MSO44 oscilloscope with 200-MHz bandwidth, for measurement periods of 4–10 ms, and sample rates ranging from 1.25–3.125 GS/s. A schematic of the optical setup is shown on the bottom right of Fig 7.8.

Before each experiment, the light intensity profile is recorded, representing the incident light intensity I_0, also referred to as the "background" signal. Another profile is recorded with a 50-mm germanium etalon (mounted on a flip mount) to characterize the laser ouput wavenumber in time, or chirp. During an experiment, the detector measurement is used to obtain the transmitted light intensity through the absorbing gas, I_t. The measurements of I_t, I_0, and the chirp profile are used to obtain an absorbance spectrum $\alpha(\nu)$ using Eqn. 7.1 for each laser scan. Sample measurements of I_0, I_{tr}, and $\alpha(\nu)$ are shown in Fig. 7.9.

The measured absorbance spectrum is fitted to obtain the P(2,20)/P(0,31) absorbance areas and the P(0,31) collision width using the fitting procedure outline in Section 3.7.3.2. The collisional widths between of the P(2,20) and P(3,14) lines are set by scaling the P(0,31) broadening by the ratio of collisional-broadening coefficients predicted by the assumed gas composition. Additionally, a 4th absorbance area is floated in some cases to capture the contribution of the RR(0,57.5) doublet of nitric oxide (NO) at 2008.25 cm^{-1} that can sometimes appear post-ignition with air as the oxidizer. Gas temperature and CO partial pressure are obtained with Eqns. 7.13 and 7.14. The gas temperature is used along with an assumption for the gas composition to infer the time-resolved collisional-broadening coefficient, γ for P(0,31). The P(0,31) collision width is divided by its collisional-broadening coefficient using Eqn. 7.21 to infer the gas pressure. The CO partial pressure is divided by the total pressure using Eqn. 7.15 to infer the CO mole fraction.

In addition to the LAS pressure measurement, a conventional electromechanical pressure measurement is collected simultaneously using piezoelectric pressure transducers. For the

shock-tube experiments, a Kistler 601B1 is used, which has a rise time of 2 µs and resonant frequency of 300 kHz. For the detonation-tube experiments, a Kistler 603CAA is used, which has a rise time of less than 0.4 µs and a resonant frequency greater than 500 kHz. The Kistler output is amplified using a charge amplifier. The amplifier applies a 100-kHz low-pass filter to the raw output signal to suppress excessive high-frequency ringing in the Kistler signal, which are magnified near the natural frequency of the transducer, near 1–5 MHz.

7.4.1 Shock-tube hydrocarbon-air kinetics

The UCLA high-enthalpy shock tube (HEST) facility has been extensively described in other works [165, 169]. Various fuel-air mixtures were shock heated in the 4.9-m driven section using a helium driver gas bursting plastic diaphragms. Optical access is provided by two 3-mm thick wedged sapphire windows located 2 cm from the endwall of the driven section. The optical path length through the inner diameter of the tube is 10.32 cm.

For the experiments, two stoichiometric mixtures of C_2H_4–air and CH_4–air were manometrically prepared in a stirred mixing tank. Both mixtures were seeded with 2% CO to allow for pre-ignition assessment of pressure. The addition of CO was found to have negligible effects on the ignition timescales (1–3% change), see Appendix G.0.2. Before each test, the shock-tube driven section was vacuumed to mTorr pressures and subsequently filled to various initial pressures to target specific post-reflected-shock conditions.

Two experiments are considered here. In experiment S1, the C_2H_4 mixture is shock-heated to near 2 atm and 1200 K. In experiment S2, the CH_4 mixture is shock-heated to a higher pressure near 4 atm at 1500 K. From the electromechanical Kistler pressure trace (see P^{Kistler} later in Fig. 7.11), distinct time periods in the experiment can be observed. Initially, before time "0" the mixture is at the pre-shock ambient condition at low pressure (not pictured). The pressure increases at time "0" due to the incident shock and at $t \sim 100$ µs due to the reflected shock. Ignition occurs at $t \sim 400$ µs where the pressure signal rises again and begins to oscillate dramatically. Due to the confined volume of the shock tube and the high concentration of reactants, this combustion process is not isobaric. The

pressure does decay slightly after its initial peak, corresponding to some gas expansion and cooling.

Post-processing of the spectrally-resolved line cluster enables inference of multiple parameters. The top-left pane of Fig. 7.9 shows sample transmitted laser intensity scan of experiment S1 before and after the ignition event, at $t = 200\,\mu s$ and $t = 585\,\mu s$, respectively. Below the raw data, the measured absorption spectra from this test are shown with the spec-

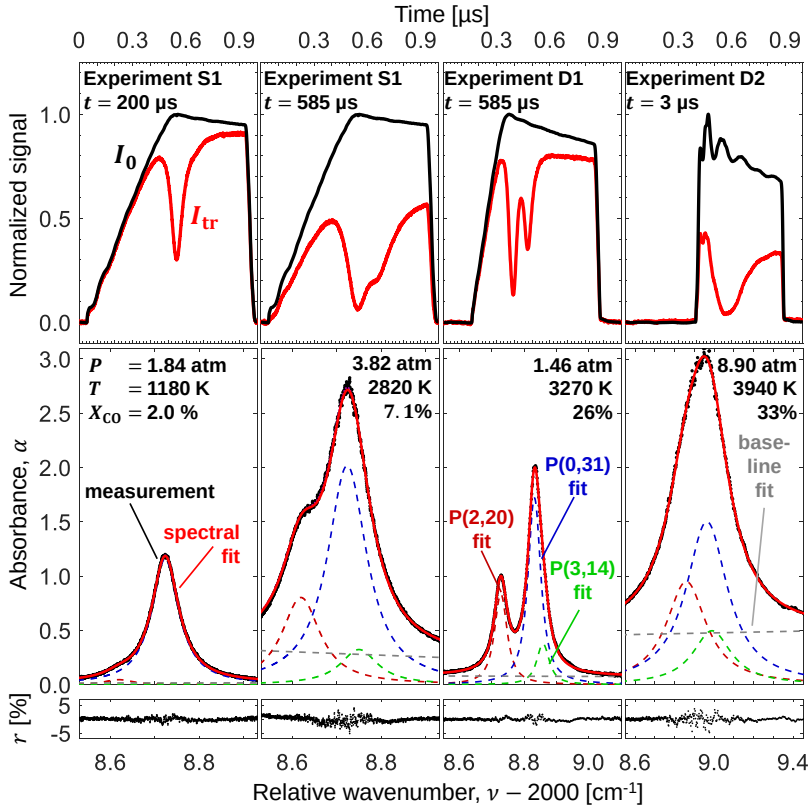

Figure 7.9: *Top*: Incident/background intensity profile (black) and transmitted intensity profile (red) plotted for select individual laser scans during shock and detonation tube experiments across various pressure and temperature conditions. *Middle*: Measured absorbance spectra of target CO transitions (black), along with overall spectral fits (red), individual transitions in each fit (dashed lines) and fit of non-absorbing baseline (dashed gray) due to high-temperature/pressure CO_2 absorption. *Bottom*: The peak-normalized residual r between the fit and measurement.

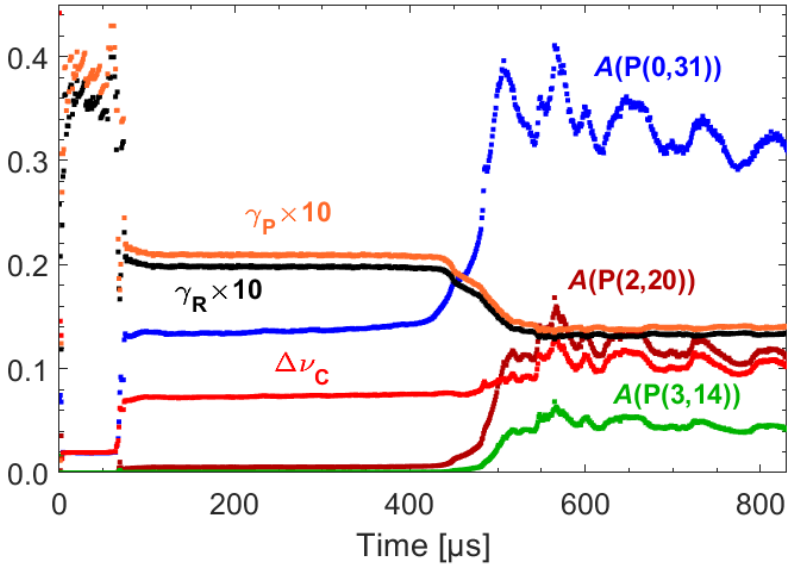

Figure 7.10: Time-resolved fitted spectral parameters, including collision-width $\Delta\nu_C$ [cm^{-1}], absorbance areas A [cm^{-1}], and collisional broadening coefficient $\gamma(T)$ [cm^{-1}·atm^{-1}]. The subscript for γ indicates whether the reactant (R) or product (P) gas composition is used to predict the broadening coefficient. The collision width and collisional broadening coefficient are given for the P(0,31) line.

tral fit of the data. The significant baseline absorption in the post-ignition scan is largely due the the broadband absorption of CO_2 [234]. In Fig. 7.10, the measured absorbance areas and collision widths from experiment S1 are plotted in time from this test. Two values of the broadening coefficient γ are plotted: the value predicted using the reactant composition (γ_R, in black) and the equilibrium product gas composition (γ_P, in orange) calculated from the CANTERA model from Section 3.7.3.3.2. Equations 7.13–7.15 and 7.21 are used to infer gas pressure, temperature, CO partial pressure, and CO mole fraction in time from the areas and collision width measurement. It should be noted that during the incident shock portion of the test, the gas temperature is quite low, so an accurate/precise measurement of the P(2,20) absorbance area is not possible, leading to an inaccurate T and p_{CO} measurement. Nevertheless, the pressure measured during this region is included due to the reduced sensitivity of

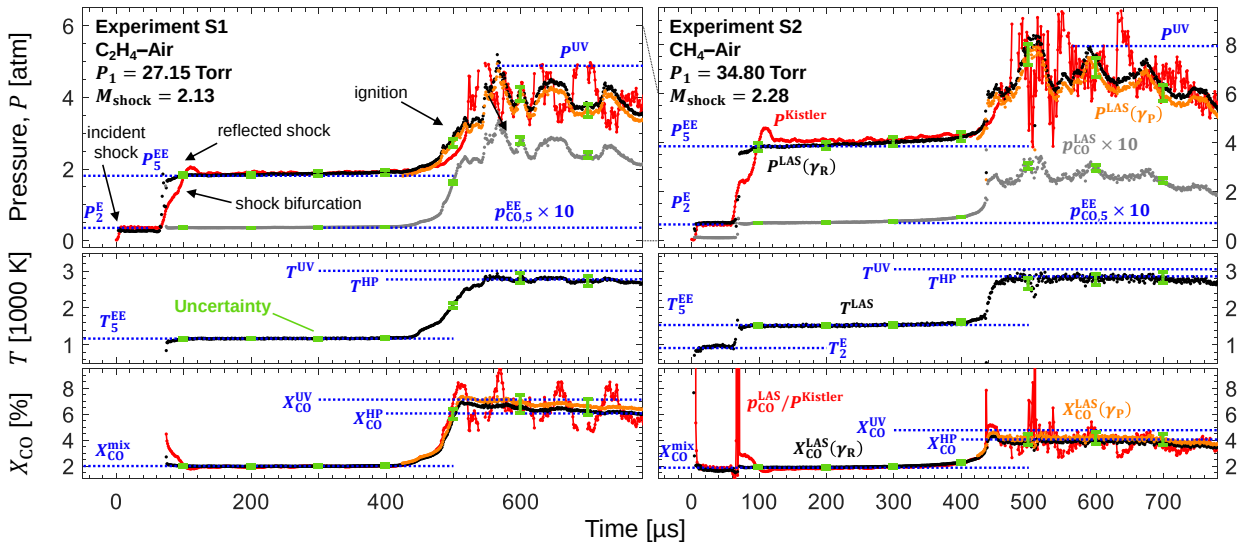

Figure 7.11: *Top*: Pressure traces for the two shock-tube experiments. The Kistler-measured pressure is indicated in red. Reference lines indicating predictions from ideal shock-relations or chemical equilibrium are indicated in blue. Two LAS measurements of pressure using the reactant collisional-broadening coefficient (black) and product collisional-broadening coefficient (orange) are indicated. The LAS-measured partial pressure of CO is shown in gray. Uncertainty is indicated with the green errorbars. *Middle*: LAS-measured temperature with uncertainties and reference values. *Bottom*: LAS-measured CO mole fraction with uncertainties and reference values. A X_{CO} measurement using the Kistler-measured pressure is shown in red.

the pressure measurement to errors in temperature. The temperature and pressure measured by the sensor can be readily compared to the temperature and pressure predicted by frozen shock tube relations, FROSH [211], from the fill pressure, temperature and composition, as well as the incident shock speed. The FROSH predictions for pressure and temperature are plotted as horizontal dashed lines in Fig. 7.11. The FROSH values predicted behind the incident shock are notated with the subscript "2" and the properties behind the reflected shock are notated with the subscript "5", assuming vibrational equilibrium in both regions (represented by the superscript "EE"). The known initial CO mole fraction is plotted as a horizontal dashed line at the bottom of Fig. 7.11 and this is combined with the P_5 prediction

to generate a prediction for $p^{\mathrm{EE}}_{\mathrm{CO},5}$, which is plotted in the top panel of the same figure (scaled by a factor of 10).

In Fig. 7.11, the measured properties from LAS for experiment S1 are shown in black, with each measured property g labeled as g^{LAS}. The CO partial pressure is plotted in grey to distinguish it from the total pressure measurement. The uncertainty for each measured property is indicated by the green errorbars, using the methods of Section 7.3. The contribution of precision error to the uncertainty is not reflected in the error bars due to the self-evident nature of the precision error in the datapoint scatter. The uncertainty is on the order of 3–6% for pressure, 2–5% for temperature, 2–7% for p_{CO} and 4–11% for X_{CO}. The contributions to the uncertainty indicated in Fig. 7.7 are generally representative of the uncertainty here, with the notable exception that the reduced potential error from ϕ, due the high certainty in the initial mixture composition. The potential error due to gas cooling is equal to zero, as this is irrelevant for the pre-ignition mixture and the temperature remains close to the equilibrium value after ignition. The potential error due to the uncertainty in reaction coordinate, Z, is also not included in the errorbar. Instead, two pressure calculations are made utilizing the reactants broadening coefficient (γ_{R}, in black) and the broadening coefficient of the products at equilibrium (γ_{P}, in orange). These two points on the reaction coordinate ($Z = 0$ and $Z = 1$) represent the two extremes in γ across the reaction, and as such bound the broadening coefficient across the ignition event. X_{CO} is also plotted as two curves corresponding to the same assumptions for γ. It can be seen that the pressure measured using γ_{R} closely aligns with P_2 and P_5 predicted by the frozen shock relations. The LAS pressure behind the reflected shock wave agrees closely with the value measured by the Kistler, with a significant exception. Immediately behind the reflected shock, the LAS pressure rises almost immediately to P_5, whereas the Kistler pressure rises to an intermediate value between P_2 and P_5, after which there is a shallower rise in pressure over 80 µs, an overshoot of P_5, and a subsequent settling of the pressure near P_5. This complex pressure structure observed by the Kistler is caused by the interaction of the reflected shock wave with the boundary layer formed by the flow behind the incident shock wave, giving rise to

a phenomena known as shock bifurcation [235]. Here the reflected shock transitions to an oblique shock near the sidewalls of the tube, leading to a localized boundary region with significantly different gas thermodynamic properties compared to the bulk gas. As a result, the Kistler is unable to probe the thermodynamic state of the bulk gas from its location on the sidewall. The LAS pressure measurement is path-integrated in nature, and as such effectively averages over these disparate regions of pressure. The ability of the LAS sensor to effectively report a path-integrated pressure is discussed in Appendix E.0.5, where knowledge of these two pressure measurements is employed to infer the radial pressure distribution at the measurement location. After the reflected shock passage, both the Kistler and LAS pressure measurements gradually rise in time, corresponding to some nominal dP/dt caused by shock-tube non-idealities [236].

It can also be seen that the temperature, CO partial pressure, and CO mole fraction closely match the region 5 values predicted by the frozen shock relations and the known concentration of seeded CO in the reactant mixture. With the temperature and CO species measurements, the ignition event is much more clear due to the abrupt rise in these two parameters along with pressure rise near 430 µs. The values of the measured gas properties after ignition can be compared to the values predicted by thermochemical equilibrium using the Cantera model from before. Here both equilibrium at constant enthalpy/pressure (labeled with "HP") and at constant internal energy/volume (labeled with "UV") are shown as references due to the fact that the combustion process here is bounded by these cases. The initial temperature and pressure conditions for these equilibrium simulations are informed by FROSH. During the lead up to ignition, the LAS pressure measurement begins to rise before the Kistler measurement. This could be due to non-uniform ignition events leading to different pressure values near the wall compared to the bulk flow. After ignition, the LAS pressure measurement tracks with the Kistler pressure, but the LAS pressure oscillates significantly less than the Kistler measurement. The accuracy of the pressure oscillations captured by the two diagnostics can be compared by examining the mole fraction measurement made using either pressure measurement, as the input to Eqn. 7.15 along with the

LAS measurement of p_{CO}. The orange curve indicates the post-combustion LAS prediction of mole fraction whereas the Kistler prediction is shown in red. The LAS measurement of X_{CO} is much more stable in time than that predicted by the Kistler pressure. It should be expected that the species concentration over a combustion process do not oscillate as drastically as the Kistler prediction, so it is likely that the extreme oscillations measured by the Kistler are non-physical, or are representative of higher pressure unsteadiness near the tube wall from boundary layer effects. The peak value of the gas properties measured by LAS are close to that predicted by the UV equilibrium: $P = 4.9$ atm, $T = 3000$ K, $p_{CO} = 0.35$ atm, and $X_{CO} = 7.1$ %. The values these parameters decay to after the initial transient are closer to the values predicted by HP equilibrium.

In Fig. 7.11, the results of the higher pressure experiment (S2) with CH_4 fuel is pictured on the right. Similar observations as for the previous experiment can be made regarding the comparison of the LAS measured values to the Kistler pressure, values predicted by frozen shock relations, and values predicted by thermochemical equilibrium. The higher gas temperature behind the incident shock for this experiment allows for a more accurate measurement of T, p_{CO}, and X_{CO}, which are now pictured in Fig. 7.11. This experiment indicates the ability of the compositional model to capture changes in γ with variation of hydrocarbon fuel. Additionally, the dynamic range of the sensor is on display, with pressure measurements made from pressures of 0.8–8 atm.

7.4.2 Ethylene-oxygen pulsed detonations

The UCLA Detonation-Impulse Tube (DIT) [149], pictured in Fig. 7.8, is used to generate near-1D detonation waves via spark ignition and deflagration-to-detonation transition (DDT). The DIT is detailed in Appendix B, but key details will be repeated here. Here, the DIT is used to generate detonations using pure O_2 as the oxidizer, yielding gas composition representative of rocket combustion product gas. The tube is 183 cm long and has a 3.81-cm internal diameter. Prior to each test, the tube was vacuumed to sub-Torr pressures after which it was filled with a pure C_2H_4–O_2 mixture to a particular sub-atmospheric

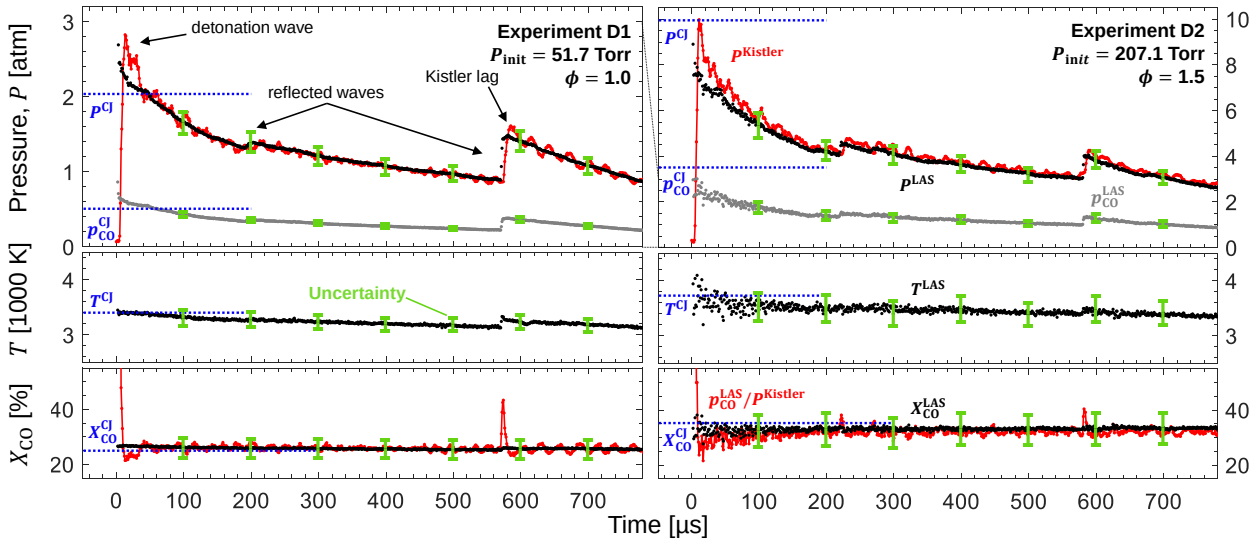

Figure 7.12: Measurements of total / CO partial pressure (*top*), temperature (*middle*), and CO mole fraction (*bottom*) for the two detonation experiments. LAS measurements are in black/gray and Kistler-derived measurements are in red. Reference lines indicating predictions from Champman-Jouguet (CJ) detonation theory are indicated in blue. Uncertainty is indicated with the green errorbars.

pressure, measured by a Baratron pressure transducer. The equivalence ratio ϕ for each experiment was set by mixing the fuel and oxidizer in a mixing manifold upstream of the detonation tube, with the flow rates of each reactant being set using MKS GE50A thermal-based mass flow controllers. After filling the tube, a valve was used to shut the tube off from the filling apparatus. The combustible mixture was ignited at one end using a spark ignition system. A Schkelkin spiral was used to accelerate DDT along the length of the tube. The presence of a detonation wave was verified comparing the detonation wave-speed predicted by Chapman-Jouguet (CJ) relations to the experimental speed derived from five piezoelectric time-of-arrival sensors located in the last 36 cm of the tube. The tube is sealed on its downstream end using a thin plastic diaphragm designed to burst upon arrival of a detonation waves. This allows for the combustion products to be evacuated into a surge tank maintained at vacuum, while also allowing for the main tube to be filled to a known pre-detonation pressure. Optical access to the detonation tube is enabled via two wedged

sapphire windows located 147 cm downstream of the tube ignition source. The Kistler pressure transducer was placed in the same plane as the optical ports to simultaneously make electromechanical pressure measurements to which the optical pressure measurements can be compared.

These experiments were simulated using a CJ detonation model implemented in CANTERA using the Caltech Shock and Detonation Toolbox and USC Mechanism Version II [142, 233, 141], providing the pressure, temperature, and gas composition for an ideal 1-D detonation wave. The predicted gas composition was used to estimate the mixture-weighted broadening coefficient γ, as done in Section 3.7.3.3.2 for deflagration combustion. The main difference here is that for detonation combustion, the pressures and temperatures are higher. The higher temperatures lead to increased dissociation of CO_2 and H_2O into smaller molecules/atoms, although some of this effect is reduced by the increased pressure.

Two representative detonation experiments are examined here. In experiment D1, the mixture is stoichiometric ($\phi = 1$) and pre-detonation fill pressure is 51.7 Torr, whereas experiment D2 is fuel-rich ($\phi = 1.5$) at higher pre-detonation fill pressure, 207.1 Torr. Figure 7.12 shows the results of experiments D1 and D2 with the same color scheme as in Fig. 7.11, with the reference CJ values plotted as blue dashed horizontal lines. After the initial rise in the measured gas properties with the passage of the detonation wave, the pressure drops by about 80% (factor 5) for both experiments over the course of 1 ms, with minor increases due to reflected waves from the diaphragm at the end of the tube. The temperature on the other hand changes by a lesser degree, on the order of 15% for experiment D1 and 25% for experiment D1. The temperature increases less dramatically than pressure across the reflected waves. The CO mole fraction does not change significantly over the test duration.

As can be expected, experiment D2 features a higher peak pressure than experiment D1, due to the higher pre-detonation pressure. The peak temperature for experiment D2 is also higher than for experiment D1 due to the decreased endothermic product dissociation at higher pressures. This effect outweighs the reduction in flame temperature when burning at fuel-rich conditions. The post-detonation CO mole fraction in experiment D2 is roughly

double that of the value in experiment D1, due to incomplete oxidation at the fuel-rich condition.

The error contributions to the pressure uncertainty are well represented by the sample C_2H_4–O_2 uncertainty breakdown presented in Fig. 7.7. Notable exceptions here include: (1) the post-detonation composition used to estimate collisional broadening is estimated from the CJ model, not from a constant-pressure combustion simulation; (2) the uncertainty in the mixture equivlance ratio is greatly reduced due to the accurate measurement of the reactant flow rate; (3) the uncertainty in the reaction progress coordinate is assumed to be negligible, as detonation combustion occurs on extremely fast time scales. As such, the uncertainty is primarily dominated by the uncertainty in the broadening parameters of the individual collision partners of CO.

The LAS measurements can be compared to the values measured by the Kistler and the CJ predictions. For experiment D1 it can be seen that both the Kistler and LAS pressure overshoot the CJ-predicted pressure, whereas for experiment D2, both peak pressure measurements closely match the CJ pressure. This can be attributed to potential pre-pressurization of the reactants before detonation passage, due to propagation of acoustic waves faster than the flame speed during the DDT process. This effect is more pronounced at lower initial pressures, due to the increased time/distance required for DDT. In a similar manner, the CO partial pressure overshoots the CJ prediction in D1 and matches the CJ prediction in D2. In both experiments, the measured post-detonation temperatures and CO mole fractions closely match the CJ predictions.

The Kistler pressure lingers near the peak pressure value for longer than the LAS pressure, due to the LAS measurement's ability to respond faster to changes in gas condition compared to the 100‘kHz filtered bandwidth of the Kistler. This effect could also be attributed to boundary-layer effects. This is especially pronounced in experiment D1. Evidence that the LAS measurement is more appropriate can be seen by looking at the CO mole fraction measurement. When using the LAS pressure to find X_{CO}, the CO mole fraction is constant after the detonation. When the Kistler pressure is used, X_{CO} starts at the CJ value, dips

below the CJ value, and returns to the CJ value afterwards in a non-physical manner.

For both experiments, after the initial pressure spike, the pressure decays substantially. At around 200 µs and 600 µs, reflected waves from the diaphragm at the end of the tube reach the measurement location and raise the pressure on the order of 10–50%. The ability of the two pressure sensors to capture the pressure changes associated with these reflected waves can be readily observed. The LAS pressure measurement responds quickly to these changes in physical pressure, whereas the Kistler measurement can be seen to lag behind by a few microseconds due to the µs-scale response time of the electromechanical sensor. This lag can be seen more clearly when looking at the X_{CO} measurements derived from these two pressure measurements. When using the LAS pressure, the X_{CO} measurement remains constant, whereas with the lagged Kistler measurement, the X_{CO} measurement non-physically spike, as the measured CO partial pressure increases behind the wave while the Kistler pressure remains roughly constant. The ringing in the Kistler measurement also leads to a lower SNR compared to the LAS measurement. The SNR of the Kistler measurement is on the order of 20 whereas the LAS pressure measurement has a higher SNR of 150. The reduced SNR of the Kistler measurement prevents it from registering the reflected wave at 200 µs. Overall, this comparison highlight the capability of the optical measurement to perform competitively with the electromechanical transducer in terms of both speed and measurement quality.

7.5 Summary

In this chapter, a high-speed optical pressure sensing strategy for dynamic combustion environments was developed based on laser absorption measurements of carbon monoxide linewidths in the mid-infrared. The single-laser, multi-line measurement technique provides for quantification of temperature, pressure, and species density simultaneously, eliminating key unknowns due to inter-dependency of these thermodynamic parameters. A thorough uncertainty-analysis framework was developed and applied to account for potential measurement error due to noise sources, spectroscopic uncertainty, and gas composition uncertainty, with cross-correlations incorporated in the analysis. The broad applicability and robustness

of the pressure measurement was shown via simulated variations in fuel, equivalence ratio, reaction progress, and other parameters. Aggregated uncertainty indicates the MHz-rate optical pressure measurement has a typical total uncertainty of approximately 10%, varying by a few percent over a large range of conditions. The most substantial uncertainty factors in this analysis are the species-specific broadening coefficients. As such, for air combustion with nitrogen as the dominant collision partner and for highly diluted gas mixtures with other inert species, the absolute uncertainty can be lower. Moreover, while absolute pressure uncertainty is limited by the ability to accurately estimate species-specific broadening coefficients, this analysis suggests that changes in pressure (dynamic pressure) will have a lower uncertainty as the directional bias would be unlikely to change for a given dynamic combustion environment. The methods outlined in this chapter and associated results allow for more specific estimation of uncertainty for a given application, and offer many useful scaling relations and guiding metrics to design LAS systems with minimized uncertainty.

The measurement technique was demonstrated in dynamic combustion experiments involving shock and detonation waves to highlight capabilities and versatility. Overall, the demonstrations indicate the ability of the pressure sensor to measure dynamically changing pressure in high-temperature air- and oxy-combustion environments with high accuracy and precision at a rate of 1 MHz, over a range of pressures and equivalence ratios. Clear advantages can be observed with the optical pressure sensor over the electromechanical pressure transducer in signal-to-noise ratio and response time. A practical advantage of overcoming boundary layer effects is shown in a shock tube experiment with shock bifurcation. The analyzed and demonstrated performance of the LAS pressure sensing strategy indicates strong potential for utilization in both laboratory and field experiments involving shock and detonation waves.

CHAPTER 8

Multi-line Boltzmann regression for near-electronvolt temperature and CO sensing via MHz-rate infrared laser absorption spectroscopy

The contents of this chapter have been published in the journal ***Applied Physics B*** *[237] under the full title "Multi-line Boltzmann regression for near-electronvolt temperature and CO sensing via MHz-rate infrared laser absorption spectroscopy".*

8.1 Introduction

At temperatures exceeding 4000 K, the line pair used to measure temperature in Chapters 4 and 5 begins to have a reduced temperature sensitivity and accordingly, the temperature measurements made using these lines become noisier and increasingly susceptible to measurement error. To combat this, a new line selection is made in a neighboring spectral region, leveraging the enhanced spectral scan depth using the waveform optimization techniques of Chapter 6. In this chapter, a mid-infrared laser absorption technique is developed for sensing of temperature and carbon monoxide (CO) number density from 2000 K to above 9000 K. To resolve multiple rovibrational lines, a distributed-feedback quantum cascade laser (DFB-QCL) is modulated across 80% of its current range using a trapezoidal waveform via a bias-tee circuit. The laser attains a spectral scan depth of 1 cm^{-1}, at a scan frequency of 1 MHz, which allows for simultaneous measurements of four isolated CO transitions near 2011 cm^{-1} (4.97 µm) with lower-state energies spanning 3,000 to 42,000 cm^{-1}. The number density and temperature are calculated using a Boltzmann regression of the four population fractions.

This method leverages the information contained in each transition and yields a lower uncertainty than using a single line pair. The sensor is validated in shock-tube experiments over a wide range of temperatures and pressures (2300–8100 K, 0.3–3 atm). Measurements behind reflected shock waves are compared to a kinetic model of CO dissociation up to 9310 K and are shown to recover equilibrium conditions. The high temperature range of the sensor is able to resolve rapid species and temperature evolution at near electronvolt conditions making it suitable for investigations of high-pressure detonation, high-speed flows, plasma applications.

8.1.1 Background for high-temperature sensing

Extreme temperatures occur frequently in combustion where, for instance, a practical rocket engine burning CH_4–O_2 at 300 bar reaches 3800 K in the combustion chamber, while detonating fuel-rich C_2H_4–O_2 mixed at 300 K and 10 atm attains 4900 K [238, 5]. Higher temperatures up to 10,000 K are obtained in industrial plasma torches [239], arc-jets [240], continuous arc discharges utilized for carbon nanotube synthesis [241, 242], and transient discharges for ignition of internal combustion engines [243, 244]. Shorter-duration arc-type discharges of several nanoseconds, employed notably for research on CO_2 conversion and plasma-assisted combustion, can present core temperatures from 1000s to 10,000s of kelvin [244, 245, 246, 247, 248]. Finally, hypersonic flows generate shock layers with temperatures in the range of 5000–10,000 K during planetary entry [249, 250]. These complex environments must be accurately characterized to inform mass-efficient thermal protection system design [251, 252].

At such extreme near-electronvolt temperatures, most physical sensors are not able to survive the associated heat flux and optical methods must be employed for in-situ detection. Within the multitude of environments aforementioned, carbon monoxide (CO) is commonly generated via oxidation of carbon or dissociation of CO_2, rendering CO an attractive optical target for gas measurements. Prior sensing of CO concentration and temperature above 3500 K has involved optical emission spectroscopy (OES), demonstrated in arc-like dis-

charges [244, 245, 246, 247, 248], plasma torches [251, 253], and shock tubes [254, 255, 252]. Emission diagnostics are well-suited to probe highly radiative sources but require optical calibration for quantitative interpretation, particularly for speciation. Laser absorption spectroscopy (LAS) can be calibration-free and highly quantitative, which makes it a valuable complement to OES at high temperatures. The advances in laser tuning rates detailed in Chapter 4 have further enabled MHz-rate LAS sensing, providing the capability to resolve high-temperature chemistry occurring at microsecond timescales [148].

8.1.2 High-speed laser absorption spectroscopy

Prior advances in high-temperature CO sensing provide a basis for the current work. CO measurements in the 3500–4000 K range were reported in shock-tube environments using LAS [256, 169]. These sensors were designed for combustion applications, with diminishing sensitivity above 4000 K and a time resolution inadequate for higher-temperature kinetics. In that context, single-line scanned LAS was developed for CO number density sensing at 100 kHz up to 8000 K, but OES measurements were needed to determine the temperature [255]. In another work, MHz single-line scanned LAS of CO demonstrated temperature measurements (2500–10,000 K) using Doppler broadening [257, 258, 153, 254]. This approach probes the translational temperature from the Doppler linewidth, but loses sensitivity at modest pressures when collisional broadening becomes substantial [257, 258, 153, 254]. These shortcomings could be circumvented using several optical transitions during one scan, the relative intensities of which depend on temperature according to the Boltzmann distribution. However, when scanning at frequencies above 10–100 kHz to track fast chemistry occurring at these temperatures, the available spectral scan-depth of tunable semiconductor lasers is reduced, such that only a single spectral feature can typically be resolved. Chapters 4 and 6 detail how this tuning limitation can be overcome with bias-tee circuitry and waveform optimization.

In Chapter 4, a bias-tee circuit was employed to diplex DC current generated from a laser controller with an RF modulation signal (AC), effectively bypassing the current-controller

bandwidth limitation (typically around 200 kHz). This modulation scheme, illustrated in Fig. 8.7, increased the scan-depth by one order of magnitude, sufficient to capture multiple rovibrational transitions of CO and CO_2 at several MHz [148]. This type of bias-tee circuit, modulated at high speeds, has also been employed in several entry-related studies where µs time resolution was needed [259, 157, 260].

Further scan-depth improvement was achieved in Chapter 6 by scanning DFB lasers below the lasing threshold and employing a squared current waveform modulation [190]. This type of modulation increased the temperature variations experienced by the laser chip within one scan and multiplied the spectral scan depth by more than 2 compared to a sine-wave modulation. Ultimately, these combined improvements resulted in a scan depth of 1 cm^{-1} at 1 MHz. This second recent advance in laser tunability enabled the development of a new CO multi-line scanned-wavelength LAS sensor presented in this chapter, able to perform accurate number density and temperature measurements at 1 MHz and in the range 2000–9000 K.

Before discussing the sensor performance, the absorption spectroscopy approach and data processing methods are presented in Section 8.2. In Section 8.3, the experimental setup is described. In Section 8.4, the sensor validation and demonstration with chemically frozen high-temperature CO mixtures is discussed. Finally, in Section 8.5, we compare the species and temperature measurements of shock-heated CO with equilibrium values and a kinetic simulation. In Appendix F, a detailed uncertainty analysis useful for line selection is conducted and the robustness of the present line selection is assessed in the case of non-uniform path-integrated temperatures. In Appendix H, uncertainty in the reflected-shock conditions generated in the demonstrations is discussed.

8.2 Methods

8.2.1 Line-selection and line-pair comparison

The methods and principles of laser absorption spectroscopy are extensively discussed in [166] and in Chapters 4 and 7. The absorbance α_i of a single line can be calculated using the incident and transmitted light intensities I_0 and I_t, respectively:

$$\alpha(\nu) = -\ln\left(\frac{I_t}{I_0}\right)_\nu. \tag{8.1}$$

For a uniform gas, the Beer-Lambert law relates the spectrally-integrated absorbance area, A_i, of a single spectral feature, i, to the CO number density, n_{CO} [cm^{-3}], the optical path-length, L [cm], and the linestrength, S_i [cm^{-1}/(molec·cm^{-2})], at the gas temperature, T [K]:

$$\int_\nu \alpha_i(\nu)d\nu = A_i = n_{CO}LS_i(T). \tag{8.2}$$

The transition lineshapes are approximated by a Voigt function. The Voigt lineshape is a convolution of the Gaussian and Lorentzian functions and is calculated using the approxi-

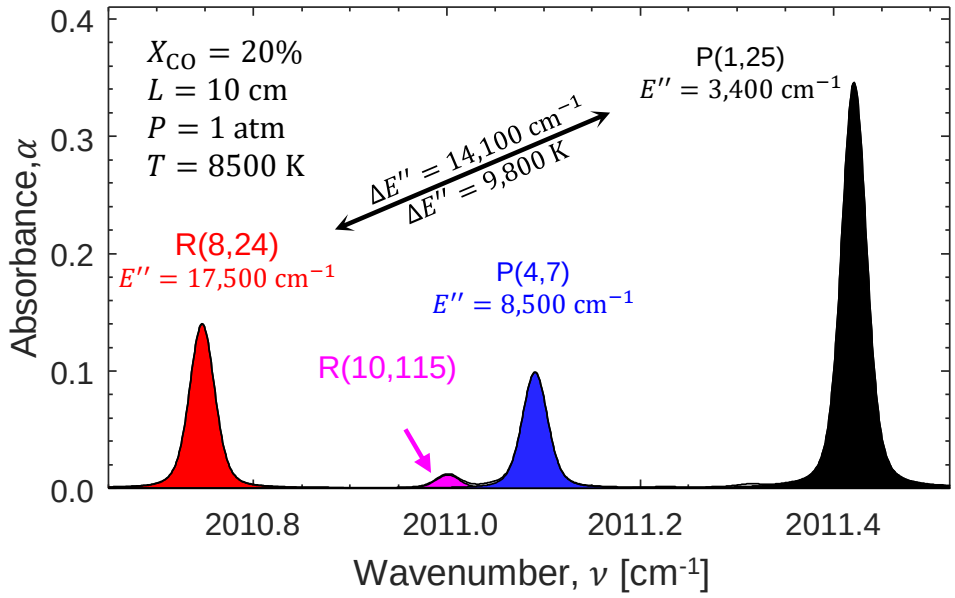

Figure 8.1: Simulated spectrum of CO on the 1-cm^{-1} range employed in this chapter with the four major lines indicated by filled areas.

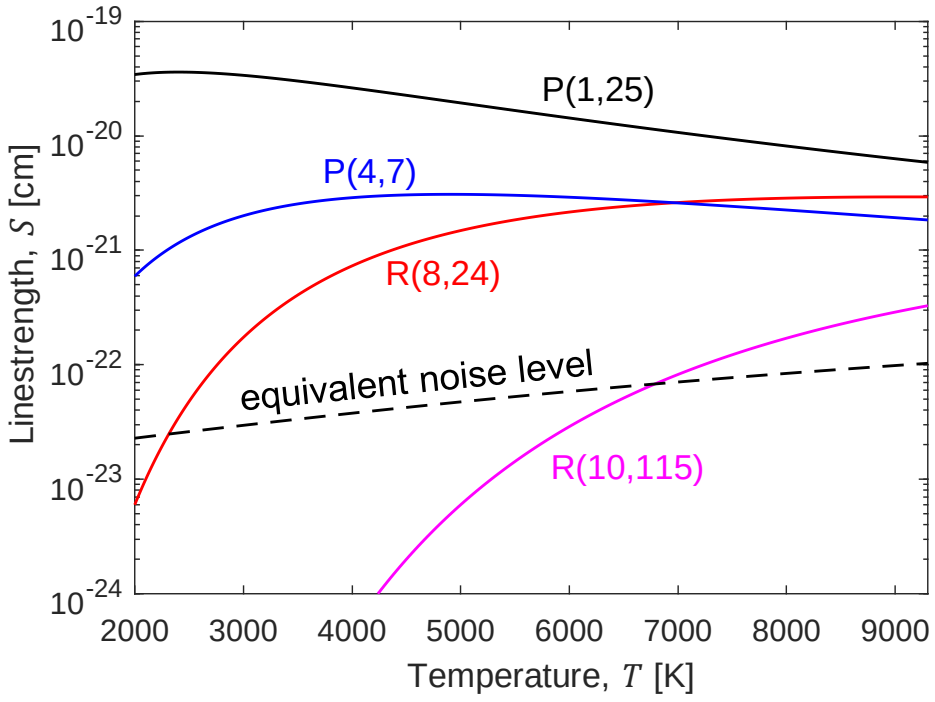

Figure 8.2: Linestrengths versus temperature of the strongest transitions in the 2010.6 - 2011.6 cm^{-1} region (∼4.97 µm). The equivalent noise level is estimated using a rectangular area, $\delta\alpha = 0.003$, $L = 10$ cm, P = 1 atm, and $X_{\text{CO}} = 10\%$.

mation of McLean [170].

In Chapters 4 and 7, CO concentration and temperature were measured using the P(2,20) and P(0,31) transitions near 2008 cm^{-1}. In this section, we show that accounting for the sensitivity of the line areas to temperature and CO number density, the 2010.6–2011.6 cm^{-1} spectral region, presented in Fig. 8.1, is favorable for temperatures above 2000 K. The linestrengths of these transitions are shown in Fig. 8.2. The complete derivation of the temperature and mole-fraction uncertainty is provided in Appendix F and only the key points are presented here. It should be noted that uncertainties are combined in quadrature in this chapter, as in Chapter 4 and unlike Chapter 7. The ratio of areas of two lines, R, is equal to the ratio of their linestrengths, solely a function of the temperature, T.

$$\frac{A_i}{A_j} = \frac{S_i(T)}{S_j(T)} = R(T). \tag{8.3}$$

After differentiation of Eqn. 8.3 and manipulation of this equation, the temperature uncer-

Table 8.1: HITEMP2019 spectroscopic data of the four main transitions utilized in this chapter (truncated values) with linestrength uncertainties given in brackets [168]

Transition	ν, cm^{-1}	S_i^0, cm	E'', cm^{-1}
R(8,24)	2010.746	$2.50 \cdot 10^{-54}$ [5-10%]	17475.86
R(10,115)	2011.000	$2.23 \cdot 10^{-106}$ [$\geq$20%]	42479.85
P(4,7)	2011.091	$3.20 \cdot 10^{-36}$ [5-10%]	8518.19
P(1,25)	2011.421	$3.26 \cdot 10^{-25}$ [1-2%]	3378.95

tainty is given by Eqn. 8.4:

$$\frac{\delta T}{T} = \frac{k_\mathrm{B}}{hc}\frac{T}{\Delta E''}\sqrt{\sum_{i=1}^{2}\left[\left(\frac{\delta S_i^0}{S_i^0}\right)^2 + \left(\frac{1}{\mathrm{SNR_{opt}}}\frac{\exp\left(\alpha_i^{\mathrm{pk}}\right)}{\alpha_i^{\mathrm{pk}}}\right)^2\right]}, \tag{8.4}$$

where k_B is the Boltzmann constant, h, the Planck constant, c, the speed of light, δS_i^0, the room-temperature linestrength uncertainty of line i, and α_i^{pk}, its peak absorbance. The spectroscopic constants of the four main transitions in the 2010.6–2011.6 cm^{-1} spectral region are given in Table 8.1. $\mathrm{SNR_{opt}}$ is the optical signal-to-noise ratio, as defined in Chapters 6 and 7. In this work, the signal-to-noise ratio reaches $\mathrm{SNR_{opt}} \sim 440$, using the root mean square noise of the raw measurement voltage, $U_{\mathrm{noise}} \sim 4.5$ mV, and the background amplitude voltage, $U_0 \sim 2$ V. As expected, a high SNR is desirable, because it will increase confidence in the measurement of the line areas, which reduces the uncertainty in the temperature measurement based on the ratio of these areas. The term $\exp\left(\alpha_i^{\mathrm{pk}}\right)/\alpha_i^{\mathrm{pk}}$ reaches a minimum around $\alpha_i^{\mathrm{pk}} = 1$. Effectively, this term indicates that the lowest line area uncertainty is reached when the peak absorbance is 1. The function $\exp\left(\alpha_i^{\mathrm{pk}}\right)/\alpha_i^{\mathrm{pk}}$ is above 5 for a peak absorbance outside the range 0.3–2.6, which mathematically shows that a spectrum that is too optically thick or thin should be avoided when possible. Finally, it should be noted that for any line pair selection, the uncertainty in the temperature measurement increases with T due to the $T/\Delta E$ factor. This increase can be compensated by choosing two lines with a high difference in their ground-state energies E''.

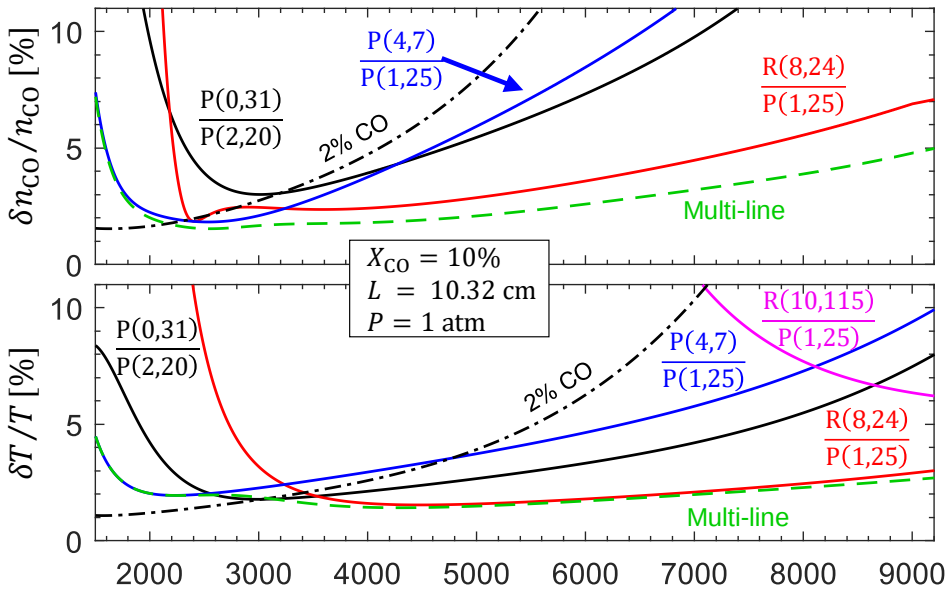

Figure 8.3: Relative temperature and number density uncertainty for given line ratios, calculated for a 10% CO mole fraction. The multi-line fit, in green, presents lower uncertainty than individual line pairs. The line pair used in Chapters 4 and 7 is shown in black at 2% and 10% CO mole fraction to highlight the different range of application of each line pair.

The number density can be derived from the Beer-Lambert law (Eqn. 8.2).

$$n_{CO} = \frac{A_i}{LS_i(T)}. \tag{8.5}$$

The differentiation of Eqn. 8.5 detailed in Appendix F provides the number density uncertainty in Eqn. 8.6:

$$\left(\frac{\delta n}{n}\right)^2 = \left(\frac{1}{\text{SNR}_{\text{opt}}}\frac{\exp\left(\alpha_i^{\text{pk}}\right)}{\alpha_i^{\text{pk}}}\right)^2 + \left(\frac{\delta L}{L}\right)^2 + \left(\frac{1}{S_i}\frac{\partial S_i}{\partial T}\delta T\right)^2 + \left(\frac{\delta S_i^0}{S_i^0}\right)^2. \tag{8.6}$$

This expression contains similar factors to the temperature uncertainty, with the addition of the linestrength derivative with respect to T, $\partial S/\partial T$, and the pathlength uncertainty $\delta L/L = 1\%$.

In Fig. 8.3, the variation of $\delta T/T$ for four line pairs is given as a function of temperature. These expressions are evaluated for a pathlength and a pressure representative of our conditions ($L = 10.32$ cm, $X_{CO} = 10\%$, and $P = 1$ atm), but can be easily applied to

other conditions. The previous line selection used by our group near 2008 cm^{-1}, P(0,31) / P(2,20), is shown in black for 2% and 10% mole fractions. At 2% concentration, these lines show their best temperature sensitivity in the 1000–4000 K region, where they were used in Chapters 4 and 7. However, above this range, their sensitivity decreases because their peak absorbance decreases. Using a CO mole fraction of 10%, this line pair can be used at higher temperatures but its sensitivity still degrades above 5000 K. Note that a neighboring line, P(3,14), is blended with P(0,31). The perturbation induced by the P(3,14) line can be taken into account to add another contribution to the uncertainty analysis, see Appendix F.0.3. For the above reasons, in this Chapter, we use the region 2010.6–2011.6 cm^{-1} to probe the P(1,25), R(10,115), P(4,7), and R(8,24) transitions that are spectrally isolated from each other. The R(10,115) / P(1,25) line pair presents the largest energy difference, $\Delta E'' \approx 39,000$ cm^{-1}, but cannot be used solely to retrieve thermodynamic properties, essentially due to the uncertainty of the R(10,115) linestrength and its low absorbance level below 7000 K. The P(4,7) / P(1,25) line pair reaches its best sensitivity near 2000 K which is suitable for many combustion applications. The R(8,24) / P(1,25) line pair is more suited for higher temperature, 2000–9000 K, leveraging the large lower-state energy difference of R(8,24) and P(1,25), $\Delta E'' \approx 14,100$ cm^{-1}. This line pair is the key to extending the temperature range of this sensor. Therefore, using two-line area ratios from 2000 K to 8000 K, the 2010.6–2011.6 cm^{-1} region provides a temperature uncertainty better than 2% and a number density uncertainty better than 6%. The best range for each line pair is leveraged and the sensitivity is improved by accounting for all of them in the Boltzmann-plot fitting procedure described in the next section.

8.2.2 Boltzmann-population fit

In this chapter, instead of using a single line pair, we leveraged the rovibrational state population information provided by the four lines fitted in the 2010.6–2011.6 cm^{-1}, see Fig. 8.4. The linestrength of a single transition i is a function of temperature, T, the partition function $Q(T)$, the ground state energy of the transition E_i'', the wavenumber of

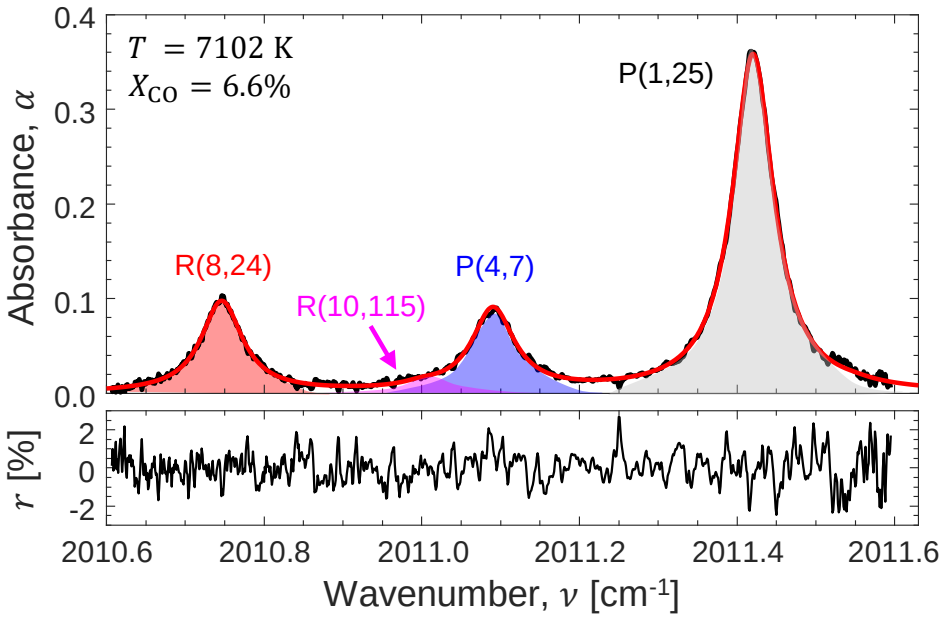

Figure 8.4: Typical fit of the CO absorption spectrum between 2010.6 and 2011.6 cm^{-1}.

the transition ν_i, and a reference temperature usually taken at $T_0 = 296$ K [166, 205].

$$S_i(T) = S_i(T_0)q(T,\nu_0)\exp\left[-\frac{hcE_i''}{k_B}\left(\frac{1}{T}-\frac{1}{T_0}\right)\right]. \tag{8.7}$$

To shorten the mathematical expressions, the reference linestrength will be noted $S_i^0 = S_i(T_0)$. The term $q(T,\nu_0)$ accounts for partition function variation multiplied by a stimulated emission factor:

$$q(T,\nu_0) \approx q(T) = \frac{Q(T_0)}{Q(T)}\frac{1-\exp\left(-\frac{hc}{k_B T}\nu_0\right)}{1-\exp\left(-\frac{hc}{k_B T_0}\nu_0\right)}. \tag{8.8}$$

We used the average wavenumber, $\nu_0 \approx 2011$ cm^{-1}, to calculate $q(T)$, which is a valid approximation[1] of the stimulated emission factor within 0.1%, such that $q(T)$ is treated as the same for all the measured spectral transitions. The line-by-line spectral information, see Table 8.1, and the partition function are retrieved from the 2020 CO HITEMP database [261, 262]. Taking the natural logarithm of Eqn. 8.7, we obtain:

$$\ln(S_i(T)) = \ln\left(S_i^0\right) + \ln(q(T)) - \frac{hc}{k_B}E_i''\left(\frac{1}{T}-\frac{1}{T_0}\right). \tag{8.9}$$

[1]This approximation is valid for any lines that are spectrally close. For spectral separation higher than 1 cm^{-1}, the impact of this approximation would have to be recalculated.

Equation 8.2 can be combined into Eqn. 8.9 to show the number density dependence:

$$\ln\left(\frac{A_i}{S_i^0}\right) = \ln(Ln_{\mathrm{CO}}q(T)) + \frac{hc}{k_{\mathrm{B}}}\left(\frac{1}{T_0} - \frac{1}{T}\right)E_i''. \tag{8.10}$$

This linear relation is a direct representation of the Boltzmann distribution of CO internal states and it can be shown[2] that A_i/S_i^0 is related to the degree which the lower state of the transition i is populated (relative to the population at T_0).

Equation 8.10 has a linear form $Y_i = aE_i + b$ with

$$Y_i = \ln\left(\frac{A_i}{S_i^0}\right), \tag{8.11}$$

$$a = \frac{hc}{k_{\mathrm{B}}}\left(\frac{1}{T_0} - \frac{1}{T}\right), \tag{8.12}$$

$$b = \ln(n_{\mathrm{CO}}Lq(T)). \tag{8.13}$$

An example of a Boltzmann distribution fit is given in Fig. 8.5. The temperature and number density can then be solved using:

$$T = \frac{1}{1/T_0 - ak_{\mathrm{B}}/hc}, \tag{8.14}$$

$$n_{\mathrm{CO}} = \frac{\exp(b)}{Lq(T)}. \tag{8.15}$$

The linear function coefficients, a and b, can be fitted accounting for uncertainty propagation [263] and, following the methods derived in Appendix F (see Eqn. F.2), the temperature uncertainty is:

$$\frac{\delta T}{T} = \frac{k_{\mathrm{B}}}{hc}T\delta a. \tag{8.16}$$

The derivation of δn_{CO} from the differentiation of Eqn. 8.15 is not as straightforward because the terms a and $q(T)$ are correlated. Therefore, with the knowledge of temperature

[2]The line area is proportional to the linestrength, which is proportional to n_i'', the lower-state population of transition i, i.e., $A_i \propto S_i(T) \propto n_i''$ [205, 166]. Thus, the term A_i/S_i^0 scales intuitively with the ratio of the transition lower-state population at T and T_0:

$$A_i/S_i^0 \propto n_i''(T)/n_i''(T_0).$$

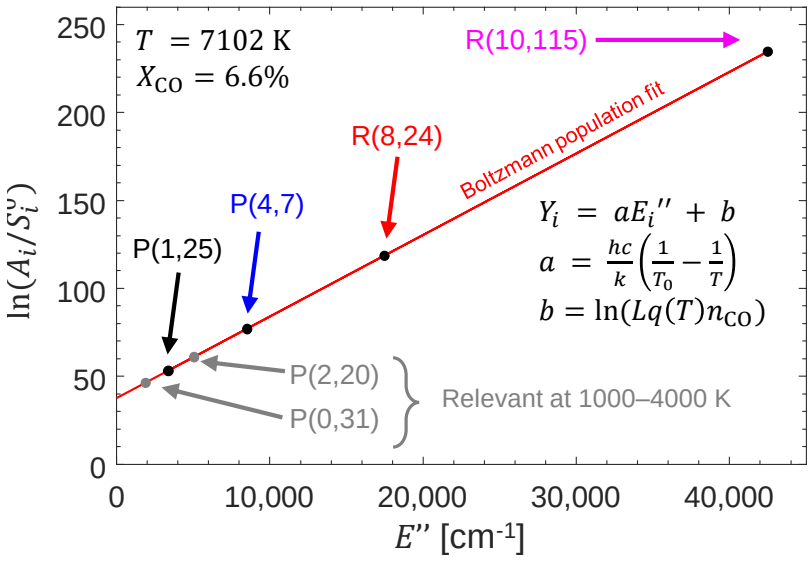

Figure 8.5: Boltzmann plot of the four rovibrational states fitted in Fig. 8.4. Error bars are too small to be visible but are propagated during the linear fit following the method of York et al. [263].

determined in Eqn. 8.14, the linestrength, $S(T)$ can now be calculated and used in the Beer-Lambert law repeated here for clarity:

$$A_i = n_{\mathrm{CO}} L S_i(T). \tag{8.2}$$

Equation 8.2 presents the form $A_i = a'S_i + b'$. In the present fitting procedure, the intercept b' is not fixed to 0 and is used to verify the validity of the fit. Fitting Eqn. 8.2 and accounting for uncertainty propagation [263], see Fig. 8.6, n_{CO} and δn_{CO} can be determined:

$$n_{\mathrm{CO}} = \frac{a'}{L}, \tag{8.17}$$

$$\left(\frac{\delta n_{\mathrm{CO}}}{n_{\mathrm{CO}}}\right)^2 = \left(\frac{\delta a'}{a'}\right)^2 + \left(\frac{\delta L}{L}\right)^2. \tag{8.18}$$

Using either Eqn. 8.15 or Eqn. 8.17 provides the same number density. However, the uncertainty derivation is more straightforward from Eqn. 8.17 and avoids dealing with correlated variables.

Therefore, in this work, Eqs. 8.14 and 8.16 are used for temperature measurements, whereas Eqs. 8.17 and 8.18 are used for number density. Assuming the same uncertainties

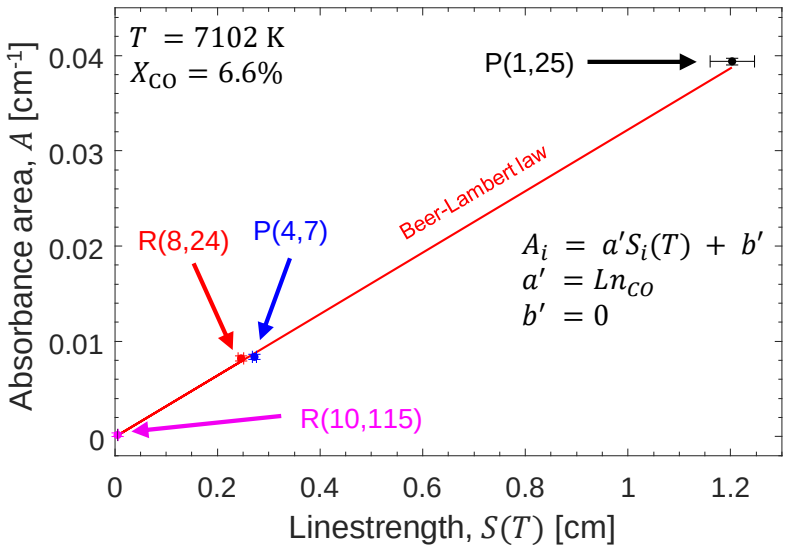

Figure 8.6: Fit of the Beer-Lambert law accounting for error-bars across the four transitions fitted in Fig. 8.4.

employed previously for the line-pair comparisons ($\delta S_i^0/S_i^0$, $\delta A_i/A_i$, and $\delta L/L = 1\%$), the uncertainty of the multi-line fit is calculated in Fig. 8.3. For $T \leq 2000$ K, the temperature and number density sensitivity is dominated by the P(4,7) / P(1,25) pair because the other transitions are too weak. In this case, the multi-line method is mathematically equivalent to the conventional two-line method and provides identical values and uncertainty. For $T \geq 2000$ K, the multi-line fit takes advantage of the P(4,7), P(1,25), and R(8,24) transitions and provides a lower uncertainty than any transition pair, whereas the R(10,115) transition improves the uncertainty for $T \geq 7000$ K. The sensitivity improvement is particularly visible in the number density uncertainty, which is below 4% across the 2000–8000 K range. To summarize, this multi-line fitting technique presents the advantage of leveraging all of the spectral information and provides: (1) A better uncertainty in temperature and number density than using a single line pair, see a comparison in Fig. 8.3. (2) A unique one-step post-processing technique across the entire range of temperature explored in this chapter.

It should be noted that rotational and vibrational temperatures could be measured independently given that at least three different vibrational levels are probed in this spectrum.

The rovibrational distribution is ideal given that the P(1,25) / R(8,24) line pair is mostly sensitive to vibrational temperature across seven vibrational levels, while the combination of the vibrational temperature and the P(1,25) / P(4,7) pair can be used to retrieve the rotational temperature. The opportunity to leverage the wide spacing in vibrational levels offered by this spectral range is however beyond the scope of this work.

8.2.3 Fitting procedure

In this section, the fitting procedure of each measurement is detailed. The entire 2010.6–2011.6 cm^{-1} spectrum is fitted by four Voigt functions, see Fig. 8.4. The area and broadening of these lines are varied until the sum of the squared difference (residual) between the experiment and the simulation reaches a minimum. A baseline is also fitted and subtracted from the experimental spectrum to account for potential background variations (beam steering, emission, laser fluctuation, etc.). Similar results are obtained with a constant or a linear baseline[3]. The spectra are fitted using Voigt profiles which provided satisfactory noise-level residuals. During the fitting loop, a single Gaussian width is floated across the entire spectrum. The collisional broadening is floated independently for the four lines and, as a verification of the fit quality, is found to track the trend of the pressure variations measured by the shock-tube piezoelectric pressure sensor. As demonstrated in Fig. 8.4, the residual normalized by the peak absorbance is typically within 2%.

Once the areas of the four main transitions are retrieved, a Boltzmann-population fit is performed using the algorithm of York et al. [263]. An example of a Boltzmann-distribution fit is shown in Fig. 8.5, corresponding to a temperature $T = 7102$ K. In this figure, the energy difference of the current line selection can be readily compared to that of the previous line pair used for combustion sensing in the 2000–3000 K range [190]. The temperature is calculated using Eqn. 8.14 and the temperature uncertainty is calculated using Eqn. 8.16. Then, the Beer-Lambert law in Eqn. 8.2 is fitted for the four measured areas to retrieve the CO number density, through Eqn. 8.17, and the corresponding uncertainty, through

[3]The effect of varying baseline fitting is explored in Appendix E.

Eqn. 8.18. An example is shown in Fig. 8.6, where the Beer-Lambert law is fitted from the data of Fig. 8.4. In this particular case, the constant of the linear fit, b', is close to zero which indicates the accuracy of the measurement.

8.3 Experimental setup

Controlled experiments at high temperatures were performed to validate the aforementioned methods and demonstrate capability. Extreme temperatures are often generated in laboratory settings using plasma torches, arc-jets, and shock tubes [239, 264, 240]. Among these devices, shock tubes can generate the highest temperatures across a range of pressure with high certainty in gas composition and thermodynamic state. Due to these advantages, shock tubes are well-suited for developing and validating a laser absorption sensor. In this study, the UCLA high-enthalpy shock tube (HEST), extensively described in previous works [265, 209] and presented in Fig. 8.7, is used to generate temperature and pressure conditions across 2000–12,000 K at 0.3–3 atm. Incident shock waves at speeds of 1.7–2.5 km/s are generated in gas mixtures of 5-20% CO–Ar. Helium is used as a driver gas. Before each shock, the driven section is turbo-vacuumed to less than 500 µTorr. The shock-wave time-of-arrival is measured by five piezoelectric sensors (Dynasen, CA-1135) located in the driven section. LAS measurements are conducted 2 cm from the shock-tube end wall through two 0.5-deg wedged sapphire windows. The reflected-shock conditions are calculated using normal shock relations, assuming vibrational equilibrium conditions in the incident shock [211].

A stainless-steel mixing tank is used to prepare the gas mixtures manometrically. The tank is vacuumed down to less than 20 mTorr before preparing the mixtures. The purity of CO and Ar gases is certified above or equal to 99.99% by Airgas. The combined pressure and gas-purity uncertainties result in a relative mixture-composition uncertainty always below 0.05%. Thus, the uncertainty of the reference mixture is assumed to be negligible.

The optical setup is schematically presented in Fig. 8.7. The mean current and temperature of a quantum cascade laser (Alpes Lasers) is regulated using a laser controller (Arroyo

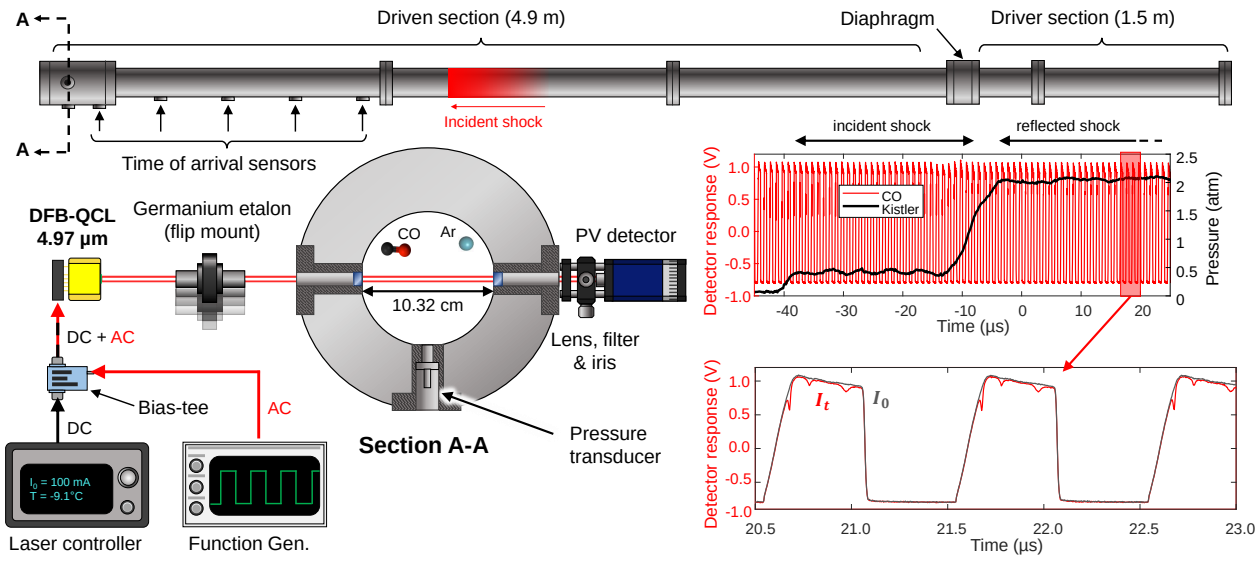

Figure 8.7: *Left*: Optical alignment setup mounted on the UCLA high-enthalpy shock tube (HEST). *Right*: Sample raw detector and pressure measurements. In the inset, the time-resolved measurements (in red) are compared with the averaged background (in grey).

6310). A fixed (DC) current is sent to the laser via the controller, while a 1-MHz modulation is added to this DC component with a bias-tee circuit [148]. In these demonstrations, we modulated the laser with a trapezoidal waveform which presents a larger spectral scan-depth compared to sine or sawtooth modulations [190]. The current amplitude is set to 80% of the maximum allowed by the laser manufacturer. This setting represents a compromise between hardware safety and spectral scan-depth, reaching 1 cm^{-1}. The trapezoidal waveform, shown in Fig. 7, presents a ramp on the increasing side. This ramp prevents the temporal frequency content of the raw electrical signal from being higher than the limiting bandwidth of the detection system (200 MHz) when narrow absorption features are present in the scan. Following the recommendations of [190], we ensured that the equivalent time to scan an FWHM of the CO line is below 10 ns (twice 1/200 MHz).

The detection is performed by a photovoltaic (PV) detector (Vigo, PVI-4TE-5-1x1, 10 Hz–205 MHz bandwidth) whose output is sent to a Tektronix oscilloscope (MSO44 model, bandwidth 200 MHz) sampling the data at 6.25 GS/s on a 12-bit scale. The laser beam is

focused on the detector chip using an AR-coated calcium-fluoride lens (20-mm focal length) and the broadband emission of the shock-heated plasma is attenuated by a narrow band-pass filter near 5 µm. The raw data acquired on the oscilloscope are presented in Fig. 8.7 and synchronized with the pressure measurement performed by a high-speed pressure transducer (Kistler, 601B1). An inset of Fig. 8.7 gives a comparison between the average background laser intensity recorded before the incident shock arrival, I_0, and the time-resolved transmitted laser intensity measured by the detector, I_t. The methods for conversion of I_0 and I_t into physical measurements were presented in the previous section. Validation and demonstration of sensor capabilities are presented in the following sections.

8.4 Sensor validation

In this section, a set of shock-tube measurements serve to validate the sensor presented in this chapter. The temperature and CO number density are compared to the values predicted by ideal-reflected shock relations from 2300 to 8100 K. The simulation of an atmospheric gas at equilibrium shows that pure CO will be dissociated by more than 20% above 6000 K [5]. Thus, for a shock-heated gas below 6000 K, the timescale of CO kinetics (mainly dissociation) is long enough to be neglected during the test time (on the order of 100s of µs). For temperatures above 6000 K, only the first few microseconds after the reflected shock are used for the temperature validation. The negligible effect of CO dissociation is ensured by comparing the post-shock CO number density with its expected level.

As an initial demonstration of the sensor, the upper panel of Fig. 8.8 shows the measured temperature, $T_{\mathrm{CO}}^{\mathrm{meas}}$= 4018 ± 53 K, and the temperature calculated using normal shock relations, T_5 = 4012 ± 130 K . The uncertainties of the shock-heated gas thermodynamic properties are calculated by numerically evaluating a Taylor expansion of the normal shock relations (see Eqn. F.2 in Appendix H) [211]. The uncertainties on the initial driven section fill pressure (p_1), the driven mixture composition, and the initial temperature have a negligible impact on the T_5 and p_5 uncertainty, which are mostly dominated by the shock speed uncertainty (1360 ± 15 m/s in this example). In the computation of T_5, we assume

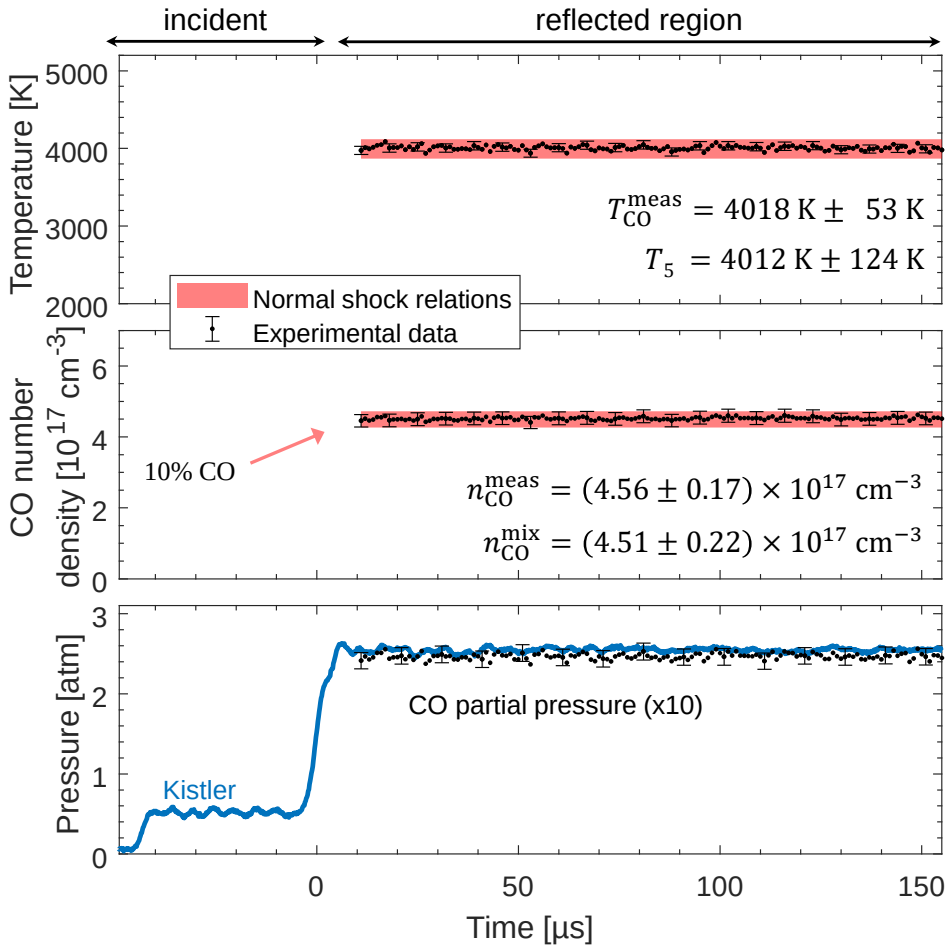

Figure 8.8: Demonstration of the measurement accuracy and precision in a non-reacting case. The red swath represents the shock relation accuracy: 2% for the temperature (T_5) and 5% for the CO number density (from T_5 and p_5).

that this incident-shock region is vibrationally relaxed before the arrival of the reflected shock. However, in the incident region, the areas of the probed transitions are sometimes not completely at steady state before the reflected shock, which indicates partial vibrational relaxation. Assuming a vibrationally-frozen incident shock would slightly reduce T_5 by only 1-2% because the mixture is mainly composed of argon. Given that the incident shock is at least partially relaxed, this contribution to the uncertainty on T_5 is assumed to be at most 1%. The resulting uncertainty is near 3% for T_5, and 4% for p_5, which is representative of all the conditions explored in this chapter. In the present example of Fig. 8.8, $T_5 = 4012 \pm$

124 K which matches the value measured by LAS.

In the middle panel of Fig. 8.8, the measured number density of CO is also compared with the mixture composition. The CO number density in the reflected region is calculated based on the ideal gas law and the normal shock calculations:

$$n_{\mathrm{CO}}^{\mathrm{mix}} = X_{\mathrm{CO}} \frac{p_5}{k_{\mathrm{B}} T_5}. \tag{8.19}$$

Therefore, as shown in Eqn. 8.20, the p_5 and T_5 uncertainties propagate to the reference CO number density and give $n_{\mathrm{CO}}^{\mathrm{mix}} = (4.51 \pm 0.22) \times 10^{17} \mathrm{cm}^{-3}$.

$$\frac{\delta n_{\mathrm{CO}}^{\mathrm{mix}}}{n_{\mathrm{CO}}^{\mathrm{mix}}} = \sqrt{\left(\frac{\delta p_5}{p_5}\right)^2 + \left(\frac{\delta T_5}{T_5}\right)^2}. \tag{8.20}$$

This value matches the measured number density, $n_{\mathrm{CO}}^{\mathrm{meas}} = (4.56 \pm 0.17) \times 10^{17} \mathrm{cm}^{-3}$, calculated

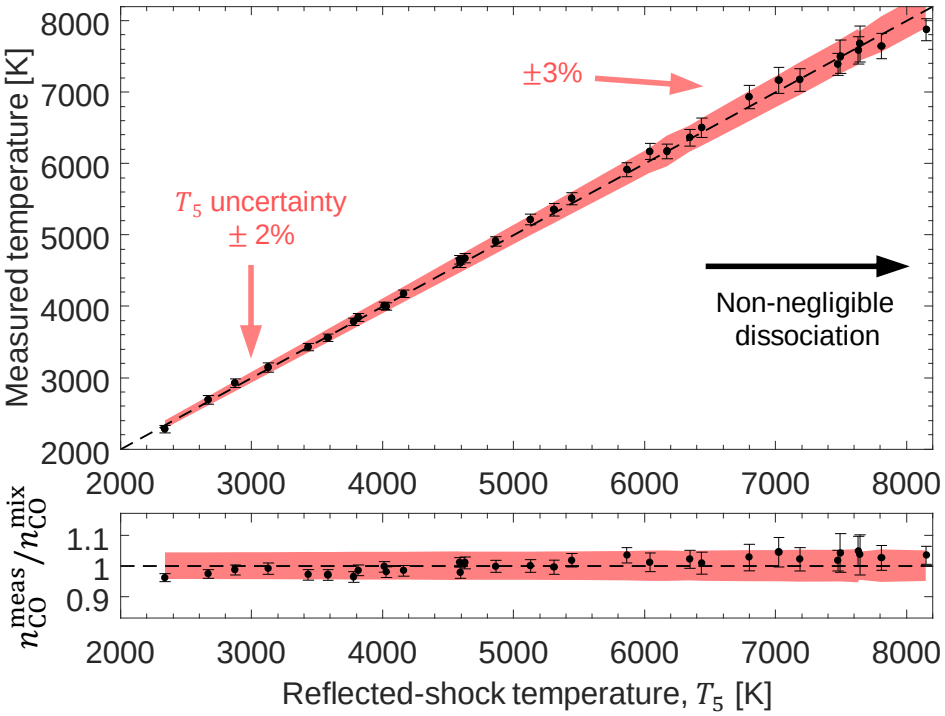

Figure 8.9: Measured temperatures and CO number densitys compared with those predicted by normal shock relations. The uncertainties of the normal-shock predictions are represented by a red swath.

using Eqs. 8.17 & 8.18. Details regarding the T_5 and p_5 uncertainty calculation are given in Appendix H.

Similar measurements of T and n_{CO} are performed for temperatures ranging from 2300 to 8100 K and compared to T_5 and $n_{\mathrm{CO}}^{\mathrm{mix}}$. The results, summarized in Fig. 8.9, show that the measured temperatures and number densities match the values determined by normal-shock relations within their uncertainties. From 2300 to 8100 K, the typical T_5 uncertainty increases from 2 to 3% and the CO number density uncertainty increases from 4 to 5 %. Further validation above 8100 K would be difficult to perform because the typical timescale of CO dissociation becomes comparable to 1 µs, the time resolution of this measurement. Quasi-steady-state conditions could be achieved with lower pressures (to slow the impact of dissociation) but would require a longer absorption pathlength (for improved SNR).

8.5 Sensor demonstrations

In this section, two time-resolved sensing demonstrations are performed to resolve thermochemical kinetics at high temperatures and the sensor performance is discussed.

8.5.1 CO dissociation above 8000 K

Above 8000 K, CO-dissociation effects can be readily observed. The temperature and number density measured for a 10% CO–Ar mixture shock-heated near 9800 K are shown in Fig. 8.10. For an initial pressure at $p_5 = 2.09$ atm, the CO number density drops and stabilizes after approximately 100 µs. At these conditions, the vibrational relaxation time is below 0.2 µs [266, 267]. In 100 µs, the temperature drops from 9000 K to 7000 K primarily due to the endothermic dissociation of CO. The partial pressure of CO ($p_{\mathrm{CO}} = n_{\mathrm{CO}} k_{\mathrm{B}} T$) is compared to the pressure reading of the piezoelectric sensor (Kistler) in the lower panel of Fig. 8.10 to quantitatively indicate the dissociation of CO. To emphasize the effect of kinetic CO dissociation, p_{CO} is rescaled to account for the initial CO dilution. At the end of the test time, t = 200 µs, the mole fraction of CO has dropped from 10% to nearly 5%.

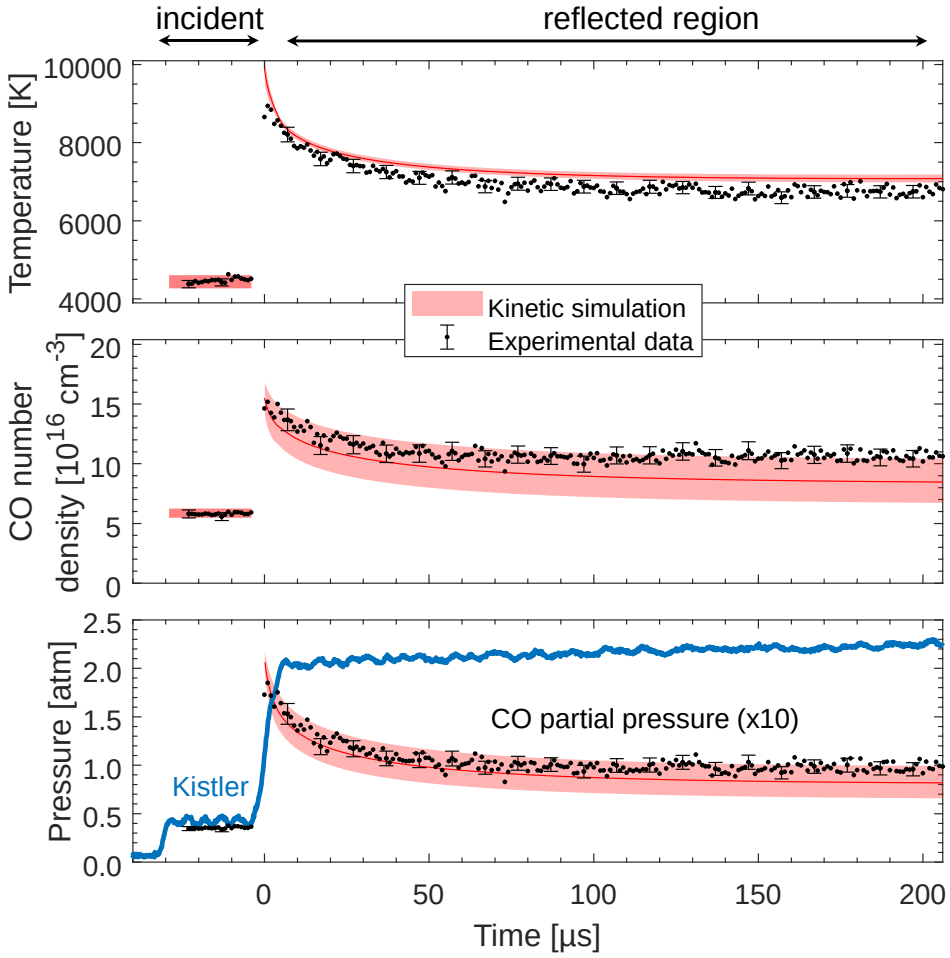

Figure 8.10: Reacting case showing CO dissociation for T_5= 9892 K, p_5 = 2.09 atm, and X_{CO} = 10%. The red swaths represent the uncertainty propagation of T_5 and p_5 in the 0-D kinetic modeling.

The measurements are compared to a 0-D kinetic simulation performed in Cantera [142] based on the high-temperature kinetic mechanisms of Johnston et al. [268] and Cruden et al. [254]. In the work of Cruden et al., relaxation temperatures measured by OES behind incident shock waves in pure CO were utilized to select two reaction sets for incident shock waves in the 3.4–6.6 km/s range (T below $\sim$ 6000 K) and 6.6–9.5 km/s range (T above $\sim$ 6000 K). The kinetic mechanism optimized for T above $\sim$ 6000 K, is employed as a baseline with the inclusion of the CO dissociation by Ar taken from Johnston et al.:

$$\mathrm{CO + Ar \longleftrightarrow C + O + Ar.} \tag{R1}$$

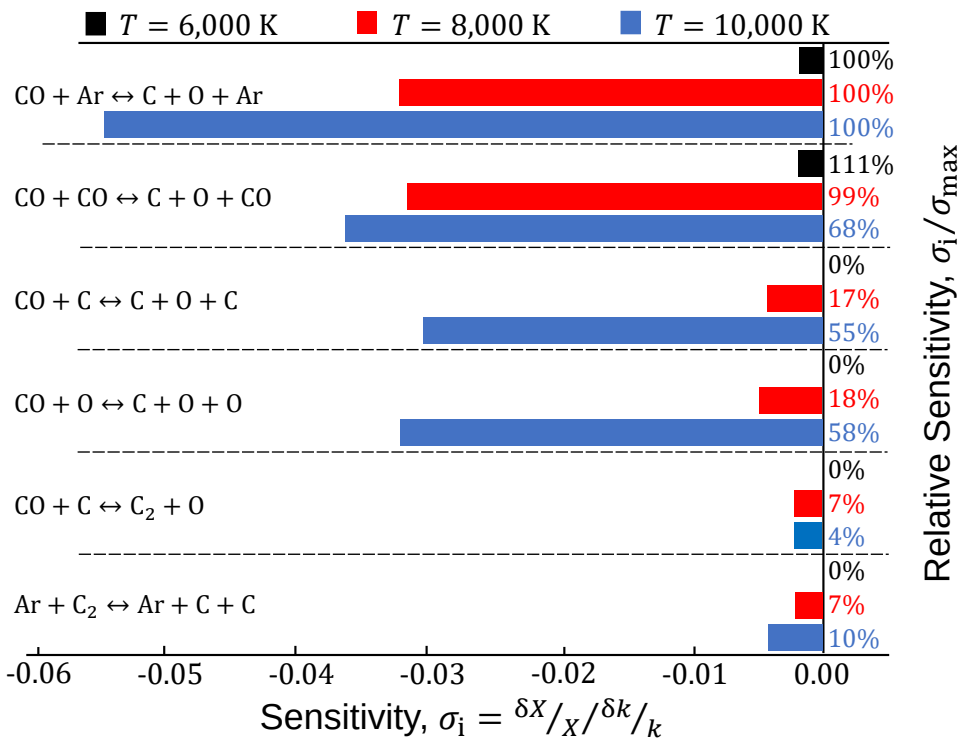

Figure 8.11: Sensitivity of CO yield at $p_5 = 2$ atm for $T_5 = 6000$, 8000, and 10000 K in a 10% CO–Ar mixture. The relative sensitivity of each reaction compared to (R1) is shown on the right panel (in %).

A Cantera 0-D constant-pressure reactor simulates the shock-heated gas. The reactor pressure and temperature are updated in the simulation time loop according to an isentropic compression law to account for the slight pressure increase measured by the piezoelectric sensor (+1 mbar/100 µs). In Fig. 8.10, our measurements are compared to a Cantera simulation performed at T_5 and p_5. Additional simulations are performed at the bounds of the combined T_5 and p_5 uncertainties and are represented by a red swath in Fig. 8.10. Note that the kinetic rate uncertainties are not included in this work. The numerical and experimental trends globally agree, with temperature and CO partial pressure dropping. For t $\geq$ 100 µs, the simulated temperature decreases slightly slower than the experimental ones, whereas the simulated CO partial pressure decreases faster than the experimental ones.

In the present chapter, sensitivity σ_i of reaction i is defined in Eqn. 8.21 where $\delta X_{\mathrm{CO}}/X_{\mathrm{CO}}$

is the relative change of CO mole fraction for a given relative change in the reaction rate k_i, $\delta k_i/k_i$.

$$\sigma_i = \frac{\delta X_{\mathrm{CO}}/X_{\mathrm{CO}}}{\delta k_i/k_i}. \tag{8.21}$$

In this case, the sensitivity is evaluated for $\delta k_i/k_i = 0.5$ and $\delta k_i/k_i = 2$. The average sensitivity of these two cases is presented in Fig. 8.11 to identify the main reactions at work. The sensitivities are calculated at $P = 2$ atm and $X_{\mathrm{CO}} = 10\%$ and qualitatively represent the 0.3–3 atm range explored in this study. As could be predicted for a highly diluted CO mixture, CO dissociation is driven by CO–Ar collisions (R1). However, the reaction rate of CO–CO collisions (R2) is one order of magnitude higher than that of (R1) and also plays a key role in the dissociation kinetics.

$$\mathrm{CO} + \mathrm{CO} \longleftrightarrow \mathrm{C} + \mathrm{O} + \mathrm{CO}. \tag{R2}$$

The slight deviation between experimental and numerical results suggests that further tuning of these rates could be performed in future work using this sensor. Other reactions are less dominant until a temperature of 10,000 K is reached, which is treated in the next subsection.

8.5.2 CO dissociation above 9000 K

In a second example presented in Fig. 8.12, the normal shock relations predict reflected conditions near 12,000 K and 3 atm. At these extreme conditions, the vibrational relaxation time is shorter than 0.1 µs [266, 267]. The effect of the kinetic dissociation is directly visible in this plot with a significant decrease in temperature ($\Delta T = 4{,}000$ K), CO number density, and CO partial pressure in less than 50 µs. A fast initial temperature drop of 200 K/µs is recorded, which can be observed accurately with the MHz-rate capabilities presented in this work.

It can be noted that the transition between the incident- and reflected-shock regions takes approximately 4 µs. This effect is a direct result of a shock bifurcation, where an oblique shock propagates in the shock-tube boundary layer and precedes the normal reflected shock in the bulk flow [235]. The boundary-layer effect is typically more pronounced with

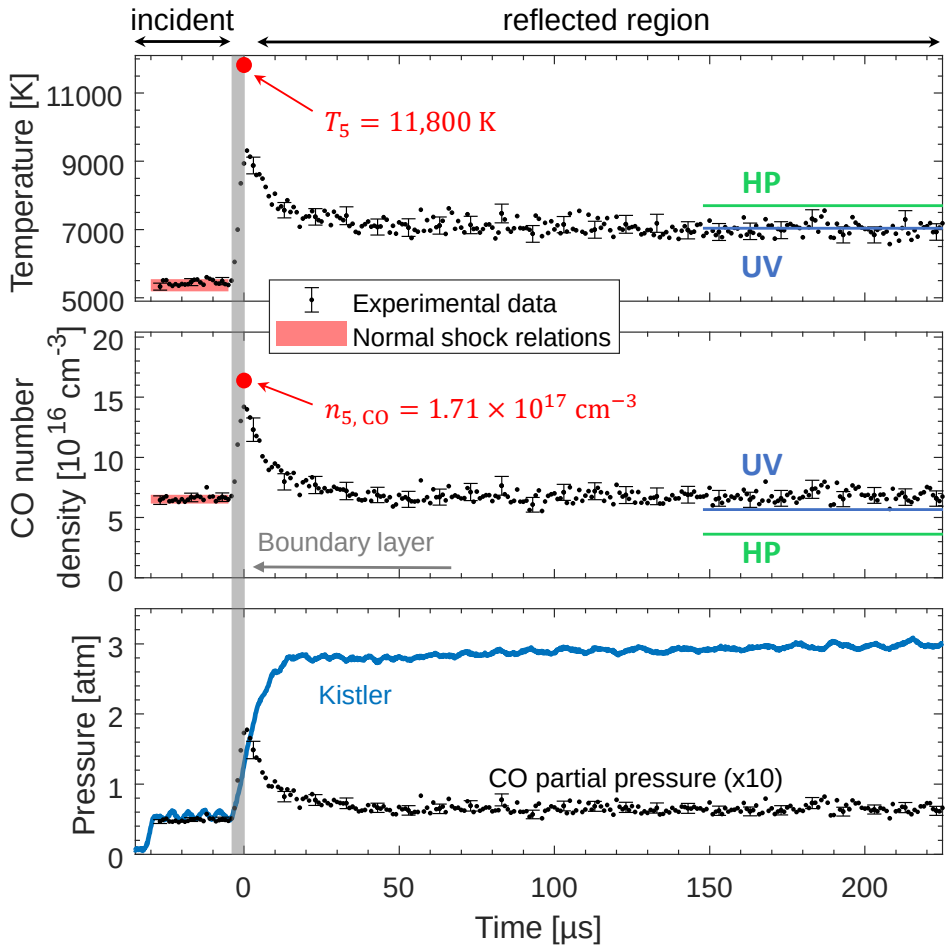

Figure 8.12: Reacting case showing CO dissociation for T_5= 11,880 K, p_5 = 2.84 atm, and X_{CO} = 10%. The solid lines represent the equilibrium values for a constant HP reactor (blue) or constant UV reactor (green).

increasing specific heat ratio and shock Mach numbers. The shock bifurcation induces a moderate beam steering effect (compared to the normal shock beam steering) but can be recorded [235]. Therefore, following the recommendations of Peterson and Hanson [235], we set the zero time using the laser scan presenting the strongest beam steering. The period of moderate beam steering preceding the zero time lasts for 4 μs and corresponds to the temperature increase period reported in Fig. 8.12. The values reported in this short period are therefore due to shock bifurcation and averaged along the beam-path. The measured temperatures are representative of the path-averaged temperature, see supporting validations

in Appendix F.1.

As demonstrated in Fig 8.11, reactions other than (R1) and (R2) are non-negligible above 10,000 K. Other reactions, such as C and O ionization by electron impact also play a role in the CO dissociation. These reaction rates are highly sensitive to the electron temperature, which is equilibrated to the translational temperature in CANTERA. The electron temperature is however known to lag behind the translational temperature [269, 270], which complicates the kinetics beyond this work's scope. Therefore, these measurements are compared to the equilibrium thermodynamic state calculated assuming constant enthalpy and pressure (HP) and constant internal energy and volume (UV), which are good approximations of the 0-D behavior of shock-heated mixtures [271]. The steady-state measurement is close to the UV case and deviates from the HP equilibrium. In this case, the UV approximation is better than the HP one. This could probably be due to the slight pressure increase in the reflected region (2% increase per 100-µs period).

Note that two temperatures of 9129 and 9310 K are reported in Fig 8.12, above the maximal tabulated temperature of the HITRAN partition function (9000 K). For these measurements, the partition function is linearly extrapolated, adding uncertainty to the number density measured at these two points. However, the temperature measurement is not dependent on the partition function. As such, despite the difficulties of validation, this sensor is suitable for temperatures well above 9000 K, near 1 eV.

8.6 Summary

A mid-infrared laser absorption sensor was developed for CO number density and temperature sensing at temperatures higher than 2000 K relevant for detonation-combustion, arc-plasma, and planetary-entry applications. Using a DFB-QCL laser, the multi-line spectrum is scanned at 1 MHz using RF-diplexing of the laser current injection and waveform tailoring. Novel line selection near 2011 cm^{-1} (4.97 µm) presents four distinct rovibrational transitions spectrally separated across $\sim$1 cm^{-1}. Compared to other line selections more adapted for

low-pressure and airbreathing combustion environments, these transitions present improved temperature and number density sensitivity at these extreme temperatures, as supported by uncertainty analysis. The temperature and number density are determined by performing a fit of the rovibrational CO Boltzmann distribution across $\Delta E''_{\max} = 39,000$ cm^{-1}. This method presents a more versatile fitting procedure and provides lower measurement uncertainties compared to using a single pair of lines that is adapted for a narrower range of temperature. The mid-range of the sensor performance exhibits uncertainty of approximately 2% in temperature and 3-4% in CO number density. In addition, the Boltzmann-population fitting of the selected transitions is more robust to temperature non-uniformity, as indicated in Appendix F.1. The precision and accuracy of the sensor are validated by shock-tube measurements from 2300 to 8100 K. The sensor utility is demonstrated during CO dissociation at near-electronvolt temperatures, matching a kinetic simulation and measuring temperatures up to 9310 K.

CHAPTER 9

Conclusions and future work

In this thesis, high-speed optical diagnostics were used and developed to gain insight on the operation of rotating detonation rocket engines.

In Chapter 2, high-speed imaging, coupled with thrust and pressure measurements, was utilized to assess one of the first rotating detonation engines fueled by the space-storable rocket propellants MMH and NTO. Experimental hot-fire testing revealed the dependency of combustor specific thrust, wave dynamics, and detonation-formation timescales on propellant flow rate, mixture ratio, injector design, and the presence of a nozzle. Additionally, additive manufacturing was shown to improve the hydraulic characteristics for detonation engine applications both computationally and experimentally.

In Chapter 3, the aforementioned hot-fire testing and high-speed imaging were used to assess the fundamental detonation length scales (detonation cell size) for MMH–NTO detonation. The technique for measuring detonation cell size can be used for a variety of propellants for which controlled laboratory detonations are difficult to produce or the cell size is too small to resolve via direction observation. The µm-scale detonation cell sizes which we measured suggest that space-storable RDREs can be exceptionally small and lightweight.

In Chapter 4, a MHz laser absorption sensor was developed to simultaneously measure four gas properties: temperature, pressure, and CO/CO_2 number densities. In Chapter 5, this sensor was utilized to provide insight on the thermodynamics of RDRE operation at various flow conditions (mixture ratio, mass flow rate, and injector design). This external campaign was performed at AFRL (Edwards Air Force Base) using gaseous CH_4–O_2 mixtures and is part of a national effort to characterize and model a single RDRE architecture.

Additionally, the cycle-resolved structure of the gas properties helped reveal non-idealities in the engine operation, such as uneven propellant injector refresh times behind detonation waves. The experimental results obtained with the sensor anchored numerical models of the engine on which measurements were made [41, 42, 272].

In chapter 6 the physics of the DFB lasers are explored and exploited to develop techniques to increase the spectral tunability and signal-to-noise ratio of MHz-rate laser absorption diagnostics. Two applications of this optimized laser tuning strategy are demonstrated, showcasing the potential for measurements at higher pressures (up to 10 bar) and temperatures (up to 9000 K). These demonstrations suggest future applications of high speed absorption sensing for detonation and shock phenomena.

Chapter 7 extends the pressure sensing technique from Chapter 4 to more broad utility for combustion applications, with demonstrations across a larger range of pressures, combustion modes, and fuels. Chapter 8 extends the temperature range of CO-based LAS sensors to nearly 10,000 K by leveraging the large scan depth provided by the techniques of Chapter 6.

Overall, the developments of this thesis have provided valuable insights into the operation of rotating detonation engines and have generated a large range of diagnostic tools and methods to enable future research on rotating detonation engines, as well as other extreme combustion or high-energy environments.

9.1 Current and future research directions

9.1.1 MMH–NTO hot-fire testing with new combustor configurations

Building upon the work of Chapters 2 and 3, further hot-fire testing has been conducted with the MMH–NTO Propulsion Test Platform. The following improvements were made to the Propulsion Test Platform: (1) line sizes were increased from 1/4" to 1/2" to reduce the pressure drops across the propellant feed system; (2) venturi flow meters were designed and implemented to measure and control system mass flow rates to a higher degree of accuracy; and (3) additional instrumentation was added to measure additional pressures across the

feed system (purge pressures, source pressure, pneumatic pressure).

Hot-fire testing was conducted with the unhoned injector from the previous campaign with the aim of assessing the effect of varying combustion chamber geometry. Based on the results of the previous campaign, it was clear that adding a nozzle was greatly beneficial to RDRE operability and performance. To further investigate the effect of the nozzle on RDRE dynamics, nozzles of varying contraction ratio and a throatless aerospike nozzle were tested.

Additionally, based on the cell size measurements of Chapter 3, which were on the order of 10–100µm, it was postulated that the combustor could be much shorter. To test this, a chamber length study was conducted and it was found that detonations could be supported at even a 25 mm (1") chamber length.

Lastly, based on the short deflagration-to-detonation transition times observed in the previous test campaign when using a nozzle at high flow rates, a pulse mode firing demonstration was executed. The test platform was retrofitted to improve valve opening/closing time by: (1) using helium as the pneumatic driver gas, (2) utilizing a pneumatic accumulator tank to minimize drop in pneumatic source pressure after opening a valve, and (3) using double-acting main propellant valves to improve valve closing time. With these improvements, pulse-mode firings were executed with pulse durations as low as 100 ms.

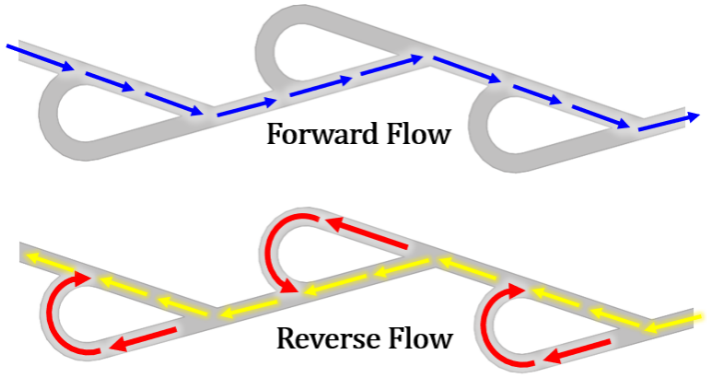

Figure 9.1: Tesla-valve geometry. Forward flow (*top*) faces minimal resistance whereas reverse flow (*bottom*) faces high resistance [273].

Work on improved injector design is ongoing. To mitigate large variation in hole sizes caused by the extrude hone process, other methods of injector honing are being explored, such as electrochemical honing. New injector designs are being developed to improve propellant mixing (by increasing the number of injector elements) and to improve injector back-flow resistance (diodicity). A "Tesla Valve" geometry is being studied to further increase back-flow resistance. A Tesla Valve, pictured in Fig. 9.1, is essentially a check-valve with no moving parts, encouraging flow in one direction and resisting flow in the opposite direction. Initial steady-state and transient CFD results indicate that this geometry has the potential to nearly double injector diodicity and improve injector refresh times by nearly 40% [273]. Current work involves printing this geometry and executing cold flow tests to assess the diodicity of this feature when printed.

9.1.2 Expanded LAS sensor suite for RDRE analysis

Building upon the work of Chapters 4 and 5, a second iteration of the multi-parameter LAS sensor was developed. For this new sensor, an additional laser was added to measure a transition of H_2O near 5 µm. This additional wavelength is multiplexed into the same InF_3 single-mode optical fiber as the wavelengths used to probe CO and CO_2, as seen in Fig. 9.2. Due to the similarity in laser wavelengths for the H_2O and CO transitions, these two laser signals could transmitted through the same spectral-bandpass filter. Using the laser current waveform tailoring developed in Chapter 6 and Appendix C, the CO and H_2O laser waveform duty cycles were each adjusted to nearly 40% to fit the two scans within a single measurement period to permit time-division multiplexing of the signals onto the same detector, allowing for the overall number of detectors (2) to stay the same. The waveform tailoring was also used to maximize all laser scan depths, extending the pressure capability of the sensor.

Additionally, a sapphire window was implemented into the combustor to allow for optical access into the annulus of the combustor. The DC-coupled Vigo PVMI-4TE-8-1x1 detectors used in the previous system iteration were replaced with AC-coupled Vigo PVI-4TE-6-1x1

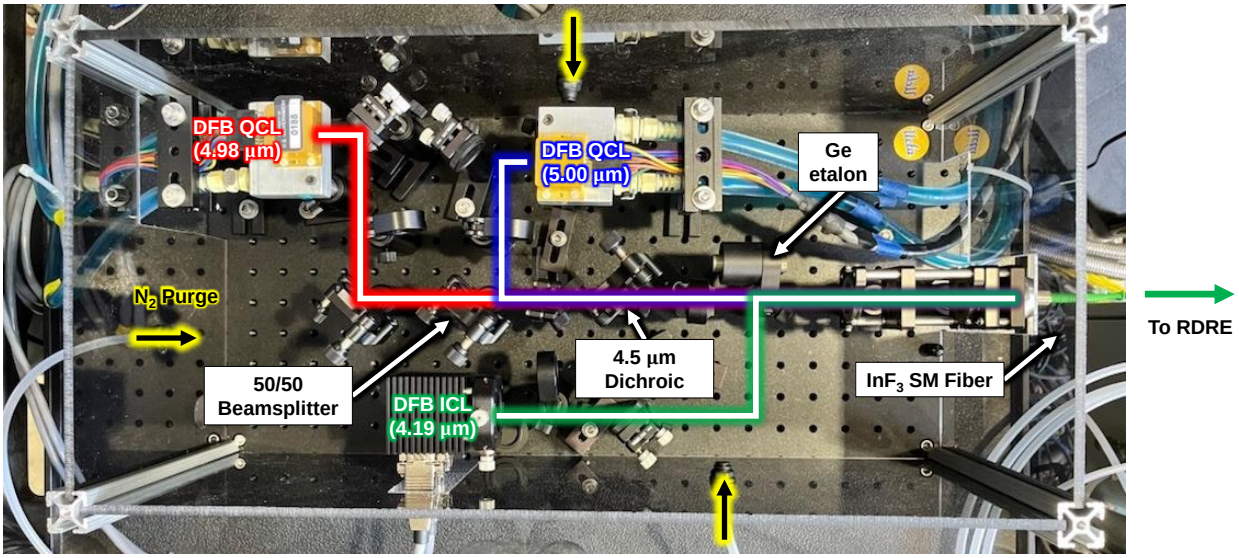

Figure 9.2: Laser breadboard for second iteration of MHz LAS sensor for RDRE in-annulus sensing.

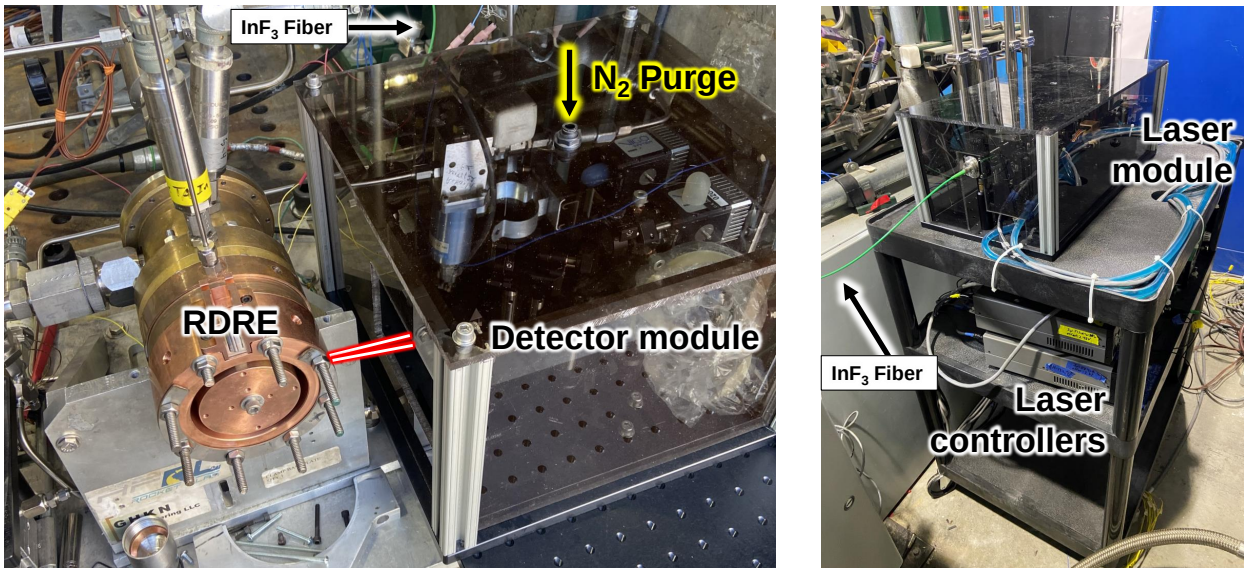

Figure 9.3: *Left*: Retro-reflection setup on RDRE with new purged enclosure and in-annulus optical access. *Right*: Laser cart with laser breadboard on top and laser controllers, function generators, and bias-tees below. Fiber output delivers light from laser module to detector module.

detectors, which performed significantly better in terms of linearity past 0.5–1 V. This enabled optical SNR improvments of up to a factor of 6. The laser and detector breadboards were housed in acrylic enclosures to facilitate purging of ambient H_2O and CO_2 and to protect the sensitive optics/photonics. The laser breadboard was secured to a cart which contained all of the laser controllers, function generators, bias-tees, and laser chillers. The enclosures and laser control cart can be seen in Fig. 9.3. This improved sensor design represents a step towards a turn-key sensor that is neatly packaged and user-friendly.

Simultaneous in-annulus 5-parameter (temperature, pressure, $CO/CO_2/H_2O$ concentration) measurements were conducted at a variety of flow conditions with the new sensor. Currently, the data is being processed to assess the time-resolved evolution of gas properties at this new measurement location, with the results to be presented at the next AIAA SciTech conference in 2023 [274].

APPENDIX A

MMH-NTO testing details

In this Appendix, the details of the equipment, facilities, and procedures used for the hypergol-fueled rotating detonation rocket engine (RDRE) testing of Chapters 2 and 3. Section A.1 details the design and operation of the UCLA Propulsion Test Platform. Section A.2 discusses the Mojave desert test facility where hot-fires were conducted. Lastly, section A.3 provides the formal standard operating procedure for setting up and operating the test stand.

A.1 Propulsion Test Platform

The UCLA Propulsion Test Platform (PTP) is a mobile, trailer-mounted, pressure-fed, liquid bi-propellant feed system that was used to hot-fire test the hypergol-fueled RDRE discussed in Chapters 2 and 3. The PTP was adapted from a trailer-mounted test stand designed and built by Polaris Propulsion in the early 2000s for gaseous H_2–O_2 engine testing. The stand was later converted for use with hypergolic propellants by Polaris. Polaris later sold the test stand to the Laser Spectroscopy and Gas Dynamics Laboratory in 2020, after which UCLA graduate students built an instrumentation and control system to operate the feed system, modified the feed-system plumbing, modified the engine interface to enable thrust measurements, and developed in-house procedures for operating the feed system for hot-fire testing. The PTP has been used for two successful hot-fire testing campaigns, in March 2021 (Chapters 2/3) and in March 2022 (discussed in section 9.1.1). The following subsections detail the design and operation of the PTP. Section A.1.1 discusses the base layout of the PTP. Section A.1.2 covers the propellant feed system used for hot-fire testing. Section A.1.3

Figure A.1: UCLA MMH–NTO mobile Propulsion Test Platform being transported to the Mojave Test Area.

details the control system used to operate the PTP. Section A.1.4 details the data acquisition system. Section A.1.5 reviews the validation tests performed for the PTP.

A.1.1 Layout

The PTP was built upon a standard flatbed utility trailer with approximate dimensions of 21'×8'. Various views of the PTP can be seen in Figs. A.1–A.3. The trailer featured an electronic braking system due to its high mass. The test stand features a single jack at the front to which a wheel could be mounted to manually maneuver the test stand (with the help of a few people). During hot-fire testing, the wheel is replaced with a 2"×4" piece of

Figure A.2: Propulsion Test Platform being hitched to a pickup truck for transport from UCLA to the Mojave Test Area.

wood which supports the weight of the front portion of the test stand. When the wheels are also chocked with wood, the test stand can withstand up to 1,000 lbf of thrust. To remain stationary under higher load, the test stand features two rear jacks, which can be bolted to the ground. This bolted joint can support thrust forces up to 5,000 lbf.

The layout of the PTP can be seen in Fig. A.3. The test article is nominally positioned at the front end of the trailer. A frame structure made from aluminum plates bolted to welded steel beams transfers the load from the test article to the main body of the trailer. The main propellant lines and propellant tanks are also mounted upon this structure. Behind this structure was a secondary structure made of much smaller steel members. Much of the gas-pressurization system plumbing was mounted upon this structure, along with enclosures which contained hand-operated regulators / pressure gauges, an electronic control system, and data-acquisition system. Behind this structure was a wooden deck mounted on another steel structure, providing for an elevated surface that could be used as a makeshift workbench during test setup. The test stand power supply box was kept on this deck during testing. A heavy-duty toolbox was bolted at the rear end of the trailer, which allowed for some tools/equipment to be directly transported with the test stand.

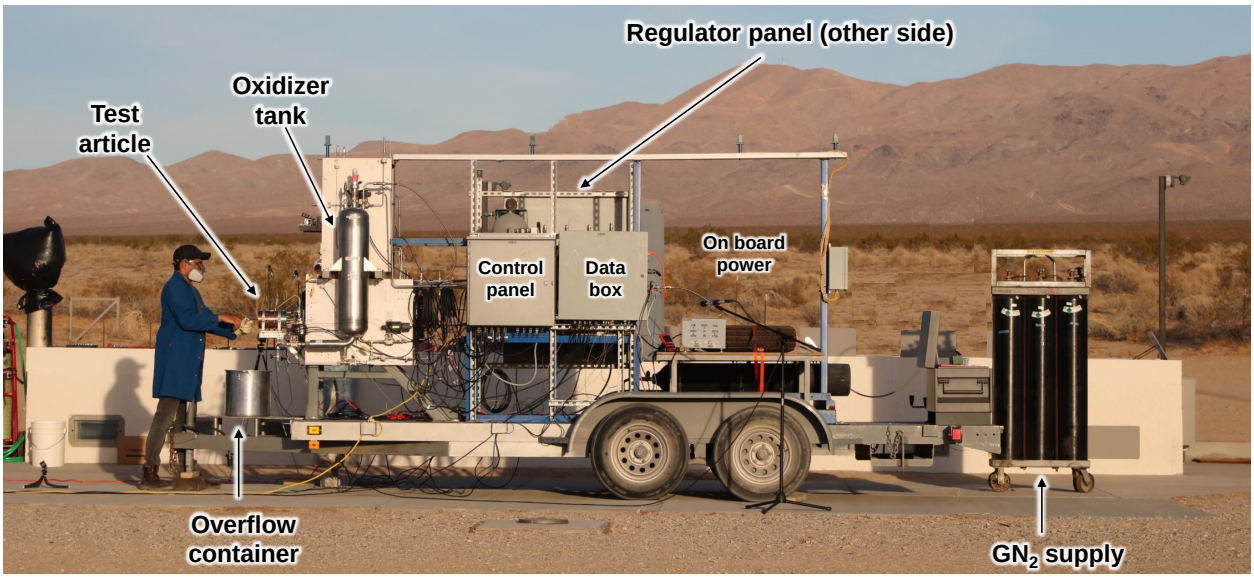

Figure A.3: NTO-side view of Propulsion Test Platform with key components labeled.

PTP modifications and validation in preparation for the March 2021 and March 2022 campaigns occurred primarily at UCLA. The test stand was transported via truck to the Mojave Test Area for hot-fire testing. When the test stand was not in use, it was stored at a storage facility in Lancaster, CA.

A.1.2 Feed-system design

The basic propellant feed system architecture was largely developed by Polaris Propulsion and was modified as required by UCLA graduate students for the RDRE testing. A side view of the PTP is shown in Fig. A.3. A plumbing and instrumentation diagram for the PTP can be seen in Fig. A.4. The trailer is divided into two sides, one which pressurizes and routes the oxidizer (NTO side) and one which pressurizes and routes the fuel (MMH side). All plumbing lines and most fittings are made from stainless steel for propellant compatibility. Most fittings/valves are produced by Swagelok, with significant exceptions noted below. Seals on the MMH side are generally made from EPDM whereas the seals on the NTO side are generally made from PTFE. The test stand featured three types of valves: (1) hand-operated ball/needle valves, (2) remotely-controlled pneumatically-actuated ball valves (in purple in Fig. A.4), and (3) remotely-controlled solenoid valves (in green in Fig. A.4). In general, all remotely controlled (two-way) valves on the test stand are normally closed to prevent unintended routing of the reactive hypergolic propellants around the system in the case of power loss.

Pneumatic and propellant-feed pressure is supplied by the GN_2 6-pack, which is plumbed into the rear of the test stand via a braided hose. A series of Tescom hand-operated spring-loaded regulators are located in a panel on the MMH side of the test stand, pictured on the left side of Fig. A.5. The panel also featured gauges that monitored N_2 bottle pressure and regulator outlet pressures. Some of these regulators support direct flow through them (i.e. for pneumatic pressure, purges). Other hand-operated regulators instead result in indirect pressurization: these regulators set the "dome-pressure" of various dome-loaded regulators, which are used to pressurize the propellant tanks due to their higher flow coefficient, C_v,

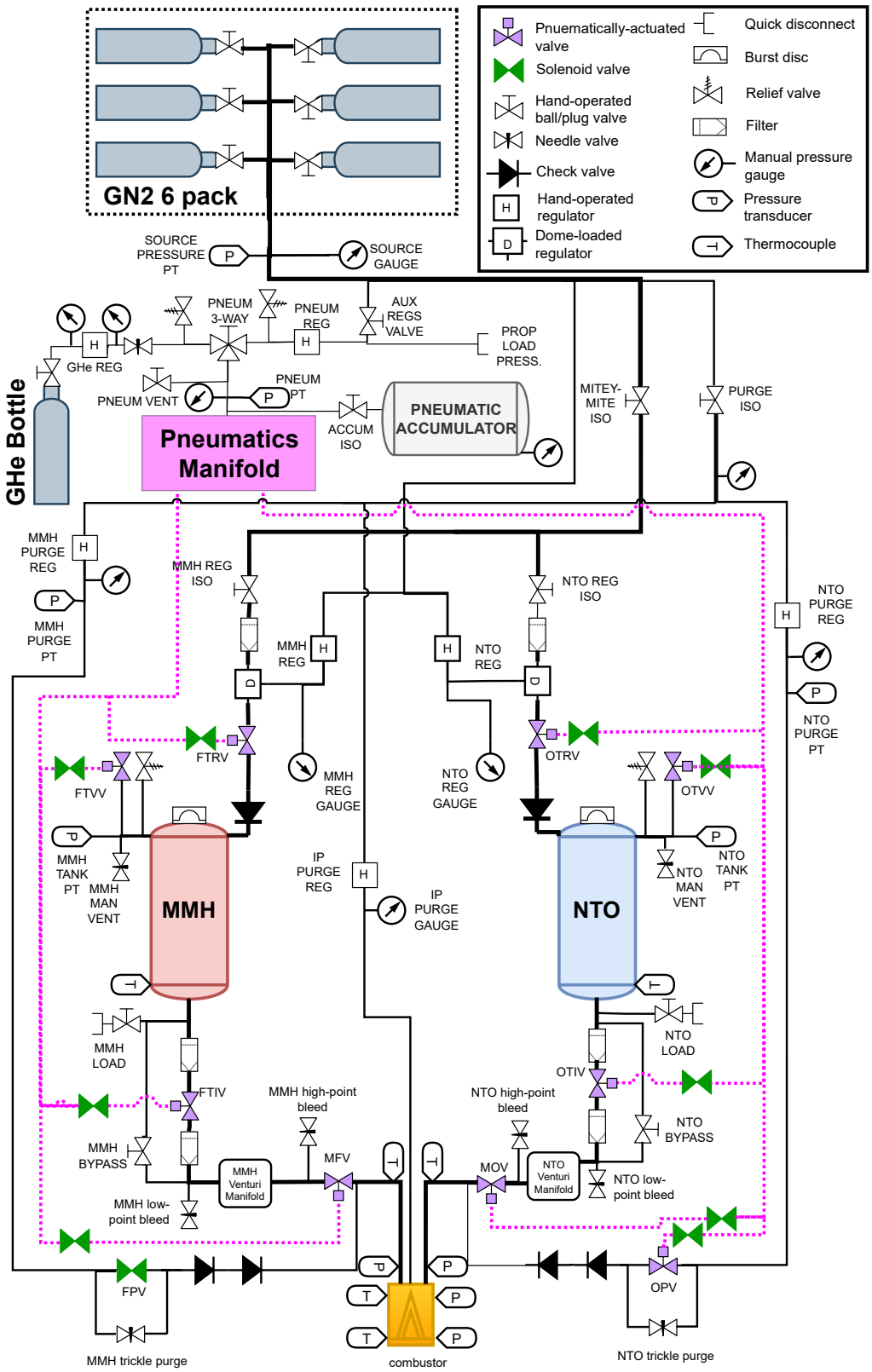

Figure A.4: Propulsion Test Platform Plumbing and Instrumentation Diagram.

see the right side of Fig. A.5. Two sets of dome-loaded regulators are present on the test stand. A set of APCO regulators with high C_v were used for the March 2021 test campaign, but experienced some issues with pressure stability—the tank pressures would often creep over time. For the March 2022 test campaign, the propellant tanks were instead pressurized using two Grove Mitey-Mite regulators with lower C_v values, which were still adequate for the relatively low N_2 flow rates required for the RDRE testing. Additionally, remotely controlled isolation valves (FTRV and OTRV) were included between the regulators and tanks to "lock in" the tank pressure before a test. The test duration was short enough (<1 s such that the tank pressure did not significantly drop due to volume expansion over the course of a test. Filters were placed upstream of the regulators to prevent clogging with foreign-object debris (FOD). Check valves are placed between the tank-pressure regulators and the propellant tanks to prevent inadvertent mixing of MMH and NTO vapors in the upstream feed system, which could result in an ignition event.

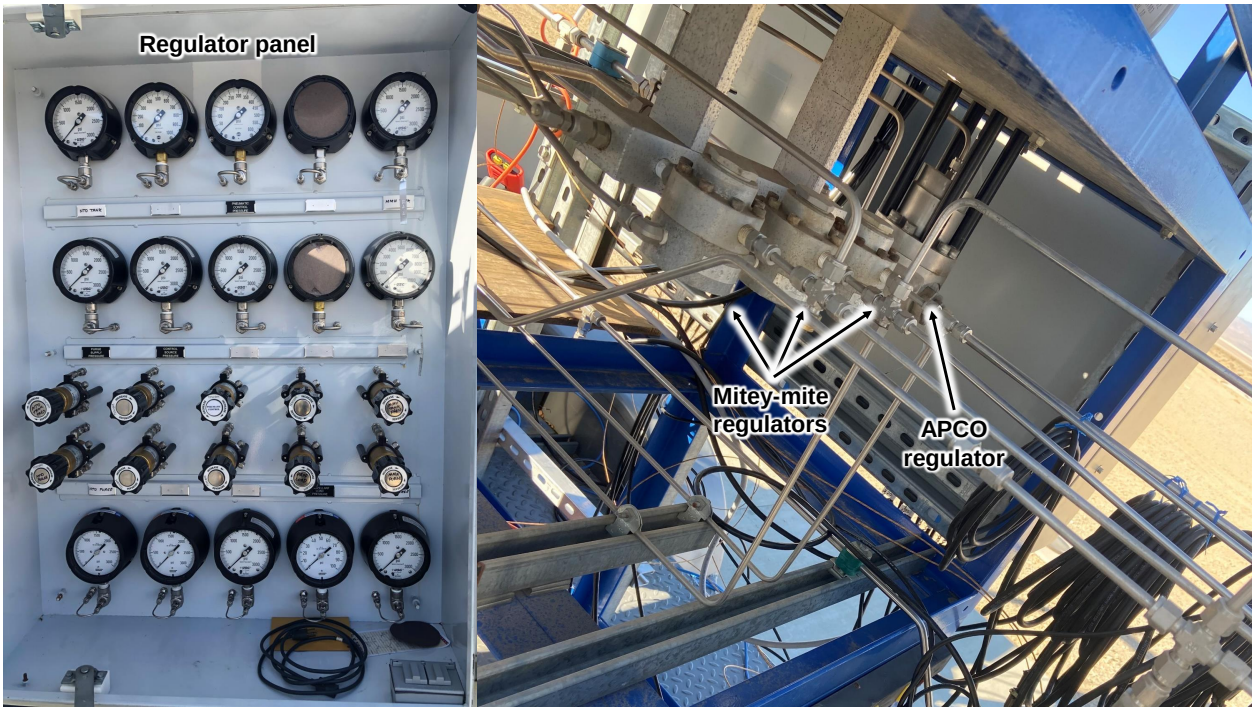

Figure A.5: *Left*: Regulator box containing hand-operated regulators. *Right*: Dome-loaded regulators used for tank pressurization.

The propellant tanks are both 1 cubic foot in volume. The top of the MMH tank can be seen on the left side of Fig A.7. The tanks were hydrostatically tested to 2000 psi. Pressure-relief valves (PRVs) were set to relieve pressure at 1300 psi, in the case of accidental over-pressurization. As a secondary safety measure, burst discs on the tank were set to burst at 1625 psi in case of extreme over-pressurization. Propellant-tank pressures were monitored remotely using the data-acquisition system discussed in Section A.1.4. Propellant-tank fluid temperatures were monitored using thermocouples attached directly to a hand-held reader. Both a manually-operated vent needle valves and a remotely-operated vent ball valves (FTVV and OTVV) were included at the top of each tank for depressurization. A gas diffuser was placed immediately downstream of each tank inlet to prevent high velocity gas jets from introducing bubbles into the propellants.

Quick-disconnect (QD) propellant load ports were included at the bottom of each tank. The two QD ports were intentionally made incompatible with each other to avoid accidental mixing of fuel and oxidizer during loading. Propellant load was conducted by Polaris Propulsion personnel. Propellants came in large drums (see Fig. A.6) that were weighed before and after loading to assess the propellant mass loaded into the test stand. The drums were fed with pressure from the test stand N_2 supply to transfer the propellants from the drum to the propellant tank. The tank vents were left open during loading.

The outlet at the bottom of each tank forms the start of each main propellant line. Each line featured a 40 µm Norman filter, a pneumatically-actuated isolation valve (1/2" size), a smaller 40 µm filter, a pneumatically-actuated "main propellant valve" (1/4" size, MFV and MOV), and a combustor manifold inlet. The MMH-side main propellant line can be seen in the middle of Fig. A.7. The two normally-closed valves act as a safety measure against accidental propellant discharge into the test article. For the March 2021 testing detailed in Chapter 2, the main propellant lines were made from 1/2" tubing up to the isolation valves and 1/4" tubing thereafter. In preparation for the more recent March 2022 campaign, discussed in section 9.1.1, the line sizes were upgraded to 1/2" all the way to the main propellant valves and 3/8" thereafter. This change was made to reduce system pressure drops

Figure A.6: Reach for positioning propellant drums near test stand for propellant load.

to increase total flow rate capability, especially due to the additional of venturi flowmeters between the isolation and main propellant valves, which added additional pressure drop into the system.

Along each main propellant line, a high-point and low-point bleed port controlled by needle valves, which allowed for excess gas or liquid to be manually expelled from the propellant line respectively. Additionally, there were bypass lines running from upstream of the large filter to downstream of the smaller filter. These bypass lines are opened via a manual ball valve along them when the test stand is in a idle (not testing) configuration. This links the small volume in the main propellant lines to the larger volume of the tanks, which prevents extreme increases in pressure (100s of psi) in those lines on sunny days, where radiative heat

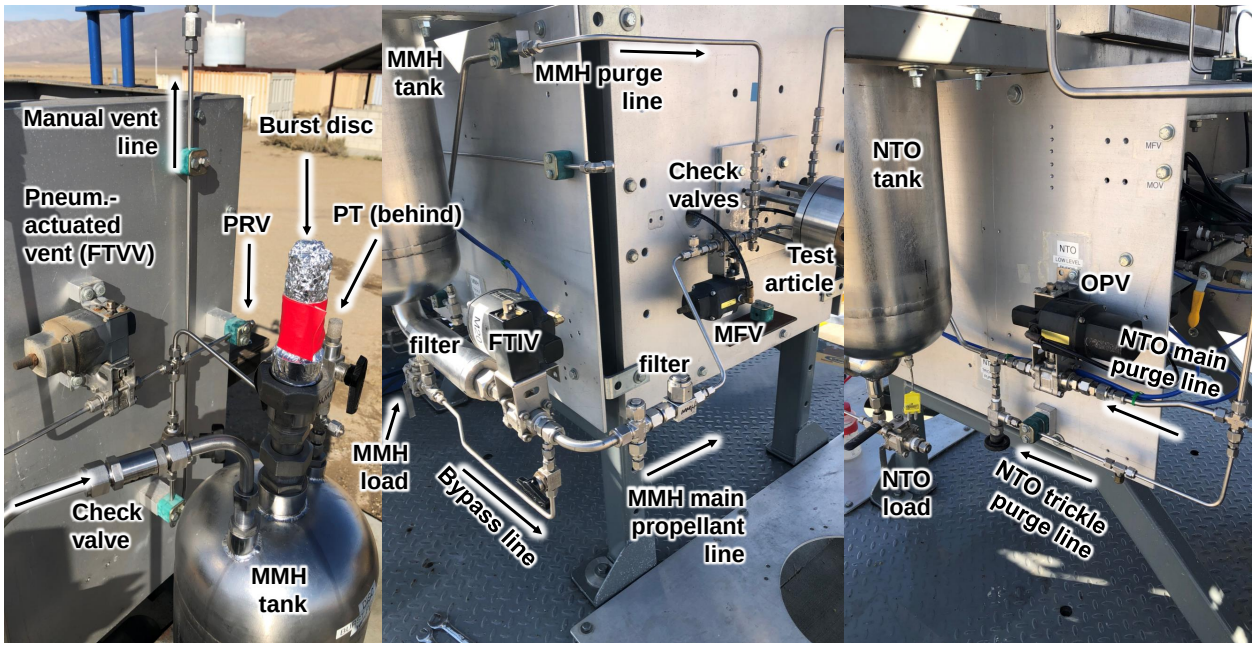

Figure A.7: *Left*: View of top of MMH tank. *Middle*: Picture of MMH-tank outlet and MMH main propellant line. Right: Image of oxidizer purge line behind NTO tank. Note: Bleed valves are not attached in these images.

transfer into the lines is high.

Each main propellant line is outfitted with various instrumentation. For the March 2021 campaign, a single pressure transducer was included downstream of each main propellant valve to assess the propellant-injector manifold pressures, which were used to assess propellant flow rates. For the March 2022 campaign, additional pressure transducers were included to measure pressures upstream, downstream, and in the throat of venturi flowmeters. In-line thermocouples are also included to measure the temperature of propellants immediately upstream of the propellant-injector manifolds to assess propellant density and phase. The aforementioned pressures and temperatures are recorded by the data-acquisition system discussed in section A.1.4.

Nitrogen purge lines were teed into the main propellant lines upstream of the combustor inlet. These purge lines served to clear the combustor of excess propellants after a hot fire test to make the test stand safe to approach. The MMH and NTO purge lines can be seen in the

middle and right images of Fig. A.7. The purge pressure for the oxidizer and fuel sides could be set independently using spring-loaded regulators on the regulator panel. These regulators have the highest flow coefficient of the spring-loaded regulators on the test stand. It was determined recently that the purge pressure and timing have a strong effect on detonation formation timescales. As such, for the March 2022 test campaign, remote purge pressure measurements were included in the data-acquisition suite. For the oxidizer-side purge, a pneumatically actuated ball valve (OPV) was used, whereas for the fuel side, a Marotta solenoid valve (FPV) was used. Both of these valves are remotely controlled. In addition to the remote controlly controlled purges, there were manually controlled "trickle purges" through needle valves. These purge lines ran parallel to the main purge lines. Immeditely upstream of the purge inlet to the main propellant lines were a set of double check valves. These double check valves served two purposes: (1) they prevented the hypergolic propellants from entering the purge system and the GN_2 supply upstream; (2) if the purge pressure was set lower than the combustor inlet pressure, the purge pressure could be left on during a test, with the check valves shutting off the purge line. After the hot fire, as the propellant feed is cut off and the line pressure drops, the pressure differential across the check valves reverse and the purges automatically activate to clear out the residual propellant. When high purge flow rate is required, the purge regulators cannot keep up with the flow demand during the engine shutdown transient. To combat this, purge accumulator tanks are included downstream of the purge regulators, which act as fluid capacitors providing relatively sustained purge pressure for a short duration.

Most of the remotely operated valves are pneumatically actuated. The pneumatic pressure can be supplied from the GN_2 supply of the test stand. Alternatively, an external gas supply can be used, such as an air compressor. During the March 2022 campaign, the test stand was re-configured to provide the option of using a helium pneumatic driver. Helium is desirable as a pneumatic driver, as its high speed of sound means that pressure forces are transmitted more quickly in a helium medium. Additionally, a pneumatic accumulator could be used, which kept the pneumatic supply pressure more constant during valve open-

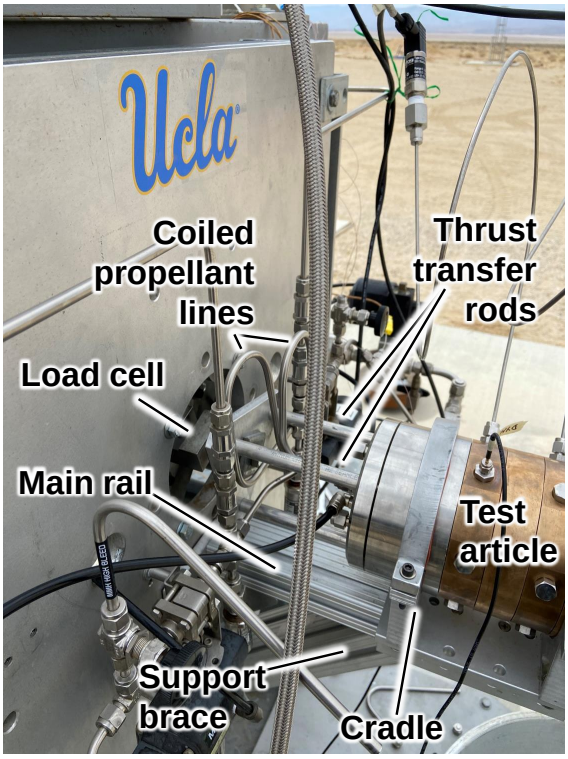

Figure A.8: Thrust structure for PTP with key components labeled.

ing. This led to improved response times (delay between valve open command and start of valve opening) by a factor of 4 and improved valve opening time (time taken for valve stem to complete 90° rotation) by a factor of 2. Pneumatic pressure distributed in a manifold block (ARO 118605-8) which features one inlet port and 8 four-way solenoid valves. In the energized state, these solenoid valves direct pneumatic pressure from the supply to each actuator, opening the corresponding main valve. In the un-energized state, these solenoid valves vent the pneumatic actuators, which allow for the spring in the actuators to return the main valves to a closed position. The solenoid valves can also be configured to support double-acting valves, such as the propellant-tank isolation valves. In this case, in the non-energized state, pressure is driven into the other side of the valve actuator, providing for more rapid valve closure, at the expense of increased valve opening time.

The combustor was mounted on support structure (see Fig. A.8) made from 6061 Aluminum T-slotted rail. One long rail protruded horizontally from the stand, with another

rail mounted diagonally between the middle of the rail and the test stand frame to reduce the bending load on the horizontal rail. The test article was held in a "cradle" which was freely allowed to slide along the horizontal rail in the axial direction while lateral motion was prohibited. This allowed for the axial loads to be entirely transmitted from the combustor into three rods, which connected to a load cell behind the combustor. Rigid tubing was used for the main propellant lines, but the lines were bent in a coil shape to reduce their stiffness, allowing for nearly all of the load to be transferred into the load cell. This was verified by manually pressing on the combustor with a weight scale and verifying that the load cell reading matched the scale reading. Below the rail was a stainless steel bucket filled with de-ionized water, which captured any overflow of residual propellants after a test.

A.1.3 Control-system design

As mentioned in the previous section, the pneumatically-actuated valves were controlled via solenoid valves, which routed pneumatic pressure from a common supply manifold. Additionally, the fuel purge valve (FPV) was a solenoid valve. All 8 of these solenoid valves required 24 V to operate. A valve control system was developed by UCLA graduate students to power and control these valves. The system was designed for three modes of operation: (1) local "manual" control at the test stand via a physical switch panel, (2) remote "manual" control via computer program, and (3) remote automated-sequence control via computer program. In this section, the design and construction of this system is detailed. The overall control system architecture is shown in Fig. A.9.

24-V power was supplied using two 12-V marine deep-cycle batteries connected in series. The batteries were contained in a "Battery Box" enclosure. The battery box can be seen on the rear deck of the PTP in Fig. A.3. A four-pin connector was used to direct 24-V power out of the box. A 25-A fuse and 20-A circuit breaker were included in series with the batteries to cut of current in the case of a short circuit. Three switches on the box were used to "enable" each battery and enable the overall circuit. 24-V LEDs activated with each switch throw to indicate the battery/box was enabled. Two 12-V battery chargers were connected

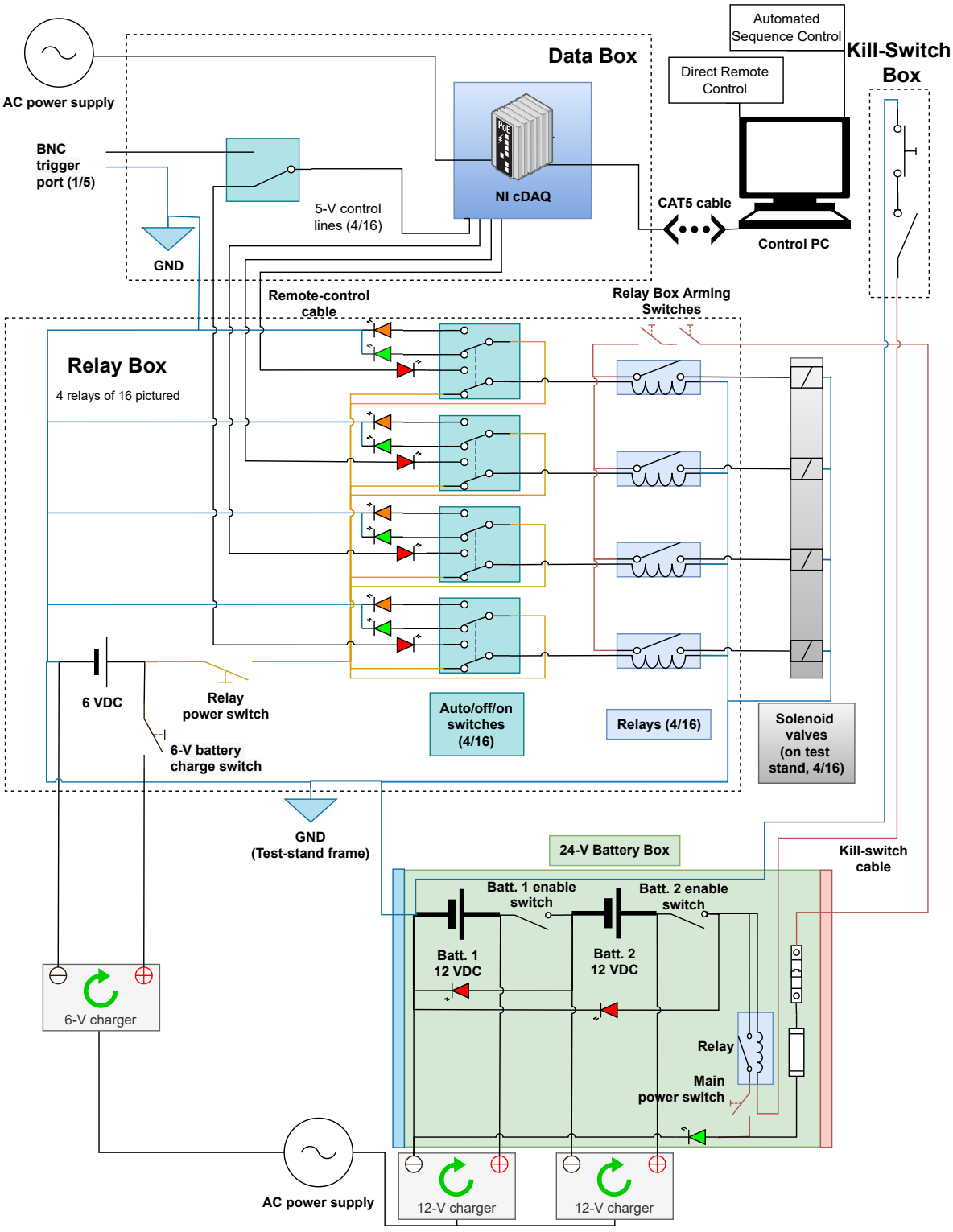

Figure A.9: Propulsion Test Platform control-system schematic.

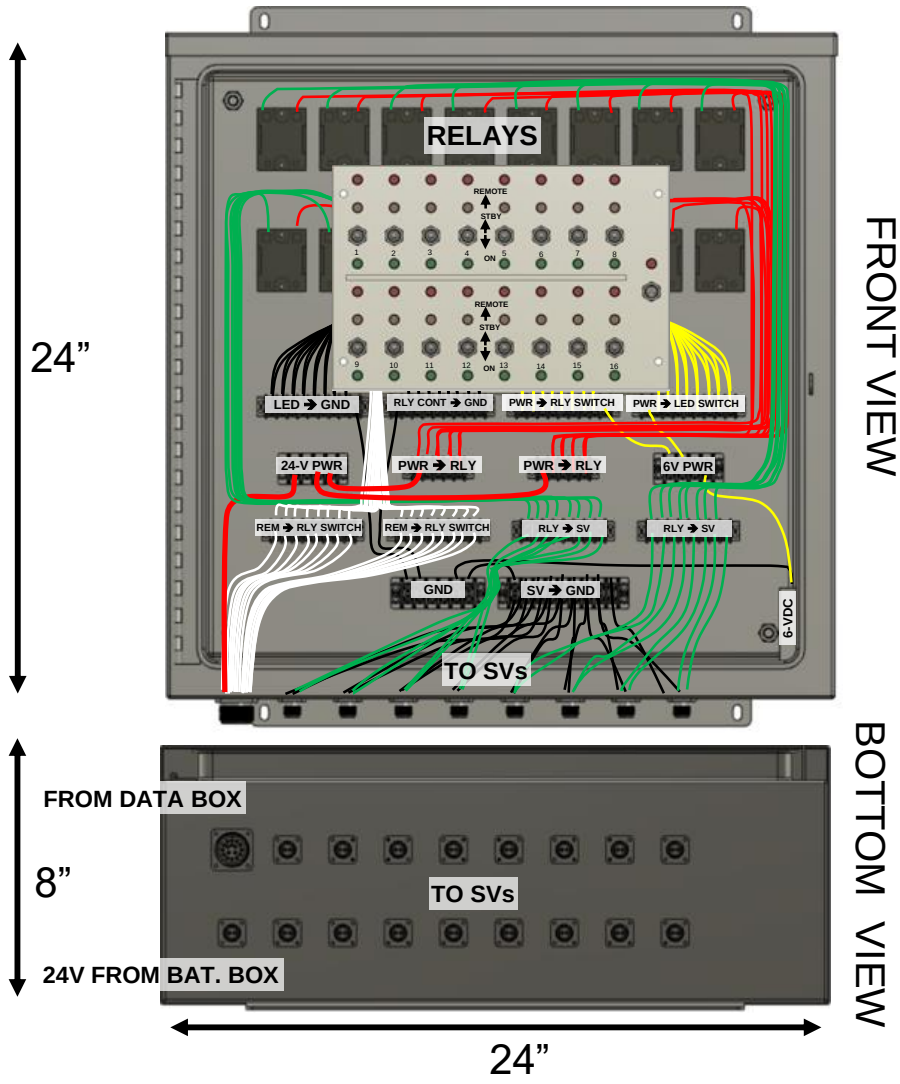

Figure A.10: Diagram of Relay-Box wiring.

across the terminals of each battery. In this way, the batteries could be left charging when AC power was available. The negative terminal of the first battery in series was connected to the box enclosure and the overall system ground, which was the test-stand chassis. The battery circuit also connected in series with the output side of an automotive relay. The input circuit of this relay also was supplied by the 24-V power. The downstream end of the input circuit was routed to a second port (2-pin) on the battery box which was connected to a 50-ft cable. This connected to a box termed the “Kill-Switch Box”. This Kill-Switch Box was typically remotely located with hot-fire test operators during a test. Both a key switch

and push-button switch were connected in series to the relay input circuit in this box. To activate the relay and enable 24-V power to leave the battery box, both they key had to be inserted/turned into the Kill-Switch Box and the push button had to be retracted. In the case of an emergency, an operator could press the large push button to immediately cut off power to the valves, safing the test stand.

Nominally, 24-V power is directed via a 4-pin cable into an enclosure termed the "Relay Box". The relay box can be seen mounted to the PTP in Fig. A.3 and the internal wiring of the box can be seen in Fig. A.10. The Relay Box served to direct power to a given solenoid valve based on user input. 24-V power was connected in parallel to the output side of 16 solid-state relays. The other terminal of the relay output was wired to a pin on 1 of 16 ports on the relay box, to which a solenoid valve cable could be connected. The other pin of each port was connected to ground. Each relay represents 1 of 16 available power channels for the system, although only 8 was used for the testing in March 2021. The input side of each relay required at least 3 V to allow current flow through the output side. This voltage was either supplied by a 6-V battery located in the relay box (for local control) or via a remote 5-V signal generated from a National Instruments (NI) relay control system, located in another box (to be discussed later). The negative terminal of the 6-V battery is connected to ground, whereas the positive terminal is connected in parallel to a set of 16 three-position, double-pole, double-throw (DPDT) switches. One "pole" of the switch is wired in "reverse" compared to conventional usage, reflecting how there is a single load (the valve) but two power sources (local and remote). As such, the input circuit of a relay is connected to the common terminal of this pole. The 6-V is supplied to one of the two "output" terminals of the same pole. The other "output" terminal is connected to the unique 5-V supply from the remote control system. Each of these 5-V supply lines is routed into the Relay Box via a 17-pin cable (one pin for ground). All 16 control switches were installed into a switch panel on the relay box, pictured in Figs. A.10 and A.11. When the switch was in the neutral position, neither the local 6-V power nor the remote 5-V power is directed into the relay. When the switch is flipped down, the local 6-V power is sent into the relay, directing 24-V

power to the corresponding solenoid valve. This is how local manual control is achieved. If the switch is flipped into the upwards position instead, the channel enters "remote standby" mode, where is awaits a signal from the remote control system. When a 5-V remote control signal is sent, the relay is energized, allowing for power to be directed to the corresponding solenoid valve.

The second pole of each switch was responsible for directing power to various LEDs on the switch panel which visually indicated the state of each valve channel. As such, the positive terminal of the 6-V battery was connected in parallel to the common terminal of the second pole of each switch. Each output terminal was directed to one of two LEDs. The output terminal corresponding to local control was connected to a green LED, located below the switch. The output terminal corresponding to remote standby was connected to an orange LED, located above the switch. A third red LED was placed above the orange LED. This LED was connected in series to the 5-V remote input line. When a remote control signal is directed to the channel in remote standby mode, the red LED is illuminated, indicating remote valve control.

In addition to the main control switches, various safety switches are located on the panel. One switch with a blue LED enables local 6-V power. A set of two switches connected in series with associated red LEDs enable 24-V power. There is also a switch to enable the charging of the 6-V battery.

Remote control was accomplished using two LabView programs. One program, termed the "direct remote control" program, featured on-screen buttons corresponding to each valve. Once the program was armed and running, the user could press these buttons to send an "open" signal to the desired valve. The computer running the program was connected via CAT5 ("ethernet") cable to a National Instruments (NI) cDAQ-9185 chassis. This chassis was located in another enclosure termed the "Data Box", which was nominally mounted on the side of the test stand, next to the relay box, see Fig. A.11. The internals of the Data Box can be seen in Fig. A.12. The cDAQ could support up to 4 cards to provide various control/instrumentation functionalities. Two of these cards were 8-channel NI relay output

modules. When the LabView program sent an "open" signal to one of these relay modules, the module would send a 5-V signal to the Relay Box via 17-pin cable, as discussed above. If the channel was set into Remote Standby mode on the Relay Box switch panel, 24 V would be directed to the solenoid-valve control line associated with the target channel. The last 5 of the 16 control channels were outfitted with the option (via a set of manual switches) to send the 5-V signal to a BNC port located on the exterior of the data box, instead of through the 17-pin connector to the Relay Box. These signals could be used to trigger other data-acquisition systems, such as the high-speed camera or Picoscope used to capture high-speed RDRE data in Chapters 2/3.

The other LabView program, termed the "Automated Sequence Control" program, was used to send a series of timed commands to the control system. This was used to generate a short repeatable test sequence for the RDRE testing, which was ofter less than 1 second in duration. For this program, the user types in a list of open and close times for each channel, after which a preview is generated for the test sequence. If the program is armed via two

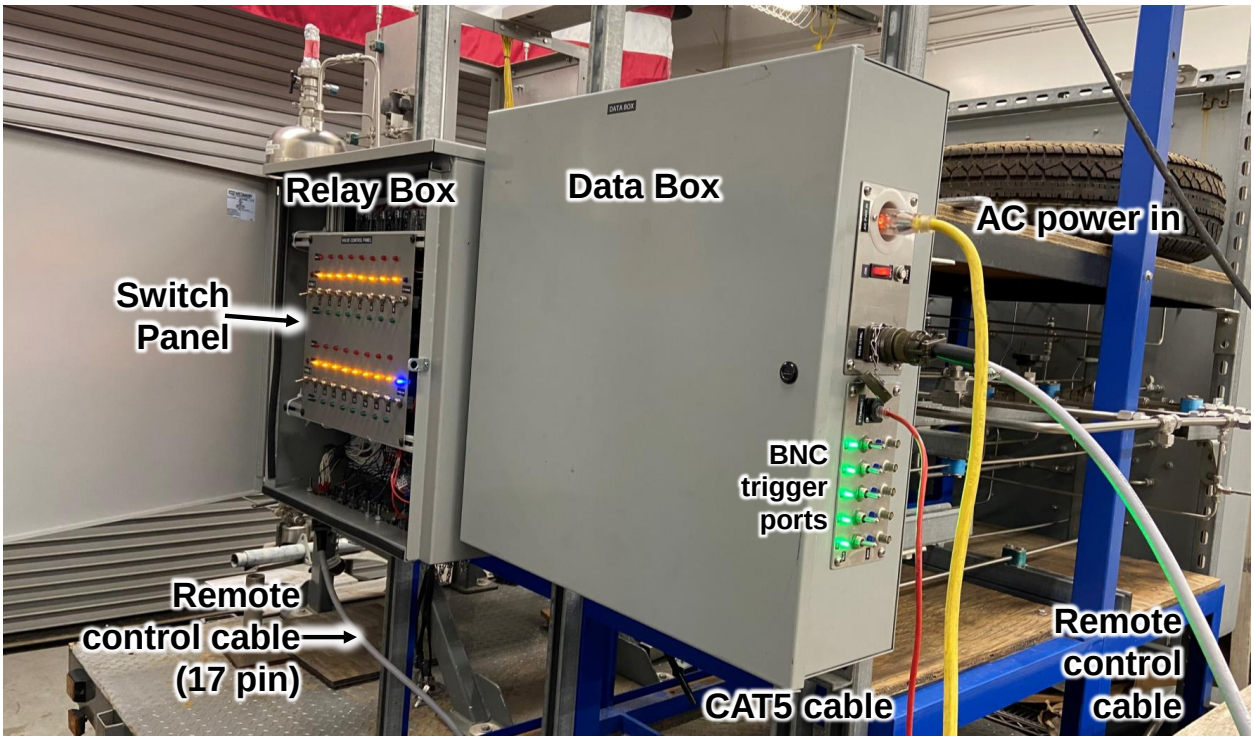

Figure A.11: Relay and Data Boxes mounted on NTO side of PTP.

buttons on the LabView VI (virtual instrument) front panel and the preview is accepted, the user can then choose to initiate the sequence, which occurs after a nominal delay/countdown. At any point during the test sequence, the user can abort the test by pressing an "abort" button on the VI front panel, which sends all of the valves into their closed state. The Kill Switch discussed above can also be used for this.

A.1.4 Data-acquisition system

In this section, the details of the PTP onboard instrumentation are discussed. Other instrumentation, such as the high-speed camera, time-of-arrival sensors, and microphones used to measure high-speed RDRE dynamics are not processed by this data-acquisition system (DAQ) and are handled with either propriety software (in the case of the camera) or via an oscillosope. On-board data was recorded using two NI-9201 cDAQ card, which were able to record a total of 16 channels of data on a ±10-V scale with 12-bit resolution and a maximum sample rate of 500 kS/s. Data collection was mediated by a custom LabView program, which displayed live readouts of data and also recorded data to text files when a trigger signal was sent to the module from the control system. Data was recorded at a sample rate of 1 kS/s. For the 2022 testing, a single NI-9205 card was used instead of the two 9201 cards. This expanded the number of available channels from 16 to 32.

On-board data included pressure, temperature, and thrust measurements. For the 2021 testing, 6 pressure transducer (Trafag Sensors and Controls) measurements were made, although the system was configured to accept 8 pressure inputs. These pressure readings included 2 tank pressures, 2 combustor inlet pressures, and 2 chamber pressure measurements on the combustor. For the 2022 testing, 10 additional pressure measurements due to the increase in total number of data channels. 6 of these were to measure pressures associated with "venturi manifolds" installed in both main propellant lines which each featured 2 cavitating and one subcritical venturi. A pressure measurement was made both upstream and downstream of each venturi manifold, and the subcritical venturis each featured a pressure measurement at their throats. These venturi pressure measurements were used to measure

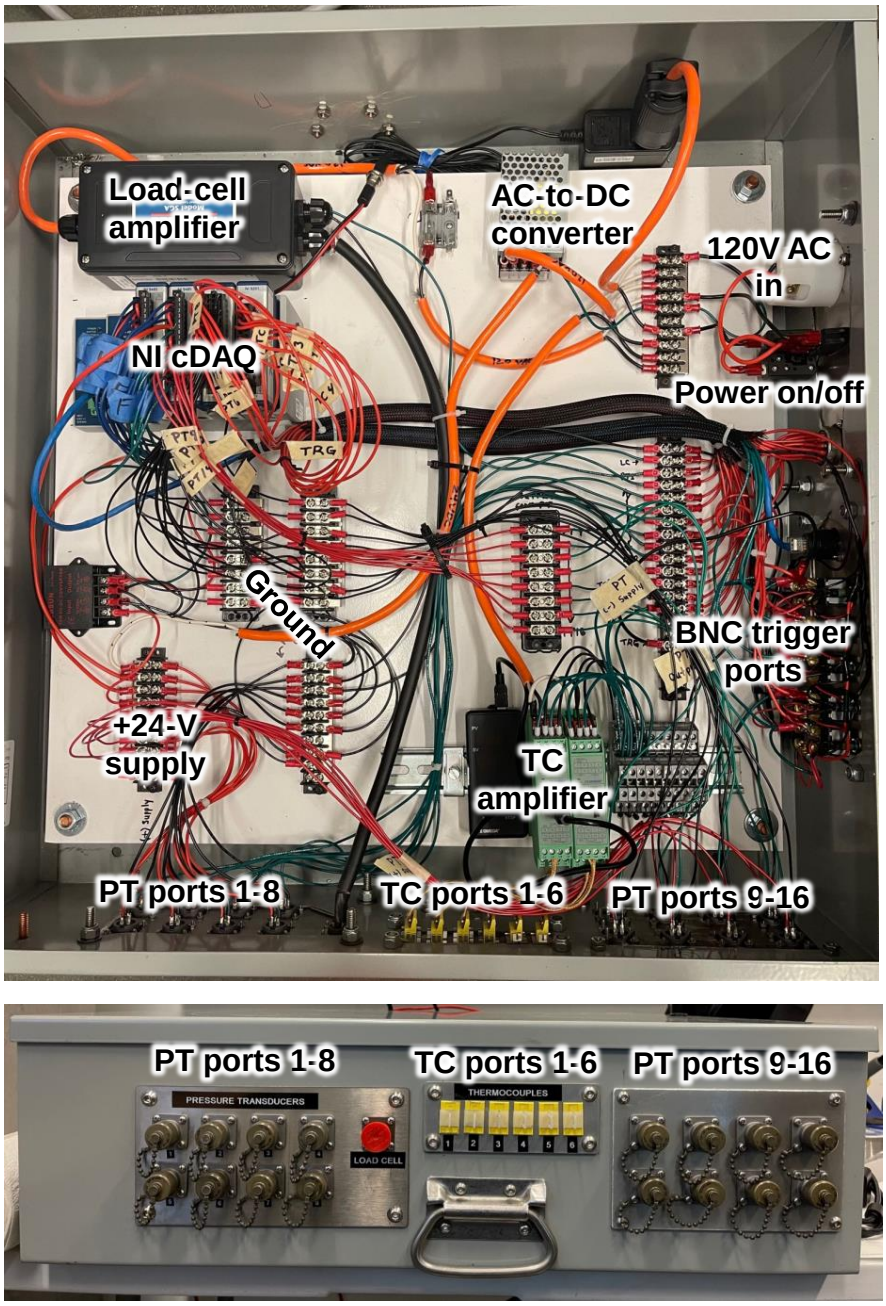

Figure A.12: *Top*: Internal view of PTP Data Box with key components labeled. *Bottom*: Bottom view of Data Box where instruments connect.

mass flow rates with high accuracy. 4 additional pressure measurements include 2 purge supply pressures, the pneumatic supply pressure, and the overall source pressure.

Four temperature measurements were recorded remotely. Two in-line K-type thermocouples (Omega KMQSS-062U-6) recorded for fluid temperature immediately upstream of the combustor. Additionally, two combustor surface temperature measurements were recorded, using Omega SA3-K-72 K-type theromcouples. As noted above, the fluid temperature inside the propellant tanks was recorded with a handheld reader attached to K-type thermocouples.

Thrust measurements were made using either an S-type load cell (Walfront PSD-S1) or low-profile load cell (Interface 1210ACK-1K-B). Both load cells had a 1000-lbf full scale.

The inside of the Data Box is shown in Fig. A.12. The bottom of the box featured connectors for up to 8 pressure transducers (upgraded to 16 in 2022), a load cell, and 6 thermocouples. The side of the box opposite the door hinge featured an AC power plug, a power switch, an CAT5 port to interface with the control computer, and switches which can direct 5-V control signals to BNC ports or the relay box (as discussed in section A.1.3). In addition to the NI cDAQ, the inside of the box housed amplifiers for the thermocouple and load-cell signals. AC-to-DC converters within the box were used to convert 120-V AC power into 5- or 24-V DC power for use with the amplifiers, the cDAQ, or any pressure transducers connected to the box.

A.1.5 On-campus testing

After the UCLA graduate student team finished modifying the PTP feed system and the control/DAQ system was developed, various validation tests were conducted to confirm proper operation of the test platform.

Instrumentation was validated by comparing to existing calibrated instruments. Pressure transducers were connected to the gas supply system of the UCLA Laser Spectroscopy and Gas Dynamics Laboratory (pictured in Fig. B.3) where various pressures were generated using inert gases. The transducer-measured pressures were compared to laboratory pressure

readers used for other experiments. Temperature measurements were also confirmed to match laboratory thermocouples. Load cell readings were verified by comparing the weight reading on a commercial weight scale to that of the load cell.

For the propellant feed system, leak testing was conducted by pressurizing the feed system with helium, due to its high propensity to leak compared to other gases. The fluid system was examined for leaks section-by-section, in order to isolate leak sources. Leaks were detected using various methods. Major leaks were audible and easily identified. Leaks could also be detected by observing a drop in pressure in the tested fluid volume once the gas-pressure supply was cut off. This method also served as an additional validation of the pressure transducer measurements. If a leak was detected in this way, the various connections and joints in the fluid system were sprayed with soapy water, in which bubbles would form if a leak was present.

After the fluid system was verified to be leak tight, the overall system was tested for functionality as a propellant feed system. This was accomplished by filling the tanks with de-ionized water and running through a simulated hot-fire sequence. Dry runs were also conducted using only nitrogen pressurization, without water, in some cases. Operating the system for cold-flow tests with water, as described in Chapter 2, provided additional confidence in the test stand operation and served as a validation of the ability to measure propellant mass flow rates.

A.2 Mojave test facility

Hot-fire testing was conducted at the Mojave Test Facility (MTA) located near Cantil, CA. This is approximately 120 miles from the UCLA campus. The Mojave Test Area is primarily operated by the Reaction Research Society (RRS), an amateur experimental rocket engineering association, which supports high-power rocket testing and education. The test facility is also leased by Polaris Propulsion, who has conducted rocket engine testing at the facility for decades. Polaris built an underground blockhouse located a few meters from a

concrete test pad where the PTP is parked during testing. The blockhouse and test pad can be seen in Figs. A.13 and A.14. The blockhouse featured windows that are several inches thick, which allowed test operators to safely view the test stand during hot-fire testing. Underground conduits run between the test pad and blockhouse interior allowing for cables to run between the PTP and blockhouse. These cables include a CAT5 cable for test-stand control, a CAT5 cable for high-speed camera control, the kill-switch cable, and BNC cables for microphone/time-of-arrival signals. These cables are connected to various computers inside the blockhouse, as pictured in Fig. A.15.

During hot-fire testing, all personnel except one, the Polaris test operator, were located inside the bunker. The Polaris test operator is responsible for setting propellant tank pressures with the regulator panel. The Polaris operator receives feedback from the test operators in the blockhouse who are actively monitoring tank pressures with the LabView system. Once tank pressures are set, the Polaris operator sets the valve channels needed for a test sequence into Remote-Standy mode, after which the operator returns to the blockhouse.

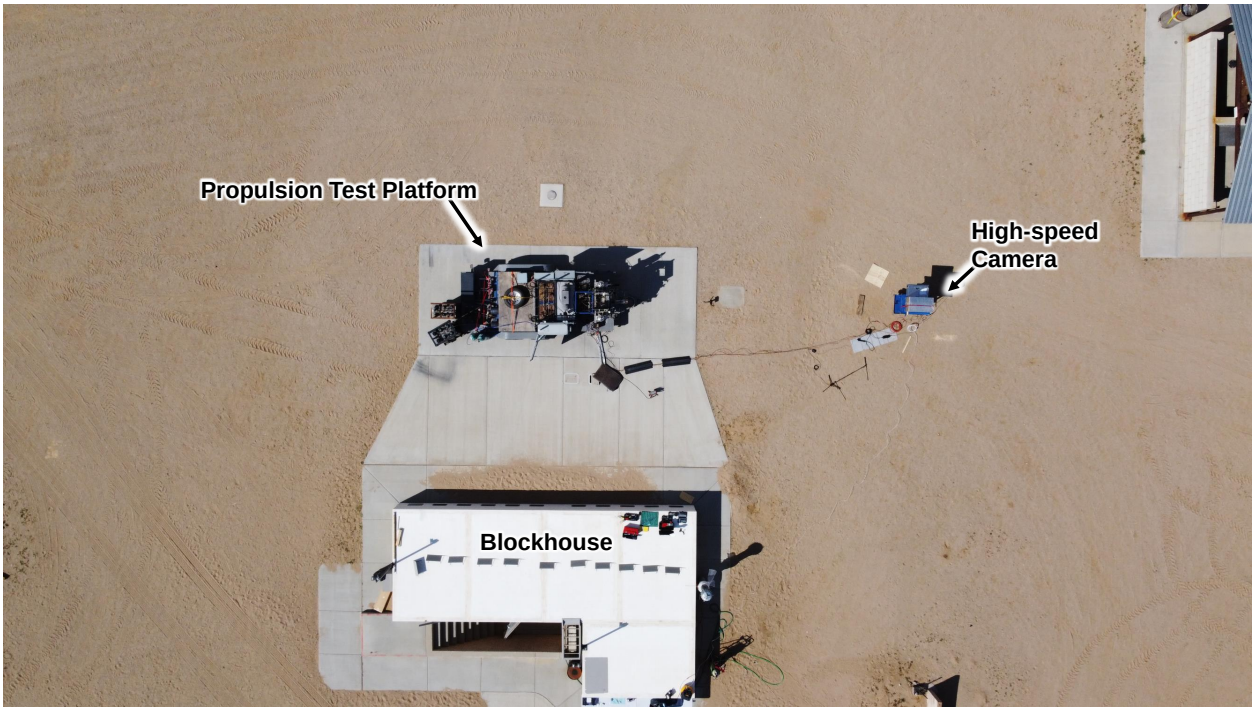

Figure A.13: Top-down view of Mojave Test Area during RDRE hot-fire testing.

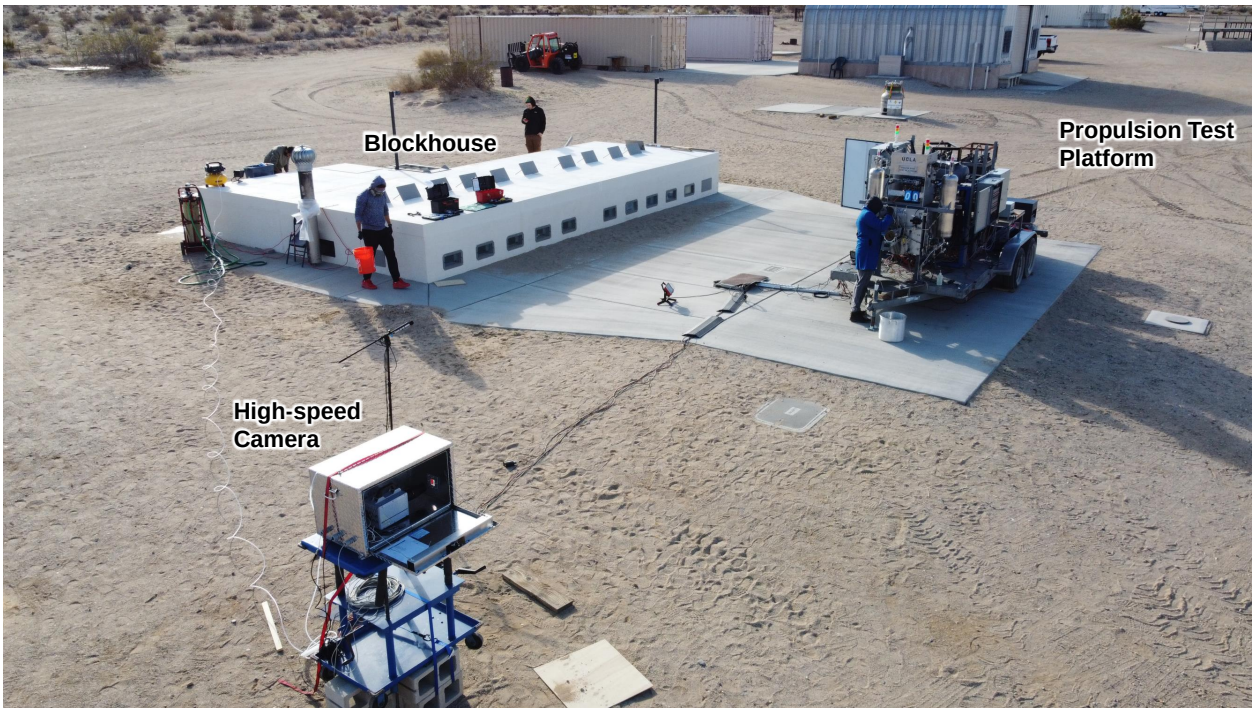

Figure A.14: Bird's-eye view of PTP at Mojave Test Area.

A.3 Standard operating procedure

This section details the standard operating procedure (SOP) used for setting up the test stand and running a hot-fire test. The procedure from the 2022 test campaign is provided, as it is more detailed and comprehensive than the 2021 version.

It should be noted that propellant loading is conducted entirely by Polaris Propulsion personnel, not UCLA graduate students. As such, the loading procedure is not included in the SOP. After hot-fire tests, propellant purges push out a majority of residual propellants, which quickly evaporate due to the volatility of the reactants. An overflow container is placed below the test article and is filled with de-ionized (DI) water, which dilutes propellants that continue to drip from the engine. Additionally, a squirt bottle of DI water is left near the test article. The test article is doused with DI water from this bottle prior to handling by personnel. If a major hardware change (such as an injector swap) is conducted, propellants are pushed back from the propellant lines into the tanks by Polaris personnel using nitrogen

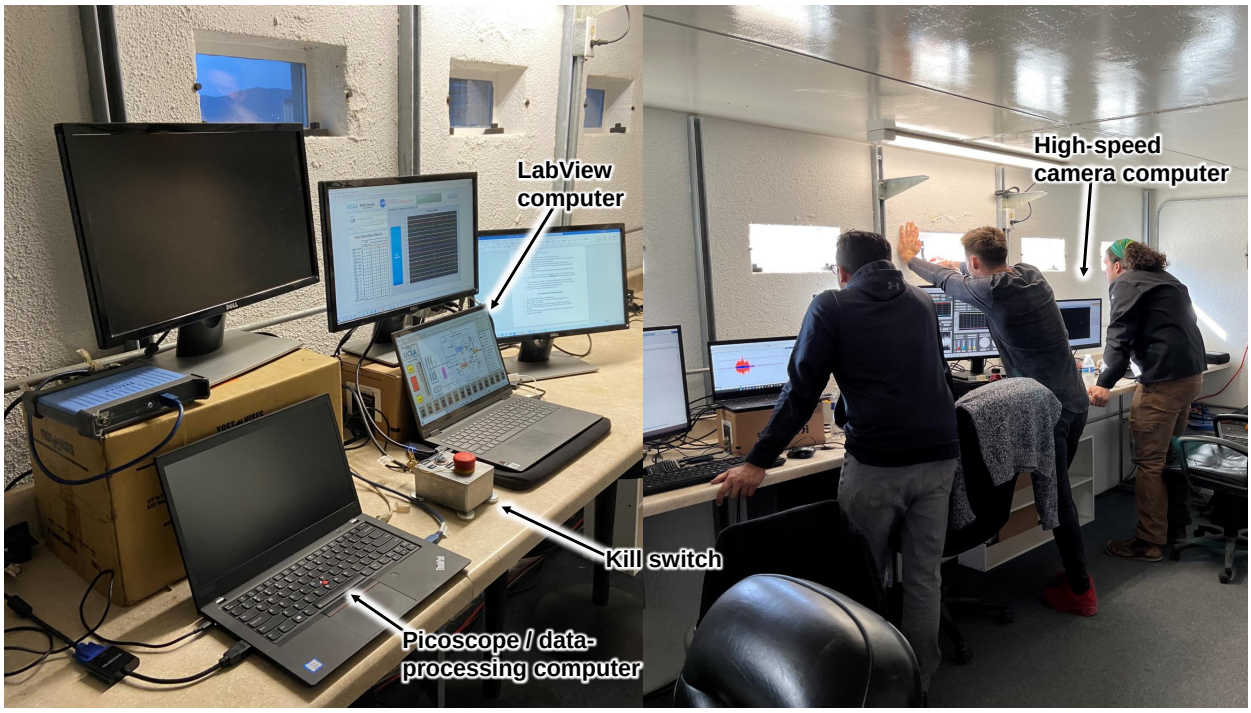

Figure A.15: UCLA graduate students during hot-fire test operation.

pressure from the test stand. The bleed ports are then used to drain trapped liquid. The test article is then flushed with DI water before removal from the test stand and disassembly. When handling contaminated hardware, UCLA personnel donned respirators with filters appropriate for filtering MMH and NTO vapors. Nitrile gloves and labcoats were always worn when handling contaminated hardware to prevent propellants from contacting skin.

After all testing is completed, propellants are transferred back into storage drums from the propellant tanks. A full DI water flush of the system is done, followed by an extended nitrogen purge to dry out the system. All system fluid ports are subsequently plugged before test stand transportation.

A.3.1 Initial setup

1. Park trailer in front of blockhouse

2. Chock wheels

3. Switch trailer jack foot from wheel to flat
4. Unlock regulator box and toolbox
5. Mount Relay Box and Data Box to left side of test stand
6. Place Battery Box on rear deck of test stand
7. Strap GHe Bottle(s) to back left side of test stand
8. Attach GN_2 hose to inlet at rear of test stand
9. Attach GN_2 hose to GHe bottle for leak check, NOT GN_2 6-pack
10. Attach load QDs to tank load lines
11. Install MMH high-point bleed, MMH low-point bleed, NTO high-point bleed, NTO low-point bleed

A.3.2 Blockhouse cable pull-through

1. Pull through into the blockhouse
   (a) the two CAT5 cables: 150 ft (off-white, camera), 50 ft (red, DAQ)
   (b) the two BNC cables for the microphone
   (c) the 50-ft PICOSCOPE TRIG BNC
   (d) the two 50-ft BNC cables designated for Dynasens
   (e) the Kill-Switch Cable
2. Power the trailer power strip using the yellow extension cord
3. Power the Data Box by connecting the orange extension cord to the trailer power strip
4. Connect Kill-Switch Cable to Kill-Switch Box

5. Ensure that Channel 16 on the Data Box is connected to both 50-ft PICOSCOPE TRIG BNC and 50-ft CAMERA TRIG BNC using a BNC tee
6. Connect 1 CAT5 Cable to the Controls & DAQ (CD) Laptop
7. Connect other CAT5 Cable to High-Speed Camera (HSC) Laptop
8. Plug in following cables to Picoscope
   (a) Ch. A – Mic A
   (b) Ch. B – Mic B
   (c) Ch. C – Dynasen 1
   (d) Ch. D – Dynasen 2
   (e) Ch. H – Picoscope Trigger

A.3.3 Test-stand controls/DAQ setup

1. Install test-number sign
2. Install 6-V battery into Relay Box
3. Plug in 6-V battery charging cable into 6-V charge port on bottom of Relay Box
4. Plug 6-V battery charging cable into test-stand power strip
5. Open lid of Battery Box
6. Attach screw labeled Left (+) to the positive terminal of the left battery (it should be taped inside a red cap)
7. Attach screw labeled Right (+) to the positive terminal of the right battery (it should also be taped inside a red cap)
8. Pull the Battery Charge 1 and Battery Charge 2 cables out of the Battery Box

9. Close the lid of the Battery Box
10. Plug in 12-V battery charging cables into 12-V charge ports coming out of lid of Battery Box
11. Plug 12-V battery charging cables into test stand power strip
12. Verify that the following switches are OFF on the Control Panel within the Relay Box
    (a) ARM 1 and ARM 2
    (b) Panel On
    (c) 6-V Charge
    (d) Channels 1–16 (neutral position)
    (e) Verify the following switches are OFF (down position) on the Battery Box
    (f) 24-V PWR
    (g) BAT 1 Enable
    (h) BAT 2 Enable
13. Verify the following switches are OFF at the Data Box
    (a) Channels 12-16 (neutral position)
    (b) Power
    (c) Plug in green safety light cable into Battery Box
14. Plug other end of green safety light cable into green port on Safety Light Box on Regulator Box
15. Plug in red safety light cable into Battery Box
16. Plug other end of red safety light cable into green port on Safety Light Box on Regulator Box
17. Connect Mil. Spec cable Z to channel 15 on Relay Box

18. Connect other end of cable Z to Mil. Spec Connector on Safety Light Box
19. Connect both 4-pin powerpole cables to both 4-pin powerpole ports on the Safety Light Box
20. Connect one 4-pin powerpole cable to the front safety light
21. Connect other 4-pin powerpole cable to the rear safety light
22. Point lights up
23. Verify that the Kill Switch key is pointing towards DISARM, the key is removed from the Kill Switch Box and the red button is pushed in
24. Connect the Kill Switch Cable to the battery box
25. Pull Kill Switch Cable through the underground conduit into the blockhouse
26. Connect the Kill Switch Cable to the Kill Switch Box
27. Plug in AC Power into the Data Box
28. Connect both ends of the REM Control cable to the Data Box and the Relay Box
29. Connect the 24-V PWR cable from the Battery Box to the Relay Box
30. Connect all 10 valve cables (A-J) to the Relay Box
    (a) Ch.1 – FTIV
    (b) Ch.2 – OTIV
    (c) Ch.3 – FTVV
    (d) Ch.4 – OTVV
    (e) Ch.5 – MFV
    (f) Ch.6 – MOV
    (g) Ch.7 – FPV

(h) Ch.8 – OPV

(i) Ch. 9 – FTRV

(j) Ch. 10 – OTRV

(k) Ch. 15 – Signal Light

31. Install Test Stand PTs (16)

32. 2000 psig PTs – Venturi Manifold, Propellant Manifolds, purge lines & CTAPS (12)

33. 3000 psig PTs – Propellant Tanks, Source Pressure (3)

34. 300 psig PTs – Pneumatics (1)

35. Connect other end of Test Stand PT cables (16) to their respective PT ports on the Data Box

    (a) Ch.1 – MMH Tank

    (b) Ch.2 – NTO Tank

    (c) Ch. 3 – MMH VM Upstream

    (d) Ch. 4 – NTO VM Upstream

    (e) Ch. 5 – MMH Venturi 3

    (f) Ch. 6 – NTO Venturi 6

    (g) Ch. 7 – MMH VM Downstream

    (h) Ch. 8 – NTO VM Downstream

    (i) Ch. 9 – MMH RDRE Manifold

    (j) Ch. 10 – NTO RDRE Manifold

    (k) Ch. 11 – Upstream CTAP

    (l) Ch. 12 – Downstream CTAP

    (m) Ch. 13 – Source Pressure

(n) Ch. 14 – Pneumatic Pressure

(o) Ch. 15 – MMH Purge

(p) Ch. 16 – NTO Purge

36. Plug load cell cable into data box

37. Connect the In-line Thermocouples to Data Box via TC extensions, don't install in line yet

    (a) Ch. 1 – MMH Inline

    (b) Ch. 2 – NTO Line

38. Connect Round-pin to Flat-pin TC Cables to Tank TCs

39. Connect Tank TC extensions to handheld TC reader

    (a) Ch. 1 – MMH Tank

    (b) Ch. 2 – NTO Tank

A.3.4 Blockhouse controls/DAQ setup

1. Verify that the following switches are OFF on the Control Panel within the Relay

    (a) ARM 1 and ARM 2

    (b) Panel On

    (c) Channels 1–16 (neutral position)

2. Verify the following switches are OFF on the Battery Box

    (a) 24-V PWR

    (b) BAT 1 Charge (neutral position)

    (c) BAT 2 Charge (neutral position)

3. Verify that the Data Box power is OFF and Relay Switches 12-16 are OFF
4. Verify that the Kill Switch key is on DISARM and the red button is pushed in
5. Power ON the Data Box
6. Power ON the Battery Box
7. Verify safety lights are flashing green
8. Open NI MAX software on the CD Laptop
    (a) Under "Devices and Interfaces," drop down "Network Devices," and drop down "NI cDAQ-9185..."
    (b) Highlight the "NI cDAQ-9185..." device and verify under Settings panel that the Status reads "Connected – Running"
    (c) When each of the 4 Chassis Cards (Mod 1-4) are highlighted, each should read Present next to Status under the Settings panel
9. Open LabVIEW Programs
    (a) Open NASA_ESI_AutoControls_V20.5_FINAL (LabVIEW VI)
    (b) Open NASA_ESI_ManualControls_V20.1_FINAL (LabVIEW VI)
    (c) Open NASA_ESI_DAQ (LabVIEW Project)
        i. First open Input_Config.vi
            A. Verify each instrumentation channel is mapped to the correct instrument with the correct respective scaling applied
            B. Verify Channel 16 is ON and mapped to "TRIGGER"
        ii. Open Main_VI.vi
            A. Choose appropriate instruments to map to their specified channels
            B. In the "Settings" box, set "Trigger Channel" to Channel 16
            C. Set "Trigger Threshold" to 2.5 V
            D. FILEPATH SAVE

A.3.5 Control System Checkouts

1. Enable Valve Pneumatics
    (a) Verify that PNEUM VENT is closed
    (b) Verify that both the NTO and MMH tanks are Empty
    (c) Verify that all regulators are closed
    (d) Ensure GHe bottle is hooked up to inlet hose on back of test stand
    (e) Ensure pneumatic 3-way valve is pointed up
    (f) Check that ACCUM ISO is closed
    (g) Confirm that all isolation valves on back of test stand are closed
    (h) Open GHe Bottle
    (i) Verify PT-13 reading matches source pressure gauge
    (j) Turn Pneumatic Control Regulator to appx. 175 psi
    (k) Verify PT-14 reading matches pneumatics gauge
2. Power ON Control System (for Checkouts)
    (a) Verify the following switches are ON at the Battery Box
        i. BAT 1 Enable
        ii. BAT 2 Enable
        iii. 24-V PWR
    (b) Verify safety light is flashing green
    (c) Put the Kill Switch key into the Kill Switch box and turn to ARM and pull the red button out
    (d) Verify the safety light is flashing red
    (e) Verify that the following switches are ON at the Control Panel within the Relay Box

i. Panel On

ii. ARM 1 and ARM 2

3. Manual Valve Checkout

   (a) One at a time, flip the 10 valve control switches and safety light switch (15) on Control Panel in Relay Box into the down position to manually open associated valve (green LED should be lit, check for visual/aural confirmation of valve actuation)

4. Remote Direct Valve Checkout

   (a) Flip channels 1-10 and 15 into REM STBY mode on Control Panel in Relay Box

   (b) On Data Box, flip Ch 15 into relay mode (green) and Ch 16 into BNC mode (blue)

   (c) Navigate to NASA_ESI_ManualControls_V20.1_FINAL (LabVIEW VI)

   (d) Verify ARM 1 and ARM 2 are ARMED (yellow)

   (e) Click "Run" and use the Open/Close buttons in the VI to actuate valves and check visually/aurally that it is working

   (f) Click "Stop" and disarm both of the ARM 1 and ARM 2 buttons

5. Remote Sequential Control Checkout

   (a) Navigate to NASA_ESI_AutoControls_V20.5_FINAL (LabVIEW VI)

   (b) Verify that the proper valves are Enabled or Disabled

   (c) Verify that the proper Open/Close times are entered in their respective valve text boxes

   (d) Click "Run"

   (e) Click "Plot Preview" in the Preview Plot tab

   (f) If the desired valve Open/Close times appear on the Preview Plot, select the Sequential Controls tab

(g) Arm both ARM 1 and ARM 2 buttons (they should be red)

(h) Select “Start” and click “GO” in the pop-up window (or Cancel if necessary)

(i) Verify that the proper valves actuate at their desired Open/Close times

(j) Disarm both the ARM 1 and ARM 2 buttons (they should be grey)

6. When finished, return valve control switches to neutral position and turn ARM 1 and ARM 2 OFF (only the blue “Panel On” LED should be lit)

7. Verify that the Kill Switch key is on DISARM and the red button is pushed in

A.3.6 Load-cell setup

1. Bring Controls Laptop out to test stand and connect to data box with short CAT5 cable

2. Re-establish labview connnection

3. Plug in load cell to load cell cable

4. Check weight of reference object on manual scale

5. Check weight of same object on LabView via load cell, confirm they are the same

6. Unplug load cell from cable

7. Route cable to test article location

8. Place back 5/8 bolt with 2 washers into rear triangular plate

9. Place 5/8 spacer onto protruding bolt

10. Screw load cell onto bolt, ensuring cable port is pointed up

11. Take front bolt and make following stackup

(a) Bolt head

(b) 3 washers

(c) Front triangle plane

(d) Washer

(e) Nut

(f) Nut

(g) Washer

12. Screw assembly into front of load cell, about 2.5 turns. Leave nuts loose

13. Add $\frac{1}{4}$" threaded rods to front plate along with standoffs

14. Slide cradle bottom onto support structure and install plastic endcap

15. Connect load cell cable

A.3.7 Test-article assembly/mounting

1. Attach fittings to manifold cap (3/8" fitting at 9 o'clock, $\frac{1}{4}$" fitting at 3 o'clock)

2. Cap 2 of the 4 fuel fittings (12 o'clock and 6 o'clock positions)

3. Put -132 EPDM o-ring on top face of injector to seal fuel manifold

4. Put -124 PTFE coated silicone o-ring on top face of injector to seal ox manifold

5. Put -149 EPDM o-ring on side of injector and grease with krytox to seal bottom of fuel manifold

6. Slide injector into manifold housing

7. Put -149 EPDM o-ring on side of manifold cap and grease with krytox to seal top of fuel manifold

8. Slide manifold cap into manifold wall

9. Place -236 silicone o-ring on instrumentation spool (IS1) and place underneath manifold
10. Put 3" long $\frac{1}{4}$-20 bolts through manifold cap and housing with washers
11. Thread fasteners into IS1 helicoils and tighten to 10 ft-lb
12. Stack desired additional outer spools (including one other instrumentation spool at end of stackup) to stackup, using -236 silicone o-rings to seal
13. Add reverse flow cap, for leak checks
14. Use six $\frac{1}{4}$"-20 bolts of appropriate length (total spool length plus $1\frac{1}{2}$") to attach extra outer spools to IS1 instrumentation spools, using the 3 aft facing helicoils
15. Attach main propellant plumbing (3 pieces for fuel, 5 pieces for ox) to manifold cap, tighten fuel and ox inlet fittings and keep other fittings loose. Fuel inlet is at 9 o' clock position and bend in line should point to 12 o'clock
16. Attach spool fittings, adding -904 silicone o-ring
    (a) On IS1, CTAP fitting at 3 o'clock, piezo fittings at 11 o'clock and 1 o'clock, cap remaining (5,7, and 9 o'clock)
    (b) On rear IS, CTAP fitting at 3 o'clock, caps on (1, 5, 7, 9, and 11 o'clock)
17. Remove caps on main propellant lines on test stand
18. Place test article on cradle
19. Remove propellant feedline caps
20. Slide engine back until contact is made with standoffs. Standoffs should be at 1, 5, and 9 o' clock. Wrap feedlines around triangular plant
21. Thread threaded rods into corresponding holes in manifold cap. Bottom out and back off 1.5 turns.
22. Loosen front load cell bolt from load cell

23. Tigthen nuts on threaded rods until standoff assembly is tight

24. Connect plumbing lines, should be able to hand tighten the fittings, otherwise, rotate engine to clocking that minimizes resistance

25. Tighten all fittings, starting from manifold cap

26. Loosen load cell front bolt nuts and slowly tighten load cell until load begins to show up on reading, then back off slightly until load disappears

27. Tighten nut on front of load cell

28. Tighten nut on back of triangle plate

29. Put top of cradle on engine, only hand tighten, then back off a half turn

30. Take scale and press up against engine, using a piece of T-slot load through the scale feet, put piece of metal in between scale and engine. Confirm that scale and load cell read the same, accounting for offset

31. Remove cap on interpropellant purge line and attach nylon purge tube to engine

32. Install RDRE manifold PTs

33. Install CTAP tubing without PT attached (swage connection removed), make sure -904 silicone o-rings are placed on test article fittings

34. Attach CTAP PTs onto swage connectors and connect to the Data Box

    (a) Ch. 11 - upstream CTAP

    (b) Ch. 12 - downstream CTAP

35. Install dynasen sensors

36. Attach BNC-Dynasen connector to Dynasens and connect to blockhouse BNC cable

37. Adhere skin thermocouples to test article (1 on each instrumentation spool)

38. Use TC extensions to connect skin TCs to Data Box

    (a) Ch. 3 – upstream TC

    (b) Ch. 4 – downstream TC

39. Connect in-line TC plumbing

A.3.8 Manual valve operation

1. Verify the following switches are ON at the Battery Box

    (a) BAT 1 Charge (enable position)

    (b) BAT 2 Charge (enable position)

    (c) 24-V PWR (LED should turn green)

2. Put the Kill Switch key into the Kill Switch box and turn to ARM and pull the red button out

3. Verify that the following switches are ON at the Control Panel within the Relay Box

    (a) Panel On

    (b) ARM 1 and ARM 2

4. Flip desired valve control switches on Control Panel in Relay Box into the down position to manually open associated valve (green LED should be lit)

5. When finished, return valve control switches to neutral position and turn ARM 1 and ARM 2 OFF (only the blue "Panel On" LED should be lit)

6. Verify that the Kill Switch key is on DISARM and the red button is pushed in

A.3.9 Remote direct valve operation

1. Verify the following switches are ON at the Battery Box

(a) BAT 1 Charge (enable position)

(b) BAT 2 Charge (enable position)

(c) 24-V PWR (LED should turn green)

2. Put the Kill Switch key into the Kill Switch box and turn to ARM and pull the red button out

3. Verify that the following switches are ON at the Control Panel within the Relay Box

   (a) Panel On

   (b) ARM 1 and ARM 2

4. Flip desired valve control switches on Control Panel in Relay Box into the up position to enable remote control (orange LED should be lit)

5. Remote Direct Valve Checkout

   (a) Navigate to NASA_ESI_ManualControls_V

   (b) 1_FINAL (LabVIEW VI)

   (c) Verify ARM 1 and ARM 2 are ARMED (yellow)

   (d) Click "Run" and use the Open/Close buttons in the VI to actuate valves and check visually/aurally that it is working

   (e) Click "Stop" and disarm both of the ARM 1 and ARM 2 buttons

6. When finished, return valve control switches to neutral position and turn ARM 1 and ARM 2 OFF

7. Verify that the Kill Switch key is on DISARM and the red button is pushed in

A.3.10 Leak check

1. Verify the following valves are closed:

(a) NTO & MMH Bypass

(b) NTO & MMH Venturis (1–6)

(c) NTO & MMH Load

(d) NTO & MMH Man Vent

(e) NTO & MMH High Point Bleed

(f) NTO & MMH Low Point Bleed

(g) NTO & MMH Trickle Purge Valves

2. Verify NTO & MMH 3-way valves pointed down
3. Verify all regulators (except pneumatic control) are in closed position
4. Check Nitrogen supply line for leaks from 6-pack to 4 rear isolation valves with leak check solution
5. Open MITY MITE ISO valve on back of test stand
6. Close FTRV
7. Open MMH tank regulator slowly to 70 psi, check for leaks up to FTRV
8. Open FTRV, pressurizing tank. Check for leaks up to bypass, load, vent valves, and FTIV.
9. Check MMH Tank PT reading matches gauge
10. Open FTIV, check for leaks up to venturis and low point bleed
11. Check MMH Venturi Manifold Upstream PT reading matches MMH Tank
12. Open one MMH Venturi, check for leaks up to MFV and high point bleed
13. Confirm MMH Venturi 3 PT and MMH Venturi Manifold Downstream PT readings match MMH Tank

14. Open MFV, check for leaks up to engine
15. Confirm MMH RDRE Manifold PT, CTAP Upstream PT, and CTAP Downstream PT readings match MMH Tank
16. Close FTIV
17. Open MMH high point bleed to vent engine
18. Close MFV
19. Back off MMH Tank Regulator
20. Vent MMH Side through MMH Man Vent
21. Close OTRV
22. Open NTO tank regulator slowly to 70 psi, check for leaks up to OTRV
23. Open OTRV, pressurizing tank. Check for leaks up to bypass, load, vent valves, and OTIV.
24. Check NTO Tank PT reading matches gauge
25. Open OTIV, check for leaks up to venturis and low point bleed
26. Check NTO Venturi Manifold Upstream PT reading matches NTO Tank
27. Open one NTO Venturi, check for leaks up to MOV and high point bleed
28. Confirm NTO Venturi 6 PT and NTO Venturi Manifold Downstream PT readings match NTO Tank
29. Open MOV, check for leaks up to engine
30. Confirm NTO RDRE Manifold PT, CTAP Upstream PT, and CTAP Downstream PT readings match MMH Tank

31. Close OTIV
32. Open NTO high point bleed to vent engine
33. Close MOV
34. Back off NTO Tank Regulator
35. Vent NTO Side through NTO Man Vent
36. Open PURGE/LOAD ISO on back of test stand
37. Open MMH purge regulator to 70 psi, check for leaks up to to FPV and MMH Trickle purge
38. Open FPV, check for leaks up to check valves
39. Close FPV
40. Back off MMH purge regulator
41. Open NTO purge regulator to 70 psi, check for leaks up to to OPV and NTO Trickle purge
42. Open OPV, check for leaks up to check valves
43. Close OPV
44. Back off NTO purge regulator
45. Vent pressure in purge lines through trickle purges, NTO high point bleed opening MOV. Close all valves when done.
46. Close all regulators EXCEPT pneumatic control
47. Remove reverse flow cap and attach correct $\frac{1}{4}$"-20 engine bolts (total spool length minus $\frac{1}{2}$") with washers

48. When finished, return valve control switches to neutral position and turn ARM 1 and ARM 2 OFF
49. Verify that the Kill Switch key is on DISARM and the red button is pushed in
50. Attach desired inner spools and nozzle to injector plate, using -015 silicone o-rings to seal
51. Shut GHe bottle
52. Vent system pressure through PNUEM VENT
53. Close PNEUM VENT and disengage pneumatic control regulator
54. Remove GN_2 hose from GHe bottle
55. Attach CGA-580 Regulator to GHe bottle
56. Attach GHe hose to CGA-580 regulator outlet attach GHe hose to GHe pneumatic line
57. Ensure GN_2 6-pack is hooked up to inlet hose on back of test stand
58. Open tanks in GN_2 6-pack and Main GN_2 6-pack valve
59. Open pneumatic accumulator tank

A.3.11 Decontamination-station setup

1. Move water deionizer tank to side of blockhouse
2. Strap tank down
3. Connect water hose from spigot to deionizer inlet
4. Connect other water hose to deionizer outlet
5. Connect hose manual handle to end of hose

6. Set up table with paper towels next to DI water

Audio-hardware setup

1. Place one microphone on microphone stand near the test article (Mic A). Ensure no cables or components are in the exhaust path.
2. Place other microphone on other microphone stand 20 ft downstream of test article (Mic B)
3. Connect both Phantom 48V Power Supplies to AC Adapters and to electrical power on trailer
4. Connect Mic A to Phantom A Input via 8 ft XLR
5. Connect Mic B to Phantom B via 8 ft + 20 ft XLR
6. Connect Both Phantom outputs to 20 ft XLR cables
7. Connect Output XLR Cables to 50 ft BNC Cables run from blockhouse with XLR/BNC Converters
8. In blockhouse, connect Mic A BNC Cable to Channel A
9. In blockhouse, connect Mic B BNC Cable to Channel B

A.3.12 High-speed video hardware setup

1. Bring enclosure out to the desired filming location, nominally 20 feet from test article
2. One at a time, take apart the cord grips and pass through power cablefrom camera power adapter, CAT5, and the CAMERA TRIG cable (TTL TRIG IN) of the camera output bundle. Leave most of the bundle inside and only pass through the TTL TRIG IN cable.
3. Reattach cord grips and fit them snugly so that the cables no longer move.

4. Install PHOTRON FASTCAM into camera enclosure with 1/4"-20 bolt on the underside, making sure to put the camera on the rubber feet inside of the enclosure.
5. Connect short CAT5 cable to camera, and connect to computer, and power on camera.
6. Connect 50 ft CAMERA TRIG BNC to CAMERA TRIG cable
7. Hook up ventilation tube to enclosure on one end and air compressor on other end
8. Set air compressor to 40 psi and turn on
9. Open PFV4 viewer to access camera. If the camera cannot be accessed, reset IP.
10. With lens cap on, click "calibrate".
11. Use "low light" mode for alignment
12. Use the zoom and pan "Quick tools" to zoom into red viewing window
13. Adjust box height and angle to center injector in red viewing window
14. Physically adjust zoom lens to fit injector in red viewing window
15. Physically adjust focus lens to focus on injector face
16. When finished checking alignment, close PV4 viewer and then turn off the camera.
17. Unplug the short cable from the laptop and re-connect long CAT5 cable to camera.
18. Close enclosure
19. From blockhouse, reconnect long CAT5 cable to laptop.
20. In blockhouse, connect to camera by opening PV4 viewer again. Ensure that the alignment has not shifted.

A.3.13 Remote photographic Setup

1. Olympus Tough setup
    (a) Ensure battery is fully charged
    (b) Install SD card
    (c) Wi-fi setup
        i. Click the “Menu” button
        ii. Navigate to the “Playback” menu
        iii. Click “Connect to smartphone” iv. Follow on-screen instructions (install “Olympus Image SHARE” on smartphone)
    (d) Install Olympus camera on tripod in desired location.
    (e) Test a burst-photo shot both while outside and in blockhouse.
2. Go-Pro setup
    (a) Install SD cards in Go-Pros
    (b) Magnetically mount one Go-Pro on steel c-strut above test article
    (c) Mount another below test article on flexible tripod
    (d) Mount another to obtain a horizontal shot of the test article
    (e) Wi-fi setup
    (f) Download “Go-Pro” app and follow on-screen instructions
    (g) Test Go-Pro connectivity in blockhouse

A.3.14 Instrumentation laptop collection

1. On Data Box flip toggle switch 16 towards green LED to illuminate blue LED
2. Plug in PicoScope to IN laptop

3. Open PicoScope software

4. Set PicoScope to collect at 1 MS, 5 second duration, (500ms/div, 1 MS)

5. PicoScope Channels A and B should be at ±500 mV, Channels C through H should be at ±10V.

6. Set Picoscope Trigger to "Single" on Channel H, with the trigger level set to 2.5 V, and pre-trigger set to 20%.

7. Set PHOTRON camera to 150 kHz frame rate, maximum exposure time.

8. Set PHOTRON trigger to "Manual," and under Trigger Settings change the pre-trigger to 150,000 frames (1 second).

A.3.15 Instrumentation checkout

1. Ensure that the Microphones register on the PicoScope signal by asking someone to tap or talk into the mics.

2. Ensure that PHOTRON camera is operational and will accept a trigger.

3. Ensure that Olympus camera and Go-Pros have fresh batteries.

4. Wirelessly connect to cameras and test functionality from inside blockhouse

5. Ensure that the Microphones register on the PicoScope signal by asking someone to tap or talk into the mics.

6. Ensure that PHOTRON camera is operational and will accept a trigger.

7. Ensure that Olympus camera and Go-Pros have fresh batteries.

8. Wirelessly connect to cameras and test functionality from inside blockhouse

9. Check load cell signal by pressing on engine

10. Ensure proper filepath is set for LabView instrumentation

11. Ensure test number panel is correct

A.3.16 Propellant load

1. Follow Polaris pyro-op directions for propellant load

A.3.17 Test-stand pressurization

1. Ensure all personnel are in blockhouse or Quonset hut

2. Ensure safety light is green

3. Ensure all pneumatic valves are closed except for FTRV and OTRV

4. Ensure valve control switches to neutral position and turn ARM 1 and ARM 2 OFF

5. Verify that the Kill Switch key is on DISARM and the red button is pushed in

6. Verify the following valves are closed:

   (a) NTO & MMH Bypass

   (b) NTO & MMH Venturis (1–6)

   (c) NTO & MMH Load

   (d) NTO & MMH Man Vent

   (e) NTO & MMH High Point Bleed

   (f) NTO & MMH Low Point Bleed

   (g) NTO & MMH Trickle Purge Valves

7. Open desired Venturi valves on MMH and NTO side (call out numbers)

8. Open pnuematics accumulator tank

9. Have Polaris pyro-op approach regulator box and set tank and purge pressures to appropriate values
    (a) Purge pressures should be ∼100 psi lower than tank pressures
10. Set IP Purge regulator to ∼70 psi
11. Outside of blockhouse, close the high-speed camera enclosure and turn on the purge system.
12. If tank pressures overshot, back off regulator, vent tank below target set pressure, and raise pressure back up, ensuring you hear check valves chattering
13. Verify the following switches are ON at the Battery Box
    (a) BAT 1 Charge (enable position)
    (b) BAT 2 Charge (enable position)
    (c) 24-V PWR (LED should turn green)
14. Verify that the following switches are ON at the Control Panel within the Relay Box
    (a) Panel On
    (b) ARM 1 and ARM 2
15. Set channels 1–10 and 15 to REM STBY at Relay Box, illuminating orange LEDs
16. Have Polaris pyro-op return to blockhouse

A.3.18 Hot-fire

1. Navigate to NASA_ESI_AutoControls_V20.5_FINAL (LabVIEW VI)
2. Verify that the proper Open/Close times are entered in their respective valve text boxes
3. Click "Plot Preview" in the Preview Plot tab

4. Prior to countdown, test triggering mechanisms of LabView DAQ, PicoScope, and PHOTRON camera by running control sequence with valves disabled (Ch 16 enabled)
5. Continually re-focus Olympus to ensure continued wireless connection.
6. Before final countdown, engage trigger for both LabView DAQ, PHOTRON (click "Record"), and PicoScope ("Running")
7. Put the Kill Switch key into the Kill Switch box and turn to ARM and pull the red button out
8. Verify that the proper valves are Enabled or Disabled
9. Click "Run"
10. Click "Plot Preview" in the Preview Plot tab
11. If the desired valve Open/Close times appear on the Preview Plot, select the Sequential Controls tab
12. Arm both ARM 1 and ARM 2 buttons (they should be red)
13. Select "Start" and click "GO" in the pop-up window (or Cancel if necessary)
14. Allow full hot-fire sequence to play out
15. Press red button in on Kill Switch turn key to DISARM and remove key
16. Disarm both the ARM 1 and ARM 2 buttons (they should be grey)
17. Look through camera data and save 5 relevant seconds
18. Save picoscope data in .mat format
19. Verify LabView data has saved
20. If done running tests, back off regulators (except pneumatics) and use the direct Control LabVIEW program to vent both the NTO and MMH tanks to 0 psig

21. When finished, have Polaris pyro-op approach test stand and return valve control switches to neutral position and turn ARM 1 and ARM 2 OFF (only the blue "Panel On" LED should be lit)

22. Close all regulators except Pneumatic Control

A.3.19 Pulse-mode setup

1. Back off pneumatic control regulator

2. Vent pneumatics through PNEUM Vent

3. Open ACCUM ISO to vent accumulator

4. Switch PNEUM 3-way to Helium

5. Close PNEUM VENT and ACCUM ISO

6. Check that CGA 580 regulator and needle valve are closed

7. Open GHe bottle and check pressure

8. Open regulator until gauge reads ∼150 psi

9. Open needle valve

10. Adjust regulator to target ∼175 psi

11. Open ACCUM ISO, allow pressure to stabilize

A.3.20 Close-out procedure

1. Close NTO REG ISO and MMH REG ISO

2. At Relay Box, set FTVV and OTVV to REM STBY and turn ARM 1 and ARM 2 ON

3. With personnel in blockhouse, arm kill switch
4. Remotely vent NTO and MMH tank
5. Disable kill switch
6. At the Relay Box, turn ARM 1 and ARM 2 OFF and return FTVV and OTVV to neutral position. Turn Panel On off
7. Refer to Polaris pyro-op on test article decontamination
8. Shut GN_2 6-pack valve
9. Close DOME CONTROL and AUX REGS needle valves
10. At the 24 V PWR Box, shut the 24 V PWR off
11. At Data Box turn Ch 16 to neutral position
    (a) Turn Data Box off
    (b) Disconnect AC Power
12. At high-speed camera
    (a) Turn off camera
    (b) Shut off air compressor
    (c) Disconnect CAT5 cable from box
    (d) Remove CAT5 cable through cord grip
    (e) Disconnect camera power
    (f) Remove ventilation hose
    (g) Disconnect BNC cable from trigger input

APPENDIX B

Detonation-Impulse Tube facility

In this Appendix, details are provided for the UCLA Detonation-Impulse Tube (DIT), used in Chapters 6 and 7. In section B.1, the basic design and operation of the DIT are reviewed. In section B.2, sample detonation experiments with LAS measurements are detailed. Lastly, in section B.3, the operating procedure for running a detonation experiment is provided. In Appendix J, a full set of drawings are provided for the DIT.

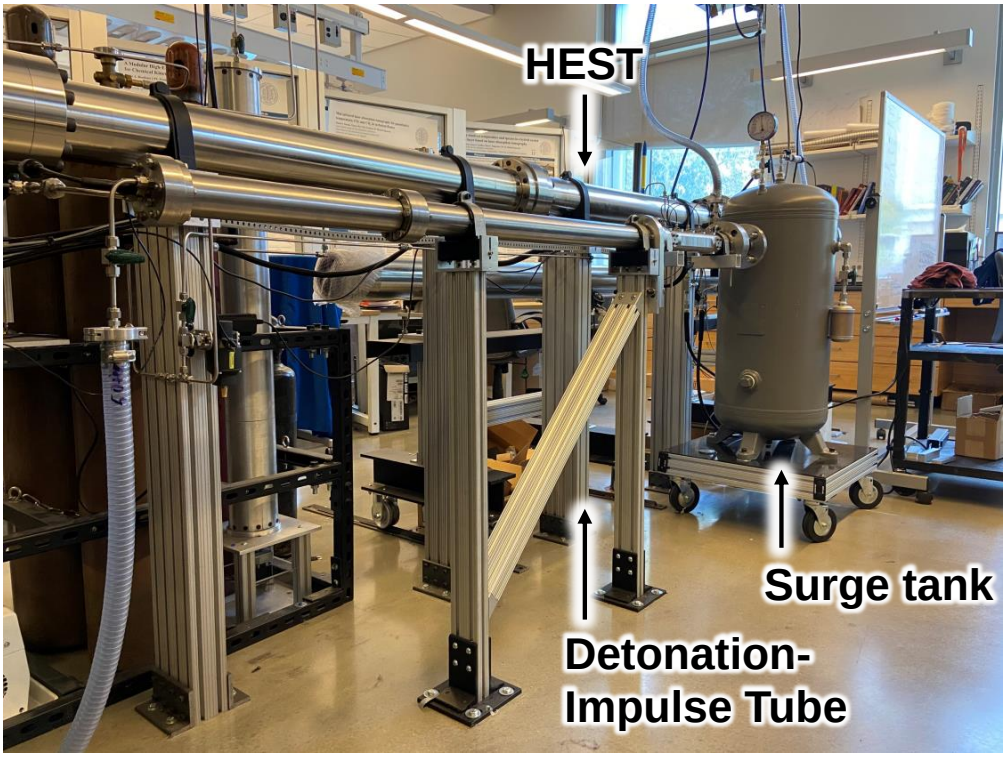

Figure B.1: Side-view of Detonation-Impulse Tube facility next to High-Enthalpy Shock Tube.

B.1 Design and operation

The Detonation-Impulse Tube facility was constructed to create controlled detonation environments with known pressure and temperature conditions for the purpose of optical sensor validation. The facility is depicted in Figs. B.1 and B.2. Critical dimensions and parameters are summarized in Table B.1. The DIT was developed as a complement to the UCLA High-Enthalpy Shock Tube (HEST) facility [209], which generates quasi-0-D high-temperature conditions behind reflected shock waves for applications such as sensor characterization, spectroscopic parameter measurements, or measurements of kinetic rates. The purpose of the DIT was to generate high-temperature gas conditions that were time-varying in nature, to demonstrate the MHz time resolution and dynamic range of the LAS sensors developed in Chapters 4–7. As such, while the HEST primarily shock heats inert or highly diluted reactive mixtures to achieve near constant-pressure and -temperature conditions, the DIT

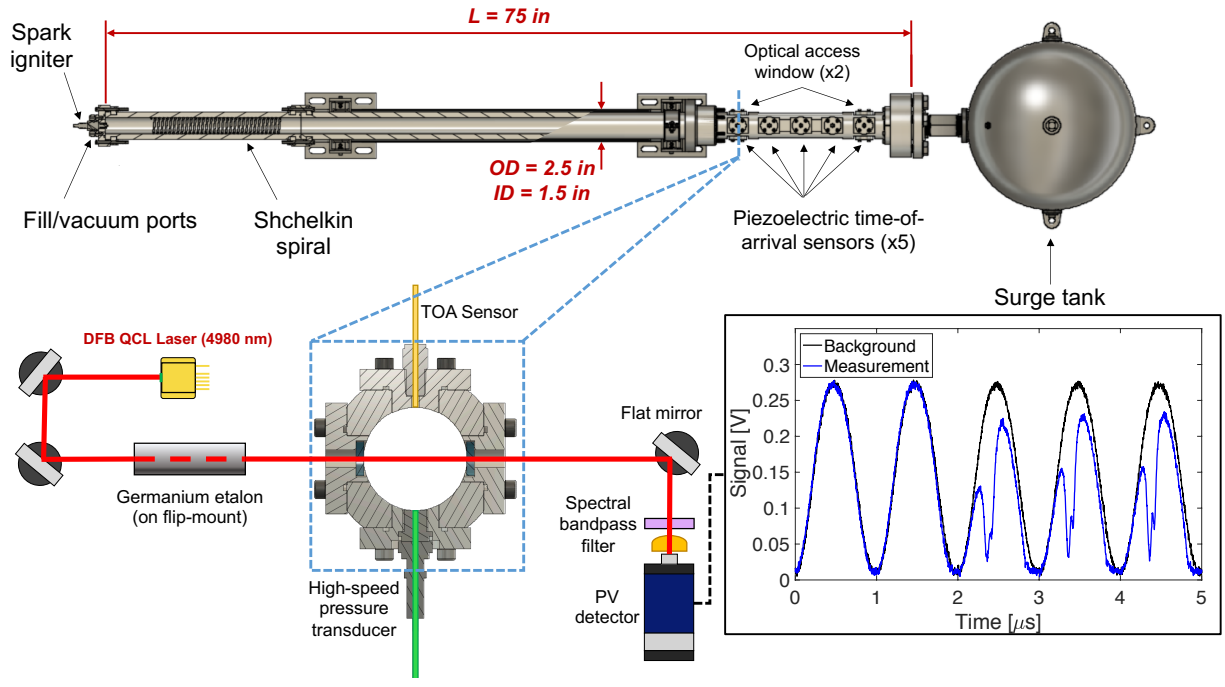

Figure B.2: Top view of Detonation-Impulse Tube facility with instrumentation and cross–sectional view of optical access with laser/detector setup. Sample MHz laser scans are shown as read by the PV detector as CO forms.

uses undiluted reactant mixtures which are directly ignited to produce a sharp detonation front and signficant post-wave gas depressurization and cooling, due to the Taylor wave effect [208]. Due to the high reactant concentrations, the tube volume must be kept significantly lower to avoid generating dangerously high quantities of reactant mixtures, which present an explosion hazard. The volume of the DIT is therefore ~ 60 times lower than that of the driven section of the HEST. Additionally, due to the higher concentration ($\times$5–10) of the targeted species for LAS (primarily CO), the path length (tube diameter) needed to be reduced compared to that of the HEST to avoid reaching optically-thick conditions. On the other hand, the tube diameter needed to be large enough to support multiple detonation cells (mm–cm scale) of the target reactants (hydrocarbons in air and O_2), in order to support the formation of an ideal 1-D detonation in a reasonable tube length. As a compromise between these two factors, the path length was reduced by a factor 2.7 from the HEST, resulting in a 1.5" (3.81-cm) inner tube diameter. The tube length was chosen to be 74.25" (188.6 cm) in order to fit within the constraints of the laboratory space, while also providing sufficient distance for a flame on one end of the tube to accelerate through a deflagration-to-detonation transition (DDT). The maximum expected operating pressure (MEOP) of the tube was set to 2,000 psi (137 bar). A minimum factor of safety (FOS) of 1.5 was introduced, setting the maximum allowable working pressure (MAWP) to 3,000 psi (207 bar). The tube was hydrostatically tested to this pressure, see below. Stress analysis detailed below also predicts that tube would only fail at a pressure of nearly 7,200 psi(500 bar), resulting in a theoretical FOS of 3.6.

The DIT was machined in-house at UCLA by graduate and undergraduate students, with support from the UCLA machine shop over the course of the 2018–2019 academic year, with the first detonation test run in October 2019. Over 120 detonation tests have been run to date.

The DIT is comprised of three tube sections made of 304 stainless steel (304 SS), mated together by weldless flanges. The flanges (304 SS) are made in halves. Sleeve pieces (304 SS) maintain concentricity between the flanges. The flanges also connect end-cap pieces (304 SS)

Table B.1: Key Detonation-Impulse Tube dimensions and parameters.

	Value	
Dimension	Imperial	Metric
Tube ID	1.5”	3.81 cm
Tube OD	2.5”	6.35 cm
Tube maximum thickness	0.5”	1.27 cm
Tube minimum thickness	0.25”	0.64 cm
Channel length (Ign. Cap to Diaphr.)	74.25”	188.6 cm
Tube elevation	40.96”	104 cm
Channel volume	131 in^3	2.15 L
Surge tank volume		114 L
Surge tank height	39.75”	100 cm
Surge tank OD	18”	45.7 cm
Surge tank thickness	1”	2.54 cm
Spiral length	36”	91.4 cm
Spiral ID	1.17”	2.97 cm
Instrumentation port bore diameter	0.6875”	1.75 cm
Port-to-port spacing	3”	7.62 cm
Flange bolt thread	1/4”-20	N/A
Flange bolt length	1.25”–4.5”	3.2–11.4 cm
Flange bolt torque	10 ft-lb	13.6 N-m
Diaphragm holder screw thread	3/4-10	N/A
Diaphragm screw length	2.25”	5.7 cm
Diaphragm screw torque	40 ft-lb	54.2 N-m
Port plug screw thread	8-36	N/A
Port plug screw length	0.5”	1.27 cm
Port plug screw torque	40 in-lb	4.52 N-m
MEOP	2,000 psi	138 bar
MAWP	3,000 psi	207 bar

which seal the ends of the tube. All seals are made using high-temperature silicone O-rings. The half-ring flanges penetrate 0.25" radially into the tube via machined grooves at the ends of each tube. As such, the tube wall thickness was set to 0.5" (1.27 cm), leaving 0.25" (0.635 cm) of material was present at the minimum tube thickness. The loading at MEOP on the flanges and grooves was assessed using finite-element analysis in Autodesk Fusion 360, resulting in a minimum FOS of 3.6, with the critical failure mode being yielding at the internal surface of the tube at the axial location of a groove. The flanges were predicted to have an FOS of 4.5. The flanges are bolted together with six 1/4"-20 black-oxide coated steel bolts and are torqued to 10 ft-lb. Hand calculations predicted an FOS of 5 for bolt tensile failure.

The first DIT tube section is terminated on one end with a cap (the "Ignitor Cap"), which features a sparkplug for ignition (discussed in detail below) and 4 fluid ports, which allow for reactant fill and vacuuming. This "Ignitor Tube" section is 18" (46 cm) long. The middle tube section, termed the "DDT Tube", is 37" (94 cm) long, and primarily exists to promote DDT, as mentioned above. DDT is assisted by a Shchelkin spiral that is 18.0" (45.7 cm) in length with a blockage ratio of 39%. The spiral is anchored axially via 2 sealing bolts accessible from the tube exterior which sit between coils of the spiral. The aftmost tube section, termed the "Instrumentation Tube", has eleven instrumentation ports located at five axial locations 3" (76.2 mm) apart, as depicted in Fig. B.2. The first and last axial location featured 4 instrumentation ports spaced around the tube circumference at 90° from each other, whereas the other three axial locations only featured a single port. Each port hole is 11/16" (1.75 cm) in diameter. The instrumentation tube section which has a lower cross-sectional area at some locations compared to the other sections due to the port holes. FEA analysis was also performed, as above, for this tube section, validating that the critical failure mode was yield at the interface grooves: the tube strength was not reduced by the port holes.

Each port is filled with a "port plug" (304 SS), which seals the instrumentation port. These port plugs can either be blank or carry optical window / instrumentation, as discussed

below. The tube is machined flat on its mating surface for the port plug to allow for an O-ring face seal. Each port plug is connected to the tube via 4 bolts. Tapped blind bolt holes on the tube are positioned 45° from the tube axis to maximize the material between the hole bottom and the tube inner diameter. The port plug bolts are 8-36 black-oxide coated steel and should be torqued to 40 lb-in. The FOS for bolt tensile failure is 4.8. Each port plug has a 0.75" (1.9-cm) radius machined into the portion which protrudes into the instrumentation port to match the inner radius of the detonation tube. After all port plugs were installed, abrasive honing was used to smooth out the tube interior. After this honing process, each port plug was assigned a specific port and orientation to maintain the internal tube geometry. The aft end of the instrumentation tube mates to a piece termed the "Diaphragm Holder" (303 SS) using the same weldless flange concept as above, with 1/4"-20 threads tapped into the Diaphragm Holder. The Diaphragm Holder adds an additional 1.25" (3.2 cm) to the internal channel length.

A key differentiating feature of this detonation tube compared to others in the literature is the ability to precisely control the pre-detonation pressure, allowing for precise estimation of the post-detonation gas properties predicted by Chapman-Jouguet (CJ) relations. Additionally, sub-atmopsheric and high-pressure detonation conditions could be achieved because the tube is not intially open to atmosphere. This precise pressure control is provided by closing the aft end of the tube. In order to prevent a large buildup of pressure post-ignition, tube end was closed using a thin plastic diaphragm (0.003" thickness, 76 µm). The diaphragm is thick enough to withstand up to a 2-atm pressure differential, but thin enough to burst/melt when exposed to the post-detonation gases. Thicker diaphragms can be used for higher initial pressure detonations. The diaphragm replaced after each test and is nominally sandwiched between two O-rings, which are compressed via a bolted-flange connection between the Diaphragm Holder and "Surge Tank Flange" (304L SS). These flanges are bolted together using four 3/4"-10 steel bolts which thread into the Diaphragm Holder. The bolts should be torqued to 40 lb-ft. Behind the diaphragm, a 30-gallon (114-L) vacuumed steel surge tank (52 times the volume of the DIT) allows for expansion and cooling of

the combustion product gases after each test.

After the tube was first assembled, the aft end of the tube was capped with a blank cap, similar to the Ignitor Cap without any sparkplug/fluid ports. Hydrostatic testing to 2,000 psi was conducted for 5 cycles, confirming that the tube was rated to its MEOP. Some initial hydrostatic tests failed due to leakage from certain port-plug O-ring seals. After hydrostatic testing, the tube was leak tested under vacuum. Leak rates as low as 0.7 mTorr/min have been achieved and the tube has reached an ultimate vacuum pressure of 2.3 mTorr. A positive-pressure leak test was also conducted with helium at 30 psi (2 atm) over 20 minutes with no noticeable drop in pressure (within 1 psi noise level of pressure transducer) was observed. After passing these qualification tests, the DIT was installed into its place in the laboratory at the Laser Spectroscopy and Gas Dynamics Laboratory, as pictured in Fig. B.1.

The DIT is mounted onto a structure which elevates it for (1) interfacing with the surge tank, and (2) ease of access to the instrumentation section, which often featured optical diagnostic setups. The main structural members were made of 3"$\times$1.5" 6061 aluminum T-slotted rail. Two vertical stanchions supported the weight of the tube and rubber pipe clamps restrained the tube from lateral motion. A metal plate termed the "Thrust Bulkhead" (Al 6061) was designed to transfer axial impulse loads generated during detonation formation to the rear stanchion. A diagonal brace, between the two stanchions transfers this horizontal load to the forward stanchion which transferred the load into the ground through concrete anchors. A truss and beam analysis confirmed that the minimum factor of safety of the structure was greater than 5 during a load condition where only the forward side of the tube was pressurized and the aft end was open. The surge tank was mounted on a rolling cart, which allowed it to be pulled away from the DIT during diaphragm installation.

Figure B.3 features a Plumbing and Instrumentation Diagram for the DIT facility. The DIT facility shares plumbing and instrumentation with the HEST facility and other laboratory facilities. Prior to each experiment, roughing pumps (Alcatel Adixen 2021i) vacuum down the DIT to mTorr pressures and the surge tank down to $<$50 Torr. The surge tank has a dedicated vacuum pump due to its large volume and the FOD (foreign object debris),

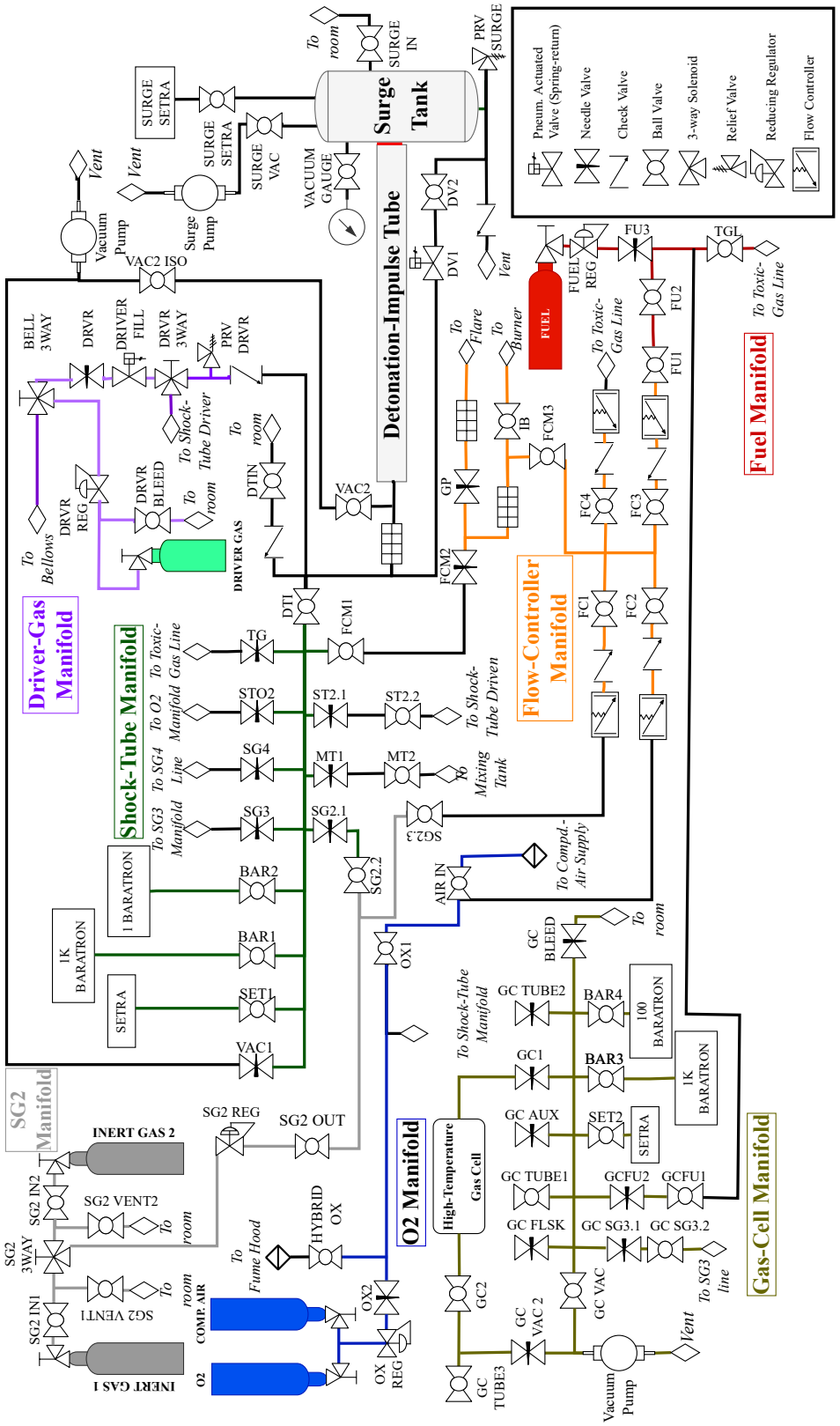

Figure B.3: Detonation-Impulse Tube facility Plumbing and Instrumentation Diagram.

which is emitted from the unfinished steel interior. The vacuum lines are opened to the DIT and surge tank with the valves denoted VAC and SURGE VAC respectively. Air intake valves (DTIN and SURGE IN) are present to repressurize the facility to atmospheric pressure after a completed or aborted test.

The test mixture composition (equivalence ratio), inert-gas dilution, and fill rate are controlled using thermally-based mass flow controllers (MKS MFC GE50A), each with a measurement uncertainty of 1.0% of the set point volumetric flow rate. These flow controllers are located at the "Flow-Controller Manifold" in the laboratory, which has oxizider, fuel, and inert gas routed to it through the various overhead lines in the laboratory. Inert gas is typically supplied by the "service gas 2" (SG2) line. The fuel supply manifold is located near the laboratory high-temperature gas cell to isolate it from the oxidizers in the room. Each gas supply has a pressure regulator, isolation valves, and a local method to vent or vacuum the gas after testing is complete. The flow controllers all have check valves attached downstream to prevent upstream mixing of reactants.

In order to allow for the establishment of steady flow in the flow controllers, which takes on the order of seconds, the mixture is initially routed into the laboratory exhaust vents. Since the mixture is combustible, a flare is set up using a glow plug to burn the reacts being exhausted. The flare is pictured in Fig. B.4. There is a flame arrester located immediately upstream of the flare. Once reactant flow has stabilized, a needle valve in parallel with the flare line is slowly opened. This diverts flow from the flare line to an overhead line which routes the reactant mixture to the "Shock-Tube Manifold". This manifold is used to prepare gas mixtures for both the High-Enthalpy Shock Tube, as well as the DIT. The reactant mixture is sent into the DIT through the Ignitor Cap after passing through a flame arrester (15 µm filter).

The initial mixture pressure in the tube is determined from a heated capacitance manometer (MKS 627D Baratron) with a full-scale pressure range of 1000 Torr, an instrument uncertainty of 0.12% of the reading, and a resolution uncertainty of 0.1 Torr. This pressure transducer is located on the Shock-Tube Manifold. The Surge Tank vacuum pressure is

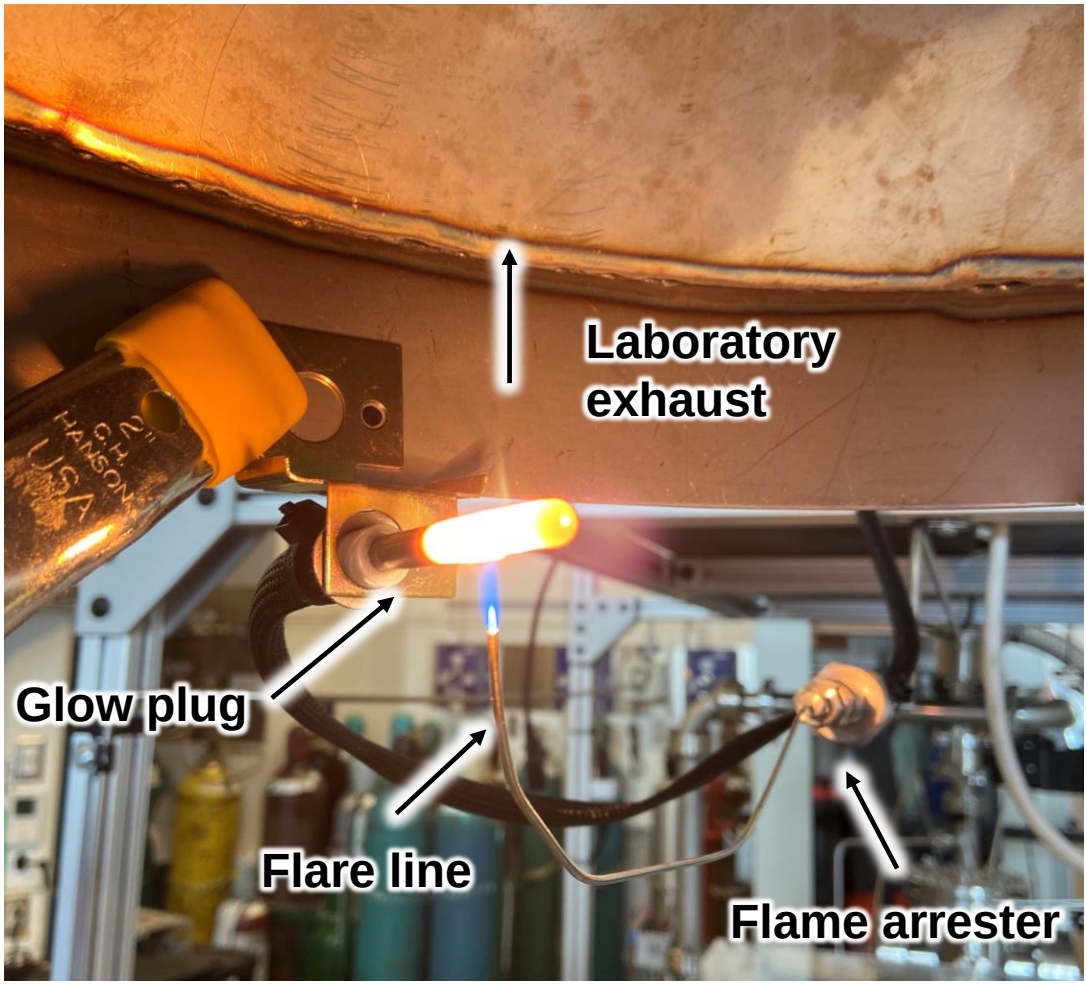

Figure B.4: Detonation-Impulse Tube glow-plug flare system used to establish steady reactant flow and equivalence ratio before filling.

monitored with a vacuum gauge, as well as a Setra 225G pressure transducer.

In addition to the aforementioned features of the facility, there are various valves that can be remotely controlled from behind a blast shield. One of these valves (DV1) allows for venting of the tube if high-pressures develop. Another valve (DRIVER FILL) routes high-pressure inert gas (usually used for the High-Enthalpy Shock Tube driver) to the tube to force diaphragm bursting and subsequent depressurization and dilution of reactant mixtures in the case of a test abort. A pressure relief valve set to 250 psi is also placed on the detonation tube in the case of accidental over-pressurization.

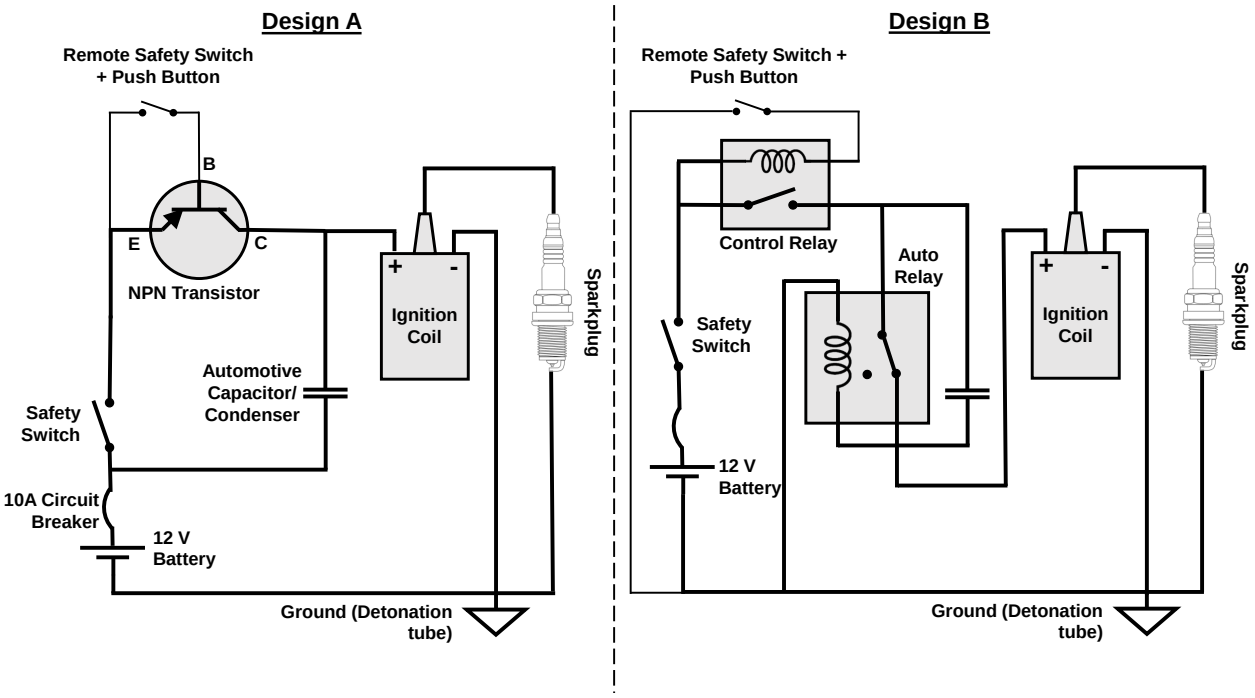

Figure B.5: Circuit diagrams for designs of the DIT spark-ignition system.

A spark plug powered by an inductive ignition circuit is used to ignite the test mixture. This circuit has undergone multiple revisions. Two successful variations will be detailed here. Variation A is pictured on the left side of Fig. B.5 and is the simpler design of the two. A 12-V battery was used send current into an automotive ignition coil, which is essentially two separate wire coils that are co-axially positioned. The current from the battery generates a current in the primary coil, which in turn generates a strong magnetic field. When the current is abruptly cut off from the primary coil, the high rate of change in magnetic field induces large inductive voltage in the secondary coil, which has many more windings than the primary coil. This amplifies the voltage to kV levels. The secondary coil is wired across an automotive sparkplug. The high voltage causes arcing across the sparkplug gap, leading to localized burst of energy which can be used to ignite combustion gas. The ground of the sparkplug, ignition coil, and battery are all connected to the detonation tube, which acts as a charge reservoir. A 10-A circuit breaker is connected in series with the battery to mitigate overcurrent in the case of a short circuit. The primary circuit is enabled via a

series of switches. One switch, termed the "Safety Switch" is located with the main circuit near the DIT. The other switch takes the form of an NPN transistor. The base of this transistor is connected to a series of remote switches that are located in the corner of the laboratory where DIT operators stand behind a blast shield during a detonation test. There is a safety switch at this remote panel and a push button, which allows the user to generate and abruptly cut off current to the primary coil, leading to spark formation. An automotive capacitor/condenser is wired in parallel to the ignition coil to absorb the energy associated with the inductive voltage generated in the primary coil. If this capacitor is not present, arcing can occur across the transistor or safety switch.

This design variation displayed inconsistent performance and had some issues related to static electricity buildup and discharge. One issue is that the downstream side of the switch was connected to the base of the NPN transistor, which did not normally connect to ground. This could lead to static electricity issues at the remote control panel. In terms of performance, this configuration often did not result in strong sparks, and there was some variability associated with the amount of time that the operator pressed the push button down for. Often, the push button had to be pressed multiple times for a spark to form. Other times, a spark was not generated at all.

To combat the above issues, a second design variation was developed. Design B is pictured on the right side of Fig. B.5. In this design variation, the NPN transistor was replaced with an off-the-shelf magnetic relay in a normally open (NO) configuration. The input circuit of the control relay was placed in series with the 12-V battery and remote switches. This time, the downstream side of the remote switches were connected to ground, mitigating static electricity issues. The output side of the control relay was not directly connected to the ignition coil. Instead, the relay output was wired into the output circuit of a second relay in a normally closed (NC) configuration, as well as one end of the capacitor. The output of the second relay was wired to the other end of the capacitor, the primary ignition coil, and to its own input circuit. The other side of the input circuit was connected to ground. The ignition coil was wired to the sparkplug in the same was as for Design A. When the

safety switches are armed and the push button is held down, the first relay is energized and its output circuit closes. This sends current into the second relay and the ignition coil, energizing it. Current is also sent to the input coil of the second relay, which begins to close the relay. This cuts off current to the primary ignition coil, resulting in a spark. Since the current to the second relay is cut off as well, the second relay opens again, allowing current flow from the first relay to resume into the ignition coil, allowing for the process to repeat again. This two-relay design allowed for a single button press to generate a high-frequency pulse-train of sparks, improving the likelihood of an ignition event occurring. Adjusting the resistance of the various circuit branches and the capacitor can change the pulse frequency and spark energy.

After the reactants are ignited, a flame travels down the length of the tube. For sufficiently detonable mixtures, the length of the tube and the spiral obstruction promote DDT, resulting in a detonation wave. When the combustion wave reaches the end of the tube, it ruptures the diaphragm, relieving pressure into the surge tank to a final gas pressure typically below 1 bar. The system is then diluted with an inert gas, evacuated with the vacuum pump, and brought back to ambient conditions. In section B.3, the standard operating procedure which codifies the above test operations/sequence is provided.

As mentioned above, the last section of the tube was outfitted with instrumentation ports at 5 axial locations. Of these five locations, two have optical ports located diametrically across from each other, allowing for an line-of-sight optical access across the tube diameter. The optical ports have 0.5° wedged sapphire windows each with a 6.35-mm (0.25") aperture. The upstream optical port—located 160 cm (63") from the spark plug—is nominally used for laser-absorption measurements due to the increased test time. The test duration is typically limited to a couple of ms by the evacuation of the combustion gases into the surge tank. The downstream optical port is outfitted with a Thorlabs PDA10D infrared light detector, which triggers the data acquisition system when the emission from the passing combustion wave is detected. The emission from an optical port during a detonation test can be seen on the right side of Fig. B.7. Fast-response, piezoelectric time-of-arrival sensors (Dynasen, Inc.) are

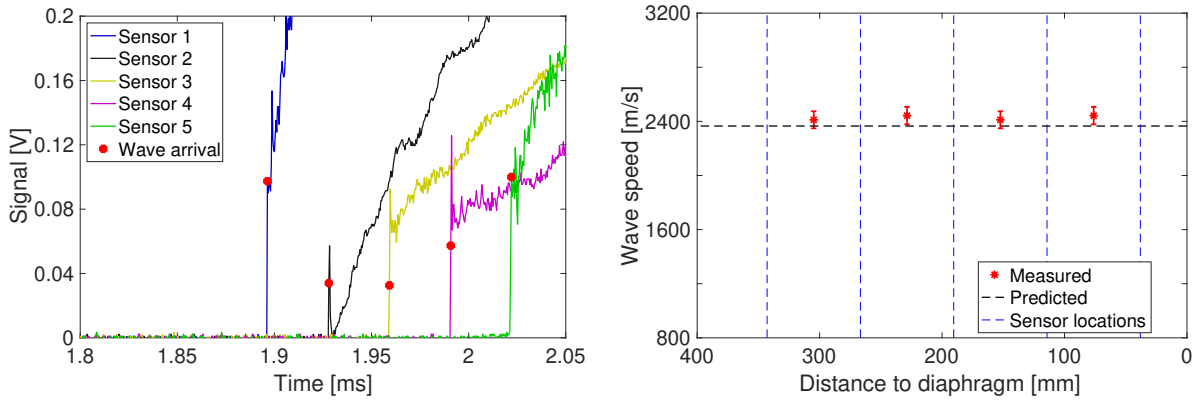

Figure B.6: Time-of-arrival signals for the five piezoelectric sensors *versus* time after DAQ triggering (*left*), indicating the times of detonation wave arrival in red. Corresponding measured wave-speed (*right*) at average location between consecutive sensors.

placed at each of the five axial locations and used to determine combustion wave-speed, U, as shown in Fig. B.6. The time-of-arrival sensors can also be seen on top of the tube on the left side of Fig. B.7. The sensors output an uncalibrated voltage pulse when exposed to a change in pressure. The time at which this voltage spike occurs can be used to infer when the detonation wave passes each axial location. Dividing the port-to-port distance by the wave travel time between the ports provides an estimate of wave-speed. This wave-speed estimate is used to assess whether the combustion wave was a deflagration (subsonic combustion) or a detonation (supersonic combustion).

Pressure traces are captured at the furthest upstream axial location using a dynamic pressure transducer (Kistler 603CAA) connected to a charge amplifier (Kistler 5018A). Laser detector and pressure data are typically collected using a Tektronix MSO44 series data acquisition module at >625 MS/s, while the time-of-arrival sensors and trigger-detector data were collected on a National Instruments PXI-6115 data-acquisition module at 2.5 MS/s. In the next section, the data captured during sample detonation experiments is detailed.

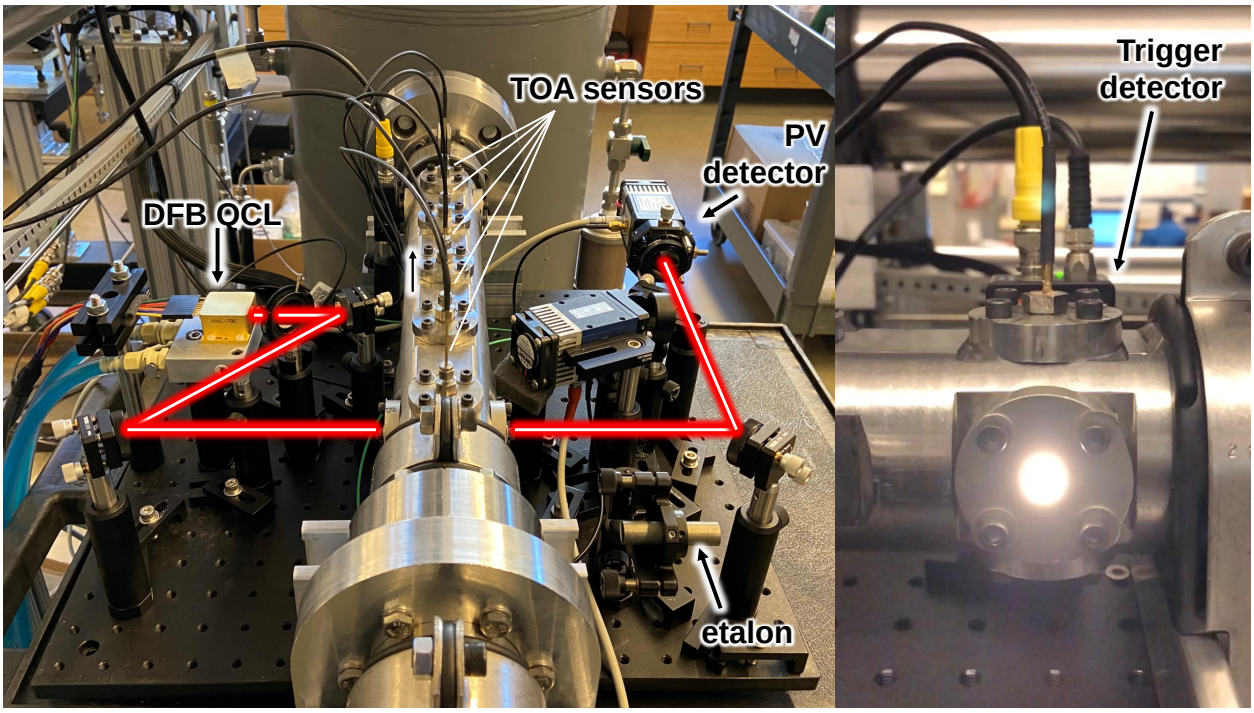

Figure B.7: *Left*: Top view of DIT instrumentation section, with time-of-arrival sensors and laser-absorption sensor optical setup on mounted breadboard. Infrared beam is highlighted in white/red for clarity. *Right*: Downstream optical port during detonation wave passage. Strong emission from detonated gases is registered by the detector on the opposite side of tube, triggering the data-acquisition system.

B.2 Sample detonation experiments

This section shows the results of two example detonation experiments that were used as a proof-of-concept for the MHz temperature and CO laser absorption sensor from Chapter 4. Both experiments were conducted at a fuel-rich equivalence ratio ϕ of 1.28, typical of rocket combustion. Informed by Chapman-Jouguet detonation models, initial conditions were selected to yield post-detonation gas conditions representative of detonation engine exhaust after some expansion has occurred. Ethylene was used as the fuel and gaseous oxygen as the oxidizer. For the first experiment, the tube was filled to an initial pressure of 58.0 Torr, while for the second experiment, the tube was initially filled to 99.4 Torr. The pressure traces collected by the Kistler pressure transducer are shown in the top of Fig. B.11, showing peak

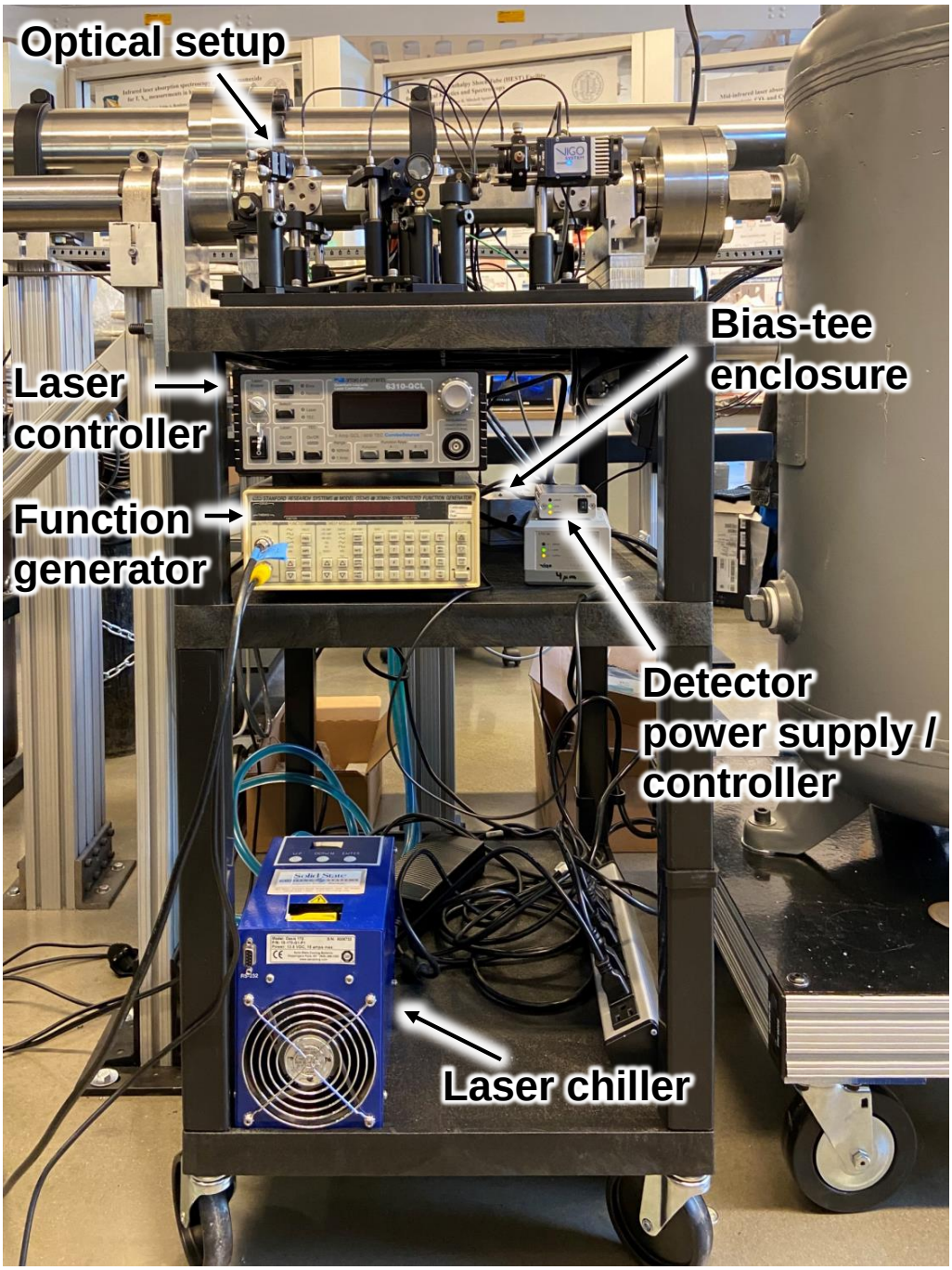

Figure B.8: Cart located underneath DIT optical breadboard which houses laser controller/chiller, function generator, bias-tee circuitry, and detector power supply / controller.

pressures of approximately 2.5 atm and 4.4 atm, respectively, followed by gas expansion. The pressure trace was fitted by a third order polynomial extrapolated backwards to the moment when CO absorbance is first observed in the laser-absorption data. Reflected waves from the diaphragm are also observed following the initial detonation wave, each of which is modeled by a separate polynomial fit. Test times are on the order of 0.5–1 ms, most of which encompasses post-detonation gas expansion.

Optical breadboards can be suspended from the Instrumentation Tube section using rubber pipe routing clamps. A 12"-wide breadboard is nominally used, with the other breadboard dimension varying from 12" to 24". Lasers and detectors have been placed directly on the breadboard, but fiber coupling schemes have also been used with a remote laser breadboard to allow for more space for multiplexed laser strategies. In the experiments discussed below, the QCL at 4.97 µm which was used for the measurements of Chapters 4 and 5 was placed on a 12"×12"-breadboard, as pictured on the left side of Fig. B.7. The light from this laser is directed through the windows of the upstream optical port into a photovoltaic detector (Vigo PVMI-4TE-8-1x1), with a measurement bandwidth of 196 MHz (note: two detectors are pictured, but only one is used for the measurement). A diagram of

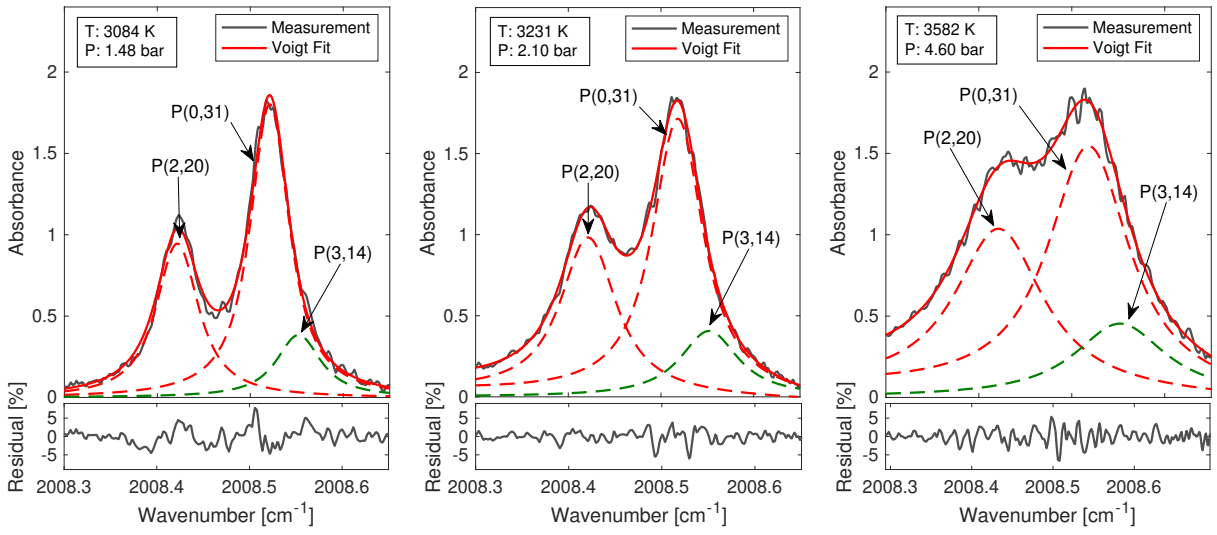

Figure B.9: Representative three-line fits for single laser scans at various conditions behind detonation waves.

the optical setup is shown on the bottom left of Fig. B.2. Below the optical breadboard was a rolling cart which held the laser controller/chiller, function generator, bias-tee circuitry, and detector controller/power supply.

Sample raw LAS data can be seen on the bottom right of Fig. B.2. The laser current was modulated sinusoidally here at 1 MHz. Strong absorption was observed on the first laser scan (within 1 µs) after the passage of the detonation wave, indicating the quick formation of CO at the high-temperature conditions. The measured incident and transmitted light intensities were parsed in 1 µs time intervals, corresponding to the scan period, and were mapped to the spectral domain using the etalon scaling technique described in sections 4.2 and 6.2. Representative absorbance spectra and corresponding multi-line spectral fits are shown in Fig. B.9 at different times behind the detonation wave, illustrating how the spectra evolves with pressure and temperature. The absorbance areas of all three lines obtained from the spectral fits and the ratio between the areas of the P(0,31) and P(2,20) lines are shown time-resolved in Fig. B.10.

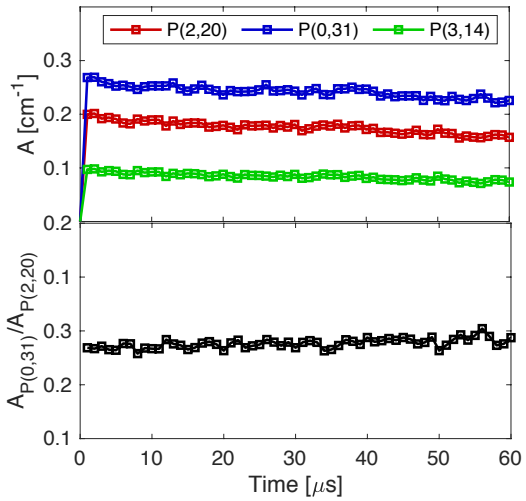

Figure B.10: Time-resolved absorbance areas for the three transitions and absorbance area ratios for the P(0,31) and P(2,20) transitions for the first 60 µs of the second detonation test.

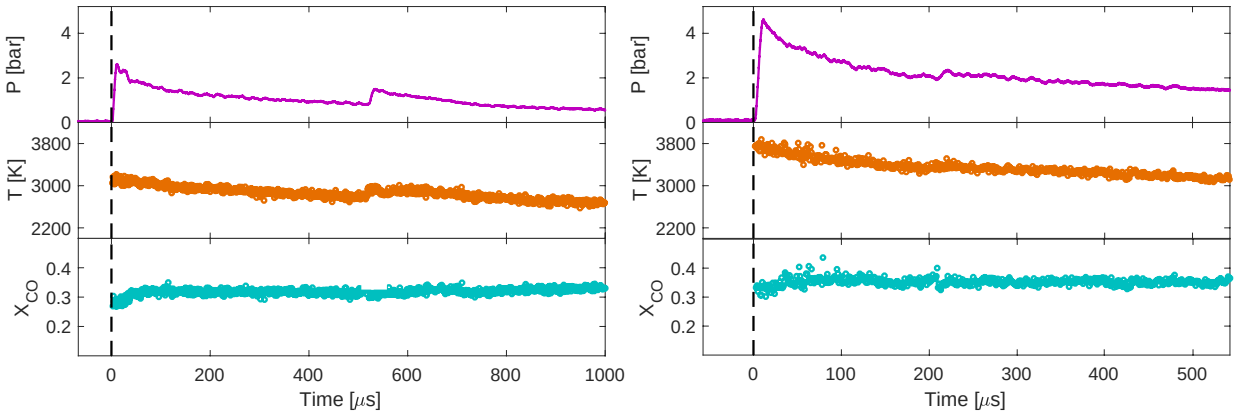

Figure B.11: Time-resolved pressure, temperature, and CO mole fraction measurements from ethylene-oxygen detonation test 1 (*left*) and test 2 (*right*).

Temperature and mole fraction were inferred using the least-squares fitting routine described in Section 4.3.1 and utilizing the pressure obtained from the pressure transducer at the same axial location as the optical line of sight. This fitting routine was repeated for each scan after the passage of the detonation wave for 1000 scans (1 ms) to produce temporally-resolved measurements of temperature and CO mole fraction for the two tests. These results are compared to a detonation model based in Cantera [142] using CalTech's Shock and Detonation Toolbox [141], which predicts the post-detonation conditions using a CJ model. The temperature and mole fraction traces are shown in Fig. B.11. The signal fluctuations produce a scatter of ± 50 K in the measured temperature and $\pm$ 0.01 in the measured CO mole fraction.

For the first test, the measured peak temperature was 3208 K, within 8% of the CJ prediction of 3473 K, while the measured mole fraction was 0.318, within 1% of the CJ prediction of 0.316, and the measured peak pressure was 2.61 bar, within 5% of the CJ prediction of 2.50 bar. For the second test, the measured peak temperature was 3788 K, within 7% of the CJ prediction of 3573 K, while the measured mole fraction was 0.363, within 7% of the CJ prediction of 0.319, and the measured peak pressure was 4.58 bar, with 5% of the CJ prediction of 4.38 bar.

These experiments were repeated using the optimized waveform strategies of Chapter 6

and the optical pressure sensing technique developed in Chapters 4 and 7. These results are shown in sections 6.3.4.1 and 7.4.2.

B.3 Standard operating procedure

Below is the standard operating procedure (SOP) to generate a detonation wave using the DIT facility located in the Laser Spectroscopy and Gas Dynamics Laboratory at UCLA. The locations of the valves referenced in this SOP (i.e. VAC1, DTIN) within the laboratory fluid system are provided in Fig. B.3.

B.3.1 Facility preparation

1. ☐ Ensure VAC1, VAC2, BAR1, BAR2, and SURGE VAC are closed
2. ☐ Change out diaphragm
   (a) If DIT and Surge Tank are at atmosphere, skip to sub-step d.
   (b) If DIT and Surge Tank are under vacuum AND are equilibrated (diaphragm burst or no diaphragm), bring to atmosphere by opening DTIN.
   (c) If DIT and Surge Tank are under vacuum AND are NOT equilibrated (diaphragm did not burst), bring DIT to atmosphere by opening DTIN and opening SURGE IN.
   (d) Remove breech canister bolts using 1-1/8" wrench
   (e) Separate surge tank from DIT
   (f) Place diaphragm at open end of DIT
   (g) Open DTI and slightly open VAC1 to keep diaphragm in place (opening VAC1 too much will cause the diaphragm to be sucked into DIT)
   (h) Close the breech canister by moving surge tank back towards DIT
   (i) Torque breech canister bolts to 40 ft-lbf

3. ☐ Ensure that the following valves are closed:

   (a) At surge tank

      i. ☐ SURGE IN

   (b) Near DIT inlet

      i. ☐ DTIN, MT1

   (c) At shock tube manifold

      i. ☐ TG, STO2, SG2.1, SG3, SG4

      ii. ☐ BAR1, BAR2

      iii. ☐ MT2

      iv. ☐ ST2.1, ST2.2, any other valves

   (d) At shock tube control panel

      i. ☐ DRVR Fill, VACUUM ET

   (e) At driver gas manifold (if first test of the day)

      i. ☐ DRVR Bottle, DRVR BLEED, DRVR REG, DNV

   (f) At flow controller manifold

      i. ☐ FC1, FC4, FCM2

      ii. ☐ GP, IB

      iii. ☐ Ensure flow controllers are closed

   (g) At remote control panels

      i. ☐ DRVR Fill (at remote ST panel), DV1 (DT Remote Panel)

4. ☐ Ensure the following 3WAY valves are correctly set

   (a) ☐ BELL 3WAY (at driver gas manifold) pointing up towards DRVR tag

   (b) ☐ DRVR 3WAY (above shock tube driver) pointing left (towards shock tube manifold)

5. ☐ Ensure that the following valves are open:

   (a) At surge tank

      i. ☐ SURGE GAUGE, SURGE SETRA, SURGE VAC

   (b) By DIT inlet

      i. ☐ DV2, VAC2

   (c) At shock tube manifold

      i. ☐ Verify that the FCM1 line is vacuumed down (using VAC1) to < 50 mTorr BEFORE opening DTI

      ii. ☐ Open DTI, FCM1, VAC1, SET1, and BAR1 (If pressure is below 15 psi on SET1)

   (d) At flow controller manifold

      i. FCM3, AUX, FC2, FC3, FC1 (if using diluent, otherwise close FC1)

6. ☐ Start filling out DT_TestLog test log while tube vacuums, located in Box under Spearrin Lab Share/Data/Detonation Tube/Experimental Data

B.3.2 Instrumentation setup

7. ☐ Kistler Pressure Transducer Setup

   (a) Check that DT Kistler cable (green) is plugged into power and is turned on

   (b) Check that DT Kistler cable (green) is plugged into DT Kistler on DIT

   (c) Check that DT Kistler cable extension (black) is plugged into "Charge" port on Kistler charge amplifier box

   (d) Set the sensitivity charge to -4.422 pC/bar on charge amplifier box by clicking the blue knob when the arrow is selected, clicking on SETTINGS, clicking on RECALL, and selecting preset number 2

   (e) Verify Low-Pass filter is set to 100kHz

(f) Ensure Kistler data cable is plugged into Channel 1 on DAQ

8. ☐ Thorlabs PDA Detector

   (a) Ensure detector is aligned with downstream window

   (b) Ensure detector power cable and BNC cable are plugged into detector

   (c) Plug in detector cable to ai5 in NI 6133 chassis

   (d) Turn power on at the power adapter by DRVR bottle and at the detector

9. ☐ Dynasen Time-of-Arrival Sensors

   (a) Ensure the correct Dynasen cables are plugged into the corresponding Dynasens; Dynasen 1 is the closest one to the ignitor and Dynasen 5 is the closest to the Surge Tank

   (b) Ensure Dynasen cables are connected to the correct BNC extenders behind the DIT optical breadboard

   (c) Ensure the BNC connectors are connected to the correct inputs channels on the NI 6133 chassis (Dyansen 1 maps to ai0 and Dynasen 5 maps to ai4)

   (d) Verify NI Trigger cable is plugged into USER1

10. ☐ Tektronix MSO44 Oscilloscope Setup

    (a) Ensure oscilloscope is plugged into power and ethernet cable is connected to NETGEAR router

    (b) Turn on oscilloscope

    (c) Ensure 10 MHz clock signal from function generator is connected to oscilloscope "Ref-In" port

    (d) Under Horizontal

        i. Set sample rate to required value (nominally 625 MS/s)

ii. Set total # of samples to achieve required test time (nominally 6.25 Mpts to achieve 10 ms test time at 625 MS/s)

iii. Set Position to 40

iv. Note sample rate and number of samples in test log

(e) Turn Channel 1 on and set vertical scale from 0-10 V

i. Double-click Ch.1 at bottom left corner of screen, set Vertical Scale to 1 V/div, and Position to -4.8 divs

(f) Plug in NI trigger cable to Aux input

(g) Click File>Save As and create new folder with today's date MMDDYY_DT (ex. 010321_DT) and make this the default folder

- Trigger setup will be explained once Background and Etalon data are collected later

11. ☐ Create folder on Box for saving data under Spearrin Lab Share/Data/Detonation Tube/Experimental Data with folder format MMDDYY (ex. 010321)

(a) Create subfolders Raw Data and Post Process

(b) ☐ LabView Dynasen program

i. Open DET_ExternalTrigger on shock tube computer by navigating to Spearrin Lab Share/Data/HEST/LabView

ii. Change trigger source to Slot 5-ai5 and the trigger level to 0.5 V, Pre-trigger to 5000, and Edge to "Rising"

iii. Fill out test log with sample rate (2.5 E+6) and # of samples (1.25 E+4) under "Dynasen" section

iv. Set save file path to the Raw Data folder created in the previous step

v. Set save name to Dynasen_runNo. (ex. Dynasen_041)

B.3.3 Gas-supply preperation

(c) ☐ Prepare driver gas for post-detonation purging

i. ☐ Check that both DRVR fill switches are turned off at the remote shock tube panel and at the manifold control panel

ii. ☐ Ensure the driver bottle, DRVR BLEED, DRVR REG and DNV are closed

iii. ☐ Ensure the 3WAY valves are routed correctly (DRVR 3WAY Left and BELL 3WAY Up)

iv. ☐ Open the driver gas bottle

v. ☐ Set DRVR REG to 100 psi

vi. ☐ Open DNV completely

(d) ☐ Prepare SG2 for diluting fill lines later and/or mixture

i. ☐ Ensure SG2.1 is closed at the shock tube manifold

ii. ☐ Ensure SG2.2 is open (overhead shock tube)

iii. ☐ Ensure SG2.3 (above flow controller table) is open if planned mixture will be diluted, close otherwise

iv. ☐ Ensure an inert gas bottle is connected to SG2 (Nitrogen, Argon, or Helium)

v. ☐ Ensure SG2 bottles are closed

vi. ☐ Ensure SG2 OUT, REG, IN2, IN1, VENT1, VENT2 are closed

vii. ☐ Check SG2 is closed at fume hoods

viii. ☐ Set SG2 3WAY to corresponding bottle

ix. ☐ Open SG2 bottle and corresponding SG2 IN

x. ☐ Set SG2 REG to ∼50 psi

xi. ☐ Open SG2 OUT completely

(e) ☐ Prepare Oxidizer

i. ☐ Ensure oxidizer bottle, OX REG, OX2, HYBRID OX and AIR IN (by flow controllers) are closed

ii. ☐ Ensure OX1 is open overhead flow controller manifold

iii. ☐ Open OX bottle

iv. ☐ Set OX REG to 35 psi

v. ☐ Open OX2 completely

(f) ☐ Prepare Fuel

i. ☐ Ensure correct fuel bottle is attached to fuel manifold

ii. ☐ Ensure fuel bottle, FUEL REG, FU3 are closed at fuel manifold

iii. ☐ Ensure GCFU2 is closed at the gas cell manifold

iv. ☐ Ensure TGL is closed overhead fuel manifold

v. ☐ Open fuel bottle

vi. ☐ If SET2 is operational, use following to set fuel pressure

A. ☐ Ensure GC VAC, GC FLSK, GCSG3.1, GC TUBE1, GC AUX, GC1, GC TUBE2, GC BLEED, BAR4, BAR3, and SET2 are closed at gas cell manifold

B. ☐ Ensure GCFU1 is open overhead gas cell manifold

C. ☐ Open GCFU2 (not all the way) and SET2

D. ☐ Open FU3 completely

E. ☐ Slowly open FUEL REG until SET2 reads 50 psi

F. ☐ Close GCFU2 and slowly open GC VAC to evacuate manifold

vii. ☐ If SET2 not operational, can use shock tube manifold to set fuel pressure

A. ☐ Verify CO bottle, CO REG, and CO Needle Valve are closed, and the TG-line is vacuumed out

B. ☐ Open TGL overhead gas cell manifold

C. ☐ Close T1-HYDROGEN fuel valve overhead flow controller manifold

D. ☐ Open NO valve in toxic gas cabinet

E. ☐ Close VAC1, FCM1, BAR1 and DTI at shock tube manifold

F. ☐ Open SET1 and TG at shock tube manifold

G. ☐ Use VAC1 to vacuum out the TG-line (below 1 Torr)

H. ☐ Close VAC1

I. ☐ Verify BAR1 and BAR2 are closed, and open FU3 needle valve all the way

J. ☐ Slowly open FUEL REG until SET1 reads 50-60 psi

K. ☐ Close TGL overhead fuel manifold

L. ☐ Open VAC1

M. ☐ Close NO valve in toxic gas cabinet when SET1 reading below 1 psi

N. ☐ Close TG

O. ☐ Open BAR1 when SET1 reading is below 15 psi

P. ☐ Open DTI and FCM1 when BAR1 reading is below 1 Torr

viii. ☐ Ensure FU1 "Ethane" and FU2 (overhead)¬ are open by flow controllers

B.3.4 Vacuuming

(a) Vacuum out fill lines

i. ☐ Open VAC1, VAC2, DTI, and FCM1 at shock tube manifold

ii. ☐ Open FCM3, AUX, FC2, FC3, and FC1 (if using diluent) at flow controller manifold

iii. ☐ Ensure pressure is below 1000 Torr (19 psi) using SET1 reading

iv. ☐ Open BAR1

v. ☐ Once BAR1 reading goes below 1 Torr, open BAR2

vi. ☐ Close VAC1 (leave VAC2 open)

(b) ☐ Perform Vacuum Test on Surge Tank

i. ☐ Ensure VACUUM ET is closed at shock tube manifold control panel

ii. ☐ If performing leak test on Surge Tank:

A. ☐ Open SURGE VAC and SURGE GAUGE

B. ☐ Wait for SURGE GAUGE reading to go below -25 in.Hg

C. ☐ Close SURGE GAUGE, then Close SURGE VAC for 30 seconds, Open SURGE GAUGE and look for visible increase in pressure which indicates presence of leak

iii. ☐ Open SURGE VAC if pressure > -25 in.Hg

A. ☐ Once an ultimate pressure of -25 in.Hg or lower has been reached in Surge Tank, close SURGE VAC

iv. ☐ Close SURGE GAUGE

(c) ☐ Perform Vacuum Test on DIT

i. ☐ Ensure DTI and FCM1 are open

ii. ☐ Open VAC2 if not already open

iii. ☐ Once pressure is below 1000 Torr (19 psi), open BAR 1

iv. ☐ Once reading on BAR1 goes below 1 Torr, open BAR2

v. ☐ Once BAR2 reading drops below 20 mTorr, record BAR2 pressure in test log

vi. ☐ Close VAC1 and VAC2, wait 1 minute, record BAR2 pressure in test log

vii. ☐ Wait 1 additional minute, record BAR2 pressure again in test log

viii. ☐ Calculate leak rate (can use leak rate from 2nd minute) and tabulate in test log

ix. ☐ Open VAC2

x. ☐ Once an ultimate pressure of 100 mTorr (at most) or lower has been reached in DIT, close VAC1 and VAC2

xi. ☐ Record DIT ultimate pressure in test log

xii. ☐ Close BAR2 and BAR1

B.3.5 Data-acquisition preperation

(a) ☐ If doing laser measurements take dark, etalon, and background

i. Turn Channel 1 off on DAQ

ii. Ensure master function generator sync port is plugged into Channel 4 and Channel 4 is turned on

iii. Set up trigger in Trigger menu

A. Switch trigger source to Channel 4

B. Set trigger mode to Edge and Slope to

C. Set trigger level to 2.5 V

iv. Press the Run/Stop button on the top right corner of DAQ and ensure Ch. 2, Ch. 3, and Ch. 4 scaling is adequate

v. Take etalon measurement

A. Flip etalon into optical path, ensure signal is maximized via alignment

B. Save all channels as waveform .mat file with naming convention Etalon_RunNo (ex. Etalon_041)

C. Remove etalon from optical path

vi. Take background measurement by saving all channels as waveform .mat file with naming convention Background_RunNo (ex. Background_041)

vii. Turn Channel 1 back on

(b) ☐ Set the Kistler pressure range such that the expected peak pressure is below 75

(c) ☐ Set up DAQ triggering

i. Ensure NI trigger cable is plugged into AUX

ii. Set up trigger in Trigger menu

A. Switch trigger source to AUX

B. Set trigger mode to Edge and Slope to

C. Set trigger level to 2.5 V

iii. ☐ Press "Single/Seq" on DAQ, and turn off all channels except for Ch. 1

iv. If using Autosave feature

A. Under the Acquisitions Tab and set number of acquisitions to 2

B. Under the Trigger Tab, go to Mode+Hold off menu

C. Under "Actions to Take" and "Trigger Event" Check Waveform Save under Act on Trigger

D. Under "Save Configuration" update filepath to today's date and save name to Measurement_RunNo (ex. Measurement_041), then press ENTER until Measurement_RunNo is bold

E. Set channels to "ALL"

F. Set format to .mat

(d) ☐ Set up LabView for Dynasen measurement/triggering

i. ☐ Ensure Dynasen file name is correct and "Save" is "On"

(e) ☐ Test DAQ triggering and prepare for test

i. ☐ Temporarily switch "Analog Trigger Source" to ai4, and "Trigger Level" to 0.05 V

ii. ☐ Press "Run once" on LabView Program

iii. ☐ Test LabView program triggering by switching MT stirrer switch on manifold control panel

A. ☐ Ensure external DAQ is triggered when LabView program is triggered

B. ☐ Check that Dynasen file is saved in Box folder & Measurement file saved in Oscope Share folder

(f) ☐ Switch "Analog Trigger Source" back to ai5, and "Trigger Level" to 0.5 V

(g) ☐ Delete test trigger files in Raw Data folder

(h) ☐ Turn Ch. 2, Ch. 3, Ch. 4 back on

(i) ☐ Press "Single/Seq" on DAQ again so that it is green

B.3.6 Reactant fill

12. ☐ Test sparkplug circuit
    (a) ☐ Check spark plug battery is plugged in (Yellow to Red, and Black to Black)
    (b) ☐ Remove spark plug indicator from sparkplug
    (c) ☐ Confirm spark plug indicator is plugged into ignition coil and spark plug
    (d) ☐ Turn off ignition battery safety
    (e) ☐ Turn off remote ignition safety
    (f) ☐ Press remote ignition button and visually confirm that sparkplug tester lights up
13. ☐ Ensure ignition battery safety is ON
14. ☐ Ensure remote ignition safety is ON
15. ☐ Move blast shield in front of DIT
16. ☐ Ensure that the following valves are closed at flow controller manifold:
    (a) ☐ FCM2, IB, FC4
    (b) ☐ FC1 (if diluent is not being used)
17. ☐ Ensure that the following valves are open at flow controller manifold:
    (a) ☐ FC2, FC3
    (b) ☐ FC1 (if diluent is being used, close otherwise)
    (c) ☐ AUX
    (d) ☐ FCM3
    (e) ☐ GP (all the way)
18. ☐ Prepare Flow Controllers (Note: Gas correction factors are relative to helium)

(a) ☐ Prepare Fuel

i. ☐ Use Up/Down Arrows to navigate to Channel C1

ii. ☐ Press “Channel Setup”

iii. ☐ Set Fuel gas correction factor by using the arrows to navigate to the number to the right of “Scale Factor,” pressing “Enter,” by using the Up/Down arrows to change the value, and by pressing “Enter” to confirm.

- Methane: 0.5
- Ethylene: 0.43

iv. ☐ Ensure “Nominal Range” is set to 2.00E+03 sccm and “Range” is set to 8.60E+02 sccm

v. ☐ Set “FlowRate SP” to target flow rate in sccm (DO NOT EXCEED 8.40E+02 sccm!)

vi. ☐ Press “ESC” to return to main menu

(b) ☐ Prepare Oxidixer

i. ☐ Use Up/Down Arrows to navigate to Channel B2

ii. ☐ Press “Channel Setup”

iii. ☐ Set Oxidizer gas correction factor by using the arrows to navigate to the number to the right of “Scale Factor,” pressing “Enter,” using the Up/Down arrows to change the value, and pressing “Enter” to confirm.

- Oxygen: 0.69
- Air: 0.71

iv. Ensure “Nominal Range” is set to 2.00E+03 sccm and “Range” is set to 1.38E+03 sccm

v. ☐ Set “FlowRate SP” to target flow rate in sccm (DO NOT EXCEED 1.38E+03 sccm!)

vi. ☐ Press “ESC” to return to main menu

(c) ☐ Prepare Diluent (if required for experiment)

i. ☐ Use Up/Down Arrows to navigate to Channel B1

ii. ☐ Press "Channel Setup"

iii. ☐ Set Diluent gas correction factor by using the arrows to navigate to the number to the right of "Scale Factor," pressing "Enter," using the Up/Down arrows to change the value, and pressing "Enter" to confirm.

- Nitrogen: 0.71

iv. Ensure "Nominal Range" is set to 5.00E+03 sccm and "Range" is set to 3.55E+03 sccm

v. ☐ Set "FlowRate SP" to target flow rate in sccm (DO NOT EXCEED 3.55E+03 sccm!)

vi. ☐ Press "ESC" to return to main menu

(d) Note that Flow Controller 2 (Channel B2) and 3 (Channel C1) have an offset of the setpoint, so the setpoint needs to be slightly higher than desired flow rate (If desired SP = 100 sccm, actual SP 115 sccm)

19. ☐ Evacuate all non-essential personnel (if Fill Pressure is above 1 atm)

(a) If below 1 atm, make sure all remaining personnel stay clear of tube axis and DIT window axes

20. ☐ Make sure VAC1, VAC2, and BAR2 are closed

21. ☐ If fill pressure < 1 atm, open BAR1 to read fill pressure and set reader to Torr

22. ☐ Turn on flare glow plug

23. ☐ Open Diluent (if necessary) flow controller by using the Up/Down arrows to navigate to Channel B1, then pressing "Setpoint" and pressing "Enter." Allow Flow Rate to stabilize before continuing.

24. ☐ Open Fuel flow controller by using the Up/Down arrows to navigate to Channel C1, then pressing "Setpoint" and pressing "Enter." Allow Flow Rate to stabilize before continuing. Note: A flame may begin to form on the glow plug at this point.

25. ☐ Open Oxidizer flow controller by using the Up/Down arrows to navigate to Channel B2, then pressing "Setpoint" and pressing "Enter." Allow Flow Rate to stabilize before continuing. Note: A very hot blue flame may form briefly before being "blown off" due to high flow velocities

26. ☐ If at any point, popping sounds are heard, flashback is occurring. Immediately close flow controllers and assess situation.

27. ☐ Verify that flow rate readings match target flow rates

    (a) ☐ If the achieved flow rate is much lower than the target, check for upstream flow restriction (needle valves not fully opened) or increase the regulator pressure

    (b) ☐ If there is a slight offset between achieved and target flow rates, slightly adjust the setpoint values until target flow rate is achieved

28. ☐ Log flow rates in test log

29. ☐ Once flow rate has stabilized slowly crack open FCM2 until target fill pressure is reached on SET1/BAR1 reading. Periodically close FCM2 to check current DIT pressure (there may be some lag). Once target pressure is reached, keep FCM2 closed

30. ☐ With flare still on, turn flow controllers off

    (a) Turn off Oxidizer

        i. Use Up/Down arrows to navigate to Channel B2

        ii. Press "Close," followed by pressing "Enter" (wait for flow rate value to stabilize around 0 sccm before continuing)

    (b) Turn off Fuel

        i. Use Up/Down arrows to navigate to Channel C1

        ii. Press "Close," followed by pressing "Enter" (wait for flow rate value to stabilize around 0 sccm before continuing)

    (c) Turn off Diluent

i. Use Up/Down arrows to navigate to Channel B1

ii. Press "Close," followed by pressing "Enter" (wait for flow rate value to stabilize around 0 sccm before continuing)

31. ☐ Turn off glow plug

32. ☐ Log initial pressure

33. ☐ Close DTI

34. ☐ Close BAR2

35. ☐ Open FCM2

36. ☐ Slowly open SG2.1 to dilute mixture to ∼50 psi, SG2 gas should be audibly flowing out of flare line during flush out

37. ☐ Close SG2.1

38. ☐ Close GP (allow pressure reading on SET 1 to return to ¡19 psi before continuing)

39. ☐ Open VAC1 and BAR1

40. ☐ Once pressure is below 1 Torr, close VAC1

41. ☐ Close BAR2, BAR1, SET1, and FCM1 at shock tube manifold

42. ☐ Close FCM2, FCM3, FC1, FC2, FC3, and AUX

B.3.7 Detonation

43. ☐ Press "Run Once" on LabView program and confirm "Save Dynasen Data" is selected

44. ☐ Confirm "Single/Seq" is pressed on DAQ (box on bottom right of screen should be yellow and say "Ready")

45. ☐ Turn Kistler on, press "Meas"

46. ☐ Flip ignition battery to “Safety OFF”

47. ☐ Move to the Remote Control panel

48. ☐ Flip remote ignition safety to “Safety OFF”

49. ☐ DETONATE: Momentarily push ignition button, no longer than 1 second

    (a) If no ignition event occurs, turn remote Ignition to “Safety ON”, and check that LabView program and DAQ have not been triggered

    (b) If they have been triggered, return to Shock Tube control panel and flip ignition battery safety to “Safety ON”

    (c) Repeat all previous steps in this section until ignition is achieved or you give up...

50. ☐ If no ignition occurs, and you would like to fill to a higher pressure and try again

    (a) Turn OFF Kistler

    (b) Stop LabView program

    (c) Turn Remote Ignition Safety & Ignition Battery Safety to “Safety ON”

    (d) Open BAR1 and FCM1

    (e) Open VAC1 until pressure goes below 1 Torr

    (f) Open BAR2 and wait until pressure drops below 100 mTorr

    (g) Close BAR2, VAC1

    (h) If Target Fill Pressure is above 1 atm, Close BAR1

    (i) Open DTI

    (j) Return to Step 31 (Ensure that the following valves are open at flow controller manifold), Skip Step 32 (Prepare Flow Controllers), and follow remaining steps

51. ☐ Flip remote ignition to “Safety ON”

52. ☐ Open DRVR Fill on remote shock tube panel for 3 seconds, and then close. If ignition has not occurred, this will burst the diaphragm, depressurizing and diluting the mixture

53. ☐ If DT SURGE SETRA reads above 14.7 psi, open DV1 on remote DIT panel until pressure drops to 14.7 psi and then close DV1

B.3.8 Post-detonation

54. ☐ Approach Shock tube manifold and flip ignition battery to "Safety ON" Note: at this point non-essential personnel may re-enter the room

55. ☐ If not using Autosave, save DAQ data on X: drive saving all channels in waveform .mat format as Measurement_RunNo (ex. Measurement_041)

56. ☐ Turn off LabView program and uncheck "Save" → change save file name to next detonation number

57. ☐ Turn Kistler OFF

58. ☐ Open SURGE VAC and VAC GAUGE

59. ☐ Once pressure reaches -25 in.Hg or less on VACUUM GAUGE, close SURGE VAC

60. ☐ Open DT IN to pressurize DIT / surge tank to atmospheric pressure

61. ☐ Open DTI, BAR1, and SET1

62. ☐ Monitoring pressure in tube via the DT SURGE reader, wait for tube/surge tank to return to 11 psi (-8 inHg)

63. ☐ Open SURGE IN to bring tube up to atmospheric pressure (14.7 psi)

64. ☐ Remove breach canister bolts with 1-1/8" wrench

65. ☐ Remove burst diaphragm, and check for broken pieces, rust, damaged o-rings, etc.

66. ☐ If running an additional test, begin at Step 1 while ignoring the entire "PREPARE GASES" and "INSTRUMENTATION" sections

B.3.9 Close-out procedure

67. ☐ Ensure VAC1, VAC2, BAR1, BAR2, and SURGE VAC are closed

68. ☐ Change out diaphragm

    (a) Place diaphragm at open end of DIT

    (b) Open DTI and slightly open VAC1 to keep diaphragm in place (opening VAC1 too much will cause the diaphragm to be sucked into DIT)

    (c) Close the breech canister by moving surge tank back towards DIT

    (d) Torque breech canister bolts to 40 ft-lbf

69. Close SURGE IN

70. Open SURGE VAC

71. Close DTIN

72. Open VAC2, FCM1, VAC1

73. Shut off DRVR Gas:

    (a) Close DRVR gas bottle

    (b) Open DRVR BLEED until bottle pressure drops to 0

    (c) Close DRVR BLEED, DRVR REG, DNV

74. Shut off SG2:

    (a) Close SG2 Bottle

    (b) Open SG2 Vent until SG2 Cylinder Pressure and Outlet Pressure drop to 0

    (c) Close SG2 Vent, SG2 IN, SG2 REG, SG2 OUT

75. Shut off Ox:
    (a) Close OX Bottle
    (b) Open Hybrid OX
    (c) Once OX Bottle and OX REG pressure drop to 0, close OX2 (Needle Valve), then close OX REG and Hybrid OX
76. Shut off Fuel:
    (a) Close Fuel Bottle
    (b) Close follow valves:
        i. GCVAC, GC FLSK, GCTUBE1, GC AUX, GC1, GCTUBE2, GCBLEED, BAR3, BAR4, GCSG3.1
    (c) Open SET2 (if operational), then open GCFU2
    (d) Slowly open GC VAC
    (e) Once SET2 reading (if operational) or fuel bottle/regulated pressure drop to 0, close FU3 and FUEL REG
77. Transfer today's DAQ files (in OScopeShare/MMDDYY_DT folder) to the appropriate Box Raw Data folder
78. Turn off ThorLabs Detector and corresponding power adapter
79. Turn off DAQ
80. If Laser measurements were made:
    (a) Turn off Function Generators
    (b) Unplug Bias-Tees
    (c) Verify Mode is on Laser, Turn Laser currents (I0) down to 0 mA
    (d) Turn off Lasers

(e) Turn Laser keys to Disable

(f) Switch Mode to TEC

(g) Bring TEC temperatures back to Chiller temperatures

(h) Turn off TEC

(i) Turn off Chillers

(j) Turn off Laser Controllers

(k) Turn off Detectors

(l) Place plastic bags over optical components

APPENDIX C

Theoretical analysis of high-speed DFB laser tuning dynamics

The contents of this chapter have been published in the journal ***Measurement Science and Technology*** *[189] under the full title "Extended tuning of distributed-feedback lasers in a bias-tee circuit via waveform optimization for MHz-rate absorption spectroscopy".*

In this Appendix, we describe a first-order model of DFB laser tuning dynamics which can be used to understand some of the trends observed in Chapter 6. The parasitic components in the laser circuitry (inductance and capacitance) are neglected and the laser output is assumed to be monochromatic. To simplify the laser tuning dynamics, a lumped-element model is used, in which the laser cavity is represented by a single thermal mass at a time-varying temperature T_{L} [K]. Two heat transfer terms are included in the model. Ohmic heating from the laser injection current $i(t)$ [A] is modeled as heat transfer into the laser, Q_{in} [W]:

$$Q_{\mathrm{in}} = \rho i^2(t). \tag{C.1}$$

Here, ρ [Ω] is the equivalent electrical resistance provided by the laser. The cooling provided by the laser heat sink is modeled as heat transfer out of the laser cavity, Q_{out} [W]:

$$Q_{\mathrm{out}} = h(T_{\mathrm{L}} - T_{\mathrm{S}}). \tag{C.2}$$

Here, T_{S} is the laser heat sink temperature and h [W·K^{-1}] is the overall heat transfer coefficient between the laser and heat sink. A key assumption in this first-order analysis is that the heat sink temperature is constant during laser modulation. This assumption becomes increasingly valid as the modulation frequency increases to high rates ($>$ kHz), because the

laser heat sink is assumed to have a much larger thermal capacity (mass) than the laser chip. Over longer timescales, such as during static tuning or Hz-rate modulation, the laser heat sink temperature may change and a higher-order analysis may be employed to analyze these situations.

Using the first law of thermodynamics, the change in thermal energy of the laser cavity, U_{L} [J], can be expressed with the following energy balance:

$$\frac{dU_{\mathrm{L}}}{dt} = Q_{\mathrm{in}} - Q_{\mathrm{out}} = \rho i^2(t) - h(T_{\mathrm{L}} - T_{\mathrm{S}}). \tag{C.3}$$

By treating the laser as a lumped thermal mass, the rate of thermal energy change of the laser can be expressed in terms of the rate of change of the laser temperature, the thermal mass of the laser cavity, m_{L} [kg], and the laser specific heat capacity c_{p} [$\mathrm{Jkg^{-1}{\cdot}K^{-1}}$]. This allows Eqn. C.3 to be rewritten as a first-order linear differential equation in T_{L}:

$$m_{\mathrm{L}} c_{\mathrm{p}} \frac{dT_{\mathrm{L}}}{dt} = \rho i^2(t) - h(T_{\mathrm{L}} - T_{\mathrm{S}}). \tag{C.4}$$

The following relationship between laser output wavenumber ν [$\mathrm{cm^{-1}}$] and temperature is adapted from [193], where α_{ex} [$\mathrm{K^{-1}}$] is the effective thermal expansion coefficient of the DFB grating:

$$\frac{d\nu}{dT_{\mathrm{L}}} = -\alpha_{\mathrm{ex}} \nu. \tag{C.5}$$

This equation can be solved to find wavenumber as a function of temperature:

$$\nu = \nu_0 \exp\left[-\alpha_{\mathrm{ex}}(T_{\mathrm{L}} - T_{\mathrm{L},0)}\right] \tag{C.6}$$

Here, ν_0 is the laser output wavenumber at an arbitrary reference temperature $T_{\mathrm{L},0}$. As the magnitude of wavenumber changes during laser scanning are relatively minor (<1%), this relation may be linearized using a Taylor Expansion:

$$\nu \approx \nu_0 \left[1 - \alpha_{\mathrm{ex}}(T_{\mathrm{L}} - T_{\mathrm{L},0)}\right]. \tag{C.7}$$

The rate of change of wavenumber with time can also be written as:

$$\frac{d\nu}{dt} = -\alpha_{\mathrm{ex}} \nu_0 \frac{dT_{\mathrm{L}}}{dt}. \tag{C.8}$$

Eqns. C.7 and C.8 can be used to recast Eqn. C.4 in terms of the laser output wavenumber:

$$\frac{m_{\mathrm{L}}c_{\mathrm{p}}}{\alpha_{\mathrm{ex}}\nu_0}\frac{d\nu}{dt}+\frac{h}{\alpha_{\mathrm{ex}}\nu_0}\nu=-\rho i^2(t)+h\left(T_{\mathrm{L},0}-T_{\mathrm{S}}+\frac{1}{\alpha_{\mathrm{ex}}}\right). \tag{C.9}$$

The case of static tuning ($d\nu/dt = 0$) can be examined to find the relationship between the reference current i_0 and the reference temperature of the laser $T_{\mathrm{L},0}$ which produces the reference output wavenumber ν_0

$$T_{\mathrm{L},0}-T_{\mathrm{S}}=\frac{\rho}{h}i_0^2. \tag{C.10}$$

We now define a new variable ν_{rel} as the difference between the output wavenumber and the reference value:

$$\nu_{\mathrm{rel}}\equiv\nu-\nu_0. \tag{C.11}$$

We also define a variable termed the "effective heating" q [A^2]as the difference in the square of the injection current and the square of the reference injection current:

$$q(t)\equiv i^2(t)-i_0^2. \tag{C.12}$$

q is the Ohmic heating of the laser chip, normalized by its electrical resistance, with the laser at its reference temperature cooling when $q < 0$ and the laser heating when $q > 0$. When modulating the injection current, the *heating amplitude* q_{A} may be defined as:

$$q_{\mathrm{A}}\equiv\frac{q_{\max}-q_{\min}}{2}=\frac{i_{\max}^2-i_{\min}^2}{2}. \tag{C.13}$$

The heating amplitude may be related to the "fractional current" F from earlier sections:

$$q_{\mathrm{A}}=i_{\mathrm{pp}}i_{\mathrm{mid}}=Fi_{\mathrm{lim}}i_{\mathrm{mid}}. \tag{C.14}$$

Here, i_{mid} is the midrange current:

$$i_{\mathrm{mid}}=\frac{i_{\max}+i_{\min}}{2}. \tag{C.15}$$

Using Eqs. C.10 – C.12, Eqn. C.9 can be rewritten in the simplified form:

$$\frac{d\nu_{\mathrm{rel}}}{dt}+\frac{\nu_{\mathrm{rel}}}{\tau_{\mathrm{L}}}=-Bq(t). \tag{C.16}$$

Here, τ_{L} [s] and B [$\mathrm{cm}^{-1}\cdot\mathrm{s}^{-1}\cdot\mathrm{A}^{-2}$] are defined as:

$$\tau_{\mathrm{L}} \equiv \frac{m_{\mathrm{L}} c_{\mathrm{p}}}{h}, \tag{C.17}$$

$$B \equiv \frac{\alpha_{\mathrm{ex}} \nu_0 \rho}{m_{\mathrm{L}} c_{\mathrm{p}}}. \tag{C.18}$$

τ_{L} is the time constant of the first-order system, and represents the time it takes for the laser output wavenumber to respond to a step change in q. B represents the magnitude of wavenumber rate of change per unit q.

The general solution of Eqn. C.16 is:

$$\nu_{\mathrm{rel}}(t) = \exp\left(-\frac{t}{\tau_{\mathrm{L}}}\right)\left[-B\int_{t_1}^{t}\exp\left(\frac{s}{\tau_{\mathrm{L}}}\right)q(s)ds + \nu_{\mathrm{rel}}(t_1)\exp\left(\frac{t_1}{\tau_{\mathrm{L}}}\right)\right]. \tag{C.19}$$

Here, t_1 [s] is an arbitrary starting time. In the following sections, we will solve Eqn. C.16 for various cases of current modulation.

C.1 Static tuning

In the case of static tuning, the injection current is a fixed value i_{st}, yielding a fixed value for $q = q_{\mathrm{st}} = i_{\mathrm{st}}^2 - i_0^2$. Additionally, $d\nu/dt = 0$, which yields the following simplified form of Eqn. C.16:

$$\nu_{\mathrm{rel,st}} = -B\tau_{\mathrm{L}}(i_{\mathrm{st}}^2 - i_0^2). \tag{C.20}$$

As mentioned in the previous section, during static tuning, the laser heat sink may change temperature due to the long timescales involved. However, this relation is informative as it indicates the locally nonlinear relationship between current and wavenumber modulation.

C.2 Sinusoidal heating modulation

Before investigating the more complicated case of sinusoidal current modulation, the idealized case of sinusoidal variation in the laser heating $q(t)$ with scan rate f [Hz] (period τ [s]) is investigated, where:

$$q(t) = q_{\mathrm{A}} \sin\left(2\pi f t\right). \tag{C.21}$$

The steady-state solution for Eqn. C.16 is:

$$\nu_{\mathrm{rel}}(t) = q_{\mathrm{A}} H_q \sin\left(2\pi f t - \phi_q\right), \tag{C.22}$$

$$H_q \equiv \frac{|v_{\mathrm{pp}}|}{|q_{\mathrm{pp}}|} = \frac{B\tau_{\mathrm{L}}}{\sqrt{(2\pi f \tau_{\mathrm{L}})^2 + 1}}, \tag{C.23}$$

$$\phi_q \equiv \tan^{-1}\left(2\pi f \tau_{\mathrm{L}}\right). \tag{C.24}$$

A sample injection-current, effective heating, and chirp profile for an idealized 1 MHz sine wave is represented by the black curves in Fig. C.1. H_q [$\mathrm{cm^{-1}{\cdot}A^{-2}}$] is the transfer function between the effective laser heating q and the wavenumber modulation of the laser which is the ratio of the wavenumber amplitude and the effective heating amplitude q_{A}. The scan depth of the laser under sinusoidal heating modulation is directly proportional to the product of the transfer function and the heating amplitude of the laser. This implies that the difference of the squares of the maximum and minimum injection current, $i^2_{\mathrm{max}} - i^2_{\mathrm{min}}$, drives the scan depth, not necessarily the linear current amplitude. As such, with the same current amplitude, current modulation at a higher mean current will result in higher scan depth than current modulation at a lower mean current. At scan rates much higher than the natural frequency of the laser ($1/\tau_{\mathrm{L}}$), the transfer function simplifies to:

$$H_q \approx \frac{B}{2\pi f}. \tag{C.25}$$

This indicates that at high modulation rates, $H_q \to 0$ which reflects the decrease in spectral scan depth at high scan rates. At very low scan frequencies relative to the laser natural frequency, H_q is maximized at $B\tau_{\mathrm{L}}$.

ϕ_q [rad] is the phase lag of the wavenumber modulation relative to the effective laser heating. As the scan-rate f becomes much larger than the natural frequency of the laser system ($1/\tau_{\mathrm{L}}$), $\phi_q \to 90°$, which is experimentally observed as the increasing phase lag between current and wavelength modulation at high scan rates, as seen in Fig. 6.2. On the other hand, at low scan rates, $\phi_q \to 0°$ which implies near zero phase lag for slow modulation. The transfer function and phase lag versus scan rate are plotted in Fig. C.2 for $\tau_{\mathrm{L}} = 240$ ns. This value, specific to the primary laser used in Chapter 6, is determined in Section C.4.

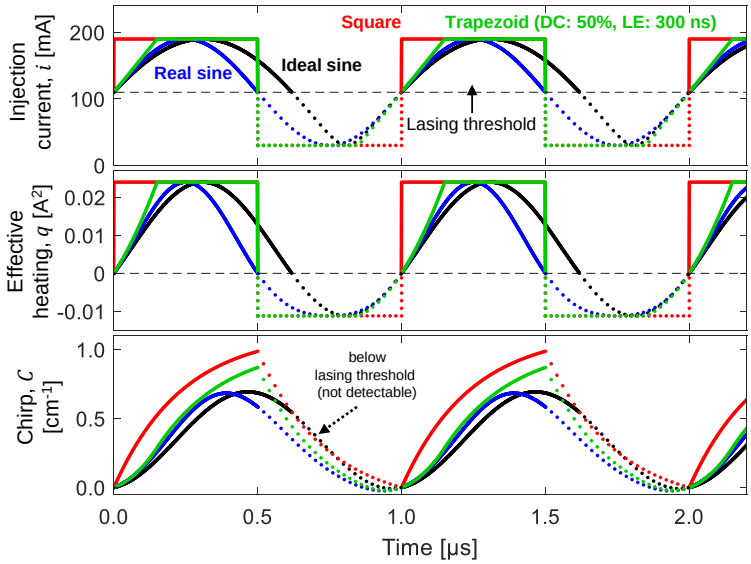

Figure C.1: Sample simulated injection current profiles (*Top*), effective heating profiles (*Middle*), and chirp profiles (*Bottom*) for an ideal sinusoidal heating (black), sinusoidal injection current (blue), square-wave modulation at 50% duty cycle (red), and trapezoid-wave modulation with 50% duty cycle and $L = 0.3$ (green). The values of B and τ_{L} are the same for each type of modulation, and are equal to the the values found for the main laser studied in Chapter 6. The values of $i_{\max}$, $i_{\min}$, and i_{th} are set to 190, 30, and 110 mA respectively. The portion of the scans for which the laser is below the lasing threshold are indicated by the dotted portion of the curves. All chirp profiles are zeroed to the beginning of the upscan above the lasing threshold.

At $f = 1$ MHz, this time constant predicts a phase lag of approximately 56° and a transfer function that is ∼55% of its maximum low-frequency value.

The transfer function is linear with B, implying that spectral scan depth is directly proportional to the thermal expansion coefficient of the DFB grating, α_{ex}, and the electrical resistance of the laser, ρ. Additionally, the transfer function and scan depth would be higher at higher wavenumbers (shorter wavelengths). The transfer function can also be increased by increasing the time constant of the laser τ_{L}. This can be achieved by either reducing the heat transfer coefficient between the laser and heat sink, h, or by increasing the overall heat capacity of the laser chip, $m_{\mathrm{L}} c_{\mathrm{p}}$ [J·K^{-1}], although this reduces B and would likely result in

an overall reduction in the transfer function. The transfer function plateaus to the value predicted by Eqn. C.25 for extremely large values of τ_{L}, implying diminishing returns for this strategy of transfer function enhancement. Increasing τ_{L} can also have potential deleterious effects on the temperature stability of the laser over long time scales, so this is a non-ideal method to improve tuning characteristics.

C.3 Sinusoidal current modulation

For a sinusoidal modulation of current with scan-rate f, current amplitude i_{A}, and midrange current $i_{\mathrm{mid}} = i_0$ (the choice of reference condition 0 is arbitrary), the time-varying current and q take the form:

$$i(t) = i_{\mathrm{A}} \sin(2\pi f t) + i_0, \tag{C.26}$$

$$q(t) = i_{\mathrm{A}}^2 \sin^2(2\pi f t) + 2 i_{\mathrm{A}} i_0 \sin(2\pi f t), \tag{C.27}$$

$$i_{\mathrm{A}} \equiv \frac{i_{\max} - i_{\min}}{2}, \tag{C.28}$$

$$i_0 = i_{\mathrm{mid}}. \tag{C.29}$$

To put the equation in terms of pure sinusoids, trigonometric double-angle identities are utilized:

$$q(t) = 2 i_{\mathrm{A}} i_{\mathrm{mid}} \sin(2\pi f t) - \frac{i_{\mathrm{A}}^2}{2} \sin\Big(4\pi f t + \frac{\pi}{2}\Big) + \frac{i_{\mathrm{A}}^2}{2}. \tag{C.30}$$

The heating function $q(t)$ is now a sum of two sinusoids with frequency $2f$, $1f$, and $0f$ (DC component). The resulting solution to Eqn. C.16 will be a linear combination of the solutions for these individual sinusoidal forcing functions. These solutions can be obtained using Eqs. C.22-C.24:

$$\nu_{\mathrm{rel}}(t) = -B q_{\mathrm{A}} \tau_{\mathrm{L}} \Bigg[\frac{\sin\left(2\pi f t - \tan^{-1}(2\pi f \tau_{\mathrm{L}})\right)}{\sqrt{(2\pi f \tau_{\mathrm{L}})^2 + 1}} + \frac{i_{\mathrm{A}}}{4 i_{\mathrm{mid}}} \frac{\sin\left(4\pi f t - \frac{\pi}{2} - \tan^{-1}(4\pi f \tau_{\mathrm{L}})\right)}{\sqrt{(4\pi f \tau_{\mathrm{L}})^2 + 1}} + \frac{i_{\mathrm{A}}}{4 i_{\mathrm{mid}}} \Bigg]. \tag{C.31}$$

This solution indicates that the wavenumber modulation is composed of two sine waves, one at the current-modulation frequency and another at a harmonic frequency twice that of the

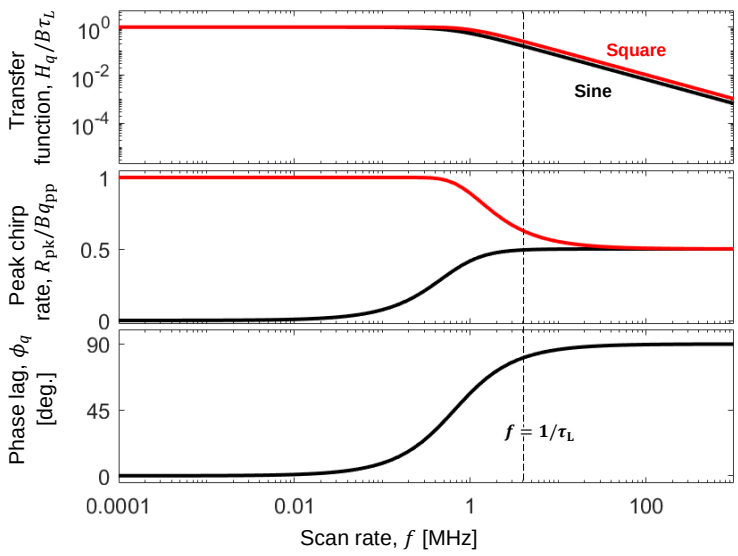

Figure C.2: *Top*: The normalized transfer function for a square wave at 50% duty cycle (red) and ideal sine wave (black) *versus* scan rate f. *Middle*: Normalized peak upscan chirp rate *versus* scan rate for the aforementioned sine and square wave. *Bottom*: The phase lag for an ideal sine wave *versus* scan rate. τ_L is set to 240 ns, the value found for the primary laser used in Chapter 6.

current-modulation. Additionally, there is an offset in the center wavenumber induced by the modulation, related to the fact that the mean current modulation is not equal to the mean value of the heating to the laser. This offset v_{off} is equal to:

$$\nu_{off} = -\frac{i_A}{4i_{mid}}\tau_L B q_A. \tag{C.32}$$

A representative injection-current, effective heating, and chirp profile for 1-MHz sinusoidal injection current modulation are represented by the blue curves in Fig. C.1. Closed form equations for the transfer function and phase lag are not easily extracted from Eqn. C.31. Equation C.31 is useful in that it reveals the functional form of the wavelength modulation due to sinusoidal current modulation. When fitting the relative wavenumber/chirp profile for a sinusoidal injection-current scan, it is thus more appropriate to fit the profile to a linear combination of a sine wave and another sine wave at double frequency, as has been performed in various works [157]. This second harmonic has been noted in analysis of

wavelength-modulation spectroscopy, where sinusoidal injection-current modulation is used and modeled.

Using Eqn. C.31, the ratio of the amplitude of the 2nd harmonic sinusoid and the sinusoid at the fundamental frequency is given by

$$\frac{\Delta\nu_{2f}}{\Delta\nu_{1f}} = \frac{i_{\mathrm{A}}}{4i_{\mathrm{mid}}} \frac{\sqrt{(2\pi f\tau_{\mathrm{L}})^2+1}}{\sqrt{(4\pi f\tau_{\mathrm{L}})^2+1}}. \tag{C.33}$$

For low values of modulation frequency, this ratio approaches $i_{\mathrm{A}}/4i_{\mathrm{mid}}$, which can range from 0 to 25%, with lower values at lower current amplitudes. For high values of the modulation frequency, this ratio approaches half of the low-speed value: $i_{\mathrm{A}}/8i_{\mathrm{mid}}$, which ranges from 0 to 12.5%. Therefore, at high modulation frequencies and moderate values of current amplitude, the higher order sinusoid may be neglected to simplify the waveform analysis, and the solution for the wavenumber profile in Eqn. C.31 can simplify to the solution of pure sinusoidal heating in Eqn. C.22, albeit with a constant offset. As such, the trends of decreasing scan depth and increasing phase lag with modulation frequency established in Section C.2 are still applicable to the case of sinusoidal current modulation.

In the following paragraph, we detail how to calculate the spectral scan depth for sine-wave modulation. If the laser is scanned below lasing threshold, i_{th}, the spectral scan depth can be found by finding the time τ_{th} at which the $i(t) = i_{\mathrm{th}}$ and computing ν_{rel} at this time. This time can be calculated as follows:

$$\tau_{\mathrm{th}} = \frac{1}{2\pi f} \sin^{-1}\left(\frac{i_{\mathrm{th}} - i_{\mathrm{mid}}}{i_{\mathrm{A}}}\right). \tag{C.34}$$

Next, the minimum value of ν_{rel} must be found. Neglecting the first harmonic term (as discussed previously), this minimum occurs at the upscan "turnaround", $\tau_{\mathrm{turn,up}}$:

$$\tau_{\mathrm{turn,up}} \approx \frac{1}{2\pi f}\left(\tan^{-1}(2\pi f\tau_{\mathrm{L}}) + \frac{\pi}{2}\right). \tag{C.35}$$

The difference between these two values is the scan depth of the sinusoidal waveform:

$$\Delta\nu_{\mathrm{sine}} = \nu_{\mathrm{rel}}(\tau_{\mathrm{th}}) - \nu_{\mathrm{rel}}(\tau_{\mathrm{turn,up}}). \tag{C.36}$$

If the laser is not being scanned below the lasing threshold, then the maximum value of the wavenumber profile must be found and subtracted by the minimum wavenumber value from

Eqn. C.35. If the second harmonic is neglected, then $\Delta\nu_{\text{sine}}$ simplifies to the following form equivalent to the form for pure sinusoidal heating (see also Eqn. C.22):

$$\Delta\nu_{\text{sine}} \approx \frac{\tau_{\text{L}} B q_{\text{A}}}{\sqrt{(2\pi f \tau_{\text{L}})^2 + 1}}. \tag{C.37}$$

To find the chirp rate of the sinusoidal waveform, the absolute value of the time-derivative of Eqn. C.31 must be taken. If the higher harmonic is neglected, the chirp rate during the upscan is given by:

$$R_{\text{up}}(t) = \frac{2\pi f \tau_{\text{L}} B q_{\text{A}}}{\sqrt{(2\pi f \tau_{\text{L}})^2 + 1}} \cos\left(2\pi f x - \tan^{-1}(2\pi f \tau_{\text{L}})\right). \tag{C.38}$$

The peak chirp rate can be found by taking the time-derivative of the chirp rate and finding the times when this derivative equals zero. The peak chirp rate can be found by evaluating the chirp rate at these times. Still neglecting the higher harmonic, the peak chirp rate during the upscan is given by:

$$R_{\text{up,peak}}(t) = \frac{2\pi f \tau_{\text{L}} B q_{\text{A}}}{\sqrt{(2\pi f \tau_{\text{L}})^2 + 1}}. \tag{C.39}$$

The peak chirp rate is plotted against scan rate in the middle row of Fig. C.2. The peak chirp rate increases as a function of the scan rate, but asymptotically approaches a maximum value of $B q_{\text{A}}$ for high modulation frequencies and can be approximated by $2\pi f \tau_{\text{L}} B q_{\text{A}}$ for low modulation frequencies.

C.4 Square-wave modulation

For the case of square-wave modulation at scan rate f (period τ) with duty cycle DC, the current and effective heating can be written as piecewise constant functions:

$$i(t) = \begin{cases} i_{\max} & \text{if } 0 \le t \le \text{DC} \times \tau \\ i_{\min} & \text{if DC} \times \tau < t \le \tau \end{cases}, \tag{C.40}$$

$$q(t) = \begin{cases} q_{\max} & \text{if } 0 \le t \le \text{DC} \times \tau \\ q_{\min} & \text{if DC} \times \tau < t \le \tau \end{cases}, \tag{C.41}$$

$$q_{\max} = i_{\max}^2 - i_0^2, \tag{C.42}$$

$$q_{\min} = i_{\min}^2 - i_0^2. \tag{C.43}$$

Equation C.16 can be solved for these two periods yielding piecewise exponential solutions for the wavenumber profile:

$$\nu_{\mathrm{rel}}(t) = \begin{cases} -B\tau_{\mathrm{L}} q_{\max} + (\nu_{\mathrm{rel}}^{\max} + B\tau_{\mathrm{L}} q_{\max}) \exp\left(-\frac{t}{\tau_{\mathrm{L}}}\right) \\ \qquad\qquad \text{if } 0 \leq t \leq \mathrm{DC} \times \tau \\ -B\tau_{\mathrm{L}} q_{\min} + \left(\nu_{\mathrm{rel}}^{\min} + B\tau_{\mathrm{L}} q_{\min}\right) \exp\left(-\frac{t-\mathrm{DC}\tau}{\tau_{\mathrm{L}}}\right) \\ \qquad\qquad \text{if } \mathrm{DC} \times \tau < t \leq \tau \end{cases}. \tag{C.44}$$

Here, $\nu_{\mathrm{rel}}^{\max}$ and $\nu_{\mathrm{rel}}^{\min}$ are the maximum and minimum values of the wavenumber profile, achieved at beginning of the upscan and downscan respectively. By enforcing the continuity of $\nu_{\mathrm{rel}}(t)$ at $t = \mathrm{DC} \times \tau$ and the periodicity of the function ($\nu_{\mathrm{rel}}(0) = \nu_{\mathrm{rel}}(\tau)$), $\nu_{\mathrm{rel}}^{\max}$ and $\nu_{\mathrm{rel}}^{\min}$ can be solved for:

$$\nu_{\mathrm{rel}}^{\max} = -B\tau_{\mathrm{L}} \left[2q_{\mathrm{A}} \frac{\exp\left(\mathrm{DC}\frac{\tau}{\tau_{\mathrm{L}}}\right) - 1}{\exp\left(\frac{\tau}{\tau_{\mathrm{L}}}\right) - 1} + q_{\min} \right], \tag{C.45}$$

$$\nu_{\mathrm{rel}}^{\min} = B\tau_{\mathrm{L}} \left[2q_{\mathrm{A}} \frac{\exp\left((1-\mathrm{DC})\frac{\tau}{\tau_{\mathrm{L}}}\right) - 1}{\exp\left(\frac{\tau}{\tau_{\mathrm{L}}}\right) - 1} - q_{\max} \right]. \tag{C.46}$$

The absolute value of these parameters are somewhat arbitrary, as they are relative to the arbitrary reference wavenumber ν_0. The difference between the two however, is interesting, as this is the spectral scan depth achievable for the square wave:

$$\Delta\nu_{\mathrm{square}} = \nu_{\mathrm{rel}}^{\max} - \nu_{\mathrm{rel}}^{\min} = 2\tau_{\mathrm{L}} B q_{\mathrm{A}} \left[\coth\left(\frac{\tau}{2\tau_{\mathrm{L}}}\right) - \frac{\cosh\left(\frac{\tau}{\tau_{\mathrm{L}}}(\mathrm{DC} - \frac{1}{2})\right)}{\sinh\left(\frac{\tau}{2\tau_{\mathrm{L}}}\right)} \right]. \tag{C.47}$$

This relation indicates that the spectral scan depth for square-wave modulation is linearly proportional to the amplitude of laser heating q_{A}. The term in the fraction encodes the dependence of the scan depth on the modulation period τ and the duty cycle DC. By taking the derivative of Eqn. C.47 with respect to the duty cycle, it can be shown that the maximum value of the scan depth is achieved at a duty cycle of 50%, which matches with

the experimental observations from Section 6.3.1 of Chapter 6. If Eqn. C.47 is evaluated for a duty cycle of 50%, the maximum scan depth for a given scan frequency can be found:

$$\Delta\nu_{\text{square}}^{\text{opt}} = 2\tau_{\text{L}} B q_{\text{A}} \left[\coth\left(\frac{\tau}{2\tau_{\text{L}}}\right) - \operatorname{csch}\left(\frac{\tau}{2\tau_{\text{L}}}\right)\right]. \tag{C.48}$$

For square-wave modulation at 50% duty-cycle, the transfer function between spectral scan depth and peak-to-peak laser heating can be written as:

$$H_{q,\text{square}}^{\text{opt}} = B\tau_{\text{L}} \left[\coth\left(\frac{\tau}{2\tau_{\text{L}}}\right) - \operatorname{csch}\left(\frac{\tau}{2\tau_{\text{L}}}\right)\right]. \tag{C.49}$$

At scan rates much greater than the natural frequency of the laser ($1/\tau_{\text{L}}$), this transfer function simplifies to:

$$H_{q,\text{square}}^{\text{opt}} \approx \frac{B}{4f}. \tag{C.50}$$

This function is generally greater than the transfer function for sinusoidal modulation (Eqn. C.25) by a factor of $\pi/2$ (+57%), which is supported by the experimental observation that spectral scan-depth is improved for square-wave modulation over sinusoidal modulation. At these high speeds, for duty cycles not equal to 50%, a factor of $4\text{DC}(1 - \text{DC})$ must be multiplied to the transfer function to account for the reduction in scan depth. In general, the transfer function is relatively insensitive to duty cycle when duty cycle is within 10% of 50%. This can be seen in the top left of Fig. C.3, where the transfer function is plotted versus scan frequency for various duty cycles. At scan rates much lower than the natural frequency of the laser, the transfer function approaches $B\tau_{\text{L}}$, which is the same value for pure sinusoidal modulation, implying reduced tuning benefits for square-wave modulation for low-speed scanning. This low-speed approximation for the transfer function is relatively insensitive to duty cycle, except at extreme values (DC$< 2f\tau_{\text{L}}$ or DC$> 1 - 2f\tau_{\text{L}}$), where the tuning performance drastically drops to near 0. Across all scan frequencies, the scan depth of a square wave is approximately equal to that of a sine wave at duty cycles near 20 or 80%.

The laser parameters for the QCL used in Sections 6.2–6.3.4.1 of Chapter 6 were determined using the relations developed above for square-wave modulation. τ_{L} was found by fitting the chirp profile for the extended square wave from Fig. 6.7 with an exponential function in the form provided by Eqn. C.44. τ_{L} was determined to be approximately 240 ns. Next,

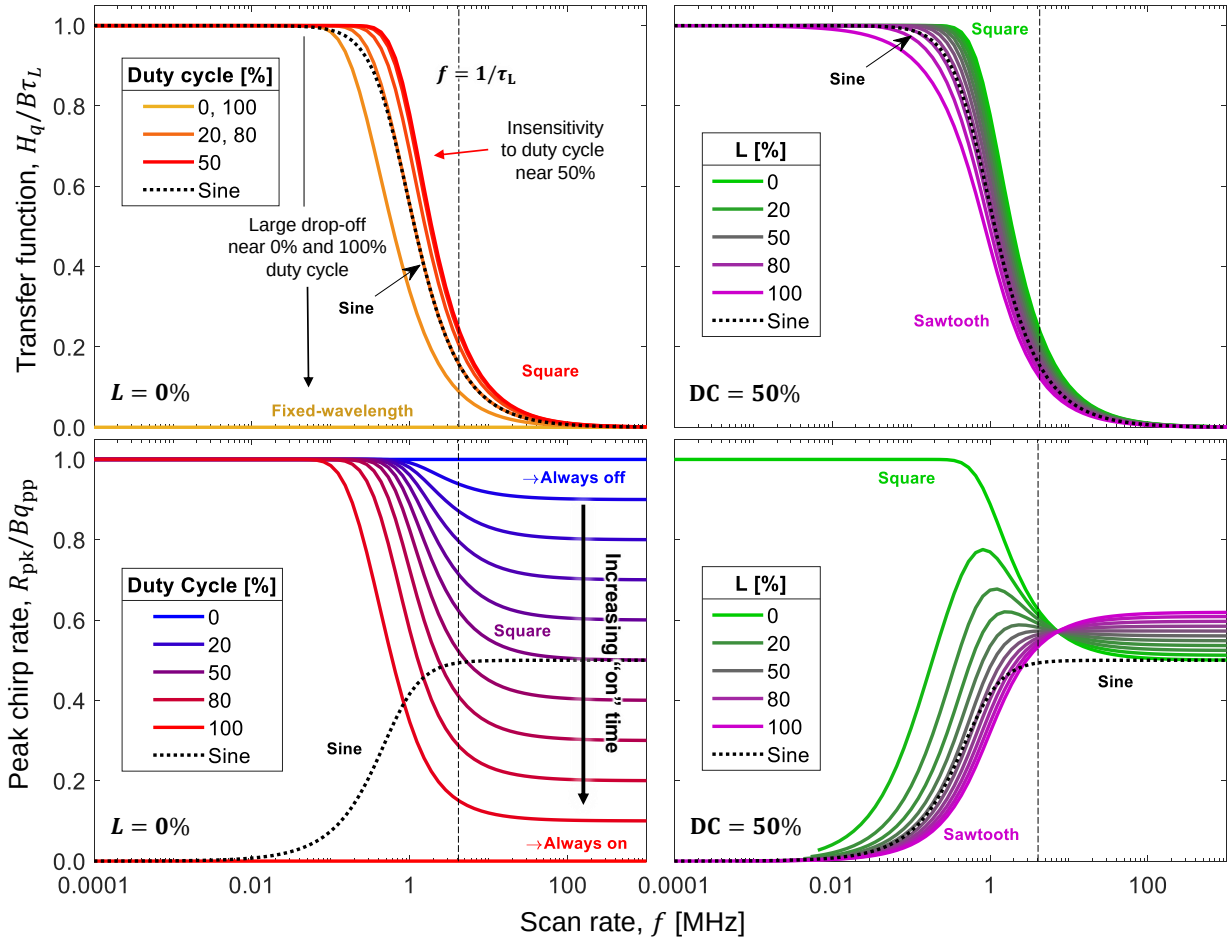

Figure C.3: Transfer function *versus* scan rate (*top*) and peak upscan chirp rate *versus* scan rate (*bottom*) for square waves of varying duty cycle (*top left*) and trapezoidal waves at 50% duty cycle with varying L.

the square-wave transfer function $H_{q,\mathrm{square}}$ at 1 MHz and 50% duty cycle was determined by observing the increase in spectral scan depth as the heating amplitude q_A was increased (by increasing the fractional current F from 42% to 84%). A linear function was fitted to the plot of scan depth versus heating amplitude and the slope of the resulting line was used to find the approximate value of the transfer function of $H^{\mathrm{opt}}_{q,\mathrm{square}} \sim 2.8 \cdot 10^{-5}$ cm^{-1}·(mA)$^{-2}$. Eqn. C.49 was then solved for B and evaluated with knowledge of τ_L, f, and $H^{\mathrm{opt}}_{q,\mathrm{square}}$. B was found to have an approximate value of $B \sim 1.5 \cdot 10^{-4}$ cm^{-1}/(mA^2·µs). A representative injection-current, effective heating, and chirp profile for 1-MHz square-wave at 50% duty cy-

cle are represented by the red curves in Fig. C.1, using the aforementioned laser parameters. The transfer functions versus scan rate for an ideal sine wave (as discussed in Section C.2 and 50% duty cycle square wave are compared in Fig. C.2 along with the phase lag, ϕ_q for an ideal sine wave.

The chirp rate for square-wave modulation may be found by taking the absolute value of the derivative of Eqn. C.44 with respect to time. The peak chirp rate R_{peak} during the upscan can be found by taking the value of the chirp rate at time zero:

$$R_{\text{peak}} = 2Bq_{\text{A}} \frac{\exp\left(\frac{\tau}{\tau_{\text{L}}}\right) - \exp\left(\text{DC}\frac{\tau}{\tau_{\text{L}}}\right)}{\exp\left(\frac{\tau}{\tau_{\text{L}}}\right) - 1}. \tag{C.51}$$

The peak chirp rate increases linearly with the heating amplitude and B. The peak chirp rate for a square wave at 50% duty cycle is plotted against scan rate in the middle row if Fig. C.2. Additionally, the peak chirp rate for multiple values of duty cycle is plotted against scan rate in the bottom left of Fig. C.3. The peak chirp rate is maximized at a duty cycle of 0, and is minimized at a duty cycle of 1, which supports the experimental observation of improved usable scan depth at duty cycles higher than 50%, as seen in Section 6.3.3 of Chapter 6. In contrast with sinusoidal modulation, the R_{peak} decreases with increasing modulation rate, as the temperature extremes of the laser become reduced, resulting in reduced heat transfer during the beginning of the upscan. At these high modulation rates, the peak chirp rate approaches $2(1-D)Bq_{\text{A}}$. For a 50% duty cycle, this value is equivalent to that for high-speed sinusoidal modulation. At low modulation rates, R_{peak} approaches $2Bq_{\text{A}}$, with a weak dependence on duty cycle, except at duty cycles near 100% (DC$> 1-2f\tau_{\text{L}}$), where the peak chirp rate rapidly drops to zero.

C.5 Trapezoidal-wave modulation

For the case of trapezoid-wave modulation at scan rate f (period τ), duty cycle DC, and leading edge ramp time LE, the current and effective heating can be written as piecewise

functions:

$$i(t) = \begin{cases} i_{\max} & \text{if } 0 \le t \le (\mathrm{DC} - \frac{L}{2})\tau \\ i_{\min} & \text{if } (\mathrm{DC} - \frac{L}{2})\tau < t \le (1-L)\tau \\ i_{\mathrm{ramp}}(t) & \text{if } (1-L)\tau < t < \tau \end{cases}, \tag{C.52}$$

$$q(t) = \begin{cases} q_{\max} & \text{if } 0 \le t \le (\mathrm{DC} - \frac{L}{2})\tau \\ q_{\min} & \text{if } (\mathrm{DC} - \frac{L}{2})\tau < t \le (1-L)\tau \\ q_{\mathrm{ramp}}(t) & \text{if } (1-L)\tau < t < \tau \end{cases}, \tag{C.53}$$

where

$$L = \frac{\mathrm{LE}}{\tau}, \tag{C.54}$$

$$i_{\mathrm{ramp}}(t) = j(t - (1-L)\tau) + i_{\min}, \tag{C.55}$$

$$q_{\mathrm{ramp}}(t) = i^2_{\mathrm{ramp}}(t) - i_0^2, \tag{C.56}$$

$$j = \frac{i_{\max} - i_{\min}}{L\tau}. \tag{C.57}$$

For a given duty cycle, L (the fraction of the scan over which the ramp occurs) has a maximal value, above which the flat part of the upscan or downscan no longer exist:

$$L_{\max} = \begin{cases} 2 \times \mathrm{DC} & \text{if } \mathrm{DC} \ge 1/2 \\ 2(1 - \mathrm{DC}) & \text{if } \mathrm{DC} \le 1/2 \end{cases}. \tag{C.58}$$

For a duty cycle of 50%, when $L = 1$, the waveform takes the form of a sawtooth wave.

Similar to the case of the square wave, the solution for $\nu_{\mathrm{rel}}(t)$ may be found by solving Eqn. C.19 for the various phases of the trapezoid wave and ensuring continuity at $t = (\mathrm{DC} - \frac{L}{2})\tau$ and $t = (1-L)\tau$, as well as ensuring the periodicity of the function $\nu_{\mathrm{rel}}(0) = \nu_{\mathrm{rel}}(\tau)$.

The resulting solution is cumbersome to write in its entirety here, but the solution may be numerically analyzed and compared to that for the pure square wave. A representative injection-current, effective heating, and chirp profile for 1-MHz trapezoid wave at 50% duty cycle with $L = 0.3$ are represented by the green curves in Fig. C.1. Unlike the pure square wave, the spectral scan depth must be found by considering the time at which the current rises

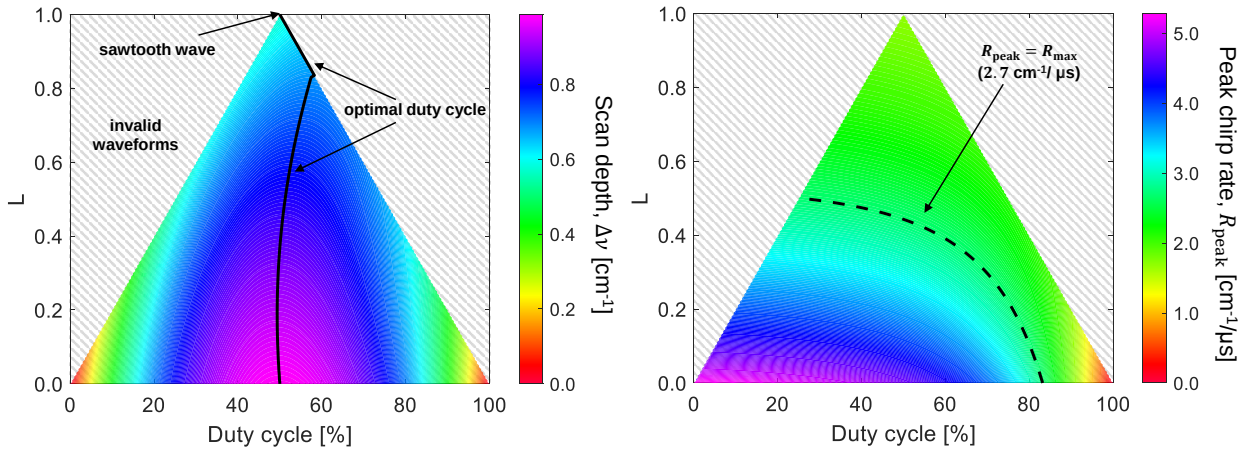

Figure C.4: *Left*: Spectral scan depth *versus* duty cycle and L for a simulated trapezoidal wave. *Right*: Peak upscan chirp rate *versus* duty cycle and L for the same simulated trapezoidal wave. B, τ_{L}, i_{max}, and i_{min} are the same as in Figs. C.1 and C.2.

above the lasing threshold during the ramp, τ_{th}. If this point occurs before the downscan "turnaround", where ν_{rel} reaches a local maximum, which occurs at time $\tau_{\mathrm{turn,down}}$ (when $d\nu_{\mathrm{ramp}}/dt = 0$), then the spectral scan depth is the difference in ν_{rel} at the turnaround and the end of the upscan. If $\tau_{\mathrm{th}} > \tau_{\mathrm{turn,down}}$, then the spectral scan depth is the difference between $\nu_{\mathrm{rel}}(\tau_{\mathrm{th}})$ and $\nu_{\mathrm{rel}}((\mathrm{DC}-1/2)\tau)$. If the current stays above the laser threshold during the entire scan period, then the spectral scan depth may be found by taking the difference between the maximum and minimum values of ν_{rel}.

The spectral scan depth is mapped as a function of each combination of duty cycle and L on the left side of Fig. C.4 for a trapezoid wave at $f = 1$ MHz, $i_{\mathrm{min}} = 30$ mA and $i_{\mathrm{max}} = 190$ mA, using the laser parameters found above ($B = 1.5{\cdot}10^{-4}$ cm^{-1}/(mA$^2{\cdot}$μs), $\tau_{\mathrm{L}} = 240$ ns), with the assumption that the lasing threshold is exceeded before the downscan turnaround (for simplicity). The scan depth is maximized at a duty cycle of 50% and when $L = 0$. The scan depth is also plotted as a function of scan frequency for trapezoidal waveforms with varying L, at a fixed duty cycle of 50% in the top right of Fig. C.3. As L is increased, scan depth generally drops for a given value of duty cycle. This is true regardless of scan frequency, although the sensitivity of the scan depth to L is reduced at

lower modulation rates. The scan depth of a trapzedoidal waveform at 50% duty cycle is similar to that of a sine wave at values of L between 70 and 80%. It is interesting to note that the duty cycle that maximizes spectral scan depth (plotted as a black curve on Fig. C.4 is greater than 50% when $L \neq 0$, as observed experimentally in Fig. 6.4 in Section 6.3.3 of Chapter 6. This is because for a pure square wave, 50% duty cycle offers an even amount of cooling and heating of the laser system, as the time averaged value of q is equal to the average between the maximum and minimum value of q. When a leading edge ramp is added to the injection-current waveform, the ramp in q is quadratic, not linear, and as such, the average value of q during the ramp is no longer equal to the average between the maximum and minimum values of q. The average value of q ends up being lower than in the linear case, resulting in increased cooling duration compared to heating over a modulation period. To compensate for this, the duty cycle can be raised to increase the heating period to balance the duration of cooling and heating, to maximize the scan depth. Above a certain value of L (in this case, $\sim$75%), the optimal duty cycle ends up being the maximum allowable value for the given value of L. This is reflected by the black curve on the left of Fig. C.4 coinciding with the right boundary of the triangle of valid waveforms. For high values of L, this implies that the optimal waveform for maximimzing spectral scan depth is closer to a sawtooth waveform.

The peak chirp rate (durng the upscan) is also mapped as a function of duty cycle and L on the right side of Fig. C.4 for the same laser parameters mentioned above. As noted for pure square waves, the peak chirp rate increases with decreasing duty cycle for a given value of L. At the presented scan frequency of 1 MHz, as L increases at a fixed duty cycle, the peak chirp rate decreases, which reflects the increasing "usefullness" of waveforms with longer leading edges when scanning narrow spectral features, as outlined in Section 6.3.3 of Chapter 6. The maximum allowable value for the chirp rate for narrow spectral detection ($\delta\nu_{\text{min}} \sim 0.027$ cm^{-1} for CO near 0.25 atm), $R_{\text{max}} = 2.7$ cm^{-1}/µs is indicated by the black dashed line on the right side of Fig. C.4. The region above and to the left of this black dashed line indicates waveforms that have limited usable scan depth when scanning features with

narrow spectral widths. This trend of decreased peak chirp rates at higher values of L and increased scan depths at duty cycles greater than 50% explain why the optimal waveforms found in Section 6.3.3 had values of L that were 30–40% and duty cycles that were 60–70%.

The peak upscan chirp rate is also plotted as a function of scan rate for various values of L at a fixed duty cycle of 50% in the bottom right of Fig. C.3. For low scan rates, the peak chirp rate generally increases with scan frequency, except for very low values of L (nearly square). At a certain scan rate, this trend reverses for low values of L, with peak chirp rate decreasing with scan rate (as for square waves). For higher values of L ($> 50\%$), the peak chirp rate always increases with scan rate (as for sinusoidal modulation). At very high modulation rates (above 6.6 MHz for the model parameters used in this work), the peak chirp rate begins to increase with L, to values above that for pure square-wave modulation. This reduces the utility of adding a leading-edge ramp at high modulation rates.

APPENDIX D

Uncertainty analysis for RDRE exhaust LAS measurements

The contents of this appendix have been published in the journal ***Applied Physics B*** *under the full title "MHz laser absorption spectroscopy via diplexed RF modulation for pressure, temperature, and species in rotating detonation rocket flows" [148].*

In Chapters 4 and 5, we presented measurements of temperature, pressure, and species column number density in rotating detonation rocket flows. To facilitate comparison with modeling and simulation, we provide experimental uncertainties for each of these measurements, and detail how they are calculated in this Appendix. Other, more detailed and general treatments of LAS-measurement uncertainty are provided in Chapter 7, as well as Appendix E and F, accoutning for effects such as fuel variation, measurement noise, baseline distortion, and line blending.

The uncertainty analysis presented here largely follows that of Pineda et. al [165]; however, here we provide more rigorous treatment of uncertainty in spectral fitting parameters, added discussion for accounting for blended spectra, and new information regarding estimating pressure from measured collisional width. As in that work, unless otherwise noted, we follow the Taylor series method (TSM) of uncertainty propagation [223], in which the uncertainty of a variable r, Δr, is given by:

$$(\Delta r)^2 = \left(\frac{\partial r}{\partial x_1}\Delta x_1\right)^2 + \left(\frac{\partial r}{\partial x_2}\Delta x_2\right)^2 + \cdots, \tag{D.1}$$

where x_i are independent variables and Δx_i are their respective uncertainties. A visual summary of the relative experimental uncertainties for each variable is shown in Fig. D.1, in

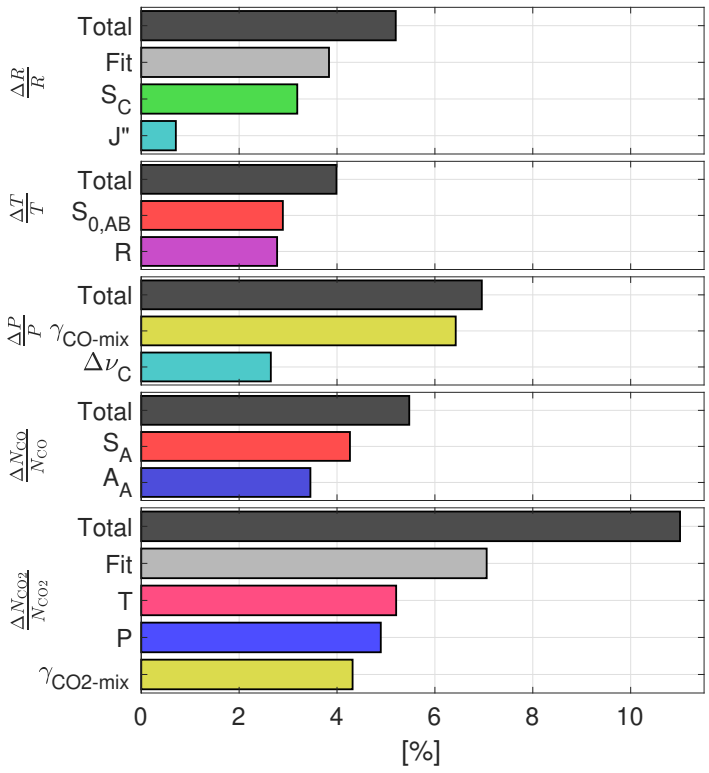

Figure D.1: Representative uncertainties for linestrength ratio R, temperature T, column density N_{CO}, total pressure P_{tot}, and column density $N_{\mathrm{CO_2}}$ performed on the test shown in Fig. 4.22. Note: these values are averaged over a time series of measurements.

which the individual contributions from dependent variables are highlighted and discussed in greater detail in the following subsections.

D.0.1 Linestrength uncertainty

For each species j, uncertainty in temperature-dependent linestrengths, $\Delta S_k(T)$, for each line k can be calculated from the expression for temperature-dependent linestrength:

$$S_k(T) = S_k(T_0)\frac{Q(T_0)}{Q(T)}\exp\left[-\frac{hcE''_k}{k_B}\left(\frac{1}{T}-\frac{1}{T_0}\right)\right]\times\frac{1-\exp\left(\frac{-hc\nu_{0,k}}{k_BT}\right)}{1-\exp\left(\frac{-hc\nu_{0,k}}{k_BT_0}\right)}, \tag{D.2}$$

where Q is the partition function for the molecule of interest, and $\nu_{0,k}$ is the linecenter of the transition k of interest.

The two uncertainties with which we are primarily concerned are the reference temperature linestrength uncertainty $\Delta S_k(T_0)$ (available in the HITEMP database [168] for the lines used in this work) and the uncertainty in temperature-dependent linestrength due to uncertainty in temperature ΔT (from the uncertainty in ΔR, discussed in Section D.0.2). We assume uncertainties in lower state energies E_k'' and line positions ν_0 are secondary and negligible contributors. The total uncertainty in the linestrength $S_k(T)$ can the be calculated by summing both primary uncertainties in quadrature:

$$\left(\frac{\Delta S_k(T)}{S_k(T)}\right)^2 = \left(\frac{\Delta S_k(T_0)}{S_k(T_0)}\right)^2 + \left(\frac{\partial S_k(T)}{\partial T}\frac{\Delta T}{S_k(T)}\right)^2. \tag{D.3}$$

For CO, the linestrengths of the P(0,31), P(2,20), and P(3,14) lines are known to within 2%, 5%, and 10%, respectively, and so $\Delta S_k(T_0)/S_k(T_0) = 0.02$ for the P(0,31) line, 0.05 for the P(2,20) line, and 0.10 for the P(3,14) line.

D.0.2 Temperature uncertainty

In this work, temperature is determined numerically from Eqns. 4.6 and D.2 by simulating linestrength $S_k(T)$ for the lines of interest using the HITEMP database [168] and comparing to the measured absorbance area ratio R. It can be seen that $R(T)$ is nonlinear, and the absolute value of dR/dT decreases as T increases. Practically speaking, this increases the sensitivity of T to R, such that a given absolute deviation in R, ΔR, will produce larger deviations in T, ΔT, at higher T. To more rigorously quantify the measurement uncertainty in temperature associated with this and other factors, we can examine an analytical expression for temperature, given by [166]:

$$T = \frac{\frac{hc}{k_B}(E_B'' - E_A'')}{\frac{hc}{k_B}\frac{(E_B''-E_A'')}{T_0} + \ln(R) + \ln\left(\frac{S_B(T_0)}{S_A(T_0)}\right)}. \tag{D.4}$$

This expression neglects stimulated emission and is used only for sensitivity analysis. In this Appendix, we use the subscripts A, B, and C to refer to line-specific parameters for the CO P(0,31), P(2,20), and P(3,14) lines, respectively. Uncertainty in measured temperature as expressed in Eqn. D.4 is assumed to be dominated by the uncertainties of the reference

temperature linestrengths in the HITEMP database, $\Delta S_k(T_0)$, and the uncertainty in the ratio of calculated absorbance areas ΔR:

$$\left(\frac{\Delta T}{T}\right)^2 = \frac{\left(\frac{\Delta R}{R}\right)^2 + \left(\frac{\Delta S_A(T_0)}{S_A(T_0)}\right)^2 + \left(\frac{\Delta S_B(T_0)}{S_B(T_0)}\right)^2}{\left(\frac{hc}{k_B}\frac{E''_B - E''_A}{T_0} + \ln(R) + \ln\left(\frac{S_B(T_0)}{S_A(T_0)}\right)\right)^2}. \tag{D.5}$$

Uncertainties in lower state energies E''_k and physical constants are not considered. Eqn. D.5 implies that ΔT decreases with increasing difference in lower state energy $E''_B - E''_A$ and increasing linestrength ratio R, highlighting the importance of line selection for accurate temperature measurements. ΔR is given by the expression:

$$\left(\frac{\Delta R}{R}\right)^2 = \left(\frac{\Delta A_A}{A_A}\right)^2 + \left(\frac{\Delta A_B}{A_B}\right)^2. \tag{D.6}$$

Thus, we are primarily concerned with the determination of ΔA_k, which for time-resolved scanned direct-absorption spectroscopy can be determined as $\Delta A_{k,\text{fit}}$, equal to the 1-σ standard deviation of the nonlinear least-squares parameter estimate for A_k from the Voigt fitting procedure. However, for the measurements reported here, there is additional uncertainty associated with the subtraction of the absorbance due to the P(3,14) line that appears appreciably at temperatures above ∼1800 K and from the assumption that the collision widths of all three lines are equal. The overall uncertainty in absorbance area is expressed as:

$$(\Delta A_k)^2 = (\Delta A_{k,\text{fit}})^2 + (\Delta A_{k,C})^2 + (\Delta A_{k,J''})^2, \tag{D.7}$$

where $\Delta A_{k,C}$ is the variation in A_k resulting from the uncertainty in the simulated absorbance from the P(3,14) line and $\Delta A_{k,J''}$ is the variation in A_k resulting from the variability in the collision widths between lines.

In practice, $\Delta A_{k,C}$ is found by re-fitting the spectra after varying the linestrength of the P(3,14) line by ±10% and finding the corresponding change in A_k. Likewise $\Delta A_{k,J''}$ is found by constraining one $\Delta\nu_{C,k}$ to be higher or lower than the others in the fitting routine by a percentage corresponding to the temperature-dependent variance in collision width across the three spectral transitions, as indicated in Fig. 4.8. The resulting area variations are added in quadrature to obtain $\Delta A_{k,J''}$. See Appendix E and F for more detailed treatments of assessing absorbance area uncertainty.

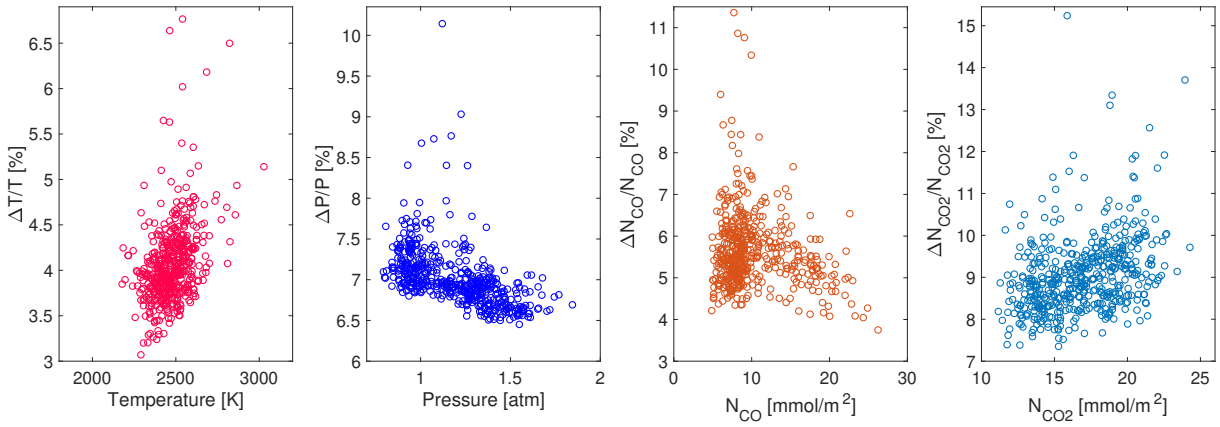

Figure D.2: Relative experimental uncertainty distributions for temperature, CO and CO_2 column number density and pressure for the test shown in Fig. 4.22.

For the experimental data presented in Chapter 4, it can be seen in Fig. D.1 that the largest influence on the magnitude of ΔR is associated with the spectral fit, while the next largest influence is the uncertainty of the linestrength of the P(3,14) line in the HITEMP database [168]. A scatterplot of $\Delta T/T$ versus T is shown in Fig. D.2, showing a range of uncertainty that tends to slightly increase with absolute temperature, and having a mean magnitude of approximately 4%.

D.0.3 Uncertainty in path-integrated measurement

As mentioned in Section 4.3.1, the temperature measured in Chapter 4 is a CO number-density weighted path-averaged temperature. In deriving Eqn. 4.5 from Eqn. 4.2, we made the following implicit assumption:

$$S_{kj}(\overline{T}) \approx \overline{S_{kj}(T)} = \frac{\int_0^L n_j S_{kj}(T) dl}{\int_0^L n_j dl}, \tag{D.8}$$

which states that the number density-weighted path-averaged linestrength is equal to the linestrength evaluated at the number density weighted path-averaged temperature. This assumption will hold regardless of the temperature distribution along the line-of-sight if the linestrength is linear in temperature across the temperature distribution [167]. To validate

this, linear temperature distributions were generated spanning 500 K for various average temperatures across a hypothetical 1 cm line-of-sight. Number density was allowed to vary with temperature. $\overline{T}$ and $\overline{S_{kj}(T)}$ (for the P(0,31), P(2,20) and P(3,14) lines) were computed numerically using Eqns. 4.4 and D.8. $S_{kj}(\overline{T})$ was computed using Eqn. D.2 for the various lines. The relative difference between $\overline{S_{kj}(T)}$ and $S_{kj}(\overline{T})$ was then calculated for each average temperature. This is plotted in the top of Fig. D.3. Disagreements are below 1% for mean temperatures ranging from 2000 K to 3000 K.

Similarly, the temperature corresponding to each absorber density-weighted path-integrated linestrength (for the P(0,31) and P(2,20) lines) was calculated by inverting Eqn. D.2. Additionally, the temperature corresponding to the ratio of the absorber density-weighted path-integrated linestrengths (which is the same as the ratio of measured absorbance areas R) was calculated. The difference between these temperatures and the actual absorber density-weighted path-averaged temperature of the distribution were calculated and plotted on the

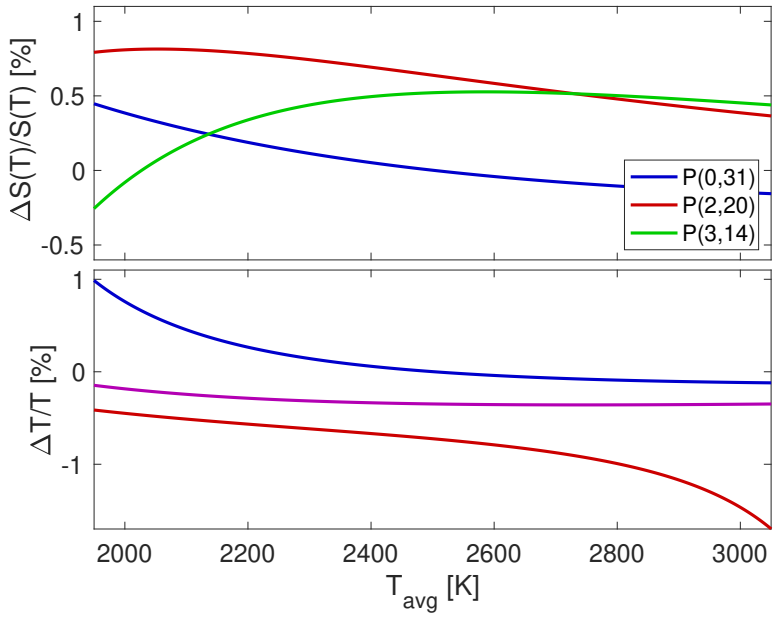

Figure D.3: The relative difference between $\overline{S(T)}$ and $S(\overline{T})$ for the P(0,31), P(2,20) and P(0,31) (top) and the difference between $\overline{T}$ and the temperature inferred from the $\overline{S}$ for the P(0,31) line (blue), the P(2,20) line (red) and from their ratio (purple).

bottom of Fig. D.3. While the errors associated with each individual lines ranged from 0.1–1.5%, the error between the temperature inferred from the absorbance area ratio and the actual path-averaged temperature was below 0.4% for all average temperatures between 2000 K and 3000 K. Due to the low values of this error relative to other experimental errors calculated in section D.0.2, it was omitted from the remainder of the uncertainty analysis. This low disagreement validates that the measurement strategy is capable of accurately retrieving $\overline{T}$, which may be compared with 3D flowfield simulations. See Appendix E.0.5 and F.1 for additional treatments of uncertainty associated with non-uniform path-integrated LAS measurements.

D.0.4 Pressure uncertainty

The uncertainty in P_{tot} calculated by Eqn. 4.9 depends on the uncertainties of $\Delta\nu_C$ and $\gamma_{\text{CO-mix}}(T)$:

$$\left(\frac{\Delta P_{\text{tot}}}{P_{\text{tot}}}\right)^2 = \left(\frac{\Delta(\Delta\nu_C)}{\Delta\nu_C}\right)^2 + \left(\frac{\Delta\gamma_{\text{CO-mix}}(T)}{\gamma_{\text{CO-mix}}(T)}\right)^2. \tag{D.9}$$

Here, the experimental uncertainty of $\Delta(\Delta\nu_C)$ is expressed in a similar fashion to the uncertainty in $\Delta A_{i,C}$ as outlined in section D.0.2:

$$(\Delta(\Delta\nu_C))^2 = (\Delta\nu_{C,\text{fit}})^2 + (\Delta\nu_{C,C})^2 + (\Delta\nu_{C,J''})^2. \tag{D.10}$$

Here, $\Delta(\Delta\nu_{C,\text{fit}})$ is the 1-σ standard deviation for the parameter estimate $\Delta(\Delta\nu_C)$ of the spectral fit, $\Delta(\Delta\nu_{C,C})$ is the variation of collision width from the linestrength uncertainty of the P(3,14) line, and $\Delta(\Delta\nu_{C,J''})$ is the uncertainty due to the assumption that the collision width is the same for the three transitions. As seen in Fig. D.1, in this work, $\Delta(\Delta\nu_C)$ contributes a smaller amount to the overall uncertainty in P_{tot} compared to $\Delta\gamma_{\text{CO-mix}}(T)$.

A generalized derivation of the temperature-dependent mixture-weighted collisional-broadening coefficient uncertainty $\Delta\gamma_{\text{CO-mix}}(T)$ is provided in the following subsection. Fig. D.2 shows that $\Delta P_{\text{tot}}/P_{\text{tot}}$ has a slight inverse trend over the range of P_{tot} measured in this work; this is largely due to the relatively constant values of $\Delta\gamma_{\text{CO-mix}}(T)$ combined with the lower values of $\Delta(\Delta\nu_C)$ at higher pressures owing to increased SNR.

See Chapter 7 and Appendix E for a more comprehensive and generalized treatment of assessing LAS-measured pressure uncertainty.

D.0.5 Broadening-coefficient uncertainty

The uncertainty in the mixture-weighted broadening coefficient $\Delta\gamma_{j-\mathrm{mix}}(T)$ for species j is given by:

$$(\Delta\gamma_{j-\mathrm{mix}}(T))^2 = \sum_Y \left[(\gamma_{j-Y}(T)\Delta X_Y)^2 + (X_Y\Delta\gamma_{j-Y}(T))^2\right]. \tag{D.11}$$

The mole fractions of the collision partners X_Y are estimated from CJ simulations, so there is a numerically-determined uncertainty ΔX_Y for each collision partner Y associated with both the uncertainty in local equivalence ratio $\Delta\phi$ and the variation of mole fraction with the assumption of either frozen or equilibrium flow $\Delta X_{Y,\mathrm{FE}}$, as shown in Fig. 4.7. This is expressed as:

$$\Delta X_Y^2 = \left(\frac{\partial X_Y}{\partial\phi}\Delta\phi\right)^2 + \Delta X_{Y,\mathrm{FE}}^2. \tag{D.12}$$

We can see from Eqn. D.11 that uncertainties associated with the major collision partners will be weighted more heavily than those associated with trace collision partners.

The temperature-dependent collisional-broadening coefficient $\gamma_{j-Y}(T)$ for species j is modeled according to Eqn. 4.10 for the collision partners CO_2, H_2O, O_2, H_2, and N_2. The uncertainty can be calculated for the collision pairs as:

$$\left(\frac{\Delta\gamma_{j-Y}(T)}{\gamma_{j-Y}(T)}\right)^2 = \left(\frac{\Delta\gamma_{j-Y}(T_0)}{\gamma_{j-Y}(T_0)}\right)^2 + N_Y^2\left(\frac{\Delta T}{T}\right)^2 + \left(\ln(T_0/T)\Delta N_Y\right)^2. \tag{D.13}$$

The uncertainties in reference temperature collisional-broadening coefficient $\Delta\gamma_Y(T_0)$, and temperature-dependent exponent ΔN_Y, are driven largely by variation with rotational quantum number[179]. For the collision partners OH, H, and O, the uncertainty is calculated as follows:

$$\left(\frac{\Delta\gamma_{j-Y}(T)}{\gamma_{jY}(T)}\right)^2 = \left(\frac{\Delta\gamma_{j-\mathrm{N_2}}(T)}{\gamma_{j-\mathrm{N_2}}(T)}\right)^2 + \left(\frac{2\Delta\sigma_{j-Y}}{\sigma_{j-Y}}\right)^2 + \left(\frac{2\Delta\sigma_{j-\mathrm{N_2}}}{\sigma_{j-\mathrm{N_2}}}\right)^2 + \varepsilon_{\mathrm{scale}}^2. \tag{D.14}$$

To account for uncertainty associated with the scaling assumptions invoked in Eqn. 4.11, the uncertainty dependencies on optical collision diameters σ are also included. $\Delta\sigma$ for

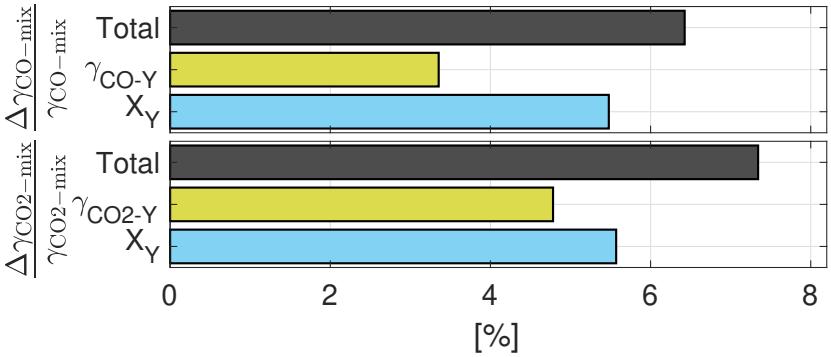

Figure D.4: Averaged representative uncertainty analysis for the mixture-weighted broadening coefficients for CO and CO_2 performed on the test shown in Fig. 4.22.

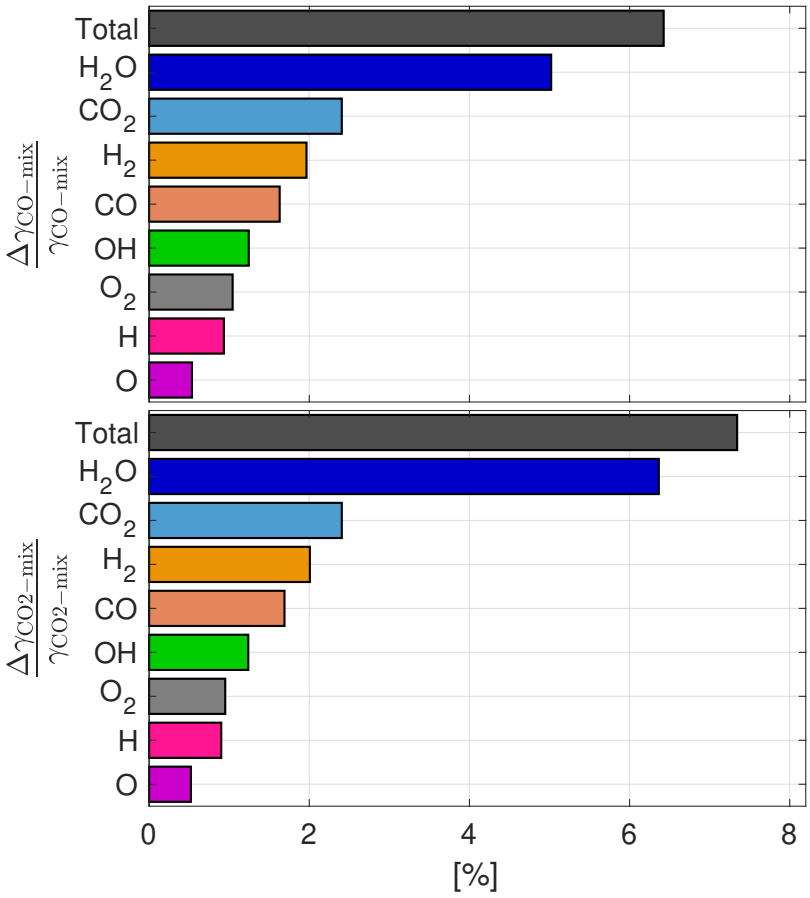

Figure D.5: Averaged representative uncertainty analysis for the mixture-weighted broadening coefficients for CO and CO_2 performed on the test shown in Fig. 4.22.

CO, N_2, CO_2, are estimated based on experimental uncertainty in virial coefficient data for these species [275], while $\Delta\sigma$ for OH, O, and H are estimated based on variations in the predictions of molecular dynamic simulations [175]. $\varepsilon_{\text{scale}}$ is the error associated with the scaling assumption, obtained by comparing the results of the scaling procedure for j-O_2 with the literature values that are actually utilized for this collision partner, which were on the order of 5%.

Overall, uncertainties in mixture composition, ΔX_Y, contribute more to $\Delta\gamma_{j-\text{mix}}(T)$ than uncertainties in species-specific broadening coefficients, $\Delta\gamma_{j-Y}(T)$, as seen in Fig. D.4. We can examine the contributors to $\Delta\gamma_{j-\text{mix}}(T)$ by looking at each species individually, as in Fig. D.5. For both CO and CO_2 measurements, we observe that uncertainties associated with both the mole fraction and the broadening coefficient of H_2O are the most significant contributors by far to the overall uncertainties in broadening coefficient, followed by those of CO_2 and H_2, owing to their magnitude. Reducing the uncertainty of either ΔX_Y or $\Delta\gamma_{j-Y}(T)$—either by measuring additional species or through additional fundamental spectroscopy investigations at high temperatures—represents an opportunity for future research.

See Chapter 7 for a more comprehensive and generalized treatment of assessing collisional-broadening coefficient uncertainty in combustion-gas mixtures.

D.0.6 Column number density uncertainty

For CO, the experimental uncertainty in column number density can be determined by applying Eqn. D.1 to Eqn. 4.7:

$$\left(\frac{\Delta N_{\text{CO}}}{N_{\text{CO}}}\right)^2 = \left(\frac{\Delta S_A(T)}{S_A(T)}\right)^2 + \left(\frac{\Delta A_A}{A_A}\right)^2. \tag{D.15}$$

$\Delta S_A(T)$ is determined from Eqns. D.2 through Eqns. D.3 (Described in Section D.0.1) in which the value of experimental ΔT used in those equations is determined using Eqn. D.5, while ΔA_A is determined from Eqn. D.7. In this work, the contributions to overall uncertainty for N_{CO} by $\Delta S_A(T)$ and ΔA_A are similar in magnitude, as shown in Fig. D.1. A slight inverse trend is noted when plotting $\Delta N_{\text{CO}}/N_{\text{CO}}$ vs. N_{CO}, as shown in Fig. D.2; overall

measurement uncertainty is typically lower as SNR increases with increasing CO density.

See Chapter 7, as well as and Appendix E and F for more comprehensive and generalized treatments of assessing LAS-measured CO concentration uncertainty.

For CO_2, the experimental uncertainty in column number density is less straightforward since N_{CO_2} is inferred directly as a free parameter of a nonlinear least-squares fit. Although there is some uncertainty associated with the 1-σ standard deviation for the parameter estimate in the spectral fit, $\Delta N_{CO_2,\text{fit}}$, this does not account for uncertainty associated with temperature, pressure, and the collisional-broadening coefficients used in the line-mixing model. The dependence of ΔN_{CO_2} on ΔT, ΔP_{tot}, and $\Delta\gamma_{CO_2-Y}(T)$ is determined by numerical application of Eqn. D.1 to the CO_2 line-mixing model. The assumed T, P, and $\gamma_{CO_2-Y}(T)$ inputs are varied by their respective experimental uncertainties, and the resulting ranges of N_{CO_2} are used to infer ΔN_{CO_2}.

$$\left(\Delta N_{CO_2}\right)^2 = \left(\Delta N_{CO_2,\text{fit}}\right)^2 + \left(\Delta N_{CO_2,\Delta T}\right)^2 + \left(\Delta N_{CO_2,\Delta P_{\text{tot}}}\right)^2 + \sum_Y \left(\Delta N_{CO_2,\Delta\gamma_{CO_2-Y}(T)}\right)^2 . \tag{D.16}$$

The most significant influence in the uncertainty for N_{CO_2} are observed to be $\Delta N_{CO_2,\text{fit}}$, largely owing to low SNR, followed by ΔT, ΔP_{tot}, and $\Delta\gamma_{CO_2-Y}(T)$, as seen in Fig. D.1. This is consistent with the sensitivity of the line-mixing model to collision-induced broadening and rovibrational energy transfers, which depend heavily on T, P_{tot}, and $\gamma_{CO_2-Y}(T)$.

D.0.7 Unquantified uncertainties

The above uncertainty analysis rigorously accounts for most theoretical and practical contributions to measurement uncertainty that are intrinsic to the technique. However, some extrinsic elements of uncertainty that are environment- and hardware-specific are not quantified here, including beam size, alignment, and steering, detector non-linearity, plume expansion, and fringe etalons. The technique has been designed to minimize most of these effects, and their influences are expected to be within the bounds of uncertainty as calculated in this section.

APPENDIX E

Extended uncertainty analysis for optical pressure sensor

The contents of this chapter have been submitted to the journal ***Applied Physics B*** *[212] under the full title "Optical pressure sensing at MHz rates via collisional line broadening of carbon monoxide: uncertainty quantification in reacting flows".*

This Appendix provides deeper analysis of the uncertainty related to the pressure sensing technique of Chapter 7. Section E.0.1 provides generalized uncertainty equations to account for correlated variables. Section E.0.2 details on uncertainty contributions to collision-width or absorbance-area measurements from white noise, spectral sampling parameters, low-frequency noise, and line blending. Sections E.0.3 and E.0.4 discuss the uncertainty of the other gas properties measured with the LAS sensor of Chapter 7 (temperature, CO concentration). Section E.0.5 estimates the effect of line-of-sight non-uniformity due to shock boundary layer effects on LAS measurements.

E.0.1 Accounting for correlated potential errors

In Section 7.3.1 of Chapter 7, Eqns. 7.16 and 7.20 were developed to combine potential errors in measured variable g from uncertainties in input variables $x_1, x_2, ..., x_N$, assuming that the input variables were all independent. In some cases, several variables x_m, x_n,...,x_p may not be independent, and depend upon a single common variable x_c. In this case, the uncertainty

in g from Eqn. 7.16 is modified as follows:

$$\delta g^{\{\theta\}} = \sum_{k\neq m,..,p} \left|\frac{\partial g}{\partial x_k}\right| \delta {x_k}^{\{d_k\}} + \left|\sum_{k=m,..,p} \frac{\partial g}{\partial x_k}\frac{\partial x_k}{\partial x_c}\right| \delta {x_c}^{\{d_c\}} + \sum_{k=m,..,p}\sum_{k'\neq c} \left|\frac{\partial g}{\partial x_k}\frac{\partial x_k}{\partial x_{k'}}\right| \delta {x_{k'}}^{\{d_{k'}\}}. \tag{E.1}$$

The first term represents the potential error contributions to g from the uncorrelated independent variables. The second term represents the potential error contribution to g from x_c via the variables with the common dependency on x_c. The term in the absolute value here is $\partial g/\partial x_c$. The final term represents the potential error contributions to g from the variables depending on x_c from (uncorrelated) sources other than x_c, represented by the variables $x_{k'}$.

Equation E.1 may be rewritten in terms of relative uncertainties (as in Eqn. 7.20):

$$\begin{aligned} E^{\{\theta\}}(g) = &\sum_{k\neq m,..,p} |s(g,x_k)|\, E^{\{d_k\}}(x_k) \quad + |s(g,x_c)|\, E^{\{d_p\}}(x_c) \\ &+ \sum_{k=m,..,p}\sum_{k'\neq c} \left[|s(g,x_k)s(x_k,x_{k'})|\, E^{\{d_{k'}\}}(x_{k'})\right]. \end{aligned} \tag{E.2}$$

E.0.2 Single-line measurement uncertainty

In this section, some details of the analysis of Section 7.3.2 are elaborated upon, notably the single-line analysis and the derivation of Eqn. 7.22. Here we investigate the precision and accuracy with which the collisional linewidth $\Delta\nu_{\mathrm{C}}$ may be obtained from measurements of a single absorption lineshape. Although CO broadening parameters are used in this section, the results of this simple analysis can be qualitatively applied to the Voigt profiles for other molecules and the analysis may be conducted by the reader for other molecules/transitions for quantitative use in other applications.

E.0.2.1 Sensitivity of Voigt lineshape to pressure

As the Voigt lineshape is a convolution of a Gaussian and Lorentzian lineshape, identification of the Lorentzian FWHM or collision width is not as straightforward as manually measuring the FWHM of the Voigt lineshape. Instead, the collision width is floated as a free parameter for a given absorption lineshape and the residual between the fitted and

measured lineshape is minimized. Across various pressures and temperatures, the relative influence of the Doppler and collision widths varies. In Fig. E.1, a, the ratio between the collision width and the Doppler, is plotted versus temperature and pressure for a given CO transition. At higher pressures and lower temperatures, collisional broadening dominates, whereas at higher temperatures and lower pressures, Doppler broadening dominates. In general, for combustion-relevant conditions ($P > 1$ atm), the collision width is higher than the Doppler width. Even so, accurate determination of the collision width requires knowledge of the Doppler width.

To quantitatively assess the effect the collision-width parameter on the Voigt lineshape, the sensitivity of the Voigtian width to changes in collision width, $s(\Delta\nu_V, \Delta\nu_C)$, is calculated using Eqn. 7.19. The Voigt profile is numerically evaluated using the McLean approximation [170] with a wavenumber resolution equal to 1% of the maximum of $\Delta\nu_C$ and $\Delta\nu_D$. Due to the linear relationship between pressure and collision width, the sensitivity of Voigtian width with pressure, $s(\Delta\nu_V, P)$, is equivalent to $s(\Delta\nu_V, \Delta\nu_C)$. Figure E.2 plots some prop-

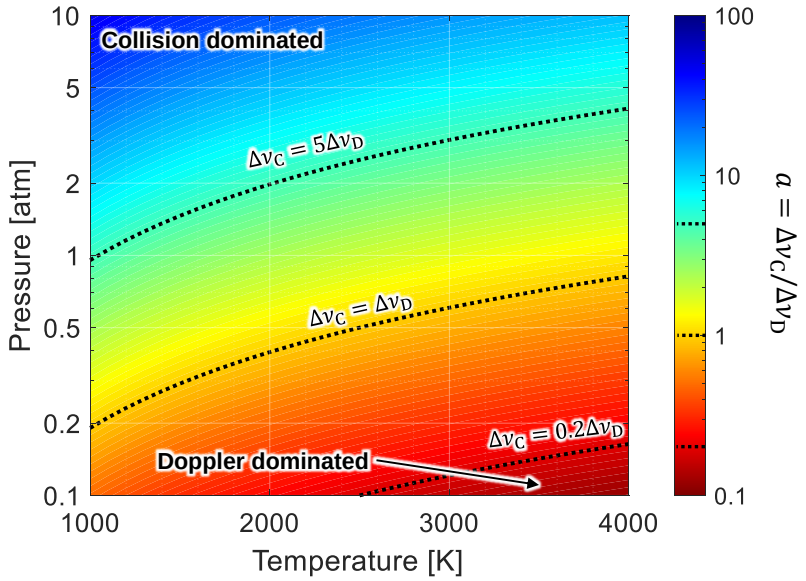

Figure E.1: Contour plot of the ratio of collision width to Doppler width, a, for a generic CO transition versus temperature and pressure. Collisional broadening is calculated using the $J'' = 20$ CO-N_2 broadening parameters: $T_0 = 1000$ K, $\gamma_0 = 0.0255$ cm^{-1} and $N = 0.55$

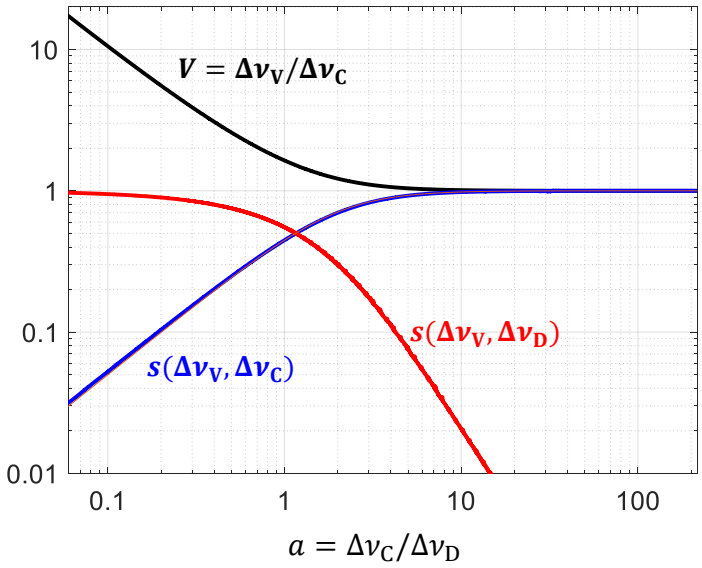

Figure E.2: Ratio of $\Delta\nu_V$ to $\Delta\nu_C$, V *versus* the ratio of the $\Delta\nu_C$ to $\Delta\nu_D$, a (black). The sensitivity of $\Delta\nu_V$ to both $\Delta\nu_C$ (blue) and $\Delta\nu_D$ (red) are also plotted.

erties of the Voigt lineshape versus this ratio of collision and Doppler widths. In black, the ratio of the Voigtian width to the collision width, V, is plotted, indicating that the Voigtian width is within a factor of 1.7 times the collision width as long as $\Delta\nu_C \geq \Delta\nu_D$. The sensitivity of the Voigtian width to both the collision width and Doppler width is also plotted. As can be expected, the sensitivity of the Voigtian width to the collision width (blue curve) correlates closely with $1/V = \Delta\nu_C/\Delta\nu_V$ (reciprocal of black curve). When $\Delta\nu_C > 4\Delta\nu_D$, the sensitivity is greater than 0.9, indicating a near linear relationship between $\Delta\nu_C$ and $\Delta\nu_V$. In the next section, the precision of $\Delta\nu_C$ measurements will be shown to scale with $1/V = \Delta\nu_C/\Delta\nu_V$.

E.0.2.2 Influence of white noise

Now that the sensitivity of the Voigt lineshape to pressure has been established, we can assess the efficacy with which the collision linewidth can be extracted from a realistic absorption measurement. In a real measurement, there is random noise that reduces the precision of the

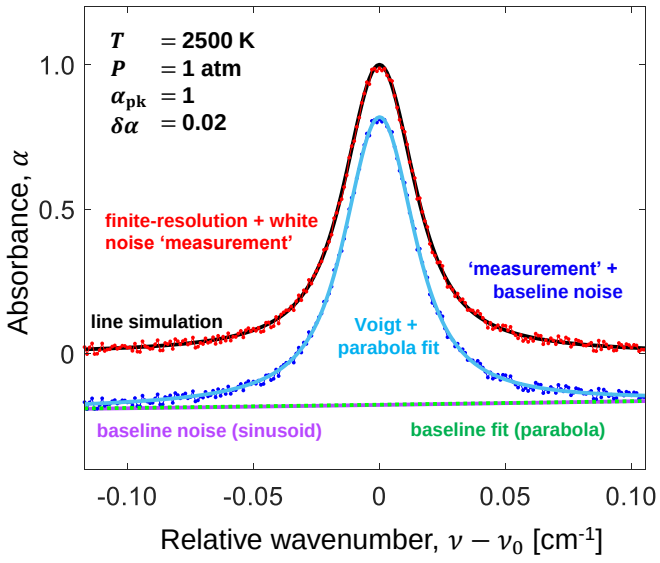

Figure E.3: Simulated generic Voigt profile for CO with peak absorbance normalized to 1 (black). Simulation with added white noise of amplitude $\delta\alpha = 0.02$ (red). Convoluting sinusoidal baseline noise (purple). Noisy simulation added to baseline (blue). Fit of Voigt profile and parabola to fit baseline (cyan).

measured absorbance spectrum. In this study, absorbance lineshapes were generated at various pressure/temperature conditions, using the same CO broadening parameters indicated in Fig. E.1, and random simulated noise was added. Then, the noisy transitions were fit with a Voigt lineshape to yield a measurement of collision width. Voigt lineshapes were generated with the spectral resolution of the measurement r_ν held fixed relative to the linewidth, such that there were 20 data points within the FWHM of the line. The scan depth D_ν was set to 8 times the linewidth.

The experimental noise content of the detection system used for the sensor demonstrations in Section 7.4 was assessed using Fourier analysis and found to be of constant amplitude between the laser scan rate (1 MHz) and the 1/2 of the data acquisition system sample rate ($\sim$1.5 GHz, also known as the Nyquist frequency). For this single-line study, all absorption lineshapes were normalized to a peak value of 1 and a fixed value of white noise (2% of the peak value) was added, see Fig. E.3. A nonlinear least-squares curve fitting routine

was employed to match the sum of a Voigt profile to the noisy Voigt simulation. For the Voigt profile, the Doppler width was fixed at a given temperature. Both the collision width, absorbance area, and absolute line position of the Voigt were allowed to float. The initial guess for the floated parameters was randomized to ±2% of the known value. 50 random noise profiles were fitted for each pressure and temperature condition. The range of the fitted collision width values (omitting outliers) was then assessed. The difference between the mean value of the fitted parameters and the true value represents a noise-induced bias of the measurement due to the non-linear relationship between the measured parameters and the Voigt profile. The range in the fitted results represents the potential error in the collision-width measurement due to measurement noise. In general, the range term is much greater than the bias term and as such, the bias term can typically be neglected. The relative potential error in the collision width from noise, plotted in Fig. E.4, is referred to as $E(\Delta\nu_C, \alpha)$ or the "precision error" in the collision width.

$E(\Delta\nu_C, \alpha)$ is plotted against pressure and temperature on the left side of Fig. E.4. The

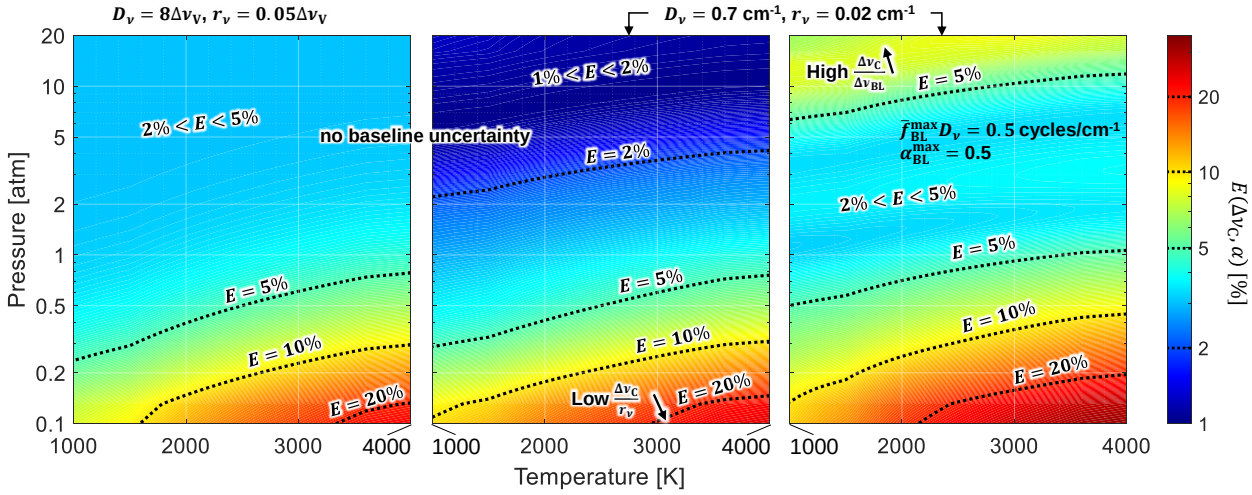

Figure E.4: Contour plots of the simulated potential precision error on the fitted collision-width $E(\Delta\nu_C, \alpha)$ of a single generic CO Voigt profile versus temperature and pressure. *Left*: The scan depth and spectral resolution scale with the FWHM of the Voigt profile. *Middle*: The scan depth and resolution are fixed. *Right*: The scan depth and resolution are fixed and baseline noise is added.

precision error in collision linewidth is under 5% for most combustion-relevant conditions and approaches 2% as pressure increases, reflecting the increased sensitivity of the Voigt lineshape to pressure. It should be noted that the precision error is a predictor of the signal-to-noise ratio of the measurement, $\mathrm{SNR}_{\mathrm{meas}}(\Delta\nu_{\mathrm{C}}) = 1/E(\Delta\nu_{\mathrm{C}}, \alpha)$. The above result indicates that the SNR of the collision-width measurement would be between 20 and 50 at combustion-relevant conditions. At higher temperatures and lower pressures, the collision width becomes small compared to the Doppler width and wavenumber resolution and measurement uncertainty exceeds 10%.

The effect of changing white noise on the absorbance measurement can now be estimated. The relative absorbance noise takes the form (as in Chapter 8):

$$E(\alpha) = \frac{\delta\alpha}{\alpha} = \frac{1}{\mathrm{SNR}_{\mathrm{opt}}}\frac{\exp\alpha}{\alpha}. \tag{E.3}$$

$\mathrm{SNR}_{\mathrm{opt}}$ refers to the "optical signal-to-noise ratio" of the incident light intensity collected by the detection system ($\mathrm{SNR}_{\mathrm{opt}}$=$I_0/\delta I$), as defined in Chapter 6. The $\exp(\alpha)/\alpha$ term describes how amplified the relative noise from the detection system ($\sim 1/\mathrm{SNR}_{\mathrm{opt}}$) becomes when absorbance is calculated. This parameter is minimized at $\alpha = 1$. In Appendix F, this parameter evaluated at the peak value of an absorption feature, α_{pk}, is shown to be a good predictor of the precision error in the fitted absorbance area. Above, $E(\alpha_{\mathrm{pk}})$ was set to 2%. In the below analysis, this parameter was varied to see its effect on the measured collision width. In Fig. E.5, the collision-width precision error $E(\Delta\nu_{\mathrm{C}}, \alpha)$ is plotted against $E(\alpha_{\mathrm{pk}})$ at four different values of $\Delta\nu_{\mathrm{C}}/\Delta\nu_{\mathrm{V}}$. It can be seen that the precision error in collision-width is indeed linear with $E(\alpha_{\mathrm{pk}})$. As the collision-width drops relative to the Voigtian width, the precision error increases by approximately $V = \Delta\nu_{\mathrm{V}}/\Delta\nu_{\mathrm{C}}$. Therefore, the following approximation can be made for the error in the collision width from white noise:

$$E(\Delta\nu_{\mathrm{C}}, \alpha) \propto \frac{\Delta\nu_{\mathrm{V}}}{\Delta\nu_{\mathrm{C}}} E(\alpha_{\mathrm{pk}}). \tag{E.4}$$

The ratio $V = \Delta\nu_{\mathrm{V}}/\Delta\nu_{\mathrm{C}}$ can quickly be approximated as $V \approx 0.5(1 + \sqrt{1 + 4/a^2})$, where $a \equiv \Delta\nu_{\mathrm{C}}/\Delta\nu_{\mathrm{D}}$ [276]. Equation E.4 was also verified with $\Delta\nu_{\mathrm{D}}$ substituted for $\Delta\nu_{\mathrm{C}}$, which is useful in the case that the Doppler broadening is floated while collisional broadening is fixed,

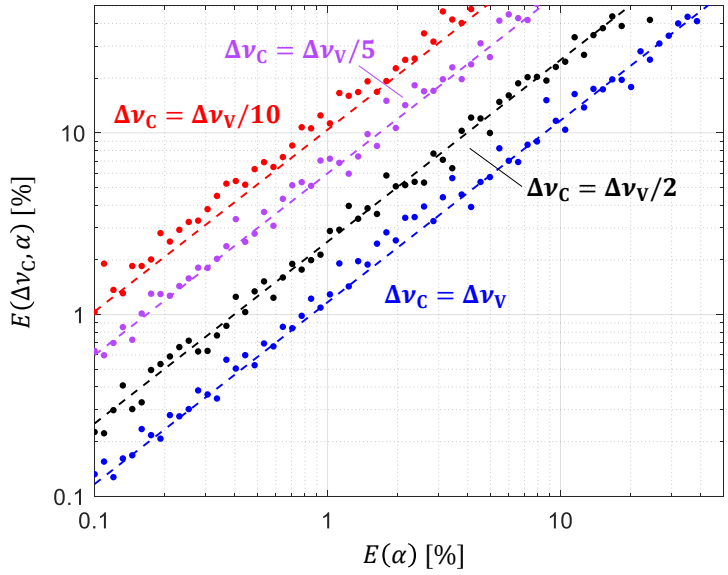

Figure E.5: Collision-width precision error $E(\Delta\nu_C, \alpha)$ versus precision error in absorbance $E(\alpha)$ for a single-line fit. Various colors indicate different pressures ratios of the collision-width to the overall voigtian width. The dashed lines represent linear fits.

as in [277]. It should also be noted that the precision error can be further reduced via signal averaging in cases where the required measurement rate f_{req} is lower than the laser scan rate f_{scan}. When averaging over $\eta = f_{\text{scan}}/f_{\text{req}}$ measurement samples, precision error is reduced by a factor $\sqrt{\eta}$. Due to the high measurement rate offered by the MHz-modulation scheme used in this work, averaged measurements at kHz rates can be produced with a factor 30 improvement in precision/SNR.

The absorbance area precision error, $E(A, \alpha)$, can also be assessed using above simulation methods. This is of relevance since absorbance area measurements are used to obtain temperature, which is used for the pressure measurement. $E(A, \alpha)$ was found to also linearly vary with $E(\alpha)$, as predicted by Appendix F, although there is not a dependence on $V = \Delta\nu_V/\Delta\nu_C$.

$E(\alpha)$ realistically varies with the temperature, pressure, and CO concentration of the gas, which affect the absorption strength. This variation can be examined for the P(0,31) transition of CO, assuming the same broadening parameters used for the single-line analysis above

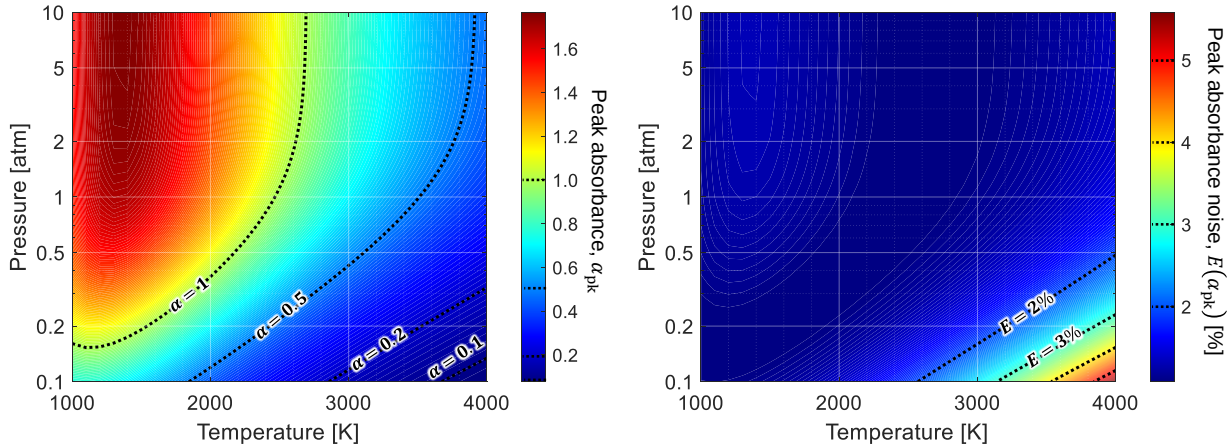

Figure E.6: *Left*: Plot of peak absorbance for the P(0,31) transition of CO versus temperature and pressure for $X_{\mathrm{CO}}L = 0.3$ cm. *Right*: Predicted relative precision error on peak absorbance of the P(0,31) line assuming an optical SNR of 250.

and using the line parameters from HITEMP [205] to calculate the temperature-dependent linestrength. Equation 7.12 is used to calculate the absorbance area at each condition, which is then multiplied by the peak Voigt lineshape to obtain the peak absorbance. The left side of Fig. E.6 plots the peak absorbance of this transition versus pressure and temperature employing values representative of the demonstration of Section 7.4 of Chapter 7, ($X_{\mathrm{CO}}L = 0.3$ cm, $\mathrm{SNR}_{\mathrm{opt}} = 250$). Above 1 atm and in the range 1000–4000 K, the P(0,31) line has an absorbance greater than 0.37. The peak absorbance noise is plotted on the right side of Fig. E.6. It can be seen that for most combustion-relevant conditions, the peak absorbance noise is $\leq$2%, indicating the 2% white noise assumption for the above single-line analysis represented a worst case. The absolute absorbance noise will also decrease away from the linecenter, tapring off to e^{-1} the peak value at the wings of the line. The resulting absorbance noise variation with gas condition and wavenumber was modelled in the multi-line fitting analysis of Section 7.3.2 to generate the absorbance noise profiles at various temperature/pressure conditions.

To summarize the results of this subsection, the Voigt lineshape is highly sensitive to pressure. This provides for very high-precision collision-width measurements using CO spec-

tral transitions across many combustion-relevant conditions. Precision error was shown to scale linearly with the noise in the raw absorbance spectra and the ratio $V = \Delta\nu_V/\Delta\nu_C$. In the following subsection, the effect of LAS sampling parameters (scan depth and spectral resolution) on the collision-width measurement will be assessed.

E.0.2.3 Effect of spectral sampling parameters

Now that the linear relationship between absorbance noise and collision-width precision error has been established, the effects of other factors which may effect precision error is assessed. In this section, the effect of the sampling of the spectral domain, both in terms of spectral tuning range (scan depth, D_ν) and the point-to-point resolution in the wavenumber domain (r_ν) Will be analyzed. These sampling parameters are related to the laser scanning parameters as well as the data acquisition system. If f_{scan} is taken as the laser scan rate, the scan depth can be approximated as the average laser chirp rate $R_{\text{chirp}} = |d\nu/dt|$ times half of the scan period, $f_{\text{scan}}^{-1}/2$ [189]:

$$D_\nu \approx \frac{R_{\text{chirp}}}{2f_{\text{scan}}}. \tag{E.5}$$

The wavenumber resolution tends to diminish with laser chirp rate at a fixed temporal sampling rate R_{samp}:

$$r_\nu = \frac{R_{\text{chirp}}}{R_{\text{samp}}}. \tag{E.6}$$

Therefore, there is a compromise between these two parameters when selecting a laser scanning waveform in order to maximize precision. To aid in the selection of these parameters, the precision error will be investigated as these parameters are varied.

To isolate the effect of scan depth, simulations of a purely Lorenztian profile with simulated noise were generated at a fixed linewidth for several different scan depths. For these Lorenztian profiles, the linewidth is simply notated as $\Delta\nu$ instead of $\Delta\nu_C$ or $\Delta\nu_V$. On the right side of Fig. 7.3, the collision-width precision error (normalized by the absorbance noise) is plotted in black against the ratio of scan depth to linewidth ($D_\nu/\Delta\nu$) for a fixed wavenumber resolution of $\Delta\nu/r_\nu = 20$ points per FWHM. In general, increasing the scan depth reduces the precision error. This benefit plateaus after the scan depth is approximately

five times the linewidth, after which the wings of the line are almost completely resolved. This can be visualized in Fig. E.7 (left). The precision error in absorbance area $E(A, \alpha)$ also presents similar variation with scan depth as $E(\Delta\nu, \alpha)$.

The effect of changing the wavenumber resolution can be observed by examining the blue curve in Fig. 7.3. The resolution can be expressed as the number of data points contained within the FWHM of the transition $n = \Delta\nu / r_\nu$. Here, the wavenumber resolution has been increased to $n = 500$ points per FWHM ($\times 25$ increase). The precision error here has significantly dropped, by nearly a factor of 5 in the plateau region with high scan depth. By examining many values of n, it was observed that $E(\Delta\nu, \alpha)$ scales with $\sqrt{n}$. When $r_\nu = 0.05\Delta\nu$ ($n = 20$ points per FWHM), the precision error in collision width is nearly equal to the absorbance noise $E(\alpha)$, making Eqn. E.4 an equality:

$$E(\Delta\nu_{\mathrm{C}}, \alpha) \approx \sqrt{\frac{20}{n}} \frac{\Delta\nu_{\mathrm{V}}}{\Delta\nu_{\mathrm{C}}} E(\alpha_{\mathrm{pk}}). \tag{E.7}$$

This square root relationship is also present for $E(A, \alpha)$ in the large scan-depth limit, such that:

$$E(A, \alpha) \approx \sqrt{\frac{20}{n}} E(\alpha_{\mathrm{pk}}). \tag{E.8}$$

It should also be noted that in many applications, the laser chirp rate is not constant. This leads to uneven spectral resolution across the measured spectrum, which will cause results to deviate slightly from the above analysis. Additionally, spectral features may not be placed in the middle of the wavenumber domain of the scan, due to optical SNR or spectral resolution maximization near a particular edge of the scan. As such, precision error may be minimized for a scan depth greater than $5\Delta\nu$. In Section S2.E.0.2.5, effect of scan depth when multiple spectral lines are present is discussed.

The single line analysis of Section S2.E.0.2.2 was repeated with fixed r_ν (0.002 cm^{-1}) and D_ν (0.7 cm^{-1}) across various pressures and temperatures, as visualized in the middle of Fig. E.4. These parameters are representative of the spectral sampling parameters used in sensor demonstrations of Section 7.4 of Chapter 7. Compared to the case where these parameters were scaled with the linewidth, there is slightly increased precision error at low

pressures due to poor resolution of the spectral feature (nearly $n = 6$ points per FWHM at the lowest pressures), but the error is dominated here by the Doppler-dominated nature of the line. On the other hand, there is reduced precision error at high pressures due to the increased points per FWHM (nearly $n = 300$ points per FWHM at 20 atm). This counteracts the limited scan depth at these high pressures, which is still greater than the linewidth. At these high pressures, uncertainty typically arises from baseline uncertainty and line blending, as will be explored in the next sections.

E.0.2.4 Effects of baseline distortion

In this section, the convoluting effects of non-absorbing baseline uncertainty is examined. At low frequencies, $1/f$ noise is present in the raw detector signal, and in realistic measurements, environmental factors such as mechanical vibration, beam steering, and broadband spectral interference can add additional noise at frequencies below 100 kHz. These factors introduce uncertainty in the non-absorbing baseline, which can cause potential fitting errors at higher

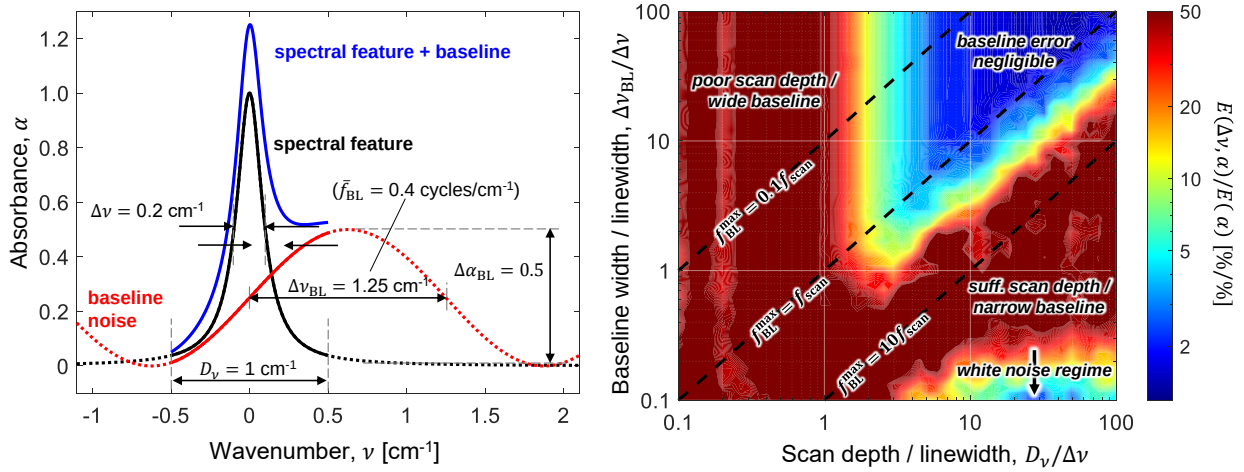

Figure E.7: *Left*: Terminology used for baseline uncertainty analysis with sample values. *Right*: Normalized precision error in collision width versus scan depth and baseline noise width. Black dashed lines indicate constant ratios of scan rate to maximum baseline temporal frequency.

pressures where there are no non-absorbing regions in the measured spectrum and as such, this type of noise is termed "baseline-uncertainty". Typically, to mitigate the effect of this uncertainty on spectral fitting, the background is treated prior to processing, or a polynomial (typically $\leq$2nd order) is fit along with the spectrum to account for the distortion, although this can still result in some potential errors in the fitted parameters. In this section, we will investigate the effect of the type of baseline noise present (amplitude and frequency), as well as the effect of the polynomial used to fit the baseline.

For the sensing strategy presented here, the laser is scanned at 1 MHz, which is much higher than the frequencies of these noise sources, so low frequency noise is modeled as the addition of a sinusoid to the absorbance. A single sine wave is used as a proxy for more complex low frequency noise to illustrate the trends associated with baseline distortion. If the baseline noise is assumed to have temporal frequency f_{BL}, then assuming the laser wavenumber rate of change (chirp rate) R_{chirp} is constant, the periodicity (cycles per cm^{-1}) of the baseline noise in the spectral domain will be $\overline{f}_{\mathrm{BL}} = f_{\mathrm{BL}}/R_{\mathrm{chirp}}$. As such, the following estimation is derived:

$$\Delta\nu_{\mathrm{BL}} = \frac{1}{2\overline{f}_{\mathrm{BL}}} \approx D_{\nu}\frac{f_{\mathrm{scan}}}{f_{\mathrm{BL}}}. \tag{E.9}$$

Here, $\Delta\nu_{\mathrm{BL}}$ is the effective FWHM of the baseline noise, or the length of half a period of the sine wave. The baseline noise width in the spectral domain, $\Delta\nu_{\mathrm{BL}}$, increases as the scan depth D_{ν} increases or when the laser scan rate f_{scan} is increased relative to the temporal frequency of the baseline distortion f_{BL}.

To isolate the effects of baseline uncertainty, pure Lorentzian profiles (with linewidth $\Delta\nu$) were simulated with white noise and a sinusoidal baseline addition. The periodicity ($\overline{f}_{\mathrm{BL}}$), amplitude ($\Delta\alpha_{\mathrm{BL}}$), and phase offset of the baseline are illustrated on the left of in Fig. E.7. This simulated noisy measurement with a baseline is fit with a Lorentzian and 2nd order polynomial, floating the linewidth, line area, line position, and polynomial coefficients. The effect of this random baseline to a spectrum simulation and corresponding fit can be visualized in Fig. E.3. Initially, the variation in collision-width precision error $E(\Delta\nu, \alpha)$ is assessed as the minimum baseline periodicity and scan depth are varied. The right side

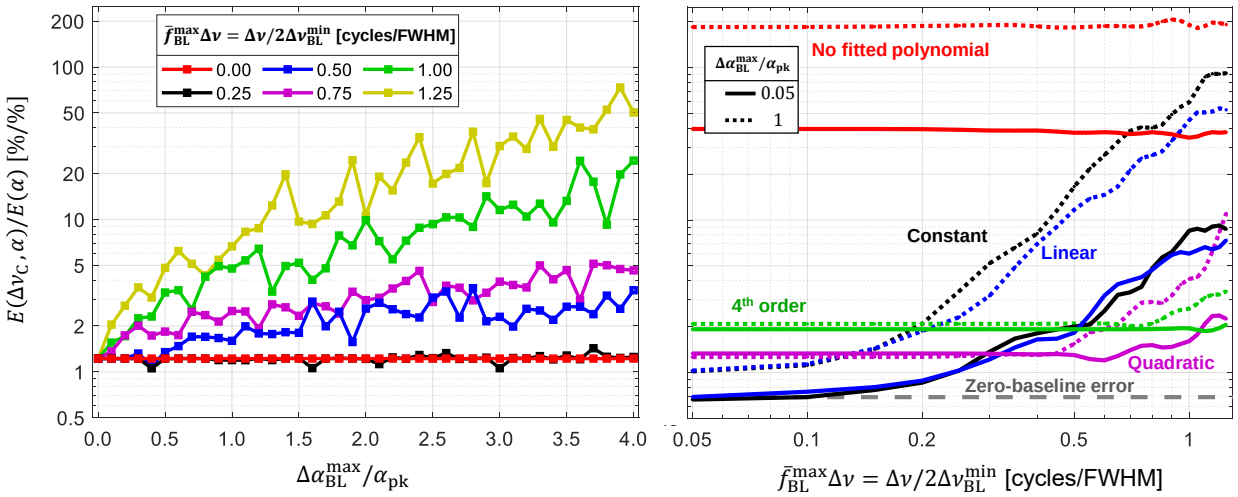

Figure E.8: *Left*: Collision-width precision error per absorbance noise versus amplitude of baseline. Different colors represent various baseline periodicities (in spectral domain) normalized by spectral linewidth. *Right*: Collision-width precision error per absorbance noise versus normalized baseline frequency. When there is minimal baseline noise (solid lines) using a linear or constant baseline fit results in the lowest error until baseline frequency exceeds nearly 0.3 cycles/FWHM. When a large baseline amplitude is present (dashed lines) a 2nd order polynomial begins to perform better starting at a lower noise frequency than before, nearly 0.15 cycles/FWHM. The scan depth is fixed at 5 times the linewidth for both plots.

of Fig. E.7 plots the precision error normalized by $E(\alpha)$ versus scan depth and baseline noise width $\Delta\nu_{\mathrm{BL}}^{\mathrm{min}} = 1/2\overline{f}_{\mathrm{BL}}^{\mathrm{max}}$, both normalized by linewidth, with the maximum baseline absorbance fixed at half the peak spectral absorbance. For high values of the baseline width (low periodicity), the trend of Section S2.E.0.2.3 is recovered— increasing scan depth up to $5\Delta\nu$ reduces precision error, after which minimal benefit is observed. When the baseline width drops below the linewidth of the spectral feature, the error becomes insensitive to scan depth, as the baseline begins to become indistinguishable from the spectral feature itself. For very high values of baseline periodicity and scan depth (bottom-right corner of Fig. E.7) the baseline noise essentially becomes white noise, and the precision error approaches the

values of Section S2.E.0.2.2. At intermediate values of the baseline width, the threshold of $D_\nu > 5\Delta\nu$ for minimizing error is still present, but there is also a maximum scan depth value beyond which the error begins to increase again. This is because an increase of scan depth causes more periods of the sine wave to enter the sampling domain, which the polynomial is unable to effectively fit. This critical scan depth value is approximately equal to the baseline width. This seems to imply that increasing scan depth is detrimental when baseline noise is present, but from Eqn. E.9, it can be seen that for a constant scan rate and baseline temporal frequency, when scan depth is increased, the baseline width in the spectral domain also increases linearly. As such, Fig. E.7 should be traversed along lines of fixed slope as scan depth increases, as indicated by the black dashed lines. In Fig. E.7, it can be seen that when the baseline temporal frequency is less than the scan rate, the precision error is minimized, highlighting the benefits of high-speed laser scanning at MHz rates. To be conservative, it is recommended to keep the scanning frequency to twice the baseline (or noise) temporal frequency to account for non-linearities associated with the conversion from light intensity to absorbance and due to the non-linear mapping of the time and spectral domains. It should be noted that the above recommendation applies when using a 2nd order polynomial to fit the baseline. With a first order polynomial, the fitting analysis reveals that scan rate should be at least 10 times the baseline noise frequency. The effect of polynomial order is discussed more later in the section. The precision error versus scan depth at a constant $f_{\text{scan}}/f_{\text{BL}}^{\text{max}}$ with a 2nd-order polynomial fit of the baseline can be seen in the green curve of Fig. 7.3. Below the scan-depth threshold valude of $5\Delta\nu$, the precision error can be seen to increase much more rapidly than for the no-baseline case.

Now that the effect of scan depth on baseline-induced precision error has been assessed, the effect of the variation of the baseline amplitude is examined. On the left of Fig. E.8, the collision-width precision error is plotted against the ratio of the maximum peak baseline absorbance to the peak transition absorbance ($r_\nu/\Delta\nu = 100$ pts/FWHM, $D_\nu = 5\Delta\nu$). The various curves represent different values of the maximum baseline peridiocity, normalized by linewidth (related to reciprocal of y-axis in Fig. E.7). It can be seen that once the baseline

frequency exceeds 0.25 cycles per scan period, the precision-error increases with the baseline absorbance amplitude, as predicted by Fig. E.7 for this scan-depth value. Beyond this limit, the precision error increases with the relative baseline noise amplitude[1].

The variation of baseline-induced precision error is plotted against maximum baseline periodicity on the right of Fig. E.8 with the maximum baseline amplitude fixed at $0.05\alpha_{\text{pk}}$ (solid line) or at α_{pk} (dashed lines). The various colors correspond to the degree of the polynomial used to fit the baseline. For both baseline noise levels, using at least a constant baseline in the fit dramatically reduces fitting error. At lower noise frequencies, the higher order polynomials (¿2) result in a larger number of free parameters in the fit which can erroneously overfit part of the actual spectra, leading to higher precision error (this phenomenon is known as the "bias-variance tradeoff" [278]). This is particularly true when $D_\nu \approx \Delta\nu \approx \Delta\nu_{\text{BL}}$, where the baseline noise and lineshape become difficult to separate from each other (this can be seen in the green curve of Fig. 7.3 when the scan depth is near the linewidth). On the other hand, at higher baseline noise frequencies, higher order polynomials help to mitigate the increase in precision error. When the baseline noise amplitude is higher (dashed lines versus solid lines), the benefit of using higher order polynomials is realized at lower noise frequencies. Judicious selection of the baseline order must be performed based on the circumstances, but in general, a lower degree polynomial is preferred. It should be noted that in this single-line analysis, even-degree polynomials and their succeeding odd-degree polynomials perform similarly (although the fit residual may decrease for higher-degree polynomials) due to the symmetric nature of the lineshape. For an asymmetric multi-line spectrum, the baseline order has a much larger effect.

On the right side of Fig. E.4, the single line analysis of Section S2.E.0.2.2 was repeated with a maximum baseline periodicity of $\overline{f}_{\text{BL}}^{\text{max}} D_\nu = 0.5$ cycles per scan and maximum baseline amplitude of $\Delta\alpha_{\text{BL}}^{\text{max}}/\alpha_{\text{pk}} = 0.5$. This led to a general increase in precision error, particularly at high pressures over 10 atm, where the linewidth approaches the baseline width.

[1]In a practical setting, high levels of baseline absorbance will reduce the raw transmitted light intensity to the detector, decreasing the optical SNR and further increasing white-noise-induced precision-error.

The above baseline effects were also analyzed for absorbance area. The trends between $E(\Delta\nu, \alpha)$, scan depth, baseline frequency, and baseline amplitude generally hold for $E(A, \alpha)$. One notable difference is that the amount by which baseline uncertainty affects absorbance area measurements is 2–5 times higher than for collision width measurements. The absorbance area is more prone to overfitting by the polynomial used to fit the baseline. This is due to the propensity of the polynomial to erroneously "steal" or "donate" area to the line near the bottom of the spectral feature. As such, it is of greater importance to minimize baseline distortion when absorbance area is being fitted.

E.0.2.5 Line-blending analysis

In this section, the isolated effect of line blending is examined. This analysis is relevant to the blending of the P(2,20) and P(0,31) lines, both of which are used for useful gas property measurements, and to the blending of the P(3,14) with the P(0,31) line at high temperatures, which tends to cause increased errors in the fitting of P(0,31). Here, two Lorentzian profiles with equal absorbance areas and linewidth $\Delta\nu$ were simulated at a fixed distance from each other. The wavenumber domain is centered in the middle of the two features. The wavenumber resolution is fixed at 20 points per FWHM. One of the lines is termed the "target", for which the error in the fitted parameters is assessed, whereas the other line is designated the "perturber", whose fitting results are deemed less important. The absorbance noise is set to be 2% of the peak absorbance of the target line.

Figure E.9 plots the normalized precision error in collision width (left) and absorbance area (middle) versus scan depth and line spacing. For values of scan depth greater than the previously established threshold ($5\Delta\nu$), the precision error in the fitted parameters significantly increases when the line spacing drops below the linewidth. The absorbance area is more strongly affected by this than the collision width, as the FWHM of two perfectly overlapped identical transitions is the same as the FWHM of each individual one, whereas it is difficult to properly allocate the correct amount of area to each line in the fit. For collision-width, the precision error in this regime scales with the factor $1+2\Delta\nu/\Delta\nu_{12}$. For absorbance

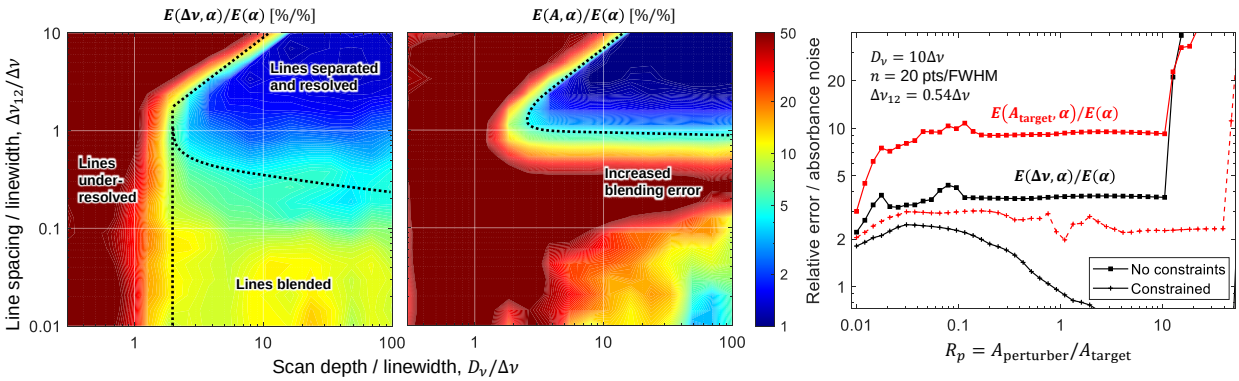

Figure E.9: Normalized precision error for collision-width *left* and absorbance area *middle*, versus scan depth and line spacing. Blacked dotted lines indicate where error behavior changes significantly. *Right*: Normalized error versus perturber-to-target area ratio R_p, with effect of fitting constraints shown.

area, the precision error does begin to drop for very high values of scan depth, even when the lines are significantly blended. The aforementioned trends are for the case where the two areas are equal to each other, as the fitting method tends to evenly distribute area on average. When the lines are set to have different areas, with ratio $R_p = A_{\text{perturber}}/A_{\text{target}}$, the target area and width error are generally insensitive for $0.02 < R_p < 10$, when the line spacing is below the linewidth. Below $R_p = 0.02$, the errors decrease and approach the value for single-line fitting. Above $R_p = 10$, the error increases dramatically and the target line becomes unresolvable.

The precision in the fitted parameters of the blended lines can be reduced by adding constraints to the fitting routine. For the fitting strategy presenting in Section 7.3.2 of Chapter 7, the relative line positions are fixed, and the ratio between the linewidths are fixed using knowledge of the relative collisional broadening of the transitions. The above blending study was repeated with the line position and linewidth of the perturber fixed relative to the target line. The results for a fixed scan depth, resolution, and line spacing ($0.54\Delta\nu$) are shown on the right side of Fig. E.9. These constraints generally reduced precision error by a factor of 4 and reduced the minimum value of line spacing from $\Delta\nu$ to $0.5\Delta\nu$. The maximum area ratio R_p for adequate target line resolution is increased from $R_p = 10$ to

$R_p = 40^2$. Due to the enhanced fitting performance with the constraints, the CO sensing technique of Chapter 7 is able to perform well at high pressures where the lines become blended. For the target CO spectrum at 2008.5 cm^{-1}, the line spacing is $\Delta\nu_{12} = 0.104$ cm^{-1}, whereas the linewidth is $\Delta\nu \approx 0.014$ cm^{-1} at $P = 1$ atm and $T = 2500$ K. Based on the limit of $\Delta\nu < 0.5\Delta\nu_{12}$, the individual fitted area precision is predicted to be resolvable up to a pressure of about 15 atm before the blending becomes too extreme for adequate separation of the lines.

For line spacing values greater than the linewidth, the scan depth threshold beyond which there are limited improvements in precision becomes $D_\nu > 5\Delta\nu + \Delta\nu_{12}$ if the center of the scan is at the midpoint of the two transitions in the spectral domain. Often, for multi-line spectra at moderate pressures, the line spacing is larger than the linewidth, so this is the dominating driver of scan depth. For the target CO spectrum at 2008.5 cm^{-1} at $T = 2500$ K, the line spacing is approximately 7.4 times the linewidth for $P = 1$ atm, making the line spacing the primary driver of scan depth. At $P = 10$ atm, $5\Delta\nu$ is now similar to the line spacing, making both factors important for chosing an adequate scan depth.

E.0.3 Temperature uncertainty

Temperature uncertainty is calculated based on the methods of Chapter D with some modification to account for positive versus negative errors, and bias effects. Using Eqn. E.2 on Eqn. 7.13, we obtain the following form for the relative temperature uncertainty:

$$E(T) = E(T, \alpha) + E(T, \text{bias}) + E(T, S_1^0) + E(T, S_2^0). \tag{E.10}$$

The potential error contributions from measurement noise, $E(T, \alpha)$, and model/fitting bias, $E(T, \text{bias})$, are quantified in Section 7.3.2 of Chapter 7, and represent the potential errors associated with the absorbance area measurements A_1 and A_2 used to obtain temperature. $E(T, \alpha)$ is plotted in Fig. 7.4 versus pressure and temperature, for $X_{\text{CO}}L = 0.3$ cm, $\text{SNR}_{\text{opt}} =$

[2]At these high area ratios, the absorbance noise on one of the two lines is likely to be signficantly higher than the other due to optically thin or thick conditions ($\alpha << 0.1$ or $\alpha >> 3$). This will lead to a greater error on one of the absorbance areas than predicted by this simple analysis.

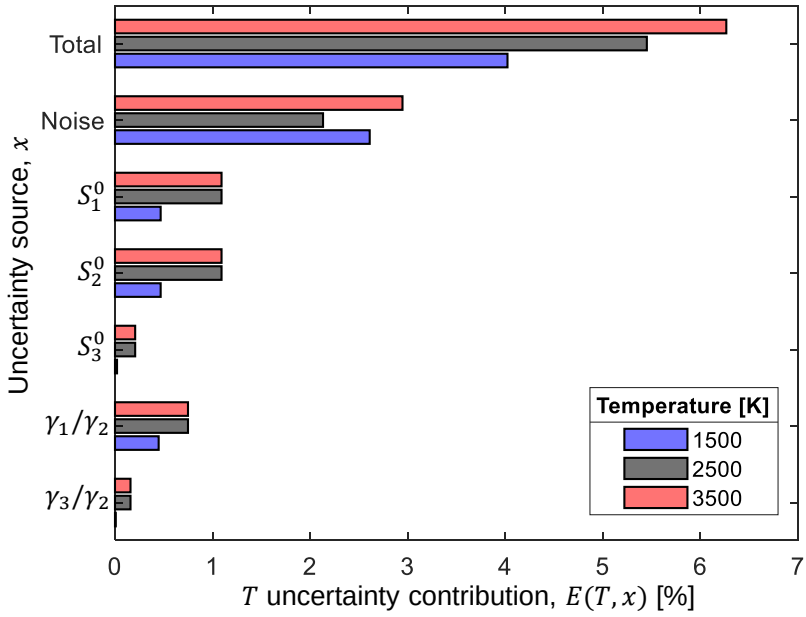

Figure E.10: Contributions of potential error sources to total temperature uncertainty (top 3 bars). Bar color corresponds to temperature condition. Noise is evaluated for $P = 1$ atm, $X_{\mathrm{CO}}L = 0.3$ cm, $\mathrm{SNR}_{\mathrm{opt}} = 250$, $D_\nu = 0.7$ cm^{-1}, $r_\nu = 0.002$ cm^{-1}, $f_{\mathrm{BL}}^{\max} D_\nu = 0.25$ cycles per scan, and $\Delta\alpha_{\mathrm{BL}}^{\max} = 0.5$.

250, $D_\nu = 0.7$ cm^{-1}, $r_\nu = 0.002$ cm^{-1}, $f_{\mathrm{BL}}^{\max} D_\nu = 0.25$ cycles per scan, and $\Delta\alpha_{\mathrm{BL}}^{\max} = 0.5$. The values at $P = 1$ atm are included at various temperatures in Fig. E.10 under the label "Noise". As mentioned in Section 7.3.2 of Chapter 7, the uncertainty on the linestrength of the minor P(3,14) line will contribute to to $E(T, \mathrm{bias})$. This effect generally increases with temperature, as the P(3,14) line becomes active. The potential error is minimized for pressures near 1 atm, but begins to increase increases above 1% beyond 3500 K at pressures above 2 atm or below 0.5 atm. The potential error contribution of this linestrength uncertainty is indicated in Fig. E.10 under the label "S_3^0".

The potential error terms related to the uncertainty in the reference linestrengths for lines 1 and 2 are as follows, from Eqn. 7.20:

$$E^+(T, S_1^0) = \frac{kT}{hc\Delta E_{12}''} E^-(S_1^0), \tag{E.11}$$

$$E^+(T, S_2^0) = \frac{kT}{hc\Delta E_{12}''} E^+(S_2^0). \tag{E.12}$$

From these relations, we can see that an overestimation of S_1^0 (the higher E'' line) will lead to an underestimation of temperature, whereas an overestimation of S_1^0 (the lower E'' line) will lead to an overestimation of temperature.

E.0.4 CO partial-pressure and mole-fraction uncertainty

The partial pressure of CO is obtained using Eqn. 7.14. By applying Eqn. E.2 to this equation, we obtain the following form for the uncertainty in p_{CO}:

$$E^+(p_{\mathrm{CO}}) = E^+(p_{\mathrm{CO}}, \alpha) + E^+(p_{\mathrm{CO}}, \mathrm{bias}) + E^+(p_{\mathrm{CO}}, S_1^0) + E^+(p_{\mathrm{CO}}, S_2^0) + E^+(L). \quad \text{(E.13)}$$

$E(L)$ refers to the relative uncertainty in the absorption pathlength L. The terms $E(p_{\mathrm{CO}}, \alpha)$ and $E(p_{\mathrm{CO}}, \mathrm{bias})$ account for the contribution to the potential errors from measurement noise and fitting model bias respectively and their effect on the correlated measurements of A_2 and $S_2(T)$. These errors are assessed using the methods of Section 7.3.2. The precision error in p_{CO} is plotted in Fig. E.11 versus temperature and pressure for $X_{\mathrm{CO}}L = 0.3$ cm, $SNR_{\mathrm{opt}} = 250$, $D_\nu = 0.7$ cm^{-1}, $r_\nu = 0.002$ cm^{-1}, $f_{\mathrm{BL}}^{\mathrm{max}} D_\nu = 0.25$ cycles per scan, and $\Delta\alpha_{\mathrm{BL}}^{\mathrm{max}} = 0.5$. The precision error term generally increases with temperature beyond 1200 K and is minimized for pressures between 1.5 and 3 atm across the 1200–4000 K temperature range, with increased precision error at higher and lower pressures. The values at $P = 1$ atm are included at various temperatures in Fig. E.10 under the label "Noise".

$E(p_{\mathrm{CO}}, S_1^0)$ is the potential error contribution to p_{CO} from the uncertainty in S_1^0 via the temperature measurement used to obtain $S_1(T)$. This error can be expressed as:

$$E^+(p_{\mathrm{CO}}, S_1^0) = \left|s(p_{\mathrm{CO}}, S_1^0)\right| \times \begin{cases} E^-(S_1^0), & \text{if } s(S_2,T)\leq 0 \\ E^+(S_1^0), & \text{if } s(S_2,T)>0 \end{cases}, \quad \text{(E.14)}$$

$$s(p_{\mathrm{CO}}, S_1^0) = \frac{kT}{hc\Delta E_{12}''} s(S_2, T), \quad \text{(E.15)}$$

$$s(S_i, T) = -1 - s(Q_{\mathrm{CO}}, T) + \frac{hcE_i''}{k_{\mathrm{B}}T} - \frac{hc\nu_{0,i}/k_{\mathrm{B}}T}{\exp\left(\frac{hc\nu_{0,i}}{k_{\mathrm{B}}T}\right) - 1}. \quad \text{(E.16)}$$

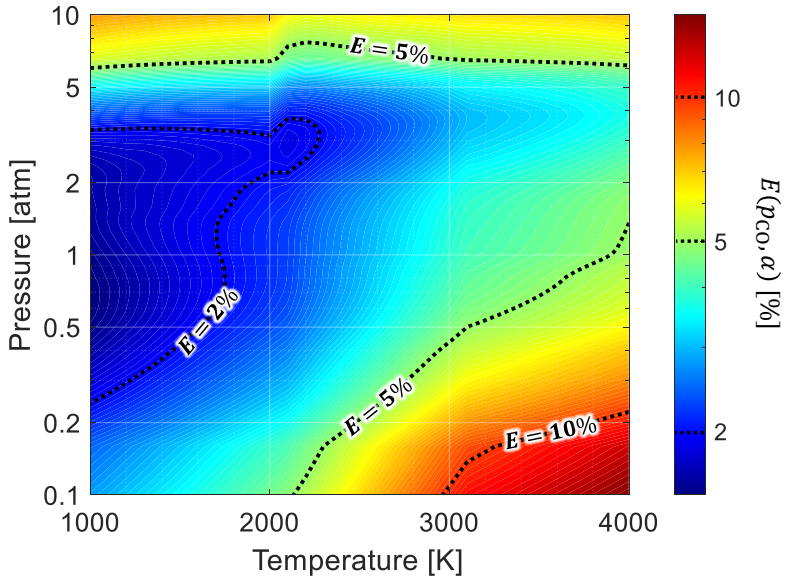

Figure E.11: Precision error in the CO partial-pressure measurement versus temperature and pressure for $X_{\mathrm{CO}}L = 0.3$ cm, $\mathrm{SNR}_{\mathrm{opt}} = 250$, $D_\nu = 0.7$ cm^{-1}, $r_\nu = 0.002$ cm^{-1}, $f_{\mathrm{BL}}^{\mathrm{max}} D_\nu = 0.25$ cycles per scan, and $\Delta\alpha_{\mathrm{BL}}^{\mathrm{max}} = 0.5$

$T_0 = 296$ K, h is the Planck constant, and Q_{CO} is the CO partition function [3]. If S_2 increases with temperature, an overestimation in S_1^0 will lead to an overestimation in p_{CO} and vice-versa if S_2 decreases with temperature.

$E(p_{\mathrm{CO}}, S_2^0)$ refers to the potential error in p_{CO} from the uncertainty in S_2^0. This relationship is not as straightforward as that for S_1^0, due to the additional directly proportional effect S_2^0 has on the linestrenth S_2 used to evaluate p_{CO}. The expression used to evaluate this potential error is:

$$E^+(p_{\mathrm{CO}}, S_2^0) = \left|s(p_{\mathrm{CO}}, S_2^0)\right| \times \begin{cases} E^-(S_2^0), & \text{if } s(p_{\mathrm{CO}}, S_2^0) \leq 0 \\ E^+(S_1^0), & \text{if } s(p_{\mathrm{CO}}, S_2^0) > 0 \end{cases}, \tag{E.17}$$

$$s(p_{\mathrm{CO}}, S_2^0) = -\left(1 + \frac{kT}{hc\Delta E_{12}''} s(S_2, T)\right). \tag{E.18}$$

Equations E.17 and E.18 show that if S_2 has a positive or weak temperature dependence, an overestimate of S_2^0 will lead to an underestimate of p_{CO}. When S_2 has a strong negative

[3] $s(Q_{\mathrm{CO}}, T)$ can be approximated as 1.13 from 300–3000 K.

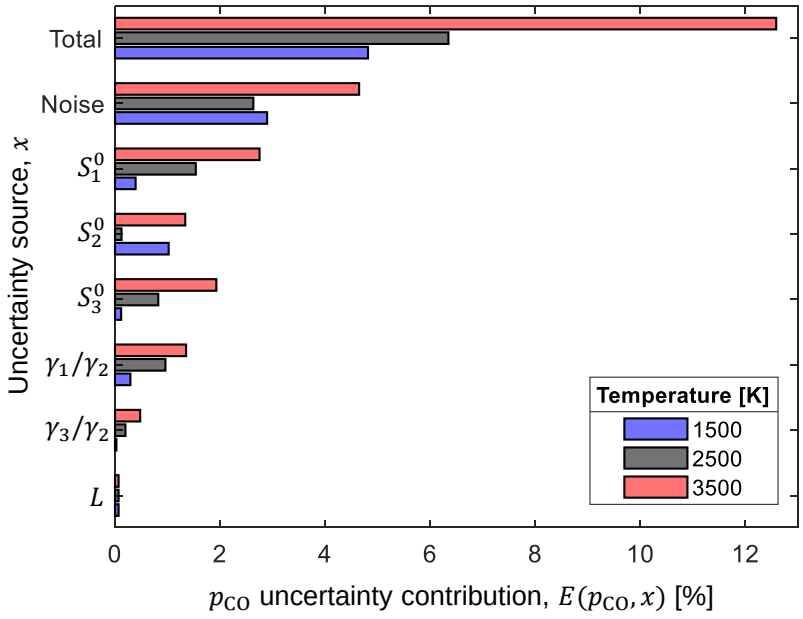

Figure E.12: Contributions of potential error sources to total CO partial pressure uncertainty (top 3 bars). Bar color corresponds to temperature condition. Noise is evaluated for the same conditions as Fig. E.10.

dependence on temperature, the temperature effect dominates such that an overestimate of S_2^0 leads to an overestimate of p_{CO}. For the P(0,31) line, the linestrength generally shows a negative correlation with temperature over the temperature range of interest (>1000 K), so the second branch of the piecewise expression is used.

The mole fraction of CO is obtained via Eqn. 7.15 using the measurements of p_{CO} and P. These two terms are highly correlated through a combined dependence on measurement noise, fitting model bias, and reference linestrength uncertainty (via the T measurement). As such, the error contributions from both of these terms must be combined using Eqn. E.2. The total error can be written as:

$$\begin{aligned} E^+(X_{CO}) = {} & E^+(X_{CO}, \alpha) + E^+(X_{CO}, \text{bias}) + E^-(L) \\ & + E^+(\gamma, \text{spec.}) + E^+(\gamma, \text{mix}) + E^+(X_{CO}, S_1^0) + E^+(X_{CO}, S_2^0). \end{aligned} \tag{E.19}$$

As for p_{CO}, the terms $E(X_{CO}, \alpha)$ and $E(X_{CO}, \text{bias})$ account for the contribution to the uncertainty from measurement noise and fitting model bias, respectively, and their effect on

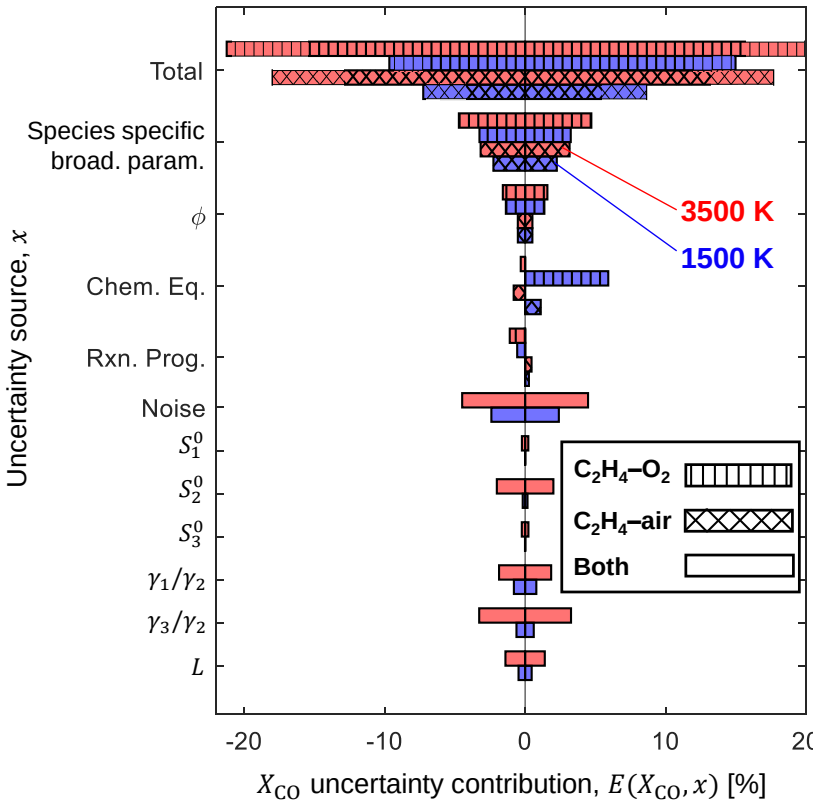

Figure E.13: Contributions of potential error sources to total CO mole fraction uncertainty (top 4 bars) for C_2H_4-fueled combustion product gas. Bar color corresponds to temperature condition. Bar hatching pattern indicates if composition-related errors/uncertainties are for air or oxygenated combustion. Noise is evaluated for the same conditions as Fig. E.10.

the correlated measurements of p_{CO} and P. These potential errors are assessed using the methods of Section 7.3.2. It is interesting to note that the precision error for X_{CO} is generally lower than that of p_{CO}, as the effects of noise on p_{CO} and P have opposing effects. Values of of $E(X_{CO}, \alpha)$ are included in Fig. E.13, evaluated for the same conditions as Fig. E.10, under the label "Noise". The term $E(X_{CO}, S_1^0)$ refers to the potential error contribution to X_{CO} from the uncertainty in S_1^0, which relates to X_{CO} via its temperature dependence through the temperature-dependent linestrength used to calculate p_{CO} and from the temperature-dependent collisional-broadening coefficient used to infer pressure. The expression for the

error is as follows:

$$E^+(X_{\mathrm{CO}}, S_1^0) = |s(X_{\mathrm{CO}}, S_1^0)| \times \begin{cases} E^-(S_1^0), & \text{if } s(X_{\mathrm{CO}}, S_1^0) \leq 0 \\ E^+(S_1^0), & \text{if } s(X_{\mathrm{CO}}, S_1^0) > 0 \end{cases}, \tag{E.20}$$

$$s(X_{\mathrm{CO}}, S_1^0) = \frac{kT}{hc\Delta E_{12}''}(s(S_1, T) + s(\gamma, T)). \tag{E.21}$$

Since both S_2 and γ generally decrease with temperature, $s(X_{\mathrm{CO}}, S_1^0)$ is generally negative, so the first branch of the piecewise expression is used.

For the effect of S_2^0 on X_{CO}, the direct inverse relationship between p_{CO} and S_2^0 must also be accounted for:

$$E^+(X_{\mathrm{CO}}, S_2^0) = |s(X_{\mathrm{CO}}, S_2^0)| \times \begin{cases} E^-(S_2^0), & \text{if } s(X_{\mathrm{CO}}, S_2^0) \leq 0 \\ E^+(S_2^0), & \text{if } s(X_{\mathrm{CO}}, S_2^0) > 0 \end{cases}, \tag{E.22}$$

$$s(X_{\mathrm{CO}}, S_2^0) = -\left[1 + \frac{kT}{hc\Delta E_{12}''}(s(S_2, T) + s(\gamma, T))\right]. \tag{E.23}$$

As for p_{CO}, since S_2 decreases with T for the P(0,31) line and because γ decreases with T, an overestimate of S_2^0 will lead to an overestimate of X_{CO}.

As for the temperature measurement, the measurements of p_{CO} and X_{CO} have potential bias errors due to the uncertainty on the P(3,14) linestrength. These potential errors are near-zero for pressures near 1.5–2 atm, and generally increase beyond 1% at other pressures after 3500 K. An exception to this is for p_{CO}, for which the potential error exceeds 1% at $P \leq 1$ atm for temperatures greater than 2400 K. These potential errors are indicated in Figs. E.12 and E.13 under the label "S_3^0".

E.0.5 Line-of-sight non-uniformity

In some situations, the gas properties along the optical line-of-sight (LOS) are not uniform, and as a result, LAS measurements represent a path-integrated quantity. In Appendix D, the effects of temperature non-uniformity were discussed in-depth for the CO line cluster near 2008 cm^{-1}. For the case of constant pressure and CO number density (or CO partial pressure) across the LOS, it was concluded that the linearity of the linestrengths with temperature

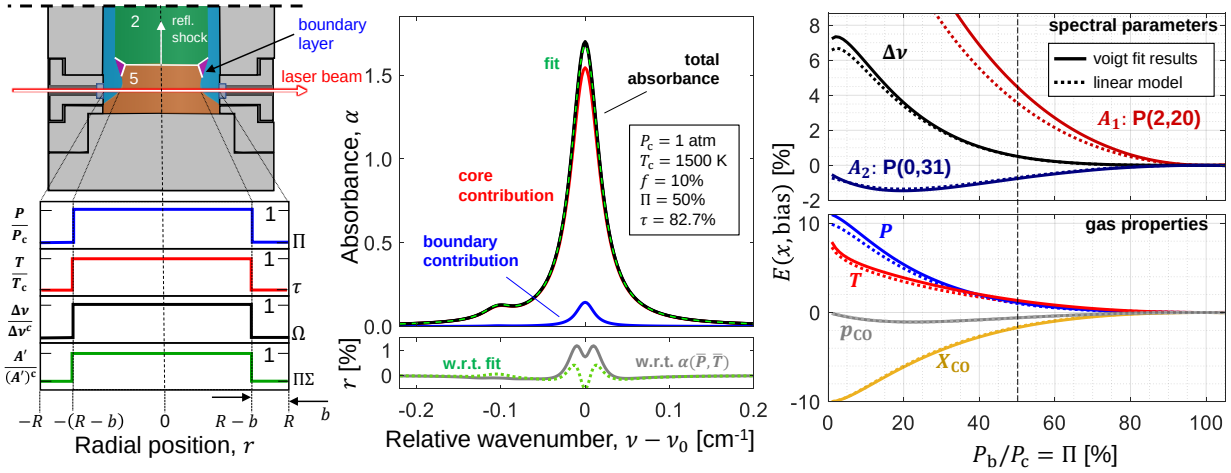

Figure E.14: *Left*: Shock-tube flow field with exaggerated boundary layer (blue) during reflected shock passage. Below is an indication of the gas/spectral properties versus radial position along the line-of-sight. A' refers to the spatial gradient of absorbance area. *Middle*: Simulated path-integrated absorbance profiles through the boundary layer (blue), core (red), and total line-of-sight (black). A Lorentzian fit of the total absorbance is shown in green. Normalized residuals between the path-integrated spectrum and the fit (green) or spectrum evaluated at the path-average P and T are shown below. *Right*: Plot of path-integration bias error versus the pressure ratio between the boundary layer and core for spectral parameters in single-line case (*top*) and for fitted gas properties derived from multi-line fit (*bottom*) at a fixed core pressure, temperature, and boundary-layer thickness. Results of first-order linear model are shown as dashed lines.

lead to 0.1–1% bias between the measured temperature and the true path averaged value for average temperatures from 2000–3000 K, assuming a uniform gradient of 500 K across the LOS. Uddi et al. [279] analyzed variation of LAS-measured temperature, accounting for a cold boundary layer in a rapid compression machine. Mathews et al. [280] performed a similar analysis for the CO lines at 2008.5 cm^{-1}, for measurements in post-detonation fireballs. In this section, we extend this type of analysis to cases where the pressure varies across the LOS. Pressure non-uniformities introduce additional complexities, as the lineshape varies across the LOS, leading to a path-integrated lineshape that is no longer purely Voigtian. We

specifically analyze the case of reflected-shock bifurcation in shock tubes, where the LOS non-uniformity is minor enough to cause minimal lineshape distortion. We first define variables describing the various gas properties. We then simulate and fit the spectrum generated in this type of non-uniform gas and assess the error between the fitted parameters and the path-averaged results. We lastly introduce a first-order model of this situation to illustrate the magnitude and contributing factors to the effect this has on the gas property measurements.

Shock bifurcation occurs when the reflected shock interacts with the cold, momentum-deficit boundary layer left behind the incident shock. This interaction is more pronounced for polyatomic driven gases, such as for the reactant mixtures used in the demonstrations of Section 7.4 of Chapter 7. The structure of the shock-boundary-layer interaction can be observed on the left side of Fig. E.14. After the normal reflected shock first passes the LAS measurement location, the majority of the LOS (the "core" flow) reaches the "region 5" condition predicted by ideal shock tube relations. Near the walls, the lack of gas momentum causes the shock wave to be replaced with a series of compression waves which gradually increase the flow pressure to P_5 [235]. There is also a region of the gas at intermediate momentum which is shock heated to an intermediate temperature and pressure behind a series of oblique shocks attached to the reflected shock (the "bifurcation" of the shock wave). Behind this series of oblique shocks, the boundary layer separates from the wall and eventually all of the flow reaches the same value as the core flow. If R is the radius of the shock tube, and b is the radial protrusion of the boundary layer from the wall, we can define f as the fraction of the path-length that is taken up by the boundary layer at the LOS during a given point in time.

$$f \equiv \frac{b}{R}. \tag{E.24}$$

It is assumed that gas properties are uniform within the boundary layer (subscript "b") and within the core region (subscript "c"). The contribution of the gas properties in the oblique shocked region is neglected due to its small radial extent [281] and for a conservative estimate of the biasing of the measured gas properties. The ratio of the boundary pressure P_b to the

core pressure P_C is labeled Π:

$$\Pi \equiv \frac{P_b}{P_c}. \tag{E.25}$$

Likewise, the ratio of the boundary temperature T_b to the core temperature T_C is labeled τ:

$$\tau \equiv \frac{T_b}{T_c}. \tag{E.26}$$

The following ratios are also defined for the linewidth and linestrength between the two regions:

$$\Omega \equiv \frac{\Delta\nu^b}{\Delta\nu^c} = \frac{\Pi}{\tau^N}, \tag{E.27}$$

$$\Sigma \equiv \frac{S(T_b)}{S(T_c)}. \tag{E.28}$$

It is assumed that the CO mole fraction is constant across the LOS. For the shock-tube experiments S1 and S2 from Section 7.4 of Chapter 7, the core pressure can be assumed to be the region 5 pressure measured via LAS once the bifurcation region has passed, where as the boundary properties can be assumed to be the values recorded by the Kistler pressure transducer which is constrained to the wall. For experiment S1, $P_c = 1.85$ atm and P_b varies, but has an inflection point at $P_b = 1.4$ atm ($\Pi \approx 0.76$). For experiment S2, $P_c = 3.9$ atm and $P_b = 2.4$ atm is an inflection point for the boundary pressure in the bifurcation region ($\Pi \approx 0.62$). For the temperature, the core value can be assumed to be the T_5 value measured after the bifurcation passes. Since a direct measurement of the boundary temperature is not possible with the current experimental setup, the isentropic assumption for temperature, assuming a diatomic gas ($\tau = \Pi^{2/7}$) will be used[4] For experiment S1, $T_c = 1200$ K ($\tau \approx 0.92$, $T_b \approx 1110$ K), and for experiment S2, $T_c = 1500$ K ($\tau \approx 0.87$, $T_b \approx 1310$ K).

To assess the error associated with making absorption measurements through shock boundary layers, the path-integrated absorbance is calculated for each transition with the following:

$$\begin{aligned} \alpha_{\text{int}}(\nu) &= 2\int_0^R P(r)X_{CO}S(T(r))\phi(\nu,r)dr \\ &= A_{\text{unif}}\left[(1-f)\phi^c(\nu) + \Pi\Sigma f\phi^b(\nu)\right], \end{aligned} \tag{E.29}$$

[4]This isentropic temperature ratio deviates from the temperature ratio for an ideal normal shock by less than 3% for pressure ratios up to 4.

$$A_{\text{unif}} \equiv 2P_{\text{c}}X_{\text{CO}}S(T_{\text{c}})R. \tag{E.30}$$

From Eqn. E.29, it can be seen that the lineshape function of the path-integrated transition is now a weighted sum of two Voigts with varying collision and Doppler width. This sum is generally not a Voigt. This non-Voigt spectrum was generated and summed for the three CO transitions used in this work and was fitted using the multi-line fitting routine described in Section 7.3.2 of Chapter 7. The middle of Fig. E.14 shows the contributions to the path-integrated spectrum from the core region (red) and boundary region (blue), as well as total spectrum (black) for $P_{\text{c}} = 1$ atm, $T_{\text{c}} = 1200$ K, $X_{\text{CO}} = 3\%$, $f = 10\%$, $\Pi = 0.5$, and $\tau = 0.827$ (CO-N_2 broadening is used). The fit of the spectrum is shown in green. The peak-normalized residual r between the path-integrated and fitted spectrum is shown below in green. The residual is very low, below 1%, reflecting the generally minimal distortion of the lineshape due to path integration. The difference between the path-integrated spectrum, and the spectrum evaluated at the path-averaged temperature and pressure is shown in gray. The higher residuals here explain why the fitted parameters deviate slightly from the path-average quantities. The fitted values for pressure, temperature, CO partial pressure / mole fraction are then compared to the path-averaged values. The path-averaged value of quantity x is notated as $\overline{x}$, and is calculated by:

$$\overline{x} \equiv \frac{1}{R}\int_0^R x(r)dr = x_{\text{c}}(1-f) + x_{\text{b}}f. \tag{E.31}$$

The bias error in parameter x due to path-integration error is denoted as $E(x, \text{bias})$ and is defined as:

$$E(x, \text{bias}) \equiv \frac{x_{\text{fit}}}{x(\overline{P}, \overline{T})} - 1. \tag{E.32}$$

$x(\overline{P}, \overline{T})$ is the quantity x evaluated at the path-averaged pressure and temperature. At the bottom right of Fig. E.14, the bias error in the fitted pressure, temperature, p_{CO}, and X_{CO} are plotted versus Π for $f = 0.10$, $P_{\text{c}} = 1$ atm, and $T_{\text{c}} = 1200$ K. In general, the bias error is sub-percent for values of Π greater than 0.5. The simulations were conducted at a variety of core pressures, temperatures, and values of f. The error generally increases at higher pressures and lower temperatures, due to line blending and the decreased linearity of

the linestrengths with temperature at lower temperatures. The error is typically maximized for values of f between 0.3 and 0.5 and is on the order of a few percent. The error is also approximately linear with f for values of f near 0 and with $1 - f$ for values of f near 1.

Based on the linearity of $E(x, \text{bias})$ with small values of f (most practical cases), a first-order model of the distortion of two isolated transitions is developed to predict the bias error at various bifurcation conditions. Here, i is used as an index to refer to the particular transition of interest, with $i = 1$ and $i = 2$ referring to the P(2,20) and P(0,31) lines respectively, as in Chapter 7. For the model, the following assumptions are made. (1) f and $E(x, \text{bias})$ are assumed to be small, so all functions of these variables are approximated by their first-order Taylor expansion. (2) A pure Lorenztian lineshape is assumed for each region, which highlights the distortion of the collision-width. (3) Only the P(0,31) and P(2,20) transitions are considered, and they are assumed to have the same collisional-broadneing parameters (same linewidth). The transitions are considered perfectly isolated from each other during fitting. (4) In finding the "fitted" transition, the sum of squared residuals (SSE) between the "measurement" and fit is found by assuming infinite scan depth and spectral resolution:

$$\text{SSE} = \int_{-\infty}^{+\infty} \left[\alpha_{\text{fit}}(\nu) - \alpha_{\text{int}}(\nu)\right]^2 d\nu. \tag{E.33}$$

The best fit of the absorbance areas $A_{\text{fit},i}$ and linewidth $\Delta\nu_{\text{fit}}$ is found by setting the partial derivatives $\partial\text{SSE}/\partial A_{\text{fit},i}$ and $\partial\text{SSE}/\partial\Delta\nu_{\text{fit}}$ equal to 0. By combining Eqns. E.33 and E.29 with the above simplifications, the following linear relationship between $E(\Delta\nu, \text{bias})$ and $E(A_i, \text{bias})$ and f can be obtained:

$$E(\Delta\nu, \text{bias}) \approx Wf, \tag{E.34}$$

$$E(A_i, \text{bias}) \approx \beta_i f, \tag{E.35}$$

where β_i and W are defined by

$$W = 1 - \Pi - N(1 - \tau) - \frac{4\Pi\Sigma_2(1 - \Omega)}{(1 + \Omega)^2}, \tag{E.36}$$

$$\beta_i = \Pi\left(\frac{4\Sigma_i\Omega}{(1 + \Omega)^2} - 1\right) + (1 - \tau)\sigma_i. \tag{E.37}$$

Here, N is the temperature exponent of the collisional-broadening coefficient of the P(0,31) transition used for the pressure measurement. σ_i is the sensitivity of linestrength i to temperature, evaluated at T_c, using Eqn. E.16:

$$\sigma_i = s(S_i, T)|_{T=T_c}. \tag{E.38}$$

The bias in the absorbance areas lead to a bias in the temperature measurement of the form:

$$E(T, \text{bias}) = \Theta f, \tag{E.39}$$

$$\Theta = \frac{k_B T_c}{hc\Delta E''_{12}}(\beta_1 - \beta_2). \tag{E.40}$$

Based on Eqn. E.34, the error in the pressure measurement obtained using the fitted collision width and $\gamma(T_{fit})$ is approximately:

$$E(P, \text{bias}) \approx \rho f, \tag{E.41}$$

$$\rho = W + N\Theta. \tag{E.42}$$

These expressions can also be used to approximate the bias-error for p_{CO} and X_{CO}:

$$E(p_{CO}, \text{bias}) \approx \Psi f, \tag{E.43}$$

$$E(X_{CO}, \text{bias}) \approx \Xi f, \tag{E.44}$$

where:

$$\Psi = \beta_2 - \Theta\sigma_2, \tag{E.45}$$

$$\Xi = \Psi - \rho \tag{E.46}$$

These relations are useful in estimating, to a first-order, the effect that step changes in the path-integrated gas properties have on the fitted parameters. As an example, if $\Pi = 0.5$, $\tau = 0.82$, $T_C = 1200$ K, $N = 0.45$, and $f = 0.10$, then $\Omega = 0.55$, $\Sigma_1 = 0.43$, $\Sigma_2 = 0.97$, $\sigma_1 = 3.7$ and $\sigma_2 = -0.086$. Compared to the spectral parameters evaluated at $\overline{P}$ and $\overline{T}$, the measured FWHM will be approximately 0.4% high and the measured absorbance areas will about 3.6% high (P(2,20)) and 0.71% low (P(0,31)). The resulting fitted temperature and pressure are predicted to be 1.1% and 1.0% high respectively. The results of this first-order

model are plotted as dashed lines against Π on the right of Fig. E.14 for $f = 0.1$. The top portion of the plot compares the error prediction for collision-width and absorbance area to values obtained from direct simulation and fitting of a single transition, whereas the lower portion of the figure compares the model prediction of pressure/temperature bias error to the multi-line fitting results. Excellent agreement is noted between the fitting results and the model. It can be seen that of the three considered spectral parameters, A_2 has the lowest bias, due to lack of sensitivity of the linestrength to temperature at this low temperatures. A_1 is the most biased (in the positive direction), due to the high sensitivity of linestrength to temperatures ($\sigma_1 \sim 4$) at these temperatures. The linewidth is biased by an intermediate amount, also in the upward direction. Of the gas parameters, the CO partial pressure is the least biased, due to the near linear relationship with the bias on A_2, which is quite low. This bias is also related to the temperature bias, which is higher, but the low sensitivity of this line with temperature reduces this effect. Temperature is biased upwards due to the relatively large upward bias of A_1 relative to A_2. The high $\Delta E''_{12}$ mitigates the biasing effect here. Pressure (and as a result, X_{CO}) are the most biased of the parameters, as they are affected most by the non-linear lineshape distortion. Pressure is biased more upward than linewidth alone, due to the additional bias from the $\gamma(T)$ calculation. The upward bias on temperature leads to a downward bias on γ, which in turn leads to an additional upward bias on pressure. Mole fraction is biased downward due to the inverse relationship with the measured pressure. It should be noted that the aforementioned trends will change as temperature changes, and the relative sensitivities of the linestrengths vary.

Both the simulation and analysis results above indicate the measurement of path-averaged collision-width and pressure is very robust to changes in gas pressure and temperature due to boundary layers arising from shock bifurcation. Using the LAS path-averaged pressure along with the sidewall pressure measurement from the Kistler for shock tube experiments S1 and S2, the shape of the shock boundary layer can be ascertained. The boundary layer thickness b can found by inverting Eqn. E.31:

$$b \approx R \frac{P_{\mathrm{c}} - \overline{P}}{P_{\mathrm{c}} - P_{\mathrm{b}}}. \tag{E.47}$$

For both shock tube experiments, this equation predicts that the boundary layer thickness peaks at roughly 10–13% of the radius (5-7 mm) and gradually decreases in size. This highlights the ability of the combined LAS and electromechanical pressure sensors to make inferences about the pressure distribution and flow structure in a spatially non-uniform flow.

APPENDIX F

Uncertainty analysis for thermometry and CO sensing via multi-line Boltzmann regression

The contents of this chapter have been published in the journal ***Applied Physics B*** *[237] under the full title "Multi-line Boltzmann regression for near-electronvolt temperature and CO sensing via MHz-rate infrared laser absorption spectroscopy".*

In this Appendix, we derive and compare the uncertainty in the temperature and number density measurements for two-line thermometry and the multi-line Boltzmann-population fit strategy presented in Chapter 8. The uncertainty analysis follows and expands analysis presented in Appendix D. The uncertainty of f, function of x_i variables, can be calculated using a Taylor expansion:

$$df(x_1, x_2, \cdots) = \frac{\partial f}{\partial x_1} dx_1 + \frac{\partial f}{\partial x_2} dx_2 + \cdots . \tag{F.1}$$

Assuming the measured variables, x_i, are independent of one another, and that the errors in the measured variables, δx_i, are independent of one another [223], we get the uncertainty of f, δf, as a function of its partial derivatives:

$$(\delta f)^2 = \left(\frac{\partial f}{\partial x_1}\delta x_1\right)^2 + \left(\frac{\partial f}{\partial x_2}\delta x_2\right)^2 + \cdots . \tag{F.2}$$

In the following sections, the relations of temperature with the linestrengths and areas of a line pair are derived and Eqn. F.2 is applied.

F.0.1 Temperature uncertainty

The temperature uncertainty for a line pair is derived from Eqs. 8.7 and 8.8, which are repeated here for clarity. The linestrength of a single line i is a function of temperature, T,

the partition function $Q(T)$, the ground state energy of the transition E_i'', the wavenumber of the transition ν_i, the Boltzmann constant k_B, and $T_0 = 296$ K [166, 205].

$$S_i(T) = S_i(T_0) q(T, \nu_0) \exp\left[-\frac{hcE_i''}{k_\mathrm{B}}\left(\frac{1}{T} - \frac{1}{T_0}\right)\right]. \tag{8.7}$$

The term $q(T, \nu_0)$ accounts for partition function variation multiplied by a stimulated emission factor:

$$q(T, \nu_0) \approx q(T) = \frac{Q(T_0)}{Q(T)} \frac{1 - \exp\left(-\frac{hc}{k_\mathrm{B}T}\nu_0\right)}{1 - \exp\left(-\frac{hc}{k_\mathrm{B}T_0}\nu_0\right)}. \tag{8.8}$$

The ratio of two linestrengths, R, is equal to the ratio of the integrated absorbance of two lines A and B, A_A and A_B:

$$R(T) = \frac{S_\mathrm{A}(T)}{S_\mathrm{B}(T)} = \frac{A_\mathrm{A}}{A_\mathrm{B}}. \tag{8.3}$$

The $q(T)$ terms cancel out in Eqn. 8.3 because ν_0 variation has a weak impact on $q(T)$ for two neighboring lines and the function $R(T)$ can be expressed as:

$$R(T) = \frac{S_\mathrm{A}^0}{S_\mathrm{B}^0} \exp\left[-\frac{hc}{k_\mathrm{B}}(E_\mathrm{A}'' - E_\mathrm{B}'')\left(\frac{1}{T} - \frac{1}{T_0}\right)\right]. \tag{F.3}$$

Differentiating Eqn. 8.3, using Eqn. F.3, and setting $\Delta E = E_A'' - E_B''$, we get:

$$\frac{dR}{R} = \frac{dS_A^0}{S_A^0} - \frac{dS_B^0}{S_B^0} + \frac{hc}{k_\mathrm{B}}\frac{\Delta E}{T^2}dT = \frac{dA_A}{A_A} - \frac{dA_B}{A_B}, \tag{F.4}$$

which can be written:

$$\frac{dT}{T} = \frac{k_\mathrm{B}}{hc}\frac{T}{\Delta E}\left(-\frac{dA_A}{A_A} + \frac{dA_B}{A_B} + \frac{dS_A^0}{S_A^0} - \frac{dS_B^0}{S_B^0}\right). \tag{F.5}$$

From here, the terms $\partial A_i/\partial T$, $\partial S_i^0/\partial T$ can be identified and, substituting Eqn. F.4 into Eqn. F.2 with T as f, the temperature uncertainty is obtained in Eqn. F.6:

$$\frac{\delta T}{T} = \frac{k_\mathrm{B}}{hc}\frac{T}{\Delta E}\sqrt{\sum_{i=1}^{2}\left[\left(\frac{\delta S_i^0}{S_i^0}\right)^2 + \left(\frac{\delta A_i}{A_i}\right)^2\right]}. \tag{F.6}$$

In this derivation, we neglected the contribution of the energy level uncertainty, $\delta E''$, which is close to the line position uncertainty and found to be $\delta E''/E'' \leq 10^{-6}$.

The area uncertainty, δA_i, is now related to the peak absorbance, α^pk. The area of the line can be approximated by the peak absorbance multiplied by the FWHM, i.e. $A_i \approx \alpha_i^\mathrm{pk}\Delta\nu$.

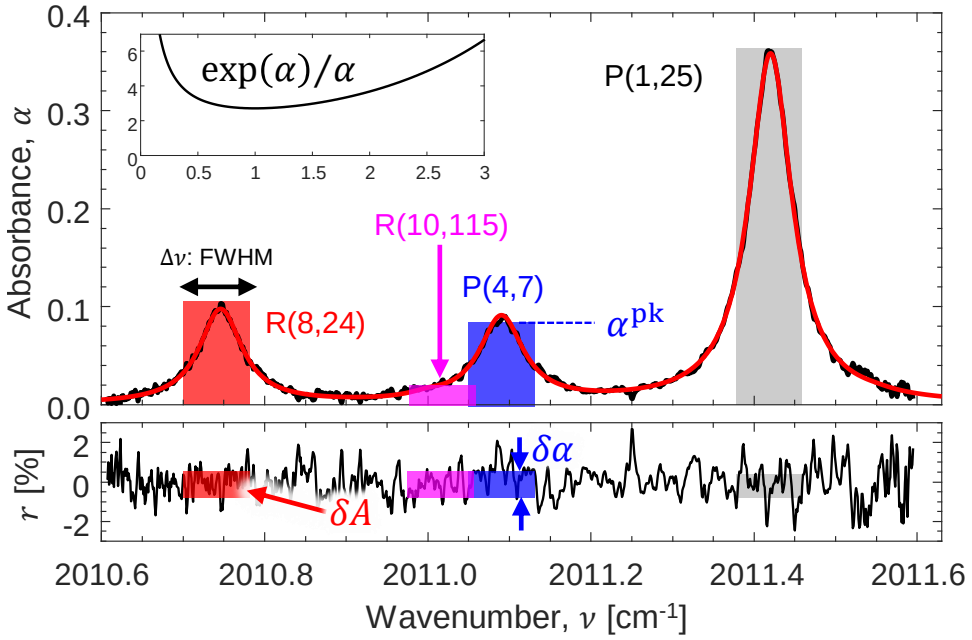

Figure F.1: Illustration of the uncertainty analysis performed assuming simplified areas, $A = \alpha^{\mathrm{pk}}\Delta\nu$, and area uncertainties $\delta A = \delta\alpha\Delta\nu$. The inset shows the uncertainty optimum reached for $\alpha = 1$, the minimum of $\exp(\alpha)/\alpha$.

The line area uncertainty can be estimated by a rectangle of height $\delta\alpha$, the absorbance noise, and width $\Delta\nu$, the FWHM of the line, i.e., $\delta A \approx \delta\alpha\Delta\nu$. An illustration of the absorbance area and area uncertainty is provided in Fig. F.1.

$$\frac{\delta A_i}{A_i} \approx \frac{\delta\alpha\Delta\nu}{\alpha_i^{\mathrm{pk}}\Delta\nu} = \frac{\delta\alpha}{\alpha_i^{\mathrm{pk}}}. \tag{F.7}$$

The validity of this approximation is shown in Appendix E.0.2.2.

The absorbance is related to the measured amplitude of the non-absorbed laser intensity, I_0, and the transmitted intensity, I_{t}, see Eqn.8.1:

$$\alpha(\nu) = -\ln\left(\frac{I_{\mathrm{t}}}{I_0}\right)_{\nu}. \tag{8.1}$$

Differentiating Eqn.8.1 we obtain:

$$d\alpha = -\frac{dI_{\mathrm{t}}}{I_{\mathrm{t}}} + \frac{dI_0}{I_0}. \tag{F.8}$$

By using Eqn. , with α as f, the absorbance noise $\delta\alpha$ can be related to the noise in the transmitted intensity, dI_t, and the noise in the background intensity, dI_0:

$$(\delta\alpha)^2 = \left(\frac{\delta I_\mathrm{t}}{I_\mathrm{t}}\right)^2 + \left(\frac{\delta I_0}{I_0}\right)^2. \tag{F.9}$$

The transmitted intensity noise, δI_t, is the root mean square of the oscilloscope voltage and hence includes the effective sum of the laser fluctuations, the detector noise and the oscilloscope noise. Unlike the analysis of Ref. [282], in this work, the noise of the background intensity is greatly reduced via signal averaging, such that $\delta I_0 \ll \delta I_\mathrm{t}$, which means that Eqn. F.9 simplifies to:

$$\delta\alpha = \frac{\delta I_\mathrm{t}}{I_\mathrm{t}}. \tag{F.10}$$

This expression can be divided by α to find the relative noise in the absorbance measurement:

$$\frac{\delta\alpha}{\alpha} = \frac{1}{\alpha}\frac{\delta I_\mathrm{t}}{I_\mathrm{t}} = \frac{1}{\alpha}\frac{\delta I_\mathrm{t}}{I_0\exp(-\alpha)}. \tag{F.11}$$

The signal-to-noise ratio of the raw laser intensity is defined as $\mathrm{SNR_{opt}} = I_0/\delta I_t$ and hence:

$$\frac{\delta\alpha}{\alpha} = \frac{1}{\mathrm{SNR_{opt}}}\frac{\exp(\alpha)}{\alpha}. \tag{F.12}$$

Equation F.12 indicates the level of noise to be expected in an absorption measurement. When α^pk is substituted for α in the denominator of both sides of the equation, the expected normalized residual r can be predicted for a well-fitted absorbance measurement. This expression is approximately equal to the uncertainty in the area measurement, as indicated by Eqn. F.7. The ratio $\exp(\alpha)/\alpha$ indicates how much the relative noise in the raw intensity ($1/\mathrm{SNR_{opt}}$) is amplified to obtain the relative absorbance noise. As shown in the inset of Fig. F.1, this function is minimized at $\alpha = 1$ at a value of e, indicating that at best, the absorbance noise is approximately 2.72 times the noise in the raw signal. When α is low, representing the optically-thin limit, the numerator is approximately 1, and the absorbance noise is inversely proportional to the absorbance. When α is high, the numerator dominates and the absorbance noise grows non-linearly with α, representing the optically-thick limit where I_t is close to 0 and below the noise level.

As indicated above, to approximate the uncertainty in an area measurement, the α in the denominator of Eqn. F.11 should be replaced by α_i^{pk}. The numerator is still a function of α, which is maximized at the peak absorbance, where the transmitted laser intensity is the lowest. To provide a conservative estimate of the area uncertainty, this peak absorbance noise is also used for the numerator, such that:

$$\frac{\delta A_i}{A_i} \approx \frac{1}{\mathrm{SNR}_{\mathrm{opt}}} \frac{\exp\left(\alpha_i^{\mathrm{pk}}\right)}{\alpha_i^{\mathrm{pk}}}. \tag{F.13}$$

The substitution of Eqn. F.13 in Eqn. F.6 gives the relative uncertainty in T for a given line pair given in Eqn. 8.4.

$$\frac{\delta T}{T} = \frac{k_{\mathrm{B}}}{hc} \frac{T}{\Delta E} \sqrt{\sum_{i=1}^{2} \left[\left(\frac{\delta S_i^0}{S_i^0} \right)^2 + \left(\frac{1}{\mathrm{SNR}_{\mathrm{opt}}} \frac{\exp\left(\alpha_i^{\mathrm{pk}}\right)}{\alpha_i^{\mathrm{pk}}} \right)^2 \right]}. \tag{8.4}$$

F.0.2 Number density uncertainty

Substituting Eqn. 8.5 to Eqn. F.2, we get:

$$\frac{\delta n_{\mathrm{CO}}}{n_{\mathrm{CO}}} = \sqrt{\left(\frac{\delta A_i}{A_i} \right)^2 + \left(\frac{\delta L}{L} \right)^2 + \left(\frac{\delta S_i}{S_i} \right)^2}. \tag{F.14}$$

The uncertainty in the linestrength due to the temperature uncertainty must be separated from the reference linestrength uncertainty. The variation in the linestrength S is convoluted with the variation of the partition function, see Eqn. 8.7, and its derivation is not straightforward to generalize to any molecule. Here, we numerically evaluate the linestrength derivative with T and use it in the following expression:

$$\left(\frac{\delta S_i}{S_i} \right)^2 = \left(\frac{1}{S_i(T)} \frac{\partial S_i}{\partial T} \delta T \right)^2 + \left(\frac{\delta S_i^0}{S_i^0} \right)^2. \tag{F.15}$$

We obtain the number density uncertainty as:

$$\left(\frac{\delta n_{\mathrm{CO}}}{n_{\mathrm{CO}}} \right)^2 = \left(\frac{1}{\mathrm{SNR}_{\mathrm{opt}}} \frac{\exp\left(\alpha_i^{\mathrm{pk}}\right)}{\alpha_i^{\mathrm{pk}}} \right)^2 + \left(\frac{\delta L}{L} \right)^2 + \left(\frac{1}{S_i(T)} \frac{\partial S_i}{\partial T} \delta T \right)^2 + \left(\frac{\delta S_i^0}{S_i^0} \right)^2. \tag{8.6}$$

In this work, the pathlength is known within $\delta L/L = 1\%$. The uncertainty $\delta n/n$ is calculated in Fig. 8.3 using three line pairs available in the 2010.6 - 2011.6 cm^{-1} region. To

minimize the overall uncertainty, the area from P(1,25) transition is taken because its peak absorbance is typically the closest to 1. This line also offers the lowest uncertainty in the reference linestrength, $\delta S^0_{P(1,25)} = 1$–2 %. Note that in the experimental results presented in this work, the uncertainty of the Boltzmann-population fit are employed. The line pair uncertainties presented in Fig. 8.3 are only used to illustrate relative measurement accuracy of the different line pair combinations leveraged by the Boltzmann-population fit method across the temperature range.

F.0.3 Non-isolated lines: perturbations due to neighboring features

The line selection used in this work presents large ΔE which improves the temperature uncertainty but also offers four spectrally separated lines. This is not the case for the line selection at 2008 cm^{-1} used in previous work, where the P(3,14) line overlaps with the P(0,31) line. This effect is evident above 3500 K, see Fig. F.3, when the P(3,14) line

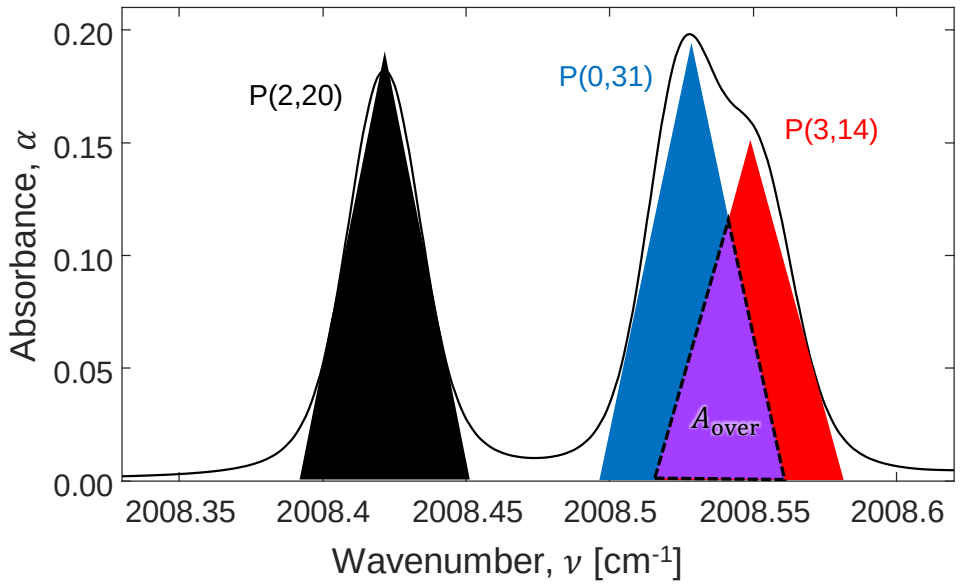

Figure F.2: Full CO spectrum calculated at $T = 8000$ K, $p = 1$ atm, and $X_{CO} = 10\%$ based on HITEMP database. The lineshapes are assumed to be triangles to calculate A_{over}, the overlap area of the P(3,14) and P(0,31) and ultimately estimate the error in fitting these lines.

has a peak absorbance similar to P(0,31). The contribution of the P(3,14) line can be subtracted using iterative Voigt fitting but it is difficult to estimate how the uncertainty of this correction propagates to the temperature and number density measurements [148, 157]. In this subsection, we numerically calculate the impact of the uncertainty generated by the subtraction of a neighboring line, taking as an example the line selection at 2008 cm^{-1}. The lineshape is assumed to be triangular to simplify the calculations, with the FWHM of the triangle set equal to that of the actual Voigt lineshape. A representation of this approximation is shown in Fig. F.2. The overlapping area of the two lines, A_{over} in Fig. F.2, can be calculated mathematically given the line peak absorbance, FWHM, and positions. When accounting for the P(3,14) line, the main source of uncertainty is estimated to arise from an erroneous allocation of the overlapping area to either P(0,31) and P(3,14). Assuming that 10% of A_{over} is wrongly attributed to P(0,31), another contribution to $\delta A_i/A_i$ in Eqn. F.6 and Eqn. F.14 leads to an increase of δT and δn. For a 2-% CO mole fraction adequate for

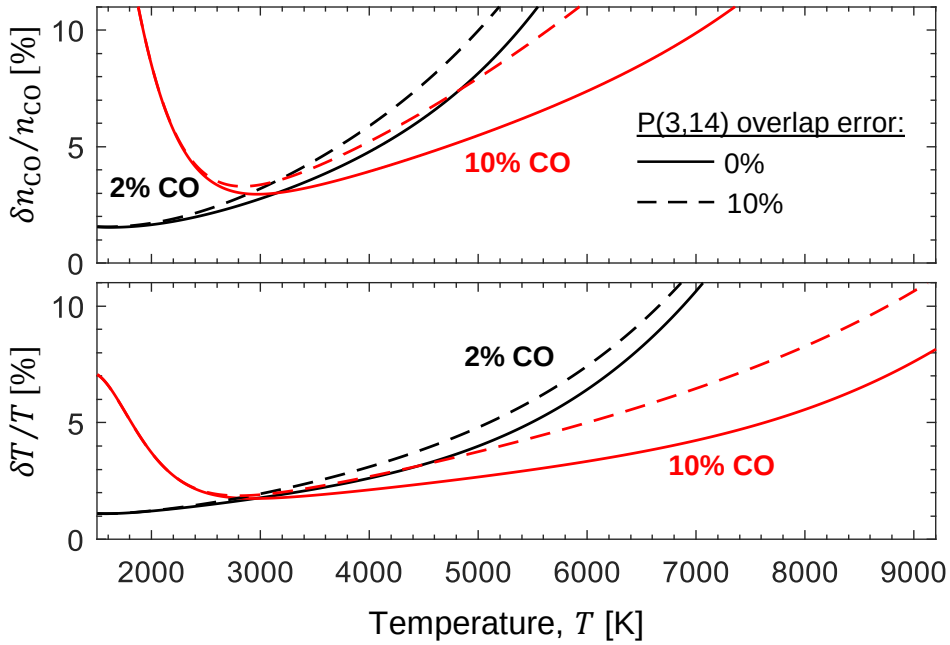

Figure F.3: δT and δn_{CO} calculated assuming the P(3,14) line area overlap, A_{over}, is perfectly taken into account, full line, and if 10% of A_{over} is erroneously attributed to the P(0,31) line, dashed line. The effect is calculated for 2% and 10% CO mixtures at 1 atm and $L = 10$ cm.

measurements in combustion environments, Fig. F.3 shows that, at 2000 K, a 10% error in the allocation of A_{over} leads to a negligible increase in temperature and number density uncertainty, 0.01% and 0.05%, respectively. This confirms that the uncertainty arising due to the P(3,14) line was negligible in previous work [148, 157]. However, at temperatures higher than 3500 K and 10% CO mole fraction, the temperature and number density uncertainty increase by several percent, which further motivates the use of the new line selection at those temperatures. The uncertainty associated with line blending is also analyzed numerically in Appendix E.0.2.5.

F.1 Non-uniform path-integrated measurements

In this section, the robustness of this line selection to non-uniform temperature distribution is assessed. This analysis follows that of Appendix D.0.3, but considers a larger temperature range and the lines near 2011 cm^{-1}. We define $\overline{S(T)}$ and $\overline{T}$ as the path-averaged linestrength and temperature weighted by the number density of the absorbing species, $n_{\text{CO}}(l)$, that varies with the position along the beampath l [148, 167]:

$$\overline{S(T)} = \frac{\int_0^L n_{\text{CO}}(l) S(T(l)) dl}{\int_0^L n_{\text{CO}}(l) dl}. \tag{F.16}$$

$$\overline{T} = \frac{\int_0^L n(l) T(l) dl}{\int_0^L n(l) dl}. \tag{F.17}$$

Assuming a linear gradient of 1000 K across a constant-pressure slab in Fig. F.4, the linestrength deviation $\delta S = \overline{S(T)} - S(\overline{T})$ is below 2% of $\overline{S(T)}$ for the three primary lines in the spectrum. This result indicates that the linestrength variation in temperature is close to linear using these lines. Hence, the temperature measurements should be close to the CO number density-weighted path-averaged temperature. This is verified by calculating δT defined in Eqs. F.18, where R^{-1} is the inverse function of R defined in Eqn. 8.3 and relating the ratio of linestrengths to temperature:

$$\delta T = R^{-1}(\overline{S(T)}) - R^{-1}(S(\overline{T})). \tag{F.18}$$

The results, shown in Fig. F.4, indicate that $\delta T/\overline{T}$ is within 1% using the ratio of R(10,115), R(8,24), and P(4,7) with P(1,25) and assuming a uniform 1000-K gradient. Performing this calculation with a Boltzmann-population fit, (in green in Fig. F.4), the difference drops below 0.2%. An extreme-case estimate with a 3000-K gradient is calculated using a Boltzmann-population fit and shows a maximum error of 4% compared to the average temperature. In conclusions, the Boltzmann fit of the four lines in the present wavenumber range is more robust to the bias induced by temperature gradients than the individual pair of lines taken separately. This robustness is essentially due to the R(10,115) transition, which positively bias non-uniform temperature measurements and compensates for the negatively bias temperature measurements induced by the other transitions. Therefore, the values reported in Fig. 8.12 during the 4-µs window displaying the propagation of the oblique shock are representative of the path-average temperature and CO number density and can be used for future studies of the oblique-shock layer.

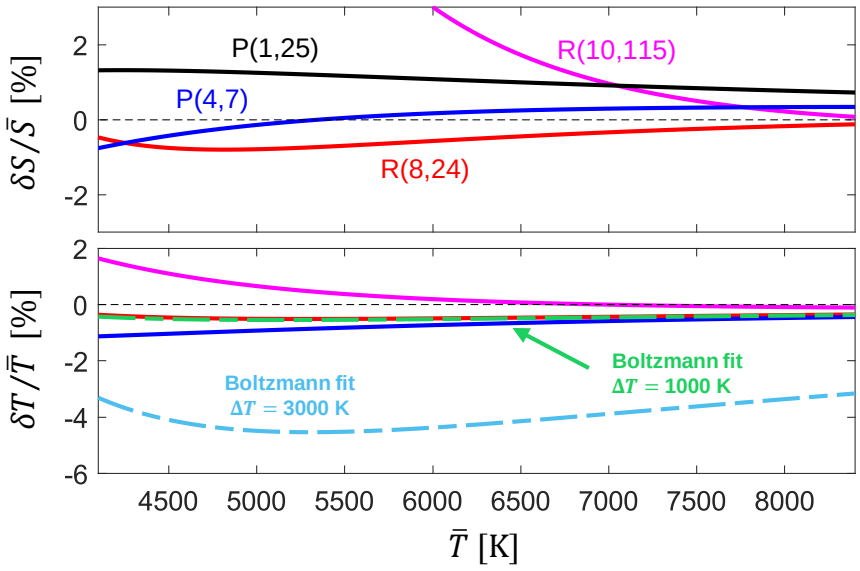

Figure F.4: *(Top)* Relative difference between $\overline{S(T)}$ and $S(\overline{T})$ assuming a linear gradient of 1000 K across an absorption slab. *(Bottom)* Relative error in temperature determination after fitting the integrated linestrength using the ratio of R(10,115), R(8,24), and P(4,7) with P(1,25), colored full lines. Two Boltzmann-distribution fits have been performed at 1000 K (green dashed) and 3000 K (grey dashed).

APPENDIX G

Combustion-kinetics analysis details

The contents of this chapter have been submitted to the journal ***Applied Physics B*** *[212] under the full title "Optical pressure sensing at MHz rates via collisional line broadening of carbon monoxide: uncertainty quantification in reacting flows".*

G.0.1 Reaction progress variable definition

In Section 7.3.3.2 of Chapter 7, a normalized reaction progress variable Z was introduce to normalize the disparate reaction time scales for various reactant combinations. Z was defined such that such that $Z = 0$ at the beginning of the reaction and $Z = 1$ at the end of the reaction. Two definitions for Z were developed, with the latter representing a more generalized definition. The initial definition of Z was as follows:

$$Z = \frac{\Delta(w_{\text{prod}} - w_{\text{react}})}{\Delta(w_{\text{prod}} - w_{\text{react}})^{\text{eq}}} = \frac{(w_{\text{prod}} - w_{\text{react}}) \quad - (w_{\text{prod}} - w_{\text{react}})^{\text{init}}}{(w_{\text{prod}} - w_{\text{react}})^{\text{eq}} - (w_{\text{prod}} - w_{\text{react}})^{\text{init}}}, \tag{G.1}$$

$$w_{\text{react}} = w_{\text{fuel}} + w_{\text{O}_2}, \tag{G.2}$$

$$w_{\text{prod}} = w_{\text{H}_2\text{O}} + w_{\text{CO}_2}. \tag{G.3}$$

w_Y refers to the mass fraction of species Y. This definition of the reaction progress was chosen to provide sufficient resolution of the initial decomposition and final oxidation phases of the reaction along the reaction coordinate.

In some of the O_2-combustion cases, the mixture would "over-react", with more H_2O and/or CO_2 temporarily being produced than the equilibrium value, with subsequent endothermic dissociation. This would lead to Z values greater than 1. This phenomenon can be observed in the top right pane of Fig. 7.6, where the overproduction of H_2O above the

equilibrium value at a value of $Z = 0.8$ can be observed for C_2H_4–O_2 ignition. To account for these cases, the reaction progress was re-defined in a piecewise fashion, with the values at the point of maximum overshoot denoted with the superscript 'os':

$$Z = \begin{cases} \dfrac{w_{\mathrm{P/R}} - w_{\mathrm{P/R}}^{\mathrm{init}}}{2w_{\mathrm{P/R}}^{\mathrm{os}} - w_{\mathrm{P/R}}^{\mathrm{init}} - w_{\mathrm{P/R}}^{\mathrm{eq}}}, & \text{if } t \leq t^{\mathrm{os}} \\ \dfrac{2w_{\mathrm{P/R}}^{\mathrm{os}} - w_{\mathrm{P/R}}^{\mathrm{init}} - w_{\mathrm{P/R}}}{2w_{\mathrm{P/R}}^{\mathrm{os}} - w_{\mathrm{P/R}}^{\mathrm{init}} - w_{\mathrm{P/R}}^{\mathrm{eq}}}, & \text{if } t > t^{\mathrm{os}} \end{cases}, \tag{G.4}$$

$$w_{\mathrm{P/R}} = w_{\mathrm{prod}} - w_{\mathrm{react}}. \tag{G.5}$$

This piecewise expression simplifies to the earlier definition of Z from Eqn. G.1 when $w_{\mathrm{P/R}}^{\mathrm{os}} = w_{\mathrm{P/R}}^{\mathrm{eq}}$.

G.0.2 Effect of CO seeding on combustion kinetics

As noted in Section 7.4.1 of Chapter 7, 2% CO was seeded into the pre-shock mixture to enable gas property sensing prior to ignition. Due to its high thermodynamic and kinetic stability, this small addition of CO has a minimal impact on the combustion chemistry. This was investigated using the chemical kinetic model in CANTERA detailed in Section 7.3.3.2 of Chapter 7. For each studied fuel-oxygen mixture, 2% CO was added to the reactant mixture. For the air-combustion cases, CO acted to replace N_2 in the reactant mixture because N_2 is already an inert component of the reactant mixture. As such, the changes to combustion chemistry from this change are reflective of the relative inertness of CO. For the oxygen-enriched mixtures, the proportion of O_2 to fuel was kept the same, with both concentrations decreasing proportionally to accommodate the addition of CO.

For each mixture, a kinetic simulation was conducted at constant pressure (1 atm) and enthalpy (HP), with an initial temperature of 1500 K. The ignition delay time was assessed by finding when the greatest rate of temperature change, dT/dt, occurred. Figure G.1 shows the simulated time-resolved temperature profile for C_2H_4-air with and without CO seeding. The changes in ignition delay time for all of the studied fuels are indicated in Table G.1. For the air-combustion cases, most of the ignition delay times were reduced by the addition

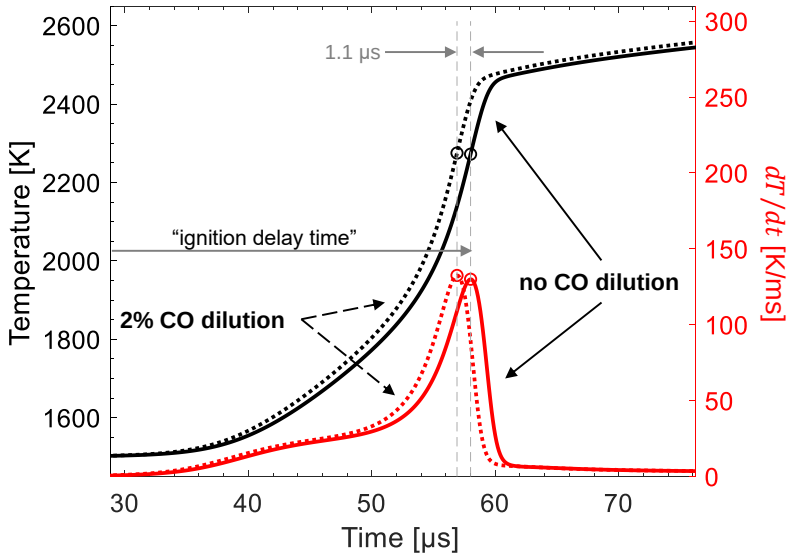

Figure G.1: Plot of temperature (black) and dT/dt (red) versus time after simulation start for stoichiometric C_2H_4-air initially at 1 atm, 1500 K. Solid lines indicate pure fuel and oxidizer, whereas the dashed lines indicate that 2% CO has been added to the mixture. The ignition delay times, corresponding to peak dT/dt are indicated with the circular markers and dashed vertical lines.

of CO, with the exception of CH_4-air combustion. The magnitude of the change in ignition delay was generally less than 3%. An outlier to these trends was NH_3, which saw a reduction in ignition delay time of 8.7%, likely due to the relatively slow ignition characteristics of NH_3 compared to the other studied fuels. Some fuels were extremely insensitive to the presence of CO, such as C_3H_8 and H_2, which saw less than 0.1% change in ignition delay. For C_2H_6 and Jet-A, the ignition delay was reduced by less than 1%. For the fuels used in the shock tube demonstrations above, there is a 2.4% ignition delay increase for CH_4 and a 1.9% ignition delay decrease for C_2H_4.

For the oxygen-enriched combustion cases, adding CO generally increased the ignition delay, as CO is generally less reactive than the pure fuel/oxidizer of the undiluted mixture. The exceptions to this trend are C_2H_4 and NH_3, which see a reduction in ignition delay from the addition of CO. The magnitude of the change in ignition delay was below 3% for most

fuels, except for CH_4, which sees a 3.8% ignition delay increase and for NH_3 which sees a 4.6% ignition delay reduction.

Table G.1: Effect of 2%-CO seeding on ignition delay time.

	Change in ignition delay time from CO dilution [%]	
Fuel	Air comb.	O_2 comb.
CH_4	+2.4	+3.8
C_2H_4	−1.9	−0.6
C_2H_2	−2.9	+0.5
C_2H_6	−0.8	+0.7
C_3H_8	+0.0	+1.3
$nC_{10}H_{22}$	−0.4	+1.1
H_2	+0.0	+2.2
NH_3	−8.7	−4.6

APPENDIX H

Uncertainties in reflected-shock conditions

The contents of this chapter have been published in the journal ***Applied Physics B*** *[237] under the full title "Multi-line Boltzmann regression for near-electronvolt temperature and CO sensing via MHz-rate infrared laser absorption spectroscopy".*

The method to calculate the uncertainty on p_5 and T_5 in the shock tube is given in this appendix. This is directly applied to the shock-tube measurements in Chapter 8, but the methodology can be applied to the shock-tube demonstrations of Chapter 7. As described in previous chapters, the reflected shock conditions are calculated using normal-shock relations processed through a MATLAB code [211]. The normal-shock relations require the knowledge of (1) p_1, the fill pressure, (2) T_1, the initial temperature, (3) x_i, the composition of the shock-heated gas, and (4) v_{end}, the speed of the shock on the endwall. The uncertainty of these parameters is propagated to the calculated T_5 and p_5 through a Taylor expansion method, see Eqn. F.2. The fill pressure uncertainty is assumed to be equal to the last digit of the most precise manometer that can be employed during the fill procedure, i.e. $\delta p_1 = 0.1$, 0.01 or 0.001 Torr. The temperature uncertainty is assumed to be $\delta T_1 = 1$ K. The mixture is prepared by subsequent filling of CO and Ar at increasing pressure. The species mole fraction uncertainty is calculated by accounting for the manometer precision in this step-by-step procedure and is negligible in this work, i.e. $\delta x_i/x_i \leq 0.05\%$. The shock position is determined through the reading of pressure transducers along the shock tube. The shock-speed uncertainty is calculated by propagating the uncertainty in the shock position versus time through a York linear fit [263] accounting for the uncertainty in the pressure sensing positions ($\delta x = 1/16$ in.) and the time-of-arrival at each sensor (near 1 µs). In the speed range of this work, these two parameters contribute within the same order of magnitude to

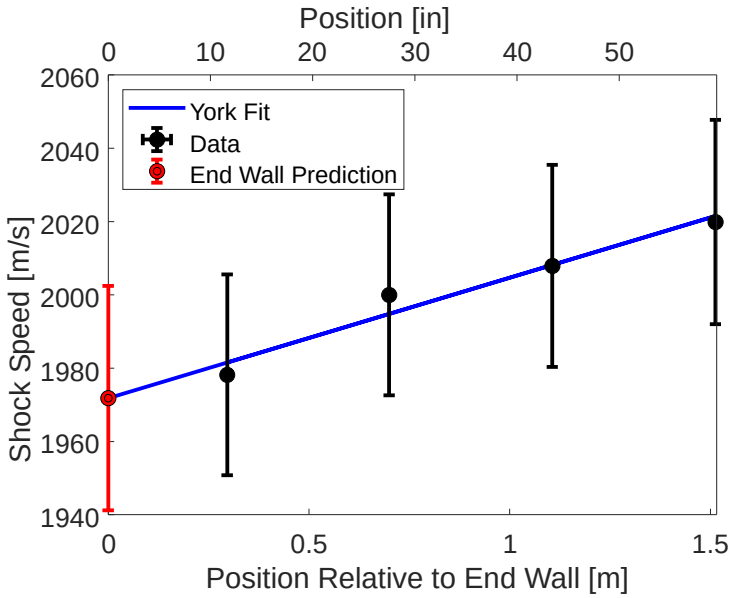

Figure H.1: Shock speed measured using five piezoelectric transducers. The end-wall speed is calculated using the linear York fit of the data [263].

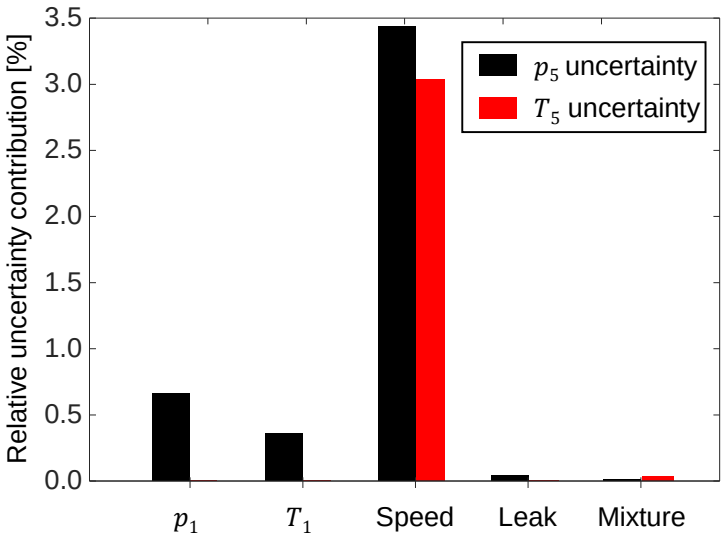

Figure H.2: Contributions to the p_5 and T_5 uncertainties.

the speed uncertainty. As illustrated in Fig. H.1, the resulting uncertainty on the speed is typically 10-30 m/s for shock speeds of 2000 m/s ($\leq 1.5\%$). We also included the uncertainty due to the shock-tube leak rate in the calculation, by adding air to the mixture. The air leaked in the shock tube represents less than 0.5% of the mixture for the lowest p_1 of this study.

For the shock used as illustration in Fig. H.1, the reflected shock heated conditions are $T_5 = 8013$ K ($\pm$ 3.1%) and $p_5 = 0.53$ atm ($\pm$ 4.5%). The contribution from each of the aforementioned sources to the total uncertainty in pressure and temperature is illustrated in Fig. H.2. The uncertainties on p_1 and T_1 have a minor contribution to the total uncertainty and would be challenging to improve further. The shock speed measurement dominates the overall uncertainty. It can also be noted that the mixture uncertainty and the leak rate have negligible impact on p_5 and T_5, which indicates that our experimental procedure is adequate.

APPENDIX I

MMH-NTO RDRE drawing package

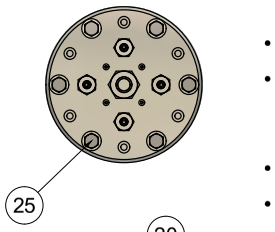

NOTE:

- ALL SURFACE FINISHES ARE MACHINE FINISH UNLESS SPECIFIED OTHERWISE
- ALL CORNER RADII ARE .031 UNLESS SPECIFIED OTHERWISE
- SCREWS, WASHERS, THREAD INSERTS, O-RINGS AND FITTINGS DO NOT NEED TO BE PROCURED. THEY WILL BE SENT TO MANUFACTURER FOR FIT CHECK.
- LUBRICANT ALL THREADS WITH KRYTOX PRIOR TO ASSEMBLY
- ALL DRILL PT. ANGLES ARE 118° UNLESS OTHERWISE SPECIFIED.

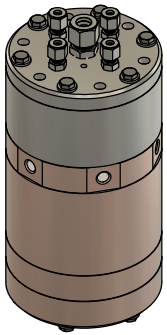

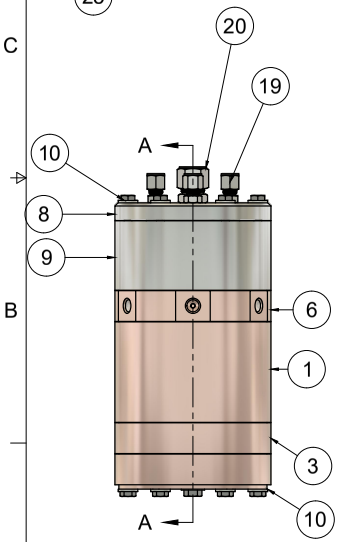

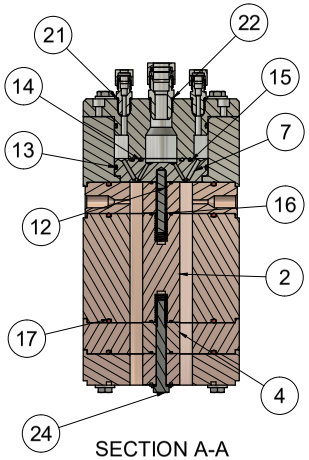

SECTION A-A
SCALE 1:2

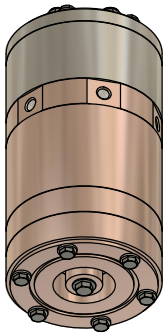

ITEM	QTY	PART NAME
24	AR	Misc. Washers for Bolts
23	AR (>0)	-908 High-Temperature Silicone O-Ring (not pict., for sealing inst. ports)
22	1	-908 PTFE O-Ring
21	4	-904 EPDM O-Ring
20	1	$\frac{1}{2}$" AN to Swage Adapter
19	4	$\frac{3}{4}$" AN to Swage Adapter
18	AR	$\frac{1}{4}$" AN Cap (not pict., for plugging inst. ports)
17	AR (>0)	-236 High-Temperature Silicone O-Ring
16	AR (>0)	-015 High-Temperature Silicone O-Ring
15	1	-132 EPDM O-Ring
14	1	-124 PTFE O-Ring
13	2	-149 EPDM O-Ring
12	AR	$\frac{5}{16}$"-24 Threaded Rod (length determined by config.)
11	1	$\frac{5}{16}$"-24 Bolt (length determined by config)
10	6 or 12	$\frac{1}{2}$"-20 Bolt (length determined by config).
9	1	Manifold Wall
8	1	Manifold Cap
7	1	Injector Plate
6	1 or 2	Instrumentation Spool
5	1 at most	Nozzle spool (not pict.)
4	AR (>0)	Inner Annulus Generic Spool
3	AR	Outer Annulus Generic Spool
2	1 at most	Main Inner Annulus
1	1 at most	Main Outer Annulus

PROJECT
HYPERGOL RDRE

TITLE
COMBUSTOR ASSEMBLY
HYPERGOL RDC

APPROVED	SIZE	CODE	DWG NO	REV
CHECKED	C		NSC000	004
DRAWN ANIL NAIR 7/5/19	SCALE 1:2	WEIGHT > 48 LBS	SHEET 1/1	

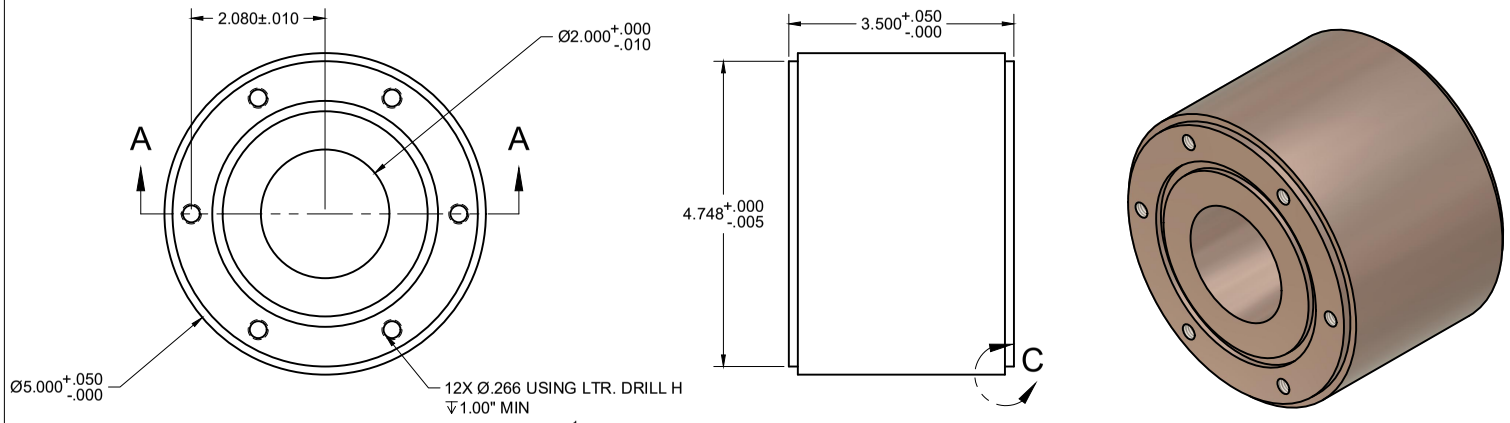

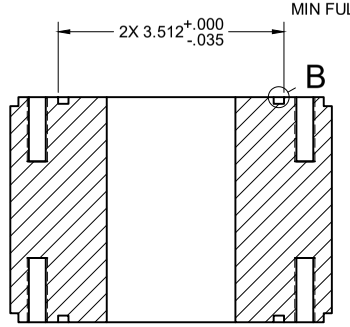

SECTION A-A
SCALE 1:1.5

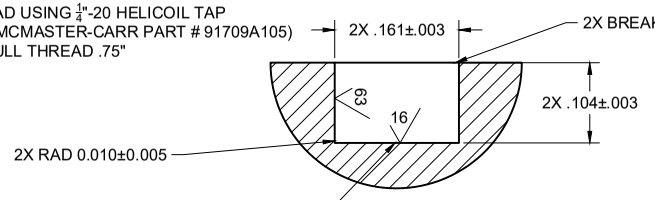

DETAIL B
SCALE 8:1

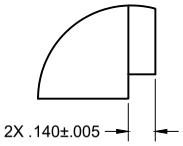

DETAIL C
SCALE 2:1

	PROJECT: HYPERGOL RDRE			
	TITLE: MAIN OUTER ANNULUS HYPERGOL RDC BERYLLIUM COPPER 172			
APPROVED	SIZE: B	CODE	DWG NO: NSC003	REV: 004
CHECKED				
DRAWN ANIL NAIR 7/5/19	SCALE 1:1.5	WEIGHT 288 OZ / 18 LBS	SHEET 1/1	

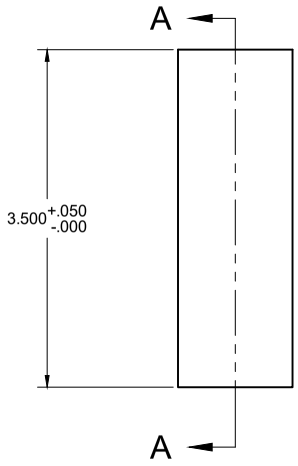

SECTION A-A
SCALE 1:1

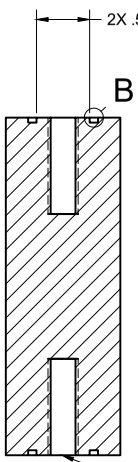

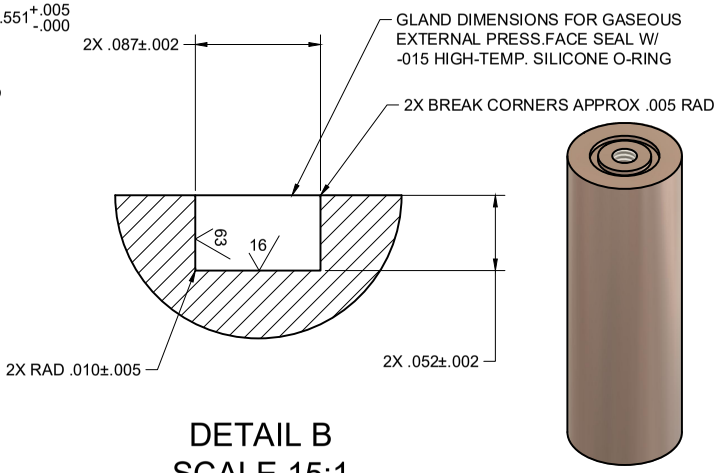

DETAIL B
SCALE 15:1

2X Ø.3281 USING $\frac{21}{64}$ DRILL BIT
↧ 1.1" MIN
THREAD USING $\frac{5}{16}$"-18 HELICOIL TAP
(REF. MCMASTER-CARR PART # 91709A153)
MIN FULL THREAD 1"

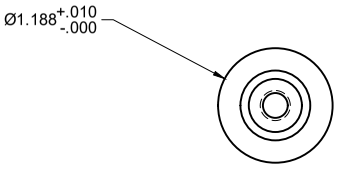

	PROJECT: HYPERGOL RDRE			
	TITLE: MAIN INNER ANNULUS HYPERGOL RDC BERYLLIUM COPPER 172			
APPROVED	SIZE: B	CODE:	DWG NO: NSC001	REV: 004
CHECKED				
DRAWN Anil Nair 7/5/19	SCALE 1:1	WEIGHT 19 OZ / 1.2 LBS	SHEET 1/1	

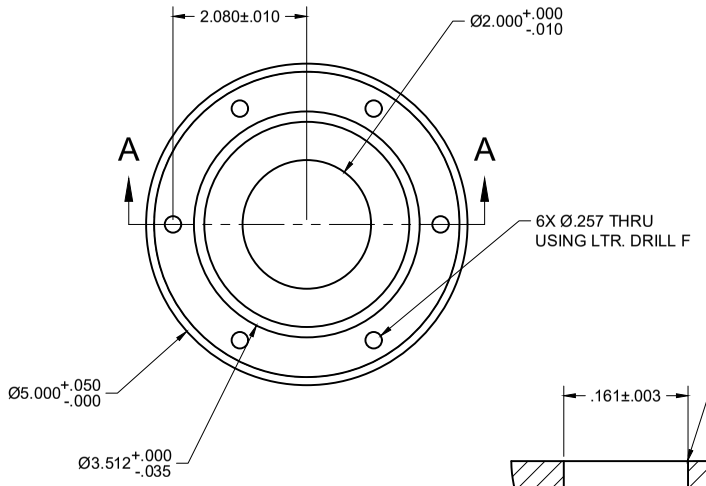

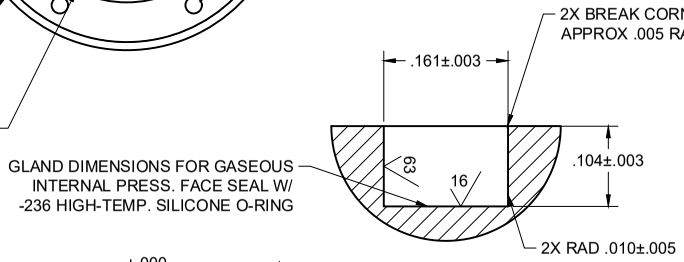

DETAIL B
SCALE 8:1

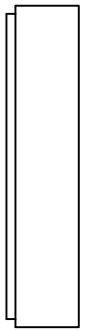

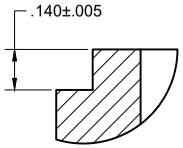

DETAIL C
SCALE 3:1

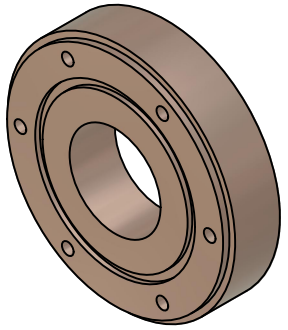

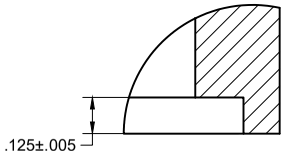

DETAIL D
SCALE 3:1

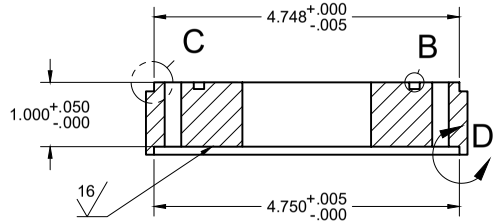

SECTION A-A
SCALE 1:1.5

	PROJECT: UCLA/POLARIS SBIR			
	TITLE: OUTER ANNULUS GENERIC SPOOL HYPERGOL RDC BERYLLIUM COPPER 172			
APPROVED	SIZE: B	CODE	DWG NO: NSC004A	REV: 004
CHECKED				
DRAWN ANIL NAIR 7/5/19	SCALE 1:1.5	WEIGHT 81 OZ / 5 LBS	SHEET 1/1	

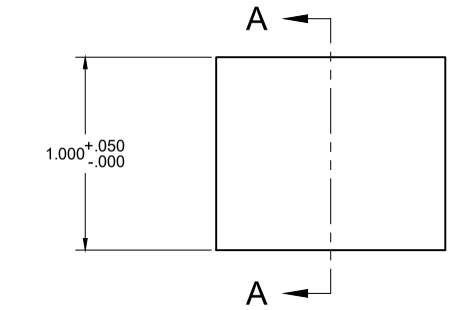

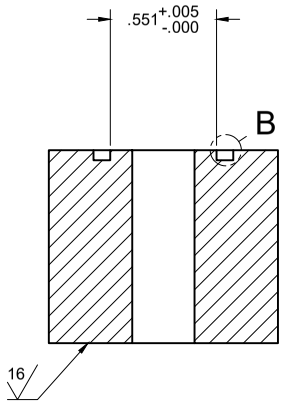

SECTION A-A
SCALE 2:1

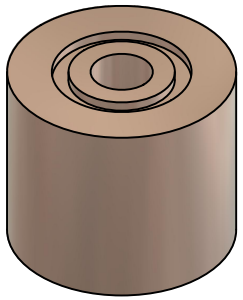

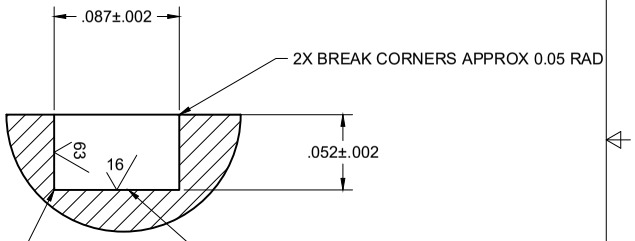

DETAIL B
SCALE 15:1

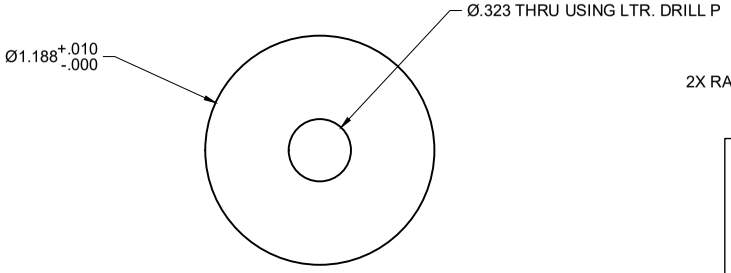

	PROJECT: UCLA/POLARIS SBIR			
	TITLE: INNER ANNULUS GENERIC SPOOL HYPERGOL RDC BERYLLIUM COPPER 172			
APPROVED	SIZE: B	CODE	DWG NO: NSC002	REV: 004
CHECKED				
DRAWN ANIL NAIR 7/5/19	SCALE 2:1	WEIGHT 5.2 OZ / 0.33 LBS	SHEET 1/1	

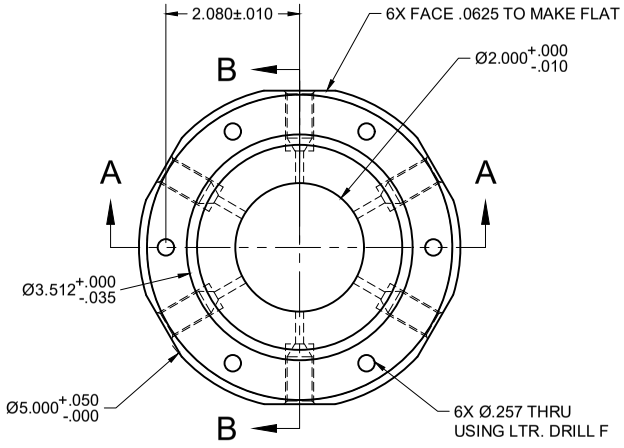

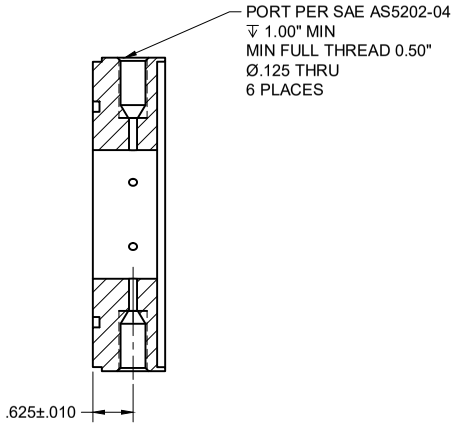

SECTION B-B
SCALE 1:1.5

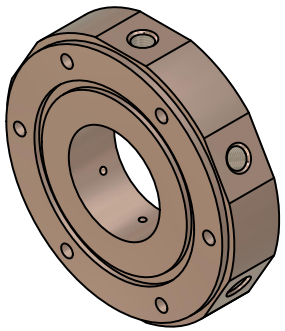

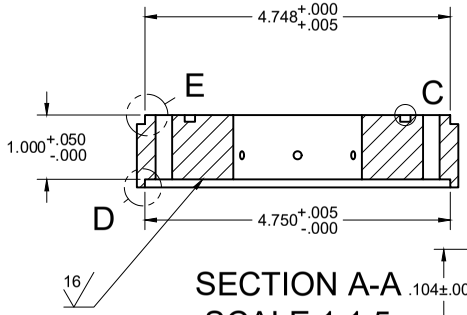

SECTION A-A
SCALE 1:1.5

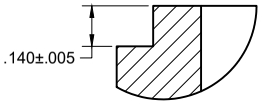

DETAIL E
SCALE 3:1

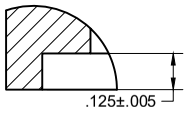

DETAIL D
SCALE 3:1

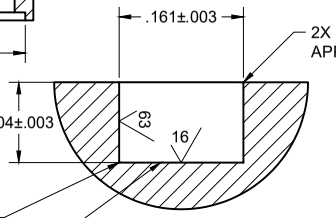

DETAIL C
SCALE 8:1

	PROJECT: UCLA/POLARIS SBIR			
	TITLE: OUTER ANNULUS AUX SPOOL HYPERGOL RDC BERYLLIUM COPPER 172			
APPROVED	SIZE: B	CODE	DWG NO: NSC004B	REV: 004
CHECKED				
DRAWN ANIL NAIR 7/5/19	SCALE 1:1.5	WEIGHT 77 OZ / 4.8 LBS	SHEET 1/1	

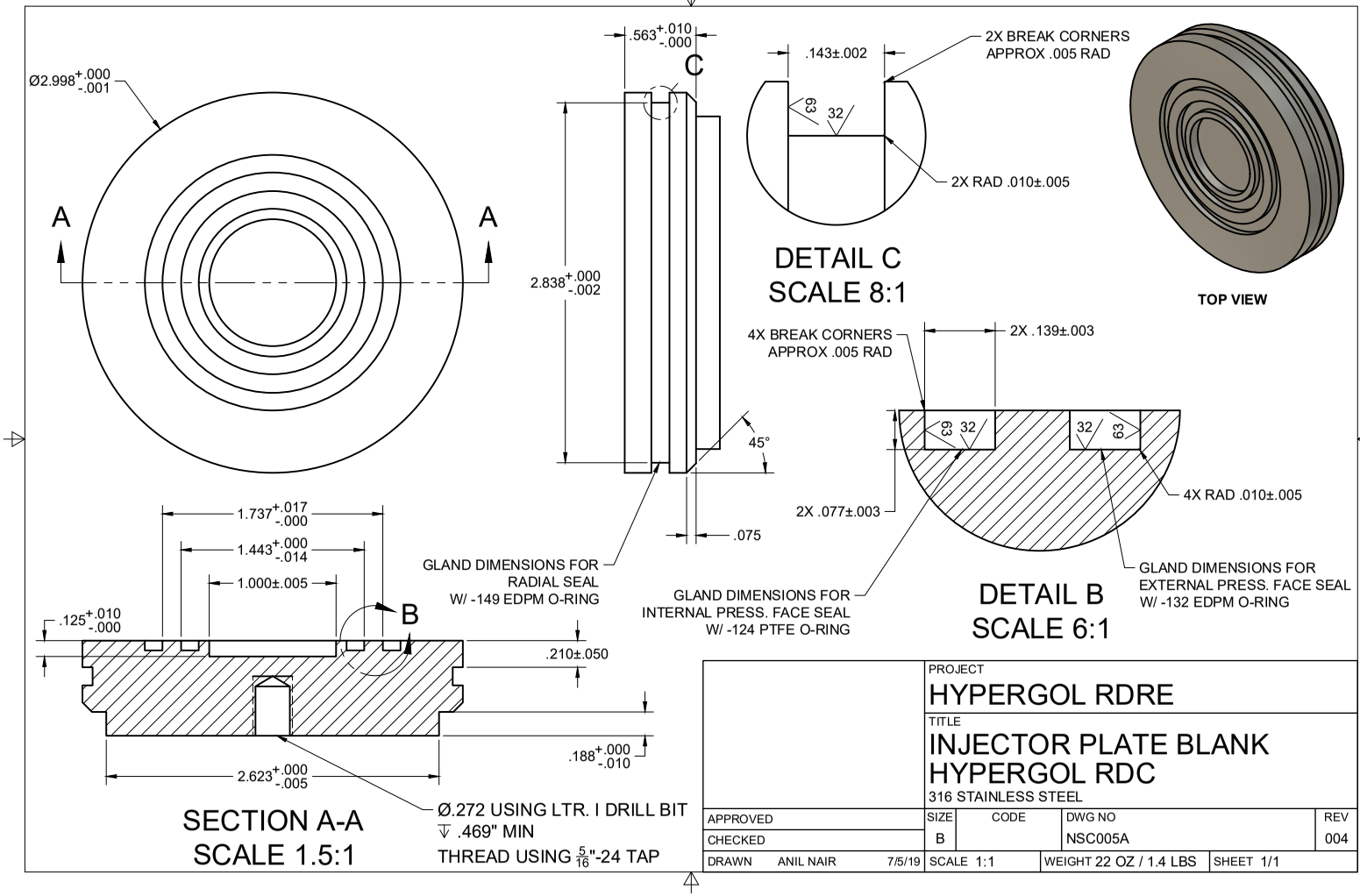

	PROJECT: HYPERGOL RDRE			
	TITLE: INJECTOR PLATE BLANK HYPERGOL RDC 316 STAINLESS STEEL			
APPROVED	SIZE: B	CODE	DWG NO: NSC005A	REV: 004
CHECKED				
DRAWN ANIL NAIR 7/5/19	SCALE 1:1		WEIGHT 22 OZ / 1.4 LBS	SHEET 1/1

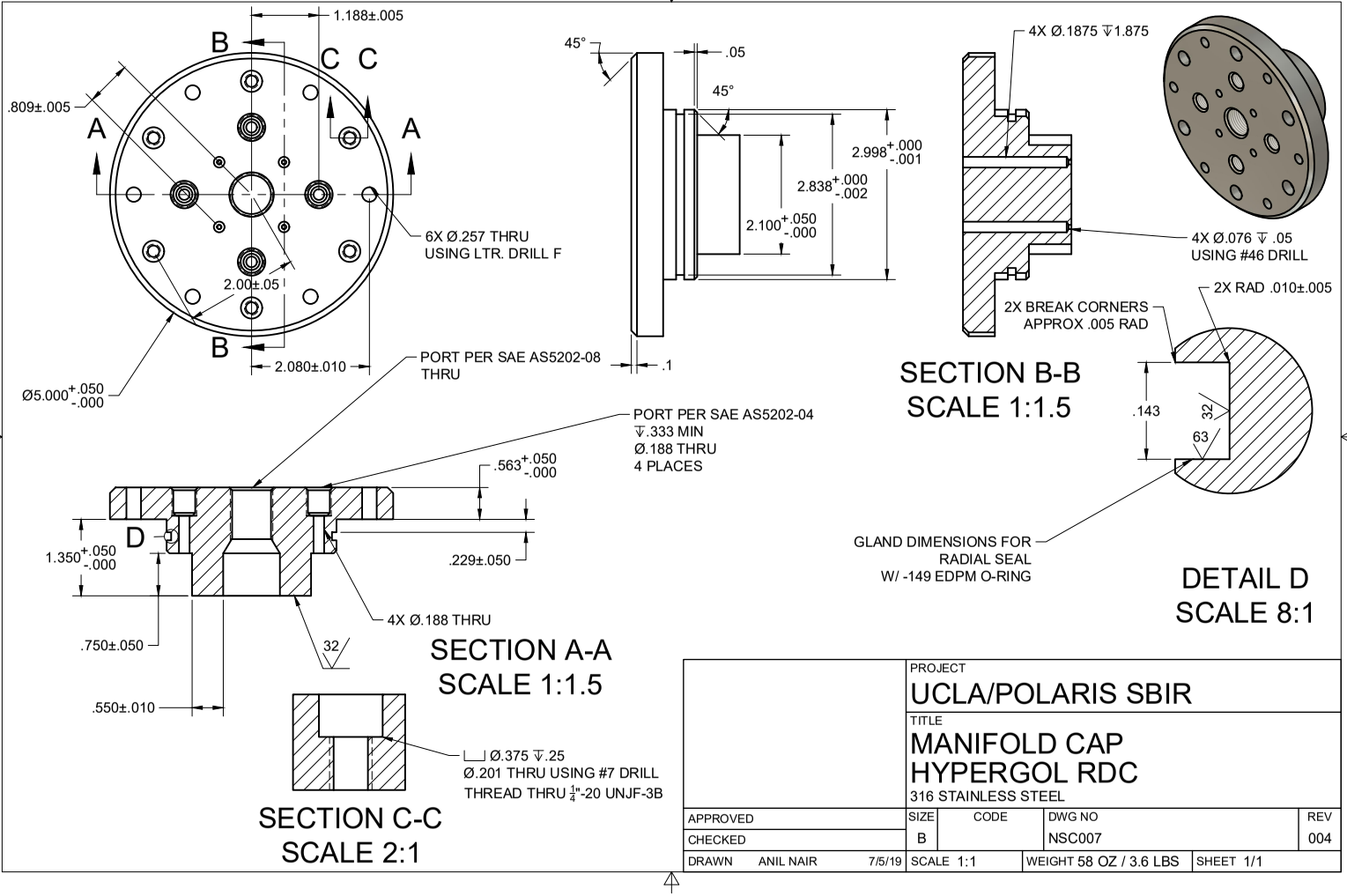

	PROJECT: UCLA/POLARIS SBIR			
	TITLE: MANIFOLD CAP HYPERGOL RDC 316 STAINLESS STEEL			
APPROVED	SIZE: B	CODE	DWG NO: NSC007	REV: 004
CHECKED				
DRAWN ANIL NAIR 7/5/19	SCALE 1:1		WEIGHT 58 OZ / 3.6 LBS	SHEET 1/1

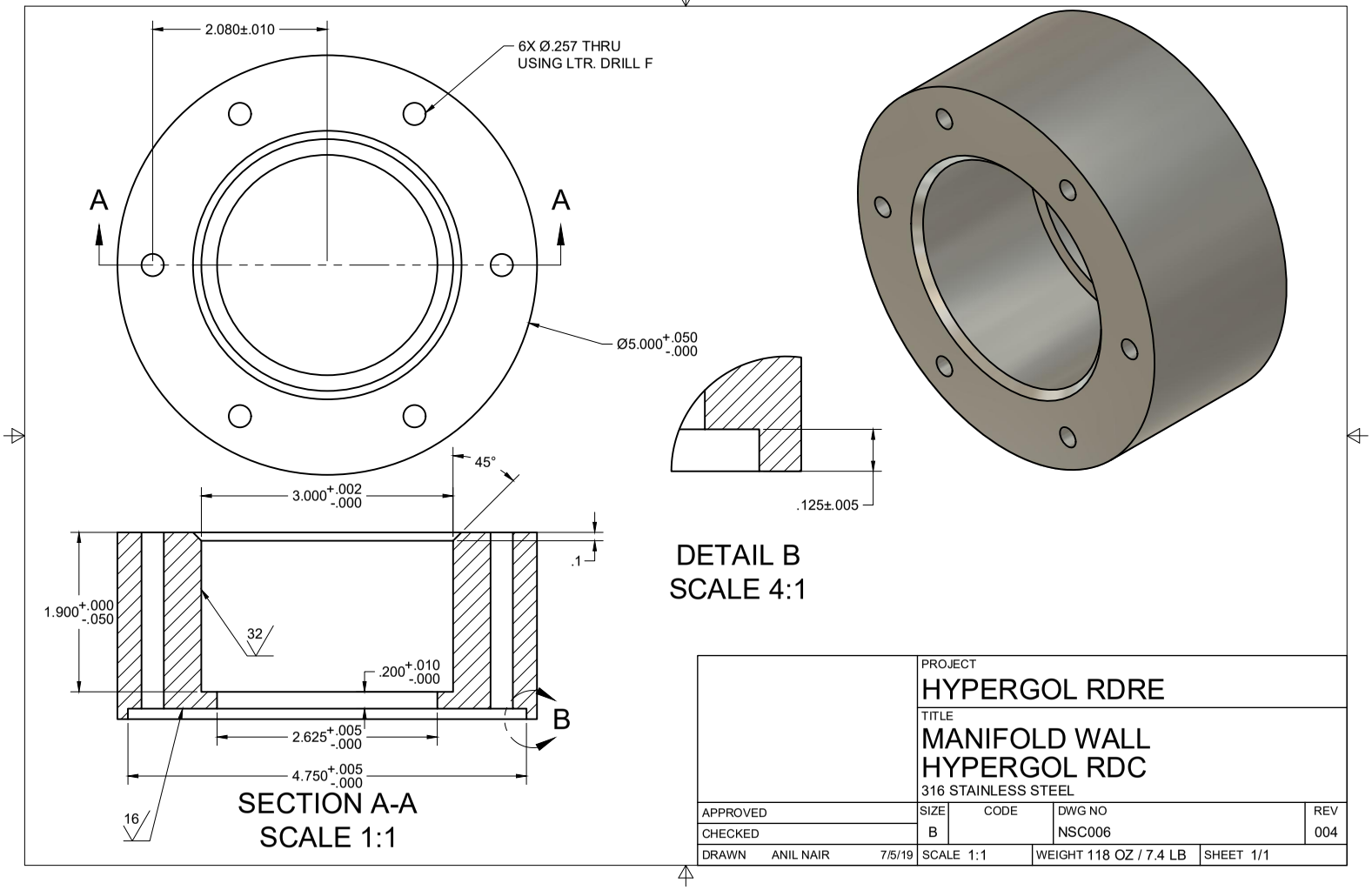

	PROJECT: HYPERGOL RDRE			
	TITLE: MANIFOLD WALL HYPERGOL RDC 316 STAINLESS STEEL			
APPROVED	SIZE: B	CODE	DWG NO: NSC006	REV: 004
CHECKED				
DRAWN ANIL NAIR 7/5/19	SCALE 1:1	WEIGHT 118 OZ / 7.4 LB	SHEET 1/1	

APPENDIX J

Detonation-impulse tube drawing package

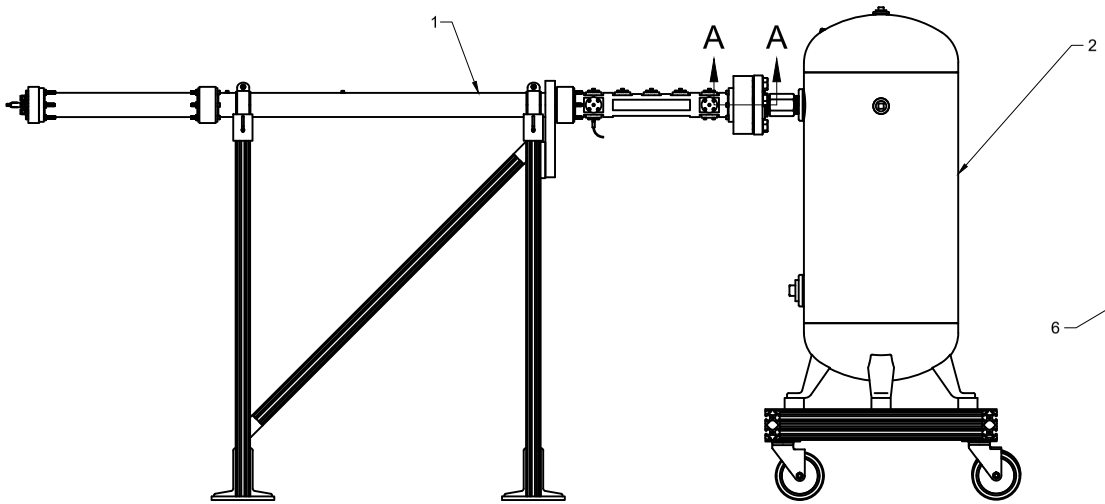

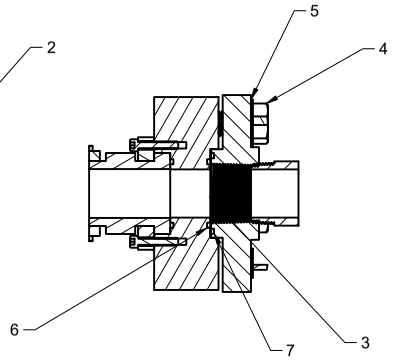

SECTION A-A
SCALE 1:3

ITEM	QTY	PART NAME
7	1	-228 High-Temperature Silicone O-Ring
6	1	-225 High-Temperature Silicone O-Ring
5	4	$\frac{3}{4}$" Washers
4	4	$\frac{3}{4}$"-10 Grade 5 Steel Hex Head Screw, Zinc-Plated, 2-1/4" Long
3	1	.003" Polyethylene Diaphragm
2	1	Mounted Surge Tank Assembly
1	1	Mounted Tube Assembly

PROJECT
Detonation-Impulse Tube

TITLE
Full Assembly

APPROVED	SIZE	CODE	DWG NO	REV
CHECKED	B			
DRAWN Anil Nair 12/3/2022	SCALE 1:10	WEIGHT	SHEET 1/1	

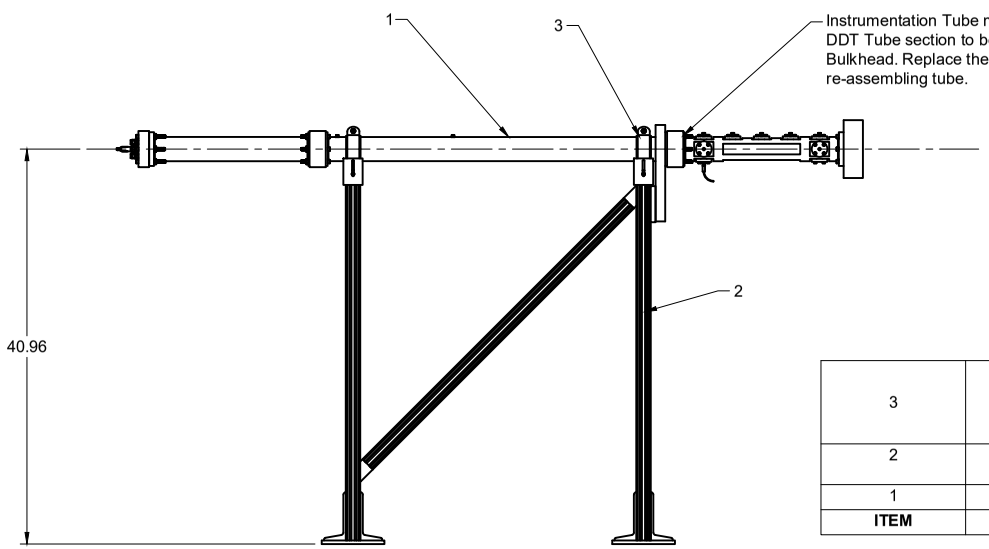

Instrumentation Tube must be disconnected from the rest of the tube to allow DDT Tube section to be inserted into the DIT Mounting Frame at the Thrust Bulkhead. Replace the 2-3/4" long bolts with 3-1/2" long bolts when re-assembling tube.

ITEM	QTY	PART NAME
3	2	Strut-Mount Routing Clamps (McMaster-Carr 32625T33)
2	1	DIT Mounting Frame
1	1	DIT Assembly

PROJECT: Detonation-Impulse Tube				
TITLE: Mounted Tube Assembly				
APPROVED	SIZE: B	CODE	DWG NO	REV
CHECKED				
DRAWN: Anil Nair 12/4/2022	SCALE: 1:10	WEIGHT	SHEET: 1/1	

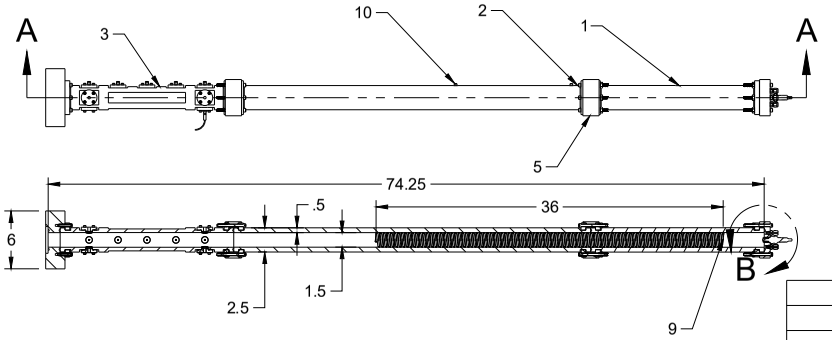

SECTION A-A
SCALE 1:10

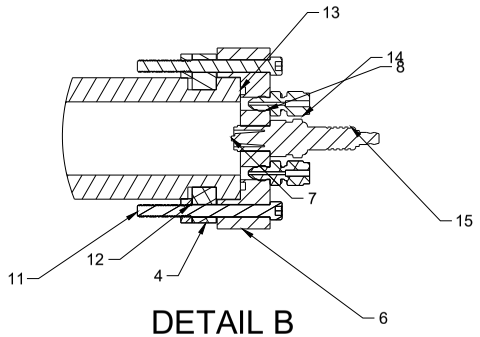

DETAIL B
SCALE 1:2

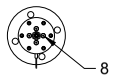

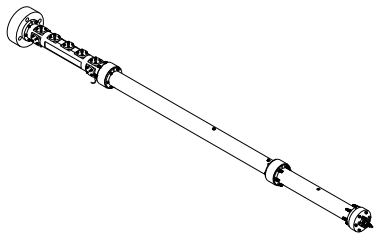

ITEM	QTY	PART NAME
16	AR	Misc. Washers to use with Bolts
15	1	-906 High-Temperature Silicone O-Ring
14	4	-902 High-Temperature Silicone O-Ring
13	3	-225 High-Temperature Silicone O-Ring
12	18	$\frac{1}{4}$"-20 Steel Nut
11	18	$\frac{1}{4}$"-20 Steel Bolt, 2-3/4" Long
10	2	Sealing bolt (McMaster Carr 92235A509)
9	1	Spiral (McMaster-Carr 9662K36)
8	4	$\frac{1}{8}$" AN-Swagelok Fittings
7	1	50-mm Sparkplug
6	1	Ignitor Cap
5	2	Flange Sleeve
4	10	Flange
3	1	Instrumentation Tube Assembly
2	1	DDT Tube
1	1	Ignitor Tube

PROJECT
Detonation-Impulse Tube

TITLE
DIT Assembly

APPROVED	SIZE	CODE	DWG NO	REV
CHECKED	B			
DRAWN Anil Nair 12/4/2022	SCALE 1:10	WEIGHT	SHEET 1/1	

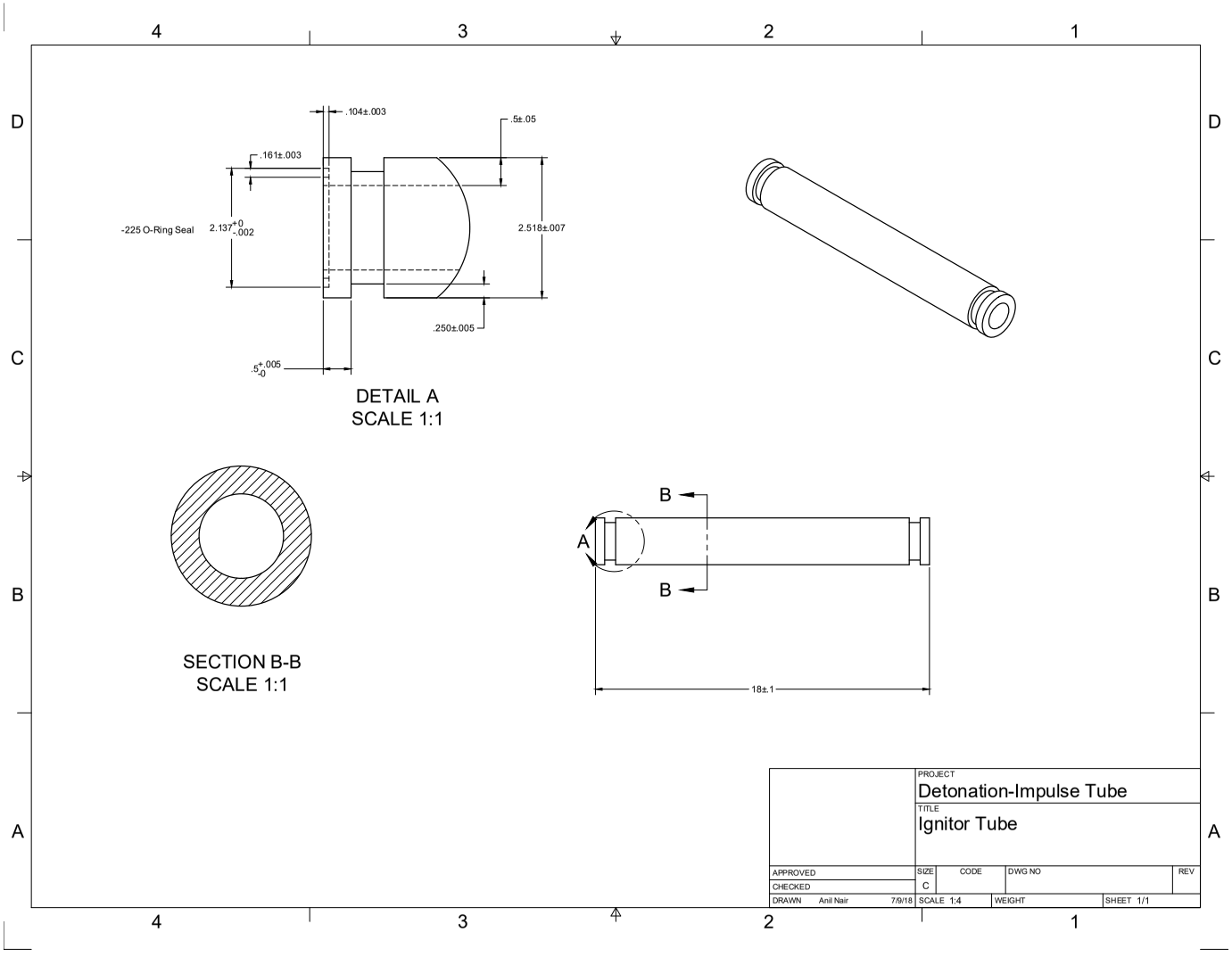
4
3
2
1
D
C
B
A
.104±.003
.5±.05
.161±.003
-225 O-Ring Seal
2.137 +0 -.002
2.518±.007
.250±.005
.5 +.005 -0
DETAIL A
SCALE 1:1
B
A
B
SECTION B-B
SCALE 1:1
18±.1
PROJECT
Detonation-Impulse Tube
TITLE
Ignitor Tube
APPROVED
CHECKED
DRAWN Anil Nair 7/9/18
SIZE C
CODE
DWG NO
REV
SCALE 1:4
WEIGHT
SHEET 1/1

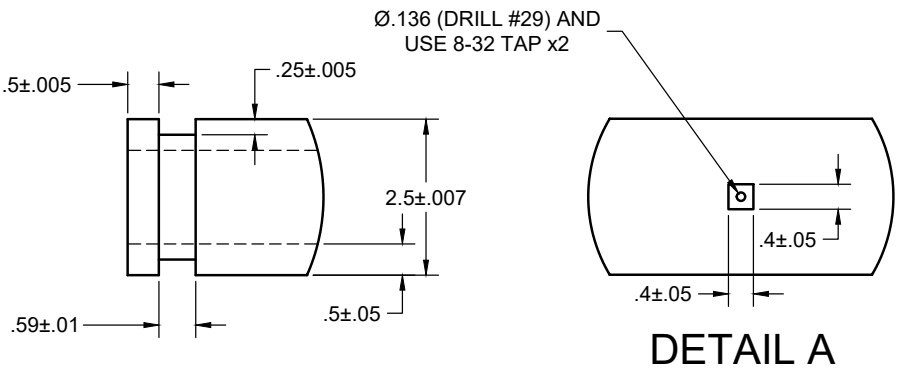

DETAIL C
SCALE 1:2

DETAIL A
SCALE 1:2

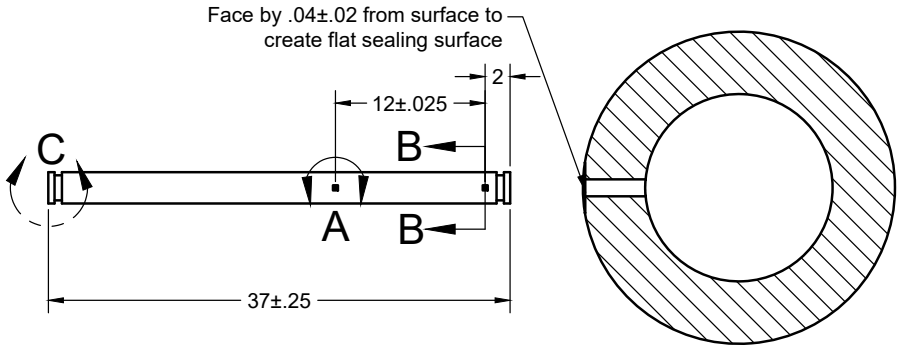

SECTION B-B
SCALE 1:1

	PROJECT: Detonation-Impulse Tube			
	TITLE: DDT Tube			
APPROVED	SIZE: A	CODE	DWG NO	REV
CHECKED				
DRAWN Anil Nair 7/9/18	SCALE 1:10	WEIGHT	SHEET 1/1	

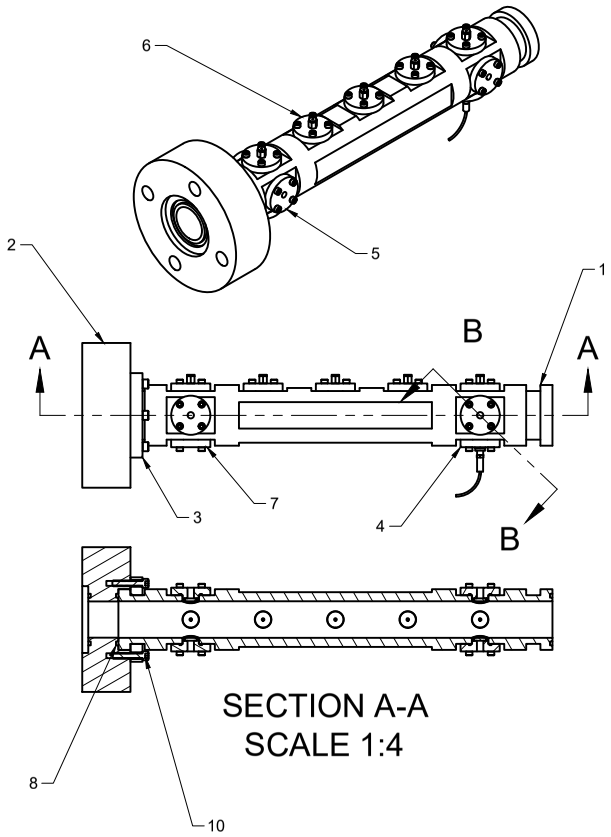

SECTION A-A
SCALE 1:4

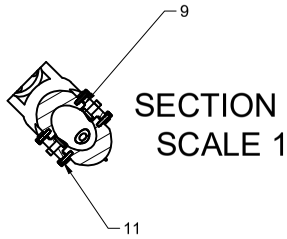

SECTION B-B
SCALE 1:4

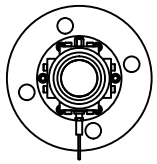

ITEM	QTY	PART NAME
12	AR	Misc. Washers for assembly
11	44	8-26 Steel Screw, $\frac{1}{2}$" Long
10	6	$\frac{1}{4}$"-20 Steel Bolt, 1-1/4" Long
9	11	-019 High-Temperature Silicone O-Ring
8	1	-225 High-Temperature Silicone O-Ring
7	1	Blank Port Plug
6	5	Time-of-Arrival Port Plug
5	4	Optical Access Port Plug
4	1	Kistler Port Plug
3	2	Flange
2	1	Diaphragm Holder
1	1	Instrumentation Tube

PROJECT
Detonation-Impulse Tube

TITLE
Instrumentation Tube Assembly

APPROVED	SIZE	CODE	DWG NO	REV
CHECKED	B			
DRAWN Anil Nair 12/4/2022	SCALE 1:4	WEIGHT	SHEET 1/1	

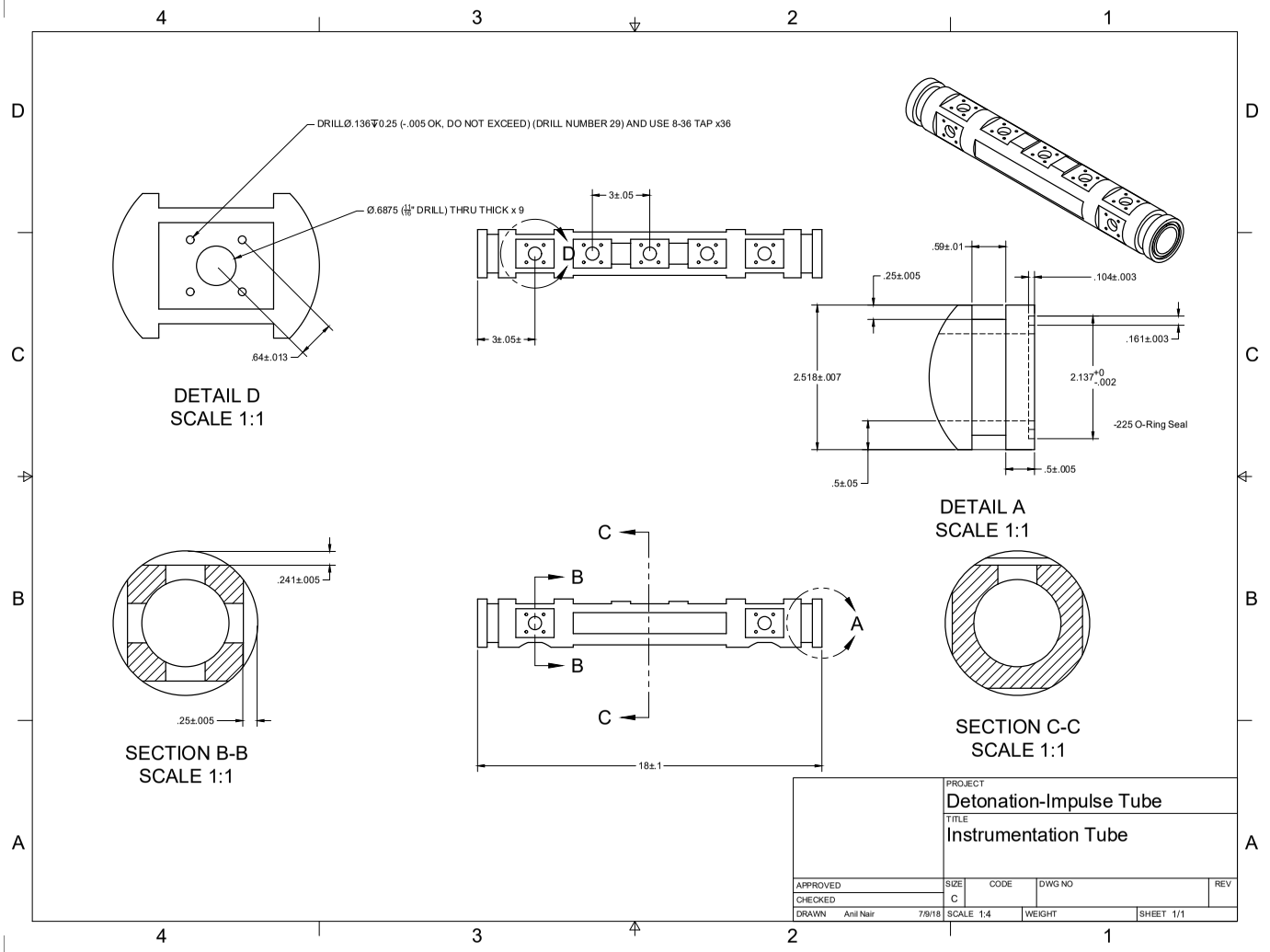
DRILLØ.136∓0.25 (-.005 OK, DO NOT EXCEED) (DRILL NUMBER 29) AND USE 8-36 TAP x36
Ø.6875 (11/16" DRILL) THRU THICK x 9
.64±.013
DETAIL D
SCALE 1:1
3±.05
3±.05±
D
.59±.01
.25±.005
.104±.003
.161±.003
2.518±.007
2.137 +0 -.002
-225 O-Ring Seal
.5±.005
.5±.05
DETAIL A
SCALE 1:1
.241±.005
.25±.005
SECTION B-B
SCALE 1:1
C
B
B
C
A
18±.1
SECTION C-C
SCALE 1:1
PROJECT
Detonation-Impulse Tube
TITLE
Instrumentation Tube
APPROVED
CHECKED
DRAWN Anil Nair 7/9/18
SIZE C
CODE
DWG NO
REV
SCALE 1:4
WEIGHT
SHEET 1/1

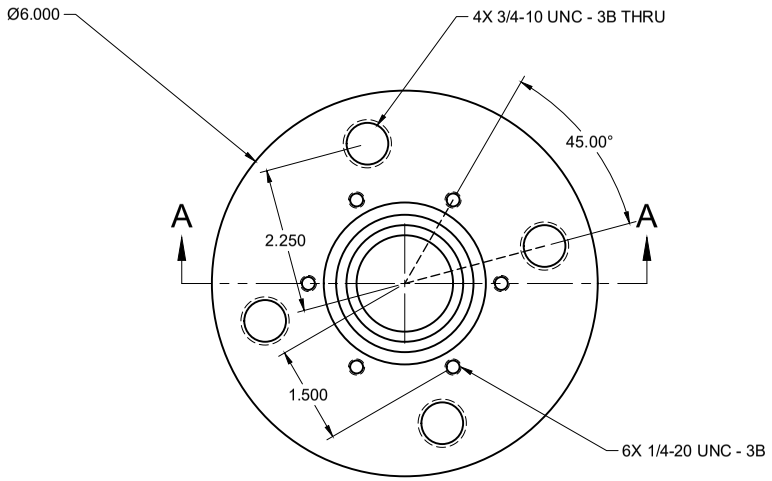

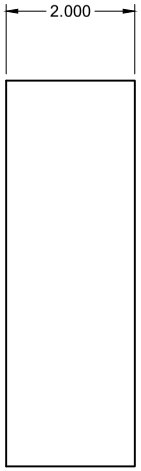

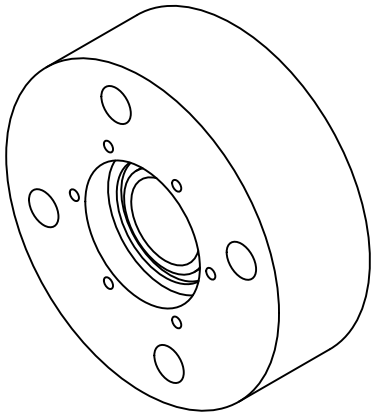

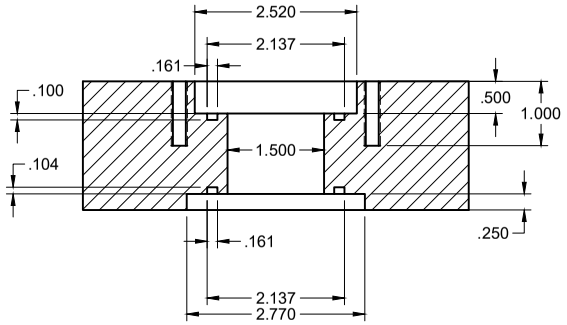

SECTION A-A
SCALE 1:1.5

	PROJECT: Detonation-Impulse Tube			
	TITLE: Diaphragm Holder			
APPROVED	SIZE: B	CODE	DWG NO	REV
CHECKED				
DRAWN: Anil Nair 12/4/2022	SCALE: 1:1.5	WEIGHT	SHEET: 1/1	

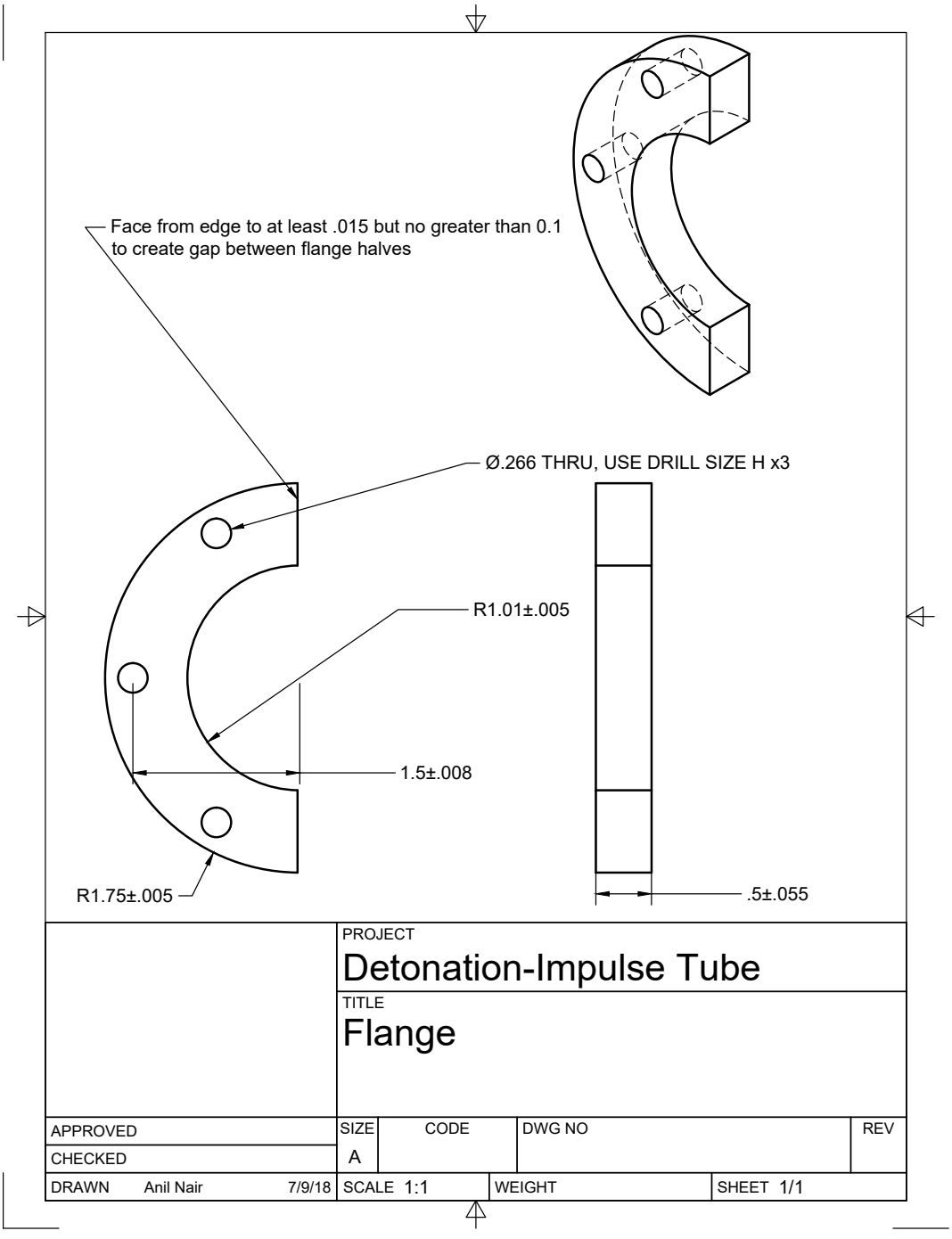

	PROJECT: Detonation-Impulse Tube			
	TITLE: Flange			
APPROVED	SIZE: A	CODE	DWG NO	REV
CHECKED				
DRAWN Anil Nair 7/9/18	SCALE 1:1	WEIGHT	SHEET 1/1	

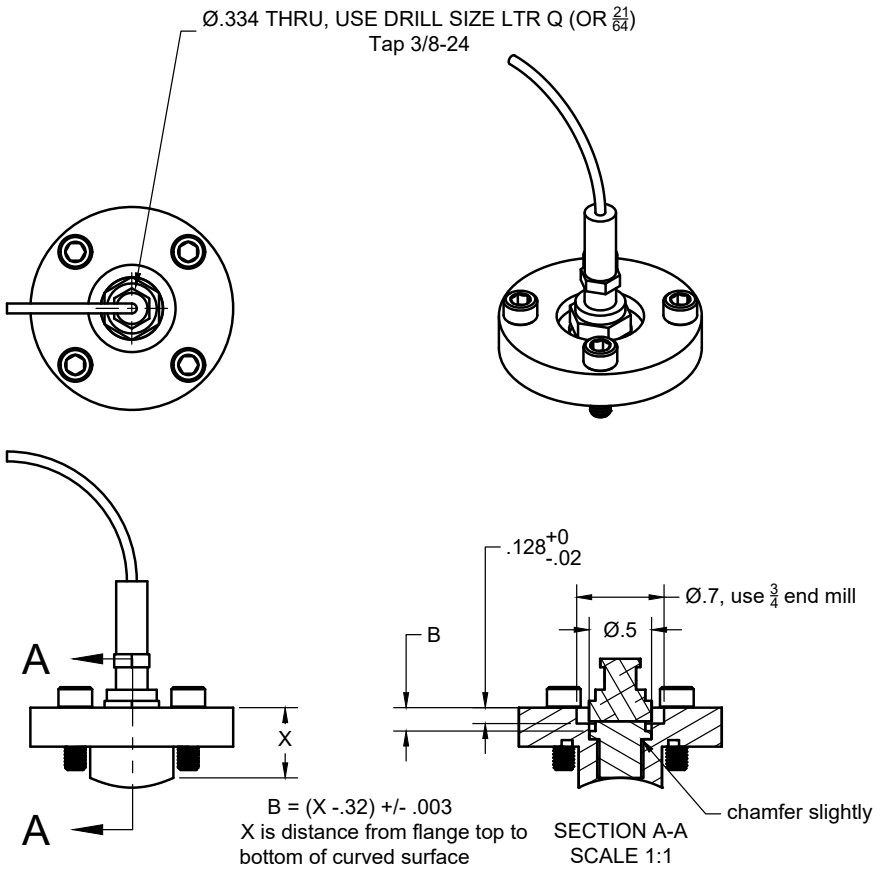

B = (X -.32) +/- .003
X is distance from flange top to bottom of curved surface

SECTION A-A
SCALE 1:1

** Can lengthen dimension on-the-fly in order to prevent hex from bottoming out

	PROJECT: Detonation-Impulse Tube			
	TITLE: Kistler Port Plug			
APPROVED	SIZE: A	CODE	DWG NO	REV
CHECKED				
DRAWN David Morrow 10/31/2019	SCALE 1:1	WEIGHT	SHEET 1/1	

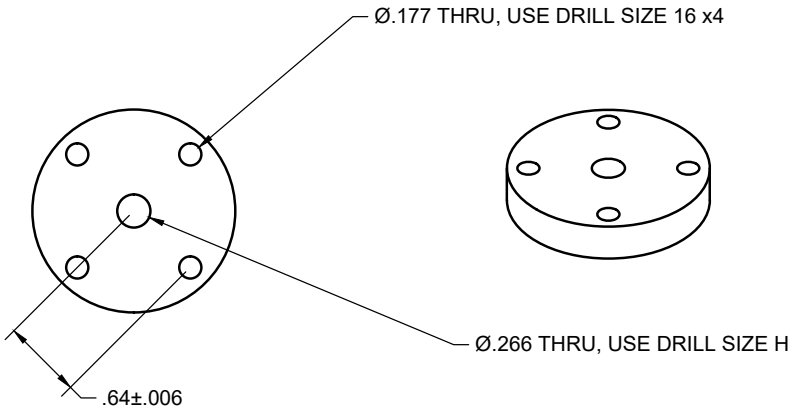

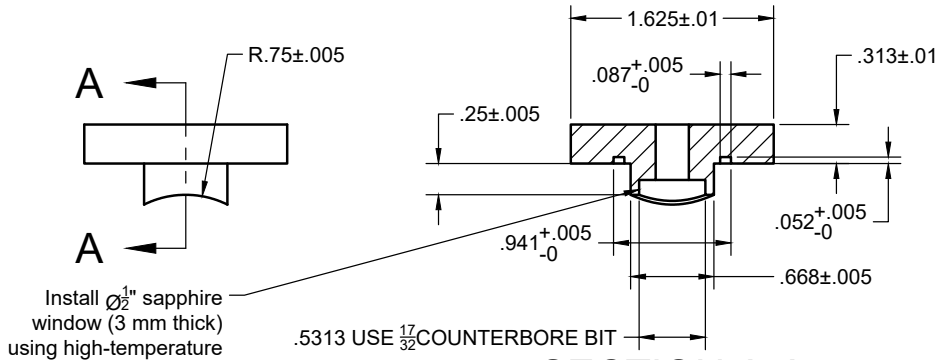

SECTION A-A
SCALE 1:1

	PROJECT: Detonation-Impulse Tube			
	TITLE: Optical Port Plug			
APPROVED	SIZE: A	CODE	DWG NO	REV
CHECKED				
DRAWN Anil Nair 7/9/18	SCALE 1:1	WEIGHT	SHEET 1/1	

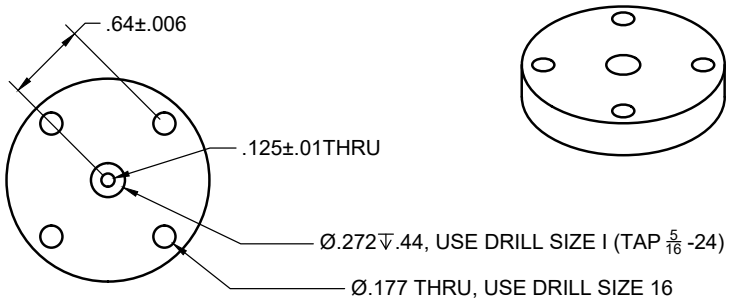

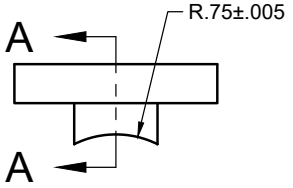

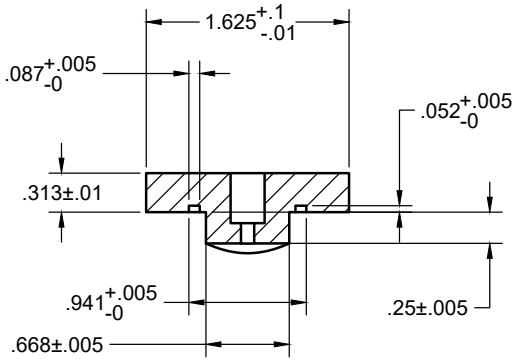

SECTION A-A
SCALE 1:1

	PROJECT: Detonation Tube			
	TITLE: Time of Arrival Port Plug			
APPROVED	SIZE: A	CODE	DWG NO	REV
CHECKED				
DRAWN Anil Nair 7/9/18	SCALE 1:1	WEIGHT	SHEET 1/1	

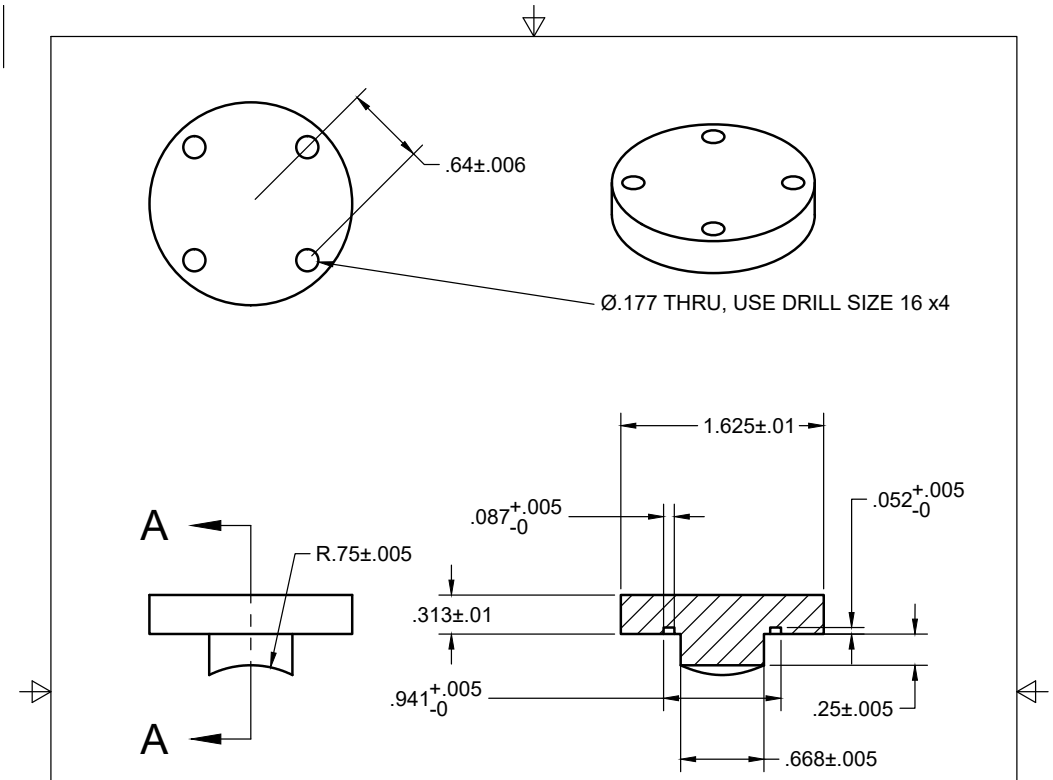

SECTION A-A
SCALE 1:1

	PROJECT: Detonation-Impulse Tube			
	TITLE: Blank Port Plug			
APPROVED	SIZE: A	CODE	DWG NO	REV
CHECKED				
DRAWN Anil Nair 7/9/18	SCALE 1:1	WEIGHT	SHEET 1/1	

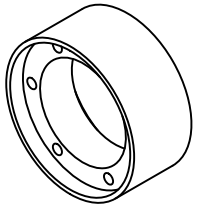

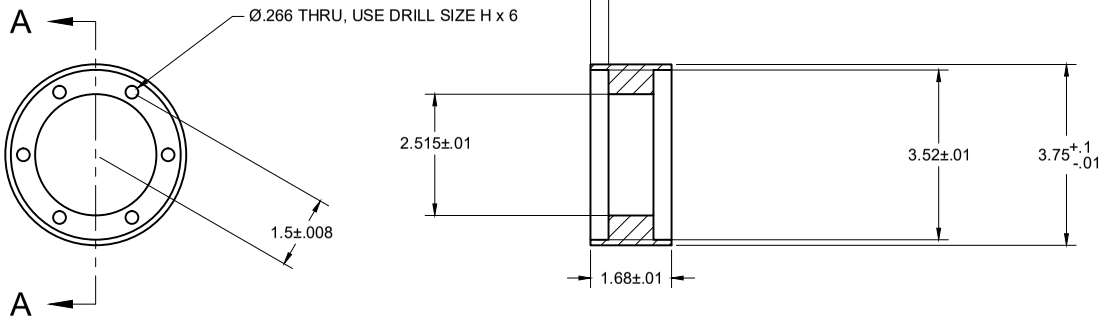

SECTION A-A
SCALE 1:2

	PROJECT: Detonation-Impulse Tube			
	TITLE: Flange Sleeve			
APPROVED	SIZE: B	CODE	DWG NO	REV
CHECKED				
DRAWN Anil Nair 7/9/18	SCALE 1:2	WEIGHT	SHEET 1/1	

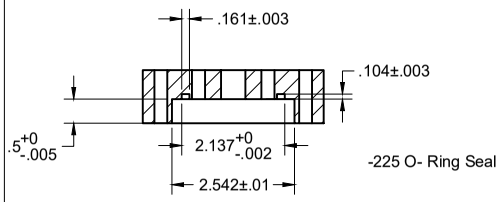

SECTION A-A
SCALE 1:2

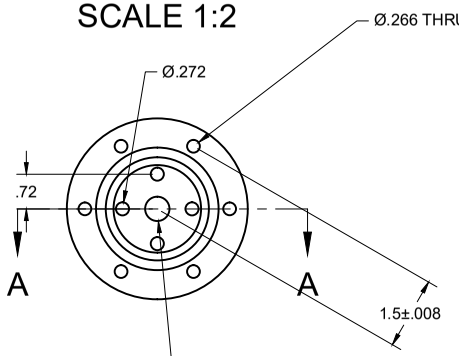

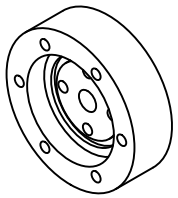

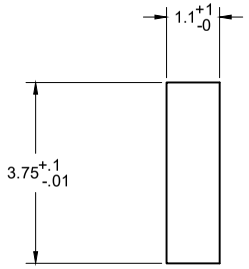

	PROJECT: Detonation-Impulse Tube			
	TITLE: Ignitor Cap			
APPROVED	SIZE: B	CODE	DWG NO	REV
CHECKED				
DRAWN Anil Nair 7/9/18	SCALE 1:2	WEIGHT	SHEET 1/1	

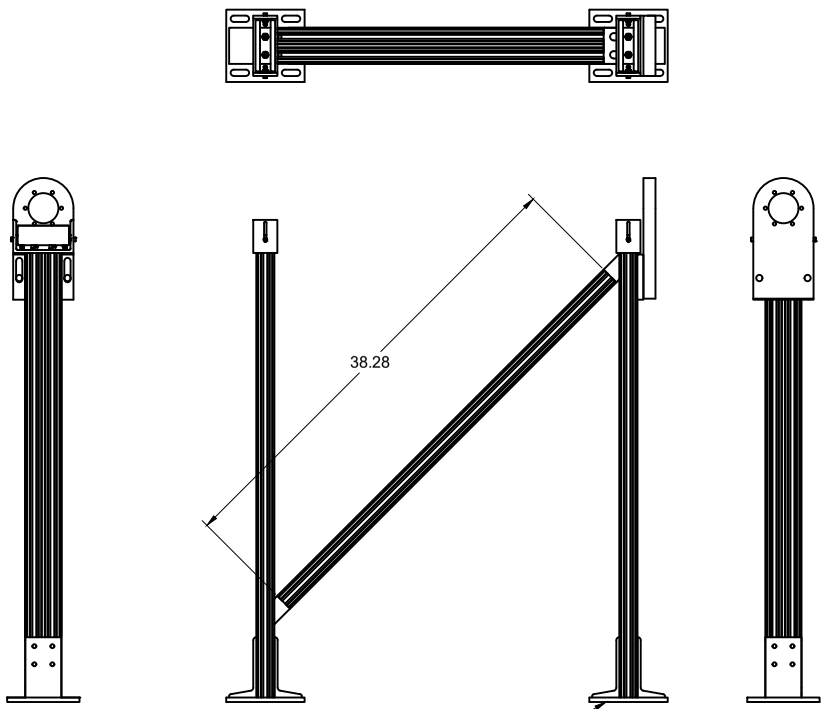

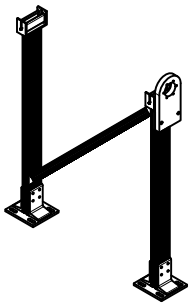

ITEM	QTY	PART NAME
6	AR	Misc. Hardware (screws, washers) to connect pieces
5	1	Thrust Bulkhead
4	1	Interface Plate
3	2	Diagonal T-Slot Brace (McMaster-Carr 47067T337)
2	1	3" T-Slotted Rail, 38.28" Long
1	2	Stanchion

PROJECT
Detonation-Impulse Tube

TITLE
DIT Mounting Frame

APPROVED	SIZE	CODE	DWG NO	REV
CHECKED	B			
DRAWN Anil Nair 12/4/2022	SCALE 1:8	WEIGHT	SHEET 1/1	

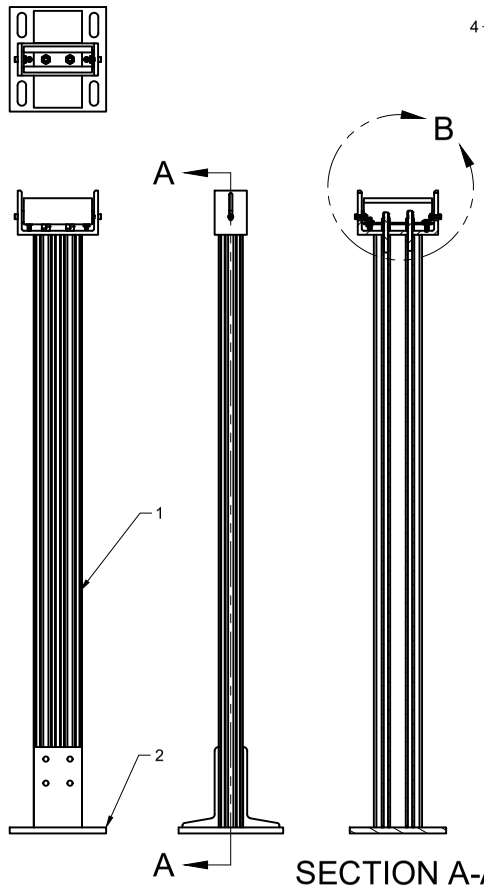

SECTION A-A
SCALE 1:6

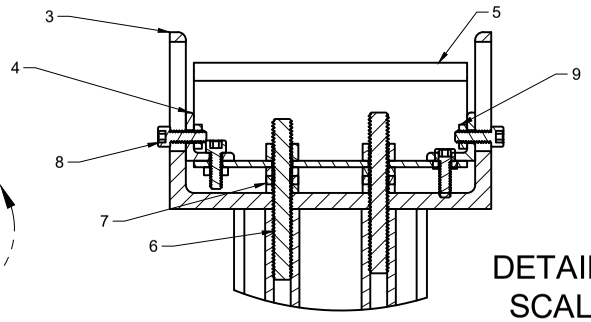

DETAIL B
SCALE
1:1.5

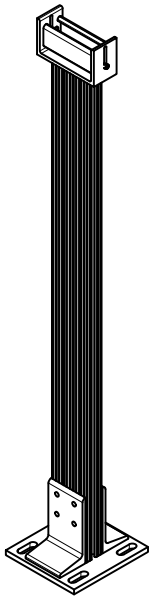

ITEM	QTY	PART NAME
10	AR	Misc. Hardware for connecting T-Rail to Mount Plate
9	4	Nut (McMaster-Carr 90480A011)
8	4	Screw (McMaster-Carr 92196A243)
7	6	Nut (McMaster-Carr 95462A030)
6	2	Threaded Rod (McMaster-Carr 90322A673)
5	1	Strut Channel
4	2	Bracket
3	1	U-Channel
2	1	3" T-Slot Floor Mount Base Plate (Motion Ai P/N 2400-Black)
1	1	3" T-Slotted Rail, 38.27" Long

PROJECT
Detonation-Impulse Tube

TITLE
Stanchion

APPROVED	SIZE	CODE	DWG NO	REV
CHECKED	B			
DRAWN Anil Nair 12/4/2022	SCALE 1:6	WEIGHT	SHEET 1/1	

1. Make from McMaster-Carr P/N 6546K81,
   6061 Al Rectangular Tube

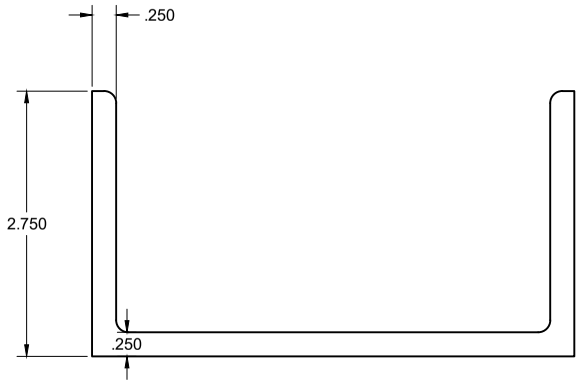

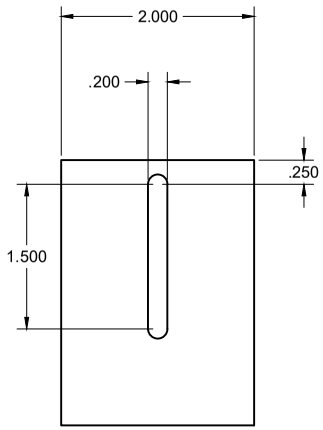

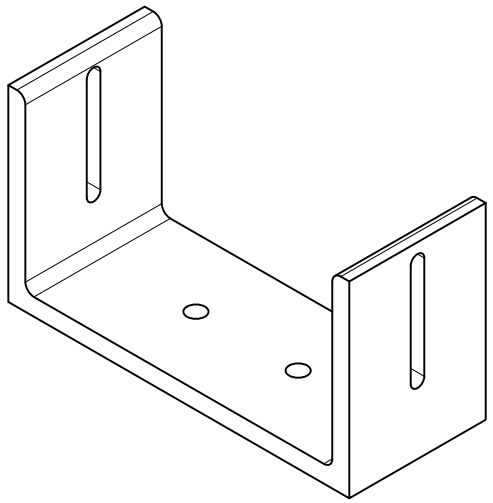

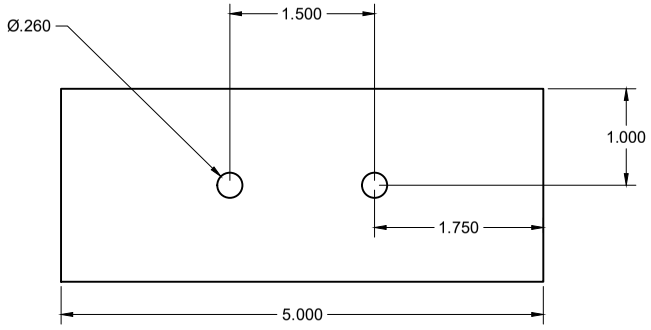

	PROJECT: Detonation-Impulse Tube			
	TITLE: U-Channel			
APPROVED	SIZE: B	CODE	DWG NO	REV
CHECKED				
DRAWN Anil Nair 4/18/19	SCALE 1:1	WEIGHT	SHEET 1/1	

1. Make from McMaster-Carr part 8982K28, 6061 Al 90 deg angle

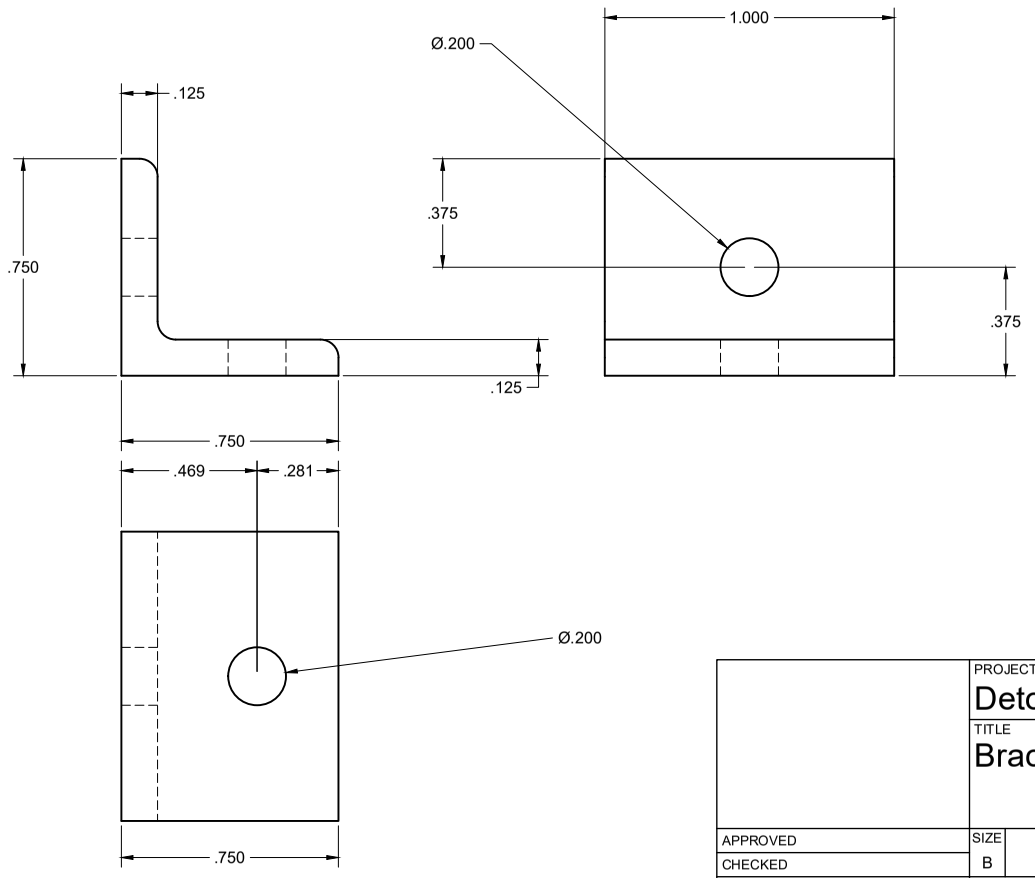

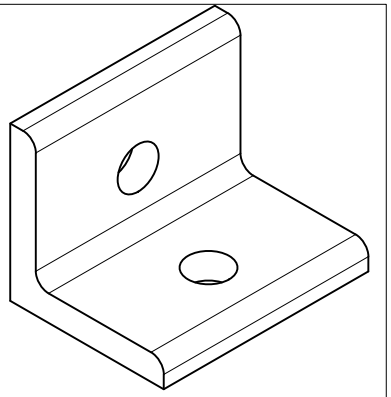

	PROJECT: Detonation-Impulse Tube			
	TITLE: Bracket			
APPROVED	SIZE: B	CODE	DWG NO	REV
CHECKED				
DRAWN Anil Nair 4/30/19	SCALE 3:1	WEIGHT	SHEET 1/1	

1. Make from McMaster-Carr P/N 3310T589, Black Powder-Coated Steel Strut Channel

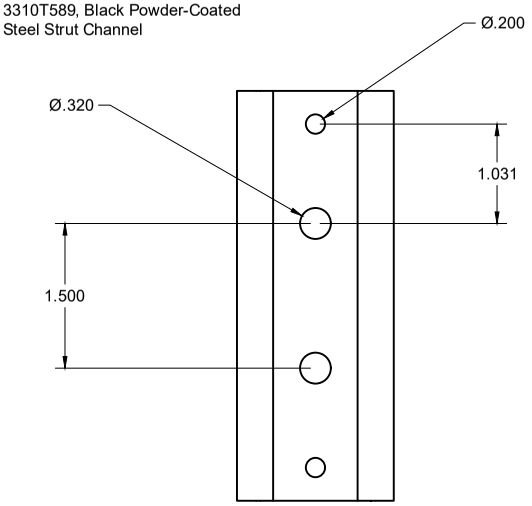

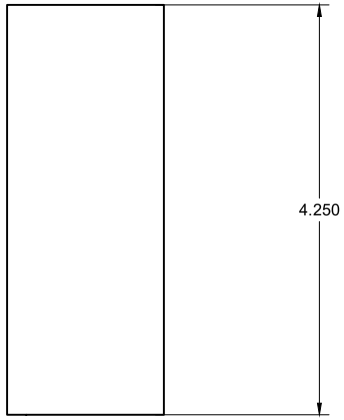

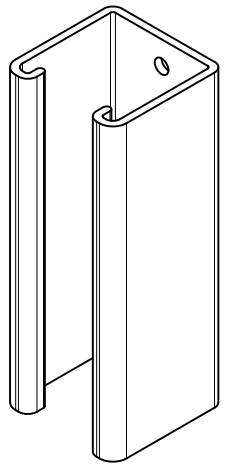

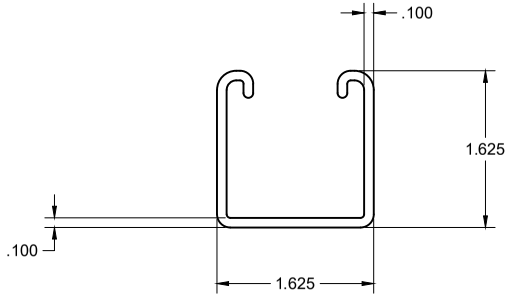

	PROJECT: Detonation-Impulse Tube			
	TITLE: Strut Channel			
APPROVED	SIZE: B	CODE	DWG NO	REV
CHECKED				
DRAWN Anil Nair 5/1/19	SCALE 1:1	WEIGHT	SHEET 1/1	

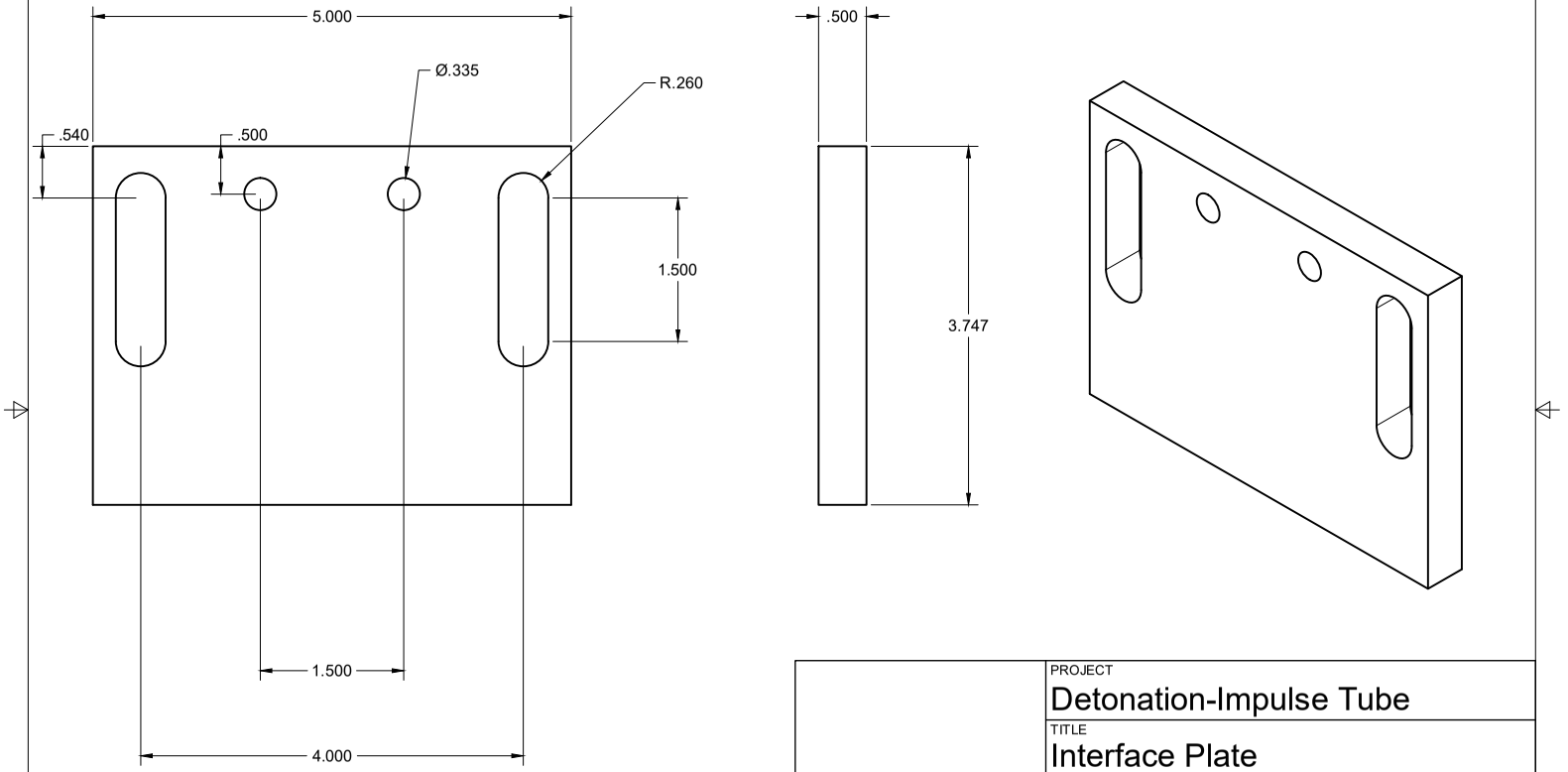

	PROJECT: Detonation-Impulse Tube			
	TITLE: Interface Plate			
APPROVED	SIZE: B	CODE	DWG NO	REV
CHECKED				
DRAWN Anil Nair 5/8/19	SCALE 1:1	WEIGHT	SHEET 1/1	

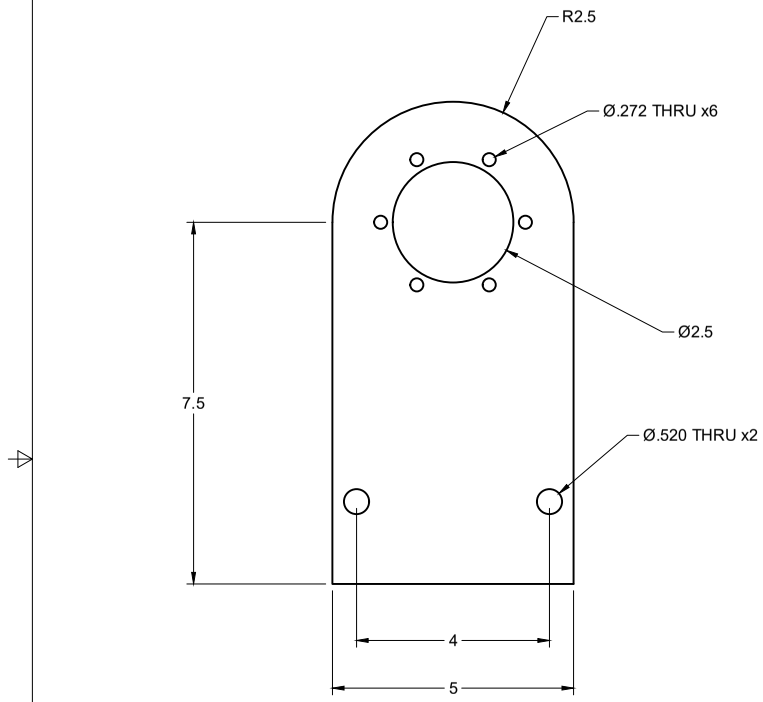

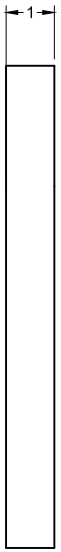

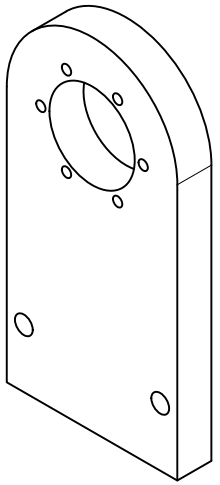

	PROJECT: Detonation-Impulse Tube			
	TITLE: Thrust Bulkhead			
APPROVED	SIZE: B	CODE	DWG NO	REV
CHECKED				
DRAWN: Anil Nair 12/4/2022	SCALE: 1:2	WEIGHT	SHEET: 1/1	

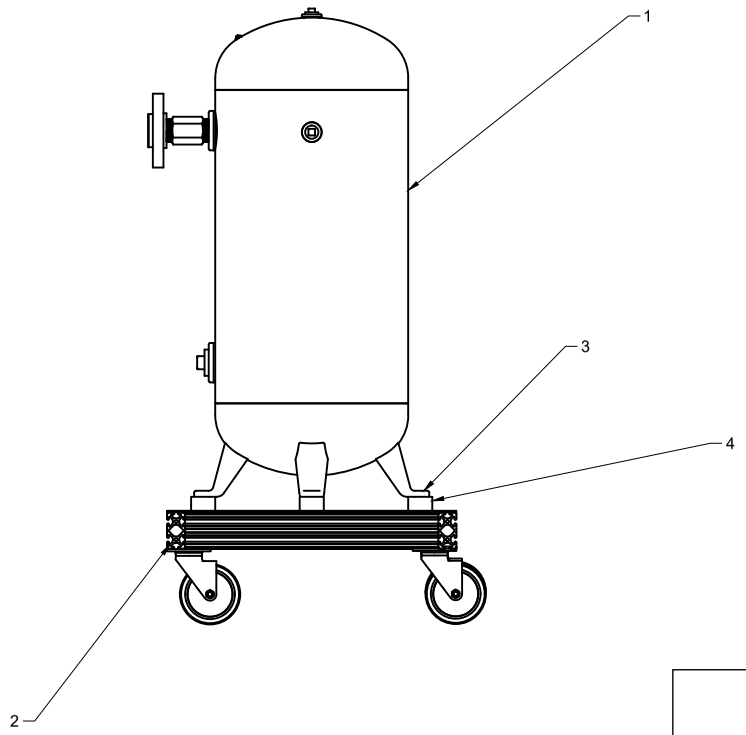

ITEM	QTY	PART NAME
4	4	2" OD, $\frac{5}{8}$" ID, 1.158" thick, shim stack
3	4	$\frac{9}{16}$"-18 socket-head screws, 3" long
2	1	Surge Tank Cart Assembly
1	1	Surge Tank Assembly

PROJECT
Detonation-Impulse Tube

TITLE
Mounted Surge Tank Assembly

APPROVED	SIZE	CODE	DWG NO	REV
CHECKED	B			
DRAWN Anil Nair 12/4/2022	SCALE 1:8	WEIGHT	SHEET 1/1	

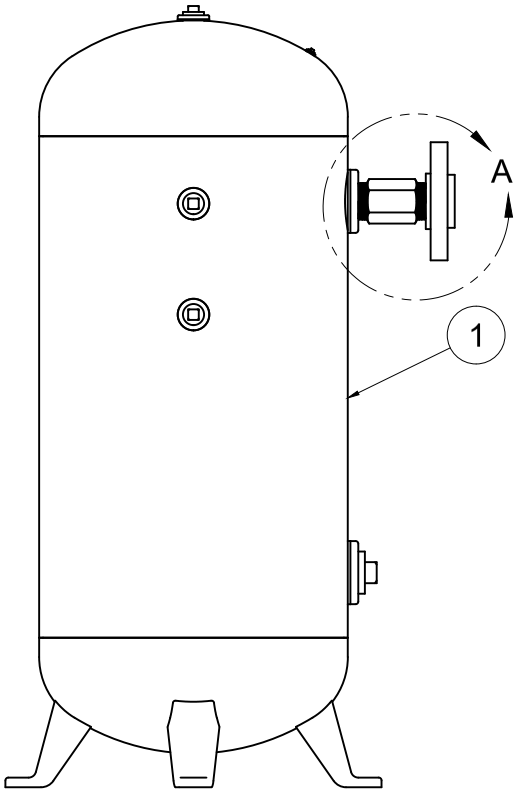

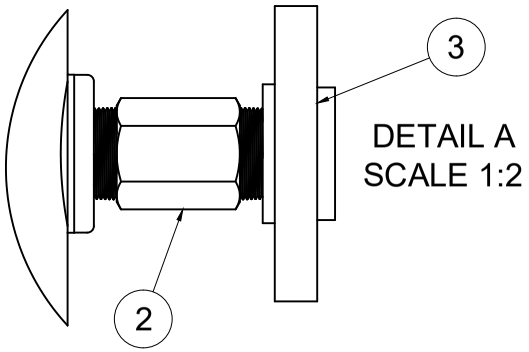

DETAIL A
SCALE 1:2

ITEM	QTY	PART NAME
3	1	Surge Tank Flange
2	1	$\frac{1}{2}$" NPT Male Straight Connector (316 Stainless Steel)
1	1	Surge Tank (McMaster-Carr 9795K1)

PROJECT
Detonation-Impulse Tube

TITLE
Surge Tank Assembly

APPROVED	SIZE	CODE	DWG NO	REV
CHECKED	B			
DRAWN Anil Nair 12/4/2022	SCALE 1:5	WEIGHT	SHEET 1/1	

Notes:

1. Make from McMaster-Carr Part 1441N29, 600 Class High-Pressure Pipe Flange, 304/304L Stainless Steel, 1-1/2 NPT
2. Machine -228 O-Ring groove

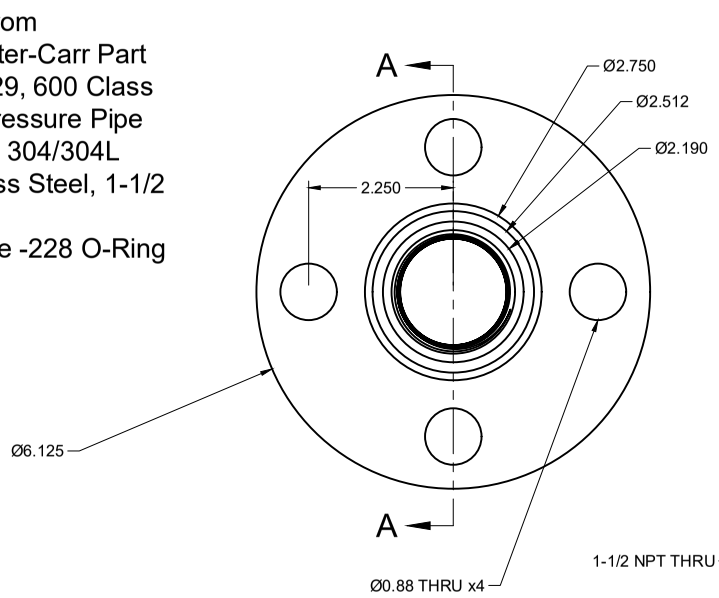

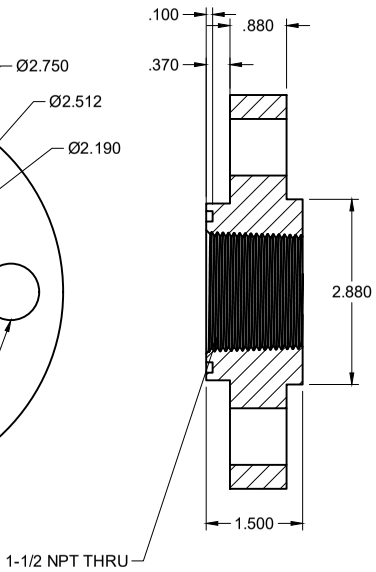

SECTION A-A
SCALE 1:1.5

	PROJECT: Detonation-Impulse Tube			
	TITLE: Surge Tank Flange			
APPROVED	SIZE: B	CODE	DWG NO	REV
CHECKED				
DRAWN Anil Nair 12/4/2022	SCALE 1:2	WEIGHT	SHEET 1/1	

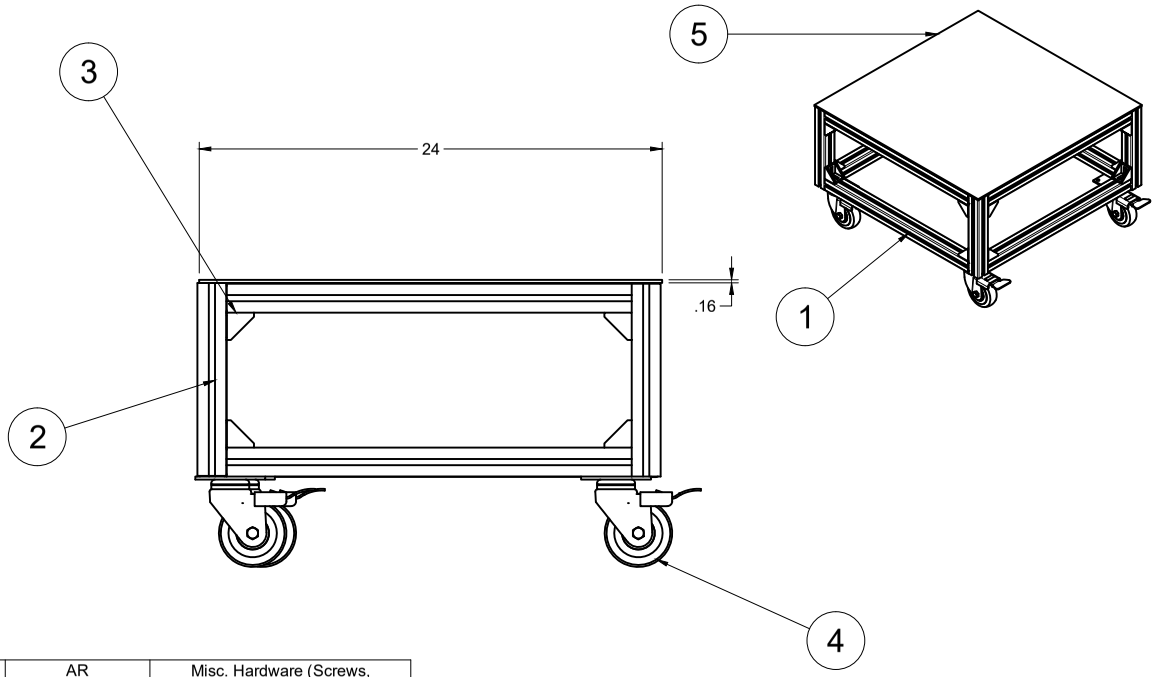

6	AR	Misc. Hardware (Screws, Washers) for assembly
5	1	Cart Baseplate
4	4	Swiveling 3-1/2" Diameter Caster (McMaster-Carr 2702T71)
3	16	Angle Bracket (McMaster-Carr 5537T51)
2	4	3" T-Slotted Rail, 10 Inch Long
1	8	3" T-Slotted Rail, 21 Inch Long

PROJECT
Detonation-Impulse Tube

TITLE
Surge Tank Cart Assembly

APPROVED	SIZE	CODE	DWG NO	REV
CHECKED	B			
DRAWN Anil Nair 12/4/2022	SCALE 1:5	WEIGHT	SHEET 1/1	

REFERENCES

[1] Philip G. Hill and Carl R. Peterson. *Mechanics and Thermodynamics of Propulsion*. Addison-Wesley Publishing Co, Reading, MA, 2nd edition, 1992.

[2] Dieter K. Huzel and David H. Huang. *Modern Engineering for Design of Liquid-Propellant Rocket Engines*. American Institute of Aeronautics and Astronautics, Washington DC, 1 1992.

[3] George P. Sutton and Oscar Biblarz. *Rocket Propulsion Elements*. John Wiley & Sons, Inc., Hoboken, NJ, USA, 8th edition, 2010.

[4] Steven Isakowitz, Joshua Hopkins, and Joseph Hopkins. *International Reference Guide to Space Launch Systems*. AIAA, 4th edition, 2004.

[5] Sanford Gordon, Bonnie J. McBride, Sanford Gordon, and Bonnie J. McBride. *Computer Program for Calculation of Complex Chemical Equilibrium Compositions and Applications*. Number January. NASA, 1996.

[6] Steering Committee for NASA Technology Roadmaps. *NASA Space Technology Roadmaps and Priorities*. National Academies Press, Washington, D.C., 5 2012.

[7] Robert L. Sackheim. Overview of United States space propulsion technology and associated space transportation systems. *Journal of Propulsion and Power*, 22(6):1310–1333, 2006.

[8] Ya. Zel'dovich. To the Question of Energy Use of Detonation Combustion. *Journal of Propulsion and Power*, 22(3):588–592, 5 2006.

[9] R. Vutthivithayarak, E. M. Braun, and F. K. Lu. On Thermodynamic Cycles for Detonation Engines. *28th International Symposium on Shock Waves*, (1):287–292, 2012.

[10] William H. Heiser and David T. Pratt. Thermodynamic Cycle Analysis of Pulse Detonation Engines. *Journal of Propulsion and Power*, 18(1):68–76, 2008.

[11] Blaine R. Bigler, Eric J. Paulson, and William A. Hargus. Idealized efficiency calculations for rotating detonation engine rocket applications. *53rd AIAA/SAE/ASEE Joint Propulsion Conference, 2017*, (July):1–11, 2017.

[12] William A. Hargus, Stephen Alexander Schumaker, Eric J. Paulson, and Stephen A. Danczyk. Air Force Research Laboratory Rotating Detonation Rocket Engine Development. In *2018 Joint Propulsion Conference*, Reston, Virginia, 7 2018. American Institute of Aeronautics and Astronautics.

[13] Chung K. Law. *Combustion Physics*. Cambridge University Press, New York, 2006.

[14] Bulat Pavel Viktorovich. About the detonation engine. *American Journal of Applied Sciences*, 11(8):1357–1364, 2014.

[15] W. Mayer, A. Schik, C. Schweitzer, and M. Schäffler. Injection and mixing processes in high pressure LOX/GH2 rocket combustors. *32nd Joint Propulsion Conference and Exhibit*, (July), 1996.

[16] Shmuel Eidelman. Pulse detonation engine: A status review and technology development road map. In *33rd Joint Propulsion Conference and Exhibit*, 1997.

[17] Elaine S. Oran and Vadim N. Gamezo. Origins of the deflagration-to-detonation transition in gas-phase combustion. *Combustion and Flame*, 148(1-2):4–47, 2007.

[18] M. Mirzaei, M. J. Torkaman Asadi, and R. Akbari. On vibrational behavior of pulse detonation engine tubes. *Aerospace Science and Technology*, 47:177–190, 2015.

[19] K. Kailasanath. The rotating-detonation-wave engine concept: A brief status report. In *49th AIAA Aerospace Sciences Meeting Including the New Horizons Forum and Aerospace Exposition*, number January, 2011.

[20] Craig Nordeen. Thermodynamics of a Rotating Detonation Engine. *University of Connecticut Doctoral Dissertations*, page 201, 2013.

[21] Fedor A. Bykovskii, Sergey A. Zhdan, and Evgenii F. Vedernikov. Continuous Spin Detonations. *Journal of Propulsion and Power*, 22(6):1204–1216, 2006.

[22] P. Wolański. Detonation engines. *Journal of KONES Powertrain and Transport*, 18(3):515–521, 2011.

[23] Frank K. Lu and Eric M. Braun. Rotating Detonation Wave Propulsion: Experimental Challenges, Modeling, and Engine Concepts. *Journal of Propulsion and Power*, 30(5):1125–1142, 2014.

[24] Richard D. Smith and Steven B. Stanley. Experimental investigation of continuous detonation rocket engines for in-space propulsion. In *52nd AIAA/SAE/ASEE Joint Propulsion Conference, 2016*, pages 1–13, Reston, Virginia, 7 2016. American Institute of Aeronautics and Astronautics.

[25] Matthew L. Fotia, Fred Schauer, Tom Kaemming, and John Hoke. Experimental study of the performance of a rotating detonation engine with nozzle. *Journal of Propulsion and Power*, 32(3):674–681, 2016.

[26] Rui Zhou, Dan Wu, and Jianping Wang. Progress of continuously rotating detonation engines. *Chinese Journal of Aeronautics*, 29(1):15–29, 2016.

[27] Brent A. Rankin, Matthew L. Fotia, Andrew G. Naples, Christopher A. Stevens, John L. Hoke, Thomas A. Kaemming, Scott W. Theuerkauf, and Frederick R. Schauer. Overview of performance, application, and analysis of rotating detonation engine technologies. *Journal of Propulsion and Power*, 33(1):131–143, 2017.

[28] John W. Bennewitz, Blaine R. Bigler, William A. Hargus, Stephen A. Danczyk, and Richard D. Smith. Characterization of detonation wave propagation in a rotating detonation rocket engine using direct high-speed imaging. *2018 Joint Propulsion Conference*, pages 1–22, 2018.

[29] K. Kailasanath. Recent developments in the research on rotating-detonation-wave engines. *AIAA SciTech Forum - 55th AIAA Aerospace Sciences Meeting*, (January):1–24, 2017.

[30] Keith D. Rein, Sukesh Roy, Scott T. Sanders, Andrew W. Caswell, Frederick R. Schauer, and James R. Gord. Measurements of gas temperatures at 100 kHz within the annulus of a rotating detonation engine. *Applied Physics B*, 123(3):88, 3 2017.

[31] Jonathan Sosa, Robert Burke, Kareem A. Ahmed, Daniel J. Micka, John W. Bennewitz, Stephen A. Danczyk, Eric J. Paulson, and William A. Hargus. Experimental evidence of H2/O2 propellants powered rotating detonation waves. *Combustion and Flame*, 214:136–138, 2020.

[32] Eric Bach, Christian Oliver Paschereit, Panagiotis Stathopoulos, and Myles D. Bohon. An empirical model for stagnation pressure gain in rotating detonation combustors. *Proceedings of the Combustion Institute*, 000:1–8, 2020.

[33] Keisuke Goto, Junpei Nishimura, Akira Kawasaki, Ken Matsuoka, Jiro Kasahara, Akiko Matsuo, Ikkoh Funaki, Daisuke Nakata, Masaharu Uchiumi, and Kazuyuki Higashino. Propulsive Performance and Heating Environment of Rotating Detonation Engine with Various Nozzles. *Journal of Propulsion and Power*, 35(1):213–223, 1 2019.

[34] Akira Kawasaki, Tomoya Inakawa, Jiro Kasahara, Keisuke Goto, Ken Matsuoka, Akiko Matsuo, and Ikkoh Funaki. Critical condition of inner cylinder radius for sustaining rotating detonation waves in rotating detonation engine thruster. *Proceedings of the Combustion Institute*, 37(3):3461–3469, 2019.

[35] Keisuke Goto, Kosei Ota, Akira Kawasaki, Hiroaki Watanabe, Nobotu Itouyama, Ken Matsuoka, Jiro Kasahara, Akiko Matsuo, and Ikkoh Funaki. Cylindrical Rotating Detonation Engine Cooling by Means of Propellant Injection. In *AIAA Propulsion and Energy 2020 Forum*, Reston, Virginia, 8 2020. American Institute of Aeronautics and Astronautics.

[36] J. W. Bennewitz, B. R. Bigler, S. A. Schumaker, and W. A. Hargus. Automated Image Processing Method to Quantify Rotating Detonation Wave Behavior. *Review of Scientific Instruments*, 90(6), 2019.

[37] John W. Bennewitz, Blaine R. Bigler, Jessica J. Pilgram, and William A. Hargus. Modal Transitions in Rotating Detonation Rocket Engines. *International Journal of Energetic Materials and Chemical Propulsion*, 18(2):91–109, 2019.

[38] Blaine R. Bigler, John W. Bennewitz, Stephen A. Danczyk, and William A. Hargus. Rotating Detonation Rocket Engine Operability Under Varied Pressure Drop Injection. *Journal of Spacecraft and Rockets*, pages 1–10, 9 2020.

[39] Douglas Schwer, Andrew Corrigan, Brian Taylor, and Kailas Kailasanath. On Reducing Feedback Pressure in Rotating Detonation Engines. In *51st AIAA Aerospace Sciences Meeting including the New Horizons Forum and Aerospace Exposition*, Reston, Virigina, 1 2013. American Institute of Aeronautics and Astronautics.

[40] Douglas A. Schwer, Andrew Corrigan, and K. Kailasanath. Towards efficient, unsteady, three-dimensional rotating detonation engine simulations. *52nd Aerospace Sciences Meeting*, (January):1–18, 2014.

[41] Christopher F. Lietz, Nathan L. Mundis, S. Alexander Schumaker, and Venkateswaran Sankaran. Numerical investigation of rotating detonation rocket engines. *AIAA Aerospace Sciences Meeting, 2018*, (210059), 2018.

[42] Christopher Lietz, Yogin Desai, Ramakanth Munipalli, Stephen Alexander Schumaker, and Venke Sankaran. Flowfield analysis of a 3D simulation of a rotating detonation rocket engine. In *AIAA Scitech 2019 Forum*, number January, Reston, Virginia, 1 2019. American Institute of Aeronautics and Astronautics.

[43] S. M. Frolov, V. A. Smetanyuk, V. S. Ivanov, and B. Basara. The Influence of the Method of Supplying Fuel Components on the Characteristics of a Rotating Detonation Engine. *Combustion Science and Technology*, 193(3):511–538, 2 2021.

[44] Blaine R. Bigler, John W. Bennewitz, Stephen Alexander Schumaker, Stephen A. Danczyk, and William A. Hargus. Injector Alignment Study for Variable Mixing in Rotating Detonation Rocket Engines. In *AIAA Scitech 2019 Forum*, number 18889, Reston, Virginia, 1 2019. American Institute of Aeronautics and Astronautics.

[45] John Z. Ma, Shujie Zhang, Mingyi Luan, and Jianping Wang. Experimental investigation on delay time phenomenon in rotating detonation engine. *Aerospace Science and Technology*, 88:395–404, 2019.

[46] Blaine R. Bigler, Jason R. Burr, John W. Bennewitz, Stephen Danczyk, and William A. Hargus. Rotating Detonation Rocket Engine Scaling using Variable Annular Width Geometries. In *AIAA Propulsion and Energy 2021 ForumForum*, 2021.

[47] Ryuya Yokoo, Keisuke Goto, Juhoe Kim, Akira Kawasaki, Ken Matsuoka, Jiro Kasahara, Akiko Matsuo, and Ikkoh Funaki. Propulsion Performance of Cylindrical Rotating Detonation Engine. *AIAA Journal*, pages 1–10, 11 2019.

[48] Yuhui Wang and Jialing Le. A hollow combustor that intensifies rotating detonation. *Aerospace Science and Technology*, 85:113–124, 2019.

[49] Blaine R. Bigler, Jason R. Burr, John W. Bennewitz, Stephen Danczyk, and William A. Hargus. Performance Effects of Mode Transitions in a Rotating Detonation Rocket Engine. In *AIAA Propulsion and Energy 2020 Forum*, number 20327, Reston, Virginia, 8 2020. American Institute of Aeronautics and Astronautics.

[50] Fabian Chacon and Mirko Gamba. Study of Parasitic Combustion in an Optically Accessible Continuous Wave Rotating Detonation Engine. In *AIAA Scitech 2019 Forum*, number January, Reston, Virginia, 1 2019. American Institute of Aeronautics and Astronautics.

[51] Hao Yang Peng, Wei Dong Liu, Shi Jie Liu, Hai Long Zhang, and Si Yuan Huang. The competitive relationship between detonation and deflagration in the inner cylinder-variable continuous rotating detonation combustor. *Aerospace Science and Technology*, 107:106263, 2020.

[52] Jumpei Fujii, Yoshiki Kumazawa, Akiko Matsuo, Soma Nakagami, Ken Matsuoka, and Jiro Kasahara. Numerical investigation on detonation velocity in rotating detonation engine chamber. *Proceedings of the Combustion Institute*, 36(2):2665–2672, 2017.

[53] C. A. Nordeen, D. Schwer, F. Schauer, J. Hoke, T. Barber, and B. M. Cetegen. Role of Inlet Reactant Mixedness on the Thermodynamic Performance of a Rotating Detonation Engine. *Shock Waves*, 26(4):417–428, 2016.

[54] Blaine Bigler, John W. Bennewitz, Stephen A. Danczyk, and William A. Hargus. Injector Mixing Effects in Rotating Detonation Rocket Engines. In *AIAA Propulsion and Energy 2019 Forum*, number 19373, Reston, Virginia, 8 2019. American Institute of Aeronautics and Astronautics.

[55] H. F. Celebi, D. Lim, K. J. Dille, and S. D. Heister. Response of Angled and Tapered Liquid Injectors to Passing Detonation Fronts at High Operating Pressures. *Shock Waves*, 2021.

[56] Douglas A. Schwer and Kailas Kailasanath. Feedback into mixture plenums in rotating detonation engines. *50th AIAA Aerospace Sciences Meeting Including the New Horizons Forum and Aerospace Exposition*, (January):1–17, 2012.

[57] Chengwen Sun, Hongtao Zheng, Zhiming Li, Ningbo Zhao, Lei Qi, and Hongbo Guo. Effects of diverging nozzle downstream on flow field parameters of rotating detonation combustor. *Applied Sciences (Switzerland)*, 9(20), 2019.

[58] John W. Bennewitz, Blaine R. Bigler, Stephen A. Danczyk, William A. Hargus, and Richard D. Smith. Performance of a rotating detonation rocket engine with various convergent nozzles. *AIAA Propulsion and Energy Forum and Exposition, 2019*, (August):1–28, 2019.

[59] Yiyuan Zhu, Ke Wang, Zhicheng Wang, Minghao Zhao, Zhongtian Jiao, Yun Wang, and Wei Fan. Study on the Performance of a Rotating Detonation Chamber with Different Aerospike Nozzles. *Aerospace Science and Technology*, 107:106338, 2020.

[60] Alexis J. Harroun, Stephen D. Heister, and Joseph H. Ruf. Computational and Experimental Study of Nozzle Performance for Rotating Detonation Rocket Engines. *Journal of Propulsion and Power*, pages 1–14, 2021.

[61] James Braun, Jorge Sousa, and Guillermo Paniagua. Numerical assessment of the convective heat transfer in rotating detonation combustors using a reduced-order model. *Applied Sciences*, 8(6), 2018.

[62] Scott W. Theuerkauf, Frederick R. Schauer, Richard Anthony, Daniel E. Paxson, Christopher A. Stevens, and John L. Hoke. Comparison of simulated and measured instantaneous heat flux in a rotating detonation engine. *54th AIAA Aerospace Sciences Meeting*, (January), 2016.

[63] Wesly Anderson, Stephen D. Heister, and Carl Hartsfield. Experimental Study of a Hypergolically Ignited Liquid Bipropellant Rotating Detonation Rocket Engine. In *AIAA Scitech 2019 Forum*, number January, Reston, Virginia, 1 2019. American Institute of Aeronautics and Astronautics.

[64] Junpei Nishimura, Kazuki Ishihara, Keisuke Goto, Soma Nakagami, Ken Matsuoka, Jiro Kasahara, Akiko Matsuo, Ikkoh Funaki, Hiroto Mukae, Kazuki Yasuda, Daisuke Nakata, Kazuyuki Higashino, and Hideki Moriai. Performance Evaluation of a Rotating Detonation Engine for Space use. In *26th ICDERS*, Boston, MA, 2017.

[65] Kazuki Ishihara, Junpei Nishimura, Keisuke Goto, Soma Nakagami, Ken Matsuoka, Jiro Kasahara, Akiko Matsuo, Ikkoh Funaki, Hideki Moriai, Hiroto Mukae, Kazuki Yasuda, Daisuke Nakata, and Kazuyuki Higashino. Study on a long-time operation towards rotating detonation rocket engine flight demonstration. In *55th AIAA Aerospace Sciences Meeting*, number January, 2017.

[66] Kosei Ota, Keisuke Goto, Noboru Itouyama, Hiroaki Watanabe, Akira Kawasaki, Ken Matsuoka, Jiro Kasahara, Akiko Matsuo, and Ikkoh Funaki. Study of Cylindrical Rotating Detonation Engine with Propellant Injection Cooling System. In *AIAA Propulsion and Energy 2021 Forum*, Reston, Virginia, 8 2021. American Institute of Aeronautics and Astronautics.

[67] Thomas A Kaemming and Daniel E Paxson. Determining the Pressure Gain of Pressure Gain Combustion. In *2018 Join Propulsion Conference*, pages 1–15, 2018.

[68] Kyle Schwinn, Brandon Kan, Swanand Sardeshmukh, Rohan Gejji, Stephen Heister, and Carson D. Slabaugh. Self-excited, Multi-kHz dynamics in a linear, semi-bounded detonation channel. In *55th AIAA Aerospace Sciences Meeting*, number January, 2017.

[69] F. A. Bykovskii, S. A. Zhdan, E. F. Vedernikov, A. N. Samsonov, A. I. Sychev, and A. E. Tarnaikin. Pressure measurement by fast-response piezo-electric sensors during continuous spin detonation in the combustor. *Combustion, Explosion and Shock Waves*, 53(1):65–73, 2017.

[70] Christopher A. Stevens, Matthew Fotia, John Hoke, and Frederick Schauer. Comparison of Transient Response of Pressure Measurement Techniques with Application to Detonation Waves. In *53rd AIAA Aerospace Sciences Meeting*, Reston, Virginia, 1 2015. American Institute of Aeronautics and Astronautics.

[71] Rohan Gejji, Ian Walters, Sarah Beard, Aaron Lemcherfi, Swanand Sardeshmukh, Stephen Heister, and Carson Slabaugh. Transducer installation effects on pressure measurements in pressure gain combustion devices. In *AIAA Aerospace Sciences Meeting, 2018*, number 210059, pages 1–12, Kissimmee, FL, 2018.

[72] Keisuke Goto, Junpei Nishimura, Akira Kawasaki, Ken Matsuoka, Jiro Kasahara, Akiko Matsuo, Ikkoh Funaki, Daisuke Nakata, Masaharu Uchiumi, and Kazuyuki Higashino. Propulsive Performance and Heating Environment of Rotating Detonation Engine with Various Nozzles. *Journal of Propulsion and Power*, 35(1):213–223, 2019.

[73] Soma Nakagami, Ken Matsuoka, Jiro Kasahara, Yoshiki Kumazawa, Jumpei Fujii, Akiko Matsuo, and Ikkoh Funaki. Experimental visualization of the structure of rotating detonation waves in a disk-shaped combustor. *Journal of Propulsion and Power*, 33(1):80–88, 2017.

[74] Ryuya Yokoo, Keisuke Goto, Jiro Kasahara, Venkat Athmanathan, James Braun, Guillermo Paniagua, Terrence R. Meyer, Akira Kawasaki, Ken Matsuoka, Akiko Matsuo, and Ikkoh Funaki. Experimental study of internal flow structures in cylindrical rotating detonation engines. *Proceedings of the Combustion Institute*, 38(3):3759–3768, 2021.

[75] Brent A. Rankin, Daniel R. Richardson, Andrew W. Caswell, Andrew Naples, John L. Hoke, and Frederick R. Schauer. Imaging of OH* chemiluminescence in an optically accessible nonpremixed rotating detonation engine. In *53rd AIAA Aerospace Sciences Meeting*, number January, 2015.

[76] Jonathan Tobias, Daniel Depperschmidt, Cooper Welch, Robert Miller, Mruthunjaya Uddi, Ajay K. Agrawal, and Ron Daniel. OH chemiluminescence imaging of the combustion products from a methane-fueled rotating detonation engine. *Journal of Engineering for Gas Turbines and Power*, 141(2):1–11, 2019.

[77] A C Eckbreth. Laser Diagnostics for Temperature and Species in Unsteady Combustion. In *Unsteady Combustion*, pages 393–410. Springer Netherlands, Dordrecht, 1996.

[78] Brent A. Rankin, Christopher A. Fugger, Daniel R. Richardson, Kevin Y. Cho, John L. Hoke, Andrew W. Caswell, James R. Gord, and Frederick R. Schauer. Evaluation of mixing processes in a non-premixed rotating detonation engine using acetone PLIF imaging. In *54th AIAA Aerospace Sciences Meeting*, volume 0, 2016.

[79] James Duvall and Mirko Gamba. Characterization of reactant mixing in a rotating detonation engine using schlieren imaging and planar laser induced fluorescence. In *2018 Joint Propulsion Conference*, 2018.

[80] Clinton Bedick, Don Ferguson, and Peter Strakey. Characterization of rotating detonation engine injector response using laser-induced fluorescence. *Journal of Propulsion and Power*, 35(4):827–838, 2019.

[81] Paul S. Hsu, Mikhail N. Slipchenko, Naibo Jiang, Christopher A. Fugger, Austin M. Webb, Venkat Athmanathan, Terrence R. Meyer, and Sukesh Roy. Megahertz-rate OH planar laser-induced fluorescence imaging in a rotating detonation combustor. *Optics Letters*, 45(20):5776, 2020.

[82] Daniel L. Depperschmidt, Jonathan R. Tobias, Robert S. Miller, Mruthunjaya Uddi, Ajay K. Agrawal, and Jeffery B. Stout. Time-resolved piv diagnostics to measure flow field exiting methane-fueled rotating detonation combustor. In *AIAA Scitech 2019 Forum*, number January, 2019.

[83] Christopher L. Journell, Rohan M. Gejji, Ian V. Walters, Aaron I. Lemcherfi, Carson D. Slabaugh, and Jeffrey B. Stout. High-speed diagnostics in a natural gas–air rotating detonation engine. *Journal of Propulsion and Power*, 36(4):498–507, 2020.

[84] Ian V. Walters, Rohan M. Gejji, Stephen D. Heister, and Carson D. Slabaugh. Flow and performance analysis of a natural gas-air rotating detonation engine with high-speed velocimetry. *Combustion and Flame*, 232:111549, 2021.

[85] Jonathan Tobias and Ajay K. Agrawal. Time Resolved Flow Field in the Radial Plane of an Aerospike Integrated with a Rotating Detonation Combustor. In *AIAA Propulsion and Energy 2021 Forum*, 2021.

[86] Venkat Athmanathan, K. Arafat Rahman, Daniel K. Lauriola, James Braun, Guillermo Paniagua, Mikhail N. Slipchenko, Sukesh Roy, and Terrence R. Meyer. Femtosecond/picosecond rotational coherent anti-Stokes Raman scattering thermometry in the exhaust of a rotating detonation combustor. *Combustion and Flame*, 231:111504, 2021.

[87] Wen Yu Peng, Séan J. Cassady, Christopher L. Strand, Christopher S. Goldenstein, R. Mitchell Spearrin, Christopher M. Brophy, Jay B. Jeffries, and Ronald K. Hanson. Single-ended mid-infrared laser-absorption sensor for time-resolved measurements of water concentration and temperature within the annulus of a rotating detonation engine. *Proceedings of the Combustion Institute*, 37(2):1435–1443, 2019.

[88] Christopher S. Goldenstein, R. Mitchell Spearrin, Jay B. Jeffries, and Ronald K. Hanson. Infrared laser absorption sensors for multiple performance parameters in a detonation combustor. *Proceedings of the Combustion Institute*, 35(3):3739–3747, 2015.

[89] R. M. Spearrin, C. S. Goldenstein, J. B. Jeffries, and R. K. Hanson. Quantum cascade laser absorption sensor for carbon monoxide in high-pressure gases using wavelength modulation spectroscopy. *Applied Optics*, 53(9):1938, 3 2014.

[90] R. M. Spearrin, C. S. Goldenstein, J. B. Jeffries, and R. K. Hanson. Mid-infrared Laser Absorption Diagnostics for Detonation Studies. In *29th International Symposium on Shock Waves 1*, pages 259–264. Springer International Publishing, Cham, 2015.

[91] Scott T. Sanders, Jeffrey A. Baldwin, Thomas P. Jenkins, Douglas S. Baer, and Ronald K. Hanson. Diode-laser sensor for monitoring multiple combustion parameters in pulse detonation engines. *Proceedings of the Combustion Institute*, 28(1):587–594, 2000.

[92] Andrew W. Caswell, Sukesh Roy, Xinliang An, Scott T. Sanders, Frederick R. Schauer, and James R. Gord. Measurements of multiple gas parameters in a pulsed-detonation combustor using timedivision-multiplexed Fourier-domain mode-locked lasers. *Applied Optics*, 52(12):2893–2904, 2013.

[93] Christopher S. Goldenstein, Christopher A. Almodóvar, Jay B. Jeffries, Ronald K. Hanson, and Christopher M. Brophy. High-bandwidth scanned-wavelength-modulation spectroscopy sensors for temperature and H2O in a rotating detonation engine. *Measurement Science and Technology*, 25(10):105104, 10 2014.

[94] Séan J. Cassady, Wen Yu Peng, Christopher L. Strand, Jay B. Jeffries, Ronald K. Hanson, David F. Dausen, and Christopher M. Brophy. A single-ended, mid-IR sensor for time-resolved temperature and species measurements in a hydrogen/ethylene-fueled rotating detonation engine. *AIAA Scitech 2019 Forum*, (January), 2019.

[95] R. M. Spearrin, C. S. Goldenstein, J. B. Jeffries, and R. K. Hanson. Fiber-coupled 2.7 µm laser absorption sensor for CO2 in harsh combustion environments. *Measurement Science and Technology*, 24(5):055107, 5 2013.

[96] L. Ma, S. T. Sanders, J. B. Jeffries, and R. K. Hanson. Monitoring and control of a pulse detonation engine using a diode-laser fuel concentration and temperature sensor. *Proceedings of the Combustion Institute*, 29(1):161–166, 2002.

[97] Adam E. Klingbeil, Jay B. Jeffries, and Ronald K. Hanson. Design of a fiber-coupled mid-infrared fuel sensor for pulse detonation engines. *AIAA Journal*, 45(4):772–778, 2007.

[98] Anil P. Nair, Alex R. Keller, David S. Morrow, Alexander B. Lima, R. Mitchell Spearrin, and Daniel I. Pineda. Hypergolic Continuous Detonation with Space-Storable Propellants and Additively Manufactured Injector Design. *Journal of Spacecraft and Rockets*, 59(4):1332–1341, 7 2022.

[99] Anil P. Nair, Alex R. Keller, Nicolas Q. Minesi, Daniel I. Pineda, and R. Mitchell Spearrin. Detonation cell size of liquid hypergolic propellants: Estimation from a non-premixed combustor. *Proceedings of the Combustion Institute*, 7 2022.

[100] Anil P. Nair, David Morrow, Alex R. Keller, Alexander Lima, Daniel I. Pineda, and R. Mitchell Spearrin. Rotating Detonation of Hypergolic Space-Storable Rocket Propellants with Additively-Manufactured Injector Design. In *AIAA Propulsion and Energy 2021 Forum*, Reston, Virginia, 8 2021. American Institute of Aeronautics and Astronautics.

[101] Anil P Nair, Alex R Keller, Alexander B Lima, and R Mitchell Spearrin. Deflagration-to-detonation transition in an annular combustor with hypergolic propellants. In *AIAA SciTech 2022 Forum*, 2022.

[102] Wesly S. Anderson, Stephen D. Heister, Brandon Kan, and Carl Hartsfield. Experimental Study of a Hypergolically Ignited Liquid Bipropellant Rotating Detonation Rocket Engine. *Journal of Propulsion and Power*, 36(6), 11 2020.

[103] Shuaijie Xue, Hongjun Liu, Lixin Zhou, Weidong Yang, Hongbo Hu, and Yu Yan. Experimental Research on Rotating Detonation with Liquid Hypergolic Propellants. *Chinese Journal of Aeronautics*, 31(12):2199–2205, 2018.

[104] Shuaijie Xue, Weidong Yang, Lixin Zhou, and Hongjun Liu. Experimental Investigation of Self-Excited Combustion Instabilities in a Small Earth Storable Bipropellant Rocket Combustor. *Aerospace Science and Technology*, 105:106008, 2020.

[105] Wesly S. Anderson and Stephen D. Heister. Response of a Liquid Jet in a Multiple-Detonation Driven Crossflow. *Journal of Propulsion and Power*, 35(2):303–312, 2019.

[106] Kosei Ota, Keisuke Goto, Noboru Itouyama, Hiroaki Watanabe, Akira Kawasaki, Ken Matsuoka, Jiro Kasahara, Akiko Matsuo, and Ikkoh Funaki. Study of Cylindrical Rotating Detonation Engine with Propellant Injection Cooling System. In *AIAA Propulsion and Energy 2021 Forum*, Reston, Virginia, 8 2021. American Institute of Aeronautics and Astronautics.

[107] William Anderson, Matthew Long, and Stephen Heister. Liquid Bipropellant Injectors. In *Liquid Rocket Thrust Chambers*, Progress in Astronautics and Aeronautics, pages 141–165. American Institute of Aeronautics and Astronautics, 1 2004.

[108] Richard D. Smith and Steven B. Stanley. Experimental Investigation of Rotating Detonation Rocket Engines for Space Propulsion. *Journal of Propulsion and Power*, 37(3):1–11, 2021.

[109] Shengbing Zhou, Hu Ma, Sihe Chen, Yepan Zhong, and Changsheng Zhou. Experimental investigation on propagation characteristics of rotating detonation wave with a hydrogen-ethylene-acetylene fuel. *Acta Astronautica*, 157(January):310–320, 2019.

[110] Bo Zhang, Hoi Dick Ng, and John H.S. Lee. Measurement and relationship between critical tube diameter and critical energy for direct blast initiation of gaseous detonations. *Journal of Loss Prevention in the Process Industries*, 26(6):1293–1299, 2013.

[111] Go Fujii, Yu Daimon, Chihiro Inoue, Daijiro Shiraiwa, Nobuhiko Tanaka, and Katsumi Furukawa. Visualization of pulse firing mode in hypergolic bipropellant thruster. *Journal of Propulsion and Power*, 36(5):671–684, 2020.

[112] Gerald W. Smith and Richard H. Sforzini. Pulse performance analysis for small hypergolic-propellant rocket engines. *Journal of Spacecraft and Rockets*, 9(9):627–628, 1972.

[113] Anil P. Nair, Daniel D. Lee, Daniel I. Pineda, Jason Kriesel, William A. Hargus, John W. Bennewitz, Blaine Bigler, Stephen A. Danczyk, and R. Mitchell Spearrin. Methane-Oxygen Rotating Detonation Exhaust Thermodynamics with Variable Mixing, Equivalence Ratio, and Mass Flux. *Aerospace Science and Technology*, 113:106683, 2021.

[114] Nan Zong and Vigor Yang. Supercritical Fluid Dynamics of Pressure Swirl Injector with External Excitations. In *43rd AIAA/ASME/SAE/ASEE Joint Propulsion Conference & Exhibit*, Reston, Virigina, 7 2007. American Institute of Aeronautics and Astronautics.

[115] Paul R Gradl, Sandy E Greene, Christopher Protz, Brad Bullard, James Buzzell, Chance Garcia, Jessica Wood, Robin Osborne, James Hulka, and Kenneth G Cooper. Additive Manufacturing of Liquid Rocket Engine Combustion Devices: A Summary of Process Developments and Hot-Fire Testing Results. In *2018 Joint Propulsion Conference*, AIAA Propulsion and Energy Forum, Reston, Virginia, 7 2018. American Institute of Aeronautics and Astronautics.

[116] Thomas W. Teasley, Christopher S. Protz, Andrew P. Larkey, Benjamin B. Williams, and Paul R. Gradl. A Review Towards the Design Optimization of High Performance Additively Manufactured Rotating Detonation Rocket Engine Injectors. In *AIAA Propulsion and Energy 2021 Forum*, Reston, Virginia, 8 2021. American Institute of Aeronautics and Astronautics.

[117] Milan Dana, Ivana Zetkova, Pavel Hanzl, and Ondrej Hronek. Accuracy of Holes Created by 3D Printing (DMLS). In *28th DAAAM International Symposium on Intelligent Manufacturing and Automation*, Vienna, Austria, 2017.

[118] G. Taubin. Estimation of Planar Curves, Surfaces, and Nonplanar Space Curves Defined by Implicit Equations with Applications to Edge and Range Image Segmentation. *IEEE Transactions on Pattern Analysis and Machine Intelligence*, 13(11):1115–1138, 1991.

[119] R. Bluemner, M. D. Bohon, C. O. Paschereit, and E. J. Gutmark. Counter-Rotating Wave Mode Transition Dynamics in an RDC. *International Journal of Hydrogen Energy*, 44(14):7628–7641, 2019.

[120] Mathias Ross, Christopher Lietz, Yogin Desai, Jason Hamilton, and William A. Hargus. Constriction-Induced Counter-Propagating Behavior in RDREs. In *AIAA Propulsion and Energy 2020 Forum*, Reston, Virginia, 8 2020. American Institute of Aeronautics and Astronautics.

[121] Lingyun Hou, Pengfei Fu, and Yantao Ba. Chemical Mechanism of MMH/NTO and Simulation in a Small Liquid Rocket Engine. *Combustion Science and Technology*, 191(12):2208–2225, 2019.

[122] M. A. Liberman, M. F. Ivanov, A. D. Kiverin, M. S. Kuznetsov, A. A. Chukalovsky, and T. V. Rakhimova. Deflagration-to-detonation transition in highly reactive combustible mixtures. *Acta Astronautica*, 67(7-8):688–701, 2010.

[123] Prankul Middha and Olav Hansen. ddt.pdf. *Process Safety Progress*, 27(3):192–204, 2007.

[124] K. Kailasanath, E. S. Oran, J. P. Boris, and T. R. Young. Determination of detonation cell size and the role of transverse waves in two-dimensional detonations. *Combustion and Flame*, 61(3):199–209, 1985.

[125] John H.S. Lee. *The Detonation Phenomenon*. Cambridge University Press, 2008.

[126] Michael Kaneshige and Joseph E. Shepherd. Detonation Database. Technical Report July, 1997.

[127] Ganbing Yao, Bo Zhang, Guangli Xiu, Chunhua Bai, and Peipei Liu. The critical energy of direct initiation and detonation cell size in liquid hydrocarbon fuel/air mixtures. *Fuel*, 113:331–339, 2013.

[128] John H.S. Lee. Dynamic Parameters of Gaseous Detonations. *Annual Review of Fluid Mechanics*, 16:311–336, 1984.

[129] F. Pintgen, C. A. Eckett, J. M. Austin, and J. E. Shepherd. Direct observations of reaction zone structure in propagating detonations. *Combustion and Flame*, 133(3):211–229, 2003.

[130] Mark Kellenberger and Gaby Ciccarelli. Simultaneous schlieren photography and soot foil in the study of detonation phenomena. *Experiments in Fluids*, 58(10):1–13, 2017.

[131] Jackson Crane, Xian Shi, Ajay V. Singh, Yujie Tao, and Hai Wang. Isolating the effect of induction length on detonation structure: Hydrogen–oxygen detonation promoted by ozone. *Combustion and Flame*, 200:44–52, 2019.

[132] Mick Carter and David L Blunck. Direct Comparison of Schlieren and Soot Foil Measurements of Detonation Cell Sizes. *Frontiers in Aerospace Engineering*, 1(June):1–11, 2022.

[133] L. Catoire, X. Bassin, G. Dupre, and C. Paillard. Shock tube study of ignition delays and detonation of gaseous monomethylhydrazine/oxygen mixtures. *Combustion and Flame*, 99(3-4):573–580, 1994.

[134] Armani Batista, Mathias C. Ross, Christopher Lietz, and William A. Hargus. Descending modal transition dynamics in a large eddy simulation of a rotating detonation rocket engine. *Energies*, 14(12):1–22, 2021.

[135] Piotr Wolanski. Rotating Detonation Wave Stability. In *23rd International Colloquium on the Dynamics of Explosions and Reactive Systems (ICDERS)*, pages 1–6, 2011.

[136] Renaud Lecourt and François Xavier D'Herbigny. MMH/NTO injection and ignition in vacuum downstream from an Aestus engine single injection element. *Aerospace Science and Technology*, 8(3):207–217, 2004.

[137] Xixuan Huang and Zhiyong Lin. Analysis of coupled-waves structure and propagation characteristics in hydrogen-assisted kerosene-air two-phase rotating detonation wave. *International Journal of Hydrogen Energy*, 47(7):4868–4884, 2022.

[138] S. A. Gubin and M. Sichel. Calculation of the detonation velocity of a mixture of liquid fuel droplets and a gaseous oxidizer. *Combustion Science and Technology*, 17(3-4):109–117, 1977.

[139] K. Kailasanath. Liquid-fueled detonations in tubes. *Journal of Propulsion and Power*, 22(6):1261–1268, 2006.

[140] S Alexander Schumaker, Andrew M Knisely, John L Hoke, and Keith D Rein. Methane – oxygen detonation characteristics at elevated pre-detonation pressures. *Proceedings of the Combustion Institute*, 000:1–10, 2020.

[141] S. Browne, J. Ziegler, and J. E. Shepherd. Numerical Solution Methods for Shock and Detonation Jump Conditions. *GALCIT Report FM2006.006*, 2004.

[142] David G. Goodwin, Harry K. Moffat, and Raymond L. Speth. Cantera: An object-oriented software toolkit for chemical kinetics, thermodynamics, and transport processes, 2018.

[143] J. E. Shepherd. Detonation in gases. *Proceedings of the Combustion Institute*, 32 I(1):83–98, 2009.

[144] Gregory P. Smith, David M. Golden, Michael Frenklach, Nigel W. Moriarty, Boris Eiteneer, Mikhail Goldenberg, C. Thomas Bowman, Ronald K. Hanson, Soonho Song, William C. Gardiner, Vitali V. Lissianski, and Zhiwei Qin. GRI-MECH 3.0, 1999.

[145] William R Anderson, Michael J McQuaid, Michael J Nusca, and Anthony J Kotlar. A Detailed , Finite-Rate , Chemical Kinetics Mechanism for Monomethylhydrazine-Red Fuming Nitric Acid Systems. Technical Report ARL-TR-5088, Army Research Laboratory, Aberdeen Proving Ground, MD, 2010.

[146] A. A. Vasil'ev. Cell size as the main geometric parameter of a multifront detonation wave. *Journal of Propulsion and Power*, 22(6):1245–1260, 2006.

[147] A. I. Gavrikov, A. A. Efimenko, and S. B. Dorofeev. A model for detonation cell size prediction from chemical kinetics. *Combustion and Flame*, 120(1-2):19–33, 2000.

[148] A.P. Nair, D.D. Lee, D.I. Pineda, J. Kriesel, W.A. Hargus, J.W. Bennewitz, S.A. Danczyk, and R.M. Spearrin. MHz laser absorption spectroscopy via diplexed RF modulation for pressure, temperature, and species in rotating detonation rocket flows. *Applied Physics B*, 126(8):138, 8 2020.

[149] Anil P. Nair, Christopher Jelloian, David S. Morrow, Fabio A. Bendana, Daniel I. Pineda, and Raymond Mitchell Spearrin. MHz mid-infrared laser absorption sensor for carbon monoxide and temperature behind detonation waves. In *AIAA Scitech 2020 Forum*, Reston, Virginia, 1 2020. American Institute of Aeronautics and Astronautics.

[150] A.P. Nair, D. Lee, D.I. Pineda, R.M. Spearrin, J. Krisel, W.A. Hargus, J.W. Bennewitz, and S. Danczyk. MHz Mid-infrared Laser Absorption of CO and CO 2 for Pressure, Temperature, and Species in Rotating Detonation Rocket Flows. In *AIAA Propulsion and Energy 2020 Forum*. American Institute of Aeronautics and Astronautics, 8 2020.

[151] Daniel D. Lee, Fabio A. Bendana, S. Alexander Schumaker, and R. Mitchell Spearrin. Wavelength modulation spectroscopy near 5 μm for carbon monoxide sensing in a high-pressure kerosene-fueled liquid rocket combustor. *Applied Physics B*, 124(5):77, 5 2018.

[152] M. Lackner, G. Totschnig, F. Winter, M. Ortsiefer, M. C. Amann, R. Shau, and J. Rosskopf. Demonstration of methane spectroscopy using a vertical-cavity surface-emitting laser at 1.68 μm with up to 5 MHz repetition rate. *Measurement Science and Technology*, 14(1):101–106, 2003.

[153] Megan E. MacDonald, Aaron M. Brandis, and Brett A. Cruden. Temperature and CO Number Density Measurements in Shocked CO and CO2 via Tunable Diode Laser Absorption Spectroscopy. In *2018 Joint Thermophysics and Heat Transfer Conference*, pages 1–23, Reston, Virginia, 6 2018. American Institute of Aeronautics and Astronautics.

[154] Benjamin D Kaebe, Nickolas P. Robins, Toby K. Boyson, Harald Kleine, and Sean O'Byrne. 16 MHz scanning rate direct absorption temperature measurements using a single vertical-cavity surface-emitting laser diode. *Applied Optics*, 57(20):5680, 2018.

[155] Mohsin Raza, Liuhao Ma, Chenyu Yao, Min Yang, Zhen Wang, Qiang Wang, Ruifeng Kan, and Wei Ren. MHz-rate scanned-wavelength direct absorption spectroscopy using a distributed feedback diode laser at 2.3 µm. *Optics & Laser Technology*, 130(May):106344, 2020.

[156] Garrett C. Mathews, Matthew G. Blaisdell, Aaron I. Lemcherfi, Carson D. Slabaugh, and Christopher S. Goldenstein. High-bandwidth absorption-spectroscopy measurements of temperature, pressure, CO, and H 2 O in the annulus of a rotating detonation rocket engine. *Applied Physics B: Lasers and Optics*, 127(12):1–23, 2021.

[157] Christopher C. Jelloian, Fabio A. Bendana, Chuyu Wei, R. Mitchell Spearrin, and Megan E. Macdonald. Nonequilibrium Vibrational, Rotational, and Translational Thermometry via Megahertz Laser Absorption of CO. *Journal of Thermophysics and Heat Transfer*, 36(2):266–275, 2022.

[158] Garrett Mathews and Christopher Goldenstein. Near-GHz scanned-wavelength-modulation spectroscopy for MHz thermometry and H 2 O measurements in aluminized

fireballs of energetic materials. *Applied Physics B: Lasers and Optics*, 126(11):1–17, 2020.

[159] C.S. Goldenstein, R.M. Spearrin, J.B. Jeffries, and R.K. Hanson. Infrared laser-absorption sensing for combustion gases. *Progress in Energy and Combustion Science*, 60:132–176, 5 2017.

[160] Arroyo Instruments. 6300 Series ComboSource User's Manual, 2015.

[161] Garrett C. Mathews and Christopher S. Goldenstein. Wavelength-Modulation Spectroscopy for MHz Thermometry and H2O Sensing in Combustion Gases of Energetic Materials. In *AIAA Scitech 2019 Forum*, pages 1–8, Reston, Virginia, 1 2019. American Institute of Aeronautics and Astronautics.

[162] Borislav Hinkov, Andreas Hugi, Mattias Beck, and Jérôme Faist. Rf-modulation of mid-infrared distributed feedback quantum cascade lasers. *Optics Express*, 24(4):3294, 2016.

[163] Robin S.M. Chrystie, Ehson F. Nasir, and Aamir Farooq. Towards simultaneous calibration-free and ultra-fast sensing of temperature and species in the intrapulse mode. *Proceedings of the Combustion Institute*, 35(3):3757–3764, 2015.

[164] R.M. Spearrin, S. Li, D.F. Davidson, J.B. Jeffries, and R.K. Hanson. High-temperature iso-butene absorption diagnostic for shock tube kinetics using a pulsed quantum cascade laser near 11.3 μm. *Proceedings of the Combustion Institute*, 35(3):3645–3651, 2015.

[165] Daniel I. Pineda, Fabio A. Bendana, Kevin K. Schwarm, and R. Mitchell Spearrin. Multi-isotopologue laser absorption spectroscopy of carbon monoxide for high-temperature chemical kinetic studies of fuel mixtures. *Combustion and Flame*, 207:379–390, 9 2019.

[166] R.K. Hanson, R.M. Spearrin, and C.S. Goldenstein. *Spectroscopy and Optical Diagnostics for Gases*. Springer International Publishing, 2016.

[167] Christopher S. Goldenstein, Ian A. Schultz, Jay B. Jeffries, and Ronald K. Hanson. Two-color absorption spectroscopy strategy for measuring the column density and path average temperature of the absorbing species in nonuniform gases. *Applied Optics*, 52(33):7950–7962, 2013.

[168] L.S. Rothman, I.E. Gordon, R.J. Barber, H. Dothe, R.R. Gamache, A. Goldman, V.I. Perevalov, S.A. Tashkun, and J. Tennyson. HITEMP, the High-Temperature Molecular Spectroscopic Database. *Journal of Quantitative Spectroscopy and Radiative Transfer*, 111(15):2139–2150, 10 2010.

[169] Fabio A. Bendana, Daniel D. Lee, Chuyu Wei, Daniel I. Pineda, and R. Mitchell Spearrin. Line mixing and broadening in the v(1→3) first overtone bandhead of carbon monoxide at high temperatures and high pressures. *Journal of Quantitative Spectroscopy and Radiative Transfer*, 239:106636, 12 2019.

[170] A.B. McLean, C.E.J. Mitchell, and D.M. Swanston. Implementation of an efficient analytical approximation to the Voigt function for photoemission lineshape analysis. *Journal of Electron Spectroscopy and Related Phenomena*, 69(2):125–132, 9 1994.

[171] J. M. Hartmann, L. Rosenmann, M. Y. Perrin, and J. Taine. Accurate calculated tabulations of CO line broadening by H2O, N2, O2, and CO2 in the 200–3000-K temperature range. *Applied Optics*, 27(15):3063, 8 1988.

[172] Ritobrata Sur, Kai Sun, Jay B. Jeffries, and Ronald K. Hanson. Multi-species laser absorption sensors for in situ monitoring of syngas composition. *Applied Physics B*, 115(1):9–24, 4 2014.

[173] SI Sandler and JK Wheatley. Intermolecular potential parameter combining rules for the Lennard-Jones 6–12 potential. *Chemical Physics Letters*, 10(4):375–378, 8 1971.

[174] D. R. Eaton and F. R. S. Thompson. Pressure broadening studies on vibration-rotation bands II. The effective collision diameters. *Proceedings of the Royal Society of London. Series A. Mathematical and Physical Sciences*, 251(1267):475–485, 6 1959.

[175] Ahren W. Jasper and James A. Miller. Lennard-Jones parameters for combustion and chemical kinetics modeling from full-dimensional intermolecular potentials. *Combustion and Flame*, 161(1):101–110, 2014.

[176] Jean Michel Hartmann, Christian Boulet, and Daniel Robert. *Collisional Effects on Molecular Spectra*. Elsevier, 2008.

[177] Fabio A Bendana, Daniel D Lee, S Alexander Schumaker, Stephen A Danczyk, and R. Mitchell Spearrin. Cross-band infrared laser absorption of carbon monoxide for thermometry and species sensing in high-pressure rocket flows. *Applied Physics B*, 125(11):204, 11 2019.

[178] Daniel D. Lee, Fabio A. Bendana, Anil P. Nair, Daniel I. Pineda, and R. Mitchell Spearrin. Line mixing and broadening of carbon dioxide by argon in the v3 band-head near 4.2 µm at high temperatures and high pressures. *Journal of Quantitative Spectroscopy and Radiative Transfer*, 253:107135, 9 2020.

[179] L. Rosenmann, J. M. Hartmann, M. Y. Perrin, and J. Taine. Accurate calculated tabulations of IR and Raman CO_2 line broadening by CO_2, H_2O, N_2, O_2 in the 300–2400-K temperature range. *Applied Optics*, 27(18):3902, 9 1988.

[180] Peter A. Strakey and Donald H. Ferguson. Validation of a Computational Fluid Dynamics Model of a Methane-Oxygen Rotating Detonation Engine. *AIAA Science and Technology Forum and Exposition, AIAA SciTech Forum 2022*, 2022.

[181] Séan J. Cassady, Wen Yu Peng, Christopher L. Strand, David F. Dausen, Joshua R. Codoni, Christopher M. Brophy, and Ronald K. Hanson. Time-resolved, single-ended laser absorption thermometry and H2O, CO2, and CO speciation in a H2/C2H4-fueled rotating detonation engine. *Proceedings of the Combustion Institute*, 21(10), 10 2020.

[182] Jan Kindracki. Experimental research on rotating detonation in liquid fuel-gaseous air mixtures. *Aerospace Science and Technology*, 43:445–453, 2015.

[183] Zhicheng Wang, Ke Wang, Qingan Li, Yiyuan Zhu, Minghao Zhao, and Wei Fan. Effects of the combustor width on propagation characteristics of rotating detonation waves. *Aerospace Science and Technology*, 105:106038, 2020.

[184] Joseph E Shepherd and Jiro Kasahara. Analytical Models for the Thrust of a Rotating Detonation Engine. *GALCIT Report FM2017.001*, 2017.

[185] Victor P. Zhukov. The impact of methane oxidation kinetics on a rocket nozzle flow. *Acta Astronautica*, 161(December 2018):524–530, 2019.

[186] Daniel I. Pineda, Fabio A. Bendana, and R. M. Spearrin. Competitive oxidation of methane and C2 hydrocarbons discerned by isotopic labeling and laser absorption spectroscopy of CO isotopologues in shock-heated mixtures. *Combustion and Flame*, 224:54–65, 2 2021.

[187] Piotr Wolański. Detonative Propulsion. *Proceedings of the Combustion Institute*, 34(1):125–158, 2013.

[188] Douglas Schwer and K. Kailasanath. Fluid dynamics of rotating detonation engines with hydrogen and hydrocarbon fuels. *Proceedings of the Combustion Institute*, 34(2):1991–1998, 2013.

[189] Anil Pradeep Nair, Nicolas Q Minesi, Christopher Jelloian, Nicholas M Kuenning, and R Mitchell Spearrin. Extended tuning of distributed-feedback lasers in a bias-tee circuit via waveform optimization for MHz-rate absorption spectroscopy. *Measurement Science and Technology*, 33(10):105104, 10 2022.

[190] Anil P. Nair, Nicolas Q. Minesi, Christopher Jelloian, Nicholas M. Kuenning, and R. Mitchell Spearrin. RF-waveform optimization for MHz-rate DFB laser absorption spectroscopy in dynamic combustion environments. *AIAA Science and Technology Forum and Exposition, AIAA SciTech Forum 2022*, pages 1–13, 2022.

[191] Wolfgang Zeller, Lars Naehle, Peter Fuchs, Florian Gerschuetz, Lars Hildebrandt, and Johannes Koeth. DFB lasers between 760 nm and 16 μm for sensing applications. *Sensors*, 10(4):2492–2510, 2010.

[192] L. Tombez, S. Schilt, J. Di Francesco, T. Führer, B. Rein, T. Walther, G. Di Domenico, D. Hofstetter, and P. Thomann. Linewidth of a quantum-cascade laser assessed from its frequency noise spectrum and impact of the current driver. *Applied Physics B: Lasers and Optics*, 109(3):407–414, 2012.

[193] Nursidik Yulianto, Bambang Widiyatmoko, and Purnomo Sidi Priambodo. Temperature Effect towards DFB Laser Wavelength on Microwave Generation Based on Two Optical Wave Mixing. *International Journal of Optoelectronic Engineering*, 5(2):21–27, 2015.

[194] R.M. Spearrin, C.S. Goldenstein, I.A. Schultz, J.B. Jeffries, and R.K. Hanson. Simultaneous sensing of temperature, CO, and CO2 in a scramjet combustor using quantum cascade laser absorption spectroscopy. *Applied Physics B: Lasers and Optics*, 117(2):689–698, 11 2014.

[195] E. Normand, M. McCulloch, G. Duxbury, and N. Langford. Fast, real-time spectrometer based on a pulsed quantum-cascade laser. *Optics Letters*, 28(1):16, 2003.

[196] Gerard Wysocki, Matt McCurdy, Stephen So, Damien Weidmann, Chad Roller, Robert F. Curl, and Frank K. Tittel. Pulsed quantum-cascade laser-based sensor for trace-gas detection of carbonyl sulfide. *Applied Optics*, 43(32):6040–6046, 2004.

[197] J. H. Van Helden, S. J. Horrocks, and G. A.D. Ritchie. Application of quantum cascade lasers in studies of low-pressure plasmas: Characterization of rapid passage effects on density and temperature measurements. *Applied Physics Letters*, 92(8):1–4, 2008.

[198] J. H. Northern, G. A. D. Ritchie, E. P. Smakman, J. H. van Helden, J. Cockburn, and G. Duxbury. Rapid passage signals induced by chirped quantum cascade laser radiation: K state dependent-delay effects in the ν_2 band of NH_3. *Optics Letters*, 35(16):2750, 2010.

[199] J. A. Nwaboh, O. Werhahn, and D. Schiel. Measurement of CO amount fractions using a pulsed quantum-cascade laser operated in the intrapulse mode. *Applied Physics B: Lasers and Optics*, 103(4):947–957, 2011.

[200] Robin S.M. Chrystie, Ehson F. Nasir, and Aamir Farooq. Calibration-free and ultrafast sensing of temperature and species in the intrapulse mode. *Optics InfoBase Conference Papers*, 39(23):6620–6623, 2014.

[201] Ehson F. Nasir and Aamir Farooq. Intra-pulse laser absorption sensor with cavity enhancement for oxidation experiments in a rapid compression machine. *Optics Express*, 26(11):14601, 2018.

[202] Michael T. McCulloch, Erwan L. Normand, Nigel Langford, Geoffrey Duxbury, and D. A. Newnham. Highly sensitive detection of trace gases using the time-resolved frequency downchirp from pulsed quantum-cascade lasers. *Journal of the Optical Society of America B*, 20(8):1761, 2003.

[203] Kevin K. Schwarm, Chuyu Wei, Daniel I. Pineda, R Mitchell Spearrin, and R. M. Spearrin. Time-resolved laser absorption imaging of ethane at 2 kHz in unsteady partially premixed flames. *Applied Optics*, 58(21):5656, 7 2019.

[204] J.J. Olivero and R.L. Longbothum. Empirical fits to the Voigt line width: A brief review. *Journal of Quantitative Spectroscopy and Radiative Transfer*, 17(2):233–236, 2 1977.

[205] I.E. Gordon, L.S. Rothman, R.J. Hargreaves, R. Hashemi, E.V. Karlovets, F.M. Skinner, E.K. Conway, C. Hill, R.V. Kochanov, Y. Tan, P. Wcisło, A.A. Finenko, K. Nelson, P.F. Bernath, M. Birk, V. Boudon, A. Campargue, K.V. Chance, A. Coustenis, B.J. Drouin, J.–M. Flaud, R.R. Gamache, J.T. Hodges, D. Jacquemart, E.J. Mlawer, A.V. Nikitin, V.I. Perevalov, M. Rotger, J. Tennyson, G.C. Toon, H. Tran, V.G. Tyuterev, E.M. Adkins, A. Baker, A. Barbe, E. Canè, A.G. Császár, A. Dudaryonok, O. Egorov, A.J. Fleisher, H. Fleurbaey, A. Foltynowicz, T. Furtenbacher, J.J. Harrison, J.–M. Hartmann, V.–M. Horneman, X. Huang, T. Karman, J. Karns, S. Kassi, I. Kleiner, V. Kofman, F. Kwabia–Tchana, N.N. Lavrentieva, T.J. Lee, D.A. Long, A.A. Lukashevskaya, O.M. Lyulin, V.Yu. Makhnev, W. Matt, S.T. Massie, M. Melosso, S.N. Mikhailenko, D. Mondelain, H.S.P. Müller, O.V. Naumenko, A. Perrin, O.L. Polyansky, E. Raddaoui, P.L. Raston, Z.D. Reed, M. Rey, C. Richard, R. Tóbiás, I. Sadiek, D.W. Schwenke, E. Starikova, K. Sung, F. Tamassia, S.A. Tashkun, J. Vander Auwera, I.A. Vasilenko, A.A. Vigasin, G.L. Villanueva, B. Vispoel, G. Wagner, A. Yachmenev, and S.N. Yurchenko. The HITRAN2020 molecular spectroscopic database. *Journal of Quantitative Spectroscopy and Radiative Transfer*, 277:107949, 2022.

[206] Junji Ohtsubo. *Semiconductor lasers and theory*. Academic Press, 1977.

[207] Xiaomin Jin and Shun Lien Chuang. High-speed modulation of semiconductor lasers. *IEEI Transactions on Electron Devices*, 32(12):2572–2584, 1985.

[208] Geoffrey Taylor. The dynamics of the combustion products behind plane and spherical detonation fronts in explosives. *Proceedings of the Royal Society of London. Series A. Mathematical and Physical Sciences*, 200(1061):235–247, 1950.

[209] Fabio Andres Bendana. *Shock tube kinetics and laser absorption diagnostics for liquid- and hybrid- propellant rocket combustion analysis*. PhD thesis, University of California, Los Angeles, 2020.

[210] John D. Anderson. *Modern Compressible Flow*. McGraw-Hill, 3rd edition, 2002.

[211] Matthew F. Campbell, Kyle G. Owen, David F. Davidson, and Ronald K. Hanson. Dependence of Calculated Postshock Thermodynamic Variables on Vibrational Equilibrium and Input Uncertainty. *Journal of Thermophysics and Heat Transfer*, 31(3):586–608, 7 2017.

[212] Anil P. Nair, Nicolas Q. Minesi, Nicholas M. Kuenning, Alex R. Keller, and R. Mitchell Spearrin. Optical pressure sensing at MHz rates via collisional line broadening of carbon monoxide: uncertainty quantification in reacting flows. *(submitted)*.

[213] K. Mathioudakis, A. Papathanasiou, E. Loukis, and K. Papailiou. Fast response wall pressure measurement as a means of gas turbine blade fault identification. *Proceedings of the ASME Turbo Expo*, 5(April):269–275, 1990.

[214] Majid Nabavi. Invited review article: Unsteady and pulsating pressure and temperature: a review of experimental techniques. *The Review of scientific instruments*, 81(3):031101, 2010.

[215] Joshua W. Hargis and Eric L. Petersen. Shock-tube boundary-layer effects on reflected-shock conditions with and without CO2. *AIAA Journal*, 55(3):902–912, 2017.

[216] Damien Nativel, Sean P. Cooper, Timo Lipkowicz, Mustapha Fikri, Eric L. Petersen, and Christof Schulz. Impact of shock-tube facility-dependent effects on incident- and reflected-shock conditions over a wide range of pressures and Mach numbers. *Combustion and Flame*, 217:200–211, 7 2020.

[217] Laura A. Kranendonk, Andrew W. Caswell, and Scott T. Sanders. Robust method for calculating temperature, pressure, and absorber mole fraction from broadband spectra. *Applied Optics*, 46(19):4117–4124, 2007.

[218] Christopher S. Goldenstein, R. Mitchell Spearrin, and Ronald K. Hanson. Fiber-coupled diode-laser sensors for calibration-free stand-off measurements of gas temperature, pressure, and composition. *Applied Optics*, 55(3):479, 2016.

[219] G.C. Mathews and C.S. Goldenstein. Wavelength-modulated planar laser-induced fluorescence for imaging gases. *Optics Letters*, 42(24):5278–5281, 2017.

[220] Robert R. Gamache and Julien Lamouroux. The vibrational dependence of half-widths of CO2 transitions broadened by N2, O2, air, and CO2. *Journal of Quantitative Spectroscopy and Radiative Transfer*, 117:93–103, 2013.

[221] Geoffrey A. Landis and Diane L. Linne. Mars rocket vehicle using in situ propellants. *Journal of Spacecraft and Rockets*, 38(5):730–735, 2001.

[222] Manijeh Razeghi, Neelanjan Bandyopadhyay, Yanbo Bai, Quanyong Lu, and Steven Slivken. Recent advances in mid infrared (3-5µm) Quantum Cascade Lasers. *Optical Materials Express*, 3(11):1872, 2013.

[223] Hugh W. Coleman and W. Glenn Steele. *Experimentation, Validation, and Uncertainty Analysis for Engineers*. John Wiley & Sons, Inc., Hoboken, NJ, USA, 3rd edition, 2009.

[224] Philip L Varghese and Ronald K Hanson. Collisional narrowing effects on spectral line shapes measured at high resolution. *Applied Optics*, 23(14):2376, 7 1984.

[225] Christopher A. Almodovar, Wey Wey Su, Christopher L. Strand, and Ronald K. Hanson. R-branch line intensities and temperature-dependent line broadening and shift coefficients of the nitric oxide fundamental rovibrational band. *Journal of Quantitative Spectroscopy and Radiative Transfer*, 239, 2019.

[226] G. J. Rosasco, L. A. Rahn, W. S. Hurst, R. E. Palmer, and S. M. Dohne. Measurement and prediction of Raman Q -branch line self-broadening coefficients for CO from 400 to 1500 K. *The Journal of Chemical Physics*, 90(8):4059–4068, 4 1989.

[227] X. Chao, J. B. Jeffries, and R. K. Hanson. Absorption sensor for CO in combustion gases using 2.3 µm tunable diode lasers. *Measurement Science and Technology*, 20(11):115201, 11 2009.

[228] Clayton R. Mulvihill, Sulaiman A. Alturaifi, and Eric L. Petersen. High-temperature He- and O2-broadening of the R(12) line in the 1←0 band of carbon monoxide. *Journal of Quantitative Spectroscopy and Radiative Transfer*, 217:432–439, 9 2018.

[229] Patrick J. Medvecz and Kenneth M. Nichols. Experimental determination of line strengths for selected carbon monoxide and carbon dioxide absorption lines at temperatures between 295 and 1250 K. *Applied Spectroscopy*, 48(11):1442–1450, 1994.

[230] Tingdong Cai, Guangzhen Gao, Xiaoming Gao, Weidong Chen, and Gang Liu. Diode laser measurement of line strengths and air-broadening coefficients of CO2 and CO in the 1.57 μm region for combustion diagnostics. *Molecular Physics*, 108(5):539–545, 2010.

[231] Peter Glarborg, James A. Miller, Branko Ruscic, and Stephen J. Klippenstein. Modeling nitrogen chemistry in combustion. *Progress in Energy and Combustion Science*, 67:31–68, 2018.

[232] H. Wang, E. Dames, B. Sirjean, D. A. Sheen, R. Tango, A. Violi, J. Y. W. Lai, F. N. Egolfopoulos, D. F. Davidson, R. K. Hanson, C. T. Bowman, C. K. Law, W. Tsang, N. P. Cernansky, D. L. Miller, and R. P. Lindstedt. A high-temperature chemical kinetic model of n-alkane (up to n-dodecane), cyclohexane, and methyl-, ethyl-, n-propyl and n-butyl-cyclohexane oxidation at high temperatures, JetSurF version 2.0, 2010.

[233] Hai Wang, Xiaoqing You, Ameya V. Joshi, Scott G. Davis, Alexander Laskin, Fokion Egolfopoulos, and Chung K. Law. USC Mech Version II. High-Temperature Combustion Reaction Model of H2/CO/C1-C4 Compounds, 2007.

[234] S. A. Tashkun and V. I. Perevalov. CDSD-4000: High-resolution, high-temperature carbon dioxide spectroscopic databank. *Journal of Quantitative Spectroscopy and Radiative Transfer*, 112(9):1403–1410, 2011.

[235] E. L. Petersen and R. K. Hanson. Measurement of Reflected-shock Bifurcation Over a Wide Range of Gas Composition and Pressure. *Shock Waves*, 15(5):333–340, 8 2006.

[236] Eric L. Petersen and Ronald K. Hanson. Nonideal effects behind reflected shock waves in a high-pressure shock tube. *Shock Waves*, 10(6):405–420, 1 2001.

[237] Nicolas Q. Minesi, Miles O. Richmond, Christopher C. Jelloian, Nicholas M. Kuenning, Anil P. Nair, and R. Mitchell Spearrin. Multi-line Boltzmann regression for near-electronvolt temperature and CO sensing via MHz-rate infrared laser absorption spectroscopy. *Applied Physics B: Lasers and Optics*, 128(12):214, 12 2022.

[238] Irvin Glassman and Richard A. Yetter. *Combustion*, volume 136. Elsevier, ed. 4 edition, 2008.

[239] N. Venkatramani. Industrial plasma torches and applications. *Current Science*, 83(3):254–262, 2002.

[240] Marcel Nations, Leyen S. Chang, Jay B. Jeffries, Ronald K. Hanson, Megan E. MacDonald, Anuscheh Nawaz, Jaswinder S. Taunk, Tahir Gökçen, and George Raiche. Characterization of a Large-Scale Arcjet Facility Using Tunable Diode Laser Absorption Spectroscopy. *AIAA Journal*, 55(11):3757–3766, 11 2017.

[241] Neha Arora and N. N. Sharma. Arc discharge synthesis of carbon nanotubes: Comprehensive review. *Diamond and Related Materials*, 50:135–150, 2014.

[242] Yanjie Su, Zhi Yang, Hao Wei, Eric Siu-Wai Kong, and Yafei Zhang. Synthesis of single-walled carbon nanotubes with selective diameter distributions using DC arc discharge under CO mixed atmosphere. *Applied Surface Science*, 257(7):3123–3127, 1 2011.

[243] Rudolf Maly and Manfred Vogel. Initiation and propagation of flame fronts in lean CH4-air mixtures by the three modes of the ignition spark. *Symposium (International) on Combustion*, 17(1):821–831, 1 1979.

[244] H. Albrecht, W. H. Bloss, W. H Herden, R. Maly, B. Saggau, and E. Wagner. New Aspects on Spark Ignition. *SAE Technical Papers*, page 770853, 1977.

[245] Lucia Daniela Pietanza, Olivier Guaitella, Vincenzo Aquilanti, Iole Armenise, Annemie Bogaerts, Mario Capitelli, Gianpiero Colonna, Vasco Guerra, Richard Engeln, Elena Kustova, Andrea Lombardi, Federico Palazzetti, and Tiago Silva. Advances in non-equilibrium CO2 plasma kinetics: a theoretical and experimental review. *The European Physical Journal D*, 75(9):237, 9 2021.

[246] Jean Maillard, Erwan Pannier, and Christophe O. Laux. Time-resolved Optical Emission Spectroscopy measurements of electron density and temperature in CO2 Nanosecond Repetitively Pulsed discharges. In *AIAA SCITECH 2022 Forum*, Reston, Virginia, 1 2022. American Institute of Aeronautics and Astronautics.

[247] M Ceppelli, T P W Salden, L M Martini, G Dilecce, and P Tosi. Time-resolved optical emission spectroscopy in CO 2 nanosecond pulsed discharges. *Plasma Sources Science and Technology*, 30(11):115010, 11 2021.

[248] Nicolas Minesi, S Stepanyan, Pierre Mariotto, Gabi Daniel Stancu, and Christophe O Laux. Fully ionized nanosecond discharges in air: the thermal spark. *Plasma Sources Science and Technology*, 29:85003, 2020.

[249] Robert D. Braun, Richard W. Powell, and Lin C. Hartung. Effect of Interplanetary Trajectory Options on a Manned Mars Aerobrake Configuration. *NASA Technical Paper 3019*, 1990.

[250] Brett A. Cruden, Dinesh Prabhu, and Ramon Martinez. Absolute Radiation Measurement in Venus and Mars Entry Conditions. *Journal of Spacecraft and Rockets*, 49(6):1069–1079, 11 2012.

[251] S. D. McGuire, A. C. Tibère-Inglesse, and C. O. Laux. Infrared spectroscopic measurements of carbon monoxide within a high temperature ablative boundary layer. *Journal of Physics D: Applied Physics*, 49(48), 2016.

[252] Steven W. Lewis, Christopher M. James, Richard G. Morgan, Timothy J. McIntyre, Christopher R. Alba, and Robert B. Greendyke. Carbon ablative shock-layer radiation with high surface temperatures. *Journal of Thermophysics and Heat Transfer*, 31(1):193–204, 2017.

[253] Denis Packan, Christophe O. Laux, Richard J. Gessman, Laurent Pierrot, and Charles H. Kruger. Measurement and Modeling of OH, NO, and CO Infrared Radiation at 3400 K. *Journal of Thermophysics and Heat Transfer*, 17(4):450–456, 10 2003.

[254] Brett A. Cruden, Aaron M. Brandis, and Megan E. Macdonald. Characterization of CO thermochemistry in incident shockwaves. *2018 Joint Thermophysics and Heat Transfer Conference*, pages 1–22, 2018.

[255] X. Lin, L. Z. Chen, J. P. Li, F. Li, and X. L. Yu. Experimental and Numerical Study of Carbon-Dioxide Dissociation for Mars Atmospheric Entry. *Journal of Thermophysics and Heat Transfer*, 32(2):503–513, 4 2018.

[256] J. Vanderover and M. A. Oehlschlaeger. A mid-infrared scanned-wavelength laser absorption sensor for carbon monoxide and temperature measurements from 900 to 4000 K. *Applied Physics B*, 99(1-2):353–362, 4 2010.

[257] Megan E. MacDonald and Brett A. Cruden. A tunable laser absorption diagnostic for measurements of CO in shock-heated gases. *46th AIAA Thermophysics Conference*, (June):1–12, 2016.

[258] Megan E. Macdonald, Aaron M. Brandis, and Brett A. Cruden. Post-Shock temperature and CO Number density measurements in CO and CO2. *47th AIAA Thermophysics Conference, 2017*, (June):1–18, 2017.

[259] Morgan D. Ruesch, Jonathan J. Gilvey, Christopher S. Goldenstein, Kyle A. Daniel, Charley R. Downing, Kyle P. Lynch, and Justin L. Wagner. Mid-Infrared Laser-Absorption-Spectroscopy Measurements of Temperature, Pressure, and NO X2 Π1/2 at 500 kHz in Shock-Heated Air. *AIAA Science and Technology Forum and Exposition, AIAA SciTech Forum 2022*, pages 1–12, 2022.

[260] Christopher C. Jelloian, Nicolas Q. Minesi, and R. Mitchell Spearrin. High-speed mid-infrared laser absorption spectroscopy of CO$$_2$$ for shock-induced thermal non-equilibrium studies of planetary entry. *Applied Physics B*, 128(12):216, 12 2022.

[261] Robert J. Hargreaves, Iouli E. Gordon, Michael Rey, Andrei V. Nikitin, Vladimir G. Tyuterev, Roman V. Kochanov, and Laurence S. Rothman. An Accurate, Extensive, and Practical Line List of Methane for the HITEMP Database. *The Astrophysical Journal Supplement Series*, 247(2):55, 4 2020.

[262] Robert R Gamache, Bastien Vispoel, Michaël Rey, Andrei Nikitin, Vladimir Tyuterev, Oleg Egorov, Iouli E Gordon, and Vincent Boudon. Total internal partition sums for the HITRAN2020 database. *Journal of Quantitative Spectroscopy and Radiative Transfer*, 271:107713, 9 2021.

[263] Derek York, Norman M. Evensen, Margarita Lopez Martinez, and Jonas De Basabe Delgado. Unified equations for the slope, intercept, and standard errors of the best straight line. *American Journal of Physics*, 72(3):367–375, 3 2004.

[264] ALIZA BALTER-PETERSON, FRANK NICHOLS, BRIAN MIFSUD, and WENDELL LOVE. Arc jet testing in NASA Ames Research Center thermophysics facilities. In *AlAA 4th International Aerospace Planes Conference*, number December, Reston, Virigina, 12 1992. American Institute of Aeronautics and Astronautics.

[265] Fabio A. Bendana, Daniel D. Lee, R. Mitchell Spearrin, Stephen A. Schumaker, and Stephen A. Danczyk. Infrared laser absorption thermometry and CO sensing in high-pressure rocket combustion flows from 25 to 105 bar. In *AIAA Scitech 2019 Forum*, number January. American Institute of Aeronautics and Astronautics, 1 2019.

[266] Chul Park, John T. Howe, Richard L. Jaffe, and Graham V. Candler. Review of chemical-kinetic problems of future NASA missions, II: Mars entries. *Journal of Thermophysics and Heat Transfer*, 8(1):9–23, 1994.

[267] Roger C. Millikan and Donald R. White. Systematics of Vibrational Relaxation. *The Journal of Chemical Physics*, 39(12):3209–3213, 12 1963.

[268] C.O. Johnston and A.M. Brandis. Modeling of nonequilibrium CO Fourth-Positive and CN Violet emission in CO 2 –N 2 gases. *Journal of Quantitative Spectroscopy and Radiative Transfer*, 149:303–317, 12 2014.

[269] Yang Li, Shengkai Wang, Christopher L Strand, and Ronald K Hanson. Two-temperature Collisional-radiative Modeling of Partially Ionized O 2 –Ar Mixtures over 8000–10,000 K Behind Reflected Shock Waves. *The Journal of Physical Chemistry A*, 124(19):3687–3697, 5 2020.

[270] Yang Li, Yu Wang, David F. Davidson, and Ronald K. Hanson. Collisional excitation kinetics for O(3s S o 5) and O(3p P3 5) states using laser absorption spectroscopy in shock-heated weakly ionized O2 -Ar mixture. *Physical Review E*, 103(6):1–15, 2021.

[271] Matthew F. Campbell, Shengkai Wang, Christopher S. Goldenstein, R. Mitchell Spearrin, Andrew M. Tulgestke, Luke T. Zaczek, David F. Davidson, and Ronald K. Hanson. Constrained reaction volume shock tube study of n -heptane oxidation: Ignition delay times and time-histories of multiple species and temperature. *Proceedings of the Combustion Institute*, 35(1):231–239, 2015.

[272] Mathias C. Ross, Christopher Lietz, and William A. Hargus. Synthetic Laser Diagnostics of Simulated RDRE Exhaust. *AIAA Propulsion and Energy Forum, 2021*, 2021.

[273] Alex R. Keller, Joel Otomize, Anil P. Nair, Nicolas Q. Minesi, and R. Mitchell Spearrin. High-diodicity impinging injector design for rocket propulsion enabled by additive manufacturing. *AIAA Science and Technology Forum and Exposition, AIAA SciTech Forum 2022*, pages 1–11, 2022.

[274] Nicholas M. Kuenning, Anil P. Nair, Alex R. Keller, Nicolas Q. Minesi, R. Mitchell Spearrin, Emre Ozen, Jason Kriesel, Blaine Bigler, John W. Bennewitz, Jason Burr, and Stephen A. Dancyzk. Simultaneous in-chamber MHz sensing of CO, H2O, temperature, and pressure via mid-infrared laser absroption in a rotating detonation rocket engine. In *AIAA SciTech 2023 Forum*, 2023.

[275] Daniel I. Pineda and Tiernan A. Casey. Virial Coefficient Data for Combustion Species. GitHub, 2017.

[276] E. E. Whiting. An empirical approximation to the Voigt profile. *Journal of Quantitative Spectroscopy and Radiative Transfer*, 8(6):1379–1384, 1968.

[277] Nicolas Q. Minesi, Anil P. Nair, Miles O. Richmond, Christopher C. Jelloian, Nicholas M. Kuenning, and R. Mitchell Spearrin. Excited oxygen kinetics at electron-volt temperatures via 5-MHz RF-diplexed laser absorption spectroscopy. *Submitted to: Applied Optics*.

[278] Pankaj Mehta, Marin Bukov, Ching Hao Wang, Alexandre G.R. Day, Clint Richardson, Charles K. Fisher, and David J. Schwab. A high-bias, low-variance introduction to Machine Learning for physicists. *Physics Reports*, 810:1–124, 2019.

[279] Mruthunjaya Uddi, Apurba Kumar Das, and Chih Jen Sung. Temperature measurements in a rapid compression machine using mid-infrared H2O absorption spectroscopy near 7.6 μm. *Applied Optics*, 51(22):5464–5476, 2012.

[280] Garrett C. Mathews, Mateo Gomez, Charles J. Schwartz, Steven F. Son, Christopher S. Goldenstein, and Daniel R. Guildenbecher. Laser-Absorption-Spectroscopy Measurements of Temperature, Pressure, and CO at 1 MHz in Post-Detonation Fireballs. *AIAA Science and Technology Forum and Exposition, AIAA SciTech Forum 2022*, 000:1–10, 2022.

[281] Kevin P. Grogan and Matthias Ihme. Regimes describing shock boundary layer interaction and ignition in shock tubes. *Proceedings of the Combustion Institute*, 36(2):2927–2935, 2017.

[282] J. J. Girard and R. K. Hanson. Minimally intrusive optical probe for in situ shock tube measurements of temperature and species via tunable IR laser absorption. *Applied Physics B*, 123(11):264, 11 2017.